Thermo-Plasticity of Fine-Grained Soils at Various Saturation States: Application to Nuclear Waste Disposal

THÈSE N^{O} 4188 (2008)

PRÉSENTÉE LE 14 NOVEMBRE 2008

À LA FACULTE ENVIRONNEMENT NATUREL, ARCHITECTURAL ET CONSTRUIT
LABORATOIRE DE MÉCANIQUE DES SOLS
PROGRAMME DOCTORAL EN MÉCANIQUE

ÉCOLE POLYTECHNIQUE FÉDÉRALE DE LAUSANNE

POUR L'OBTENTION DU GRADE DE DOCTEUR ÈS SCIENCES

PAR

Bertrand FRANÇOIS

ingénieur civil des constructions, Université de Liège, Belgique
et de nationalité belge

acceptée sur proposition du jury:

Prof. J.-F. Molinari, président du jury
Prof. L. Laloui, directeur de thèse
Prof. R. Charlier, rapporteur
Dr V. Labiouse, rapporteur
Dr P. Marschall, rapporteur

ÉCOLE POLYTECHNIQUE
FÉDÉRALE DE LAUSANNE

Suisse
2008

à mes parents

à ma soeur

Remerciements

Je suis intimement convaincu que ce sont les échanges et les contacts humains qui font de nous ce que nous sommes. Ce travail est le fruit d'une succession de rencontres et de discussions, scientifiques mais surtout humaines. A ce titre, j'aimerais remercier toutes les personnes qui, de près ou de loin, ont contribué au bon déroulement de cette thèse.

Il me tient tout particulièrement à cœur de consacrer mes premiers remerciements à Monsieur le Professeur Lyesse Laloui qui est la source et le fil conducteur de ce travail de recherche. Le cheminement de ce travail s'est construit à partir d'une certaine autonomie scientifique encadrée par ses conseils avisés. L'atmosphère stimulante de son groupe de recherche a permis un épanouissement scientifique propice au bon déroulement de cette thèse. Qu'il trouve dans ce travail ma reconnaissance pour tout ce qu'il m'a apporté tant d'un point de vue professionnel que personnel.

J'ai eu la chance d'évoluer dans une structure de recherche performante et conviviale. J'aimerais sur ce point remercier vivement Monsieur le Professeur Laurent Vulliet pour l'accueil qu'il m'a réservé au sein de son laboratoire. Je lui suis également très reconnaissant pour la confiance qu'il m'a accordée dans la tâche d'assistanat du cours de Mécanique des Sols.

L'aboutissement de ce travail est le fruit de nombreuses rencontres et échanges scientifiques qui ont fortement influencé ma vision des choses sur les sujets abordés dans cette dissertation. Je pense, tout particulièrement, à Monsieur le Professeur Robert Charlier qui m'a fourni l'outil de calcul utilisé dans cette thèse, m'a accueilli à plusieurs reprises au sein de son groupe de recherche et m'a fait part de ses conseils éclairés. C'est aussi beaucoup grâce à lui que j'ai pu effectuer ce travail à Lausanne. Je le remercie pour tout cela et également pour m'avoir fait l'honneur d'accepter d'évaluer ce travail de doctorat. Dans le même cadre, le dernier volet de cette thèse n'aurait pas pu voir le jour sans l'aide et les conseils éclairés de Monsieur le Docteur Frédéric Collin à qui je dois beaucoup pour l'implémentation et l'utilisation du code de calcul. J'ai également très apprécié les contacts humains, avec lui et avec toute l'équipe du Professeur Charlier, qui ont découlé de cette collaboration.

J'ai retiré beaucoup d'enseignements dans les collaborations scientifiques qui ont agrémenté ce travail. Je pense tout particulièrement aux membres de l'équipe de recherche du laboratoire LMGC de l'Université Montpellier II, Messieurs les Professeurs Christian Saix et Saïd El Youssoufi et le Docteur Simon Salager, qui ont fortement contribué au bon déroulement de la campagne expérimentale. Mes remerciements s'adressent également à Monsieur le Docteur Lorenzo Sanavia, de l'Université de Padoue, pour sa collaboration efficace.

Je remercie sincèrement Messieurs les Docteurs Vincent Labiouse et Paul Marschall d'avoir accepté de réviser et d'évaluer cette thèse de doctorat. Dans la problématique traitée dans ce travail, leur expérience liant la recherche et les attentes des agences nationales est précieuse. Merci également à Monsieur le Professeur Jean-François Molinari d'avoir accepté de présider le jury de cette thèse.

Bien que les domaines abordés soient quelque peu différents, j'ai retiré beaucoup d'enseignements, avant et pendant le début de cette thèse, au contact de Monsieur Christophe Bonnard. Il m'a apporté une rigueur scientifique et une approche qui allie le fondamental et le terrain. Au même titre, j'aimerais mentionner et remercier Monsieur le Docteur Moustafa Gencer pour le contact direct qu'il m'a apporté avec la pratique du géotechnicien.

J'ai pu bénéficier, tout au long de ce travail, de l'aide de plusieurs stagiaires: David Ubals Picanyol, Clément Laurent et Victor Martin. Merci pour vos contributions efficaces et précieuses.

La convivialité et la bonne humeur dans laquelle s'est effectuée cette recherche a enjolivé les quatre années passées au sein des Laboratoires de Mécanique des Sols et des Roches. Ce n'est donc pas à des collègues, mais plutôt à une bande de copains, que je consacre ces remerciements qui me tiennent tout particulièrement à cœur. Mathieu, Hervé et Azad (alias « The Lyesse's angels »), un chaleureux merci pour la conviviale émulation scientifique qui a découlé de notre collaboration efficace. Emilie, Suzanne, Federica et Irène, mille mercis pour cette touche de féminité dans ce monde d'ingénieur. Julian, Rafal, Patrick, Simon, Alessio, Laurent, Marta, Claire, Stefano, Nina et Véronique, ce fut un plaisir de partager tous ces bons moments en votre compagnie. Une petite pensée à l'entourage du LMS-R : Solène, Azin, Mohamed, Jan, Jennifer, Eva, Jonathan, Pénélope et … Joachim ;-). Mille mercis au reste de l'équipe qui a contribué à faire de mon séjour à Lausanne, une magnifique aventure.

J'ai la précieuse chance de pouvoir compter sur des amis qui me sont chers. Merci au kot 23 (Thom, Oli, Phred, Ad, Laurence, Mira et Angela) pour la fidélité de leur amitié. Une pensée toute particulière également à l'Orval Pro Tour.

Je n'ai pas de mots assez forts pour exprimer ma reconnaissance envers le soutien inestimable que m'a apporté ma famille dans la réalisation de ce travail. Que mes parents et ma sœur trouvent dans ce manuscrit, que je leur dédie, le fruit de leur affection au quotidien. Ils sont les racines qui ont permis aux bourgeons d'éclore.

Enfin, rien n'aurait été possible sans l'amour, le soutien de tous les instants et la compréhension de ma douce complice. Anne-Christine, amoureusement, merci.

Contents

Abstract

Soil is a particulate material that may undergo irreversible strain as the relative positions of the constituent particles change. That irreversible behaviour may be induced not only by an external stress variation but also by temperature or suction changes. The geomaterials that will be involved in the confinement of radioactive waste in deep geological formations will be submitted to strong thermal, hydraulic, and mechanical modifications. Those modifications may produce a significant change of the characteristics of the confinement barrier. A safety assessment of such facilities must be performed that considers the potential thermo-plasticity effects in the confining soil.

Following the need for understanding and quantifying such effects, a constitutive model that deals with the thermo-mechanical modelling of unsaturated soils is proposed. In light of elasto-plasticity, this model is based on the relevant temperature and suction effects on the mechanical behaviour of fine-grained soils, as observed in experiments. In addition, an experimental program has been undertaken in order to corroborate and to extend the existing results. Finally, the developed constitutive model has been properly implemented in a finite element code in order to study the behaviour of the soils that confine the nuclear waste. Therefore, this work addresses the issue from three different directions: a constitutive, experimental, and numerical point of view.

(i) *Constitutive study.* The elaboration of a thermo-plastic constitutive model for unsaturated soils is done in a systematic manner. Starting from a hardening plasticity model for isothermal and saturated conditions, the constitutive relations are progressively extended to non-isothermal conditions and then to unsaturated states. For the more advanced model, a generalized effective stress framework is adopted, which includes a number of intrinsic thermo-hydro-mechanical connections, to represent the stress state in the soil. Two coupled constitutive aspects are used to fully describe the soil behaviour. The mechanical constitutive part is built on concepts of bounding surface theory and multi-mechanism plasticity, while water retention characteristics are described using elasto-plasticity to reproduce the hysteretic response and the effect of temperature and dry density on the soil's water retention properties. The theoretical formulation is supported by comparisons with experimental results.

(ii) *Experimental study.* Aiming at a better understanding of the non-isothermal mechanical behaviour of unsaturated soils, a series of oedometric compression tests under controlled temperatures and suction conditions has been carried out on a silty material. The characteristics and the calibrations of the experimental apparatus are presented. The main results are interpreted in light of the proposed constitutive framework. The compressibility of the soil tested appears not to be affected by the temperature, but it decreases with a suction increase. As far as the preconsolidation stress is concerned, the results show a decrease of the yield limit with increasing temperature, while a suction increase tends to enhance this limit. Finally, an analytical expression is proposed to describe the evolution of the preconsolidation stress with respect to temperature and suction.

(iii) *Numerical study.* In the issue of nuclear waste disposal, the quantification of the temporal and spatial distributions of the thermo-hydro-mechanical phenomena that occur in the confining soils

requires that numerical simulations be carried out under imposed boundary conditions. To this end, the last part of this work presents finite element modelling results of several in-situ or laboratory simulation tests through using the developed constitutive model that was implemented in an advanced finite element code. The parameters of the different materials involved in the simulated experiments are determined by means of an extensive literature analysis on their thermal, hydraulic, and mechanical characteristics. The simulation results are interpreted in light of the elasto-thermoplasticity of saturated and unsaturated soils, which emphasizes the significant role of thermo-plastic processes in the global thermo-hydro-mechanical response of the confining materials.

In that sense, this work supplies, in a systematic and progressive manner, constitutive explanations that may help to provide a better understanding of *what the effects of thermo-plasticity in soils involved in the confinement of nuclear waste are.*

Keywords: Nuclear waste disposal, fine-grained soils, thermo-plasticity, temperature, constitutive modelling, hardening plasticity, unsaturated soils, generalized effective stress, thermo-hydro-mechanical processes, oedometric tests, numerical modelling, finite element simulation.

Résumé

Le sol est un matériau qui peut subir des déformations irréversibles suite à un réarrangement des particules qui le constituent. Ce comportement irréversible peut être induit par une sollicitation mécanique extérieure mais également par une modification de la température et/ou de la succion du matériau. Les géomatériaux qui contribueront au confinement des déchets nucléaires en formations géologiques profondes seront soumis à de fortes modifications thermiques, hydrauliques et mécaniques. Ces sollicitations peuvent induire des changements importants des caractéristiques de la barrière de confinement. Une évaluation de la sécurité de tels ouvrages doit être effectuée en incluant les effets thermo-plastiques pouvant se produire dans le sol entourant les déchets nucléaires.

Face au besoin de comprendre et de quantifier de tels effets, ce travail propose un modèle constitutif avancé décrivant le comportement thermo-mécanique des sols non-saturés. Dans un cadre élasto-plastique, ce modèle se base sur des résultats expérimentaux qui mettent en évidence les effets de la température et de la succion sur le comportement mécanique des sols fins. De plus, une campagne expérimentale a été réalisée afin de corroborer et de compléter les résultats existant dans la littérature. Finalement, le modèle de comportement développé a été introduit dans un code aux éléments finis afin d'étudier le comportement des sols intervenant dans le confinement des déchets nucléaires. Ainsi, le sujet de ce travail est traité du triple point de vue constitutif, expérimental et numérique.

(i) *Etude constitutive.* Un modèle thermo-plastique pour les sols non-saturés est développé d'une manière systématique. Partant d'un modèle à écrouissage pour les sols en conditions saturées et isothermes, les relations constitutives sont progressivement étendues afin de considérer les conditions non-isothermes et ensuite non-saturées. Le modèle le plus avancé utilise un cadre de contrainte appelé contrainte effective généralisée qui inclu de façon intrinsèque une série de couplages thermo-hydro-mécaniques. Deux schémas constitutifs couplés sont utilisés pour décrire le comportement du sol. Le cadre mécanique est fondé sur les concepts de « bounding » surface et de plasticité à multi-mécanismes. Le cadre hydrique, quant à lui, est décrit en utilisant un concept élasto-plastique qui reproduit l'hystérèse hydrique et l'effet de la température et de la variation volumique du sol sur la courbe de rétention. La formulation théorique est validée par des comparaisons avec des résultats expérimentaux.

(ii) *Etude expérimentale.* Afin d'améliorer la compréhension du comportement mécanique non-isotherme des sols non-saturés, une série de compressions oedométriques à température et succion contrôlées a été réalisée sur un matériau limoneux. Les caractéristiques et les calibrations du dispositif expérimental sont présentées. Les résultats sont interprétés dans le cadre constitutif proposé. La compressibilité du sol semble indépendante de la température mais diminue lorsque la succion augmente. Concernant la contrainte de préconsolidation, les résultats montrent une décroissance de la limite d'élasticité avec la température et une augmentation avec la succion. Finalement, une expression analytique est proposée pour décrire cette évolution avec la température et la succion.

(iii) *Etude numérique.* Une quantification rigoureuse des distributions temporelle et spatiale des processus thermo-hydro-mécaniques se produisant autour des déchets nucléaires enfouis en

profondeur nécessite des simulations numériques avec des conditions de contour imposées. Dans ce cadre, la dernière partie du travail présente des résultats de modélisation par éléments finis de plusieurs essais in-situ ou de laboratoire, en utilisant le modèle de comportement développé. Ce modèle a été implémenté dans un code aux éléments finis performant. Les paramètres des différents matériaux considérés dans les expériences simulées ont été déterminés grâce à une analyse de la littérature sur leurs caractéristiques thermique, hydraulique et mécanique. Les résultats de simulation sont interprétés dans un cadre elasto-thermoplastique en conditions saturées ou non-saturées. Ces interprétations démontrent le rôle majeur des phénomènes thermo-plastiques dans la réponse globale des matériaux de confinement.

Ainsi, ce travail fournit, d'une façon systématique et progressive, une approche constitutive qui peut aider à une meilleure compréhension *des effets thermo-plastiques se produisant dans les sols et en particulier autour des déchets nucléaires enfouis en profondeur*.

Mots clés : Stockage de déchets nucléaires, sols fins, thermo-plasticité, température, modèle constitutif, écrouissage, sols non-saturés, contrainte effective généralisée, processus thermo-hydro-mécaniques, essai oedométrique, modélisation numérique, simulation par éléments finis.

List of symbols

Roman symbols

a	material parameter controlling the rate of plasticity inside the external deviatoric yield limit
A	Hamaker constant (=2.2 10^{-13} ergs)
A	proportion of adsorbed water in the total volume of the material
b	material parameter defining the shape of the deviatoric yield limit
$\mathbf{b}$	body force vector
B	proportion of solid skeleton in the total volume of the material
c	material parameter controlling the rate of plasticity inside the external isotropic yield limit
c	ionic concentration
c'	cohesion
$\mathbf{C}$	mechanical constitutive tensor
C^e_{ijkl}	elastic stiffness matrix
C^s	elastic hydraulic modulus matrix
C^1_{ijkl}, C^2_{ijkl}	constitutive tensors (generic form)
CEC	cation exchange capacity
$CKW1$	coefficient for the relation between water permeability and degree of saturation
C_p	specific heat of the soil mixture
$c_{p,a}$	specific heat of dry air
$c_{p,s}$	specific heat of solid
$c_{p,v}$	specific heat of water vapour
$c_{p,w}$	specific heat of liquid water
c^{peak}	cohesion characterizing the peak strength
c^{peak}_{p-q}	cohesion in the (p-q) plane
d	ratio between the preconsolidation pressure, p'_c, and the critical pressure, p'_{cr}
D	dielectric constant
D	air diffusion coefficient
e	void ratio
e_0	initial void ratio

e_0	electronic charge (=4.81 10^{-10} esu)
e_c	void ratio corresponding to a given preconsolidation pressure p'_c
e_{c0}	void ratio corresponding to the initial preconsolidation pressure p'_{c0}
E	Young's modulus
E_{ijkl}, $\mathbf{E}$	elastic modulus matrix
$EXPN$, $EXPM$	material parameters of the Kozeni-Karman relation
$\mathbf{F}$	vector of the yield limits $\begin{pmatrix} f_{dev} & f_{iso} \end{pmatrix}$
f	mechanical yield limit
f_{dev}	isotropic yield limit
f_{iso}	deviatoric yield limit
$\mathbf{F_{hyd}}$	vector of the water retention yield limits $\begin{pmatrix} f_{dry} & f_{wet} \end{pmatrix}$
f_{dry}	drying yield limit
f_{wet}	wetting yield limit
$\mathbf{f_g}$	macroscopic velocity of the gas phase
$\mathbf{f_l}$	macroscopic velocity of the liquid phase
$\mathbf{f_T}$	heat flow
$\mathbf{f_w}$	macroscopic velocity of the liquid water
$\mathbf{F}$	vector of nodal values (fluxes and forces)
$\mathbf{F^i}$	vector of nodal values at step *i*
$\mathbf{F^{i+1}}$	vector of nodal values at step *i*+1
$\mathbf{F_G}$	nodal gas flux
$\mathbf{F_M}$	nodal mechanical force
$\mathbf{F_T}$	nodal thermal flux
$\mathbf{F_W}$	nodal water flux
F_α	mass fraction of the α component
g	gravity acceleration
g	slope of variation of friction angle with temperature
g	plastic potential
g_{dev}	plastic potential of the deviatoric mechanism
g_{iso}	plastic potential of the isotropic mechanism
$\mathbf{G}$	vector of the plastic potentials $\begin{pmatrix} g_{dev} & g_{iso} \end{pmatrix}$
G	shear elastic modulus
G_{ref}	shear elastic modulus at a reference pressure (p_{ref})
h	relative humidity

$\mathbf{H}$	matrix of hardening moduli
H	hardening modulus
H_b	plastic modulus on the bounding surface in the model of Dafalias et al.
H_s	Henry's coefficient, defining the proportion of dissolved air in the liquid phase
$\mathbf{i}$	suction-gradient of the loading function $\mathbf{F}$
$\mathbf{I}$	identity matrix
$\mathbf{i_a}$	nonadvective flux of dry air
$\mathbf{i_v}$	nonadvective flux of water vapour
I_p	plasticity index
$\mathbf{j}$	stress-gradients of the loading function $\mathbf{F}$
k	Boltzmann constant (=1.38 10^{-16} ergs/K)
k_w	intrinsic water permeability
$k_{w,h}$	horizontal intrinsic water permeability
$k_{w,v}$	vertical intrinsic water permeability
$k_{w,r}$	relative water permeability
$k_{w,sat}$	saturated water permeability
$k_{w0,sat}$	saturated water permeability corresponding to the reference porosity n_0
$\mathbf{k_g}$	tensor of intrinsic gas permeability
$\mathbf{k_w}$	tensor of intrinsic water permeability
$\mathbf{K}$	stiffness matrix
$\mathbf{K_{MM}}$	mechanical sub-matrix of the stiffness matrix
$\mathbf{K_{WW}}$	water flow sub-matrix of the stiffness matrix
$\mathbf{K_{GG}}$	gas flow sub-matrix of the stiffness matrix
$\mathbf{K_{TT}}$	thermal sub-matrix of the stiffness matrix
K	bulk elastic modulus
K_{ref}	bulk elastic modulus at a reference pressure (p_{ref})
K_0	coefficient of earth pressure at rest
K_α	bulk modulus of the α component
L	latent heat of water vaporisation
$\mathbf{L}$	displacement ($\mathbf{u}$) gradient defined in the global axis ($\mathbf{X}$)
l_α	length of the constituent α
$\mathbf{m}$	vector collecting the flow directions
M	slope of the critical state line in the (p'-q) plane
M_0	slope of the critical state line at ambient temperature T_0

M_{peak}	slope of the line characterizing the peak strength in the (p-q) plane
m_a	mass of air
M_a	molar mass of dry air (= 28.8 10^{-3} kg/mol)
M_v	molar mass of water vapour (=0.018 kg/mol)
M_w	molar mass of water (=0.018 kg/mol)
$\mathbf{n}$	unit normal vector
n	porosity
n_0	electrolyte concentration
N_0	Avogadro's number (=6.02 10^{23} mol^{-1})
n^e	non-linear elasticity exponent
OCR	overconsolidation ratio
p	mean total stress
p'	mean effective stress
p_{net}	mean net stress
p'_0	initial mean effective stress
p'_{ref}	reference mean effective stress (= unity in the Cam-Clay model; = 1MPa in the ACMEG model)
p'_{cyc}	effective mean stress at the last change of direction of solicitation (unloading – reloading)
p'_c	preconsolidation pressure
p'_{c0}	initial preconsolidation pressure (for $\varepsilon_v^p = 0$; $T = T_0$; $s \leq s_e$)
p'_{cr}	mean effective stress at the critical state
p'_{cr0}	initial value of the critical pressure
p_{peak}	mean stress at the peak state
p'_k	reduced mean effective stress in the model of Hujeux
P_{appl}	applied vertical pressure in the loading chamber of the oedometer
P_{meas}	pressure measured in the sample chamber of the oedometer
p_a	pore (dry) air pressure
p_g	gas pressure
$\hat{p}_g$	imposed gas pressure at the boundary of the modelled domain
p_{g0}	initial value of gas pressure
p_v	pore water vapour pressure
$p_{v,0}$	saturated vapour pressure
p_w	pore water pressure

$\hat{p}_w$	imposed pore water pressure at the boundary of the modelled domain
p_{w0}	initial values of pore water pressure
p_w^p	pore water pressure induced by soil plasticity
q	deviatoric stress
q_{cr}	deviator stress at the critical state
q_{peak}	deviatoric stress at the peak state
q_{rad}	thermal flux through radiation
Q_a	volume source of dry air in water
Q_{da}	volume source of dissolved air
Q_T	volume heat source
Q_v	volume source of water vapour
Q_w	volume source of liquid water
r	radius of the capillary tube
r_{dev}	degree of mobilization of the deviatoric mechanism
r_{dev}^e	size of the elastic nuclei of the deviatoric mechanism
r_{iso}^e	size of the elastic nuclei of the isotropic mechanism
r_{iso}	degree of mobilization of the isotropic mechanism
R	constant of perfect gases (=8.3143 J/(mol K))
R_s	radius of curvature of the air-water interface
s	(matric) suction
s_0	initial suction
s_π	osmotic component of the total suction
s_t	total suction
s_d	drying yield limit
s_{d0}	initial drying yield limit
s_e	air-entry suction
s_{e0}	air-entry suction at reference temperature T_0 in the initial state $(\varepsilon_v = 0)$
s_{hys}	material parameter considering the size of the water retention hysteresis
s_k	stress vector in the model of Hujeux
S_r	degree of saturation
S_{r0}	initial degree of saturation
$S_{r,res}$	residual degree of saturation
S_T	enthalpy of the system
SS	specific surface

$\mathbf{t}$	temperature-gradient of the loading function $\mathbf{F}$
$\mathbf{t}$	imposed traction vector
t	thickness of the clay platelet
t	time
T	temperature
T_0	reference or initial temperature
$\hat{T}$	imposed temperature at the boundary of the modelled domain
T_{cyl}	temperature of the cylinder
T_{lab}	ambient temperature of the laboratory
$\mathbf{u}$	displacement vector
$\mathbf{u}_0$	initial value of displacement vector
UCS	unconfined compression strength
V	volume of the soil mixture
V_a	volume of air
V_α	volume of the constituent α
V_A	attractive potential
V_R	repulsive potential
V_{voids}	volume of void in the soil sample
V_w	pore water volume
w	water content
w_L	liquid limit
w_P	plastic limit
W	work input per unit volume
W^e	part of the work input recoverable upon unloading (elastic energy)
W^p	part of the work input irrecoverable upon unloading (plastic work)
$\mathbf{x}$	vector of nodal values
$\mathbf{x_M}$	nodal displacements
y	vertical, upward directed coordinate

Greek symbols

α	hardening function in the model of Dafalias et al.
α	flow rule parameter
$\alpha_{g,T}$	material parameter defining the linear decrease of the dynamic viscosity of gas with temperature
$\alpha_{w,T}$	material parameter defining the linear decrease of the dynamic viscosity of water with temperature
β	plastic compressibility modulus

β^*	parameter of the Nova-Wood model
β_h	slope of the desaturation curve in the $(S_r - s)$ plane
β'_w	volumetric thermal expansion coefficient of water or of liquid phase
β'_{s0}	volumetric thermal expansion coefficient of the solid skeleton at reference temperature
$\bar{\beta}'_{sG,\alpha}$	linear thermal expansion coefficient of the constituent (grain) α
$\bar{\beta}'_{sG,P}$	linear thermal expansion coefficient of solid grain in the direction parallel to the crystallographic axis
$\bar{\beta}'_{sG,N}$	linear thermal expansion coefficient of solid grain in the perpendicular direction to the crystallographic axis
$\beta'_{sG,\alpha}$	volumetric thermal expansion coefficient of the solid grain α
β'_{sG}	volumetric thermal expansion coefficient of the solid grain
β'_s	volumetric thermal expansion coefficient of the solid skeleton
$\bar{\beta}_s'$	linear thermal expansion coefficient of the solid skeleton
$\bar{\beta}_a'$	linear thermal expansion coefficient of the oedometer ring
$\beta_{T,ij}$	component of the thermal expansion coefficient vector
$\boldsymbol{\beta}_{\mathbf{T}}$	thermal expansion coefficient vector
γ_d	dry unit weight
γ_s	material parameter defining the shape of the isotropic yield limit with respect to suction
γ_T	material parameter defining the shape of the isotropic yield limit with respect to temperature
γ_{ij}	shear strain component of the strain tensor/vector
δ	inter-particle distance
δ	distance between actual stress point (σ'_{ij}) and associate stress point on the bounding surface ($\bar{\sigma}'_{ij}$) in the model of Dafalias et al.
δ_0	distance between O and associate stress point on the bounding surface $\bar{\sigma}'_{ij}$ in the model of Dafalias et al.
δ_{ij}	Kronecker's symbol
Δh_{cell}	measured vertical displacement due to the deformation of the cell
Δh_T	thermal deformation of the oedometric cell structure
ΔV_w	volume of exchanged water measured during oedometric tests
$\Delta V_{w,1}^T$	volume change of the drainage system during a thermal cycle
$\Delta V_{w,2}^T$	volume change of the pore water during a thermal cycle

$\Delta V_{w \to a}$	volume of air diffused through the ceramic disc of the oedometer
θ	effective contact angle of the fluid-fluid interface with the solid surface
θ_T	material parameter describing the logarithmic evolution of air-entry suction with respect to temperature
θ_e	material parameter describing the logarithmic evolution of air-entry suction with respect to volumetric strain
κ	swelling index
κ'	swelling index measured in the generalized effective stress reference
κ'_{un}	swelling index determined from the unloading elastic path in the generalized effective stress reference
λ	compression index
λ_a	thermal conductivity of gas phase
λ_s	thermal conductivity of solid phase
λ_w	thermal conductivity of liquid water
λ'	compression index measured in the generalized effective stress reference
λ^p	plastic multiplier
$\boldsymbol{\lambda}^{\mathbf{p}}$	plastic multiplier vector of the mechanical constitutive part
λ^p_{dev}	plastic multiplier of the deviatoric mechanism
λ^p_{iso}	plastic multiplier of the isotropic mechanism
λ^p_{dry}	plastic multipliers of the drying mechanism
λ^p_{wet}	plastic multipliers of the wetting mechanism
$\boldsymbol{\lambda}^{\mathbf{p}}_{\mathbf{hyd}}$	plastic multiplier vector of the water retention constitutive part
Λ^1_{kl}, Λ^2_{kl}	independent stress variable vectors (generic term)
ε_0	static permittivity
ε	emissivity
$\boldsymbol{\varepsilon}$	total strain tensor/vector
$\boldsymbol{\varepsilon}^{\mathbf{e}}$	elastic strain tensor/vector
$\boldsymbol{\varepsilon}^{\mathbf{p}}$	plastic strain tensor/vector
$\boldsymbol{\varepsilon}^{\mathbf{e}}_{\mathbf{T}}$	thermal elastic strain vector
ε_{ij}	component of the strain tensor/vector
ε_1	axial strain in triaxial conditions
ε_3	radial strain in triaxial conditions
ε_i	principal strains in the i direction
ε_v	volumetric strain
ε_d	deviatoric strain
ε^e_v	volumetric elastic strain

ε_d^e	deviatoric elastic strain
ε_v^p	volumetric plastic strain
ε_d^p	deviatoric plastic strain
$\varepsilon_v^{p,iso}$	volumetric plastic strain induced by the isotropic mechanism
$\varepsilon_v^{p,cyc,iso}$	volumetric plastic strain produced by the isotropic mechanism since the last change of direction of solicitation (unloading – reloading)
ε_{sk}	volumetric strain of the solid skeleton without considering the adsorbed water
ε_{ij}^{me}	elastic strain induced mechanically
ε_{ij}^{Te}	thermal elastic strain
ε_{cell}^T	thermal strain of the oedometric cell structure
ϕ'	friction angle at critical state
ϕ_0'	friction angle at critical state at temperature T_0
ϕ^{peak}	friction angle characterizing the peak strength
Ω	approximation of the thickness of the double layer
Ω	modelled domain
π_i	internal variable i (generic term)
$\boldsymbol{\pi}$	internal variable vector of the mechanical model
$\boldsymbol{\pi}_{\mathbf{hyd}}$	internal variable vector of the water retention model
Γ	specific volume on the critical state line for p′=1 kPa in the Cam-Clay model
Γ	thermal conductivity of the soil mixture
Γ_π	boundary of the modelled domain
τ	tortuosity of the material
μ_g	dynamic viscosity of gas
μ_{g0}	dynamic viscosity of gas at initial temperature T_0
μ_w	dynamic viscosity of water
μ_{w0}	dynamic viscosity of water at initial temperature T_0
υ	ionic valence
υ	Poisson's ratio
v	specific volume ($v = 1 + e$)
ρ	bulk density of the soil mixture
ρ_α	bulk density of the α component
ρ_a	bulk density of dry air
ρ_d	bulk dry density
ρ_g	bulk density of gas

ρ_v	bulk density of water vapour
ρ_s	bulk density of solid
ρ_w	bulk density of water
ρ_{w0}	initial values of water bulk density (at $p_w = p_{w0}$ and $T = T_0$)
ρ_{sat}	bulk density of saturated soils
$\rho_{ads\ wat}$	bulk density of adsorbed water
σ^*	stress in the solid skeleton
σ'	effective stress
σ	total stress
σ	Stephan-Boltzmann constant (=5.67 10^{-8} W/(m^2K^4))
σ_1	axial total stress in triaxial conditions
σ_3	radial total stress in triaxial conditions
σ_1'	axial effective stress in triaxial conditions
σ_3'	radial effective stress in triaxial conditions
$\sigma_{1,net}'$	axial net stress in triaxial conditions
$\sigma_{3,net}'$	radial net stress in triaxial conditions
σ_i	principal total stress in the i direction
σ_i'	principal effective stress in the i direction
σ_{ij}'	component of the effective stress tensor/vector
σ_{ij}	component of the total stress tensor/vector
$\sigma_{ij,net}$	component of the net stress tensor/vector
$\boldsymbol{\sigma}$	total stress tensor/vector
$\boldsymbol{\sigma}'$	effective stress tensor/vector
σ_v	applied vertical stress (in oedometer) or applied normal stress (in direct shear test)
σ_{v0}	initial vertical stress
σ_v'	vertical effective stress
σ_{vc}'	vertical preconsolidation stress
σ_{vc0}'	initial vertical preconsolidation stress
$\sigma_c^{e_{c0}}(T_0, s_0)$	initial vertical preconsolidation stress corresponding to a void ratio e_{c0}
$\sigma_c^{e_c}(T_i, s_i)$	vertical preconsolidation stress determined after temperature and suction loadings corresponding to a void ratio e_c
σ_A	Van der Waals attraction between soil particles

σ_R	repulsive pressure between soil particles
σ_{R-A}	interaction stress between soil particles
σ_c	surface charge density
σ_{r0}	initial radial total stress in the hollow cylinder test
σ_{y0}	initial axial total stress in the hollow cylinder test
σ'_{r0}	initial radial effective stress in the hollow cylinder test
σ'_{y0}	initial axial effective stress in the hollow cylinder test
σ_x	total radial stress in the ATLAS experiment
σ_z	total vertical stress in the ATLAS experiment
σ_s	surface tension
ζ	slope of the variation of β'_s with respect to the current temperature, T, at $\xi = 1$
ξ	ratio between mean effective stress and the critical state pressure
ξ	variable proportional to the distance to the particle in the diffuse double layer theory
ξ_δ	variable describing the effect of inter-particle distance on the increment of the interaction stress between particles
ξ_T	variable describing the effect of temperature on the increment of the interaction stress between particles
Ψ	electrostatic potential in a plane at a distance x from the surface of the clay platelet
Ψ_0	electrostatic potential in a plane at the surface of the clay platelet ($x = 0$)
Ψ_d	electrostatic potential in a plane at the mid-plane between two clay platelets ($x = \delta/2$)
ψ	dilatancy angle
χ	effective stress parameter
χ_w	water bulk modulus

Superscripts

′	refer to the effective stress
e	elastic component
p	plastic component

Subscripts

0	initial value
a	property of dry air
c	preconsolidation value
cr	value at critical state

da	property of dissolved air in water
dev	value related to the deviatoric mechanism
dry	value related to the drying mechanism
g	property of dry air
iso	value related to the isotropic mechanism
ref	reference value of a parameter
s	property of solid phase
v	property of water vapour
w	property of liquid water
wet	value related to the wetting mechanism

Operators

.	inner product of tensors with single contraction
:	inner product of tensors with double contraction
d (.)	increment
div (.)	divergence
grad *(.)*	gradient
Δ *(.)*	variation
Σ *(.)*	summation

Nota Bene

Throughout this dissertation, the sign convention is the usual convention of soil mechanics which is that compression is positive. Appendix A reports the used stress-strain conventions.

Chapter 1

Thermo-plasticity in soil: an introduction

Understanding the behaviour of real objects is improved if intelligent simplifications of reality are made and analyses are performed using simplified object of the real objects. […]. The objective of using conceptual models is to focus attention on the important features of a problem and to leave aside features which are irrelevant. The choice of model depends on the application.[1]

---

[1] Muir Wood D. (1990). *Soil Behaviour and Critical State Soil Mechanics.* Cambridge University Press, Cambridge.

1.1 General introduction

1.1.1 Thermal effect in soils and nuclear waste disposal

Interest in thermal effect on geomechanical problems dates back to the 1960s, when the first conference concerning *the effect of temperature and heat on the engineering behaviour of soil* was held in Washington (Highway Research Board, 1969, reported by Cekerevac, 2003). Already by that time, the scope of the conference revealed the need to study accurately the thermal effects in soils:

Knowledge of soil thermal properties is of primary importance in understanding the characteristic soil profile, water accumulation, frost heave, stability loss, corrosion and other problems that must be solved by highway engineer. Qualitative use of thermodynamics can indicate the direction in which a soil system changes under known or expected environmental influences and can point out the type of testing or experimentation that should be done on the system to obtain meaningful information.

The birth of this new discipline in geomechanics was mainly motivated by the need for the road engineers to understand and to assess the effect of temperature on the mechanical behaviour of subgrades soils. However, as discussed in Section 1.2, since that time, an accurate characterization of the thermo-mechanical behaviour of soils has been considered with respect to many other geotechnical applications. In particular, a feasibility study of nuclear waste disposal in deep geological formations involves the consideration of temperature as one of the main agents that affect the confining materials surrounding the radioactive wastes.

This thesis is mainly motivated by the challenging task of characterising, understanding, and modelling the effect of temperature on the geomaterials involved in the confinement of underground nuclear waste disposal. In most of the concepts developed in different countries, the argillaceous materials constitute either the main barrier or an important element aimed at confining the nuclear waste and isolating it from the biosphere. A typical scheme for a deep geological repository is shown in Figure 1.1. In addition to the temperature action, the confining barrier may also be subjected to drastic changes of the pore fluid pressures in combination with temperature and mechanical variations. Such thermo-hydro-mechanical (THM) loading has a considerable influence on the soil, not only in terms of the mechanical response, but also on the material's water retention properties. In particular, clayey materials are prone to plastic strains during temperature, hydraulic, or mechanical loading. The order of magnitude of these plastic effects can be much greater than the elastic strains, and this may have considerable impacts on the behaviour of the soil surrounding heat-emitting radioactive waste.

The stability of such a repository has to be ensured during the period needed for the radioactivity to decrease under an acceptable threshold. Since this matter concerns long time periods, the safety assessment of this option must be based mainly on predictions. A rigorous characterisation, understanding, and model of the highly coupled and non-linear THM processes occurring in the clayey barrier must be undertaken in order to contribute to the performance assessment of such facilities.

Facing this ambitious objective, this dissertation addresses the *thermo-plasticity in soils at various saturation states, as it applies to nuclear waste disposal issues*.

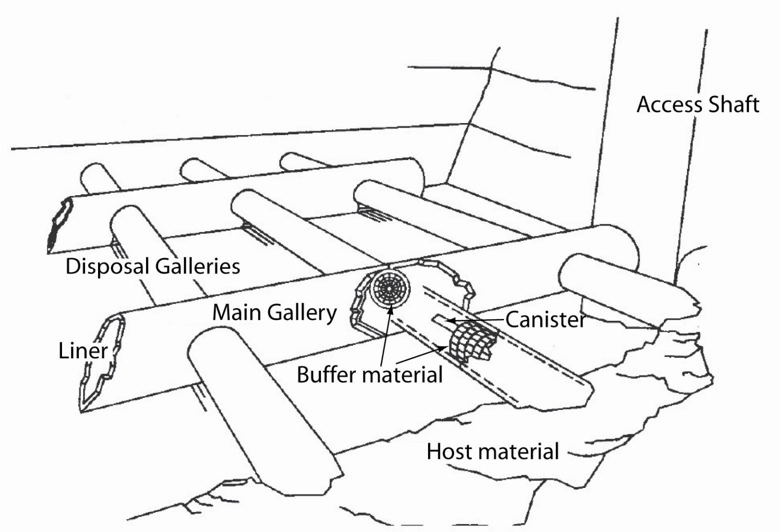

Figure 1.1 : Typical scheme of a deep geological repository for nuclear waste (modified from Gens and Olivella, 2001).

1.1.2 Objectives

In this dissertation, the problem of thermo-plasticity in saturated and unsaturated soils (in particular, in the clayey materials involved in the confinement of radioactive waste), is addressed in a progressive and systematic way. This issue is treated from an experimental, constitutive, and numerical point of view, leading to the following objectives:

- To provide a state of knowledge of the thermo-mechanical behaviour of saturated and unsaturated fine-grained soils via a literature analysis of the experimentation performed in the past, and to display additional experimental results on thermo-hydro-mechanical tests to help fill the gap between the needs of modelers and the available experimental data.
- To develop a constitutive model that considers the non-linear and highly coupled behaviour of soils, not only in terms of mechanical response (as it is affected by temperature and water retention variations) but also in terms of how the water retention behaviour is affected by the temperature and mechanical state.
- To use the developed model to study the transient THM processes that affect the confining materials surrounding the nuclear waste disposal. These simulations aim at underlining the role of thermo-plasticity of saturated and unsaturated soils in the global response of the buffer materials and the host formation.

The theoretical developments and the experimental program in this thesis consider soils as isotropic materials without induced or natural internal structure. It aims at keeping a general framework in the interpretation of experimental results and at constructing a conceptual constitutive model. Within this approach, the behaviour of structured materials (e.g. natural bonded soils or aggregated soils) is a specific case for which further adaptations of the developed constitutive tools are required.

This research was performed in a context that deals with constitutive modelling of multi-physics processes occurring in unsaturated soils. Consequently, in addition to these thermo-plasticity aspects, this work contributes to a global context of constitutive modelling that is more or less in connection with the present study (Koliji, 2008; Peron 2008; Laloui et al., 2008).

The study of the thermo-plasticity of fine-grained soils is a long-standing practice in the research group in which this work has been performed. Among the perspectives stated in the concluding remarks of previous works performed in the this field (Laloui, 1993; Cekerevac, 2003), the extension of the existing thermo-plastic models available for saturated conditions towards unsaturated conditions, as well as computing solutions of boundary value problems, was defined as a main concern. Even if the topic is broad and many research axes are still to be investigated, we hope that this work may help to provide a better understanding of *what the effects of thermo-plasticity in saturated and unsaturated soils are; in particular, what the effects are around a nuclear waste disposal site.*

1.1.3 Outline of the thesis

In the present study, the treated problems are addressed progressively and in a systematic manner. In the first section (Chapters 2 and 3), water saturated conditions are assumed, and a mechanical constitutive model for fine-grained soil is developed. The model is developed first for isothermal conditions, and then the thermal effects are considered. In the second section (Chapters 4 to 6), the partial water saturation of the soil is introduced, and the constitutive model is extended towards the unsaturated state. Finally, the third section (Chapters 7 and 8) applies the developed model to boundary value problems related to the nuclear waste disposal issue.

In particular, the material of this thesis is presented as follows:

Chapter 2 …
… presents the main families of the elasto-plastic constitutive models for soils and focuses on the hardening plasticity and the critical state concept. From those considerations, a constitutive model for isothermal and saturated conditions is developed. This model is the constitutive base on which the further developments of the next chapters will be established.

Chapter 3 …
… is devoted to the thermo-mechanical behaviour of saturated fine-grained soils. The reasons behind the temperature-induced modification of the macroscopic mechanical behaviour of soils are first investigated at the particle-scale. Then, the macroscopic thermo-plastic experimental evidence is underlined, and the constitutive model developed in Chapter 2 is extended in order to consider the thermal effects.

Chapter 4 …
… introduces the partial saturation in soils and the suction-induced effects on the mechanical behaviour of soils. In that sense, the behaviour of unsaturated soils is reviewed and extended in order to consider the thermal effects.

Chapter 5 …
… presents an experimental program performed on a silty material, which investigates the combined effect of temperature and partial saturation on the stress-strain behaviour of soils. The calibration of the experimental apparatus is also presented.

Chapter 6 …
… extends the constitutive model developed in Chapter 2 and 3, considering the unsaturated and non-isothermal soil mechanics. This implies that is considers not only the stress-strain behaviour of the material but also its water retention response, with a strong interaction between the two constitutive frameworks.

Chapter 7 …

… introduces the THM governing equations of the finite element code used in the last part of the thesis. The implementation of the constitutive model in the code is validated by means of a comparison between the known numerical solutions and results from finite element simulations.

Chapter 8 …

… reports the results of finite element simulations of THM processes in soils with regard to the issue of nuclear waste disposal. In the interpretation of the simulation results, particular attention is paid to the advancements brought by the thermo-plasticity concepts used in the simulations. As an application, this chapter unifies all the theoretical developments obtained in the present work.

Chapter 9 …

…, finally, states the concluding remarks of the present work and proposes outlooks for further studies in the field.

1.2 THM applications in geotechnics

1.2.1 Temperature and environmental geomechanics

The recent increase in geotechnical problems, where temperature effect coupled with the hydro-mechanical behaviour of soil is of paramount importance, have placed the thermo-mechanics of fine-grained soils at the centre of many challenging research programs. Thermo-hydro-mechanical (THM) coupling effects are therefore becoming one of the major issues in environmental geomechanics (Vulliet et al., 2002). In addition to issues of nuclear waste disposal, thermal impact may play a major role in many other geotechnical applications as well. As shown below, temperature affects not only the fluid flow in soils, but also the mechanical response of the geological formation under consideration.

1.2.2 THM applications

1.2.2.1 *Natural ground temperature variations*

Subsurface soils may undergo thermal variations due to daily or seasonal evolution of atmospheric temperature. Heat supply in the ground is mainly provided by surface conduction and geothermal heat flow. In the upper part of the underground, ground temperature varies with time and depends on the amount of heat absorbed by the ground as well as on its thermal properties. Many factors contribute to the high variability of heat adsorption, such as air temperature, snow cover, slope orientation, vegetal cover, wind, and rain (Burger et al., 1985). Generally, the ground temperature evolution presents a cyclical and almost simple allure. For instance, sinusoidal variations can be considered (Williams and Gold, 1977), where the phase shift between air temperature (almost in phase with that of the ground surface) and ground temperature is proportional to depth (Figure 1.2).

In addition, many changes in terrain can modify the ground temperature field. In particular, in road design, temperature variations of the subgrade soil induced by the heat absorption of the road pavement may alter the mechanical response of the road foundation. The changes in temperature and moisture conditions underneath the pavement are thought to induce modifications in the resilient modulus of the subgrade soil, the bearing capacity, or the durability of the structure. Figure 1.3 gives an example of monthly temperature variations of a subgrade soil which occur in parallel with the change of its resilient modulus (Jin et al., 1994).

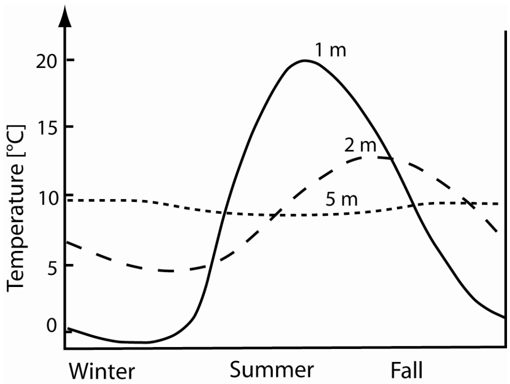

Figure 1.2 : Annual evolution of ground temperatures in Ottawa (Williams and Gold, 1977).

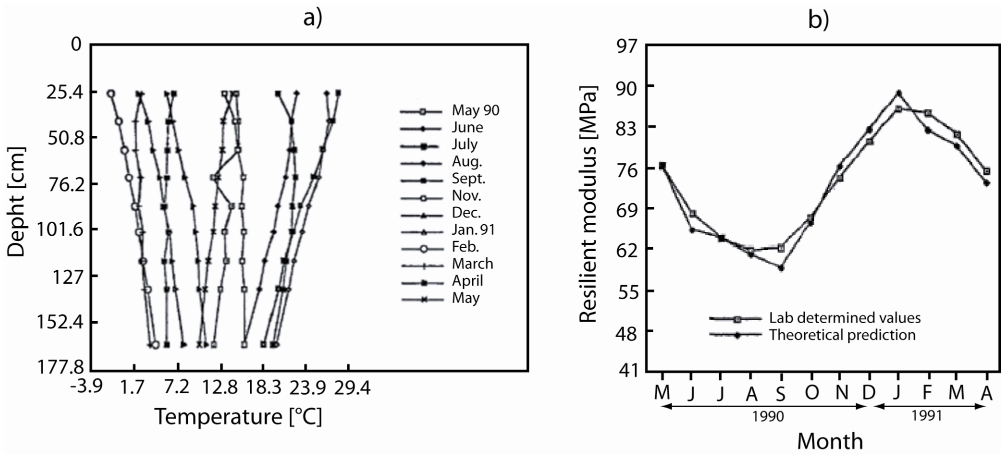

Figure 1.3 : (a) Monthly temperature variations of subgrade soil, and (b) corresponding variations of the resilient modulus (Jin et al., 1994).

1.2.2.2 *Energy storage in building foundations*

The amplitude of ground temperature fluctuations attenuates with depth. In the context of geothermal energy, ground temperature is considered constant below 20 meters. In regards to regulating the ambient temperature of live-space, this underground temperature stability allows thermal energy from the surface to be stored during the hot period and to be extracted from the ground during the cold period. These exchanges could be carried out using various systems, such as geothermal probes, heat exchanger piles, or energetic geostructures (Brandl, 2006).

By modifying ground temperature distribution (Figure 1.4), such energetic exchanges could have significant impacts on ground behaviour. In particular, the settlement has to be quantified in order to ensure ground and structure stability and to optimize systems design parameters (Gabrielsson et al., 2000). For example, piles designed to work as heat exchangers are frequently oversized. A deeper knowledge of the thermal effects acting both on soil and piles could allow designers to optimize their dimensions (Laloui et al., 2006).

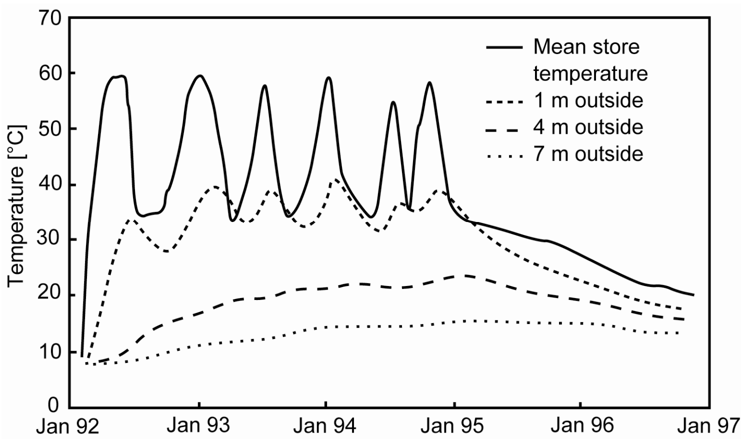

Figure 1.4 : Measured temperatures at various distances from a heat store test (Gabrielsson et al., 2000).

1.2.2.3 *Exploitation of geothermal fields*

Mean ground temperature increases with depth, and down to the depths accessible by drilling, the average geothermal gradient is about 27°C/km; in the presence of geological anomalies, it can reach more than 200°C/km. At great depth, ground temperatures are therefore significantly greater than surface temperature, and this thermal energy can be exploited for heat or electricity production. This process is usually undertaken by extracting hot water out of the geothermal reservoir and re-injecting cold water into it. However, production and re-injection of reservoir fluids may cause significant decreases in subsurface pressure and temperature. Figure 1.5 depicts an example of such a temperature decline. These modifications could lead to land-surface displacements (Sorey, 2000). Therefore, in order to optimize the exploitation rate of the field while keeping the disturbance acceptable at the ground surface, a proper understanding of the thermal behaviour of the reservoir materials is needed.

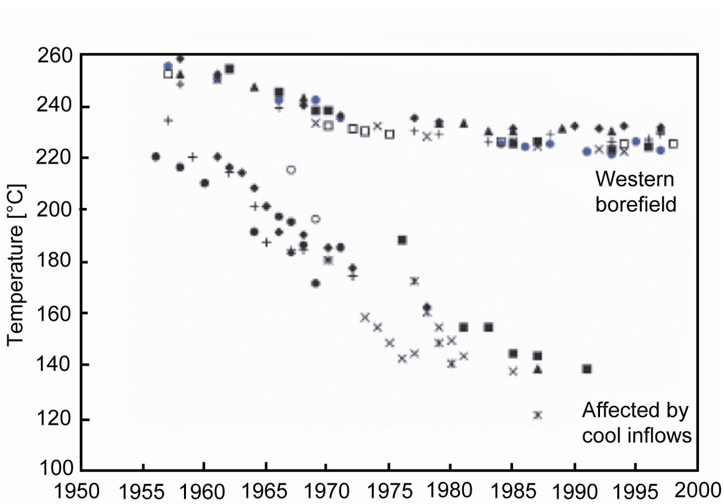

Figure 1.5 : Average temperatures from liquid feedzones in the production areas of the geothermal field at Wairakei, New Zealand (Clotworthy, 2000).

1.2.2.4 *Large and rapid landslides*

In a rapid landslide, friction along the slip surface induces heating (Figure 1.6a). In order to understand the dynamic behavior of complex landslides, consideration of thermal effect may help in identifying the main mechanisms that govern the velocity of the moving mass. If the rate of shearing is high enough, the heat produced can enhance pore water pressure in the shear zone (Figure 1.6b) and result in a significant decrease in effective stresses. Amongst these phenomena, the Vaiont landslide in Italy on 9th October 1963 (Semenza and Ghirotti, 2000; Vardoulakis, 2002; Gerolymos et al., 2007) and the East Abbotsford landslide in New Zealand on 8th August 1979 (Smith and Salt, 1988), must be mentioned.

1.2.2.5 *Buried cables or pipelines*

Heat losses in underground high-voltage cables (mainly caused by Joule's effect) induce a temperature increase in the cable core, causing a thermal gradient in the surrounding soil (Figure 1.7). Maximal temperatures depend on the operating tension, and therefore, soil response must then be computed in order to ensure thermal stability. The thermal behaviour of the soil and its ability to dissipate the generated heat imposes a major restriction on its load capability. Thus, since soil materials are frequently used for cable backfill, an accurate reproduction of soil and backfill thermal behaviour may allow enhancement of the current rating of buried cables. Also, the temperature fields generated around a buried pipeline are the cause of similar concerns (Cui and Ye, 2005; Da Costa et al., 2002).

1.2.2.6 *Furnace foundations*

In the ground and foundations under blast furnaces, temperature may reaches more than 800°C. Moreover, erosion of the ground may enhance foundation temperatures up to more than 1000°C (Figure 1.8). That very high temperature produces deep holes and cracks in the furnace foundations. In order to optimize design parameters, interactions between the ground and their foundations need to be studied.

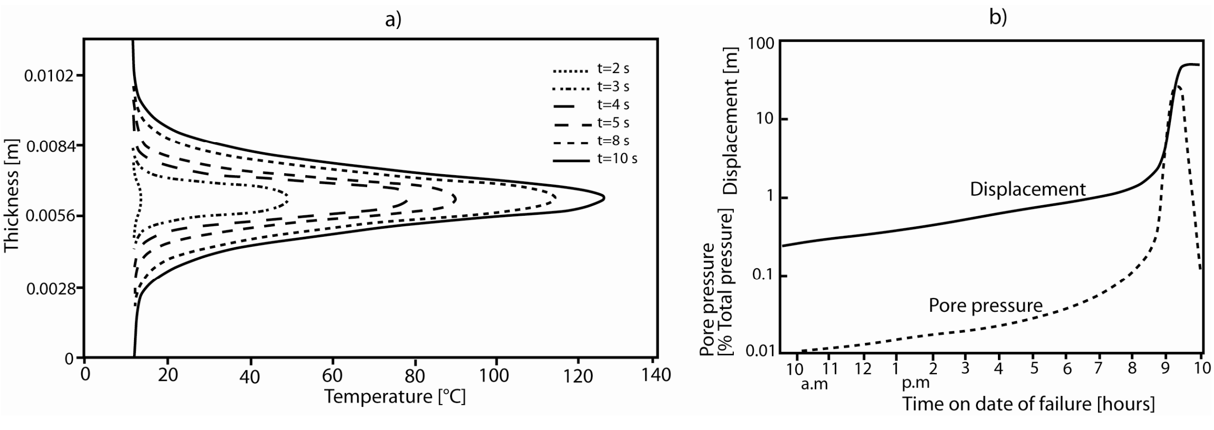

Figure 1.6 : Effect of temperature induced by friction in shear band of rapid landslides. (a) Simulation of temperature isochrones in the vicinity of the shear band of Vaiont landslide (Vardoulakis, 2002). (b) Calculated excess pore pressures within the clay band in parallel with displacement of the East Abbotsford landslide (Smith and Salt, 1988).

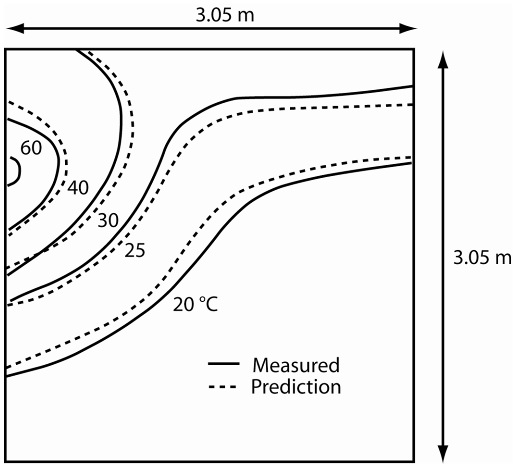

Figure 1.7 : Predicted and measured temperature distributions in field test section around a buried cable 10 days after heating the cable from 20°C to 60°C (Mitchell et al., 1979).

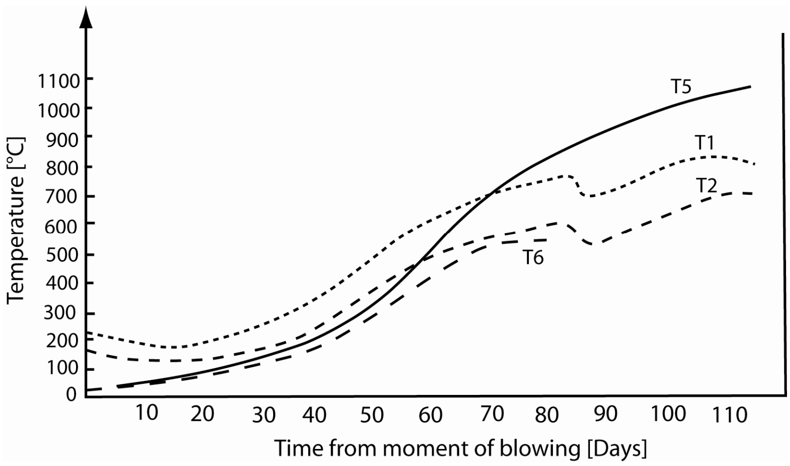

Figure 1.8 : Example of thermocouple readings (T1, T2, T5, T6) placed at different locations in the earth for a furnace foundation (Krepyshev, 1958).

1.2.2.7 *Underground storage of natural gas*

Disposal or storage of pressurized carbon dioxide (CO_2) in deep saline aquifers has been suggested as a promising concept for reduction of emission of greenhouse gases into the atmosphere (Holloway, 1997). In general, injection of CO_2 results in a pore pressure increase which can significantly modify the stress state and cause deformation of the media. CO_2 should be injected in a supercritical state. The temperature of this gas should then remain above 31.04°C. In addition, the processes of fluid flow, CO_2 dissolution, and phase change produce variation of the temperature field in the ground (Figure 1.9). Therefore, the influence of such temperature changes on the distributions of stresses and deformation should be properly considered (Pruess, 2003; Rutqvist and Tsang, 2002).

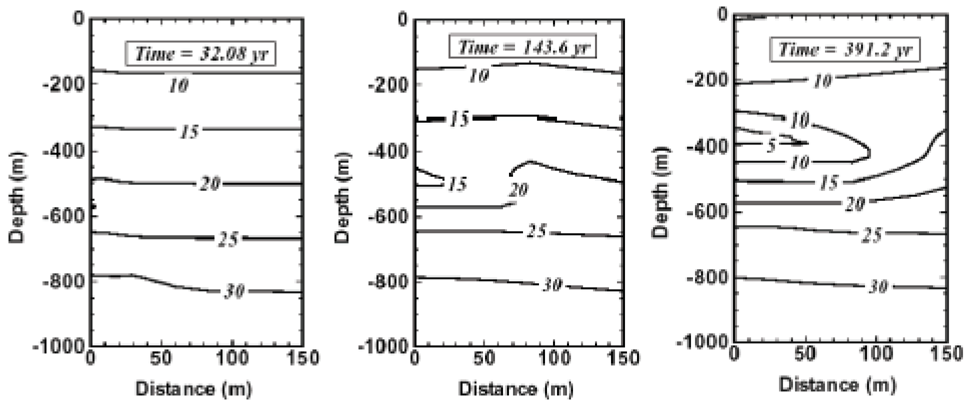

Figure 1.9 : Simulation of ground temperature distribution (°C) in a reservoir submitted to CO_2 injection at the bottom boundary. Temperature at three different times after injection (Pruess, 2003). Significant decrease of ground temperature due to CO_2 vaporisation.

1.2.2.8 *Hydrocarbon exploitation*

The petroleum industry may harbour applications of THM coupling such as petroleum drilling, injection, and production activities. In particular, fire-flooding involves high fluid pressure and high temperature in a petroleum reservoir. This technique is used to enhance hydrocarbon recovery for heavy oil by injecting compressed air into the petroleum reservoir and burning some of the oil. Thermal stress fields are then generated during fire-flooding, which must be taken into account during modelling of mechanical behaviour of the reservoir (Dusseault et al., 1988) (Figure 1.10).

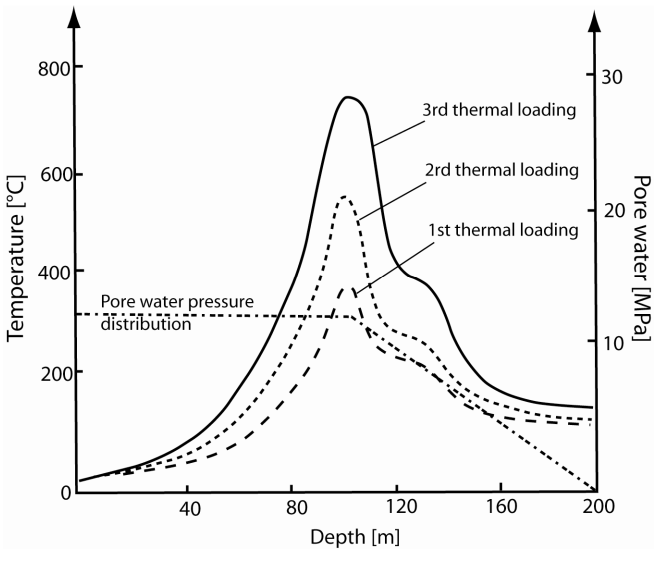

Figure 1.10 : Indicative distribution of temperature and pore pressure for a horizontal section of the Bodo reservoir in Alberta, synthesized from field and laboratory data (Dusseault et al., 1988).

1.2.2.9 *Thermal evolution of sample properties*

In most experimental tests on soil samples, the temperatures existing *in situ* are different from those in the laboratory. Typically, the temperature modifications caused by sampling, storing and laboratory testing are applicable to a temperature range of 10°C to 50°C (Moritz, 1995; Leroueil and Marques, 1996). Since the behaviour of soils is affected by thermal effects, this can induce errors in sample characterization. For instance, a sample of a marine sediment may have been subjected to a temperature increase of 20°C between the time it was recovered from the ocean floor and was brought to the laboratory for the testing (Plum and Ersig, 1969).

1.2.2.10 *Landfills*

Waste stored in landfill facilities can generate significant heat, and the local increase of surface temperature is correlated to biogas release. Since temperature affects the mechanical behaviour of landfills, this factor cannot be neglected during the design of such facilities. The landfill must be properly designed to limit the disturbance of the landfill efficiency (Neusinger et al., 2005) caused by temperature.

Section I

Thermo-mechanical constitutive behaviour of saturated fine-grained soils

Chapter 2

ACMEG, an isothermal constitutive model

Soils having cohesion and internal friction are often considered to be perfectly plastic solids. […]. However, such an idealized treatment will often result in a marked difference between prediction and experimental fact. In particular, the strong dependence of the volume change under shearing action on the prior history of the soil cannot be properly taken into account. It is suggested herein that soil be treated as a work-hardening material which may reach the perfectly plastic state.[1]

[1] Drucker D.C., Gibson R.E. and Henkel D.J. (1957). Soil mechanics and working hardening theories of plasticity. *Transaction of ASCE*, 122: 338-346.

2.1 Introduction

Soil mechanics concepts have been developed for about a century. In the first half of the twentieth century, the basic concepts of classical soil mechanics were established. Terzaghi's work, explaining notions such as consolidation and effective stress of saturated porous media, opened the classical soil mechanics era (Terzaghi, 1943). Then, other famous authors contributed to the understanding of the mechanical behaviour of soil materials. In particular, Casagrande, Hvorslev, Skempton, Bishop, Biot or Drucker made major contributions with works on the concept of preconsolidation pressure (Casagrande, 1936), soil strength (Hvorslev, 1937), the distinction between drained and undrained soil behaviour (e.g. Skempton and Golder, 1948), shearing strength (Skempton and Bishop, 1950; Bishop, 1966), the effect of transient flow of the pores-fluids through the voids (Biot, 1956) and the work-hardening theory of plasticity (Drucker et al., 1957).

However, beyond this empirical or analytical analysis of soil behaviour, the need for describing the soil deformation for various stress loading led to elaborate appropriate constitutive theories of the stress-strain relations for geomaterials. Because soil is a complex porous medium facing particle rearrangements upon loading, elasticity generally fails to predict the real behaviour of soil in most geotechnical applications. In order to consider irreversible processes together with yielding phenomena and shear-induced dilatancy, more sophisticated models were required. Consequently, the theory of plasticity, initially developed to describe the behaviour of metals (see, among others, the pioneering works of Von Mises, 1928; Hill, 1948; Prager, 1955; Drucker, 1958), was adapted for soil mechanics. The key role of the volume change during soil shearing required the elaboration of advanced theories, leading to the concept of soil hardening (Calladine, 1963) and the flow rule upon yielding (Drucker et al., 1957).

Those developments led to the fundamental works of Schofield, Worth, Roscoe and co-workers at Cambridge University (Roscoe et al., 1958; Schofield and Worth, 1968; Roscoe and Burland, 1968) which initiated "Modern Soil Mechanics". They studied and modelled, in the deviatoric $(\varepsilon_1 - q)$ and volumetric $(\varepsilon_1 - \varepsilon_v)$ planes, the behaviour of soil subjected to triaxial and oedometric mechanical solicitations and introduced the critical state concept stating that '*when soils or others granular materials are continuously distorted until they flow as a frictional fluid, they will come into a well-defined critical state determined by two equations*

$$q = Mp' \tag{2.1}$$

$$\Gamma = v + \lambda \ln p' \tag{2.2}$$

where M , Γ *and* λ *represent basic soil material properties.* p' is the mean effective stress, q the deviatoric stress and v the specific volume ($v = 1 + e$, e being the void ratio) (Figure 2.1).

Thus, '*the total change from any initial state to an ultimate critical state can be precisely predicted*', and the problem is reduced to determining how the mechanical behaviour evolves between these two extreme states.

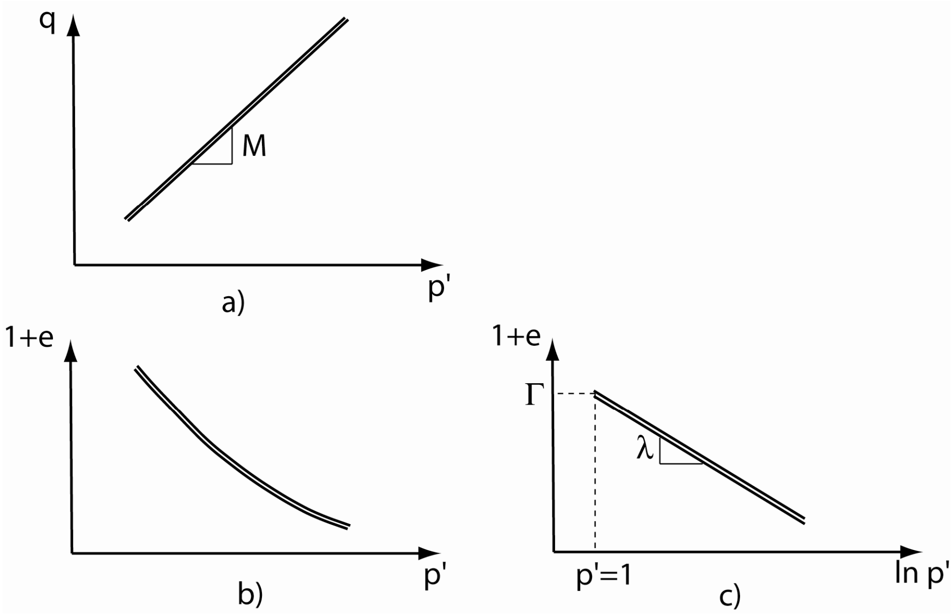

Figure 2.1: Representation of the critical state (a) in the (p′ - q) plane, (b) in the (p′ - (1+e)) plane and (c) in the (ln p′ - (1+e)) plane. M, λ and Γ are the material parameters characterizing the critical state (Schofield and Worth, 1968).

On the basis of this critical state concept, the Cambridge team built the Granta-Gravel model (Schofield and Worth, 1968), which is the first modern elasto-plastic constitutive soil model. It is built from a general yield function formulated in the $(p'-q)$ plane (which can be extended in the principal stress space by a rotation of this yield curve around the p' axis) (Figure 2.2) and an associated flow rule based on the suggestion of Drucker et al. (1957). The well-known Cam-Clay family models spring from this precursory model.

In this chapter, the basic concept of soil plasticity theory is addressed. The constitutive equations of the Cam-Clay model are introduced and interpreted based on its response on triaxial compression tests. Then, some advanced developments in elasto-plasticity for soils are presented. Finally, a new constitutive model founded on the Original Cam-Clay model is presented and validated by experimental results.

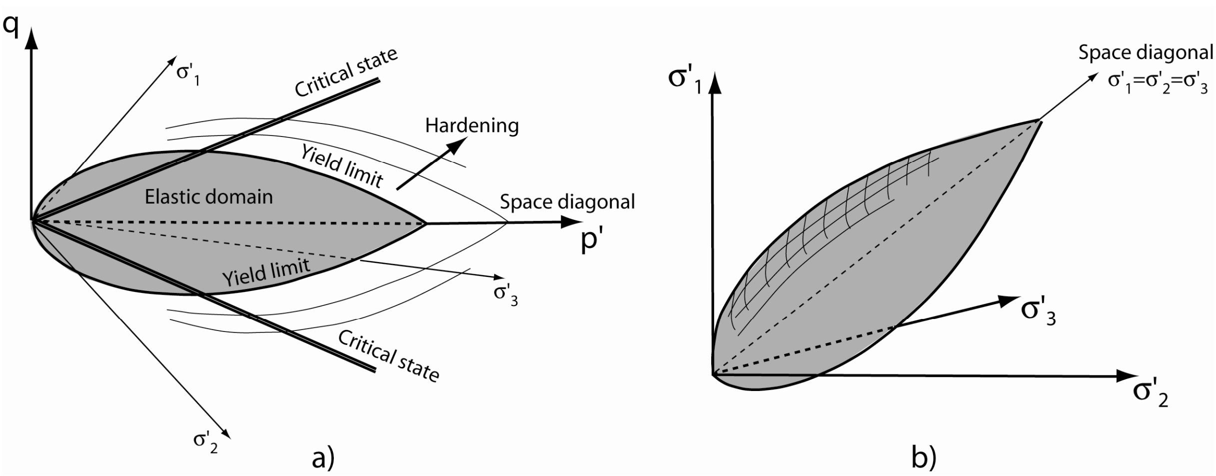

Figure 2.2: Cam-Clay yield limit (a) in the (p′-q) plane, (b) in the principal stress space (Schofield and Worth, 1968).

2.2 Soil elasto-plasticity

2.2.1 Some concepts of plasticity in soils

2.2.1.1 *Work input and elasto-plasticity*

Elasto-plasticity is based on the decomposition of the total strain increment $d\varepsilon_{ij}$ into both elastic and plastic strain increments, $d\varepsilon_{ij}^{e}$ and $d\varepsilon_{ij}^{p}$, respectively. Within the small strain assumptions, it yields:

$$d\varepsilon_{ij} = d\varepsilon_{ij}^{e} + d\varepsilon_{ij}^{p} \tag{2.3}$$

The elastic part of the strain produced by a given loading is directly recoverable after unloading. On the contrary, the plastic part of the strain remains irrecoverable even once the applied stress is removed. This aspect can be interpreted in term of work input per unit volume dW of a material submitted to a strain increment $d\varepsilon_{ij}$:

$$dW = \sigma'_{ij} d\varepsilon_{ij} = \sigma'_{11} d\varepsilon_{11} + \sigma'_{22} d\varepsilon_{22} + \sigma'_{33} d\varepsilon_{33} + \sigma'_{12} d\gamma_{12} + \sigma'_{13} d\gamma_{13} + \sigma'_{23} d\gamma_{23} \tag{2.4}$$

In combination with the elasto-plastic assumption (Equation (2.3)), it gives:

$$dW = \sigma'_{ij} d\varepsilon_{ij}^{e} + \sigma'_{ij} d\varepsilon_{ij}^{p} = dW^{e} + dW^{p} \tag{2.5}$$

where dW^{e} is the elastic energy recoverable upon unloading while dW^{p} is the plastic work that cannot be recovered. This quantity of energy is dissipated by the material during loading. In that sense, the work done on the plastic strain must be positive:

$$dW^{P} = \sigma'_{ij} d\varepsilon_{ij}^{p} > 0 \tag{2.6}$$

That is *the condition of irreversibility* as stated by Prager (1949).

2.2.1.2 *Elastic domain and yield criterion*

Most of the elasto-plastic constitutive approaches developed for soils are based on the concept of the yield criterion, also called the loading surface or yield limit.

The yield criterion is a condition that defines the limit of elasticity and the beginning of plastic deformation under any possible combination of stresses. In the elastic region, all the deformation will be recovered once the applied stress is removed. However, once the yield condition is reached, some of the deformation will be permanent in the sense that it cannot be recovered even after the stress is removed completely (Yu, 2006).

This yield limit is expressed in terms of the effective stresses (σ'_{ij}) and may depend on one or several internal variables, π_i. Mathematically, the general form of this limit can be expressed as follows:

$$f\left(\sigma'_{ij}, \pi_i\right) = 0 \tag{2.7}$$

2.2.1.3 *Plastic potential and stress-strain relations*

Once the boundary between elastic and elasto-plastic domain is established in the stress space, it is necessary to specify the relative magnitude of the various components of the plastic strain when this boundary is reached. In order to answer this point, a plastic potential g must be defined to relate the plastic strain to the stress state as follows:

$$g\left(\sigma'_{ij},\pi_i\right)=0 \tag{2.8}$$

$$d\varepsilon_{ij}^p=\lambda^p\frac{\partial g}{\partial\sigma'_{ij}} \tag{2.9}$$

where $d\varepsilon_{ij}^p$ is the (i,j) component of the plastic strain increment and λ^p is a non-negative variable called the plastic multiplier. $\partial g/\partial\sigma'_{ij}$ defines the direction of the plastic strain while λ^p governs its magnitude. If the plastic potential is the same as the yield limit, the plastic flow rule (Equation (2.9)) is called the associated flow (or normally flow) rule. Otherwise, if g is different from f, the flow rule is said to be non-associated.

So, Equation (2.3) can be re-written as the following:

$$d\varepsilon_{ij}=d\varepsilon_{ij}^e+d\varepsilon_{ij}^p=E_{ijkl}^{-1}d\sigma'_{kl}+\lambda^p\frac{\partial g}{\partial\sigma'_{ij}} \tag{2.10}$$

where E_{ijkl}^{-1} is the elastic modulus matrix. Inversely, in an incremental stress path, the effective stress increment is:

$$d\sigma'_{ij}=E_{ijkl}\left(d\varepsilon_{kl}-\lambda^p\frac{\partial g}{\partial\sigma'_{ij}}\right) \tag{2.11}$$

At this level, it is important to demand that the solution of the stress-strain relation be unique. *The uniqueness condition*, as it is called by Prager (1949), guaranties that the sum of the plastic strain increments obtained from several sets of stress increments $d\sigma'_{ij,\alpha}$ will be the same as the plastic strain increment resulting from $d\sigma'_{ij}=\sum_{\alpha}d\sigma'_{ij,\alpha}$. Hill (1950) demonstrated that this condition is fulfilled for any associated flow rule in the small strain approach. As far as non-associated flow rules are concerned, the incremental problem can be uniquely solved under certain conditions.

2.2.1.4 *Hardening and consistency conditions*

When the stress point reaches the yield limit, plastic strains occur for all stress paths directed towards the exterior of the yield limit. In any other case, the material behaviour is commonly assumed to be purely elastic. Consequently, three possible conditions may be defined:

$$\text{Unloading:}\quad f\left(\sigma'_{ij},\pi_i\right)=0\quad\text{and}\quad df=\frac{\partial f}{\partial\sigma'_{ij}}d\sigma'_{ij}<0 \tag{2.12}$$

Neutral loading: $f\left(\sigma'_{ij},\pi_i\right)=0$ and $df=\dfrac{\partial f}{\partial \sigma'_{ij}}d\sigma'_{ij}=0$ (2.13)

Loading: $f\left(\sigma'_{ij},\pi_i\right)=0$ and $df=\dfrac{\partial f}{\partial \sigma'_{ij}}d\sigma'_{ij}>0$ (2.14)

That is *the condition of continuity* formulated by Prager (1949). By definition, the exterior of the elastic domain limited by the yield criterion is unattainable. Therefore, in the loading case, the inequality of Equation (2.14) must be counterbalanced by an evolution of the yield function f in order to guaranty that the yield criterion is satisfied as long as the material is in a plastic state. That is *the condition of consistency* (Prager, 1949). This process, called hardening, leads to a change in size, location or shape of the elastic domain. Strictly speaking, if the elastic domain is expanding in size, the material is said to be hardening. On the contrary, if the elastic domain contracts, the material undergoes softening.

The evolution of the yield function f is governed by the internal variables π_i in agreement with Prager's consistency condition (Prager, 1949):

$$df=\frac{\partial f}{\partial \sigma'_{ij}}d\sigma'_{ij}+\frac{\partial f}{\partial \pi_i}d\pi_i=0 \tag{2.15}$$

Two different main hypotheses can be made on the internal variables. The work hardening hypothesis assumes that the hardening depends only on the plastic work (Hill, 1950) while the strain hardening hypothesis links the hardening to the plastic strain (reported by Desai and Siriwardane (1984)):

Work hardening : $f=f\left(\sigma'_{ij},\pi_i\right)=f\left(\sigma'_{ij},W^p\right)$ (2.16)

Strain hardening : $f=f\left(\sigma'_{ij},\pi_i\right)=f\left(\sigma'_{ij},\varepsilon^p_{ij}\right)$ (2.17)

In the following, only the strain hardening hypothesis will be addressed. Thus, Equation (2.15) can be re-written in the following form:

$$df=\frac{\partial f}{\partial \sigma'_{ij}}d\sigma'_{ij}+\frac{\partial f}{\partial \varepsilon^p_{ij}}\frac{\partial \varepsilon^p_{ij}}{\partial \lambda^p}\lambda^p=0 \tag{2.18}$$

Combining this consistency condition with Equation (2.11) gives the value of the plastic multiplier, which rates the magnitude of plastic strain increment:

$$\lambda^p=\frac{1}{H}\frac{\partial f}{\partial \sigma'_{ij}}E_{ijkl}d\varepsilon_{kl} \tag{2.19}$$

The plastic (or hardening) modulus H depends on the stress state, the plastic potential and the elastic rigidity of the material:

$$H=\frac{\partial f}{\partial \sigma'_{ij}}E_{ijkl}\frac{\partial g}{\partial \sigma'_{kl}}-\frac{\partial f}{\partial \varepsilon^p_{ij}}\frac{\partial \varepsilon^p_{ij}}{\partial \lambda^p} \tag{2.20}$$

Finally, it is necessary to mention that all of these developments assume isotropic hardening, which does not modify the shape, the centre and the orientation of the yield surface and allows only expansion or contraction uniformly about the centre of the yield surface.

2.2.2 Cam-Clay family models

2.2.2.1 *The main constitutive equations*

All of the above-mentioned concepts of plasticity were established before the 1960's. Based on those theories, the Cam-Clay model considers four main aspects of soil behaviour: the soil response under isotropic loadings, the critical state concept, the stress-dilatancy relation and the associated flow rule.

Two main versions of the Cam-Clay model exist, differing from each other in their yield function equation. These two versions are called "*the Original Cam-Clay*" and "*the Modified Cam-Clay*". The yield limit of the Modified Cam-Clay is elliptic while the Original Cam-Clay uses an almond-shaped yield criterion. Figure 2.3 shows the representation of the Original Cam-Clay yield limit in the mean effective stress p', deviatoric stress q, void ratio e space. The model considers a unique state boundary surface outside which no state of the soil is permissible. A given size of the state surface corresponds to a given void ratio. Any densification of the material tends to enhance the elastic domain (i.e. hardening).

The volumetric response of soil under isotropic loading can be divided in two main parts (Figure 2.4).

(i) The behaviour inside the yield limit is governed by the loading-unloading curve (also called κ curve) which is characteristic of the isotropic elastic behaviour:

$$e = e_0 - \kappa \ln \frac{p'}{p'_0} \tag{2.21}$$

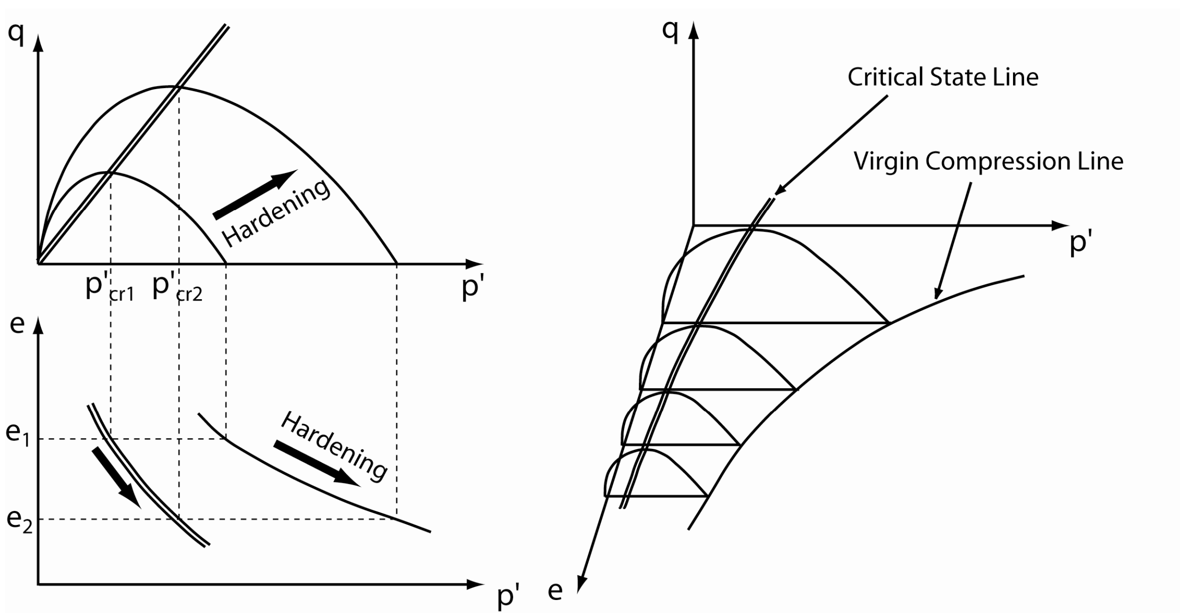

Figure 2.3: Original Cam-Clay yield limit in the (p', q, e) space.

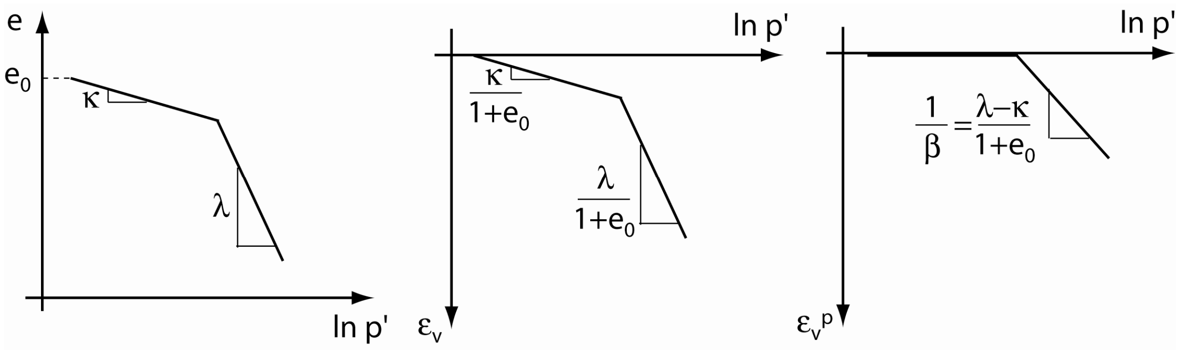

Figure 2.4: Schematic representation of Cam-Clay prediction on an isotropic compression path. (a) (e-ln p′); (b) (ε_v – ln p′); (c) ($\varepsilon^v{}_p$ – ln p′).

where e_0 is the initial void ratio and p'_0 the initial mean effective stress. κ, the swelling index, is a material parameter (the slope of the κ curve in the ($e-\ln p'$) plane).

(ii) On the isotropic yield criterion, a loading process induces both elastic and plastic evolutions of the void ratio following the normally consolidated line (also called λ curve or virgin compression line):

$$e = e_0 - \lambda \ln \frac{p'}{p'_0} \tag{2.22}$$

where λ, the compression index, is a material parameter (the slope of the λ curve in the ($e-\ln p'$) plane).

The evolution of void ratio can easily be transformed into volumetric strain ε_v (contraction being positive):

$$\varepsilon_v = \frac{e_0 - e}{1+e_0} \tag{2.23}$$

By doing so, Equation (2.21) can be expressed in term of the incremental stress-strain relation:

$$d\varepsilon_v^e = \frac{dp'}{K_{ref}\left(p'/p'_{ref}\right)} \quad ; \quad K_{ref} = \frac{1+e_0}{\kappa} p'_{ref} \tag{2.24}$$

where K_{ref} is the bulk modulus at the unity mean effective stress p'_{ref}.

In order to extract the plastic component of the total evolution of void ratio in Equation (2.22), the swelling index κ must be subtracted from the compression index λ, leading to the definition of the plastic compressibility:

$$\beta = \frac{1+e_0}{\lambda - \kappa} \tag{2.25}$$

This parameter is used in the hardening equation, which describes the evolution of the critical pressure p'_{cr} with the generated volumetric plastic strain ε_v^p:

$$p'_{cr} = p'_{cr0} \exp\left(\beta \varepsilon_v^p\right) \tag{2.26}$$

where p'_{cr0} is the initial value of the critical pressure. Equation (2.26) is another way to express the evolution of the normally consolidation line (Equation (2.22)).

As far as the deviatoric stress is concerned, the shape of the yield limit differs according to the version of the Cam-Clay model used. The Original Cam-Clay model considers an almond-shaped yield limit (Schofield and Worth, 1968):

$$f = q - Mp'\left(1 - \ln\frac{p'}{p'_{cr}}\right) = 0 \tag{2.27}$$

where M is the slope of the critical state in the $\left(p' - q\right)$ plane. The corresponding associated flow rule is the following:

$$\left.\begin{array}{l} d\varepsilon_v^p = \lambda^p \dfrac{\partial g}{\partial p'} = \lambda^p \left(M - \dfrac{q}{p'}\right) \\ d\varepsilon_d^p = \lambda^p \dfrac{\partial g}{\partial q} = \lambda^p \end{array}\right\} \Rightarrow \frac{d\varepsilon_v^p}{d\varepsilon_d^p} = M - \frac{q}{p'} \tag{2.28}$$

$d\varepsilon_d^p$ is the increment of deviatoric strain, and g the plastic potential expressed below.

Actually, these expressions for the yield limit and dilatancy rule (Equations (2.27) and (2.28)) are based on two main assumptions.

(i) All the plastic work is dissipated entirely by friction (according to the assumption made by Taylor (1948)):

$$dW^p = p'\, d\varepsilon_v^p + q\, d\varepsilon_d^p = Mp' d\varepsilon_d^p \tag{2.29}$$

leading, after further rearrangement, to Equation (2.28) (Schofield and Worth, 1968). This flow can be integrated to find a plastic potential:

$$g = q - Mp'\left(1 - \ln\frac{p'}{p'_{cr}}\right) = 0 \tag{2.30}$$

(ii) The yield function follows from the associated flow rule assumption ($f = g$).

Equations (2.27) and (2.28) were modified by Roscoe and Burland (1968) by adopting a revised work equation to derive the yield function and plastic potential, leading to the elliptic yield function of the Modified Cam-Clay model:

$$f = g = q^2 - M^2 p'^2 \left(\frac{2p'_{cr}}{p'} - 1\right) = 0 \tag{2.31}$$

$$\left.\begin{aligned} d\varepsilon_v^p &= \lambda^p \frac{\partial g}{\partial p'} = \lambda^p p'\left(M^2 - \left(\frac{q}{p'}\right)^2\right) \\ d\varepsilon_d^p &= \lambda^p \frac{\partial g}{\partial q} = \lambda^p 2q \end{aligned}\right\} \Rightarrow \frac{d\varepsilon_v^p}{d\varepsilon_d^p} = \frac{M^2 - \left(\frac{q}{p'}\right)^2}{2\frac{q}{p'}} \tag{2.32}$$

2.2.2.2 *Application on triaxial compression paths*

The Cam-Clay model, aiming to unify the observed shearing of clay into a coherent framework, is mainly founded on the experimental observations of drained and undrained triaxial compression tests. The drained test aims to maintain a constant pore water pressure in the soil sample while the undrained samples are constrained to keep constant volume. In spite of the different effective stress paths followed by the drained and undrained tests, the line of failure points appears to be similar for both families of tests, for a given soil. This line is called the critical state line. For a better understanding of the main concept of Cam-Clay family model, the Original Cam-Clay prediction of both drained and undrained response of normally consolidated specimen submitted to triaxial compression loading is discussed below. In this section, the choice has been made to focus on the Original Cam-Clay, rather than the Modified Cam-Clay, because the model developed in this thesis is based on the original version.

First of all, the mechanical response of the specimen is governed by the Terzaghi's effective stress (Terzaghi, 1943):

$$\sigma_i' = \sigma_i - p_w \tag{2.33}$$

where σ_i' and σ_i are the ith components of the principal effective and total stress vector, respectively, while p_w is the pore water pressure.

On the triaxial compression path, the deviatoric stress and strain are respectively defined as:

$$q = \sigma_1' - \sigma_3' \tag{2.34}$$

$$\varepsilon_d = \frac{2}{3}(\varepsilon_1 - \varepsilon_3) \tag{2.35}$$

where σ_1' and ε_1 are the axial effective stress and axial strain and σ_3' and ε_3 are the radial effective stress and radial strain. The mean effective stress and the volumetric strain are

$$p' = \frac{1}{3}(\sigma_1' + 2\sigma_3') \tag{2.36}$$

$$\varepsilon_v = \varepsilon_1 + 2\varepsilon_3 \tag{2.37}$$

In the context of elasto-plasticity, the total strain increment $d\varepsilon_i$ is split into elastic and plastic components, $d\varepsilon_i^e$ and $d\varepsilon_i^p$, respectively:

$$d\varepsilon_i = d\varepsilon_i^e + d\varepsilon_i^p \tag{2.38}$$

The elastic strain component is governed by tensor of elasticity.

$$d\varepsilon_v^e = \frac{dp'}{K_{ref}\left(p'/p'_{ref}\right)} \tag{2.39}$$

$$d\varepsilon_d^e = \frac{dq}{3G} \tag{2.40}$$

where K_{ref} is the bulk modulus at unity mean effective stress p'_{ref} while G is the shear modulus.

Undrained triaxial compression tests

In undrained conditions, the soil specimen is distorted without any volume change ($d\varepsilon_v = d\varepsilon_v^e + d\varepsilon_v^p = 0$). The generated volumetric plastic strain must be exactly matched by a variation of the volumetric elastic strain, opposite in sign. The combination of Equations (2.28) and (2.39) gives:

$$\lambda^p\left(M - \frac{q}{p'}\right) = \frac{-dp'}{K_{ref}\left(p'/p'_{ref}\right)} \tag{2.41}$$

In this equation, the mean effective stress is obtained by subtracting the generated pore water pressure from the mean total stress (from Equation (2.33)):

$$p' = p - p_w \tag{2.42}$$

The plastic multiplier λ^p is determined by the consistency equation:

$$df = \frac{\partial f}{\partial q}dq + \frac{\partial f}{\partial p'}dp' + \frac{\partial f}{\partial \varepsilon_v^p}\frac{\partial \varepsilon_v^p}{\partial \lambda^p}\lambda^p = 0 \tag{2.43}$$

In the Cam-Clay prediction of a stress-controlled undrained triaxial compression test, the unknown is the pore water pressure generated, which can be determined by the combination of Equations (2.41), (2.42) and (2.43).

The effective stress path is obtained by subtracting the generated pore water pressure (Figure 2.5a) from the total stress path (slope of 1/3 in the $(p'-q)$ plane). As long as the deviatoric stress increases, the mean effective stress decreases, which increases the q/p' ratio. Consequently, the flow rule (Equation (2.28)) indicates that the $d\varepsilon_v^p/d\varepsilon_d^p$ ratio continuously decreases to zero on the critical state line $q = Mp'$. At that point, q remains constant because no more hardening is possible $(d\varepsilon_v^p = 0)$ while the deviatoric plastic strain increment is at a maximum. It yields the plateau in the deviatoric plane (Figure 2.5b). The constant volume of the specimen produces an horizontal line in the volumetric planes from the normally consolidated line (NSL) to the critical state line (CSL) (Figure 2.5c,d).

Several normally consolidated specimens isotropically compressed to a different initial value of $p' = p'_c$ (p'_c being the preconsolidation pressure) exhibit a similar shape for the $(q-\varepsilon_d)$ curves, but the specimens that were compressed to higher value of p' sustain a higher value of q. Nevertheless, in normalized stress references ($\left(p/p_c'\right)-\left(q/p_c'\right)$), all the curves join into one.

Drained triaxial compression tests

The drained triaxial compression test produces a linear stress path in the ($p'-q$) plane with $\frac{dq}{dp'}=3$. The initial stress point is on the yield limit, so the hardening process occurs from the beginning of the loading. For low deviatoric stress levels, the volumetric plastic strain is high with respect to the deviatoric plastic strain. However, as long as the deviatoric stress increases, the stress point approaches the critical state and the volumetric plastic strain decreases asymptotically to zero when it reaches the critical state line. The $d\varepsilon_v^p/d\varepsilon_d^p$ ratio governs the relation between the stress state and the plastic strain all along the triaxial compression tests (Figure 2.6) (Equation (2.28)). Similar to the undrained case, the curves of drained tests starting from different value of $p'=p_c'$ present a similar shape that join into one in the normalized stress reference.

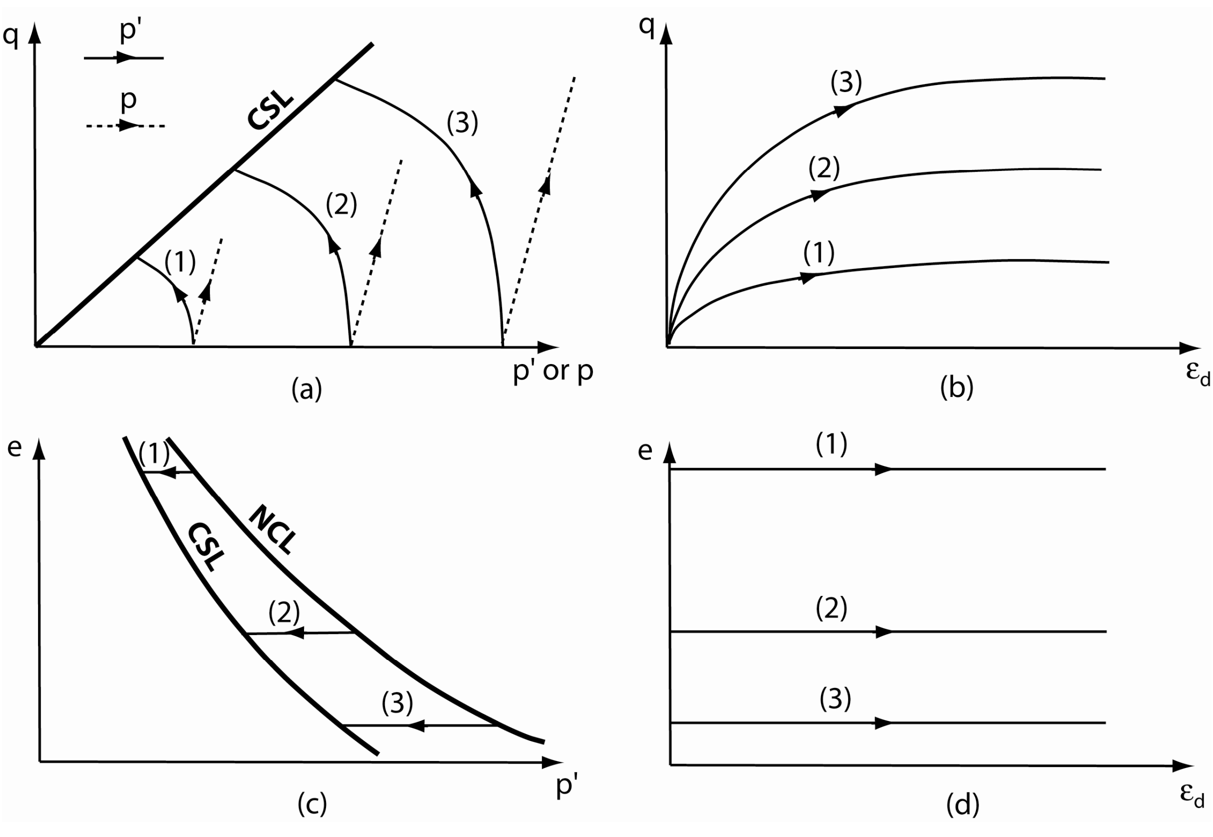

Figure 2.5: Stress-strain response in (p′ or p - q) (a), (q - ε_d) (b), (p′ - e) (c) and (e - ε_d) (d) planes for the undrained triaxial test on normally consolidated samples (from Atkinson and Bransby, 1978).

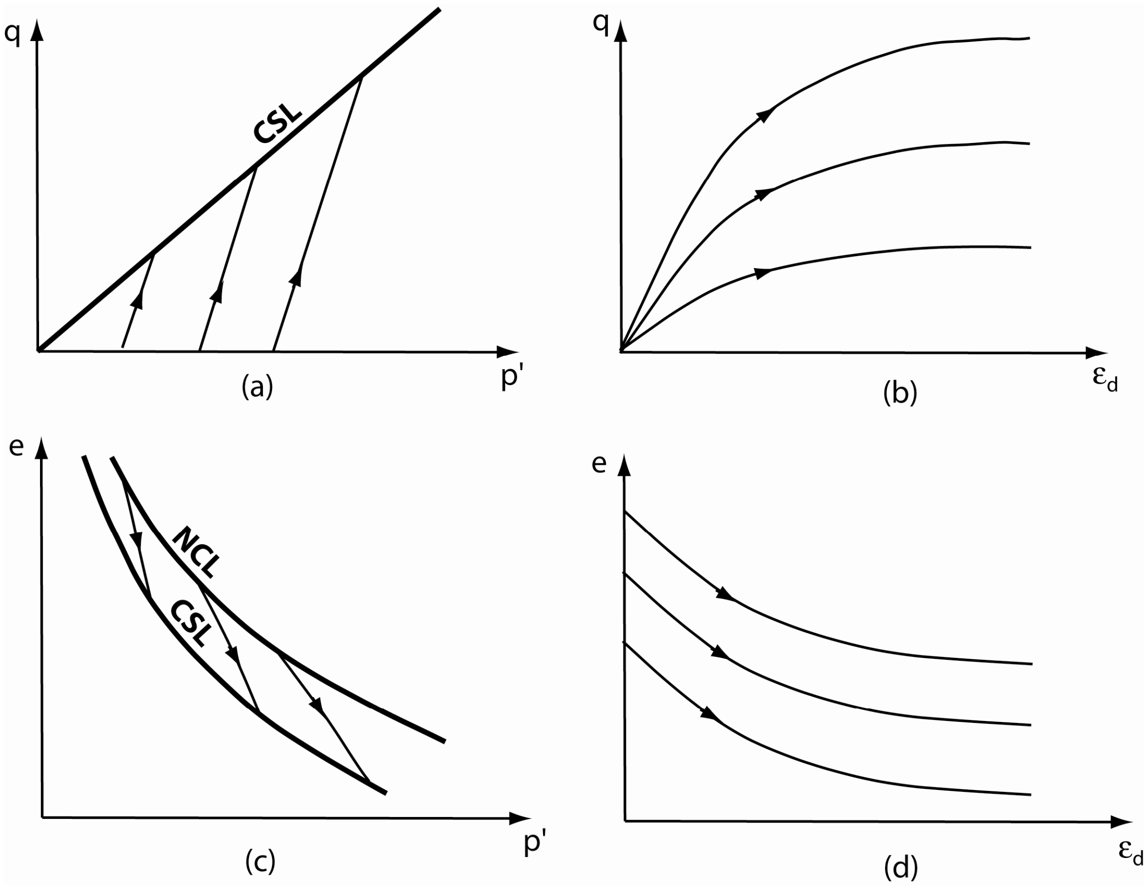

Figure 2.6: Stress-strain response in (p' - q) (a), (q - ε_d) (b), (p' - e) (c) and (e - ε_d) (d) for drained triaxial test on normally consolidated samples (from Atkinson and Bransby (1978)).

Discussions

Comparisons between drained and undrained behaviour clearly point out the key role of the volumetric plastic strain ε_v^p in the global behaviour of soils. In undrained conditions, ε_v^p is constrained by the constant volume of the specimen. The low hardening process producing volumetric plastic strain must compensate the volumetric elastic strain. Consequently, the volumetric behaviour is constrained, but the followed stress path depends on the elastic and plastic modulus (K_{ref} and β). On the contrary, in drained conditions, the stress path is fixed, but the volumetric behaviour depends on the elastic and plastic moduli.

For slightly overconsolidated soils, the first part of the response is purely elastic before reaching the yield limit. From that state, the behaviour is similar to the one explained in the case of normally consolidated soil. However, for heavily consolidated soils, the yield criterion can be reached on the left of the critical state line (for $q > Mp'$). In this case, in agreement with Equation (2.28), the induced volumetric plastic strain is negative, and the yielding process produces a softening of the material with shrinkage of the elastic domain.

2.2.2.3 *Limitations of the Cam-Clay models*

The Cam-Clay models were a great advance in constitutive modelling. They could account for the main experimental observations (reversible and irreversible volumetric strain under isotropic loadings, volumetric strain during shearing, coupling between volumetric changes and shear strength…), but several limitations exist. In particular, these models do not consider (i) the structural and stress-induced anisotropy, (ii) the mechanical response of soil under cyclic loading,

(iii) the viscous behaviour (time-dependent stress-strain response) and (iv) the behaviour of non-associated materials (Prevost and Popescu, 1996). Also, the Original Cam-Clay model predicts a sharp transition between elastic and plastic behaviour, and the peak behaviour of overconsolidated soils is badly reproduced. Finally, the hardening process upon isotropic loading predicts not only volumetric plastic strain but also deviatoric plastic strain which is incongruous. To remove some of these limitations, several more advanced models have been developed. Each of them has its own improvements but generally keeps the framework of the loading surface separating the elastic from the plastic domain and the critical state line. These advanced models can be classed into several families:

- Models based on the multi-surface theory (Mroz, 1967)
- Models based on the bounding surface theory (Dafalias and Popov, 1975, 1977; Krieg, 1975)
- Models based on the multi-mechanism theory (Koiter, 1960; Mandel, 1965)

In the next sections, these three types of models will be described in more detail. For each of the model families, reference is made to recent constitutive approaches. Those references are instances of possible applications but are obviously non-exhaustive. Yu (2006) addresses a comprehensive description of those different plasticity concepts.

In parallel to this framework using the concept of loading surfaces, some alternative theories of plasticity that do not require a prior yield criterion have been developed, such as the generalised plasticity (Zienkiewicz and Mroz, 1984) or the hypoplasticity (Green, 1956). However, those alternative approaches will not be detailed in the following.

Added to these mechanical basic models, several environmental solicitations or specific features of behaviour can be taken into account by keeping the same original model. Leroueil and Hight (2003) made a very complete overview of all these possible extensions. They address the influences of non-linear elasticity, of anisotropy, of strain rate and time, of temperature, of microstructure, of discontinuities, of soil water chemistry and of partially saturation.

2.2.3 Family of advanced models

2.2.3.1 *The multi-surface theory*

Mroz (1967) developed the multi-surface theory to represent the evolution of the plastic modulus during the hardening of metals. In this concept '*a configuration of surfaces of constant workhardening moduli is defined in the stress space*'. When the stress point reaches a surface, this surface is allowed to translate without changing form and orientation (kinematic hardening) and/or expand or contract (isotropic hardening) in the stress space. Each surface that is activated by the stress point cannot intersect but are tangent and push each other. The activation of the successive loading surfaces produces successive modifications of the hardening modulus. Thus, the stress-strain curve is approximated by a succession of linear segments of constant tangential moduli. This theory permits to model the material behaviour for complex loading paths, in particular for cyclic loadings. Figure 2.7 reproduces a typical prediction of the stress-strain response of a material subjected to a simple one-dimensional compression and extension.

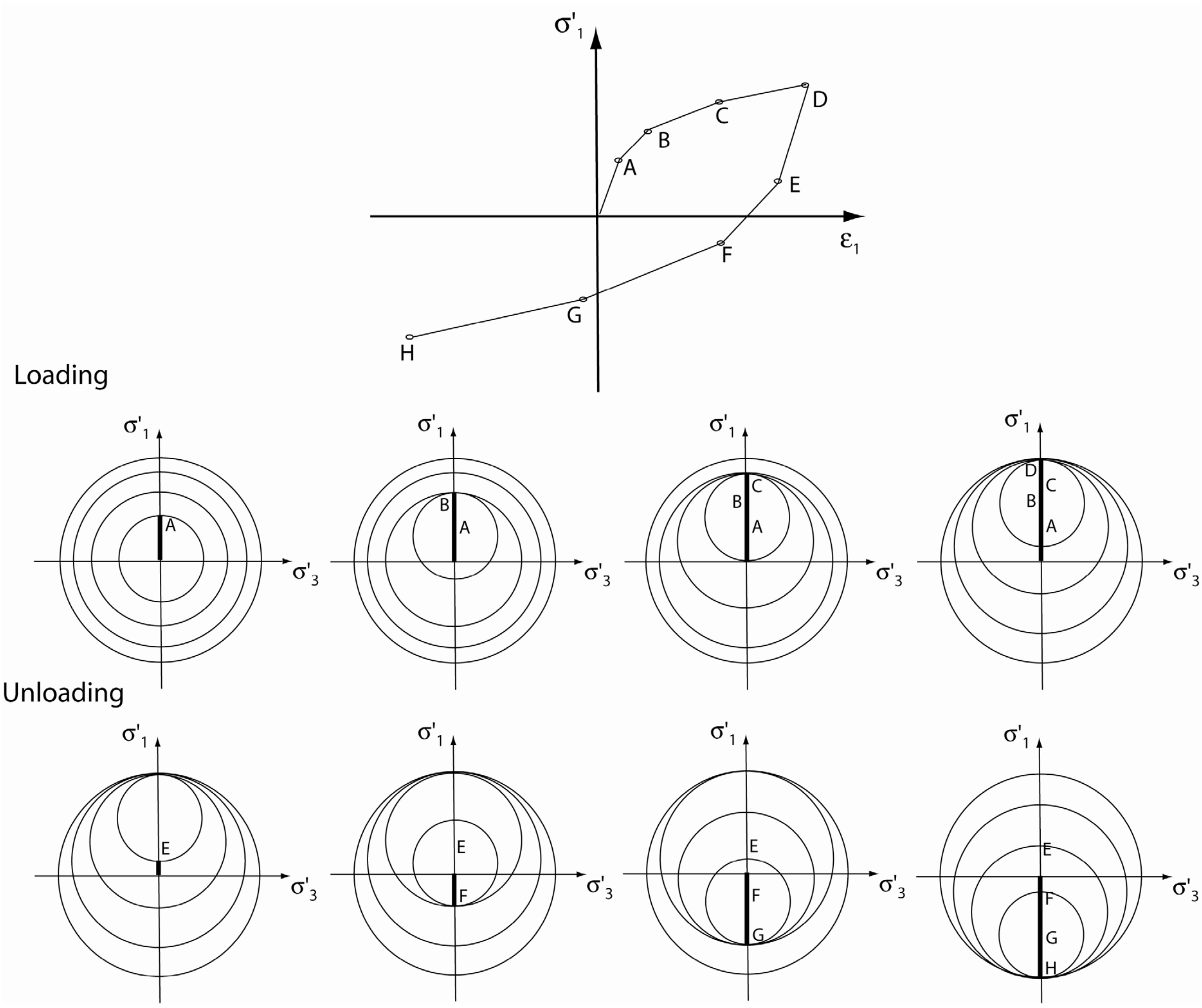

Figure 2.7: Concept of the multi-surface theory in the simplified case of uniaxial compression and extension (after Mroz, 1967). σ'_1 is the axial effective stress, σ'_3 the radial effective stress and ε_1 the axial strain.

This concept, initially used to describe metal behaviour, was adapted by the same authors and co-workers (Mroz et al., 1981) for soil behaviour by using the critical state concept. The basic idea of this adaptation is that the so-called consolidation surface, which is the biggest yield limit induced by the highest loading subjected by the materials, encloses one, several or an infinite numbers of nesting surfaces. All of these surfaces have the same elliptic shape. The first loading induces an isotropic hardening of the consolidation surface, which expands. At the first reverse-loading, a second surface is activated. This new surface can translate and/or expand (kinematic and/or isotropic hardening). At each change of direction, a new surface is activated (Figure 2.8). The consolidation surface grows only when the stress point reaches this yield limit. An additional parameter, which increases with accumulated deviatoric strain, is introduced to model the stiffness degradation during the course of cyclic loading (Mroz et al., 1981). Two versions of this model exist: a modified two surfaces model which is closer to the bounding surface theory expressed below (Mroz et al., 1978, 1979) and a model with an infinite number of nesting surfaces (Mroz et al., 1981).

At the same time, Prevost (1977) adapted the initial concept from Mroz (1967) for modelling the behaviour of undrained clays (in total stress reference). In this continuation, Prevost (1985) extended the model to simulate the behaviour of cohesive-frictional soils.

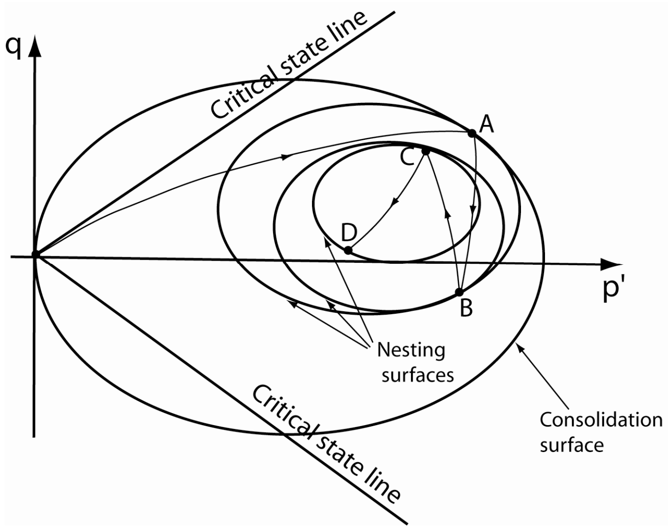

Figure 2.8: Schematic representation of the concept of multi-surface theory in the case of cyclic loading. Model with an infinite number of surfaces (Mroz et al., 1981).

2.2.3.2 *The bounding surface theory*

Dafalias and co-workers (Dafalias and Popov, 1975, 1977) and, in parallel, Krieg (1975) developed the concept of the "bounding surface" in stress space with the framework of critical state soil plasticity. For this thesis, the bounding surface concept to which we will refer is that of Dafalias and Herrmann (1980), for the explicitness and the conciseness of their explanation of the concept. The basic idea of this model family is that '*plastic deformation may occur when the stress state lies on or within the bounding surface, by allowing the plastic modulus to be a decreasing function of the distance of the stress state from a corresponding point on the bounding surface*'. This principle can easily be represented by Equation (2.44), illustrated by Figure 2.9:

$$H = H_b + \alpha \frac{\delta}{\delta_0 - \delta} \tag{2.44}$$

where H is the actual hardening modulus, H_b, the hardening modulus on the bounding surface, α, the hardening function, δ, the distance between actual stress point (σ'_{ij}) and associate stress point on the bounding surface ($\bar{\sigma}'_{ij}$) (O, σ'_{ij} and $\bar{\sigma}'_{ij}$ are on the same straight line) and δ_0, the distance between O and $\bar{\sigma}'_{ij}$ (Figure 2.9).

An extension of this model is the introduction of an elastic nucleus in which the mechanical response of the material is purely elastic ($H = \infty$).

The great advantage of this formulation is that '*any classical yield surface soil plasticity model* (such as the Cam-Clay models) *can be easily transformed into a corresponding and more flexible bounding surface model*'.

In recent years, several constitutive models based on the bounding surface theory have been proposed in order to capture some specific characteristic features of soils, such as particle crushing (Russell and Khalili, 2004), cyclic behaviour of soils (Hujeux, 1979; Yu et al. 2006; Khalili et al., 2005), unsaturated soil behaviour (Russell and Khalili, 2006), visco-plastic effects (Kaliakin and Dafalias, 1990) or anisotropy and progressive loss of initial structure of natural and reconstituted clay (Gajo and Muir Wood, 2001).

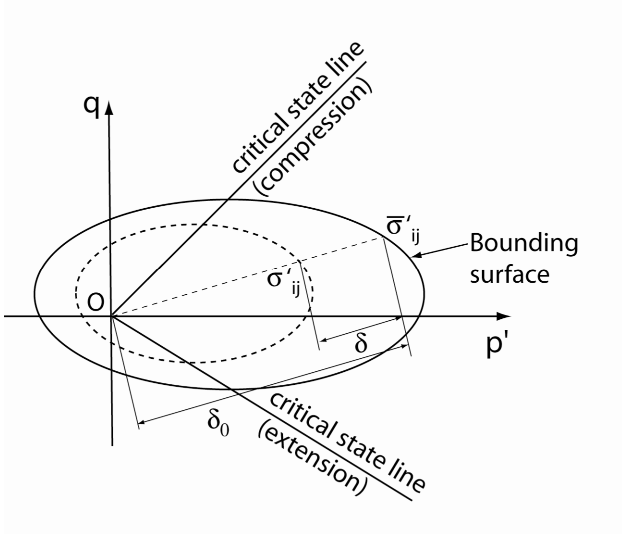

Figure 2.9: Schematic representation of the concept of a bounding surface (Dafalias and Herrmann, 1980).

2.2.3.3 *The multi-mechanism theory*

The multi-mechanism theory is based on the fact that plastic strains may occur according to several distinct planes. A mechanism of yielding can be defined for each plane. This multi-mechanism theory has been developed by Koiter (1960) who considered, as first approximation, mutually independent mechanisms of yielding. Further, Mandel (1965) extends the concept by considering non-independent mechanisms, which is more realistic. This extension argues that the shearing according to one loading direction may influence the shearing strength according to another loading direction. This theory was initially developed for metals. In this case, the direction of the shearing planes depends on the microstructure (at crystal-scale). Later, it was adapted for soils.

Hujeux (1979) (see also Aubry et al., 1982; Hujeux, 1985) developed a multi-mechanism model for soils recognizing that, in a three dimensional stress state, there are usually three distinct mechanisms of plasticity in three perpendicular planes. For each mechanism, the critical state concept can be applied and the stress state is defined by the coordinate of the Mohr circle $p'_k = \left(\sigma'_{ii} + \sigma'_{jj}\right)/2$ and the vector $s_k = \left(\left(\sigma'_{ii} + \sigma'_{jj}\right)/2, \sigma'_{ij}\right)$ (Figure 2.10). Besides these three deviatoric mechanisms (shearing), an isotropic mechanism can be added for the purely volumetric consolidation.

The global elastic domain is the intersection of the elastic domain relative to each mechanism. These four mechanisms are coupled via the critical pressure (p'_{cr}), which is common to all mechanisms. Aubry and Modaressi (1992) used such a framework to predict the conditions and directions of strain localization in soils while Modaressi and Laloui (1997) extended the Hujeux model to consider visco-thermo-plasticity.

A multi-laminate framework for developing constitutive models is also an efficient way to consider the inelastic deformations occurring in soils. This theory assumes that soil is made of an assemblage of perfectly fitting polyhedral blocks. Irreversible deformations occur due to sliding, separation/closing of the boundaries through an infinite number of oriented planes in space (Pietruszczak and Pande, 1987).

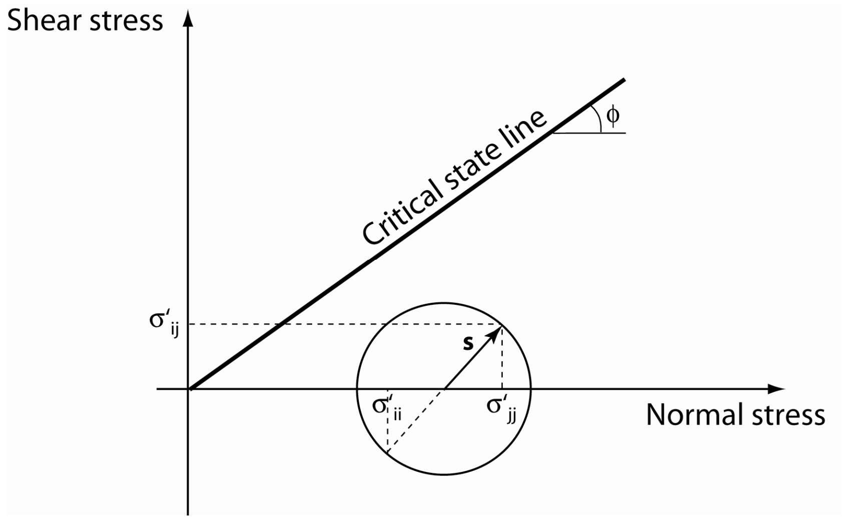

Figure 2.10: Multi-mechanism theory: Stress state in the (i,j) plane of one deviatoric mechanism (Hujeux, 1979).

In the same vein of multiple sources of energy dissipation, Sanchez et al. (2005) proposed a model for double structure materials. Contrary to Hujeux (1985), the multi-mechanism of plasticity does not arise from different elementary directions of loading but from the multi-scale aspect of the material. The macroscopic behaviour described by a conventional elasto-plastic model is coupled with a microstructural model accounting for the basic physical-chemical phenomena at the clay particle level. Multi-dissipative mechanisms can also encompass the combination of plasticity with elastic degradation (e.g. Hansen and Schreyer, 1994) or the coupled effect of mechanical and thermo-plasticity (Cui et al., 2000). Rizzi et al. (1996) developed a general setting for elasto-plastic model accounting for several possible active dissipation modes which constitutes a consistent framework to determine the tangent operators.

2.3 The ACMEG model

2.3.1 Introduction

Keeping in mind the main limitations of the Original Cam-Clay model to describe the real stress-strain behaviour of clayey soils, many research groups improved this original model in order to obtain a constitutive tool able to predict soil response upon various mechanical loading encountered in geotechnical applications.

At the present stage, considering isothermal and saturated conditions, the main features that are to be reproduced by the model, which is developed in this thesis, can be divided into two main aspects: (i) the volumetric response upon isotropic loadings and (ii) the stress-strain behaviour upon soil distortions (e.g deviatoric loading). Both parts of the soil behaviour require considering several specific behavioural features.

(i) Under isotropic stress conditions, the constitutive model must address:

- The effect of stress level on the elastic rigidity of soil.
- The plastic volumetric strain generated when the preconsolidation pressure is surpassed.
- The progressive transition between the reversible elastic and the irreversible elasto-plastic responses.

- The existence of an elastic nucleus in the stress space in which the produced strains are fully reversible.
- The volumetric response of soil upon several isotropic loading-unloading-reloading cycles (without accommodations effects).

(ii) Under deviatoric stress conditions, the following points must be considered:

- The effect of stress level on the elastic rigidity of soil.
- The unique critical state reached upon various distortional paths.
- The hardening process occurring from the elastic domain to the critical state of normally or slightly overconsolidated soils.
- The peak behaviour observed on distortion paths of highly overconsolidated soils.
- The progressive transition between the reversible responses and the full mobilization of the hardening or softening processes.
- The existence of an elastic nucleus in the stress space in which the produced strains are fully reversible.
- The accurate volumetric response upon distortional paths which can involve a non-associated flow rule.

In order to satisfy all of these points, it is required to introduce some advanced modelling development in the basic Original Cam-Clay model. The model presented in this chapter, ACMEG, which stands for "Advanced Constitutive Model for Environmental Geomechanics", will be the constitutive base on which further developments dealing with non-isothermal and unsaturated conditions will be established. Consequently, this basic constitutive model must be robust and straightforward in order to make further developments easy. Regarding to the Original Cam-Clay, the successive improvements of the model are detailed in the following sections.

The successive improvements of the isothermal model are founded on several constitutive works, all built upon the critical state concept. In particular, the constitutive developments in this chapter are closely related to the works of Hujeux and co-workers (Hujeux, 1979; Hajal, 1984; Lassoudière, 1984; Michalski and Rahma, 1989; Piccuezzu, 1991). Those improvements also take place in the continuation of the constitutive developments of Modaressi and Laloui (1997) and Laloui and Cekerevac (2008).

2.3.2 The successive improvements

2.3.2.1 *Non-linear elasticity*

In the elastic domain (e.g. in the initial range of loading of overconsolidated soils and during unloading and reloading), soil undergoes reversible strains which appear strongly non-linear because of a strong dependence of the elastic moduli on the mean effective stress. The clearer evidence of this non-linearity is the logarithmic stress-strain relationship of the swelling line considered in the Cam-Clay model upon isotropic or oedometric unloading (Figure 2.4). As shown previously (Equation (2.24)), to consider this behavioural feature, the following expression of the bulk modulus is needed:

$$K = K_{ref} \frac{p'}{p'_{ref}} \tag{2.45}$$

where K_{ref} is the bulk modulus at the unity mean effective stress p'_{ref}. Nevertheless, this expression may be insufficient to reproduce some behaviours of stiff clay, which exhibits elasticity closer to linear (such as metals) than logarithmic (such as soft soils). In order to overcome this limitation, an additional elastic exponent n^e can be added, which governs the role of the mean effective stress on the elastic stiffness (Hujeux, 1985):

$$K = K_{ref}\left(\frac{p'}{p'_{ref}}\right)^{n^e} \tag{2.46}$$

As far as the elastic stiffness upon distortional path is concerned, the shear modulus is also strongly affected by the mean effective stress. The most evident form for the shear modulus expression is similar to Equation (2.46) with the same elastic exponent n^e:

$$G = G_{ref}\left(\frac{p'}{p'_{ref}}\right)^{n^e} \tag{2.47}$$

where G_{ref} is the bulk modulus at the unity mean effective stress p'_{ref}. Expressions (2.46) and (2.47) have been adopted in the improved version of the model. However, a rigorous thermodynamical analysis of those elastic moduli may prove that this non-linear elasticity is non-conservative in terms of the work input. Indeed, upon any purely elastic loading-unloading path for which the final stress state corresponds to the initial one, the total work input must be null (e.g. the stored energy during loading must be totally released upon unloading). The use of the proposed elastic moduli does not guarantee such a conservation condition. The dependence of G on the mean effective stress must imply a dependence of K on the deviatoric stress (Hueckel et al., 1992; Wroth, 1971). Since this coupling effect remains significantly less important in practice, it has been neglected in the development of the present model. This aims also to keep the elastic part of the model simple enough to be used easily.

2.3.2.2 *The multi-mechanism theory*

The Original Cam-Clay model suffers from some inconsistencies in the prediction of the behaviour of normally consolidated soils. An isotropic loading should produce only volumetric strain while the Original Cam-Clay predicts a deviatoric component of the plastic strain. In this thesis, when dealing with non-isothermal and unsaturated conditions, the isotropic behaviour will play a major role in the global mechanical response of the soil for various temperature and suction paths. It clearly points to a need to improve the model capability to predict accurate behaviour upon isotropic loadings. In agreement with the work of Hujeux (1979), an isotropic yielding mechanism is added to the Original Cam-Clay deviatoric yielding mechanism:

$$f_{iso} = p' - p'_c = 0 \tag{2.48}$$

where p'_c is the preconsolidation pressure which evolves with the generated volumetric plastic strain ε_v^p:

$$p'_c = p'_{c0}\exp\left(\beta\varepsilon_v^p\right) \tag{2.49}$$

with p'_{c0} being the initial preconsolidation pressure and β the plastic compressibility.

This second mechanism is coupled to the original one through their unique hardening variable, the volumetric plastic strain ε_v^p. Thus, the theory of multi-mechanism plasticity must be introduced in order to deal with the interconnection between both mechanisms of plasticity (Mandel, 1965). The two yield functions define a closed domain in the effective stress space inside which the behaviour of the material is reversible. If the volumetric plastic strain increases due to the activation of one of the mechanisms, the yield limit of the other mechanism will also move. When the two mechanisms are activated simultaneously, two consistency conditions must be met leading to two interrelated plastic multipliers (λ_{iso}^p and λ_{dev}^p). Thus, the total increment of volumetric plastic strain, $d\varepsilon_v^p$ is the sum of the increment of volumetric plastic strain induced by each mechanism ($d\varepsilon_v^{p,iso}$ for the isotropic mechanism and $d\varepsilon_v^{p,dev}$ for the deviatoric one):

$$d\varepsilon_v^p = d\varepsilon_v^{p,iso} + d\varepsilon_v^{p,dev} \tag{2.50}$$

In agreement with the multi-mechanism theory (Rizzi et al., 1996), the generic form of the two related consistency conditions is:

$$\begin{cases} df_{iso} = \dfrac{\partial f_{iso}}{\partial \sigma'_{ij}} d\sigma'_{ij} + \dfrac{\partial f_{iso}}{\partial \varepsilon_v^p}\dfrac{\partial \varepsilon_v^p}{\partial \lambda_{iso}^p}\lambda_{iso}^p + \dfrac{\partial f_{iso}}{\partial \varepsilon_v^p}\dfrac{\partial \varepsilon_v^p}{\partial \lambda_{dev}^p}\lambda_{dev}^p = 0 \\ df_{dev} = \dfrac{\partial f_{dev}}{\partial \sigma'_{ij}} d\sigma'_{ij} + \dfrac{\partial f_{dev}}{\partial \varepsilon_v^p}\dfrac{\partial \varepsilon_v^p}{\partial \lambda_{iso}^p}\lambda_{iso}^p + \dfrac{\partial f_{dev}}{\partial \varepsilon_v^p}\dfrac{\partial \varepsilon_v^p}{\partial \lambda_{dev}^p}\lambda_{dev}^p = 0 \end{cases} \tag{2.51}$$

where f_{dev} is the yield function of the Original Cam-Clay. At this first stage of improvement, the elastic domain is limited by the almond-shaped Original Cam-Clay yield locus (Equation (2.27)) cut by an isotropic yield limit (Figure 2.11).

2.3.2.3 *Ratio between critical pressure and preconsolidation pressure*

At a given void ratio, the Original Cam-Clay assumes that the ratio between the preconsolidation pressure p'_c and the critical pressure p'_{cr} is equal to 2.718, while the elliptic shape of the Modified Cam-Clay assumes that the critical pressure is the half of the preconsolidation pressure. In practice, this value may vary depending on the soil type. The introduction of the isotropic mechanism enables to impose freely this ratio between 1 and 2.718 through an additional parameter d (Hujeux, 1979):

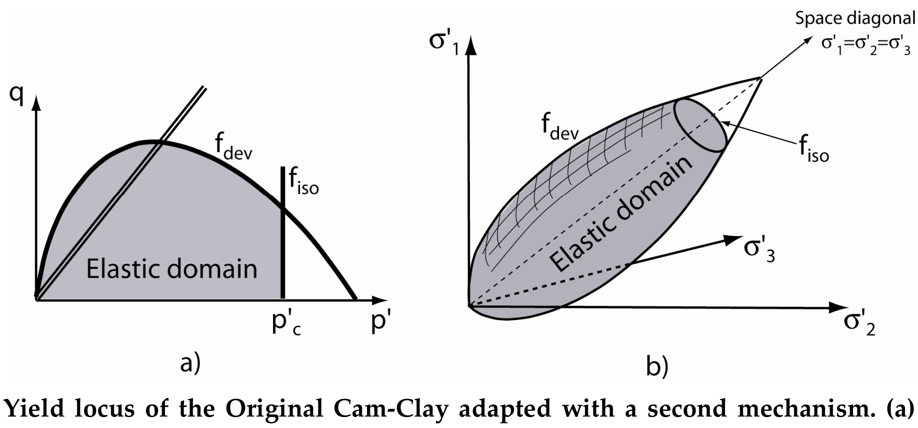

Figure 2.11: Yield locus of the Original Cam-Clay adapted with a second mechanism. (a) View in the ($p' - q$) plane and (b) the principal stress space (from Hujeux (1979) and Michalski and Rahma (1989)).

$$d = \frac{p'_c}{p'_{cr}} \tag{2.52}$$

Thus, the deviatoric yield limit (Equation (2.27)) can be expressed with respect to the preconsolidation pressure instead of the critical pressure:

$$f_{dev} = q - Mp'\left(1 - \ln\frac{d\ p'}{p'_c}\right) = 0 \tag{2.53}$$

2.3.2.4 *Behaviour of heavily overconsolidated soils*

The shape of the Original Cam-Clay yield locus significantly overestimates peak stresses on the left side of the critical state line (i.e. for heavily overconsolidated soils). To overcome this limitation, many models used an alternative yield limit on the right side of the critical state, such as the Hvorslev surface, which is a straight line in the deviatoric plane. However, the two separated yield surfaces for hardening (on the right side of the critical state line) and softening (on the left side of critical state line) produce a discontinuity in the yield surface that may cause significance numerical difficulties (Gens and Potts, 1988; Yu, 2006).

In order to avoid such problems linked to the addition of a new failure limit, a more efficient way to proceed is to adapt the existing Original Cam-Clay yield limit. Hujeux (1985) proposed to include a parameter b to control the shape of the yield limit:

$$f_{dev} = q - Mp'\left(1 - b\ln\frac{d\ p'}{p'_c}\right) = 0 \tag{2.54}$$

The expression is similar to the failure locus proposed by Nova and Wood (1979) with $b = \beta^*/M$, β^* being a parameter of the Nova-Wood model. The b parameter varies from 0 (corresponding to a Mohr-Coulomb criterion) to 1 (for the Original Cam-Clay model) (Figure 2.12). As stated by Hujeux (1985), the role of this parameter is particularly important for highly overconsolidated soils. Generally, the value of b is lower for sand than for clays.

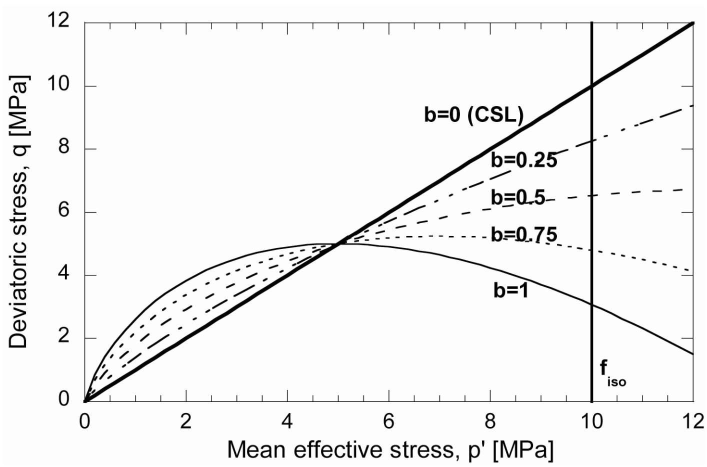

Figure 2.12: Example of the deviatoric yield limit shaped for different values of the parameter b. p'c = 10 MPa, d = 2; M = 1 (from Hajal (1984)).

2.3.2.5 *Plasticity inside the external yield limits*

Typical isotropic compression experimental results on a remoulded soil, as shown in Figure 2.13, clearly exhibit progressive mobilization of the plasticity before reaching the virgin consolidation line. Therefore, even before surpassing the isotropic yield limit (i.e. the preconsolidation pressure), the soil undergoes generally irreversible strains upon isotropic loading. This behavioural feature can have a major effect on the response of an overconsolidated soils submitted to loading-unloading cycles. In order to reproduce this effect, the model needs to be improved by means of an additional constitutive artifice. In Section 2.2.3 of this chapter, two main theories are presented in order to catch the progressive loss of stiffness induced by plasticity inside the external yield limit (i.e. the multi-surface and the bounding surface theories). As stated by Dafalias and Herrmann (1980), *'the main value of the bounding surface formulation is that any sound classical yield surface soil plasticity model can be easily transformed into a corresponding and more flexible bounding surface model'*. In that sense, the isotropic yielding mechanism has been enhanced by considering such a bounding surface concept. The isotropic yield limit is modified as follows (Hujeux, 1979):

$$f_{iso} = p' - p'_c \, r_{iso} = 0 \tag{2.55}$$

where r_{iso} is the degree of mobilization of the isotropic mechanism. During loading, r_{iso} is a hyperbolic function of the volumetric plastic strain induced by the isotropic mechanism, $\varepsilon_v^{p,iso}$:

$$r_{iso} = r_{iso}^e + \frac{\varepsilon_v^{p,iso}}{c + \varepsilon_v^{p,iso}} \quad \text{and} \quad dr_{iso} = \frac{(1 - r_{iso})^2}{c} d\varepsilon_v^{p,iso} \tag{2.56}$$

where c is a material parameter and r_{iso}^e the radius of the isotropic elastic nuclei inside which the produced strains are fully reversible. During unloading the behaviour is purely elastic.

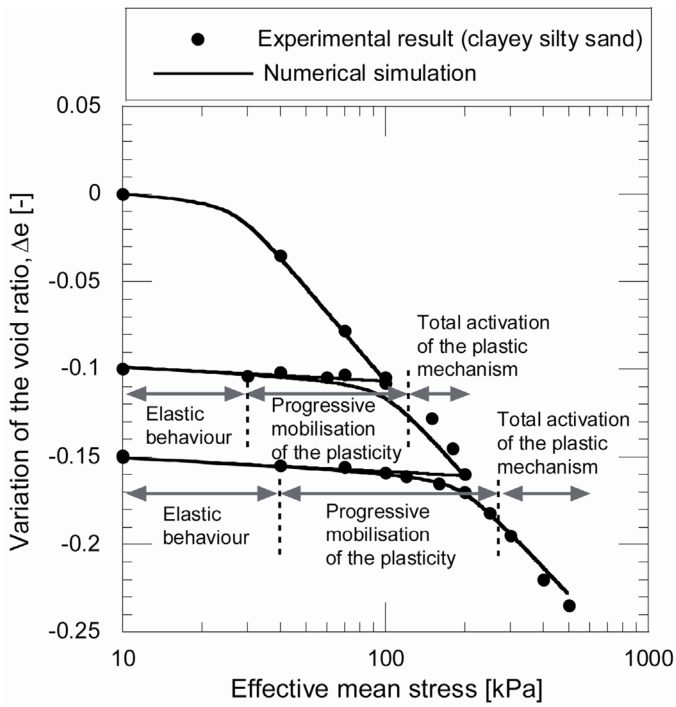

Figure 2.13: Illustration of the bounding surface theory. Isotropic compression test. Comparison of experimental results (Jamin, 2003) and a numerical simulation using the ACMEG model.

Under distortional paths, the Original Cam-Clay mechanism also predicts a too sharp transition between elastic and plastic behaviours. In the same way as the isotropic mechanism, the deviatoric mechanism needs to be enhanced by a progressive plasticity process inside the external deviatoric yield limit. Hujeux (1979) proposed to introduce an additional hardening variable, the deviatoric plastic strain ε_d^p, governing the evolution of the degree of mobilization of the deviatoric mechanism r_{dev}. The deviatoric yield limit is modified as follows:

$$f_{dev} = q - Mp'\left(1 - b\ln\frac{d\,p'}{p'_c}\right)r_{dev} = 0 \tag{2.57}$$

During deviatoric loading, r_{dev} is a hyperbolic function of the deviatoric plastic strain:

$$r_{dev} = r_{dev}^e + \frac{\varepsilon_d^p}{a + \varepsilon_d^{p,dev}} \quad \text{and} \quad dr_{dev} = \frac{(1 - r_{dev})^2}{a}\, d\varepsilon_d^p \tag{2.58}$$

where a is a material parameter and r_{dev}^e the radius of the deviatoric elastic nuclei inside which the strains produced are fully reversible. Thus, it introduces a double deviatoric hardening process that may occur not only due to the volumetric plastic strain but also through the deviatoric plastic strain. Hujeux (1979) demonstrated the drastic improvement of the prediction of triaxial tests due to this new progressive hardening process.

2.3.2.6 *Response upon several isotropic loading-unloading-reloading cycles*

In order to enable the progressive plasticity upon each isotropic reloading, as shown in Figure 2.13, r_{iso} must not only evolve properly during loading (Equation (2.56)), but must also be re-initialized during unloading. Thus, during unloading, r_{iso} decreases to follow the decrease in the mean effective stress, p', and at reloading, at the moment of change of direction of solicitation (unloading – reloading), r_{iso} is adjusted to keep a constant defined elastic nuclei (r_{iso}^e):

$$r_{iso} = r_{iso}^e + \frac{p'_{cyc}}{p'_c} + \frac{\varepsilon_v^{p,cyc,iso}}{c + \varepsilon_v^{p,cyc,iso}} \leq 1 \tag{2.59}$$

where p'_{cyc} is the effective mean stress at the last change of direction of solicitation (unloading (i.e. decrease of p'_c) – reloading (i.e. increase of p'_c)) and $\varepsilon_v^{p,cyc,iso}$ is the volumetric plastic strain produced by the isotropic mechanism since this change of direction of solicitation. This process is illustrated in Figure 2.14.

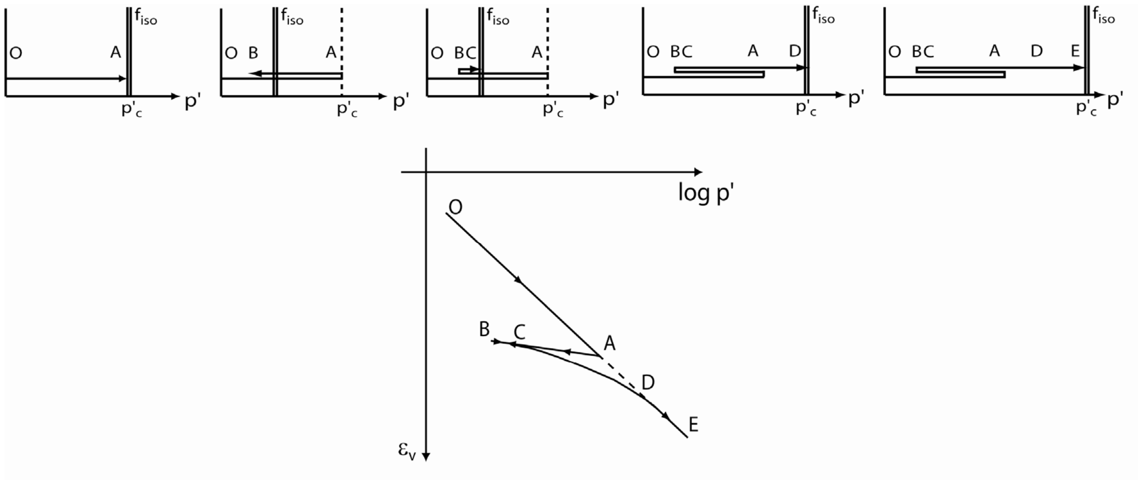

Figure 2.14: Schematic representation of the isotropic plastic mechanism behaviour over a mechanical isotropic loading-unloading-reloading cycle.

During the first loading (O-A, the initial yield limit being in O), conventional hardening of the yield surface occurs ($r_{iso} = 1$; $d\varepsilon_v^p > 0$, p'_c increases following Equation (2.49)). The unloading (A-B) takes place elastically and so does not produce plastic strain ($d\varepsilon_v^p = 0$, p'_c remains constant). The first part of the reloading (B-C) takes place inside the elastic nuclei ($r_{iso} = r_{iso}^e + \dfrac{p'_{cyc}}{p'_c}$; $d\varepsilon_v^p = 0$, p'_c remains constant). During the second part of the reloading (C-D), the yield surface is activated, and plastic strains are produced to keep the yield limit on the stress point; r_{iso} increases according to Equation (2.59) and produces a shift of the yield limit. When p'_c is reached, the conventional hardening of the yield limit occurs again (D-E) ($r_{iso} = 1$; $d\varepsilon_v^p > 0$, p'_c increases). Thus, the preconsolidation pressure can be seen as the pressure for which the isotropic mechanism is totally active. Indeed, when $p' = p'_c$ in Equation (2.55), the degree of mobilisation of the isotropic mechanism r_{iso} is equal to one.

2.3.2.7 *Flow rules*

As far as the isotropic mechanism is concerned, the flow rule must remain associated. Indeed, this plastic mechanism must produce only volumetric plastic strain. This requires that the normal unit vector of the isotropic plastic potential must be oriented in the direction of the isotropic axis, which is also the case of the isotropic yield limit ($g_{iso} = f_{iso}$).

If the Original Cam-Clay expression for dilatancy is kept (Equation (2.28)), the modification of the deviatoric yield function by the introduction of the b parameter produces a non-associated flow rule. Indeed, even if the plastic potential of the deviatoric mechanism g_{dev} is unchanged, the expression of the yield locus f_{dev} is modified. Thus, f_{dev} and g_{dev} do not coincide anymore. However, many studies prove that the Original Cam-Clay plastic potential disagrees with experimental observations. The main limitation is related to the discontinuity of the plastic potential at $q = 0$ (i.e. under normally consolidated conditions) producing non-zero shear strains under isotropic stress changes (Gens and Potts, 1988). In the second version of the Cam-Clay model, this obstacle was overcome with the elliptic shape of the modified Cam-Clay model. In the present case, which retains the Original Cam-Clay basis, this limitation is of no account due to the isotropic mechanism, which cuts off the deviatoric yield limit for low values of q/p'.

Nevertheless, for highly overconsolidated soils, the Original Cam-Clay plastic potential also fails to predict the volumetric changes during plastic straining accurately. Thus, it seems that one additional parameter must be introduced in order to catch the various volumetric responses depending on the soil type. Following the proposal of Simpson (1973) and resumed by Nova and Wood (1979), the plastic dilatancy can take the following form:

$$\frac{d\varepsilon_v^p}{d\varepsilon_d^p} = \alpha\left(M - \frac{q}{p'}\right) \tag{2.60}$$

where the additional parameter α is a positive constant that modifies the dilatancy rule of the Original Cam-Clay model. After some algebra, the expression of the plastic potential is (Nova and Wood, 1979):

$$g_{dev} = q - \frac{\alpha}{\alpha - 1} Mp'\left[1 - \frac{1}{\alpha}\left(\frac{d\,p'}{p'_c}\right)^{\alpha-1}\right] = 0 \tag{2.61}$$

It can be proven that

$$\lim_{\alpha\to 1}\left[q - \frac{\alpha}{\alpha - 1} Mp'\left[1 - \frac{1}{\alpha}\left(\frac{d\,p'}{p'_c}\right)^{\alpha-1}\right]\right] = q - Mp'\left(1 - \ln\frac{d\,p'}{p'_c}\right) \tag{2.62}$$

Consequently, if $\alpha = b = 1$, the flow rule of the deviatoric mechanism is associated (i.e. $f_{dev} = g_{dev}$), while in any other configuration it is not. Moreover, if $\alpha = b = 1$ and $d = 2.71$, the deviatoric mechanism corresponds to the Original Cam-Clay yielding mechanism.

2.3.3 The constitutive relations

Starting from the Original Cam-Clay model, the ACMEG model is the outcome of the different improvements detailed in the previous section. Here, the constitutive equations are summarized in a concise way. References and physical interpretations of each relation can be found in Section 2.3.2. Within the small strain assumptions, the concept of loading surface allows the total strain increment vector, $\mathbf{d\varepsilon}$, to be split into elastic, $\mathbf{d\varepsilon^e}$, and plastic, $\mathbf{d\varepsilon^p}$, components:

$$d\varepsilon_{ij} = d\varepsilon_{ij}^e + d\varepsilon_{ij}^p \tag{2.63}$$

2.3.3.1 *Non linear elasticity*

$d\varepsilon_{ij}^e$ is the (i,j) strain increment component that does not modify the hardening state of the material. In the following, it will be understood that the generic subscript notation of the strain component ε_{ij} includes the shear strain components γ_{12}, γ_{13} and γ_{23}, which are the conjugated variables of the shear stress components σ'_{12}, σ'_{13} and σ'_{23}:

$$\boldsymbol{\varepsilon} = \begin{pmatrix}\varepsilon_{11} & \varepsilon_{22} & \varepsilon_{33} & \gamma_{12} & \gamma_{13} & \gamma_{23}\end{pmatrix}^T \tag{2.64}$$

$$\boldsymbol{\sigma}' = \begin{pmatrix}\sigma'_{11} & \sigma'_{22} & \sigma'_{33} & \sigma'_{12} & \sigma'_{13} & \sigma'_{23}\end{pmatrix}^T \tag{2.65}$$

Due to the reversible process, the elastic constitutive part is not affected by the loading history of the material and is entirely defined by:

$$d\varepsilon_{ij}^{e} = E_{ijkl}^{-1} d\sigma'_{kl} \tag{2.66}$$

where contraction is taken as positive. E_{ijkl} is the mechanical elastic tensor:

$$\mathbf{E} = \begin{bmatrix} K+\frac{4}{3}G & K-\frac{2}{3}G & K-\frac{2}{3}G & 0 & 0 & 0 \\ & K+\frac{4}{3}G & K-\frac{2}{3}G & 0 & 0 & 0 \\ & & K+\frac{4}{3}G & 0 & 0 & 0 \\ & Sym & & G & 0 & 0 \\ & & & & G & 0 \\ & & & & & G \end{bmatrix} \tag{2.67}$$

The hypo-elastic moduli depend on the mean effective stress:

$$K = K_{ref}\left(\frac{p'}{p'_{ref}}\right)^{n^e} \quad ; \quad G = G_{ref}\left(\frac{p'}{p'_{ref}}\right)^{n^e} \tag{2.68}$$

where K_{ref} and G_{ref} are the reference bulk and shear elastic moduli, respectively, at the reference mean effective stress, p'_{ref} ; n^e is a material parameter.

The volumetric and deviatoric parts of the elastic strain increment are, respectively:

$$d\varepsilon_v^e = \frac{dp'}{K} \quad ; \quad d\varepsilon_d^e = \frac{dq}{3G} \tag{2.69}$$

where ε_v^e is the volumetric elastic strain and ε_d^e the deviatoric elastic strain. q and p' are the deviatoric and effective mean stress, respectively.

2.3.3.2 *Plastic mechanisms*

The feature of the present model is that the total strain increment induced by plasticity (hardening of the material) is a linear combination of two irreversible processes: an isotropic as well as a deviatoric process. Therefore, the total plastic strain increment, $d\varepsilon_{ij}^{p}$, is the sum of "partial" plastic strain increments, induced by the isotropic and the deviatoric mechanisms, $d\varepsilon_{ij}^{p,iso}$ and $d\varepsilon_{ij}^{p,dev}$, respectively:

$$d\varepsilon_{ij}^{p} = d\varepsilon_{ij}^{p,iso} + d\varepsilon_{ij}^{p,dev} \tag{2.70}$$

In the following sections, yield functions, plastic potentials and the procedure to determine plastic multipliers are introduced for each mechanism.

Isotropic plastic mechanism

The yield limit, f_{iso}, of the isotropic plastic mechanism is expressed by:

$$f_{iso} = p' - p'_c \, r_{iso} \tag{2.71}$$

where r_{iso} is the degree of plastification (mobilised hardening) of the isotropic yield limit enabling a progressive evolution of the isotropic yield limit during loading and a partial comeback of this limit during unloading. During loading, r_{iso} is a hyperbolic function of the plastic volumetric strain induced by the isotropic mechanism, $\varepsilon_v^{p,iso}$ (Hujeux 1979):

$$r_{iso} = r_{iso}^e + \frac{\varepsilon_v^{p,iso}}{c + \varepsilon_v^{p,iso}} \quad \text{and} \quad dr_{iso} = \frac{(1 - r_{iso})^2}{c} d\varepsilon_v^{p,iso} \tag{2.72}$$

where c is a material parameter.

During unloading, r_{iso} decreases to follow the decrease of effective mean pressure, p', and at reloading, at the moment of change of direction of solicitation (unloading – reloading), r_{iso} is adjusted to keep a defined elastic nuclei (r_{iso}^e):

$$r_{iso} = r_{iso}^e + \frac{p'_{cyc}}{p'_c} + \frac{\varepsilon_v^{p,cyc,iso}}{c + \varepsilon_v^{p,cyc,iso}} \leq 1 \tag{2.73}$$

where p'_{cyc} is the effective mean stress at the last change of direction of solicitation (unloading – reloading) and $\varepsilon_v^{p,cyc,iso}$ is the volumetric plastic strain produced by the isotropic mechanism since the change of direction of solicitation.

The preconsolidation pressure, p'_c, is expressed as a function of the volumetric plastic strain ε_v^p:

$$p'_c = p'_{c0} \exp\left(\beta \varepsilon_v^p\right) \tag{2.74}$$

p'_{c0} is the value of the initial preconsolidation pressure, and β is the plastic compressibility modulus (the slope of the linear function $\varepsilon_v^p - \log p'_c$).

The flow rule is associated ($f_{iso} = g_{iso}$):

$$d\varepsilon_{ii}^{p,iso} = \lambda_{iso}^p \frac{\partial g_{iso}}{\partial \sigma'_{ii}} = \frac{\lambda_{iso}^p}{3} \tag{2.75}$$

The plastic multiplier, λ_{iso}^p, is determined using Prager's consistency equation (Prager, 1949), as presented below.

Deviatoric plastic mechanism

The expression of the deviatoric yield limit is:

$$f_{dev} = q - Mp'\left(1 - b \ln \frac{d\, p'}{p'_c}\right) r_{dev} = 0 \tag{2.76}$$

where b is a material parameter defining the shape of the deviatoric yield limit, and d is the ratio between the preconsolidation pressure, p'_c, and the critical pressure, p'_{cr}. M is the slope of the critical state line in the ($p' - q$) plane:

$$M = \frac{6 \sin \phi'}{3 - \sin \phi'} \tag{2.77}$$

where ϕ' is the friction angle at critical state.

r_{dev}, in the same way as for the isotropic mechanism, is the degree of plastification of the deviatoric mechanism and also enables a progressive evolution of the deviatoric yield limit during loading:

$$r_{dev} = r^e_{dev} + \frac{\varepsilon^p_d}{a + \varepsilon^p_d} \quad \text{and} \quad dr_{dev} = \frac{(1 - r_{dev})^2}{a} d\varepsilon^p_d \tag{2.78}$$

where r^e_{dev} and a are material parameters defining the size of the elastic nuclei of the deviatoric mechanism and the evolution of r_{dev}, respectively, while ε^p_d is the deviatoric plastic strain.

Assuming the following dilatancy rules,

$$\frac{d\varepsilon^p_v}{d\varepsilon^p_d} = \alpha\left(M - \frac{q}{p'}\right) \tag{2.79}$$

the plastic potential can be expressed as:

$$g_{dev} = q - \frac{\alpha}{\alpha - 1} Mp'\left[1 - \frac{1}{\alpha}\left(\frac{d\, p'}{p'_c}\right)^{\alpha - 1}\right] = 0 \tag{2.80}$$

Consequently, the hardening rule can be established as:

$$d\varepsilon^{p,dev}_{ij} = \lambda^p_{dev} \frac{\partial g_{dev}}{\partial \sigma'_{ij}} = \lambda^p_{dev} \frac{1}{Mp'}\left[\frac{\partial q}{\partial \sigma'_{ij}} + \alpha\left(M - \frac{q}{p'}\right)\frac{1}{3}\delta_{ij}\right] \tag{2.81}$$

$$\text{with} \qquad \frac{\partial q}{\partial \sigma'_{ij}} = \begin{cases} \dfrac{3}{2q}\left(\sigma'_{ij} - p'\right) & \text{if} \quad i = j \\[2ex] \dfrac{3\sigma'_{ij}}{q} & \text{if} \quad i \neq j \end{cases} \tag{2.82}$$

$$d\varepsilon_v^{p,dev} = \lambda_{dev}^p \frac{\partial g_{dev}}{\partial p'} = \lambda_{dev}^p \frac{\alpha}{Mp'}\left[M - \frac{q}{p'}\right] \tag{2.83}$$

$$d\varepsilon_d^p = \lambda_{dev}^p \frac{\partial g_{dev}}{\partial q} = \lambda_{dev}^p \frac{1}{Mp'} \tag{2.84}$$

α is a material parameter introducing the non-associative behaviour. The plastic multiplier, λ_{dev}^p, must be determined, as well as the isotropic mechanism, using Prager's consistency condition (Prager, 1949).

Coupling between the two mechanisms

The isotropic and the deviatoric yield limits are coupled through the hardening variable, ε_v^p which appears in the expression of the two yield limits. When the two mechanisms are activated simultaneously, the total volumetric plastic strain increment, $d\varepsilon_v^p$, is the sum of the volumetric plastic strain increments due to each mechanism (Equations (2.75) and (2.83)):

$$d\varepsilon_v^p = \lambda_{dev}^p \frac{\partial g_{dev}}{\partial p'} + \lambda_{iso}^p \frac{\partial g_{iso}}{\partial p'} = \lambda_{dev}^p \frac{\alpha}{Mp'}\left[M - \frac{q}{p'}\right] + \lambda_{iso}^p \tag{2.85}$$

The two consistency conditions must be met simultaneously, leading to the solving of two equations with two unknowns (Rizzi et al., 1996):

$$\mathbf{dF} = \frac{\partial \mathbf{F}}{\partial \boldsymbol{\sigma}'} : d\boldsymbol{\sigma}' + \frac{\partial \mathbf{F}}{\partial \boldsymbol{\pi}} . \frac{\partial \boldsymbol{\pi}}{\partial \boldsymbol{\lambda}^{\mathbf{p}}} . \boldsymbol{\lambda}^{\mathbf{p}} = \mathbf{j} : d\boldsymbol{\sigma}' - \mathbf{H}.\boldsymbol{\lambda}^{\mathbf{p}} \le 0 \ ; \ \boldsymbol{\lambda}^{\mathbf{p}} \ge 0 \ ; \ \mathbf{dF}.\boldsymbol{\lambda}^{\mathbf{p}} \ge 0 \tag{2.86}$$

$$\mathbf{dF} = \begin{pmatrix} df_{iso} \\ df_{dev} \end{pmatrix} \tag{2.87}$$

where $\boldsymbol{\sigma}'$ is the stress vector (Equation (2.65)) and $\boldsymbol{\pi}$ the internal variable vector. $\mathbf{j}$ collects the stress-gradients of the loading function $\mathbf{F}$:

$$\mathbf{j} = \begin{pmatrix} \frac{\partial f_{iso}}{\partial \sigma'_{11}} & \frac{\partial f_{iso}}{\partial \sigma'_{22}} & \frac{\partial f_{iso}}{\partial \sigma'_{33}} & \frac{\partial f_{iso}}{\partial \sigma'_{12}} & \frac{\partial f_{iso}}{\partial \sigma'_{13}} & \frac{\partial f_{iso}}{\partial \sigma'_{23}} \\ \frac{\partial f_{dev}}{\partial \sigma'_{11}} & \frac{\partial f_{dev}}{\partial \sigma'_{22}} & \frac{\partial f_{dev}}{\partial \sigma'_{33}} & \frac{\partial f_{dev}}{\partial \sigma'_{12}} & \frac{\partial f_{dev}}{\partial \sigma'_{13}} & \frac{\partial f_{dev}}{\partial \sigma'_{23}} \end{pmatrix} \tag{2.88}$$

$\boldsymbol{\lambda}^{\mathbf{p}}$ is the plastic multiplier vector:

$$\boldsymbol{\lambda}^{\mathbf{p}} = \begin{pmatrix} \lambda_{iso}^p \\ \lambda_{dev}^p \end{pmatrix} \tag{2.89}$$

$\mathbf{H}$ is the matrix of hardening moduli $H_{\alpha\beta} = -\partial f_\alpha / \partial \lambda_\beta^p$:

$$\mathbf{H} = \begin{bmatrix} H_{ii} & H_{id} \\ H_{di} & H_{dd} \end{bmatrix} \tag{2.90}$$

$$\text{with}\quad\begin{cases} H_{ii} = -\dfrac{\partial f_{iso}}{\partial r_{iso}}\dfrac{\partial r_{iso}}{\partial \lambda^p_{iso}} - \dfrac{\partial f_{Tiso}}{\partial \varepsilon^p_v}\dfrac{\partial \varepsilon^p_v}{\partial \lambda^p_{iso}} = p'_c\dfrac{\left(1-r_{iso}\right)^2}{c} + p'_c\beta r_{iso} \\ H_{id} = -\dfrac{\partial f_{iso}}{\partial r_{dev}}\dfrac{\partial r_{dev}}{\partial \lambda^p_{dev}} - \dfrac{\partial f_{iso}}{\partial \varepsilon^p_v}\dfrac{\partial \varepsilon^p_v}{\partial \lambda^p_{dev}} = -\dfrac{\partial f_{iso}}{\partial \varepsilon^p_v}\dfrac{\partial \varepsilon^p_v}{\partial \lambda^p_{dev}} = p'_c\beta r_{iso}\dfrac{1}{Mp'}\left(M-\dfrac{q}{p'}\right)\alpha \\ H_{di} = -\dfrac{\partial f_{dev}}{\partial r_{iso}}\dfrac{\partial r_{iso}}{\partial \lambda^p_{iso}} - \dfrac{\partial f_{dev}}{\partial \varepsilon^p_v}\dfrac{\partial \varepsilon^p_v}{\partial \lambda^p_{iso}} = -\dfrac{\partial f_{dev}}{\partial \varepsilon^p_v}\dfrac{\partial \varepsilon^p_v}{\partial \lambda_{iso}} = Mp'b\beta r_{dev} \\ H_{dd} = -\dfrac{\partial f_{dev}}{\partial r_{dev}}\dfrac{\partial r_{dev}}{\partial \lambda^p_{dev}} - \dfrac{\partial f_{dev}}{\partial \varepsilon^p_v}\dfrac{\partial \varepsilon^p_v}{\partial \lambda^p_{dev}} = -\left(1-b\ \ln\dfrac{p'd}{p'_c}\right)\dfrac{\left(1-r_{dev}\right)^2}{a} - b\beta\left(M-\dfrac{q}{p'}\right)\alpha r_{dev} \end{cases} \tag{2.91}$$

$\mathbf{dF} \leq 0$ expresses Prager's consistency condition (Prager, 1949) extended to multiple dissipation processes (Rizzi et al. 1996). The elasto-plastic framework enables the stress increment response with respect to prescribed strain increment to be expressed as:

$$d\boldsymbol{\sigma}' = \mathbf{E}:\left(d\boldsymbol{\varepsilon} - \mathbf{m}.\boldsymbol{\lambda}^{\mathbf{p}}\right) \tag{2.92}$$

where $\mathbf{E}$ is the current elastic stiffness tensor of the material (Equation (2.67)), $\mathbf{m}$ defines the collection of flow directions; $\mathbf{m} = \dfrac{\partial \mathbf{G}}{\partial \boldsymbol{\sigma}'}$ with $\mathbf{G}$ being the potential vector function:

$$\mathbf{m} = \begin{pmatrix} \dfrac{\partial g_{iso}}{\partial \sigma'_{11}} & \dfrac{\partial g_{iso}}{\partial \sigma'_{22}} & \dfrac{\partial g_{iso}}{\partial \sigma'_{33}} & \dfrac{\partial g_{iso}}{\partial \sigma'_{12}} & \dfrac{\partial g_{iso}}{\partial \sigma'_{13}} & \dfrac{\partial g_{iso}}{\partial \sigma'_{23}} \\ \dfrac{\partial g_{dev}}{\partial \sigma'_{11}} & \dfrac{\partial g_{dev}}{\partial \sigma'_{22}} & \dfrac{\partial g_{dev}}{\partial \sigma'_{33}} & \dfrac{\partial g_{dev}}{\partial \sigma'_{12}} & \dfrac{\partial g_{dev}}{\partial \sigma'_{13}} & \dfrac{\partial g_{dev}}{\partial \sigma'_{23}} \end{pmatrix}^T \tag{2.93}$$

Thus, the consistency equation can be re-written as follows:

$$\mathbf{dF} = \mathbf{j}:\mathbf{E}:d\boldsymbol{\varepsilon} - \left(\mathbf{H} + \mathbf{j}:\mathbf{E}:\mathbf{m}\right).\boldsymbol{\lambda}^{\mathbf{p}} \leq 0 \quad ; \quad \boldsymbol{\lambda}^{\mathbf{p}} \geq 0 \quad ; \quad \mathbf{dF}.\boldsymbol{\lambda}^{\mathbf{p}} \geq 0 \tag{2.94}$$

2.3.4 Numerical validation

2.3.4.1 *Introduction*

In this section, the performance of the model devoted to isothermal and saturated conditions is demonstrated. For the numerical simulations, the driver of the constitutive law LAWYER developed at the Ecole Centrale de Paris (Modaressi et al.) was used. The existing Hujeux model, already modified by Laloui (1993) at the BRGM (Bureau de Recherche Géologique et Minière, France) and Cekerevac (2003) at EPFL, has been completed in order to introduce the ACMEG model. The original LAWYER code has also been adapted for all of the following developments of this thesis dealing with non-isothermal and unsaturated conditions. The final version of the model subroutine, written in FORTRAN, is given in Appendix B. We wish to thank the BRGM (Professor H. Modaressi) and the Ecole Centrale de Paris (Professor D. Aubry) for providing us with the original LAWYER code.

In the following, the model predictions are compared to experimental results for a remoulded clay in different loading configurations. The experimental program investigates the soil behaviour upon various loading directions. The model parameters have been determined from three conventional tests (one triaxial compression, one isotropic compression and one isotropic extension) while the simulations of the other tests are blind predictions.

2.3.4.2 *Description of the tests numerically simulated*

Costenza et al. (2006) performed a large experimental program on reconstituted French silty clay (Beaucaire Marl). Those tests carried out on specimens normally consolidated to an initial state which is either isotropic or anisotropic aim to investigate, in a systematic manner, the soil response upon stress-controlled loading in different directions of the stress space. The choice of this experimental program to validate the developed model was made for several reasons:

- The experimental tests are carried out on reconstituted samples. It reduces to a minimum the unavoidable differences between the various specimens and enables reproducible tests.
- The experimental procedure is systematic and performed with a unique experimental device. It avoids discrepancy in results due to various laboratory conditions.
- The different tests point in different directions in the triaxial plan. It enables investigation of the performance of the model under non-conventional distortional loadings.
- Two initial stress states (isotropic and anisotropic) are considered. It enables calibration of material parameters on some specific paths starting from one initial state and performing blind simulations from the other initial state.

The tests were performed on reconstituted Beaucaire Marl, which is a low plasticity (CL) silty clay, with a liquid limit of 38%, and an average plasticity index of 17% consisting of slightly less than 30% of clay and 34% of calcium carbonate. The soil was prepared by thoroughly mixing known quantities of natural soil with distilled water, to a water content approximately equal to 1.5 times the liquid limit and consolidated in a large consolidometer up to a nominal vertical effective stress of 75 kPa. Initial states from which distortional stress path were performed are (i) located on the isotropic axis at 150 kPa; and (ii) at a deviator stress of 60 kPa with the same mean effective stress as state (i). Given the stress level previously experienced by the soil inside the consolidometer, they both represent virgin states for the material (Costenza et al. 2006). All the tests were performed under drained conditions.

Model calibration

In order to assess the performance of the model, it is essential to select the minimum numbers of tests required to calibrate the material parameters and carry out blind simulations on the remaining tests. Consequently, the conventional triaxial compression (i.e. sloping 1/3 in the ($p'-q$) plane – test number 121) was used to establish the deviatoric parameters (G_{ref}, b, d, ϕ', α, a and r^e_{dev}). The isotropic plastic parameters (β, c and r^e_{iso}) were fixed from the isotropic compression path (i.e. horizontal path in the ($p'-q$) plane – test number 128). The elastic isotropic parameters were calibrated from the isotropic extension path (test number 127). A detailed explanation on the way to determine the material parameters is presented in Section 3.5.5.1. These three tests used for the calibration of material parameters start from the isotropic stress state. The six remaining tests starting from the isotropic stress state as well as the ten tests carried out from anisotropic stress state consist of blind predictions. The set of material parameters is reported in Table 2.1.

Elastic parameters		
K_{ref} , G_{ref} , n^e	[MPa], [MPa], [-]	66, 46, 1
Isotropic plastic parameters		
β , c , r^e_{iso} , p'_{c0}	[-], [-], [-], [kPa]	33, 0.018, 0.01, 150
Deviatoric plastic mechanical parameters		
b , d , ϕ' , α , a , r^e_{dev}	[-], [-], [°], [-], [-], [-]	1, 1.9, 33, 1.8, 0.001, 0.84

Table 2.1: The Beaucaire clay material parameters.

2.3.4.3 *Numerical simulations*

In Figure 2.15 and Figure 2.16, the results of simulations are given and compared with experimental curves in the four representative stress-strain planes: ($\varepsilon_d - (\sigma'_1 - \sigma'_3)$), ($p' - (\sigma'_1 - \sigma'_3)$), ($\varepsilon_d - \varepsilon_v$), and ($p' - \varepsilon_v$), with σ'_1 and σ'_3 being the axial and radial effective stresses, respectively. The simulation results of the tests starting from the isotropic stress state agree very well with experiment (Figure 2.15). In particular, the generated volumetric strain with respect to the axial strain or the mean effective stress (Figure 2.15c,d) is predicted remarkably well. It proves the efficiency of the dilatancy rule (Equation (2.79)). In particular, the parameter α, which has been added in the improvement of the model, plays a major role in this good agreement. Also, the parameters d and b affecting the plastic volumetric strain are efficient for whichever path is followed. In the deviatoric plane $(\varepsilon_d - (\sigma'_1 - \sigma'_3))$, the prediction is also excellent for tests experiencing positive deviatoric stresses (tests number 121, 123, 126). For negative deviatoric stresses (tests number 122, 124, 125), the spread between experiment and simulation results is a bit higher, although it remains very satisfactory. This point may be due to the fact that the slope of the critical state line on the compression path ($(\sigma'_1 - \sigma'_3) > 0$) is slighty different from the one on the tension path ($(\sigma'_1 - \sigma'_3) < 0$) which is not considered in the ACMEG model.

Figure 2.16 gives the comparison between experiment and simulation results for the tests starting from the anisotropic stress state. All of these tests are blind predictions. The same comments as those for Figure 2.15 can be made. Under positive deviatoric stress, simulation results match perfectly with experimental results in terms of volumetric as well as deviatoric generated strains. As far as deviatoric extension paths ($(\sigma'_1 - \sigma'_3) < 0$) are concerned, some slight discrepancies can be observed.

This set of simulations on non-conventional triaxial paths reveals the performance of the ACMEG model to reproduce the mechanical behaviour of fine-grained soils under isothermal and saturated conditions on any complex stress paths. Though the ACMEG model is founded on a very simple Original Cam-Clay model mainly devoted to soil behaviour upon triaxial and isotropic compression path, the successive improvements permit us to accurately reproduce the material response along various loading paths. It is of particular interest to validate the model on such non-conventional loading directions since many important engineering applications involve similar stress paths. Moreover, the efficiency of the ACMEG model is strengthened by the small amount of testing required to calibrate the material parameters. All of the model constants have been fixed using only 3 tests results.

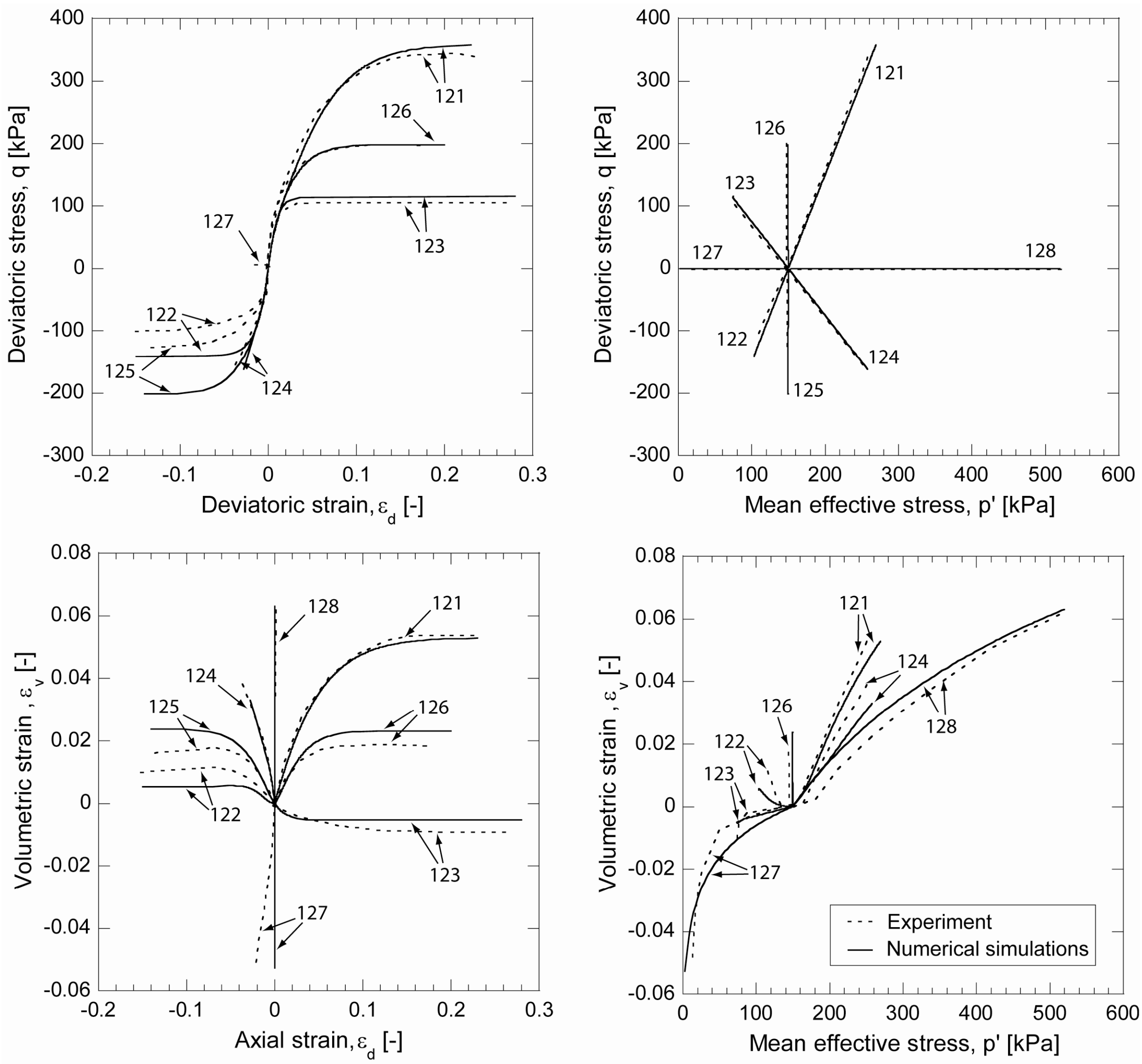

Figure 2.15: Validation of the ACMEG model on drained non-conventional triaxial loadings starting from a virgin isotropic stress state and pointing in different directions in the stress space. Comparison of simulation results with experimental curves of Costanza et al. (2006) in the four representative planes.

In a companion paper of Costenza et al. (2006), Masin et al. (2006) investigated the performance of several advanced constitutive models for soils with respect to this experimental program. They concluded that the Modified Cam-Clay model remains a performing model as long as continuous loading paths are considered. In unloading, however, substantial improvement can be achieved with the kinematic hardening approach. Though the purpose of the present section is not to carry out such an accurate comparative evaluation of different constitutive models, it seems that the successive modifications of the present model also provide noticeable enhancements to the prediction accuracy.

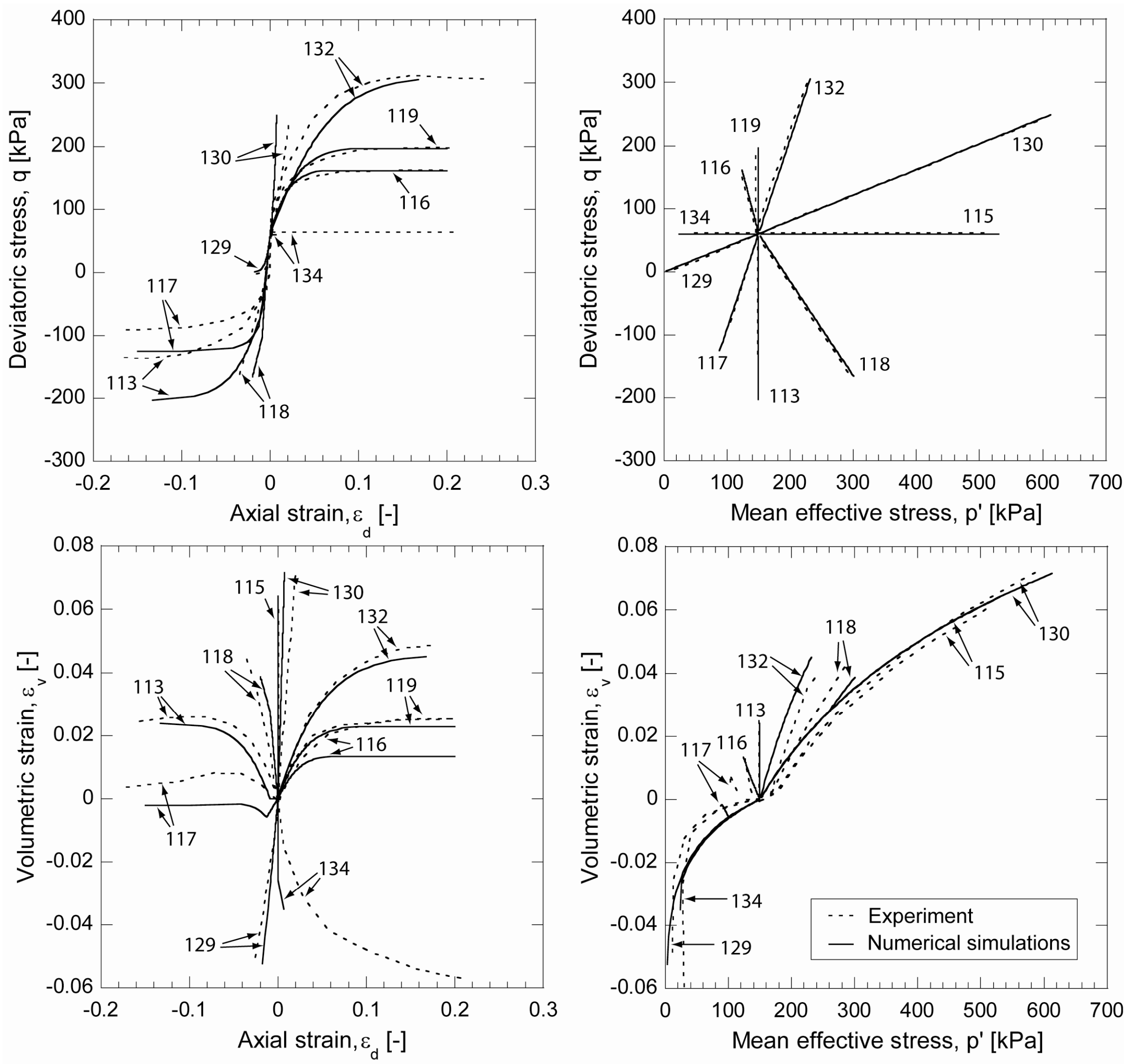

Figure 2.16: Validation of the ACMEG model on drained non-conventional triaxial loadings starting from a virgin anisotropic stress state and pointing in different directions in the stress space. Comparison of simulation results with experimental curves of Costanza et al. (2006) in the four representative planes.

2.4 Conclusions

Starting from the Original Cam-Clay model and based on several improvements aiming to overcome the main limitations of this well-known constitutive model, a constitutive law, "Advanced Constitutive Model for Environmental Geomechanics", or ACMEG, has been developed. The ACMEG model retains the concepts of classical elasto-plasticity and critical-state soil mechanics. Using the contributions of Hujeux (1979, 1985), the shape of the deviatoric yield limit of the Original Cam-Clay has been refined by two additional material parameters, b and d, which have comprehensive physical meanings. In particular, the b parameter, varying between 0 and 1, enables the model to reproduce the behaviour of different kinds of soil (from sand to clay). Moreover, the Original Cam-Clay deviatoric yield surface has been cut off by an isotropic yield limit using the principle of multi-mechanism plasticity. A major advance in the prediction accuracy has been achieved using the possible progressive plasticity inside the external yield limit. This concept, termed the bounding surface plasticity, substantially improves the transition between purely elastic and fully elasto-plastic behaviour. These improvements, which are mainly based on the works of Hujeux and co-workers (Ecole Centrale Paris), make the model efficient for different kind of materials. The Original Cam-Clay model has been shown to be a special case of the ACMEG model.

All of these constitutive developments aim to create a model not only simple enough to be used easily in practice but also to capture, in a quantitative way, the main features of the behaviour of fine-grained soil. In that sense, this model remains straightforward enough to be used as the basis of further developments dealing with thermo-plasticity of saturated and unsaturated soils. The material parameters also retain a comprehensive and explicit physical meaning, which makes parameter calibration easy.

Because engineering applications generally involve non-conventional stress paths, it is essential to prove the efficiency of the model to consider stress paths pointing in various directions. This validation reveals the ability of the model to predict the soil response under such complex loadings. Thus, the ACMEG model represents an efficient and useful extension of the Cam-Clay model and overcomes most of the Original Cam-Clay limitations.

The ACMEG model is mainly devoted to soil behaviour upon monotonic loading. Some specific responses related to mechanical anisotropy, time-related effects (e.g. viscosity) or stress-strain response upon dynamics loadings require improved versions of the model, which are not addressed in this dissertation. Moreover, this model is most suitable to describe the mechanical response of fine-grained soils (silts and clays). The prediction of stiff overconsolidated clays and sand behaviours is subject to some limitations although it can provide satisfactory results for some specific applications.

Chapter 3

ACMEG-T, a non-isothermal mechanical constitutive model

Altering the temperature of a soil specimen can produce effects similar to changes in stress history and can produce change in the pore water pressure of the material. Clearly, any such changes, if not recognized, may have important engineering implications. […]. There is experimental evidence to indicate that heating of cohesive soil will cause it to decrease in volume, to decrease in undrained shear strength, and, perhaps, to exhibit a decrease in shear strength parameters obtained from one effective stress analysis.[1]

[1] Plum L. and Esrig M.I. (1969). Some temperature effects on soil compressibility and pore water pressure. Special report, Report 103, Highway Research Board, Washington.

3.1 Introduction

In addition to the mechanical behaviour of soil under isothermal conditions, a fine-grained material submitted to non-isothermal loading may exhibit some complex behavioural features related to temperature change. This behaviour depends on the soil type, the stress state, the stress and temperature history and the drainage conditions. In order to reproduce such behaviour, an accurate description of the thermo-mechanical processes observed in soils is required. Once those processes are identified and quantified, rigorous constitutive models describing the mechanical behaviour of soils under non-isothermal conditions may be developed.

Within that framework, this chapter aims to address the stress-strain-temperature relations that are experienced by fine-grained soils. In the first section, soil is considered at the micro-scale level as a composition of clay platelets and/or fine grains that are affected by thermal changes. From those micro-scale considerations, a way to evaluate the macroscopic response of soil undergoing temperature variations is proposed. Then, experimental results underlining the temperature effects on the mechanical behaviour of soils are presented from a literature analysis. Also, the most relevant constitutive approaches in the field are briefly introduced, with a focus on the gradual improvement displayed by the successive constitutive models of the literature. The developed thermo-mechanical model, named ACMEG-T, is then presented. This model is an extension toward the non-isothermal conditions of the ACMEG model addressed in the previous chapter. Finally, the qualitative prediction of this model is compared with a model from the literature, and the performance of ACMEG-T is demonstrated through comparison of quantitative numerical predictions and experimental results.

3.2 Thermal effect on microstructural aspects of clayey soils

3.2.1 Introduction

Soil is a particulate material undergoing complex physico-chemical interactions at the particle level. In general, the fineness of the soil governs the balance between gravimetric forces and surface-related forces acting in the material. In that sense, the quantity of clay mineral affects the role of interaction forces between particles regarding the macroscopic gravimetric forces. In this thesis, only fine-grained soils are considered. According to the Unified Soil Classification System (USCS), *fine-grained soils are those that have more than 50% by weight passing the No. 200 sieve* (corresponding to a grain size of 0.06 mm). Because of the prevalence of surface forces acting between particles with respect to volumetric gravimetric forces, *fine-grained soils* are often confusingly termed *cohesive soils*, even though, in the absence of cementation or any capillary effects, such soils do not exhibit any cohesion at a critical state (Santamarina, 2001). Indeed, the inter-particle attraction cannot be the cause of any significant cohesion in the medium. So, in the entire thesis, the term *fine-grained soils* will be preferred over the confusing term *cohesive soils*.

In this section, the main micro-mechanical interactions between clayey particles are described. Then, an extension to non-isothermal conditions is considered. Based on the diffuse double layer theory, the predominant temperature effects on the interaction forces between particles are described. Finally, those micro-structural considerations are used to describe the behaviour of the material at the macro-scale. Indeed, it is reasonable to assume that the thermal phenomena observed at the macro-scale (i.e. by considering soil as a continuum) are a consequence of the micro-structural changes of the clays. The distinction between *micro-* and *macro-scale* must be understood as a distinction between *the scale of the clay particle* and *the scale of the conventional experimental test*.

3.2.2 Interactions in clay-water system

3.2.2.1 *Clayey soil mineralogy*

Clay mineral is a phyllosilicate made up of combinations of two simple structural units, the silicon tetrahedron, producing a silica sheet $(Si_4O_{10})^{4-}$ by the sharing of three of the four oxygens ions in each tetrahedron, and the aluminium or magnesium octahedron, forming an octahedral sheet by the sharing of oxygens or hydroxyls (Figure 3.1) (Mitchell, 1976).

Clay minerals differ from each other mainly in two aspects (Figure 3.2):

- The type of 'glue' that holds the successive layers together. Unit layers can be stacked closely together, or a water layer or potassium atoms may intervene.
- The stacking arrangement of the sheets. The minerals have units cells consisting of two, three, or four sheets that combine together to form different kind of clays.

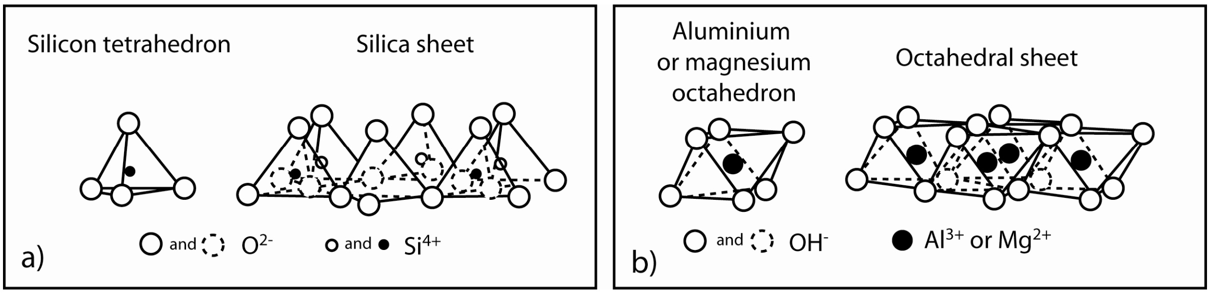

Figure 3.1: (a) Silicon tetrahedron and silica sheet; (b) Aluminium or magnesium octahedron and octahedral sheet (Mitchell, 1976).

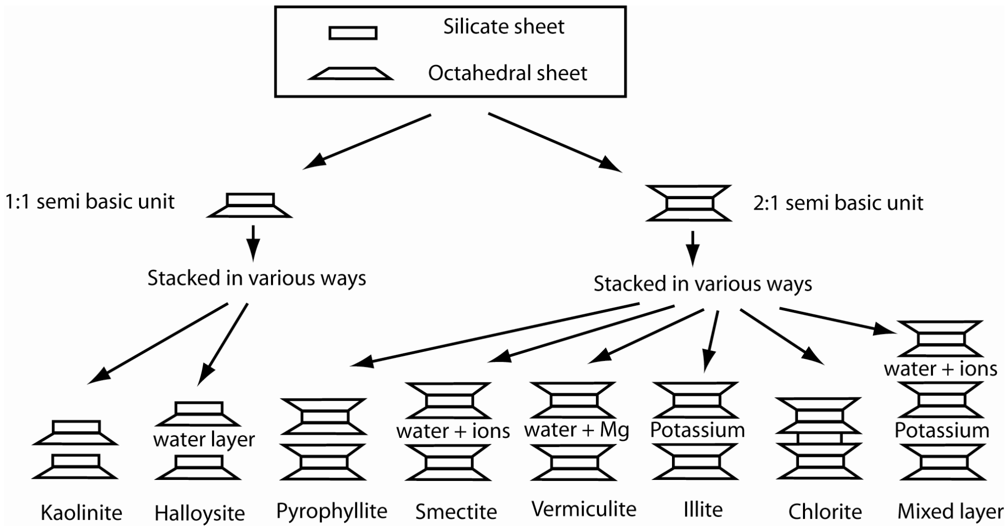

Figure 3.2: Patterns of clay minerals (Mitchell, 1976).

3.2.2.2 *Diffuse double layer theory*

The diffuse double layer theory, based on the work of Chapman (1913) and Gouy (1919), describes the water-clay particle interactions at the vicinity of the particle. The unit cell of the clay mineral has a residual negative charge that is balanced by the adsorption of cations from solution. In the neighbourhood of the particle, the cations are strongly attracted by the particle, and the water has many of the characteristics of a crystalline solid. This layer of attracted water, called adsorbed water, is considered by many authors as a part of a solid skeleton (Hueckel, 1992a; Hueckel and Pellegrini, 1989). The electric charge carried by this layer extends over a certain distance from the particle surface, and it dies out gradually with increasing distance (Verwey and Overbeek, 1948) (Figure 3.3). Outside a given distance to the particle, which depends on the properties of the solution, the water can be considered to be free water, also called bulk water.

3.2.2.3 *Water in saturated clays*

Under saturated conditions, water fills all the pores. According to their size, the pores can be categorized as: (i) the inter-aggregate (average size of 1.5 to 16 μm), (ii) the inter-particle (average size of 20 to 150 nm) and (iii) the inter-lamellar pores (average size of 1.5 to 2.5 nm) (Robinet et al., 1994; Touret et al., 1990). The diffuse double layer theory predicts that the water mobility vanishes at the small-range distance (i.e. smaller than 20 Å) from the clay particles. In the small pores (inter-lamellar and some inter-particle pores), water is essentially adsorbed, while, in the larger pores, water is mainly free to move. So, during a consolidation process, the proportion of large pores decreases, and the percentage of adsorbed water out of the total volume of water increases.

3.2.2.4 *Physico-chemical interactions between particles*

The well-established diffuse double layer theory considers a unique particle surrounded by a solution (dissolved ions in water). This theory can easily be applied for colloids for which mineral particles are dispersed in a continuous liquid phase. However, the density of clayey soil is such that particles interact through their diffuse double layer. Looking at the potential of one isolated particle surrounded by water, the quantity Ω is a good approximation of the thickness of the double layer (Mitchell, 1976):

$$\Omega = \left(\frac{\varepsilon_0 DkT}{2n_0 {e_0}^2 \upsilon^2} \right)^{1/2} \tag{3.1}$$

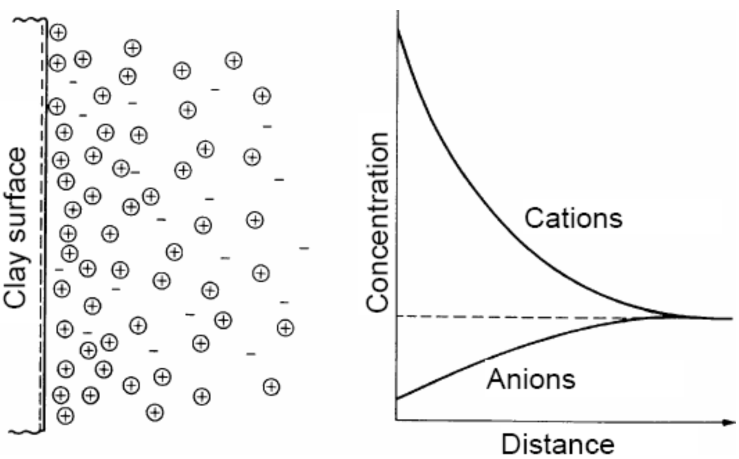

Figure 3.3: Representations of the diffuse double layer (Mitchell, 1976).

where ε_0 is the static permittivity of the medium [$C^2J^{-1}m^{-1}$], D is the dielectric constant of the medium [-], k is the Boltzmann constant ($=1.38\ 10^{-16}\,ergs/K$), T is the temperature [K], n_0 is the electrolyte concentration [ions/m^3], υ is the ionic valence of the solution [-], and e_0 is the electronic charge ($=4.81\ 10^{-10}\,esu$).

The diffuse double layers of two platelets close to each other overlap and a repulsion force takes place. Assuming two parallel platelets, this repulsion force can be quantified by a potential energy dependent on the inter-particle distance δ (Verwey and Overbeek, 1948).

In addition to this repulsive force, a long-range attractive interaction between particles, related to Van der Waals forces, must be considered. Assuming two parallel platelets, this attractive force may also be quantified by a potential energy dependent on the inter-particle distance δ (Verwey and Overbeek, 1948).

Combining the repulsive and attractive potential, V_R and V_A, respectively, the total potential curve is obtained as a function of the inter-plate distance. V_R exponentially decreases with δ, while V_A decreases quadratically with δ. Since the exponential decreases faster than any negative power decreasing function, the attractive potential will always be greater than the repulsive one for large distances. In the intermediate distance, two possibilities exist. Either V_R is greater than V_A, which produces a repulsive barrier preventing direct contact between particles (Figure 3.4, case A), or else V_R remains smaller than V_A for all distances, and this repulsive barrier does not exist (Figure 3.4, case B).

The interaction force between plates is proportional to the negative derivative of the energy potential. Thus, the resultant force depends on the inter-particle distance in case A (attractive between 0 and 1, repulsive between 1 and 2 and still attractive between 2 and 3). On the contrary, in case B, the force is always attractive.

For parallel clay layers of constant surface charge density in a 1:1 electrolyte solution, the interaction stress between platelets σ_{R-A} may be assessed by subtracting the Van der Waals attraction σ_A from the repulsive pressure σ_R. σ_R can be assessed as follows (Van Olphen, 1977):

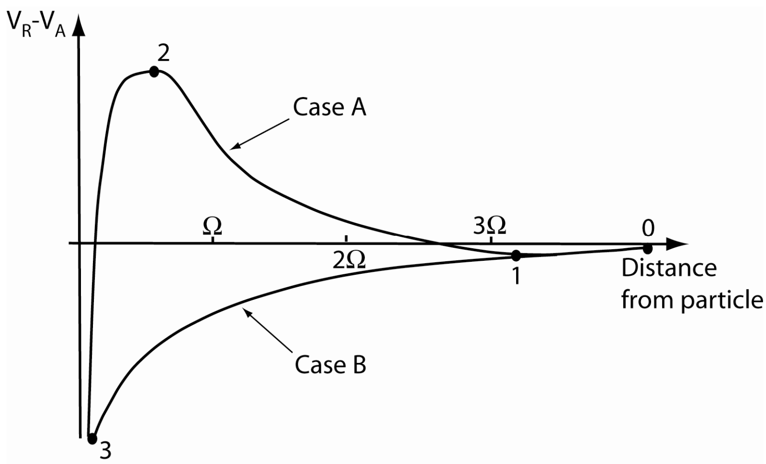

Figure 3.4: Curve of total potential energy (repulsion + attraction).

$$\sigma_R = 2n_0 kT\left(\cosh u - 1\right) \tag{3.2}$$

$$\frac{dy}{d\xi} = -\left(2\cosh y - 2\cosh u\right)^{1/2} \tag{3.3}$$

$$\text{For } y = z \qquad \left(\frac{dy}{d\xi}\right)_0 = \frac{4\pi e_0 \upsilon \sigma_c}{DkT\kappa} \tag{3.4}$$

$$\int_z^u \left(2\cosh y - s\cosh u\right)^{-1/2} dy = -\kappa\frac{\delta}{2} \tag{3.5}$$

$$\kappa = \left(\frac{8\pi n_0 e_0{}^2 \upsilon^2}{DkT}\right)^{1/2} \tag{3.6}$$

where $y = \upsilon e_0 \Psi / kT$, $z = \upsilon e_0 \Psi_0 / kT$, and $u = \upsilon e_0 \Psi_d / kT$. Ψ, Ψ_0 and Ψ_d are the electrostatic potentials in a plane at a distance x from the surface of the layer, at the surface of the platelet ($x = 0$) and at the mid-plane between two platelets ($x = \delta/2$), respectively. σ_c is the surface charge density. Equation (3.5) cannot be integrated analytically. However, Van Olphen (1977) presents tables relating the u and z with $\kappa \times \delta/2$ for different values of $\left(dy/d\xi\right)_0$. It enables the determination of the repulsive pressure σ_R with respect to the charge density at the surface of the clay σ_c, the inter-platelet distance δ and the temperature T. In addition, the Van der Waals attraction force is given by

$$\sigma_A = \left(\frac{A}{6\pi}\right)\left[\left(\frac{1}{\delta}\right)^3 - \frac{2}{\left(\delta + t\right)^3} + \frac{1}{\left(\delta + 2t\right)^3}\right] \tag{3.7}$$

where t is the thickness of the clay platelet. A is the Hamaker constant, which may be taken to be 2.2 10^{-13} ergs (Israelachvili and Adams, 1978).

From Equations (3.2) to (3.7), it is possible to compute the interaction stress between platelets of clay depending on the properties of the electrolyte solution and on the clay density. In Appendix C, such a development is performed for Boom clay, leading to an interaction stress between particle σ_{R-A} of 901 kPa. This numerical application that aims to quantify the interaction stress between particles at a micro-scale level underlines the dependency of the solute and the clay platelet properties, as well as the porosity, on the repulsive force acting between particles. As will be shown below, those properties are affected by temperature.

3.2.2.5 *Effective stress concept in clays*

The physico-chemical forces acting between clayey particles affect the equilibrium between the inter-particle forces and the external load. The influence of the physico-chemical forces on the macroscopic behaviour mainly depends on the pore size. As a consequence, the smaller the pores, the higher the effect of the attractive and repulsive forces is. On the contrary, in larger pores, the contact forces between particles are predominant. The physico-chemical forces strongly affect the behaviour of small pores with the same order of magnitude as the thickness of the diffuse double layer. Hueckel (1992b) distinguishes three stress components in clay: the stress in the solid skeleton σ^*, the bulk water pressure p_w and the physico-chemical specific force per unit area σ_{R-A}, which was referred to in the previous section as the interaction stress between particles. The role of each stress component depends on the dry density of the material.

In soil mechanics, it is essential to assess the effective stress state in the medium because it controls the macroscopic behaviour of the material. As stated by Terzaghi (1943), an increment of external stress applied on a porous media is supported by an increment in the combination of the pore water pressure and the effective stress. The effective stress was initially defined by Terzaghi (1936) as *"the stress seated exclusively in the solid phase of the earth"*. This definition then progressively evolved into *"the vector sum of all the inter-particle forces in a given direction divided by the total area being considered"* (Mitchell, 1976). According to this second definition, it seems obvious that the effective stress is affected by the physico-chemical interactions between particles. Those interactions being strongly influenced by the density of the material, Hueckel (1992b) stated that the effective stress state may be related to the microstructural stress component in two different ways, according to the density of the clay.

(i) In dense clay, there is a majority of small pores, and the contacts between plates are mostly face-to-face (i.e. parallel platelets). In that configuration, it can be assumed that the external stress is almost totally supported by the interaction stress between particles. A stress increment tending to reduce the inter-particle distance produces an increase of the repulsive force (Figure 3.4, case A). As long as the potential barrier (point 2 on Figure 3.4) is not reached, this drop in inter-particle distance produces a reversible straining of the material. The effective stress state in dense soil can be assessed by the Lambe-Bolt series connection model (Figure 3.5a):

$$\sigma' = \sigma^* = \sigma_{R-A} = \sigma - p_w \tag{3.8}$$

(ii) In loose soil, the pores are larger, which makes the interaction stress between particles negligible with respect to the edge-to-edge or edge-to-face contact forces. An increase in the external stress mainly induces an irreversible relative slide of the edge-to-edge contacts, producing an irreversible strain of the material. In this case, the microstructural interpretation of the effective stress proposed by Sridharan and Venkatappa Rao (1973) seems appropriate (Figure 3.5b):

$$\sigma' = \sigma^* = \sigma - p_w - \sigma_{R-A} \tag{3.9}$$

A consolidation process can be understood as a progressive transition from the Sridharan and Venkatappa Rao model, with a majority of edge-to-face contacts, into the Lambe-Bolt series connection model, with a majority of face-to-face contacts (Hueckel, 1992b).

The effective stress concept as defined by the classical Terzaghi equation has been shown to include some limitations in saturated clays. However, as already discussed by many authors studying various porous media (Skempton, 1960a, b; De Boer and Ehlers, 1990, among others), *it is very unlikely that an effective stress expression will be found that is applicable to the full range of porous materials. The correct combination of total stresses, pore pressures* and other interaction forces *depends on the constitutive features and/or internal structure of the material, losing in this way its desired universality* (Jardine et al., 2004). Nonetheless, the simple effective stress expression usually remains applicable provided that the grain compressibility is negligible compared to the skeleton compressibility. As a consequence, in this dissertation, the constitutive approaches based on macroscopic considerations will be developed from the Terzaghi equation.

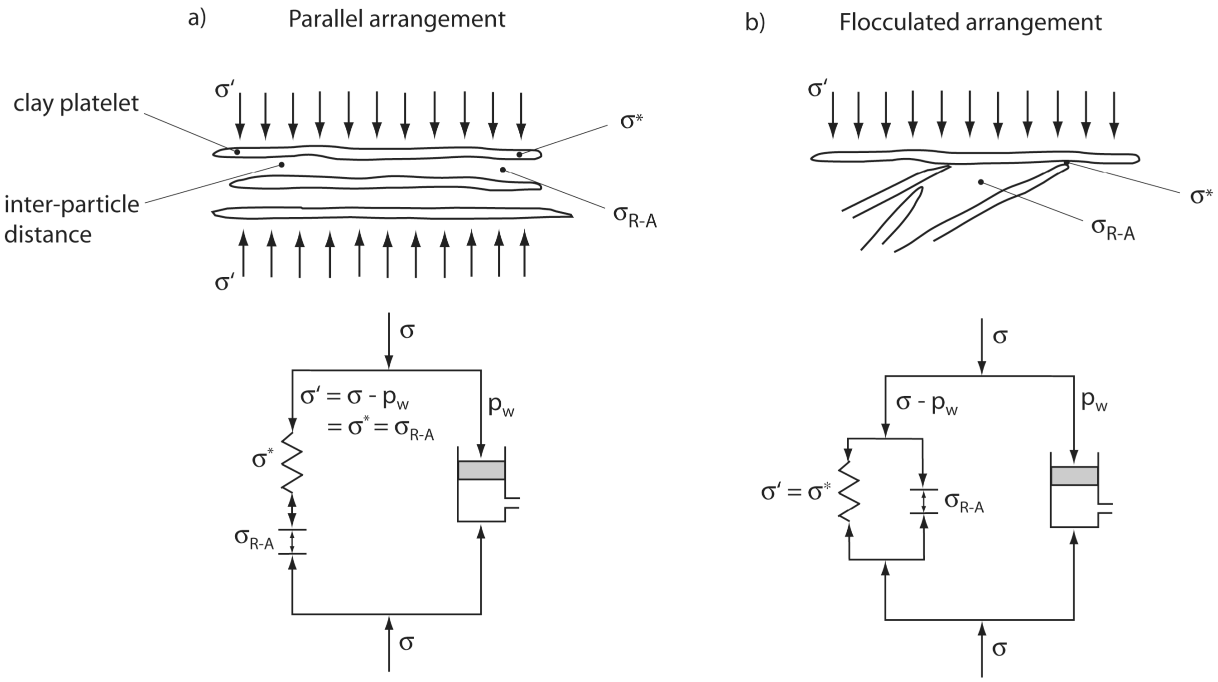

Figure 3.5: Type of contact in clay medium and model of microscopic distribution of stress in clay-water system. (a) Dense clay – Parallel arrangement of particles and Lambe-Bolt series connection model; (b) Loose clay – Flocculated arrangement of particles and parallel connection model (from Hueckel, 1992b).

3.2.3 Temperature effect on the clay-water system

3.2.3.1 *Temperature effect on macroscopic volumetric behaviour*

Thermal expansion of solid skeleton

When the temperature increases, all the constituents of soils (i.e. solid minerals, adsorbed and free waters) dilates. Under drained conditions, the effects of bulk water thermal expansion dissipate with time, depending on the permeability of the medium. On the contrary, the thermal volume change of adsorbed water and minerals produces a macroscopic thermal strain proportional to the temperature variation.

For a constituent α, its length and volume changes are related to temperature variation through the linear and volumetric thermal expansion coefficients $\overline{\beta}'_{sG,\alpha}$ and $\beta'_{sG,\alpha}$, respectively:

Linear thermal expansion $$\frac{dl_\alpha}{l_\alpha} = \overline{\beta}'_{sG,\alpha} dT \quad (3.10)$$

Volumetric thermal expansion $$\frac{dV_\alpha}{V_\alpha} = \beta'_{sG,\alpha} dT \quad (3.11)$$

l_α and V_α being the length and volume of the constituent α, respectively. The coefficients $\overline{\beta}'_{sG,\alpha}$ and $\beta'_{sG,\alpha}$ depend on the temperature level. Those coefficients usually increase with temperature. For instance, the linear thermal expansion coefficient of the mineral Al_2O_3 shifts from 6.5 10^{-6} °C^{-1} at ambient temperature to 12.10^{-6} °C^{-1} at 1000°C (Kingery et al. 1976). However, in the range of temperatures encountered in geotechnical applications, constant values are often assumed.

For most of the minerals, the linear thermal expansion varies along different crystallographic axes. The volumetric thermal expansion coefficient may be assumed to be the sum of the three components of the linear thermal expansion coefficient. For some crystals, the expansion coefficient in one direction may be negative and the resulting volume expansion coefficient may be very low. Table 3.1 reports the thermal expansion of some typical crystals, depending on the direction with respect to the crystallographic axis, as well as the resulting volumetric thermal expansion coefficient. A compilation of thermal expansion coefficients of many substances of geological interests may be found in Fei (1995). To calculate the resulting volumetric coefficient, the direction parallel to the crystallographic axis must be considered twice:

$$\beta'_{sG} = 2\overline{\beta}'_{sG,P} + \overline{\beta}'_{sG,N} \tag{3.12}$$

The effect of adsorbed water on the macroscopic response of soil strongly depends on its volume with respect to the volume of mineral present in the soil. Two different assumptions may be considered (Baldi et al. 1988). For loose soil, the diffuse double layers of two neighbouring particles do not intersect, and in addition to adsorbed water, there is a volume of free water. Consequently, adsorbed water does not occupy all the voids, and its volume may be deduced by multiplying the specific surface area of the soil by the thickness of adsorbed water. The second hypothesis, more realistic for dense soil, is that all the water is adsorbed water. In that case, the layers of water adsorbed by neighbouring particles overlap, and there is no space for free water.

Baldi et al. (1988) determined a theoretical volumetric thermal expansion coefficient of adsorbed water. This coefficient depends on temperature and distance from the clay platelet. In the middle region between two platelets, the water expansion is considerably reduced, while, at the contacts between platelets, the adsorbed water undergoes a larger expansion than free water. An average value of this coefficient can be approximated as 4.5 10^{-4} °C^{-1}.

	Crystal	Normal to the crystallographic axis $\overline{\beta}'_{sG,N}$	Parallel to the crystallographic axis $\overline{\beta}'_{sG,P}$	Volumetric thermal expansion coefficient β'_{sG}
(1)	Al_2O_3	8.3	9.0	26.3
(1)	Al_2TiO_5	-2.6	11.5	46.7
(1)	$3Al_2O_3.2SiO_2$	4.5	5.7	15.9
(1)	TiO_2	6.8	8.3	23.4
(1)	$ZrSiO_4$	3.7	6.2	16.1
(1)	$CaCO_3$ (calcite)	-6	25	60.1
(1)	SiO_2 (quartz)	14	9	32
(1)	$NaAlSi_3O_8$ (albite)	4	13	30
(1)	C (graphite)	1	27	55
(2)	Muscovite	17.8	3.5	24.8
(2)	Phlogopite	17.8	14	45.8
(2)	Kaolinite	18.6	5.2	29
(2)	Dickite	14.9	5.9	26.7
(2)	Halloysite	10	6	22
(2)	Talc	16.3	3.7	23.7
(2)	Chlorite	9	11.1	31.2
(3)	Illite	-	-	25
(3)	Smectite	-	-	39

Table 3.1 : Linear and volumetric thermal expansion coefficients for several minerals (x10^{-6} °C^{-1}). From (1) Kingery et al. (1976), (2) McKinstry (1965) and (3) Dixon et al. (1993).

Soils are generally made of a mixture of several minerals in different proportions surrounded by adsorbed water. In the soil arrangement, a temperature change will produce a volume change of each constituent according to their volumetric thermal expansion coefficient. However, each particle is restrained by the surrounding particles so that it cannot freely extend or shrink. Those differences in expansion propensity produce a micro-stress field in the material. Consequently, the most rigid particles may expand more easily than compressible particles. In the limiting situation, if gas is considered as a possible constituent of the material, it will not affect the macroscopic thermal expansion of the medium because of its very high compressibility. Based on the theory developed for ceramics, Kingery et al. (1976) proposed the following expression to determine the global thermal expansion coefficient of a composite material β_s' :

$$\beta_s' = \frac{\sum_\alpha \beta_{sG,\alpha}' F_\alpha K_\alpha / \rho_\alpha}{\sum_\alpha F_\alpha K_\alpha / \rho_\alpha} \tag{3.13}$$

where F_α, K_α and ρ_α are the mass fraction, the bulk modulus and the bulk density of the α component, respectively. This expression assumes that no cracks develops, that the expansion or contraction of each grain is the same as the overall expansion or contraction, that all micro-stresses are purely hydrostatic (no interfacial shear) and that no micro-stresses are large enough anywhere to disrupt the structure. Table 3.2 reports the bulk modulus and the bulk density of some typical clay minerals.

Thermal expansion of clay-water system

In addition to the effect of expansion of each constituent on the macroscopic thermal dilation of the medium, the stress distribution between solid particles and adsorbed water (Equations (3.8) and (3.9)) may be modified due to a temperature change. As shown in Section 3.2.2.5, this stress distribution depends on the density of the material. Therefore, it can be expected that the thermal dilation of a clayey material is affected by its density.

Starting from the consideration of the effective stress concept at the micro-scale level (Equations (3.8) and (3.9)), Hueckel (1992b) proposed to express the relationship between stress, strain and environmental loads including physico-chemical effects. They stated that the stress increment in a porous skeleton $d\sigma^*$ is proportional to the volumetric strain increment of the porous skeleton $d\varepsilon_{sk}$, while the increment of the interaction stress between particles $d\sigma_{R-A}$ is expressed in term of increments of inter-particle distance $d\delta$, of dielectric constant dD, of ionic concentration dc and of temperature dT. In the present work, it is proposed to keep the same framework, considering only the effects of inter-particle distance and temperature changes on the increment of the interaction stress between particles. Also, under non-isothermal conditions, the volumetric strain rate of the porous skeleton $d\varepsilon_{sk}$ must be related not only to incrementation of the solid skeleton stress, but also to thermal expansion of the particle. It yields the two following equations describing, respectively, the behaviours of the solid skeleton and of the diffuse double layers:

$$d\varepsilon_{sk} = \frac{d\sigma^*}{K} - \beta_s' dT \tag{3.14}$$

$$d\sigma_{R-A} = \xi_\delta \frac{d\delta}{\delta} + \xi_T dT \tag{3.15}$$

	Mineral	Bulk modulus K_α [GPa]	Bulk density ρ_α [kg/m³]
(1),(3)	Smectite	9	2394
(1)	Kaolinite	46	2442
(1)	Illite	60	2706
(1)	Chlorite	127	2681
(2)	Quartz	38	2650
(2)	Calcite	73	2712
(2)	Muscovite	52	2790
(2)	Dolomite	94	2860
(2)	Anhydrite	55	2970
(2)	Pyrite	143	5010

Table 3.2 : Bulk modulus and bulk density of some typical clay minerals. From (1) Wang et al. (2001), (2) Gebrande (1982) and (3) Lambe (1969).

where K is the bulk modulus of the solid skeleton. ξ_δ and ξ_T are variables describing the effect of inter-particle distance and temperature on the increment of the interaction stress between particles, respectively. As shown in Figure C.1 (Appendix C), the repulsive force decreases as the inter-particle distance increases. So, ξ_δ has a negative value. In contrast, Figure C.2 (Appendix C) predicts an increase of the repulsive force with heating, if constant inter-particle distance is assumed. So, ξ_T has a positive value. In Equation (3.15), it is assumed that the modification of the dielectric constant with temperature is directly considered in the ξ_T variable. Also, the thermal expansion of adsorbed water is taken into account in the thermal expansion of the solid skeleton (in the term $\beta_s' \times dT$).

Below, the two models describing the effective stress state in clay (Equations (3.8) and (3.9)) are investigated for the case of heating under constant external stress (i.e. $d\sigma = 0$). It is assumed that the process is fully drained, which eliminates the bulk water pressure variation dp_w .

Let us consider first the Lambe-Bolt series connection model (Equation (3.8)), which seems to fit the effective stress state of dense soil well. In this series model, the solid skeleton stress and the increment of the interaction stress between particles are assumed to be equal. Thus,

$$d\sigma' = d\sigma^* = d\sigma_{R-A} = d\sigma = 0 \tag{3.16}$$

The model being a series model, all the stress increments equal zero (because the external stress is assumed to be constant). In a series model, the total volumetric strain of the material is determined by adding up the strain of each constituent (i.e. the thermal expansion of solid particles and the change in inter-particle distance) (Hueckel, 1992b) (contraction is considered as positive):

$$d\varepsilon_v = -\left(\mathrm{A}\beta_s' dT + \mathrm{B}\frac{d\delta}{\delta} \right) = \mathrm{A}d\varepsilon_{sk} - \mathrm{B}\frac{d\delta}{\delta} \tag{3.17}$$

where A and B are the proportion of adsorbed water and solid skeleton in the total volume of the material. If all the water is adsorbed water, which is realistic in dense clay, then $\mathrm{A} = n$, and $\mathrm{B} = 1 - n$, n being the porosity. Combining of Equations (3.14), (3.15), (3.16) and (3.17) gives the expression of the volumetric strain induced by the heating process under constant external stress:

$$d\varepsilon_v = \left(n\frac{\xi_T}{\xi_\delta} - (1-n)\beta_s' \right) dT \tag{3.18}$$

As discussed previously, ξ_δ is negative while ξ_T is positive. As a consequence, the ratio ξ_T / ξ_δ is negative.

Considering now the parallel model of Sridharan and Venkatappa Rao (1973) appropriated for loose soils (Equation (3.9)), the external stress increment may be expressed as the sum of the solid skeleton stress increment and the interaction stress between particles:

$$d\sigma = d\sigma^* + d\sigma_{R-A} = 0 \tag{3.19}$$

Moreover, in such a parallel configuration, the relative change of the inter-particle distance is constrained to be equal to the strain in the solid skeleton (Hueckel, 1992b):

$$d\varepsilon_{sk} = -\frac{d\delta}{\delta} = d\varepsilon_v \tag{3.20}$$

Some algebraic combinations of Equations (3.14), (3.15), (3.19) and (3.20) enable the expression of the macroscopic volumetric strain induced by the heating process under constant external stress as follows:

$$d\varepsilon_v = -\frac{K}{K+\xi_\delta}\left(\frac{\xi_T}{K} + \beta_s' \right) dT \tag{3.21}$$

The ratio ξ_T / K being positive, the thermal effect on the diffuse double layer behaviour tends to increase the global thermal coefficient of loose clay. This coefficient depends on the rigidity of the solid skeleton. Adsorbed water and solid skeleton are assumed to have parallel effects. As a consequence, the higher the rigidity is of the solid skeleton, the smaller the effect is of the collapse of adsorbed water.

3.2.3.2 *Discussion*

Equations (3.18) and (3.21) have been established from theoretical considerations. This proves that the thermal expansion of clayey soil is highly non-linear and depends on the density of the material. This information is valuable from a qualitative point of view. However, in practice, the determination of the thermo-mechanical soil behaviour based on such microstructural aspects is subject to some limitations:

- Determination of the required parameters governing the microstructural properties of soils is often a strenuous process.
- As far as soil-water interaction in the vicinity of the particle is concerned, hypothesis and experimental data are often contradictory, and there is no clear understanding of the precise physico-chemical mechanisms occurring in clays.
- Viani et al. (1983) shows experimentally that the relation between interaction forces that act between particles and interlayer separations is not in strict agreement with the double layer theory. They stated that the double layer forces are too weak to account for the observed swelling pressures.

- The particle arrangement has been assumed to be fixed. No relative displacement between particles has been considered. Thus, only reversible processes can be reproduced. It seems obvious that the difference in rigidity and in thermal expansion between particles and adsorbed water may generate micro-stress upon heating, which could induce rearrangements of particles in an irreversible way. In particular, the degradation of the adsorbed layer, which tends to group particles closer together, may produce large voids between the platelet aggregates (Pusch, 1987). That meta-stable configuration may lead to particle rearrangements if the available energy (i.e. the stress level) is sufficiently high.
- The interaction of two single plates has been considered, while the real field of physico-chemical forces is produced by the arrangement of an infinite number of clay platelets.
- Soil particles have been considered to be regular plates, while they are often irregular and may consist of a combination of platelets and spherical particles.
- All the water in the material has been assumed to be adsorbed water. In practice, this assumption is consistent for bentonite but is inappropriate for most of the soils.
- According to several authors (Ninham, 1981; Low, 1979), the double layer theory fails to predict correctly the physico-chemical interaction between particles for interstices smaller than 2 nm. It corresponds to a water content smaller than 158% for smectites and 16 % for illites (Hueckel, 1992b).

3.3 Experimental evidence on thermo-mechanical behaviour of clayey soils

3.3.1 Soil response to heating-cooling cycles

Under normally consolidated conditions (NC), clay contracts when it is heated, and a significant part of this deformation is irreversible upon cooling. This thermal contraction is an unusual behaviour for any material. During heating, the NC sample settles with a non-linear volume variation. In the course of cooling, soil undergoes a relatively linear volume expansion that is much smaller than the contraction upon heating. The behaviour over the whole cycle indicates the irreversibility of strain due to thermal loading, which is representative of thermal hardening. Even though there has been no physical change in effective stresses, this can be interpreted as the soil undergoing densification.

Thus, in contrast to most of the other materials, the thermal volume change of NC soils upon the heating phase is governed not by classical thermo-elasticity, but by irreversible rearrangements of particles producing thermo-plasticity. This temperature-induced plasticity may be explained by the combination of several micro-mechanical processes:

- The shearing strength of inter-particle contacts governed by physico-chemical interactions (see Section 3.1) decreases as temperature increases. This decrease in interparticle bond strength acts to increase the probability of bond slippage or failure. As a consequence, there is a partial collapse of the soil structure and a decrease in void ratio until a number of additional bonds are formed sufficient to enable the soil to carry the stress at the higher temperature (Campanella and Mitchell, 1968). The maximal probability of bond slippage or failure occurs when a maximal number of interparticle contacts are in the limit state with respect to slippage. That is when the acting force producing bond slippage or failure is the highest (i.e. under normally consolidated conditions).

- The thermal degradation of the adsorbed layer, which tends to group particles closer together, may produce large voids between the platelet aggregates (Pusch, 1987). That meta-stable configuration may lead to particle rearrangements if the available energy (i.e. the stress level) is sufficiently high.
- Because soil is a composite body, the difference in rigidity and in thermal expansion between the dissimilar minerals forming the solid skeleton generates a modification of the contact force networks as temperature increases (Kingery et al., 1976). Such temperature-induced changes in the internal micro-stress distribution may cause a collapse of the soil structure until a new micro-stress equilibrium is reached.
- The thermal expansion of each soil constituent would produce a global dilation of the solid skeleton if the particle arrangement were assumed to be fixed. This global dilatation increases the pore size and the inter-particle distance. In agreement with diffuse double layer theory (Section 3.2.2.4), it changes the equilibrium between the Van der Waals attractive forces and the electrostatic repulsive forces, which results in the particles rearranging to reach a new equilibrium (Laloui, 2001).

Most of those factors that contribute to increasing the temperature-induced plasticity are related to the physico-chemical interaction between clay particles. The soil plasticity index is a good indicator of the importance of the water-mineral interactions in clays. So, there should be a correlation between the plasticity index of soil and the irreversible strain induced by a thermal cycle on normally consolidated soils. Demarks and Charles (1982) show this relation for six different clays. Table 3.3 and Figure 3.6 extend this observation for other clays. Even if a clear analytical expression is difficult to extract, the volumetric thermo-plastic strain of normally consolidated soil, reported by unit temperature change, seems to increase when the plasticity index increases. This is in agreement with the observation of Demarks and Charles (1982).

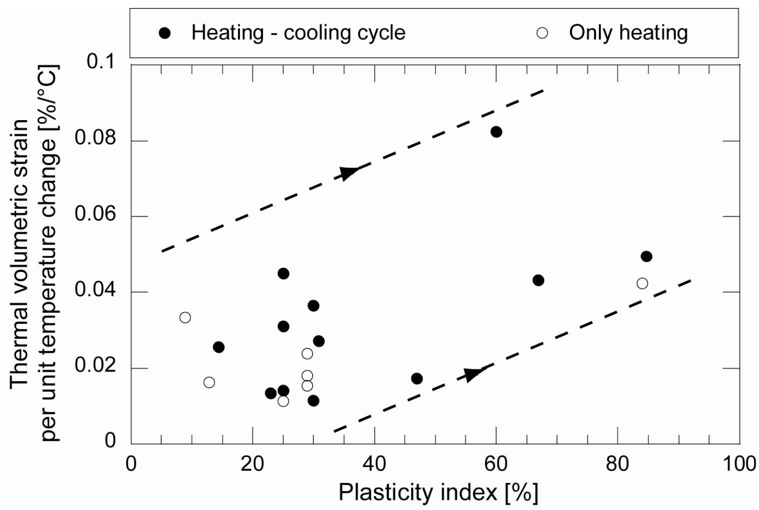

Figure 3.6 : Relation between the plasticity index and the temperature-induced contractile strain. The numerical values are reported in Table 3.3.

Authors	Clay type	T_0 [°C]	T_1 [°C]	ΔT [°C]	Thermal Cycle	I_p [%]	ε_v [%]	$\varepsilon_v/°C$ [%/°C]
Campanella and Mitchell (1968), Campanella (1965)	Remoulded illite	5	60	55	Yes	47	0.95	0.017
Paaswell (1967)	Penn soil	30	60	30	No	8.9	1	0.033
Plum and Ersig (1969)	Illite	24	50	26	No	84	1.1	0.042
Hueckel and Baldi (1990)	Boom clay	22	80	58	Yes	25	1.8	0.031
	Pontida clay	22	60	38	No	12.9	0.62	0.016
Robinet et al. (1997)	Bassin Parisien clay	20	80	60	Yes	30	0.69	0.011
	Boom clay	20	80	60	Yes	25	0.85	0.014
Abuel-Naga et al. (2007)	Bangkok clay	22	90	68	Yes	60	5.6	0.082
Del Olmo et al. (1996), Hueckel et al. (1998)	Spanish clay	20	100	80	Yes	23	1.08	0.013
Laloui and Cekerevac (2003)	Kaolin clay	20	95	75	No	23	0.85	0.011
Demarks and Charles (1982)	Atlantic Marine clay	25	50	25	Yes	25	1.24	0.049
	Atlantic Marine clay	25	50	25	Yes	84.7	1.08	0.043
	Atlantic Marine clay	25	50	25	Yes	66.9	0.68	0.027
	Atlantic Marine clay	25	50	25	Yes	30.8	0.64	0.025
Burghignoli et al. (2000)	Todi clay	22	48	26	Yes	14.4	0.95	0.036
Sultan et al. (2002)	Boom clay	22	100	78	Yes	30	3.5	0.044
Towhata et al. (1993)	MC clay	20	90	70	No	25	1.66	0.023
	MC clay	20	90	70	No	29	1.08	0.015
	MC clay	20	90	70	No	29	1.26	0.018

Table 3.3: For different clayey soils, contractile volumetric strain induced by a temperature change at constant mean effective stress under normally consolidated conditions. Correlation with the plasticity index of the soil. Thermal cycle: Yes: Heating-cooling cycle; No: only heating.

In contrast to the NC state, the highly overconsolidated (OC) soils produce mainly reversible dilation when they are heated. The micro-mechanical processes that could explain the thermo-plasticity of NC soils remain active for highly OC soils. However, the low stress level does not supply enough acting force between particles to modify the soil structure. In that sense, the particle arrangement remains fixed, and only thermo-elastic strain is produced. As explained in Section 3.2.3, this reversible thermal strain depends on the thermal expansion of each mineral constituent, on the porosity and on some other electrostatic properties of the soils.

Between these two opposite stress states (NC and highly OC), an intermediate one (low overconsolidation ratio) first produces dilation and then a tendency toward contraction. Upon such transitional states, contacts between particles have low stability with regard to sliding or failure. A small change in temperature does not produce sufficient micro-mechanical modifications to generate particle rearrangements. However, as far as temperature change, the contact particle becomes progressively unstable, which allows relative displacements between particles.

In summary, during drained heating, the response of fine-grained soil is strongly affected by the stress level (through the overconsolidation ratio, OCR). The soil exhibits irreversible contraction for NC soil, reversible expansion for highly OC soils and transition behaviour for slightly OC soils. This behaviour is illustrated in Figure 3.7 for four different soils. Figure 3.7a and Figure 3.7b reproduce complete heating-cooling cycles on Boom clay and Bangkok clay, respectively. Figure

3.7c and Figure 3.7d represent the soil response within the heating phase for Kaolin clay and Pasquasia clay, respectively. In Figure 3.8, the influence of OCR on the thermally-induced volumetric strain is summarized for six different materials.

3.3.2 Temperature effect on compression behaviour

3.3.2.1 *Temperature effect on the preconsolidation pressure*

Preconsolidation pressure, p_c', is considered here as the stress yield limit that separates "elastic" pre-yield from "plastic" post-yield behaviour under isotropic or oedometric conditions. Several results from the literature show a decrease in the preconsolidation pressure with increasing temperature. Therefore, the elastic domain under isotropic loading is reduced as temperature increases, which is representative of thermo-plasticity. Laloui and Cekerevac (2003) proposed the following equation to describe this thermo-mechanical behavioural feature:

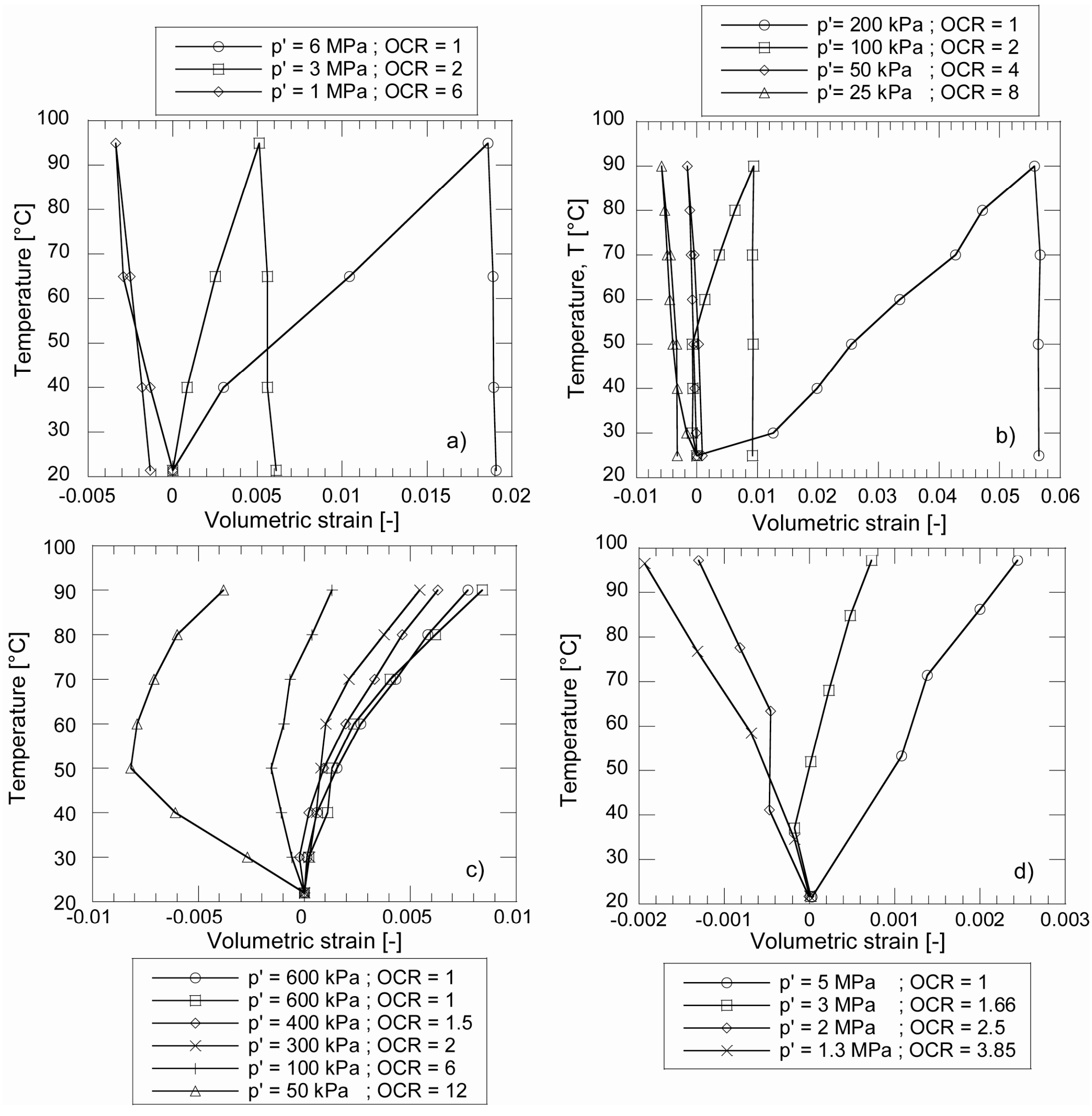

Figure 3.7 : Typical volumetric strain induced by heating-cooling cycles at different overconsolidation ratios. (a) Boom clay (Baldi et al., 1991); (b) Bangkok clay (Abuel-Naga et al., 2007); (c) Kaolin clay (Cekerevac and Laloui, 2004); (d) Pasquasia clay (Del Olmo et al., 1996).

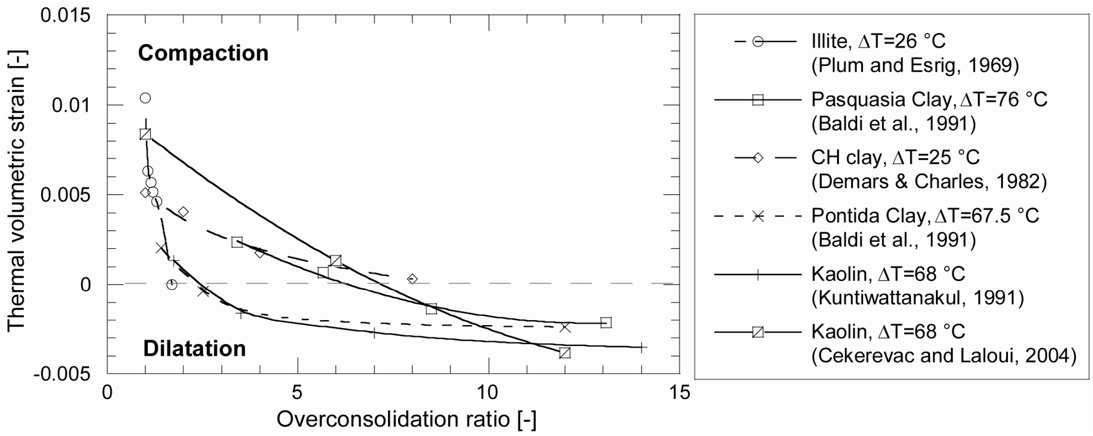

Figure 3.8 : Influence of overconsolidation ratio on the thermal strain of fine-grained soils (from Cekerevac and Laloui, 2004).

$$p'_c = p'_{c0}\left(1-\gamma_T \log\left[T/T_0\right]\right) \tag{3.22}$$

where p'_c is the preconsolidation pressure at a given temperature T, while p'_{c0} is the preconsolidation pressure at the reference temperature T_0. γ_T is a material parameter that varies with the soil considered. Laloui and Cekerevac (2003) validated Equation (3.22) with several experimental results on various clayey materials.

During a consolidation process, the yield limit corresponds to the stress level that begins to produce a change of the soil structure. In that sense, the decrease of yield limit with temperature may be ascribed to the temperature-induced physico-chemical modifications in clay at the micro-scale. The combinations of several micro-mechanical processes tend to make the rearrangements of particles easier, reducing the yield limit of the material. In the same way as the thermal contractile volumetric strain, the decrease in preconsolidation pressure should be linked to the plasticity index, which is a good indicator of the importance of the water-mineral interaction in clays. Table 3.4 and Figure 3.9 report the value of γ_T with respect to the plasticity index. Although there is some spread of the point distribution, Figure 3.9 seems to validate the assumptions of the increase of thermo-plastic effects as the plasticity index increases.

In addition to Equation (3.22) proposed by Laloui and Cekerevac (2003), several authors suggested analytical expressions to describe the shrinkage of the yield limit with increasing temperature:

$$p'_c(T) = p'_c(T_0)\exp\left(-\alpha_0\left[T-T_0\right]\right) \quad \text{(Cui et al., 2000)} \tag{3.23}$$

$$p'_c(T) = p'_c(T_0) + 2\left(a_1\left[T-T_0\right] + a_2\left[T-T_0\right]\left|T-T_0\right|\right) \quad \text{(Hueckel and Baldi, 1990)} \tag{3.24}$$

$$p'_c(T) = p'_c(T)\left(1+C\left[T-T_0\right]\right) \quad \text{(Boudali et al., 1994)} \tag{3.25}$$

$$p'_c(T) = p'_c(T_0)\left[\frac{T_0}{T}\right]^n \quad \text{(Moritz, 1995)} \tag{3.26}$$

where α_0, a_1, a_2, C, and n are material parameters.

Figure 3.10 compares the best fit of these expressions with different experimental results on Swedish clays (Eriksson, 1989; Moritz, 1995; Tidfors and Sällfors, 1989), on a natural clay from Canada (Boudali et al., 1994) and on artificial Kaolin clay samples (Cekerevac and Laloui, 2004). Those experimental results are reported in Cekerevac (2003). Most of the analytical expressions catch the good trend of the experimental evolution p_c' with temperature. However, a linear relation is unable to reproduce the attenuation of the preconsolidation pressure decrease under elevated temperature. The general trend shows that the more the temperature increases, the more the preconsolidation pressure tends toward stabilisation. Thus, a logarithmic or a non-linear relation seems to be more appropriate. Also, the quadratic expression of Hueckel and Baldi (1990) requires two parameters instead of one for the other expressions.

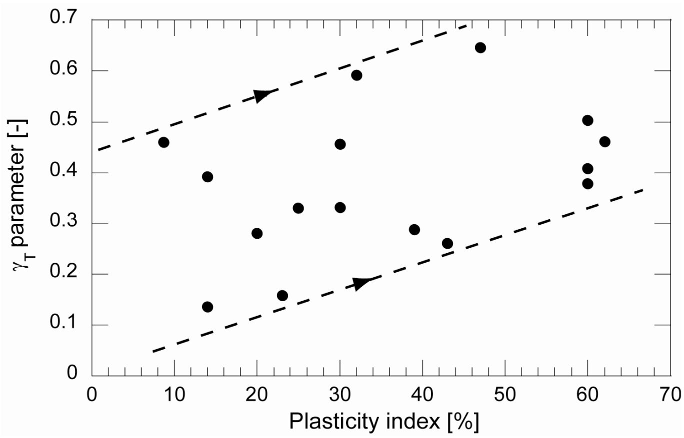

Figure 3.9 : Relation between the plasticity index and the γ_T parameter quantifying the decrease of the preconsolidation pressure with temperature. The numerical values are reported in Table 3.4.

Authors	Clay type	I_p [%]	T_0 [°C]	T_1 [°C]	T_1/T_0 [-]	p'_{c0} [kPa]	p'_{c1} [kPa]	p'_{c1}/p'_{c0} [-]	γ_T [-]
Tidfors and Sällfors (1989)	Backebol clay	60	7	30	4.28	62	46	0.74	0.41
Campanella and Mitchell (1968)	Remoulded illite	47	25	51	2.04	200	160	0.8	0.65
Boudali et al. (1994)	Bertheville clay	25	5	35	7	68	49	0.72	0.33
	Louiseville clay	39	5	35	7	198	150	0.76	0.29
	Saint-Jean Vianney clay	14	5	35	7	1040	921	0.89	0.14
Burghignoli et al. (2000)	Todi clay	30	18	48	2.66	184	158	0.89	0.33
Marques et al. (2004)	Saint-Roch de l'Achigan clay	43	10	50	5	165	135	0.82	0.26
Eriksson (1989)	Lulea clay	60	5	55	11	61	37	0.61	0.38
Abuel Naga et al. (2006)	Bangkok clay	60	25	90	3.6	200	144	0.72	0.50
Hueckel and Baldi (1990)	Pontida clay	14	22	90	4.09	2500	1900	0.76	0.4
Cekerevac (2003)	Kaolin clay	23	22	95	4.32	600	540	0.9	0.16
Sultan et al. (2002)	Boom clay	30	22	100	4.54	6000	4200	0.7	0.46
Robinet et al (1997)	Kaolinite	20	20	60	3	1500	1300	0.86	0.28
	Smectite	62	20	60	3	1500	1170	0.78	0.46
Despax (1976)	Argile noire	32	20	95	4.75	-	-	-	0.6
Salager et al. (2008)	Sion silt	8.7	22	80	3.64	-	-	-	0.46

Table 3.4: For different soils, reduction of the preconsolidation pressure (from p'_{c0} to p'_{c1}) induced by a temperature variation (from T_0 to T_1). Correlation with the plasticity index of the soil.

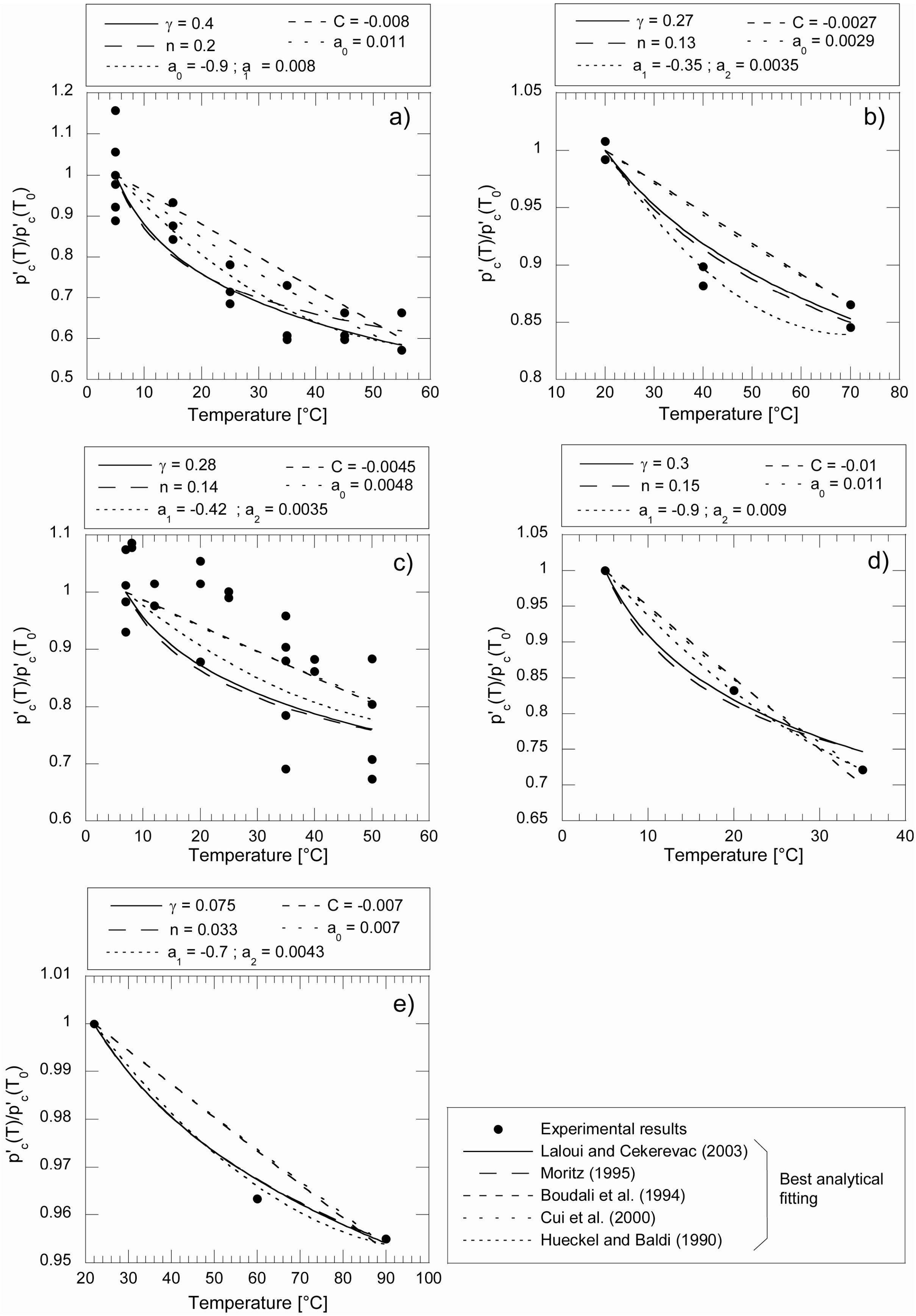

Figure 3.10 : Various analytical fits of the evolution of the preconsolidation pressure with temperature, compared with experimental results from (a) Eriksson (1989), (b) Moritz (1995), (c) Tidfors and Sällfors (1989), (d) Boudali et al. (1994) and (e) Cekeravec and Laloui (2004).

3.3.2.2 *Temperature effect on the compression and swelling indexes*

As far as the compression index is concerned, the slope of the compression line seems to be essentially independent of temperature (Finn, 1951; Campanella and Mitchell, 1968; Graham et al., 2001; Despax, 1976; Laloui and Cekerevac, 2003). The normally consolidated line moves in parallel toward lower stress levels with increasing temperature, due to the temperature-induced reduction of the yield limit. However, a few contradictory experimental results show non-parallel consolidation curves at different temperatures (Plum and Ersig, 1969; Tanaka et al., 1997; Sultan et al., 2002). Under mechanical unloading, the swelling index also remains unaffected by temperature change. At least, most of the experimental studies at different temperatures show variability in the swelling index, but remaining in the range of usual variation for different samples of the same material. Figure 3.11 exhibits typical consolidation curves at different temperatures.

3.3.2.3 *Temperature-induced overconsolidated behaviour*

Several research studies have shown that a heating-cooling cycle produces overconsolidated behaviour in the material (Plum and Ersig, 1969; Sultan et al., 2002; Hueckel and Baldi, 1990). This behavioural feature is due to the thermal hardening process generated upon heating. Even though there has been no physical change in effective stresses, the soil undergoes irreversible densification, similar to a consolidation process. As a consequence, after the subsequent cooling, the soil, which is denser than before the thermal cycle, behaves as an overconsolidated material. Figure 3.12 illustrates such a feature in two different materials.

3.3.3 Temperature effect under undrained conditions

3.3.3.1 *Undrained thermal loading under constant isotropic stress conditions*

Many authors studied the thermally-induced pore water pressure under isotropic conditions (Henkel and Sowa, 1963; Campanella and Mitchell, 1968; Plum and Ersig, 1969; Houston et al., 1985; Agar et al., 1986; Hueckel and Pellegrini, 1992; Tanaka et al., 1997; Abuel-Naga et al., 2007, among others).

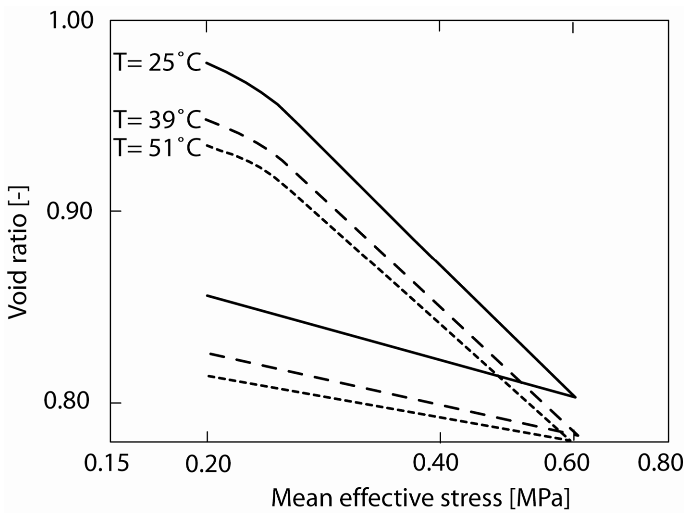

Figure 3.11 : Isotropic consolidation of a remoulded illite at three different temperatures (Campanella and Mitchell, 1968).

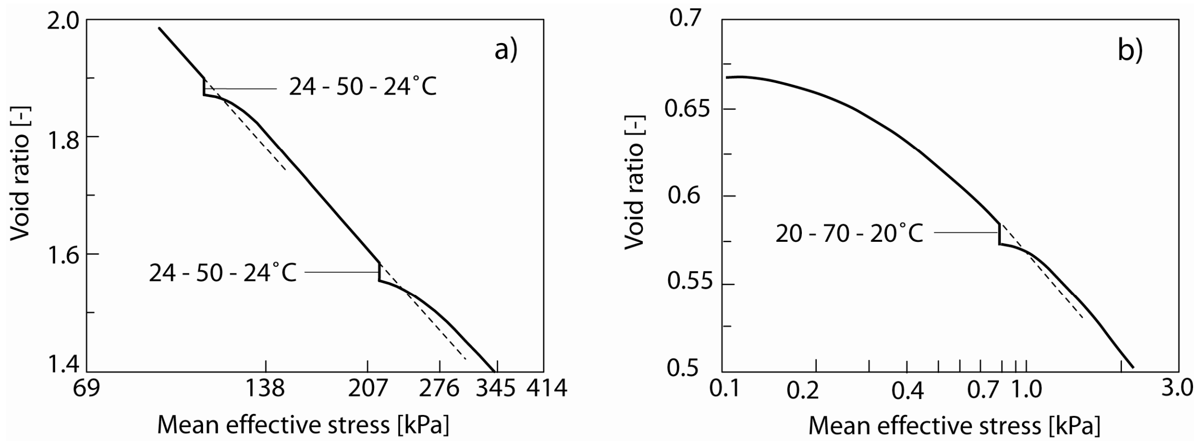

Figure 3.12 : Effect of heating-cooling cycle on the consolidation of (a) Illite (Plum and Ersig, 1969) and (b) Boom clay (Sultan et al., 2002). Smoothed experimental results.

The higher thermal expansion of water than that of the solid skeleton induces pore water pressure increase when a saturated soil is heated under undrained conditions. A temperature increase tends to enhance the pore space of the material proportionally to the thermal expansion coefficient of the solid skeleton. Nevertheless, this effect is more than counterbalanced by the thermal dilation of water (Campanella and Mitchell, 1968). So, the main factor controlling the pore water pressure generated upon undrained heating is the difference between the coefficients of thermal expansion for the solid skeleton and for the water. The thermal expansion coefficient of the water ($\beta'_w \approx 4\ 10^{-4}$) is more than one order of magnitude greater than that for the usual mineral phases ($\beta'_s \approx 2\ 10^{-5}$). Campanella and Mitchell (1968) identified several other factors affecting the generation of pore water pressure under undrained conditions: the temperature range, the porosity and the compressibility of the soil structure.

Under heating-cooling cycles, the pore pressure-temperature relation forms a hysteresis loop (Figure 3.13). Many authors explained this loop through the changes in soil compressibility during mechanical rebound and recompression. When pore water pressure increases, the soil undergoes a mechanical unloading (i.e. a decrease of the mean effective stress). During this unloading, the soil rigidity is governed by the unloading rigidity. On the contrary, upon cooling, the pore water pressure decrease and the rigidity corresponds to a rigidity of recompression. The temperature-induced pore water pressure being dependent on the soil rigidity, the pore water pressures during the heating and cooling phases do not coincide. In the overconsolidated state, this difference in rigidities may induce the generation of irreversible negative pore water pressure (Abuel-Naga et al., 2007). In contrast, thermo-plastic effects produce irreversible positive pore water pressure following a thermal cycle (Hueckel and Pellegrini, 1992).

3.3.3.2 *Undrained thermal loading under constant deviatoric stress conditions*

Under anisotropically, normally consolidated conditions, undrained monotonic heating may produce failure of soils. The combination of the pore water pressure increase (i.e. a decrease of the mean effective stress) and the temperature-induced shrinkage of the elastic domain lead the soil up to a critical state. As long as the temperature increases, the mean effective stress decreases, but the deviatoric stress remains constant. In addition, the elastic domain is reduced due to the decrease of the preconsolidation pressure. If the shrinkage of the elastic domain is faster than the decrease of the mean effective stress, it induces a plastic process that tends to generate an axial strain increase until the critical state is reached.

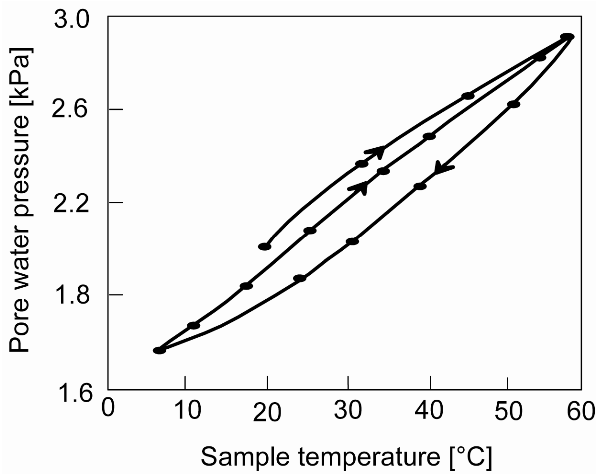

Figure 3.13 : Temperature-induced pore water pressure on normally consolidated remoulded illite under undrained conditions (after Campanella and Mitchell, 1968).

Hueckel and Pellegrini (1992) (see also Hueckel and Pellegrini, 1989) observed such a process in Boom clay. The specimen was isotropically consolidated at 5.75 MPa and then subjected to a stress difference of 2 MPa under undrained conditions. Then, the specimen was heated under undrained conditions at a constant total stress leading to failure at 92°C ($\Delta T = 71°C$) (Figure 3.14). Agar et al. (1986) noticed similar thermally-induced failure under shearing. On the contrary, Hueckel and Pellegrini (1989) observed that, in a non-isotropic overconsolidated state, undrained heating does not seem to lead to failure.

3.3.4 Temperature effect on shearing behaviour

3.3.4.1 *Temperature effect on elastic modulus*

Temperature seems to have a stiffening effect on the elastic behaviour of soil upon distortional paths. The little experimental data provided in the literature seems, more or less, to agree on that sense. In a Kaolin clay, Cekerevac and Laloui (2004) observed a higher soil stiffness at 90°C than at 22°C (Figure 3.15a). Kuntiwattanakul et al. (1995) noticed also that the secant modulus under a 0.1% strain increases with increasing temperature for both normally consolidated and highly overconsolidated soils (Figure 3.15b).

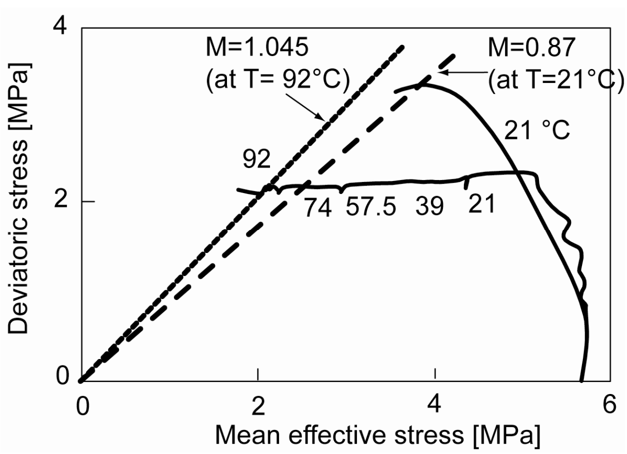

Figure 3.14 : Effective stress path undergone by Boom clay upon undrained heating under constant non-isotropic stress condition (from Hueckel and Pellegrini, 1992).

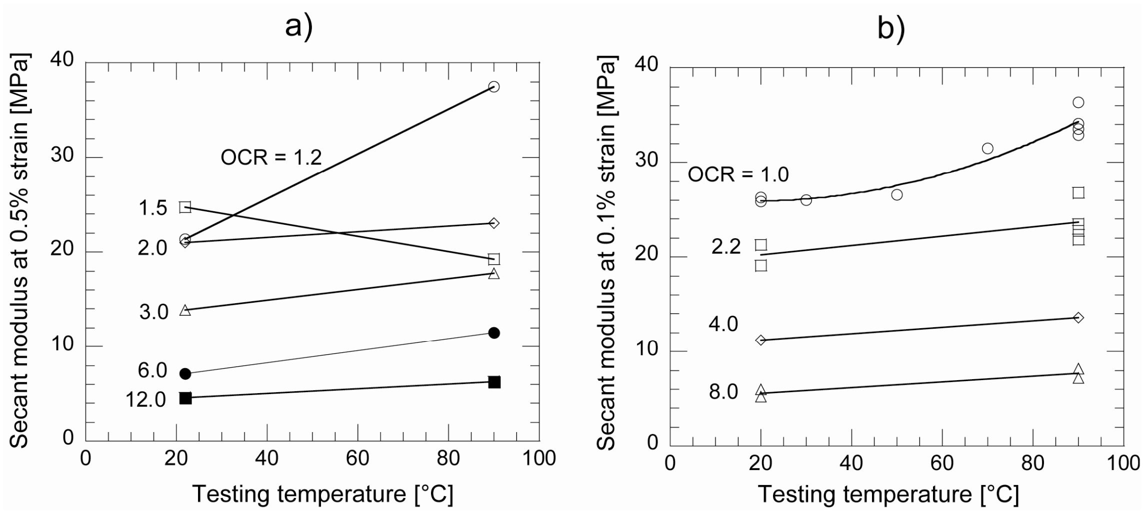

Figure 3.15 : Effect of temperature on the secant elastic modulus observed upon triaxial shearing. (a) Kaolin clay (Cekerevac and Laloui, 2004); (b) MC clay (Kuntiwattanakul et al., 1995). The OCR is calculated at ambient temperature.

In the same vein, Abuel-Naga (2005) detected a similar increase in stiffness with temperature in a Bangkok clay. On the contrary, Burghignoli et al. (2000) did not observe a significant effect of temperature on Tody clay stiffness, if that temperature is the highest temperature experienced by the soil. However, they noted that a thermal cycle performed before triaxial shearing tends to increase the stiffness of the soil. This increase can be explained in terms of temperature-induced overconsolidated behaviour.

3.3.4.2 *Temperature effect on shear strength*

Until recently, the thermal effect on shear strength lacked confirmation. Some researchers concluded that heating caused a decrease in strength, while others reported slightly increased strength. Some experimental results are summarised by Cekerevac and Laloui (2004), which tend to confirm that the friction angle at the critical state can either slightly increase or decrease with temperature. However, comparison is not always possible due to the variability in experimental techniques, stress and strain paths and drainage conditions during heating and shearing. For instance, Hueckel and Pellegrini (1989) observed that the slope of the friction angle at the critical state of Pontida clay is unaffected by temperature under both drained and undrained shearing. In contrast, the same authors noticed a slight increase in friction angle of Boom clay under undrained shearing. They attributed this difference to the relatively high amount of illite and smectite in Boom clay. Such minerals are surrounded by an appreciable amount of adsorbed water, which is sensitive to temperature change.

In term of maximal deviatoric stress, Cekerevac (2003) as well as Kuntiwattanakul et al. (1995) observed a slight increase in the peak strength as temperature increases, in a Kaolin clay and MC clay, respectively (Figure 3.16). However, drawing any general conclusions remains delicate because of the discrepancy among some results in the literature. For instance, Abuel-Naga et al. (2006) also noticed an increase of the maximal deviatoric stress upon triaxial shearing of normally consolidated Bangkok clay, while Hueckel et al. (1998) suggested that the peak strength of a Spanish clay decreases by about 25% for a temperature increase from 22° to 120 °C.

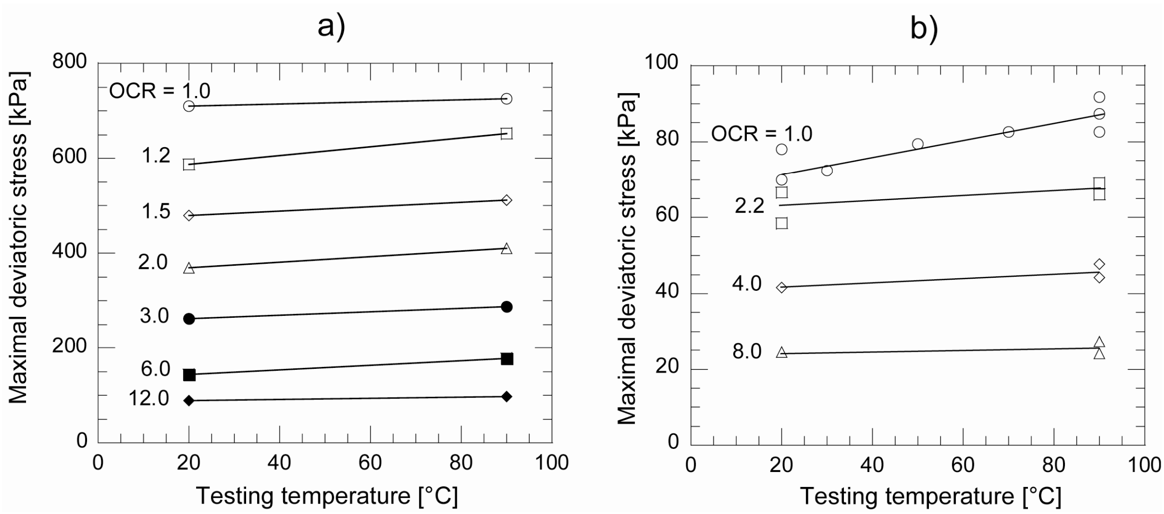

Figure 3.16 : Effect of temperature on the maximal deviatoric stress observed upon triaxial shearing. (a) Kaolin clay (Cekerevac, 2003); (b) MC clay (Kuntiwattanakul et al., 1995). The OCR is calculated at ambient temperature.

3.3.4.3 *Temperature effect on flow rule*

Upon distortional yielding, the flow rule defines the ratio between volumetric plastic strain increment $d\varepsilon_v^p$ and deviatoric plastic strain increment $d\varepsilon_d^p$. The associated flow rule postulates that, irrespective of the stress increment vector, beyond the yield limit the corresponding plastic strain increment vector should be normal to the yield limit (Schofield and Worth, 1968). However, most of the soils do not obey an associated flow rule. The yield limit and plastic strain increment can be examined together by aligning $d\varepsilon_v^p$ with p' and $d\varepsilon_d^p$ with q. For Kaolin clay, Cekerevac and Laloui (2004) investigated the effect of temperature on the deviatoric yield locus and the plastic strain increment vector, calculated for a stress increment of 60 kPa. These two data are reported in Figure 3.17a in a normalized plane. The normality rule not being satisfied, Cekerevac and Laloui (2004) studied the effect of temperature on the deviation of the plastic strain increment vectors with respect to the normal to the yield limit (Figure 3.17b). They concluded that, for highly overconsolidated states, the deviation is not affected by temperature. In contrast, when the OCR decreases, the directions of plastic strain obtained at 90°C are quite different from those observed at 22°C. So, they concluded that temperature may have an effect on the flow rule.

Contrary to this, on non-conventional triaxial test paths, Graham et al. (2001) noted that remoulded illite appears to approximately conform to the associated flow rule, no matter the temperature of the test. The authors suggested (with some caution) that an associated flow rule could be assumed without serious error, although some variations in the results were detected.

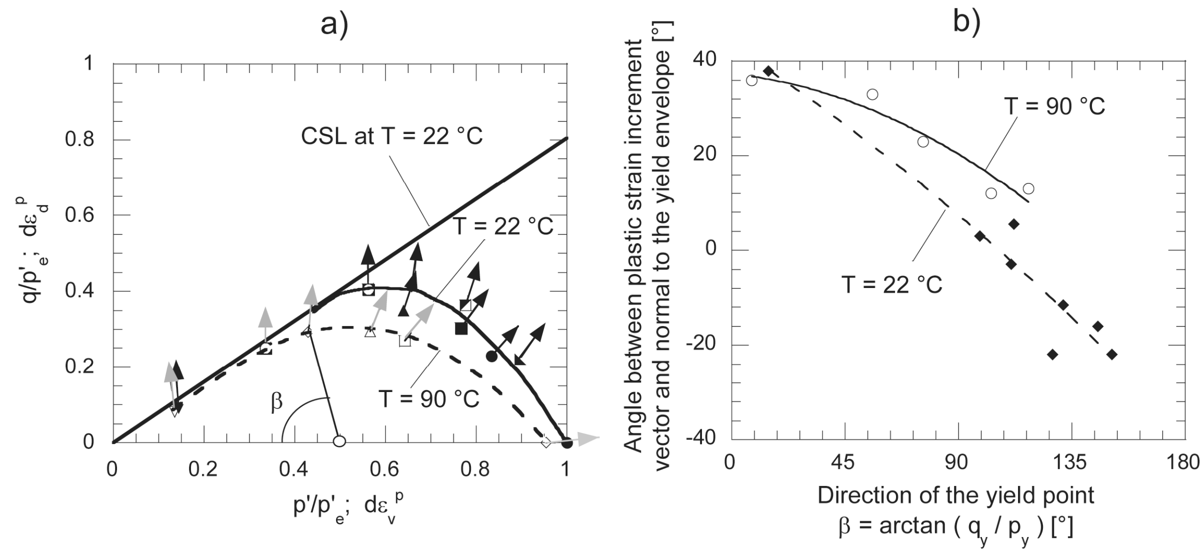

Figure 3.17 : Effect of temperature on the flow rule of Kaolin clay (T = 22°C and 90°C) (Laloui and Cekerevac, 2004). (a) Normalized yield envelope and plastic strain increment vectors, (b) deviation of the plastic strain increment vector from normal to the yield envelope.

3.3.5 Conclusions

In this section, a literature analysis of the experimental evidence on the thermo-mechanical behaviour of soils has been carried out. It reveals the necessity to consider thermal effects on the mechanical response of soils not only in terms of reversible phenomena, but also in term of thermo-plasticity. Such thermo-plastic processes are affected by the microstructure of the materials. The correlation between the temperature-induced macroscopic irreversibility and the plasticity index of the soil was underlined. The predominant effect of temperature on the behaviour of fine-grained soils is the causation of successively lower void ratios with temperature increasing for a given stress level. The normally consolidated lines at different temperatures are parallel and shifted to the left with increasing temperature. As a consequence, in a normally consolidated state, the soil undergoes thermal hardening (i.e. densification) upon heating in order to reach the normally consolidated line corresponding to the current temperature. This densification produces overconsolidated behaviour of the soil after the heating-cooling cycle.

Under undrained conditions, the generation of pore water pressure upon heating is a consequence of a higher thermal expansion coefficient of water than of the mineral phase. Also, thermo-plastic processes may induce additional pore water pressure. As far as distortional paths are concerned, temperature may affect the elastic modulus, the friction angle at the critical state, the peak strength and the post-yielding flow rule. Nevertheless, those temperature effects seem to depend on the soil type as well as the experimental conditions.

3.4 Relevant contributions to the thermo-mechanical constitutive modelling of soils

The constitutive developments dealing with the thermo-mechanical behaviour of saturated soils were investigated by the precursory works of Campanella and Mitchell (1968), wherein the mechanical response of soil along non-isothermal paths was interpreted by means of constitutive relations. The volume change in drained conditions or the generated pore water pressure in undrained conditions on non-isothermal paths were estimated through theoretical analyses based on the thermal dilatation coefficients of each soil constituent (water and solid), the repartition between phases (i.e. porosity) and the compressibility of water. In addition, the irreversible processes due to temperature were related to physico-chemical structural adjustments.

Noting the lack of experimental data on the thermal effects on soils at the micro-scale, Hueckel and Borsetto (1990) proposed a macroscopic thermo-mechanical model based on phenomenological experiments. This model introduced thermo-plasticity in addition to classical thermo-elasticity of soil. Starting from a modified Cam-Clay model (Roscoe and Burland, 1968), the thermal shrinkage of the yield surface was introduced through the decrease of the preconsolidation pressure with temperature increase. The consistency equation had to be substantially adapted to consider temperature as a state variable. This work pioneered modern thermo-plasticity constitutive modeling of fine-grained soils. However, some specific behavioural features were not fully reproduced by this precursory model. In particular, the irreversible thermal strain observed at intermediate degrees of surconsolidation (OCR) was not considered.

In the same vein, further developments were proposed by Modaressi and Laloui (1997), who started from an isothermal elasto-plastic multi-mechanism model (Hujeux, 1979) to develop a visco-thermo-plastic model that examines the decrease of the preconsolidation pressure with temperature. This matches with the concluding remarks of Hueckel and Borsetto (1990), who state that, for the sole mechanical part of soil behaviour, a more sophisticated model should be chosen over the modified Cam-Clay. Later, Laloui and Cekerevac (2003) enhanced this model by introducing a logarithmic expression for the evolution of preconsolidation pressure with temperature that required only one material parameter.

Aware of the need to improve the role of the OCR on the thermal expanding/contracting behaviour in the aforementioned models, Cui et al. (2000) added a new thermal yield curve to allow for the generation of thermal irrecoverable strain, even at high OCR. As a consequence, the yield surface initially proposed by Hueckel and Borsetto (1990) was coupled with this new thermal yield limit.

3.5 The ACMEG-T model[1,2]

3.5.1 Introduction

The ACMEG-T model is an extension toward the non-isothermal state of the ACMEG model, addressed in the previous chapter (Section 2.3) devoted to isothermal and saturated conditions. The ACMEG-T model aims to consider the thermo-mechanical features of soil behaviour in addition to the mechanical response (Laloui et al., 2005; Laloui and François, 2008). So, this thermo-mechanical model keeps the structure of the isothermal model (non-linear elasticity, critical state theory, multi-mechanism plasticity and the bounding surface concept).

The following section details the specifics of the unified mechanical and thermal parts of the model. The main constitutive relations, already addressed in Section 2.3, are completed in the context of non-isothermal conditions. Following this, typical responses of the ACMEG-T model on thermo-mechanical paths are depicted. Finally, some selected comparisons between model

[1] Laloui L., Cekerevac C. and François B. (2005). Constitutive modelling of the thermo-plastic behaviour of soils. *Revue Européenne de Génie Civil* 9, 5-6 : 635-650.

[2] Laloui L. and François B. (2008). ACMEG-T: A soil thermo-plasticity model. *Journal of Engineering Mechanics.* (Accepted).

simulations and experimental results for different combinations of thermo-mechanical loading paths are presented.

Here, the considered temperature range is from 5 °C to 95 °C, which corresponds to that of the principal geo-environmental applications concerned (without freezing or boiling of the pore water).

3.5.2 Thermo-mechanical constitutive equations

3.5.2.1 *Thermo-elasticity*

In addition to the mechanically induced hypo-elastic strain increment $d\varepsilon_{ij}^{me}$ (Equation (2.66)), the total elastic strain increment must consider a reversible thermal strain increment of the solid skeleton $d\varepsilon_{ij}^{Te}$ (Duhamel-Neumann equation):

$$d\varepsilon_{ij}^{e} = d\varepsilon_{ij}^{me} + d\varepsilon_{ij}^{Te} = E_{ijkl}^{-1} d\sigma'_{kl} - \beta_{\mathrm{T},ij} dT \tag{3.27}$$

The mechanical elastic tensor E_{ijkl} is defined in Equations (2.67) and (2.68). $\beta_{\mathrm{T},ij}$ is the expansion coefficient vector which depends on temperature, T. Considering an isotropic thermal dilatation, one can express the thermal coefficient as $\beta_{\mathrm{T},ij} = (1/3)\beta'_s\ \delta_{ij}$ with β'_s being the volumetric thermal expansion coefficient of the solid skeleton and δ_{ij} Kronecker's symbol. The volumetric and deviatoric parts of the tensor of the elastic strain increment are, respectively:

$$d\varepsilon_{v}^{e} = d\varepsilon_{v}^{me} + d\varepsilon_{v}^{Te} = \frac{dp'}{K} - \beta'_s dT \tag{3.28}$$

$$d\varepsilon_{d}^{e} = \frac{dq}{3G} \tag{3.29}$$

The volumetric thermal expansion coefficient of the solid skeleton, β'_s, increases with temperature and decreases as stress level increases:

$$\beta'_s = \left[\beta'_{s0} + \zeta\left(T - T_0\right)\right]\xi \tag{3.30}$$

in which β'_{s0} is the isotropic thermal expansion coefficient at a reference temperature, T_0 (usually ambient temperature), and ξ the ratio between the initial critical state pressure at ambient temperature, p'_{cr0}, and the mean effective stress, p':

$$\xi = \frac{p'_{cr0}}{p'} \tag{3.31}$$

ζ corresponds to the slope of the variation of β'_s with respect to the current temperature, T, at $\xi=1$. The ζ dimension is °C^{-2}. Experimental evidence shows that this parameter (ζ) could be approximated by $\left[-\beta'_{s0}/(100°C)\right]$ (Laloui, 1993).

3.5.2.2 *Thermo-plasticity*

From Equations (2.63) and (3.27), the thermo-plastic strain increment can be expressed as the part of the total strain increment which is not recoverable:

$$d\varepsilon_{ij}^{p} = d\varepsilon_{ij} - d\varepsilon_{ij}^{e} = d\varepsilon_{ij} + \beta_{\mathrm{T},ij}\ dT - E_{ijkl}^{-1}\ d\sigma'_{kl} \tag{3.32}$$

Within the multi-mechanism concept, the two plastic mechanisms (Section 2.3.2.2) are affected by temperature. In the two following sections, the yield limits of the isotropic and deviatoric mechanism, respectively, are recalled and the temperature-induced modifications of those relations are presented.

Isotropic thermo-plastic mechanism

Similarly to Equation (2.71), the yield limit, f_{iso}, of the isotropic thermo-plastic mechanism is expressed by :

$$f_{iso} = p' - p'_c\ r_{iso} \tag{3.33}$$

r_{iso} corresponds to the degree of plastification (mobilised hardening) of the isotropic yield limit (Equation (2.72)). The thermal effect on the isotropic mechanism is introduced through the evolution of the preconsolidation pressure p'_c with temperature (Figure 3.18a). As shown in Section 3.3.2.1 (Equations (3.22) to (3.26) and Figure 3.10), several authors suggested analytical expressions to describe the shrinkage of the yield limit with increasing temperature. The evolution of p'_c with temperature being rapid for low temperature changes and becoming asymptotic for the high ones, the logarithmic function of Laloui and Cekerevac (2003) is a very suitable expression to model this phenomenon (Equation (3.22)). The preconsolidation pressure must also be expressed as a function of the volumetric plastic strain (Equation (2.74)). Finally, the thermo-mechanical evolution of the preconsolidation pressure is expressed as:

$$p'_c = p'_{c0} \exp\left(\beta\, \varepsilon_v^{P}\right)\left(1 - \gamma_T \log\left[T/T_0\right]\right) \tag{3.34}$$

where p'_{c0} is the initial value of the preconsolidation pressure at the reference temperature, T_0, β is the plastic compressibility modulus (the slope of the linear function $\varepsilon_v^p - \log p'_c$) and γ_T is the material parameter defining the shape of the isotropic yield limit with respect to temperature (Figure 3.18b).

The flow rule of the isotropic mechanism remains unchanged regarding to the isothermal mechanism (Equation (2.75)).

Deviatoric thermo-plastic mechanism

Similarly to Equation (2.76), the yield limit, f_{dev}, of the deviatoric thermo-plastic mechanism is expressed by (Hujeux, 1979):

$$f_{dev} = q - Mp'\left(1 - b\ \ln\frac{d\ p'}{p'_c}\right) r_{dev} = 0 \tag{3.35}$$

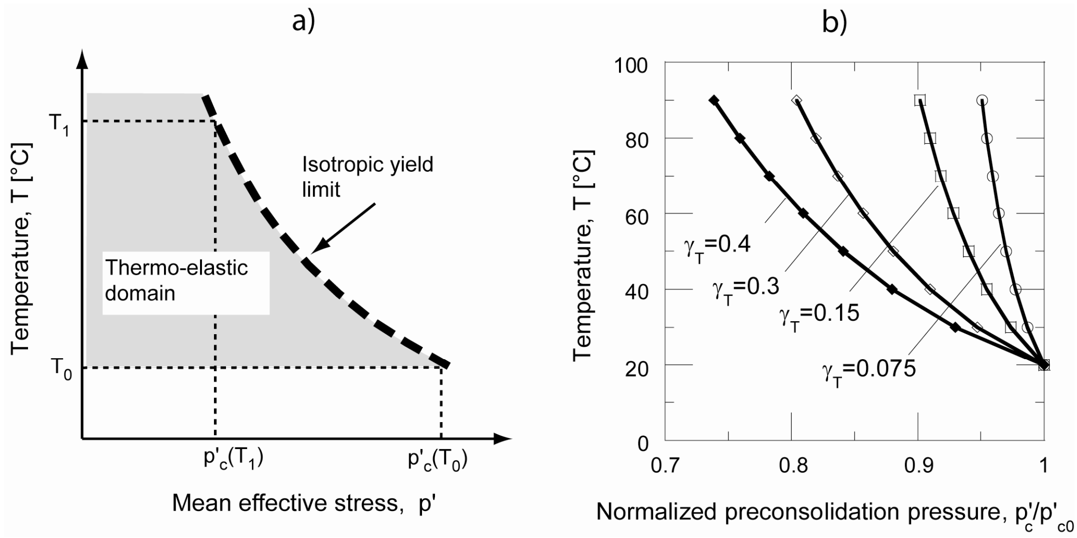

Figure 3.18 : Isotropic thermo-plastic yield limit (a) and its dependency on the γ_T parameter (b) (Laloui and Cekerevac, 2003).

where b is a material parameter defining the shape of the deviatoric yield limit and d the ratio between the preconsolidation pressure, p'_c, and the critical pressure, p'_{cr}. r_{dev}, in the same way as for the isotropic mechanism, is the degree of plastification of the deviatoric mechanism (Equation (2.78)). M is the slope of the critical state line in the ($q-p'$) plane (Equation (2.77)). As shown in Section 3.3.4.2, the friction angle may depend on temperature. So, the following expression is proposed (Laloui 1993):

$$M = M_0 - g\left(T - T_0\right) \tag{3.36}$$

where M_0 is the slope of the critical state line at ambient temperature T_0 and g is an average slope of variation of friction angle at critical state with temperature.

Through a combination of Equations (3.34), (3.35) and (3.36), the deviatoric yield surface becomes, under non-isothermal conditions (Figure 3.19):

$$f_{dev} = q - r_{dev} p' \left[M_0 - g\left(T - T_0\right)\right]\left(1 - b\ \ln \frac{d\ p'}{p'_{c0}\exp\left(\beta\varepsilon_v^p\right)\left[1-\gamma_T \log\left[T/T_0\right]\right]}\right) = 0 \tag{3.37}$$

The hardening and dilatancy rules of the deviatoric mechanism remain unchanged regarding to the isothermal mechanism (Equations (2.79) to (2.84))).

Coupling between the two thermo-plastic mechanisms

The coupling between the two thermo-plastic mechanisms is similar to the isothermal model (Section 2.3.3.2). However, inclusion of the derivation of the yield limits with respect to temperature is required in the consistency conditions for multi-mechanism (Equation (2.86)) due to the evolution of both yield limits with temperature state (Prager, 1958). In that sense, the effective stress and the temperature are the two state variables of the model:

$$\mathbf{dF} = \frac{\partial \mathbf{F}}{\partial \boldsymbol{\sigma}'} : d\boldsymbol{\sigma}' + \frac{\partial \mathbf{F}}{\partial \mathrm{T}}.d\mathrm{T} + \frac{\partial \mathbf{F}}{\partial \boldsymbol{\pi}}.\frac{\partial \boldsymbol{\pi}}{\partial \boldsymbol{\lambda}^{\mathbf{p}}}.\boldsymbol{\lambda}^{\mathbf{p}} = \mathbf{j} : d\boldsymbol{\sigma}' + \mathbf{t}.d\mathrm{T} - \mathbf{H}.\boldsymbol{\lambda}^{\mathbf{p}} \leq 0\ ;\ \boldsymbol{\lambda}^{\mathbf{p}} \geq 0\ ;\ \mathbf{dF}.\boldsymbol{\lambda}^{\mathbf{p}} \geq 0 \tag{3.38}$$

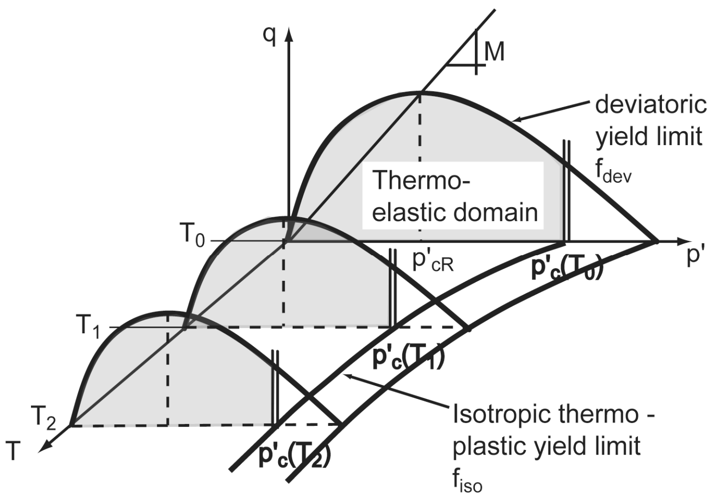

Figure 3.19 : Coupled thermo-plastic yield limits.

All the isothermal terms are detailed in Section 2.3.3.2. $\mathbf{t}$ collects the temperature-gradient of the loading function $\mathbf{F}$. The elasto-plastic framework (Equation (3.32)) enables the stress increment response with respect to prescribed strain increment to be expressed as:

$$d\boldsymbol{\sigma}' = \mathbf{E} : \left(d\boldsymbol{\varepsilon} - d\boldsymbol{\varepsilon}^{\mathbf{Te}} - \mathbf{m}.\boldsymbol{\lambda}^{\mathbf{p}} \right) = \mathbf{E} : \left(d\boldsymbol{\varepsilon} - \boldsymbol{\beta}_{\mathbf{T}} dT - \mathbf{m}.\boldsymbol{\lambda}^{\mathbf{p}} \right) \tag{3.39}$$

where $\mathbf{E}$ is the current elastic stiffness tensor of the material, $\mathbf{m}$ defines the collection of flow directions; $\mathbf{m} = \dfrac{\partial \mathbf{G}}{\partial \boldsymbol{\sigma}'}$ with $\mathbf{G}$ being the potential vector function.

So, the consistency equation can be re-written as follows:

$$\mathbf{dF} = \mathbf{j} : \mathbf{E} : d\boldsymbol{\varepsilon} - \left(\mathbf{H} + \mathbf{j} : \mathbf{E} : \mathbf{m} \right).\boldsymbol{\lambda}^{\mathbf{p}} - \left(\mathbf{j} : \mathbf{E} : \boldsymbol{\beta}_{\mathbf{T}} - \mathbf{t} \right).dT \le 0 \quad ; \quad \boldsymbol{\lambda}^{\mathbf{p}} \ge 0 \quad ; \quad \mathbf{dF}.\boldsymbol{\lambda}^{\mathbf{p}} \ge 0 \tag{3.40}$$

where

$$\boldsymbol{\beta}_{\mathbf{T}} = \begin{pmatrix} \dfrac{\beta'_s}{3} & \dfrac{\beta'_s}{3} & \dfrac{\beta'_s}{3} & 0 & 0 & 0 \end{pmatrix}^T \tag{3.41}$$

$$\mathbf{t} = \begin{pmatrix} \dfrac{\partial f_{iso}}{\partial T} \\ \dfrac{\partial f_{dev}}{\partial T} \end{pmatrix} = \begin{pmatrix} p'_{c0} \exp\left(\beta \varepsilon_v^p \right) \dfrac{\gamma_T}{T \ln 10} r_{iso} \\ \dfrac{M \; r_{dev} \; p' \; b \; \gamma_T}{\left[1 - \gamma_T \log\left(\dfrac{T}{T_0} \right) \right] T \ln 10} + p' \left[1 - b \ln\left(\dfrac{d \; p'}{p'_c} \right) \right] g \; r_{dev} \end{pmatrix} \tag{3.42}$$

3.5.2.3 *Undrained conditions*

The experimental evidences presented in Section 3.3.3 clearly show that the undrained non-isothermal behaviour of soils must be addressed by means of a two-phase approach. In this context, three distinct thermal expansion coefficients must be considered, the water, the grain and the solid skeleton thermal expansion coefficients, β'_w, β'_{sG} and β'_s, respectively. β'_w may be implemented according to the linear thermal dependency proposed by Campanella and Mitchell (1968) with $\beta'_w\left(22°C\right)=2.73\ 10^{-4}\ °C^{-1}$ and $\beta'_w\left(80°C\right)=6.27\ 10^{-4}\ °C^{-1}$.

The non-isothermal mass conservation equations of the two-phase soil can be expressed as follows with the assumption of incompressible grains (Lewis and Schrefler, 1987):

$$n\left(1/\chi_w\right)dp_w=\left[n\beta'_w+\left(1-n\right)\beta'_{sG}\right]dT+d\varepsilon_v \tag{3.43}$$

where $1/\chi_w$ is the water compressibility and n is the porosity. Through the decomposition of the volumetric strain increment into elastic and plastic components (Equations (2.63), (3.28) and (2.85)), Equation (3.43) results in the expression of pore water pressure variation:

$$dp_w=\frac{\left[n\beta'_w+\left(1-n\right)\beta'_{sG}-\beta'_s\right]dT+\dfrac{dp'}{K}+\lambda^p_{dev}\dfrac{\alpha}{Mp'}\left[M-\dfrac{q}{p'}\right]+\lambda^p_{iso}}{n\left(1/\chi_w\right)} \tag{3.44}$$

Being under undrained conditions, the mean effective stress increment, dp', must be deduced from the total mean stress increment, dp, and the pore water pressure increment, dp_w, through the expression of Terzaghi's effective stress ($dp'=dp-dp_w$). Finally, the increment of pore water pressure generated by any thermo-mechanical load is equal to:

$$dp_w=\frac{\left[n\beta'_w+\left(1-n\right)\beta'_{sG}-\beta'_s\right]dT+\dfrac{dp}{K}+\lambda^p_{dev}\dfrac{\alpha}{M\left(p-p_w\right)}\left[M-\dfrac{q}{p-p_w}\right]+\lambda^p_{iso}}{n\left(1/\chi_w\right)+\left(1/K\right)} \tag{3.45}$$

It should be mentioned that the determination of plastic multipliers, λ^p_{dev} and λ^p_{iso}, requires the use of the mean effective stress increment, which also implies knowledge of the pore water pressure increment. This results in the fact that the calculation of pore water pressure variation involving elasto-thermoplasticity requires an iterative procedure.

3.5.3 Some typical thermo-mechanical responses predicted by ACMEG-T

In addition to classical elasto-plastic behaviour under isothermal conditions, the framework of ACMEG-T may reproduce some non-linear and irreversible behaviour induced by temperature change. The following sections explain the main mechanisms governing these processes. In particular, thermal collapse response depending on soil type, plasticity and stress level (measured in terms of OCR) is illustrated. The pore water pressure induced by a heating-cooling cycle under undrained conditions is also presented.

3.5.3.1 *Volumetric response under temperature increase*

As explained in Section 3.3.1, the response of fine-grained soil upon drained heating exhibits irreversible contraction for normally consolidated soil, reversible expansion for highly overconsolidated soils and transition behaviour for slightly overconsolidated soils. This behaviour is reproduced by the ACMEG-T model, as illustrated in Figure 3.20. The separation between these elastic "pre-yield" and elasto-plastic "post-yield" behaviours can be represented by the isotropic yield limit. When the temperature of a normally consolidated soil increases, the decrease trend of the preconsolidation pressure must be counterbalanced by the activation of the isotropic yield limit to keep constant the preconsolidation pressure (Figure 3.20a). On contrary, when the soil is highly overconsolidated, even if the hardening process is possible inside the external yield limit (through the bounding surface theory), the temperature-induced decrease of the yield limit is not sufficient to overpass the elastic nucleus. Thereby, the stress point remains inside the elastic domain and only thermal expansion is produced (Figure 3.20c). For intermediate case, the initial elastic nucleus can be overpassed for elevated temperatures. So, after an initial elastic behaviour (expansion), thermal hardening takes place that generates thermal volumetric plastic strain (compaction) (Figure 3.20b).

The four main parameters governing this mechanical response on non-isothermal paths are r_{iso}^{e}, c, γ_T and β, controlling the size of elastic nuclei of the isotropic mechanism, the rate of plasticity inside the external yield limit, the shape of the isotropic yield limit in the ($T - p'$) plane and the plastic compressibility, respectively.

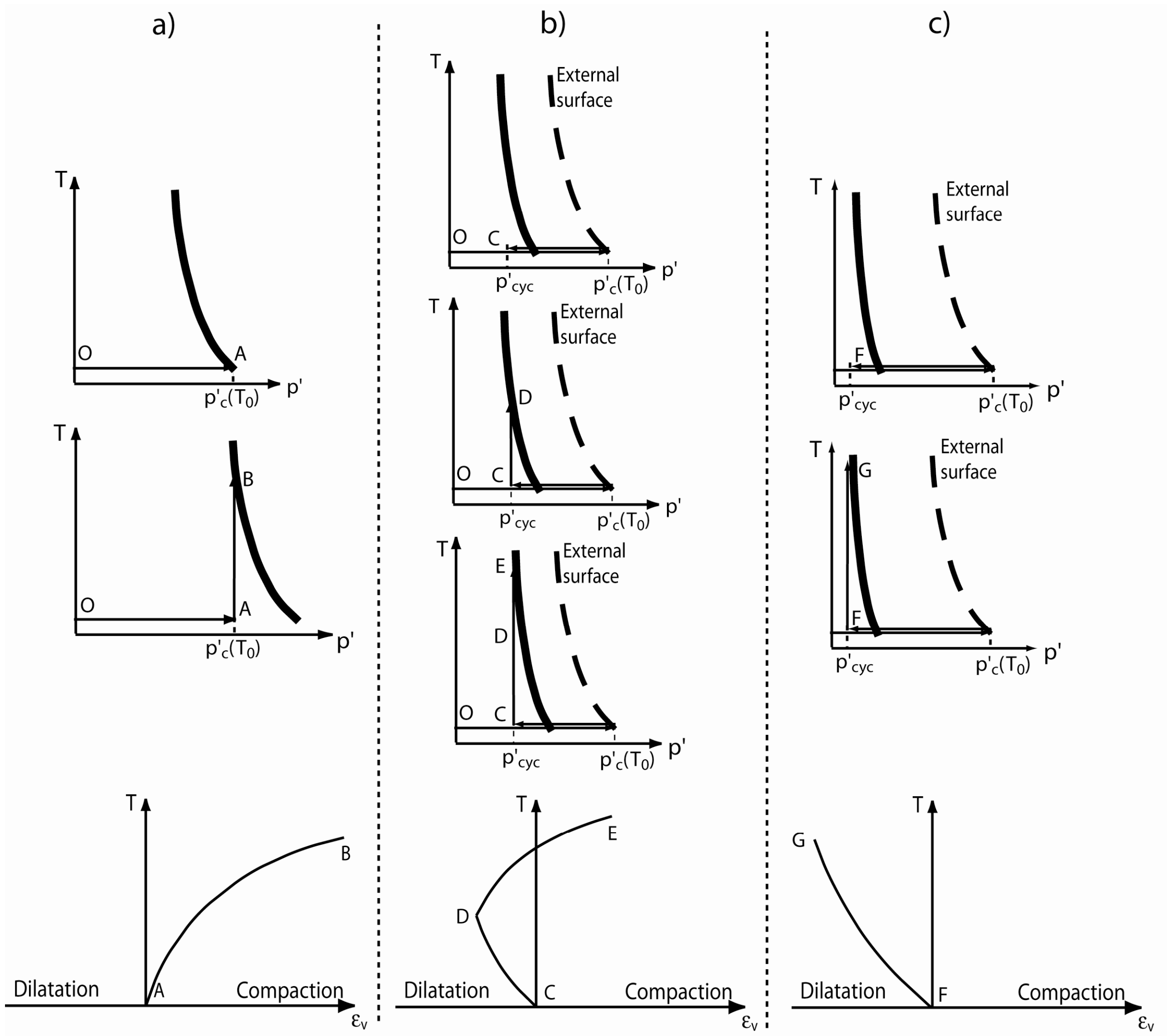

Figure 3.20 : Qualitative explanation of the response of the isotropic thermo-plastic mechanism under heating at different degrees of consolidation. a) normally consolidated, b) slightly overconsolidated and c) highly overconsolidated conditions.

3.5.3.2 *Pore water pressure induced by a undrained thermal cycle*

A heating under undrained conditions produces a pore water pressure increase due to the higher thermal expansion of water than that of the solid skeleton. At constant external (total) stress, the generation of pore water pressure induces a drop of the mean effective stress which is similar to a mechanical unloading. As a result, on the one hand, the yield limit decreases with increasing temperature; however, on the other hand, the mean effective stress also decreases. Thus, as shown in Figure 3.21, two cases may appear.

If the mean effective stress decreases (due to pore water pressure increase) faster than the isotropic yield limit, the process is elastic (i.e. the plastic multipliers λ_{dev}^{p} and λ_{iso}^{p} are equal to zero in Equation (3.45)) (Figure 3.21a). On the contrary, if the mean effective stress decreases more slowly than the isotropic yield limit, the stress point reaches the yield limit, which activates the isotropic mechanism. Plasticity is then induced. However, due to the fact that the hardening process could not occur under undrained conditions, additional pore water pressure, p_{w}^{p}, is generated in order to maintain the stress point on the isotropic yield surface (Figure 3.21b).

The fact that the variation of the mean effective stress could be faster or slower than the isotropic yield limit variation mainly depends on the soil type, represented by the material parameter, γ_T.

3.5.4 Thermo-plasticity: one notion, two approaches

3.5.4.1 *The two approaches*

As explained in Section 3.4, constitutive models dealing with thermo-mechanical behaviour of fine-grained soils have been successively improved by different authors (among others, Hueckel and Borsetto, 1990; Modaressi and Laloui, 1997; Cui et al., 2000; Laloui and Cekerevac, 2003). The decrease of the preconsolidation pressure as temperature increases has been well-reproduced by each model. In contrast, the irreversible thermal strains generated upon heating at intermediate degrees of over-consolidation (OCR) were rarely well modelled. Aware of the need to improve the description of the role of the OCR in the thermal expansion/contraction behaviour in the model of Hueckel and Borsetto (1990), Cui et al. (2000) added a new thermal yield curve to allow for the generation of thermal irrecoverable strain, even at high OCR.

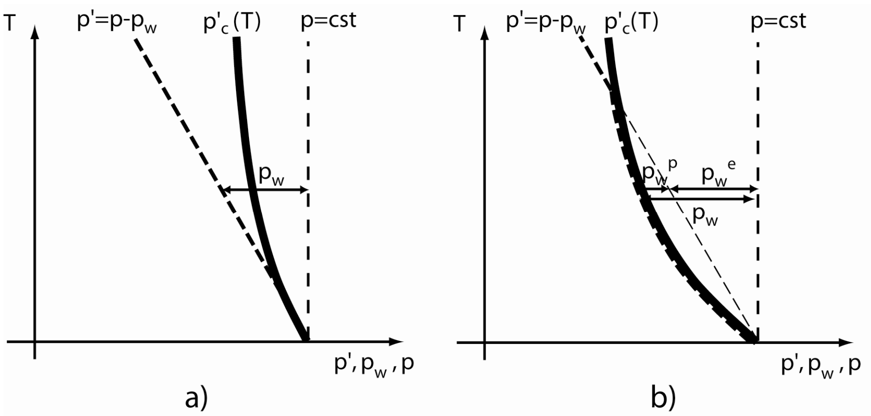

Figure 3.21 : Schematic representation of the evolution of pore water pressure and effective mean stress when a normally consolidated soil is heated. a) The effective mean stress decreases faster than the yield limit - Elastic behaviour; b) The effective mean stress decreases more slowly than the yield limit - Elasto-plastic behaviour.

In the concept of Cui et al. (2000), two coupled isotropic mechanisms are needed to fully describe the thermo-mechanical irreversible strain induced upon heating or mechanical loading. The great asset of this model is the comprehensive distinction between thermal hardening, mainly induced by the TY yield limit, and mechanical hardening, mainly produced by the LY yield limit (Figure 3.22). However, the coupling between LY and TY requires additional constitutive relations, which induce complexity in the model.

On the contrary, the ACMEG-T model keeps a unique isotropic thermal yield surface and considers the thermal irrecoverable strains at the intermediate OCR by means of the bounding surface theory, which allows for a progressive plasticity inside the external yield limit. In that way, no distinction is made between mechanical and thermal hardening. In the isotropic plane, both processes are described by a unique yield surface that shrinks with increasing temperature.

So, in terms of the isotropic thermo-mechanical soil response, the model of Cui et al. (2000) and the ACMEG-T model aim to reproduce similar behavioural features. However, the approaches are different. In the following section, the qualitative predictions of each model on two characteristic loadings are compared: (i) isotropic compressions at two different temperatures and (ii) heating-cooling cycles at different overconsolidation ratios (OCR).

3.5.4.2 *Qualitative comparison*

Isotropic compressions at two different temperatures

Figure 3.23 sketches and compares the qualitative responses of the models of Cui et al. (2000) (Figure 3.23a) and of ACMEG-T (Figure 3.23b) upon isotropic compression at two different temperatures.

The model of Cui et al. (2000). Upon isotropic loading at ambient temperature, the sample behaves elastically until the initial LY curve (path 0-1). The subsequent isotropic loading at the same temperature moves LY_1 rightward to LY_2 (path 1-2). Since no change of temperature occurred, there is no effect on TY_0. The volume response of the soil between 1 and 2 is plastic. Under elevated temperatures, the TY curve is directly mobilized upon isotropic loading. So, the behaviour on the path 0′-1′ is not purely elastic, but is governed by a tiny plastic mechanism controlled by the evolution of TY (from TY_0 to $TY_{1'}$). The coupling between TY and LY produces a small shift of the LY curve to the right (from LY_0 to LY_1). After reaching $LY_{1'}$, the standard plastic compression occurs between 1′ and 2′. So, the main differences between isotropic compressions at ambient and elevated temperatures are the decrease of the preconsolidation pressure and the transient plastic mechanism observed at elevated temperatures.

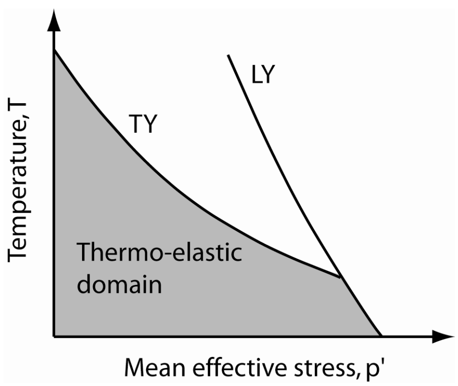

Figure 3.22 : Isotropic yield limits of the thermo-mechanical model of Cui et al. (2000).

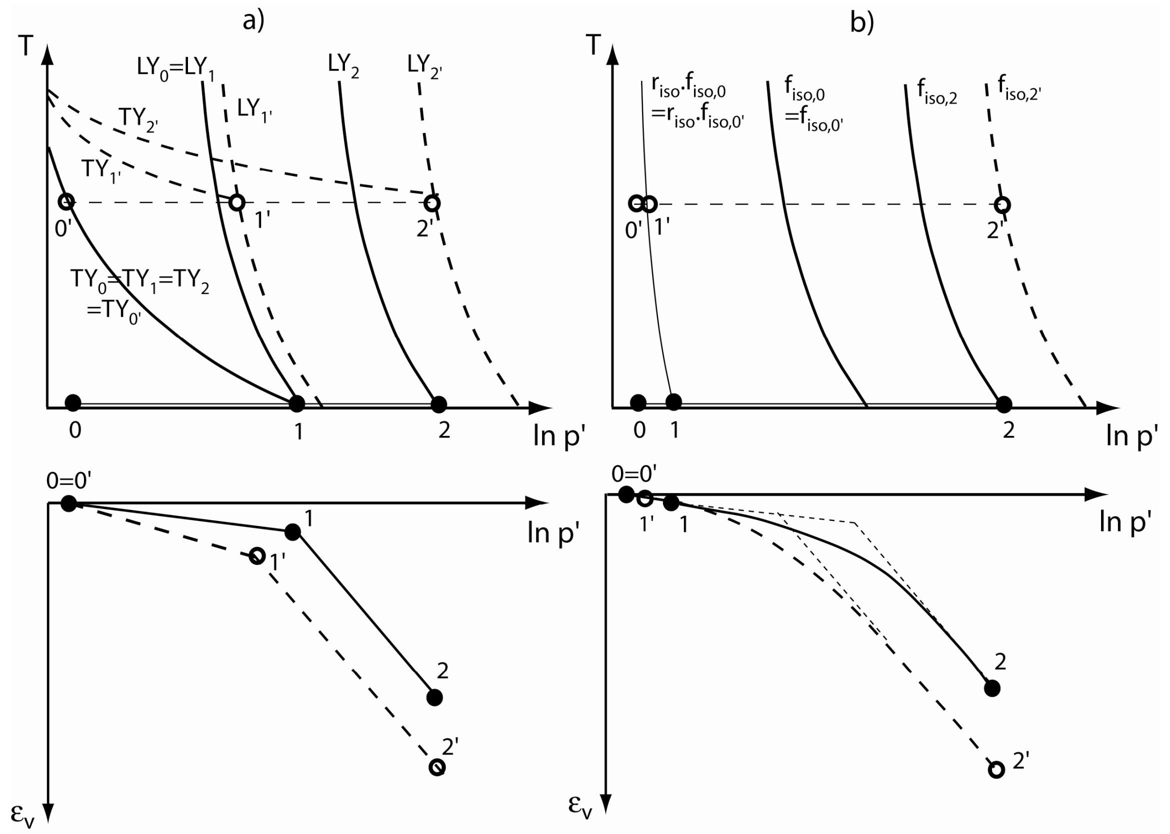

Figure 3.23 : Compression behaviour of soils at two different temperatures. Qualitative comparison of the predictions of (a) the model of Cui et al. (2000) and (b) the ACMEG-T model.

The ACMEG-T model. Through the bounding surface theory and the decrease of the preconsolidation pressure with temperature, the unique isotropic yield limit of the ACMEG-T model is able to reproduce the same features of behaviour as the model of Cui et al. (2000). At ambient temperatures, after the elastic nuclei (path 0-1), the soil undergoes progressive plasticity until reaching the normally consolidated line (path 1-2). At elevated temperatures, the soil is subjected to a similar transient process from being purely elastic to having full mobilization of the plastic mechanism. The difference is that the elastic nucleus is surpassed more rapidly under elevated temperatures (point 1′ is reached at a lower stress than point 1), and the normally consolidated line is shifted to the right at elevated temperatures.

Heating-cooling cycles at two different OCR

Figure 3.24 sketches and compares the qualitative responses of the model of Cui et al. (2000) (Figure 3.24a) and of ACMEG-T (Figure 3.24b) upon a heating-cooling cycle at two different overconsolidation ratios.

The model of Cui et al. (2000). Under the normally consolidated state, a temperature increase (path 0-1) mobilizes the TY curve (from TY_0 to TY_1), and the TY-LY coupling also moves LY (from LY_0 to LY_1). It gives rise to plastic thermal contraction of the soil. Under cooling (path 1-2), the process is elastic and does not modify the TY and LY yield limits. In overconsolidated soils, the first part of the heating (path 0′-1′) occurs elastically (i.e. thermal dilatation). Then, when the TY curve is reached, the thermo-plastic process takes place (path 1′-2′). The TY curve moves from $TY_{1'}$ to $TY_{2'}$, and the TY-LY coupling also moves LY (from $LY_{1'}$ to $LY_{2'}$). The cooling phase is elastic (path 2′-3′).

The ACMEG-T model. As already explained in Section 3.5.3.1, heating under normally consolidated conditions directly activates the isotropic yield limit, which produces thermal contraction of the soil (path 0-1). Under slightly overconsolidated conditions, a temperature increase first produces elastic expansion when the stress point remains inside the elastic nuclei (path 0′-1′). The thermal hardening takes place when the elastic domain is surpassed (path 1′-2′). In both cases, the cooling phases appear elastically (i.e. thermal dilatation) (paths 1-2 and 2′-3′).

3.5.4.3 *Discussion on the comparison of the two approaches*

The model of Cui et al. (2000), as well as the ACMEG-T model, follows from the need to accurately reproduce the thermo-plastic processes occurring in soil under various thermo-mechanical paths and stress states. In particular, the generation of thermal contractile strain upon intermediate overconsolidation required an improvement with respect to the first-developed thermo-mechanical models (see for instance Hueckel and Borsetto (1990)). Cui et al. (2000) introduced a second isotropic plastic mechanism, while the ACMEG-T model used the concept of bounding surface to overcome the limitation of the first-developed thermo-mechanical models. The two approaches give similar results. However, the advantage of the bounding surface concept used by the ACMEG-T model is that it considers a unique isotropic plastic mechanism that does not require any additional coupling equations between the thermal and the mechanical hardenings. Also, the plasticity is generated progressively from an elastic nucleus to a full mobilization of the plastic mechanism. This concept is closer to the real phenomenological behaviour of the soil response.

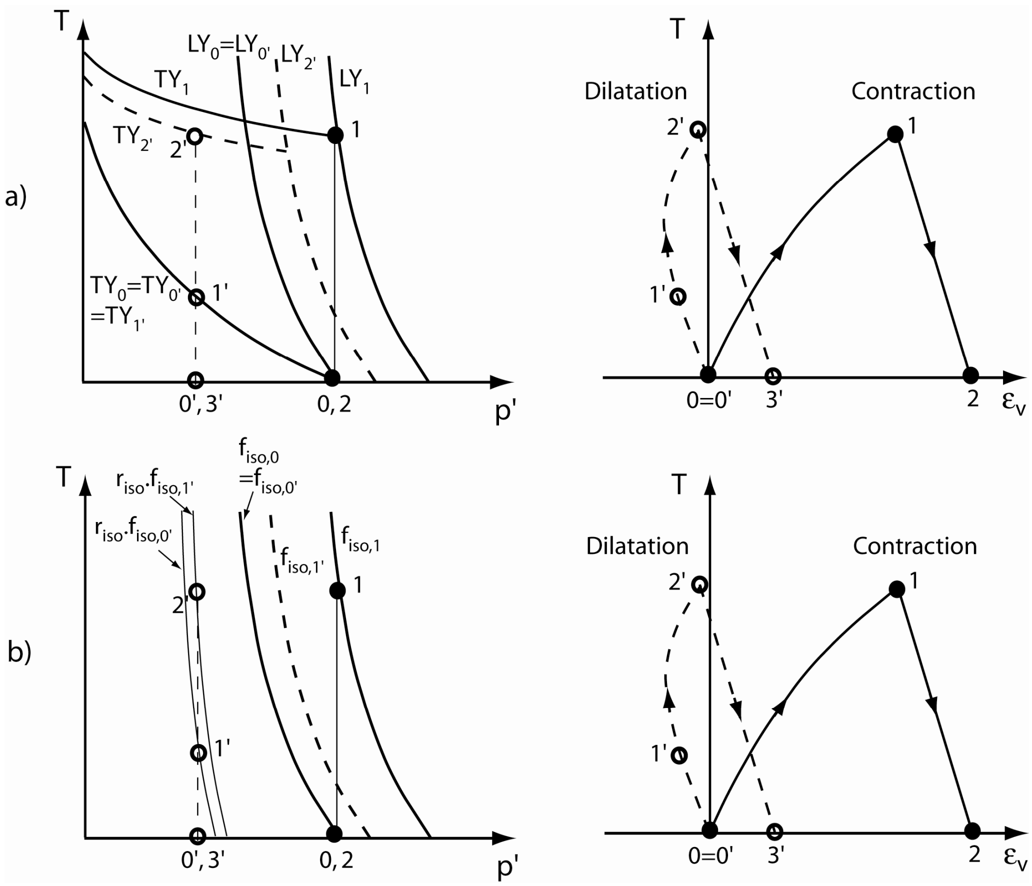

Figure 3.24 : Volumetric response of soil upon heating at two different OCRs. Qualitative comparison of the predictions of (a) the model of Cui et al. (2000) and (b) the ACMEG-T model.

3.5.5 Validation of the ACMEG-T constitutive model

As a numerical validation of the ACMEG-T constitutive model, thermo-mechanical experimental results on Bangkok clay under drained and undrained conditions are used (Abuel-Naga et al., 2006; Abuel-Naga et al., 2007).

3.5.5.1 *Parameter determination*

The model parameters were determined using a minimum amount of tests. Thus, two isotropic compression tests performed at two constant temperatures (25°C and 90°C) were used to establish the isotropic parameters K_{ref}, β, γ_T and c. The determination of the compressibility indexes (κ and λ) of these curves enables the reference bulk elastic modulus, K_{ref}, and the plastic compressibility modulus to be obtained easily using the following expressions:

$$K_{ref} = \frac{1+e_0}{\kappa} p'_{ref} \quad ; \quad \beta = \frac{1+e_0}{\lambda - \kappa} \tag{3.46}$$

where p'_{ref} is the reference mean effective pressure for which K_{ref} is defined (p'_{ref} =1 MPa in the present case) and e_0 is the initial void ratio for which both parameters are established. The slope of the logarithmic decrease of the preconsolidation pressure with temperature, γ_T, is evaluated by comparing the values of mean effective pressures corresponding to the inflection point of the compression curves (e.g. the preconsolidation pressure) obtained at 25°C ($p'_c(T_0)$) and 90°C ($p'_c(T_1)$):

$$\gamma_T = \frac{1 - \dfrac{p'_c(T_1)}{p'_c(T_0)}}{\log\left(\dfrac{T_1}{T_0}\right)} \tag{3.47}$$

Finally, the parameter c is determined by curve fitting in order to obtain the best transition between elastic and elasto-plastic isotropic behaviour. The thermo-elastic parameter, β'_{s0}, has been calculated using the quantification of the volumetric strain induced by a heating test on a highly overconsolidated soil (p'_c =25 kPa and OCR=8).

The deviatoric parameters, G_{ref}, b, d, ϕ'_0, α and a, have been determined using one triaxial test at ambient temperature. The determination of the slope of the critical state line M_0 requires only one triaxial test:

$$M_0 = \frac{q_{cr}}{p'_{cr}} \tag{3.48}$$

where q_{cr} and p'_{cr} are the deviator stress and the mean effective stress at the critical state (e.g. when $\partial q / \partial \varepsilon_{11} = 0$ and $\partial \varepsilon_v / \partial \varepsilon_{11} = 0$, ε_{11} being the axial strain).

The parameter d can be deduced through the plastic compressibility parameter, β, and the total volumetric plastic strain produced during the test, ε_v^p:

$$d = \frac{p'_{c0} \exp\left(\beta \varepsilon_v^p\right)}{p'_{cr}} \tag{3.49}$$

where ε_v^p is unknown but can be obtained by subtracting the volumetric elastic strain, ε_v^e, from the total measured volumetric strain, ε_v:

$$\varepsilon_v^p = \varepsilon_v - \varepsilon_v^e = \varepsilon_v - \frac{\Delta p'}{K} = \varepsilon_v - \left(\frac{p'_{ref}}{p'}\right)^{n^e} \frac{\Delta p'}{K_{ref}} \tag{3.50}$$

The three other deviatoric parameters, b, α and a, have been determined by curve fitting. Finally, the temperature influence on the friction angle, g, has been determined by comparing friction angle values at 25°C and 90°C. The slope of the critical state line at 90°C, M_1, can be compared with M_0 to deduce g:

$$g = \frac{M_0 - M_1}{T_1 - T_0} \tag{3.51}$$

All of these parameters are summarized in Table 3.5.

3.5.5.2 *Drained simulations*

Numerical simulations of drained isotropic compression tests at three different temperatures are shown in Figure 3.25. Two of the experimental results (at 25°C and 90°C) have been used to determine isotropic parameters and, therefore, are back-predictions, while the test at 70°C is a blind simulation. Figure 3.26 shows the comparison between the predicted and experimental results on a combined thermo-mechanical path. The test consists in oedometric loading in a normally consolidated state until an effective vertical stress of 100 kPa, followed by a thermal cycle (25-90-25°C) and finishing with vertical loading up to 200 kPa. Figure 3.27 shows experimental and numerical results on heating-cooling cycles for different overconsolidation ratios (OCR=8, 4, 2 and 1) under oedometric conditions. The test for the higher OCR was used to determine the thermal dilatation coefficient on the cooling path. The other numerical results are blind predictions. Figure 3.25 to Figure 3.27 clearly show good agreement between the numerical predictions of ACMEG-T and experimental results on thermo-mechanical isotropic paths. Moreover, the strain induced by each thermal cycle in Figure 3.27 (e.g. thermo-plastic strain) is given with respect to the overconsolidation ratio in Figure 3.28. This underlines the capability of the model to consider the great dependence of the stress history on the thermo-plastic induced strain.

Elastic parameters		
K_{ref}, G_{ref}, n^e, β'_{s0}, β'_{sG}	[MPa], [MPa], [-], [°C^{-1}], [°C^{-1}]	42, 15, 1, 2.10^{-4}, 2.10^{-4}
Isotropic plastic parameters		
β, γ_T, c, r_{iso}^e	[-], [-], [-], [-]	5.49, 0.52, 0.04, 0.15
Deviatoric plastic mechanical parameters		
b, d, ϕ'_0, g, α, a, r_{dev}^e	[-], [-], [°], [-], [-], [-], [-]	0.2, 1.6, 22.66, 1.10^{-3}, 2, 0.02, 0.1

Table 3.5: The model parameters for the simulation of the thermo-mechanical response of Bangkok clay

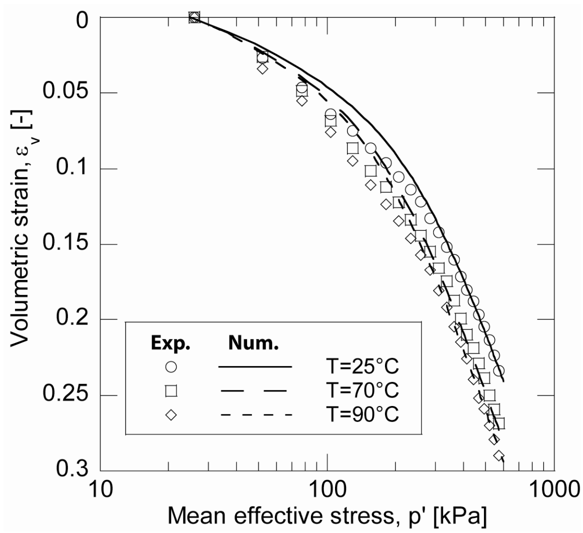

Figure 3.25 : Numerical simulations of isotropic compression tests of Bangkok clay at three different temperatures. Comparison with experimental results.

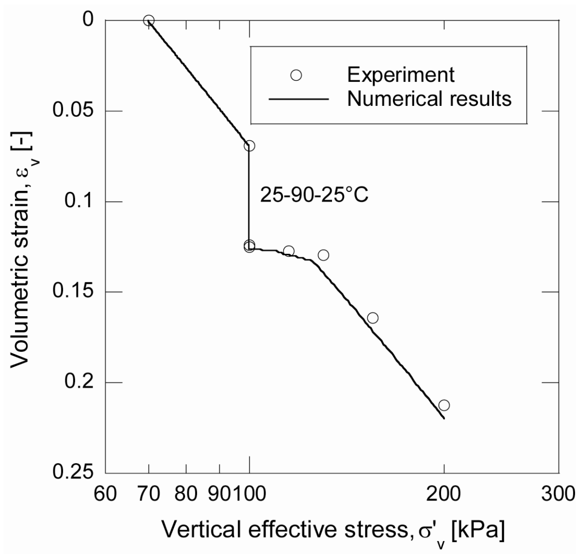

Figure 3.26 : Numerical simulations of a combined thermo-mechanical oedometric path of Bangkok clay. Comparison with experimental results.

Numerical simulations of drained triaxial tests at 3 different constant temperatures for initially normally consolidated states have been performed and are compared with experimental results in Figure 3.29. The isotropic stress has been first applied. Then the temperature of the test has been imposed and finally the triaxial compression has been performed. These results show the thermal strengthening of the material, which results in an increase in strength of about 25% for a thermal gradient of 70°C. Such an effect is well reproduced by the numerical simulations.

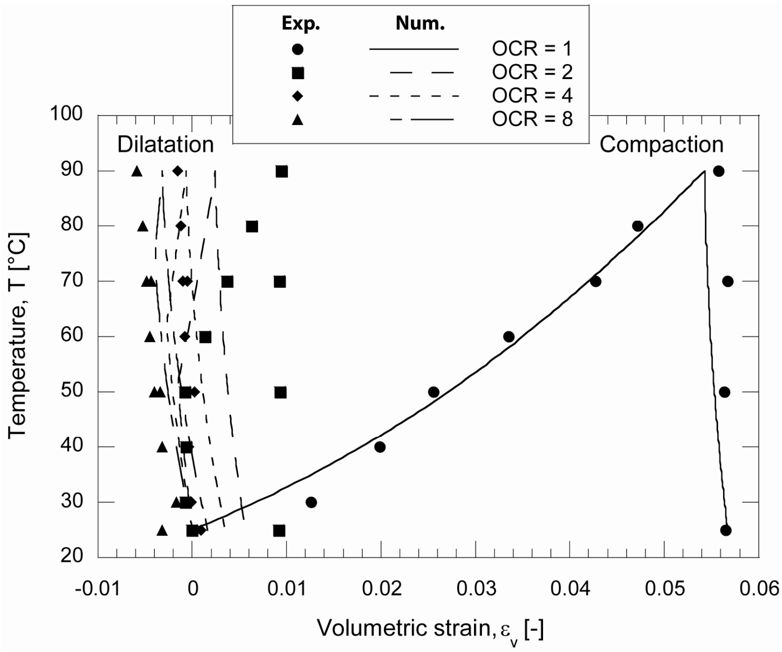

Figure 3.27 : Numerical simulations of a heating-cooling cycle of Bangkok clay at different degrees of consolidation under oedometric conditions (vertical preconsolidation pressure = 200 kPa). Comparison with experimental results.

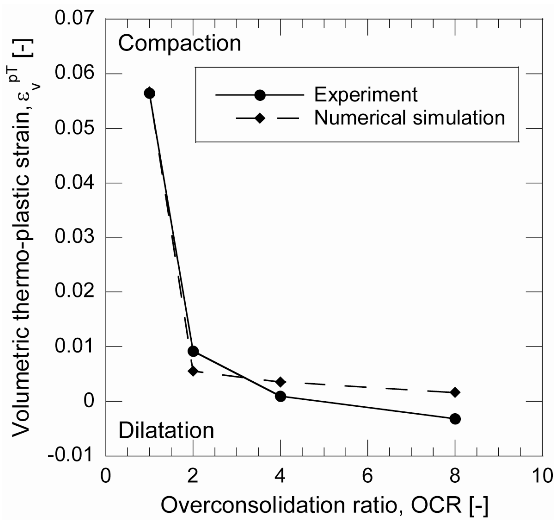

Figure 3.28 : Effect of overconsolidation ratio on the mechanical response of Bangkok clay along a heating-cooling cycle. Comparison between numerical simulations and experiments.

3.5.5.3 *Undrained simulations*

The numerical simulations of induced pore water pressure for undrained heating-cooling cycles at three different isotropic stress states (i.e. OCR) are shown in Figure 3.30 and are compared with experimental results. On the heating paths, the ACMEG-T computations fit very well with the experimental points. The soil response is purely elastic for any overconsolidation ratio. As explained in Section 3.5.3.2, this corresponds to a faster decrease in mean effective stress than the shrinkage of the isotropic yield surface with temperature (Figure 3.21). Thus, the induced pore water pressure is only governed by the first term of Equation (3.45). The non-linearity of the curve is due to the evolution of the bulk modulus and of the thermal expansion coefficients of the solid skeleton and water with stress state and/or temperature. As shown in Equation (3.45), the increment of pore water pressure is affected by these three variables (K, β'_s and β'_w).

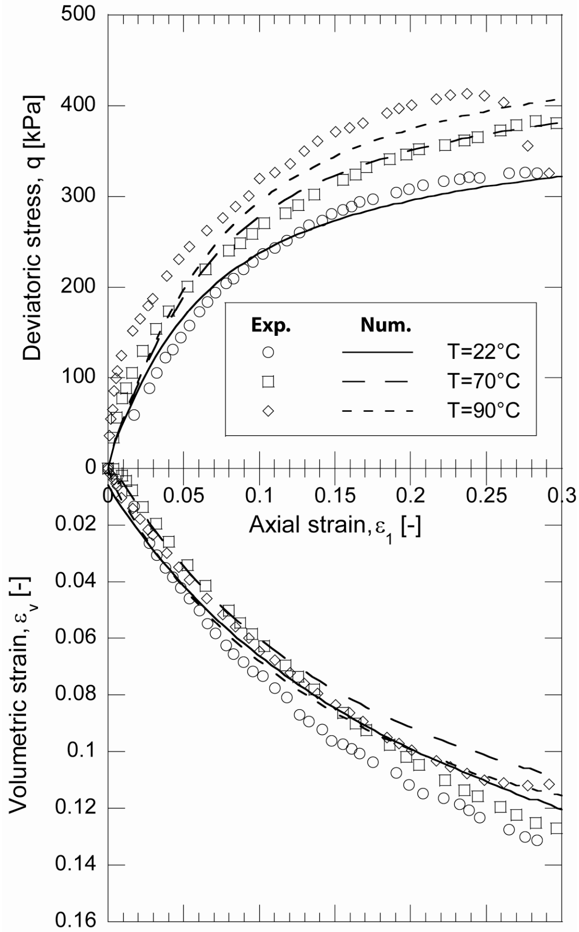

Figure 3.29 : Numerical simulations of drained triaxial compression tests on normally consolidated Bangkok clay (p'_c=200 kPa). Comparison with experimental results.

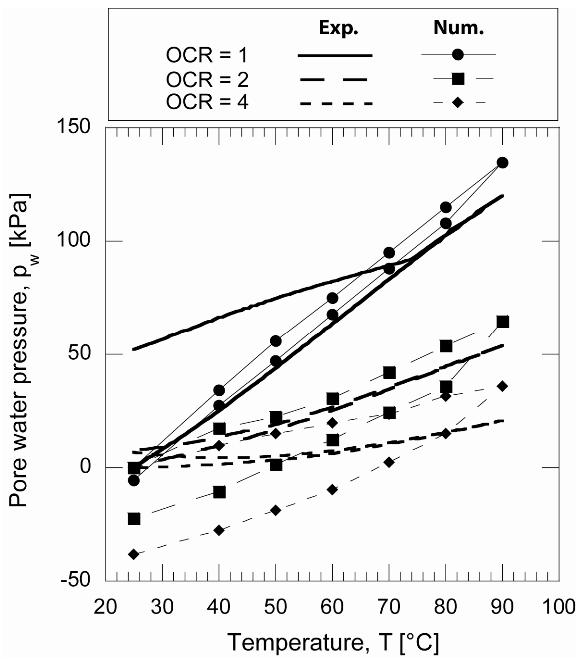

Figure 3.30 : Numerical simulations of undrained heating-cooling cycles at different degrees of consolidation under oedometric conditions (vertical preconsolidation pressure = 200 kPa). Comparison with experimental results.

On the cooling paths, the numerical predictions exhibit almost reversible behaviour for overconsolidated states, while irrecoverable positive pore water pressure is generated for the normally consolidated state. This irreversible response provided by the ACMEG-T model occurs during the decrease in pore water pressure (i.e. the increase of the mean effective stress), which is equivalent to a mechanical load. Because the model used the bounding surface theory, this increase of the mean effective stress may produce plastic strain, even if the stress state lies within the external yield surface. At this cooling stage, the experimental points differ from the numerical predictions.

3.5.5.4 *Discussion of ACMEG-T numerical predictions*

This set of numerical simulations of the thermo-mechanical response of clay along isotropic and deviatoric paths under drained and undrained conditions compares well with the experiments. Therefore, it has been shown that, with very few experimental tests, the thermo-mechanical model parameters can be determined. Indeed, only two isotropic compression tests, one heating test on a highly overconsolidated sample and two drained triaxial tests at two different temperatures, are needed to get the whole set of model parameters. In other words, based on only 5 test results, the constitutive model is able to reproduce the mechanical response of soils on any complex thermo-mechanical path under drained and undrained conditions.

3.6 Conclusions

Temperature effects on the mechanical response of soil are governed by complex phenomena that are mainly induced by physico-chemical changes at a micro-scale level. A qualitative understanding of those processes acting at the micro-scale is possible to achieve by considering the diffusive double layer theory. However, such analysis is subject to several limitations due to the lack of well-established experimental evidence, including some contradictory observations at that scale. As a consequence, a rigorous quantification of the thermo-mechanical processes governing the soil response requires considering soil as a continuum. At that macro-scale, much experimental evidence enables identification of the main temperature-induced effects on the soil response.

Based on those observations, the ACMEG-T model has been built. It is an extension toward the non-isothermal conditions of the ACMEG model presented in the previous chapter. The model response has been qualitatively explained on some typical thermo-mechanical paths. It enables a good understanding of the constitutive mechanisms that are considered by the model. Analytical relations to determine the model parameters have been presented. Finally, the performance of the proposed model has been assessed by means of comparisons between thermo-mechanical experimental results, under drained and undrained conditions, and numerical predictions. This set of numerical simulations has shown that ACMEG-T is able to reproduce the mechanical response of soils on any complex thermo-mechanical path under drained and undrained conditions, using only five test results required to calibrate material parameters.

Section II

Thermo-mechanical constitutive behaviour of unsaturated fine-grained soils

Chapter 4

Thermal effect on the mechanics of unsaturated soils

Any soil could be unsaturated and, therefore, there could be no reason why a fundamental approach, already successful in the case of saturated soils, could not be applied also to this type of materials. […]. Instead of considering unsaturated soils as a separate class of materials, there should be a seamless continuity with the by now well-established understanding of saturated soil behaviour.[1]

[1] Gens A., Sanchez M. and Sheng D. (2006). On the constitutive modelling of unsaturated soils. *Acta Geotechnica*, 1: 137-147.

4.1 Introduction

Most of the engineering applications in geotechnical engineering are in relation with unsaturated soils. Consequently, the predominance of unsaturated soils was recognized early in the field of soil mechanics.

In a saturated soil, the pore fluid pressure can generally be assumed as a neutral stress in most of the cases. On the contrary, under unsaturated conditions, a new internal stress, namely the suction, plays a significant role in the behaviour of unsaturated soils and must be, directly or indirectly, considered in the formulation of the stress-strain relationship. Since the beginning of 1960s, the key role of suction in the global soil behaviour was investigated by the means of experimental tests. Those experiments reveal that suction not only governs the hydraulic diffusion in soils but also affects the mechanical response of the material.

After giving general definitions related to partially saturated soils, the stress framework issue is addressed in this chapter. Then, the experimental evidence underlying the mechanical behaviour (stress-strain relationship) and the water retention behaviour (degree of saturation-suction relationship) are presented, considering isothermal conditions. In the second part of this chapter, the temperature effect on the behaviour of unsaturated soils is presented from mechanical and water retention points of view. In particular, the effect of temperature on the water retention is studied from both microscopic and macroscopic scales.

4.2 Isothermal behaviour of unsaturated soils

4.2.1 Partial saturation in soils

4.2.1.1 *A negative pore water pressure*

The pore space in soil can be filled with a combination of fluids. Under saturated conditions, as considered in the first section of this thesis, the entire pore space is filled with one fluid (usually water). However, when the pores are filled with two (or more) immiscible fluids, the state of the soil is termed *unsaturated* or *partially saturated*. In this dissertation, it will be assumed that those fluids are exclusively air and water.

In addition to that definition of unsaturated soils, the particular state of soils that sustains a negative pore water pressure, that is a pressure lower than the atmospheric pressure, but remains fully water-saturated is also enclosed in the present framework.

At the boundary between the liquid and gas phases, the air-water interface has some specific properties which govern the mechanics of unsaturated soils. Unlike a molecule in the interior of the water that experiences equal force in all directions, a water molecule within the air-water interface is subject to an unbalanced force towards the interior of the water (Figure 4.1a). In order for that interface to be in equilibrium, a tensile pull is generated along that boundary (Fredlund and Rahardjo, 1993). The surface tension, σ_s, is the property of the air-water interface that allows this tensile pull. The mechanical equilibrium between air pressure, water pressure and surface tension is controlled by the radius of curvature R_s of the air-water interface (Kelvin's capillary model equation, Figure 4.1b).

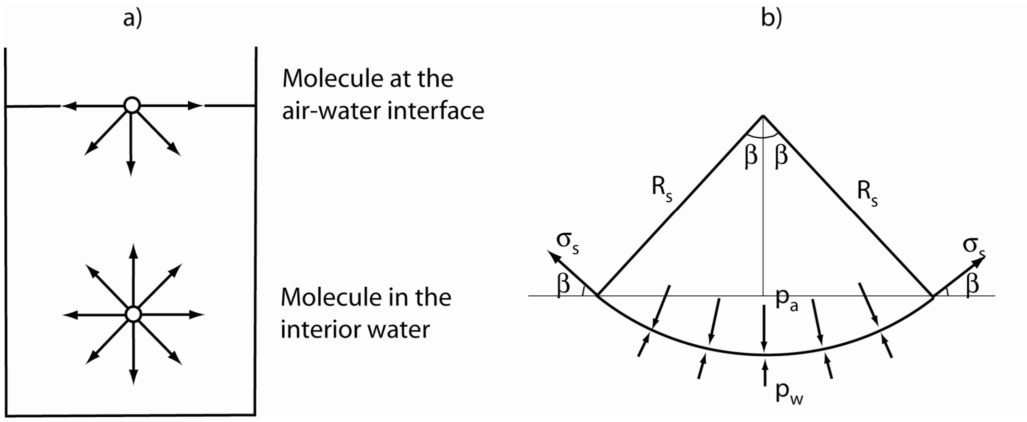

Figure 4.1: The surface tension phenomenon at the air-water interface: a) Unbalanced force at the water surface; b) Equilibrium between air, water and surface tension acting on a curved surface (meniscus).

$$p_a - p_w = \frac{2\sigma_s}{R_s} \tag{4.1}$$

where p_a and p_w are the pore air and pore water pressures, respectively.

4.2.1.2 *Water potential and suction*

In unsaturated soils, pore water pressure is usually less than the pore air pressure, the difference between both fluid pressures being sustained by the curved tensile skin, often called the *meniscus*. This deficit of water pressure with respect to air pressure assigns a certain potential to water. The *water potential* is defined as the potential energy of water relative to pure water in a reference state. It quantifies the tendency of water to move from one area to another. For instance, the negative potential of water in unsaturated soils implies that an unsaturated soil, when in contact with a reservoir of free water, is capable of drawing water through the liquid and gas phase. The soil *suction* quantifies this thermodynamic potential of soil pore water relative to a reference potential of free water (Lu and Likos, 2004).

The total soil suction is the sum of several physical and physico-chemical additive processes that decrease the potential of the pore water relative to the reference state. Neglecting temperature, gravity, and inertial effects, the primary mechanisms include (i) capillary effects, (ii) short-range adsorption effects and (iii) osmotic effects. The former mechanism is unique to unsaturated soil, while the latter two may occur under either saturated or unsaturated conditions (Lu and Likos, 2004).

(i) Capillary effects are those related to the negative pore water pressure with respect to the pore air pressure, as described by Equation (4.1). Those effects are also termed mechanical effects because they arise from the difference in the pore fluid pressures. (ii) Short-range adsorption effects are mainly related to the attraction of water by solid particles. Those effects, already discussed in Section 3.2.2 by the means of the diffuse double layer theory, are most important in fine-grained soils. Through this process, water is tightly bonded to the soil particle in its vicinity. The potential of the adsorbed water is highly negative relative to the free water potential. (iii) The last effect, the osmotic effect, is linked to dissolved solutes in pore water. The difference in solute concentration between pore water with dissolved ions and reference pure water reduces the chemical potential of the pore water.

The term *matric suction* usually groups the suction linked to capillary mechanisms and short-range adsorption mechanisms. Suction arising from the presence of dissolved ions is refereed to *osmotic suction*. In this way, total suction s_t is the algebraic sum of the matric and osmotic components, s and s_π, respectively:

$$s_t = s + s_\pi \tag{4.2}$$

Throughout this study, the term suction refers to matric suction. In absence of high solute concentration in the pore fluids, that component of suction is recognized as the main component governing the mechanical response of unsaturated soils.

4.2.2 Stress frameworks

An accurate description of the mechanical response of unsaturated soils, at a macro-scale level, requires a rigorous definition of the stress state in the medium. Unlike the case of saturated conditions, the soil suction, which is specific to a unsaturated medium, has a direct impact on the state of stress acting at the particle-particle contact. Consequently, the macroscopic mechanical behaviour of the soil is directly affected by the suction level. Clearly, the use of suction, or a modified version of it, is required to define the stress state of the medium accurately (Nuth and Laloui, 2008). In addition, the relative amounts of the pore air and pore water phases play a key role in the mechanical properties of the unsaturated soil. This proportion, usually defined by the degree of saturation, should be considered, directly or indirectly, in the complete description of the hydro-mechanical soil state.

When considering unsaturated media, the above considerations clearly reveal the need to modify Terzaghi's (1936) effective stress developed for the particular case of saturated soil. Accordingly, various thermo-dynamically consistent stress frameworks have been elected for constitutive modeling of unsaturated soil. Two main families of approaches can be distinguished: *the independent stress variables* and *the averaged pseudo-effective stress* (Jardine et al., 2004). The choice of stress framework appears to be mostly a matter a convenience. On the one hand, approaches with two independent stresses use measurable stresses which have an experimental significance (Fredlund and Rahardjo, 1993). On the other hand, a pseudo-effective stress converts a multi–phase porous media into a mechanically equivalent, single-phase, single-stress state continuum which has noticeable advantages in the elaboration of a constitutive framework (Jommi, 2000; Khalili et al., 2004; Laloui and Nuth, 2005, Nuth and Laloui, 2008). The two families of approaches are briefly addressed in the next sections (see Nuth and Laloui (2008) or Wheeler and Karube (1995), for more complete treatment).

4.2.2.1 *Approaches using two independent stresses*

The approaches using independent stress variables postulate that the elastic strain emerges from the variation of two distinct stress variables. This hypothesis may be expressed by the following generic equation:

$$d\varepsilon_{ij}^e = C_{ijkl}^1 d\Lambda_{kl}^1 + C_{ijkl}^2 d\Lambda_{kl}^2 \tag{4.3}$$

where C_{ijkl}^1 and C_{ijkl}^2 are constitutive tensors, while Λ_{kl}^1 and Λ_{kl}^2 are the two stress variable vectors that govern independently the elastic strain of unsaturated soil. Based on multiphase continuum mechanics, Fredlund and Morgenstern (1977) show that any combination of two of the three stress variables (the total stress σ_{ij}, the pore water pressure p_w and the pore air pressure p_a) can be used to define the stress state. These combinations are:

$$\begin{aligned}&\left(\sigma_{ij} - p_a\delta_{ij}\right) \quad \text{and} \quad \left(p_a - p_w\right)\delta_{ij}\\&\left(\sigma_{ij} - p_w\delta_{ij}\right) \quad \text{and} \quad \left(p_a - p_w\right)\delta_{ij}\\&\left(\sigma_{ij} - p_a\delta_{ij}\right) \quad \text{and} \quad \left(\sigma_{ij} - p_w\delta_{ij}\right)\end{aligned} \tag{4.4}$$

where $\left(\sigma_{ij} - p_a\delta_{ij}\right)$ is the net stress vector $\sigma_{ij,net}$ while $\left(p_a - p_w\right)$ is the suction s. δ_{ij} is the Kronecker's symbol. Wheeler and Karube (1995) discussed the merits of each possible combination. Most of the models using two independent stress variables are formulated by adopting the net stress and suction as fundamental variables (see e.g. Alonso et al. (1990)). In this case, the generic Equation (4.3) takes the form:

$$d\varepsilon_{ij}^{e} = C_{ijkl}^{e}\left(d\sigma_{kl} - dp_a\delta_{kl}\right) + C^{s}\left(dp_a - dp_w\right)\delta_{kl} \tag{4.5}$$

where C_{ijkl}^{e} and C^{s} are the elastic stiffness matrix and the elastic hydraulic modulus, respectively. Those models will be further discussed in Section 4.2.5.1.

4.2.2.2 *Approaches using the pseudo-effective stress*

With the aim to use a single stress to describe the mechanical behaviour of unsaturated soils, combinations between mechanical stresses and fluid pressures are assessed in the approaches using pseudo-effective stresses. In the sense of Terzaghi's (1936) definition, the effective stress should be such that *all the measurable effects of a change in stress, such as compaction, distortion and a change in shearing resistance, are exclusively due to a change in the effective stress*. Consequently, the effective stress enters the elastic and elasto-plastic constitutive equations of the soil matrix. The effective stress can thus be defined as that inducing the mechanical elastic strain of the solid skeleton:

$$d\varepsilon_{ij}^{e} = C_{ijkl}^{e}d\sigma_{ij}' \tag{4.6}$$

Bishop (1959) first attempted to extend the concept of effective stress, as defined by Terzaghi (1936) in saturated conditions, to unsaturated porous media:

$$\sigma_{ij}' = \sigma_{ij} - p_a\delta_{ij} + \chi\left(p_a - p_w\right)\delta_{ij} \tag{4.7}$$

In this formulation, χ, called the effective stress parameter, varies with the degree of saturation, from zero for dry soil to unity for fully saturated conditions. This expression enables a simple transition from partially to fully saturated states, recovering Terzaghi's expression for $S_r = 1$ (i.e. $\chi = 1$). Several authors attempted to identify the relationship between the effective stress parameter and the degree of saturation, based on various criteria, such as the volume change and shear strength (Bishop et al., 1960), comparison between soil response upon change in applied external stress and applied suction (Jennings, 1960) or critical state (Vanapalli and Fredlund, 2000). It yields to the relations reported in Figure 4.2.

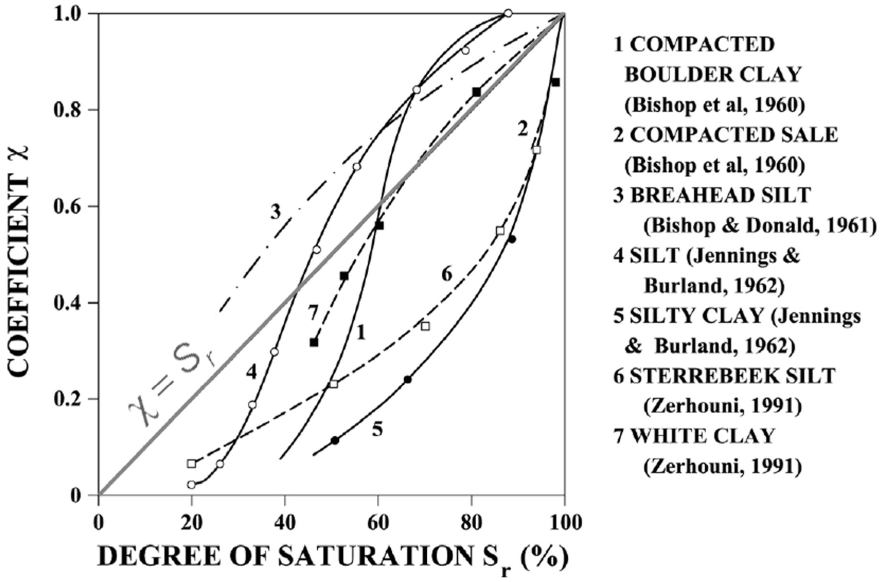

Figure 4.2: Effective stress parameter with respect to the degree of saturation for various soils, as reported by Zerhouni (1991).

Schrefler (1984) proposed the elementary choice:

$$\chi = S_r \tag{4.8}$$

Others authors proposed expressions for χ which depend on a suction ratio rather than on the degree of saturation (see i.e. Aitchison (1960); Khalili and Khabbaz (1998)). From a micromechanical standpoint, theoretical approaches were also developed to evaluate the χ parameter by examining the forces and fluid pressures that arise in unsaturated soils with idealized soil particles. That kind of analysis shows that the shape and the arrangement of grains, as well as the contact angle at the solid-liquid interface, may have a significant impact on the behaviour of the χ parameter (Likos and Lu, 2004).

Since Bishop's 1959 paper on the effective stress for unsaturated soils, the validity of the constitutive developments based on a pseudo-effective stress framework has often been challenged. The limitations of Bishop's effective stress were hastily attributed to its apparent non-efficiency to reproduce the collapse phenomenon as well as the definition and the use of the χ parameter. The constructive contributions of Gens (1995a) and Jardine et al. (2004) brought substantial clarification to the validity of the pseudo-effective stress approaches. More recently, Nuth and Laloui (2008) showed that a Bishop-type effective stress implemented in a consistent elasto-plastic framework coupled with a rigorous description of the water retention behaviour of soil provides an efficient structure for modelling the mechanical response of unsaturated soils.

4.2.3 Mechanical behaviour

This section presents the stress-strain behaviour of unsaturated soils under isothermal conditions. The mechanical soil response is significantly affected by soil suction. The characterization of the mechanical response of unsaturated soils depends strongly on the stress reference used in the representation of the experimental results. The curves obtained from laboratory tests are usually displayed according to net stresses because they are the direct data monitored during the experiments. This provides a consistent framework to analyse the obtained results. However, the pseudo-effective stress approach may bring substantial clarification to some observed features of soil behaviour. Therefore, where possible in this section, the experimental evidence will be presented using the Bishop-type effective stress reference with $\chi = S_r$, called the generalized effective stress as termed by Nuth and Laloui (2008), in parallel with the net stress reference. This interpretation is possible only if the water retention information is available.

4.2.3.1 *Effect of suction on compression behaviour*

The apparent preconsolidation pressure increases remarkably upon desaturation. This increase in the elastic domain with suction is narrowly linked to capillary effects. During a consolidation process, the yield limit corresponds to the stress level that begins to produce a rearrangement of particles. As suction increases, air enters in pores and menisci that form at the air-water interface stabilize the particle-particle contact. This stabilizing effect pushes back the soil yielding limit. Figure 4.3 shows the evolution of the preconsolidation pressure with suction, as determined from compression tests on compacted Boom clay in both net stress and generalized effective stress references (Romero, 1999).

The evolution of the preconsolidation pressure appears to be rapid for low values of the suction and then becomes asymptotic for higher ones (Figure 4.3a). However, the logarithmic scale on the y-axis, which emphasizes very low suction levels (Figure 4.3b), shows that the increase in the elastic limit is noticeable only for suction higher than a given limit suction, the air-entry suction, which is when air begins to enter the pores. Above this limit, a logarithmic function might be suitable to model this phenomenon. Based on its similarity with the temperature effect and the evolution law proposed by Laloui and Cekerevac (2003) (Section 3.3.2.1), Nuth and Laloui (2007) used the same logarithmic formulation to quantify the one-to-one relationship between suction and preconsolidation pressure in the generalized effective stress reference:

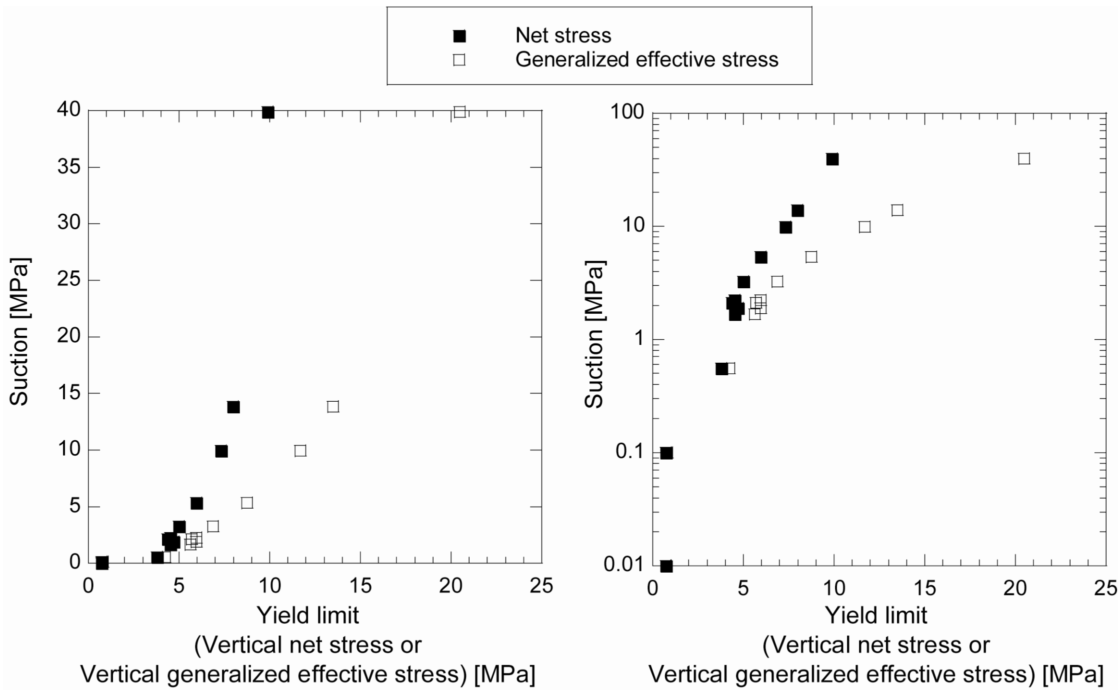

Figure 4.3: Evolution of the yielding limit with respect to suction determined from oedometric compression tests on compacted Boom clay at ambient temperature (Romero, 1999): a) linear y-axis; b) logarithmic y-axis.

$$p'_c = \begin{cases} p'_{c0} & \text{if } s \le s_e \\ p'_{c0}\left(1+\gamma_s \log\left(\dfrac{s}{s_e}\right)\right) & \text{if } s \ge s_e \end{cases} \tag{4.9}$$

where p'_{c0} is the preconsolidation pressure at saturation, p'_c is the preconsolidation pressure at a given suction s, s_e is the air-entry suction and γ_s is a material parameter. In the saturated domain (i.e. for suction lower than the air-entry value), Equation (4.9) assumes that a positive suction can take place without affecting directly the preconsolidation pressure, which remains equal to its saturated reference, provided that no volumetric plastic strain is produced during the suction evolution. Figure 4.4 validates this evolution law on two different soils.

Suction variation does not only affect the preconsolidation pressure but also tends to modify the compression indices. This effect depends on the stress reference. Geiser et al. (2006) reported the evolution of the compression index with suction for different fine-grained soils in the net stress reference (Figure 4.5). It reveals the non-monotonic evolution of the compression index with suction. For most of the soils shown in Figure 4.5, an initial increase in λ is noticeable at low suction values, followed by a reduction. A possible interpretation of this evolution is that λ increases with suction up to the air-entry suction, which initiates the desaturation process (see 4.2.4.1, below), and then below this limit, suction tends to reduce the soil compressibility. This should be coherent with respect to the possible stabilizing effect of the capillary meniscus, which acts when soil is unsaturated.

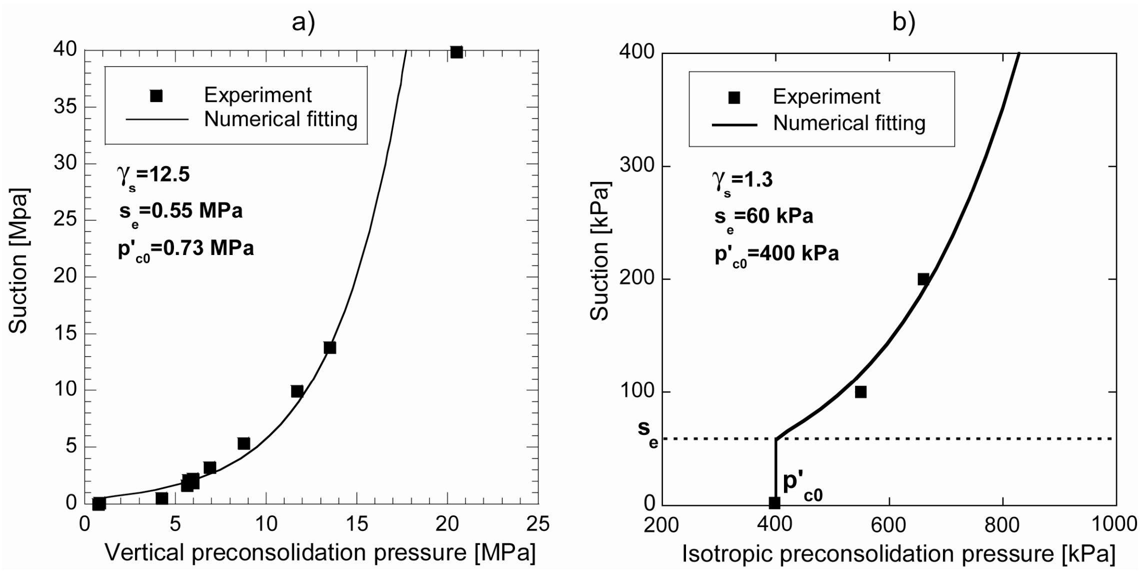

Figure 4.4: Analytical fitting of the evolution of preconsolidation pressure with suction compared with experimental results of (a) Romero (1999) on compacted Boom clay under oedometric conditions and (b) Geiser (1999) on Sion silt under isotropic conditions. The x-axes are drawn in the generalized effective stress reference.

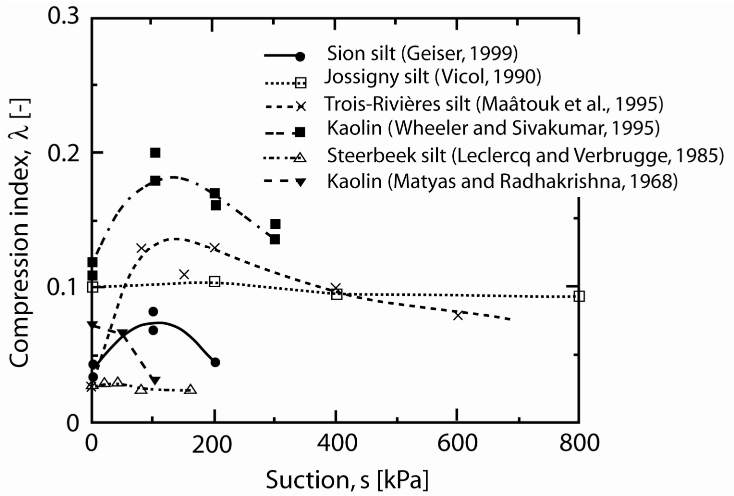

Figure 4.5: Evolution of the compression index of various soils with respect to suction, as reported by Geiser et al. (2006). The compressibilities were calculated in the net stress reference.

In light of the generalized effective stress, the evolution of the compression index with suction (denoted λ' as opposed to λ in the net stress reference) lacks confirmation. Some researchers concluded that drying causes a decrease in the slope of normal consolidation lines, while others noticed an increase. Nuth and Laloui (2008) observed that the use of the generalized effective stress reference enables one to obtain linear normal consolidation lines in the ($\ln p' - \varepsilon_v$) plane, while the net stress reference could lead to curved normal consolidated lines (Figure 4.6). The same conclusions were drawn by Salager et al. (2008) (see also François et al. (2007a) and Chapter 5, below).

4.2.3.2 *Effect of suction on shearing behaviour*

In unsaturated soils, the suction enhances the apparent shear strength of the soil if the experimental results are interpreted in the net stress reference (e.g. Blight, 1966, 1967; Escario 1980; Ho and Fredlund, 1982; Escario and Saez, 1986; Cui and Delage, 1996; Geiser et al., 2006). Figure 4.7 reports the critical state line with respect to suction, as determined by Escario (1980) from direct shear tests.

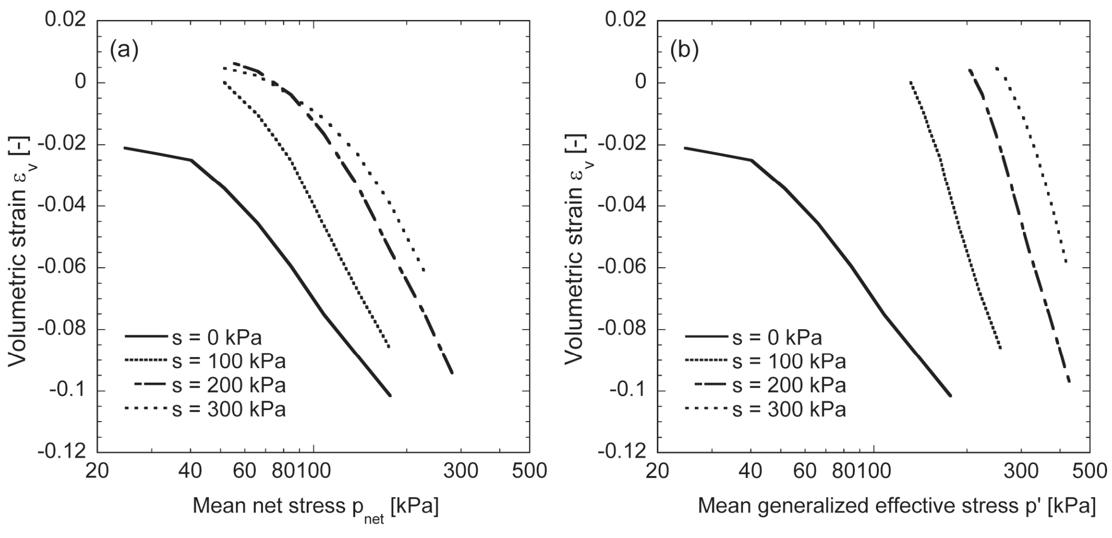

Figure 4.6 : Isotropic compression of kaolin at different suctions in both the net stress (a) and generalized effective stress (b) references. Experimental data: Sivakumar (1993), reported by Nuth and Laloui (2008).

Based on such experimental evidence, Fredlund and Morgenstern (1977) proposed a shear strength equation for unsaturated soil formulated in terms of independent stress state variables (net stress and suction) in which the friction angle is assumed to be unaffected by the soil suction, while the cohesion under saturation condition increases linearly with suction.

In opposition to the analysis of results using the net stress approach, the generalized effective stress framework brings substantial simplification in the critical state expression, in the sense that the slope of the critical state line can reasonably be interpreted as unique (Khalili et al., 2004; Nuth and Laloui, 2007, 2008). Result interpretations in light of the generalized effective stress clearly evidence a convergence of all critical state points towards a single line, whatever the suction. Khalili et al. (2004) investigated the uniqueness of the critical state line in the ($p'-q$) plane with different suctions. They used a particular suction ratio for the χ parameter. Similarly, Nuth and Laloui (2008) reinterpreted several shearing data with the generalized effective stress reference (i.e. with $\chi = S_r$). The results of that work are depicted in Figure 4.8.

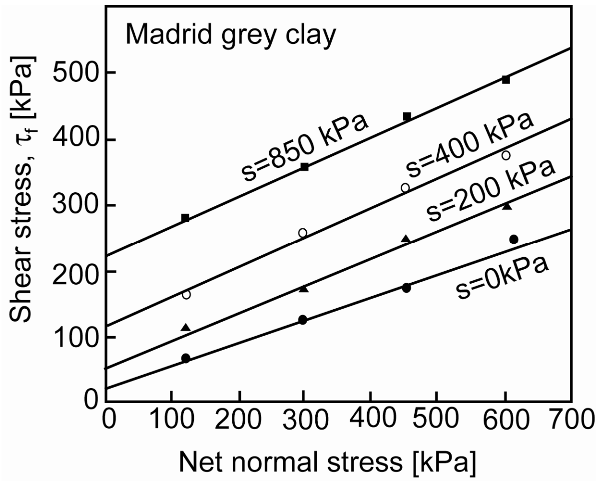

Figure 4.7: Increase in the shear strength with suction, as observed by Escario (1980) from direct shear tests, reported by Fredlund and Rahardjo (1993).

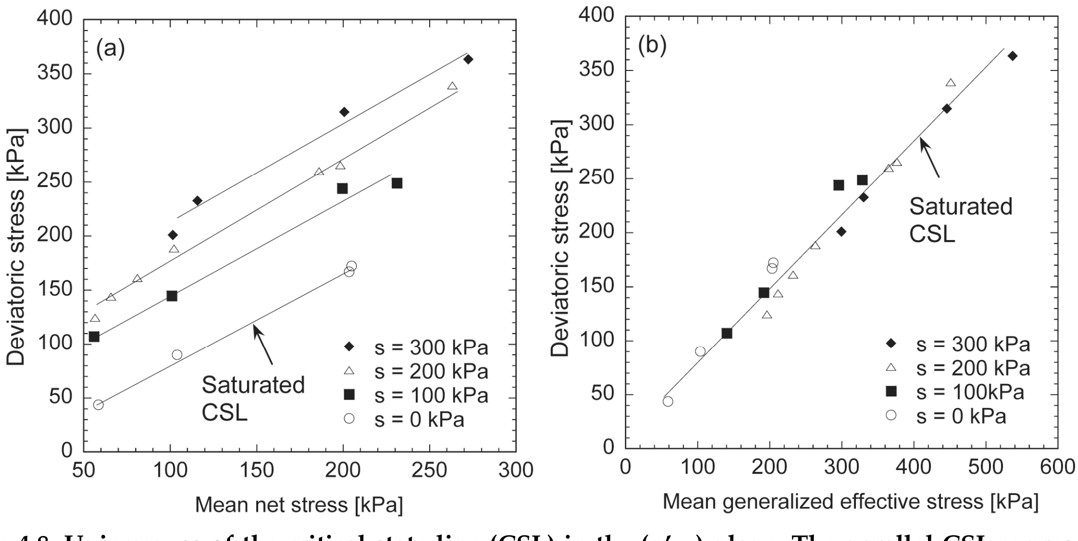

Figure 4.8. Uniqueness of the critical state line (CSL) in the (p'-q) plane. The parallel CSL expressed in the net stress reference (a) converge to a unique CSL in the generalized effective stress reference (b),. Experimental data: Sivakumar (1993), reported by Nuth and Laloui (2008).

In terms of yield behaviour, the critical state concept offers a consistent framework in which to interpret the evolution of the yield curve (defined as the limit of the elastic domain) with suction. Upon soil shearing, the elastic domain becomes enhanced with increasing suction. Evidently, the yield surface, as well as its evolution, depends on the stress representation. Figure 4.9 reports the yielding points experimentally obtained by Cui and Delage (1996) and Geiser et al. (2006) with their respective constitutive representation. In term of constitutive modelling, the evolution of the yield limit is usually governed by the evolution of the preconsolidation pressure, the friction angle and the cohesion of the soil with suction. However, in the generalized effective stress reference, the two last variables remain unaffected by suction.

4.2.3.3 *Volumetric response upon wetting-drying paths*

One of the key issues in study of unsaturated soils is the modelling of the volumetric response of soil submitted to wetting-drying cycles. The modelling of that behaviour requires a good identification of the characteristic response of soil undergoing variations in suction. Under low or zero external stress, soil swells when it is humidified. In both approaches, either using a single effective stress or two independent stress variables, this process is interpreted as elastic. The humidification provokes a drop in the suction and consequently a drop in the effective stress. Equation (4.5), using independent stresses, and Equation (4.6), using the pseudo-effective stress, both predict an expansion strain of the material. On the other hand, under high stress levels, i.e. under normally consolidated or slightly overconsolidated conditions, soil contracts when it is humidified. This process, called *wetting collapse*, is representative of irreversible strain in the material. Such a process requires that the elasto-plasticity concept be reproduced by the constitutive modelling.

At a same external stress, depending on the hardening state of the material, soil may undergo reversible volume change, for dense soil, or irreversible contraction, for loose soil. In the case of compact materials, the compaction process induces high initial soil suction. When in contact with a wetter environment, such relatively dry material tends to soak water, inducing a wetting process. In that specific case, the density of the compacted soil (related to the energy of compaction) must be optimized in order to avoid undesired wetting collapse under soil humidification.

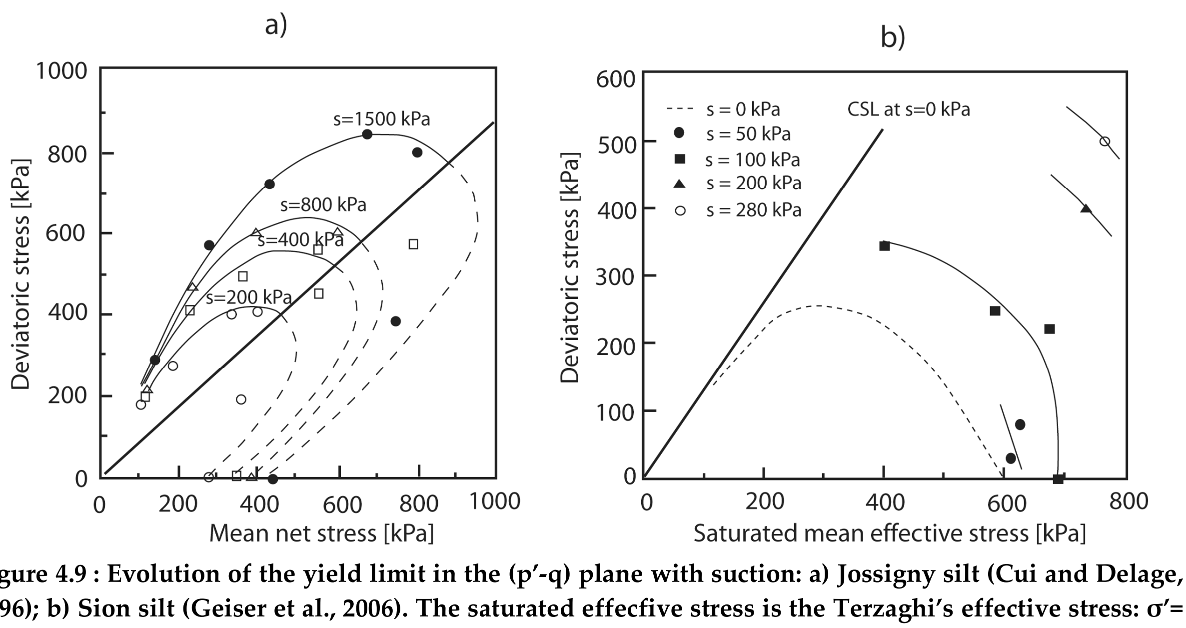

Figure 4.9 : Evolution of the yield limit in the (p'-q) plane with suction: a) Jossigny silt (Cui and Delage, 1996); b) Sion silt (Geiser et al., 2006). The saturated effecfive stress is the Terzaghi's effective stress: $\sigma' = \sigma - p_w$.

In order to mirror that fact, Romero et al. (2003) performed a comparative experimental study of the volumetric response of compacted Boom clay at different dry densities during wetting-drying cycles (Figure 4.10). Either swelling or collapse is observed according to the soil density and the external stress level. Under several wetting-drying cycles, most of the deformations are undergone during the first wetting path. This behaviour is characteristic of irreversible strains.

In the case of virgin or slightly overconsolidated saturated soil, a drying process produces successive distinct responses delimited by characteristic constitutive limits. Figure 4.11 depicts such behaviour on a white clay (Fleureau et al., 1993) and a Bioley silt (Péron, 2008). During the initiation of the drying process, at low suction, the soil may undergo very limited volume variations (Domain I). Below a given suction limit, soil enters a normally consolidated state corresponding to a drastic increase of the volume variation (Domain II). This state extends up to the air entry suction. Beyond this limit, the compressibility is reduced, and the drying process continues with very little shrinkage (Domain III). In light of the constitutive modelling, Domains I and III correspond to the elastic overconsolidated state, while Domain II is mainly governed by plastic processes. In Domain II, the slope in the ($e-s$) plane is similar to the compression index obtained from compression of saturated soil. In such a domain, where the soil remains saturated (i.e. the suction is lower than the air-entry suction), suction plays the role of a negative pore pressure, and Terzaghi's effective stress remains valid. Under re-wetting, the soil undergoes elastic swelling.

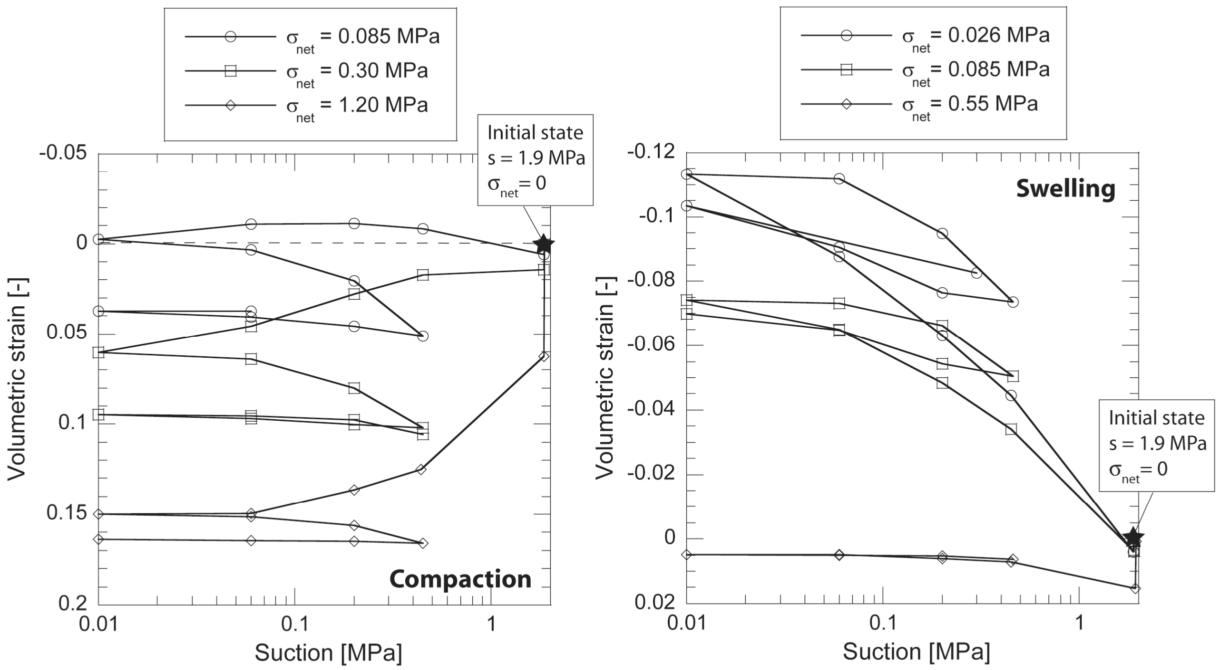

Figure 4.10: Effect of the dry density and the external vertical stress on the swelling and/or collapse behaviour upon wetting. Compacted Boom clay (Romero et al., 2003): a) Collapse (i.e. compaction) of loose soil (γ_d=13.7 kN/m^3); b) Swelling of dense soil (γ_d=16.7 kN/m^3).

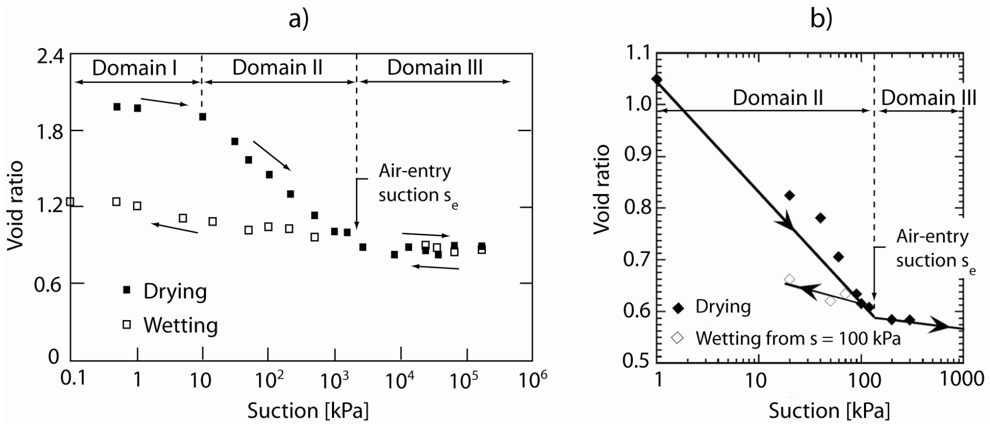

Figure 4.11 : Volume variation of virgin or slightly overconsolidated soil upon drying-wetting cycle: a) White clay (Fleureau et al., 1993); b) Bioley silt (Péron, 2008).

4.2.4 Water retention behaviour

4.2.4.1 *Water retention curve*

The relation between the amount of water presents in soil pore space (quantified by the degree of saturation or the water content) and the soil suction is usually referred to as the *soil-water characteristic curve*. In this dissertation, we will term it the *water retention curve* instead. Indeed, the adjective *characteristic* could be misleading in the sense that the water retention curve is not an intrinsic (i.e. characteristic) soil property but depends on many soil variables.

Evaporation from a soil or air-drying a soil brings the soil to a drier state. As the soil dries, the degree of saturation, or alternatively the water content, decreases and the suction increases. However, the process of desaturation occurs only at suction values greater than the *air entry-suction*. Below this limit, the soil remains saturated while suction is positive. Above this limit, desaturation occurs until it reaches a residual saturation state. In soil science, the state of soil saturation is generally conceptualized as having three regimes: the *capillary state,* where the soil remains saturated, the *funicular state,* where soil is unsaturated with a continuous water phase and the *pendular state,* characterized by an isolated, discontinuous water phase (Newitt and Conway-Jones, 1958; Mitarai and Nori, 2006).

Under re-wetting, a hysteresis effect occurs. At a same suction, the degree of saturation is lower on a wetting path than on a drying path. For a soil in a given state, the drying and wetting curves can be assimilated to limit curves inside of which hysteretic loops can be present. This hysteretic phenomenon can be attributed to several effects at the particle-scale: the "ink-bottle" effect, capillary condensation, entrapped air, solid skeleton deformation and contact angle hysteresis (Lu and Likos, 2004).

Discrete data points obtained from experiments can be described in a continuous mathematical form through fitting curves or more elaborate water retention models. Brooks and Corey (1964), Van Genuchten (1980) and Fredlund and Xing (1994), among others, proposed analytical expressions based on various meaningful soil characteristics to provide a continuous relation between soil suction and the degree of saturation. Figure 4.12 shows the water retention curves fitted with the Brooks and Corey (1964) and the Van Genuchten (1980) models, as well as experimental data.

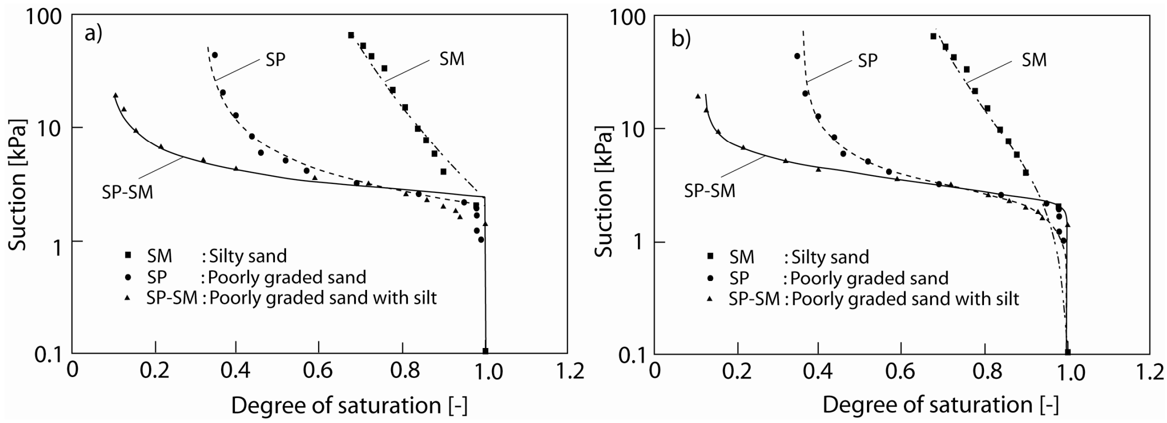

Figure 4.12: Analytical expressions fitting the water retention curves of three different soils at constant void ratio (experimental data from Clayton, 1996): a) the Brooks and Corey (1964) model; b) the Van Genuchten (1980) model, from Lu and Likos (2004).

In the case of the constitutive model for unsaturated soils using the generalized effective stress, a rigorous assessment of the degree of saturation with respect to suction is essential, because this information is used directly in the stress variable. In other words, not only the suction but also the degree of saturation directly affects the mechanical response of the material.

4.2.4.2 *Effect of dry density*

The effect of soil deformation on the water retention curve is mainly related, at the micro-scale, to the changes in the dimensions of voids and of connecting passageways between voids (Gallipoli et al., 2003a). The smaller the pores, the higher the suction that the capillary meniscus can sustain before air enters the pores. The corresponding changes in the water retention curve are usually assessed through the evolution of the air-entry value, a meaningful soil parameter. The denser the soil, the higher its water retention capacity. Figure 4.13 shows the water retention curve of compacted Boom clay at four different void ratios obtained by Romero (1999). The soil was deformable upon drying-wetting cycles, so it was not possible to obtain a curve corresponding to a constant void ratio from one unique sorption-desorption cycle. The results at various constant void ratios of Figure 4.13 were obtained from interpolations of different tests results starting from different initial void ratio. This figure reveals some key characteristics of the degree of saturation – suction relationship which must be considered in order to build an accurate water retention model. Those observations summarize the behavioural features explained in this section:

- On a drying path, the soil remains saturated below a given suction, that is, the air-entry suction. On a wetting path, the suction corresponding to the expulsion of air from the media, which must be surpassed to re-saturate the material, is lower than the air-entry suction.
- The transition between the saturated and unsaturated domains is smooth.
- The desaturation process seems to occur according to a logarithmic slope (linear in the ($S_r - \ln s$) plane.
- The logarithmic slopes appear to be parallel for different constant void ratios, at least for a range of degree of saturation between 20% and 80%.
- A decrease in the void ratio produces a shift in the water retention curve towards a higher suction level, for the same degree of saturation.
- The hysteresis behaviour induces a lower degree of saturation on wetting path than that on drying path for a same suction.

- The residual state is not visible on this graph, but matric suction tends to a common limiting value in the range of 600 – 1000 MPa, as the degree of saturation approaches 0% (Fredlund and Rahardjo, 1993).

From the relationship proposed by Fredlund and Xing (1994), Salager et al. (2007a) proposed a model to deduce the evolution of the water retention curve with the void ratio, by knowing the water retention curve at a given void ratio on monotonic drying path. Gallipoli et al. (2003a) and François et al. (2007b) (see also François and Laloui, 2008a) introduced the hysteresis and the dry density effect in a water retention model coupled with a unified stress-strain framework.

4.2.5 Constitutive modelling of unsaturated soils

4.2.5.1 *Elasto-plastic models using two independent stresses*

The first extension to unsaturated soils of a constitutive elasto-plastic model initially developed for saturated conditions was performed by Fredlund and Morgenstern (1977). They adapted the Mohr-Coulomb criterion by introducing a dependency of the cohesion on suction. Later, an hardening plasticity model describing the mechanical behaviour of unsaturated soils was presented by Alonso et al. (1990). This model, known as the Barcelona Basic Model (BBM), is based on the modified Cam-Clay ellipse expressed in the ($p' - q$) plane and extended into a third dimension, suction. The model incorporates the dependency of the cohesion and the preconsolidation pressure with suction. An isotropic yield limit, called the LC curve, considers plastic processes occurring upon wetting and isotropic stress loading. A second yield surface (the SI surface) is introduced to reproduce the plasticity upon drying. Using the same core, Wheeler and Sivakumar (1995) modified the Cam-Clay ellipse considered in the BBM to fit closely to the experimental results obtained on their materials. Similarly, Cui et al. (1995) considered an anisotropic yield surface using the same BBM framework.

In an innovative stress framework, using suction and the Terzaghi effective stress, Geiser et al. (2000) (see also Laloui et al., 2001) developed a model based on two yield surfaces. The surfaces, coupled through the hardening variable, reproduce the plasticity hardening induced by mechanical and hydraulic loading, respectively.

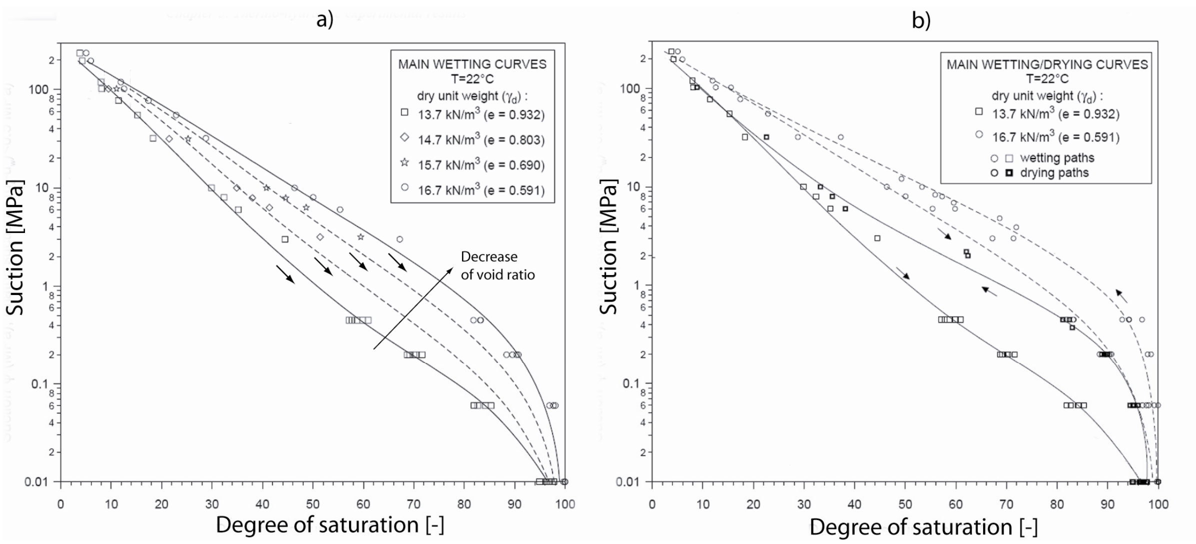

Figure 4.13: Effect of the void ratio on the water retention curve, as observed by Romero (1999) on compacted Boom clay: a) wetting curve at four different void ratios; b) wetting-drying curve for two particular void ratios.

4.2.5.2 *Elasto-plastic models using a pseudo-effective stress*

The approaches using a pseudo-effective stress are usually based on the tentative equation proposed by Bishop (1959) (Equation (4.7)) with different interpretations of the χ parameter. However, as stated by Gens (1995a), a unique effective stress variable is not sufficient to fully describe the mechanical response of unsaturated soils. A second stress variable, usually the suction, must be introduced to define the soil state. Consequently, the use of the *effective stress* term may be misleading. The authors using a homogenized stress prefer the term *pseudo-effective stress, average skeleton stress* or *generalized effective stress*.

Among others, Bolzon et al. (1996), Jommi (2000), Wheeler et al. (2003), Gallipoli et al. (2003b), Loret and Khalili (2002), Sheng et al. (2004), Tamagnini (2004) and Nuth and Laloui (2008) developed constitutive models based on the pseudo-effective stress. Among those contributions, the original state variable framework considered by Gallipoli et al. (2003b) is worthy of mention. Their model considers two constitutive variables: an averaged skeleton stress and an additional scalar variable related to the magnitude of the bounding effect exerted by the meniscus water. More recently, based on the so-called generalized effective stress (i.e. with $\chi = S_r$), François and Laloui (2008a) proposed a unified framework which considers not only the effect of water retention state on the mechanical behaviour, but also the reciprocal coupling from the mechanical state to the water retention behaviour.

Gens et al. (2006) (see also Gens (1995a)) enumerated the benefits and difficulties related to the use of a pseudo-effective stress:

- No special difficulties arise in unsaturated-saturated transition provided that the limiting case of the pseudo-effective for $S_r = 1$ is Terzaghi's effective stress.
- Hydraulic hysteresis is naturally incorporated if the effective stress parameter is related to the degree of saturation.
- The strength increase with suction results directly from the definition of the constitutive stress.
- The stress path is more complex, and it becomes impossible if data on water content is not available or unreliable.

4.2.5.3 *Specific constitutive developments*

The study of the unsaturated soil behaviour encompasses many annex fields, which arise from a need to describe the behaviour of some specific materials. In particular, materials with a double porosity fabric show significant swelling and/or collapse that, in some cases, cannot be easily accommodated by conventional elasto-plastic unsaturated soil models (Gens and Alonso, 1992). Alonso et al. (1999) proposed a conceptual model for double structure expansive clays, in which two levels of formulation are presented: the microstructure model, where the interactions at particle level occur, and the macrostructure model that accounts for the overall fabric arrangement of the material, including aggregates and macropores. This model was re-formulated in the framework of generalized plasticity and multi-mechanism theory by Sanchez et al. (2005). Koliji (2008) developed an elasto-plastic model using a parameter to quantify the soil structure physically in terms of macroporosity. This parameter evolves with the generated plastic strain.

During drying processes, soil may undergo desiccation cracks. This phenomenon usually arises from the constrained soil shrinkage, which induces tensile stress in the materials. If this stress reaches the tensile strength, the soil may crack. The prediction of such events requires an accurate constitutive model founded on the concept of the mechanics of unsaturated soils. Based on Bishop-type effective stress and tensile strength criterion, Deng and Sheng (2007) and Péron (2008) (among others) presented constitutive approaches which predict crack occurrences during soil drying.

4.3 Non-isothermal behaviour of unsaturated soils

4.3.1 Mechanical behaviour

In addition to the observed behaviour of unsaturated soils at ambient temperature (Section 4.2) and of saturated soils under non-isothermal conditions (Section 3.3), some coupled effects between suction and temperature arise in soils when unsaturated and non-isothermal conditions are simultaneously met. Those interactions must be considered in the development of constitutive models in order to cover the range of thermo-hydro-mechanical couplings occurring in fine-grained soils. Those coupling effects, experimentally observed on compression and wetting-drying paths, are detailed in the two following sections, respectively.

4.3.1.1 *Compression paths*

From experimental programs studying the thermal effect and the suction effect on the compression behaviour of soils separately, the experimental results clearly underline a decrease in the preconsolidation pressure with temperature and an increase in that pressure with suction. However, the combined effect of temperature and suction on the preconsolidation pressure lacks of confirmation. On compacted Boom clay loaded under oedometric conditions, Romero (1999) noticed a very small effect due to temperature, regarding the suction effect, on the evolution of the preconsolidation pressure (Figure 4.14a). However, the results confirm the usual decrease in p_c' with temperature and increase with suction. Tang et al. (2008) observed similar behaviour on MX80 bentonite (Figure 4.14b). Note that the experimental curves were analysed in net stress reference for both materials.

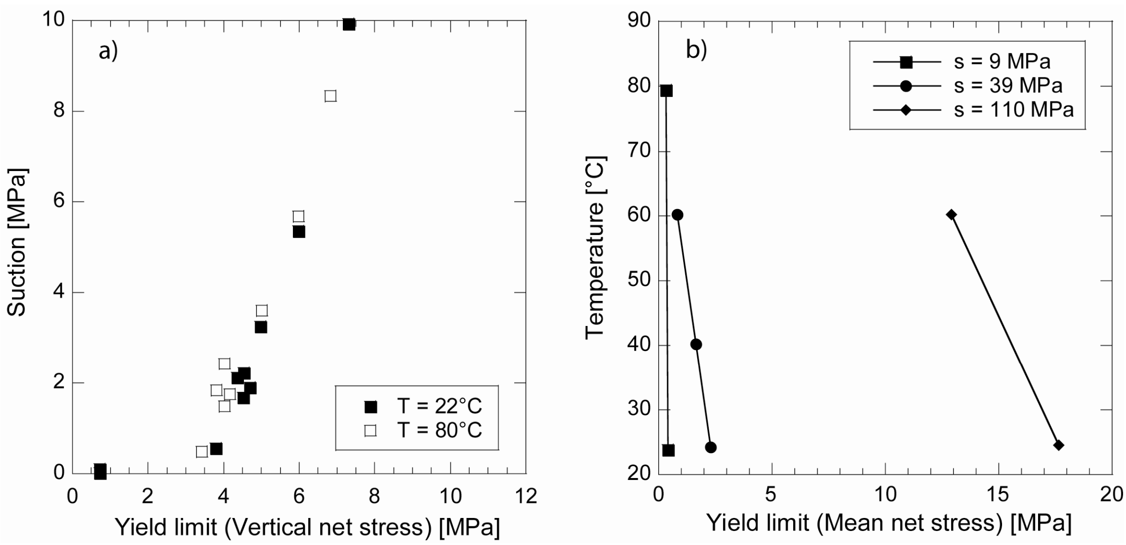

Figure 4.14. Combined effect of temperature and suction on the evolution of the yield limit in the net stress reference: a) Oedometric compression tests on compacted Boom clay (Romero, 1999); b) Isotropic compression tests on MX 80 bentonite (Tang et al., 2008).

In contrast, Saix et al. (2000) (see also Saix, 1991 and Saix and Jouanna, 1990) observed an unusual increase in the preconsolidation pressure with temperature on an unsaturated clayey silty sand. This increase in the yield limit was observed for temperatures above 40°C. Salager et al. (2008) (see also François et al., 2007a) performed an experimental investigation to study the combined effects of temperature and suction on the preconsolidation pressure and compressibility indices of a sandy silt. This experimental study is addressed in Chapter 5, below.

4.3.1.2 *Wetting-drying paths*

It was also observed that the temperature level influences the mechanical response of fine-grained soils along wetting-drying paths, mainly because of the thermal effect on the physico-chemical interactions between clay particles. Romero et al. (2003) observed that the swelling potential of compacted Boom clay increases with temperature. This increase in the swelling strain upon wetting a high-density sample of compacted Boom clay was observed for various vertical stress levels. In particular, Figure 4.15 depicts the swelling response under 0.085 MPa of vertical stress at 22° and 80°C. On the contrary, Villar and Lloret (2004) observed a decreasing swelling capacity of FEBEX bentonite with increasing temperature (Figure 4.16). Villar and Lloret (2004) noticed that the temperature effect is consistent with the observations of Lingnau et al. (1996) on a sand/bentonite mixture.

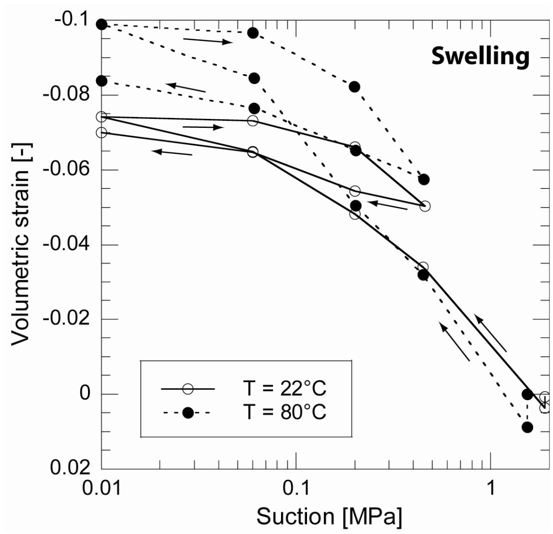

Figure 4.15 : Effect of temperature on the swelling strain of compacted Boom clay, experimental results from Romero et al. (2003). The vertical net stress is 0.085 MPa.

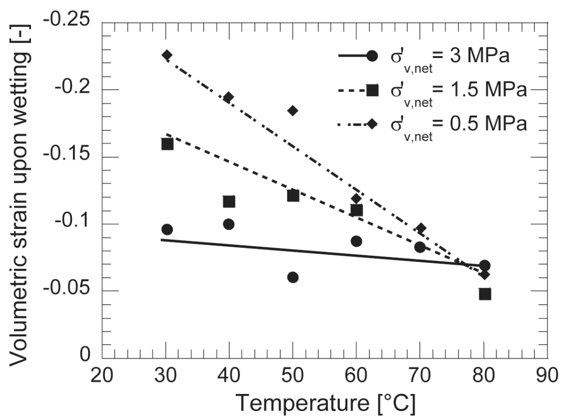

Figure 4.16: Effect of temperature on the volumetric strain upon wetting (swelling strain) of FEBEX bentonite, experimental results from Villar and Loret (2004).

In term of collapse propensity, for loose-density Boom clay, Romero et al. (2003) observed that the contraction strain upon wetting is higher at elevated temperatures than that at room temperature.

4.3.2 Water retention behaviour

The effect of temperature on the water retention properties of fine-grained soils, as observed at the macro-scale, is the consequence of several physical mechanisms that act at the particle scale. These thermal phenomena are related to the role of temperature on the capillary mechanisms, on the short-range solid-liquid interaction or on the phase change mechanisms. These processes are addressed in the following section, starting from micro-scale considerations. In a second section, thermal effect on the water retention curve are presented from macroscopic observations.

4.3.2.1 *Microstructural aspects*

The volume of water stored in soil pore space can be split into two categories: adsorbed and bulk water. The closer the particle is to the water, the higher its attraction to the particle and lower its mobility. In the vicinity of the particle, the water is essentially adsorbed (Section 3.2.2). The retention capability of a soil, at a micro-scale, results from the equilibrium between stresses of both fluid phases, capillary forces acting at the interface of each phase and the attractive force between adsorbed water and particles.

In particular, the equilibrium between the capillary forces and the suction is governed by Jurin's law:

$$p_a - p_w = s = 2\sigma_s \frac{\cos\theta}{r} \tag{4.10}$$

where σ_s is the surface tension between both fluids, θ is the effective contact angle of the fluid-fluid interface with the solid surface and r is the radius of the capillary tube (which can be assumed to be the radius of the soil pore).

As a consequence, for a given suction, a meniscus is not able to form in pores with a radius greater than the suitable radius meniscus. Each pore size has a corresponding suction beyond which a meniscus is not able to sustain difference between air and water pressures. It implies that at each pore size there is a critical suction beyond which water is drained from the pore. Thus, the continuity of water is maintained as long as the pore radius is smaller than a critical radius defined by Jurin's law (Mercury et al., 2003).

Also, the equilibrium between adsorbed water and particles is governed by the diffuse double layer theory, as addressed in Section 3.2.2.2. The quantity Ω is a good approximation of the measure of the thickness of the double layer (see Equation (3.1)):

$$\Omega = \left(\frac{\varepsilon_0 DkT}{2n_0 {e_0}^2 \upsilon^2} \right)^{1/2} \tag{4.11}$$

where ε_0 is the static permittivity of the medium [$C^2J^{-1}m^{-1}$], D the dielectric constant of the medium [-], k the Boltzmann constant ($=1.38\ 10^{-16} ergs/K$), T the temperature [K], n_0 the electrolyte concentration [ions/m^3], υ the ionic valence of the solution [-] and e_0 the electronic charge ($=4.81\ 10^{-10} esu$). To quantify the amount of adsorbed water in a soil, Equation (4.11), valid for a single particle, must be multiplied by the specific area [m^2/g] of the considered soil to get the volume of adsorbed water by unit weight of dry soil.

As revealed by Equation (4.10), the volume of free water stored by the medium depends on the size of the pores, the properties of phase interfaces and the suction. However, the amount of adsorbed water depends on the physico-chemical properties of fluids and particle surfaces in addition to the specific surface of the soil (Equation (4.11)).

The effect of temperature on the volumetric fraction of each phase in a soil must be separated into *long term* and *short term* effects. A change of temperature in the soil induces a modification of the properties of the different phases and also of their interfaces. These modifications may generate dissipative or non-dissipative consequences. In other words, some thermal effects will dissipate with time by means of the diffusion of fluid phases, while other effects directly affect the intrinsic properties of materials and are not dampened with time, except if the temperature recovers its initial value.

Therefore, unlike short term effects, the long term effects must be understood as effects which subsist even if a new equilibrium has been reached. The long-term volumetric equilibrium between each phase is governed by the geometry of the media (size and forms of pores and grains) and the interaction force between each phase through Equations (4.10) and (4.11), respectively.

Thermal modification of the volume repartition of each phase (short term effect)

When temperature increases in soil, each constituent dilates. The volume change of each component is proportional to the temperature variation and the thermal dilatation coefficient of the phase considered. Because the thermal dilatation coefficients of air, water and solid grains are different, the volumetric proportion of each phase will be modified by a temperature change.

For a temperature change of 50°C, the volume of water increases 2%, because the thermal dilation coefficient of water β'_w is 4.10^{-4}. Similarly, if the solid skeleton expansion is possible, the pore space increases 0.1 %, with a thermal dilation of solid skeleton β'_s of 2.10^{-5}. The dilatation of air is governed by the perfect gas equation. However, because the air phase is much more compressible than the liquid and solid phases, this air dilatation is constrained by the neighbouring water and solid media. Therefore, the dilatation of air is not considered. As a consequence, and according to the following equation, a temperature increase of 50°C induces, in the short term, an increase in degree of saturation of 1.9 %:

$$\Delta S_r = \Delta\left(\frac{V_w}{V_{voids}}\right) = \frac{\Delta V_w \; V_{voids} - V_w \; \Delta V_{voids}}{V_{voids}^2} = \frac{2\;10^{-2} V_w}{V_{voids}} - \frac{V_w 1\;10^{-3}}{V_{voids}} = 1.9\;10^{-2} S_r \qquad (4.12)$$

Thermal modification of Henry's coefficient (short term effect)

The solubility of air in water changes with temperature. Considering that air is at athmospheric pressure, the solubility of air in water varies from 0.0232 kg/m^3 at a temperature of 0°C to 0.0103 kg/m^3 at 60°C (calculated from Mercury et al., 2003). Accordingly, during soil heating from 0°C to 60°C, 0.0129 kg of air is released from one cubic meter of water in the form of air bubbles. The Clapeyron equation enables us to express the corresponding volume of such a mass of desorbed air:

$$V_a = \frac{m_a.R.T}{M_a.p_a} = 1.24\ 10^{-2}\, m^3 \quad \text{released from one cubic meter of pore water} \tag{4.13}$$

with m_a the mass of air [kg]; $R = 8.314\ J/(K.mol)$, the gas constant; $T = 333.15\ K$, the temperature in Kelvins; $M_a = 28.8\ 10^{-3} kg/mol$, the molar mass of air; and $p_a = 1.10^5 Pa$, the pore air pressure, assumed equal to atmospheric pressure.

Assuming constant pore space, the desorbed air from water causes, in the short term, an desaturation of 1.24 %, according to the following mathematical transformations:

$$\Delta S_r = \frac{\Delta V_w}{V_{voids}} = \frac{\Delta(V_{voids} - V_a)}{V_{voids}} = \frac{-\Delta V_a}{V_{voids}} = \frac{-\Delta V_a}{V_w}\frac{V_w}{V_{voids}} = -1.24\ 10^{-2}\, S_r \tag{4.14}$$

Thermal modification of surface tension of water (long term effect)

In Equation (4.10), the surface tension between air and water phases depends on thermal conditions, while the temperature sensitivity of the wetting coefficients is not well established (She and Sleep, 1998). If it is admitted that the wettability of clay particles is temperature independent (i.e. θ is constant), as assumed by Philip and De Vries (1957), the effect of the temperature on the equilibrium described by Equation (4.10) can easily be assessed. Grant and Salehzadeh (1996) proposed a linear regression of the surface tension evolution with temperature, over the temperature range -10°C to 70°C:

$$\sigma_s = 0.0752 - 0.000153\ T \tag{4.15}$$

T being expressed in degrees Celsius [°C]. For a given pore size distribution, the radius of the meniscus is directly related to the degree of saturation of the media. Two cases may be considered: (i) a constant degree of saturation and (ii) a constant suction

(i) Assuming a constant degree of saturation means that the geometry of the meniscus remains unchanged. However, in agreement with Equation (4.10), for the same curvature of the capillary meniscus, the sustained difference between pore air and pore water pressure (i.e. the suction) will be modified due to the thermal change of the surface tension. A heating from 0°C to 60°C decreases surface tension from 0.0751 N/m to 0.066 N/m, inducing a suction decrease of 12 % at a constant degree of saturation

(ii) On the contrary, if the suction is assumed constant, the decrease of surface water-air tension with temperature decreases the radius of the meniscus. As a consequence, some pores which were water-filled are drained and cause the degree of saturation to decrease. However, this effect is difficult to quantitatively assess in terms of the degree of saturation variation, because it strongly depends on the pore size distribution of the material.

Thermal modification of adsorbed water thickness (Long term effect)

In Equation (4.11), the temperature change directly affects the product $D \times T$. For a variation of temperature from 20°C to 70°C, the decrease of $D \times T$ is about 6 % (Mitchell, 1976) which induces a decrease in the thickness of the adsorbed water layer of the same value. Accordingly, a temperature variation of 50°C in clayey soils induces a change in the volume of adsorbed water of 6%. Assuming that, in pure clay, the large majority of the pore water is adsorbed water (Pusch and Carlsson, 1985), it produces a decrease in the degree of saturation of approximately 5% (assessing that 80% of water is adsorbed water).

Conclusions

The two main long term temperature effects on the water retention curve, namely the changes in the surface tension of water and in the adsorbed water thickness, contribute to a decrease in the retention capability of a soil with increasing temperature. Even if these two thermal contributions are the predominant effects, some secondary effects, such as thermal modifications of the contact angles or of the solubility of salt in water, should also contribute to changes in the moisture content of soil with temperature. In addition, short term effects tend to make the thermal-induced desaturation of the soil faster. However, those short term effects tend to dissipate with time, when a new equilibrium is recovered.

A rigorous quantification of the thermal effects on the water retention curve at the micro-scale is delicate in the sense that it depends on many factors (the grain size distribution, the density, the arrangement of grains, the clay fractions, and the solute concentration in pore water, among others). Romero et al. (2001) and Imbert (2005) proposed, respectively, adaptations of the Van Genuchten (1980) empirical expression and of the Brustaert's relation (Bear and Bachmat, 1986) to incorporate only the effect of temperature on the surface tension in the water retention curve. Similarly, Salager et al. (2006) proposed a model predicting the effect of temperature on the water retention curve based on the differential partial derivative of suction with respect to the water content, the temperature and the void ratio (see also Salager et al., 2007a).

4.3.2.2 *Macrostructural aspects*

As shown in the previous section, many factors contribute to the decrease in the water retention capability of soil as temperature is increased. From a macroscopic point of view, this means that, at constant suction, the degree of saturation of a given soil is lower under elevated temperature than at room temperature. On the contrary, for a given amount of water in the soil, the suction is reduced when temperature increases.

Many authors noticed such a decrease in the water retention capability as the temperature is increased. Among many others, Imbert et al. (2005) observed such an effect on the monotonic drying of FoCa compacted clay (Figure 4.17a). Loret et al. (2004) observed similar effects on FEBEX bentonite submitted to a wetting-drying cycle at 40°C, 60°C and 80°C (Figure 4.17b).

As explained in the previous section, some authors quantify the thermal effect on the water retention curve using microscopic considerations. However, to the author's knowledge, the only macroscopic water retention model considering the influence of temperature on the $S_r - s$ relationship has been proposed by François and Laloui (2008a). This model is based on the evolution of the air-entry suction with temperature. This meaningful soil parameter, which is clearly temperature dependent, is used to control the shift of the water retention curve with temperature change (see Section 6.3.2, below).

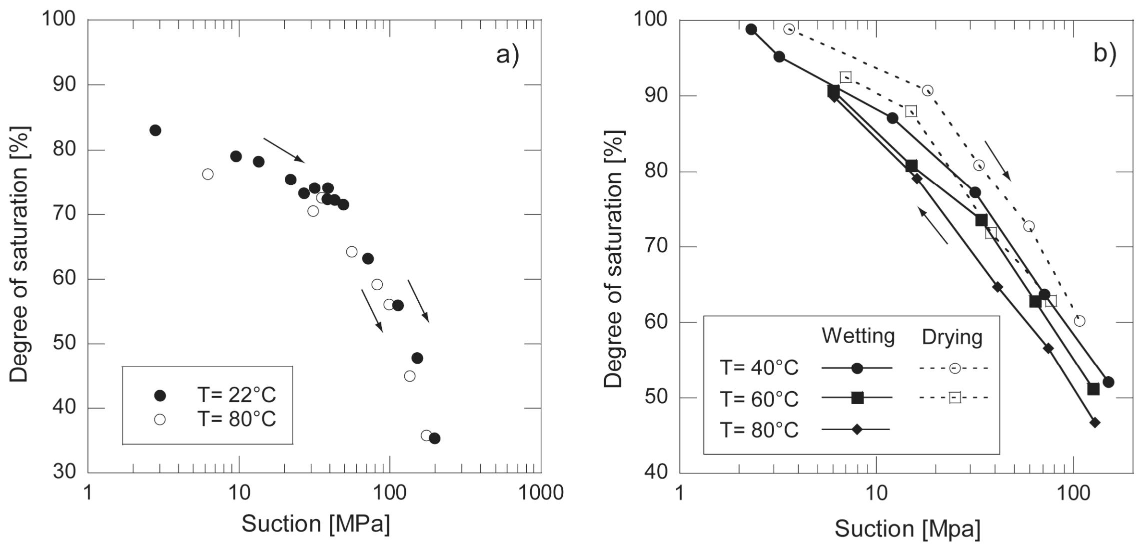

Figure 4.17 : Effect of temperature on the water retention curve: a) FoCa clay (Imbert et al., 2005); b) FEBEX bentonite - dry density of 1.65 kN/m³ (Loret et al., 2004, corrected with a density of water set at 1.1 g/cm³).

4.4 Conclusions

In this chapter, a literature analysis of the experimental evidence for the mechanics of unsaturated soil has been conducted. In the first part, isothermal conditions were considered, while the second part presented the influence of temperature on the response of unsaturated soils. This analysis shows the strong link between the mechanical behaviour and the water retention behaviour. Moreover, because temperature affects both the stress-strain and degree of saturation-suction relationships, temperature plays an important role in the global response of unsaturated soils.

Any interpretation of experimental results, as well as any development of constitutive models, requires a consistent stress framework. Provided that the choice of the state variables remain acceptable from a thermodynamics point of view, that is to say that the stress and strain variables remain work conjugate, the choice of the stress framework appears to be mostly a matter of convenience.

The strong irreversibilities in the unsaturated soil response have been emphasized. In particular, the generated plastic strains upon various thermo-hydro-mechanical paths have been shown to be closely related to the temperature and suction of the soil. Among other examples, the collapse propensity of a soil, occurring upon soil humidification, is not only affected by the external stress level but also by temperature. Similarly, the elastic domain is enhanced with increasing suction, while it decreases with increasing temperature.

In terms of water retention capability, the water retention curve is affected by the mechanical state of the soil and by the temperature. The denser the soil, the higher its degree of saturation for an equivalent suction. On the other hand, temperature tends to reduce the degree of saturation at a given suction. This thermal effect has been studied from both microscopic and macroscopic points of view.

Chapter 5

Experimental characterization of the THM behaviour of soils

There is a need, therefore, to examine more systematically the combined effects of suction and temperature on the mechanical behaviour of unsaturated soils under more controlled conditions. […]. To achieve such an understanding it is necessary to perform tests under the simultaneous control of suction and temperature. A main challenge for such an undertaking is the devising of a reliable controlled-suction apparatus capable of working at elevated temperatures.[1]

[1] Romero E., Gens A. and Lloret A. (2003). Suction effects on a compacted clay under non-isothermal conditions, *Géotechnique*, 53(1): 65-81.

5.1 Introduction

When a fine soil is simultaneously submitted to thermal, hydraulic and mechanical loads, strong thermo-hydro-mechanical (THM) couplings occur. In particular, the mechanical behaviour of soils is affected by unsaturation and thermal effects. In the field of environmental geomechanics, several relevant applications require an accurate knowledge of the thermo-mechanical behaviour of unsaturated soils (Vulliet et al., 2002). However, a literature analysis (Chapter 4) reveals a lack of accurate experimental results describing the combined effects of temperature and suction on the mechanical response of fine soils. Moreover, the few available results are mainly focused on compacted materials (Wiebe et al., 1998; Romero et al., 2005; Romero et al., 2003; Tang et al., 2008), which have an aggregated structure giving them specific behavioural features. The main results focusing on the behaviour of remoulded fine soils at different temperature and suction levels have been obtained on a clayey, silty sand (Saix, 1991; Saix et al., 2000; Saix and Jouanna, 1990).

In order to corroborate and to extend the results obtained on remoulded soils, it was decided to perform an experimental program on a sandy silt in a THM oedometer. This program was designed to determine the coupled influence of temperature and suction on the compression behaviour of soil. The tests in the oedometer cell were carried out in parallel with others tests performed at the Montpellier II University (France) on the same soil, but with an isotropic cell. These results are presented in Section 5.3.6 and compared with the results obtained in the THM oedometer.

Before addressing this experimental program with the obtained results, a literature analysis of the existing devices used to investigate the mechanical behaviour of soils under unsaturated and non-isothermal conditions is presented.

5.2 Literature analysis on the THM experimental devices

5.2.1 Introduction

Despite the technical difficulties related to the control and measurement of suction applied to soil specimens, there exists a relatively large number of experimental studies concerning the mechanical behaviour of unsaturated soils under isothermal conditions. Under such unsaturated conditions, the measurement of the volume change of the soil sample requires specific techniques which involve rigorous calibrations. Early experimental results were obtained by Bishop and Donald (1961) in a triaxial apparatus. After that, most tests were performed under oedometric or isotropic stress conditions (among others, Escario, 1969; Fredlund and Morgenstern, 1976; Jennings and Burland, 1962). Direct shear box testing has also been carried out (Escario, 1980). Finally, since 1980, the triaxial technique has again been used to determine stress-strain curves under controlled suction (e.g. Ho and Fredlund, 1982). Each technique has its own specificities with its advantages and disadvantages. Oedometric compression tests enable an accurate direct volume change determination and minimize effects due to the anisotropic loading because the stress path followed is similar to the static compaction process used in the fabrication of the sample. Nevertheless, stress state information is usually incomplete. The great advantage of isotropic and triaxial tests is that the stress state of the sample is totally known. However, the volume change measurement is usually subject to calibrations and indirect procedures.

As far as non-isothermal conditions are concerned, a great number of experimental studies concerning temperature effects on saturated soils have also been carried out. The difficulties with these tests are related to the control of undesirable effects on various parts of the equipment and the calibration to correct errors in the measurement due to the temperature effects. The first thermo-mechanical devices used for soil testing were oedometers adapted for applying, measuring and acquiring temperature data (Finn, 1951; Paaswell, 1967; Plum and Ersig, 1969). Later, in order to completely control the stress state of the sample, temperature-controlled triaxial cells were used. The first triaxial equipment permitting the control of both temperature and stress was developed by Campanella and Mitchell (1968). Since that time, many authors have performed thermo-mechanical triaxial tests (Eriksson, 1989; Baldi et al., 1991; Hueckel and Pellegrini, 1991; Kuntiwattanakul, 1991; Moritz, 1995; Sultan, 1997; Cekerevac, 2003; Abuel-Naga, 2005).

In contrast, experimental studies concerning the joint effect of unsaturation and temperature on the mechanical behaviour of soils are very limited. In these kinds of tests, the number of parameters that must be controlled increases considerably and substantial precautions to ensure accurate results must be taken. The most relevant contributions to the experimental investigations of the thermo-mechanical behaviour of soils under unsaturated conditions with simultaneous control of temperature, suction and stress state have been performed by Recordon (1993) and Romero (1999) under oedometric conditions and Saix and Jouanna (1990), Saix (1991), Wiebe et al. (1998), Romero (1999), Saix et al. (2000), Romero et al. (2003), Romero et al. (2005), Salager et al. (2008), and Tang et al. (2008), under triaxial conditions. In the following section, the existing techniques to impose and measure suction, temperature and stress state as well as techniques to measure the volume variation of the soil specimen are presented.

5.2.2 Overview of experimental methods

In such experimental thermo-mechanical tests under unsaturated conditions, it is necessary to control four parameters: suction, temperature, sample volume evolution throughout the test and air or water exchange quantities. The control and/or the measurement of each of these parameters requires specific experimental techniques and their calibrations.

5.2.2.1 *Control of suction*

Three main techniques are generally used to control the suction within a soil sample: the axis translation technique, the osmotic technique and the imposed relative humidity technique. Delage et al. (1998) has described the principle of each method with its advantages and drawbacks (see also Hoyos et al., 2008).

Axis translation technique

The axis translation technique (also called the overpressure technique) involves a translation of the reference pore air pressure, p_a, which can be seen as an artificial increase in the atmospheric pressure under which the test is performed. This technique requires the maintenance of a difference between the pore air and pore water pressures. To this end, a high air-entry value ceramic disc (HAED) with air-entry value greater than the maximum applied suction must be used as an interface between the unsaturated soil sample and the pore water pressure system. This ceramic disc acts as a link between the pore water in the soil and the water in the measuring system, avoiding the passage of free air into the water compartment.

The validity of this technique requires that an increase of pore air pressure induces similar effects to a decrease of pore water pressure. As reported by Fredlund and Rahardjo (1993), the radius of curvature of the meniscus, which controls the effect of suction on the mechanical response of the soil, only depends on the difference between pore air and pore water pressures, which makes the axis translation technique valid. Bishop and Donald (1961) and Fredlund and Morgenstern (1977) experimentally proved the validity of the axis translation technique in the positive range of pore water pressure. More recently, Mongiovi and Tarantino (1998) developed an apparatus to investigate the validity of the axis translation technique in unsaturated soils in the negative range of pore water pressure by preventing sample deformation and water content changes. They conclude that matrix suction seems unaffected by air pressure changes. This overpressure method enables one to impose suction up to 1500 kPa. This limitation is related to the ceramic stones, which are not able to sustain differences between air and water pressures higher than this limit.

The main benefit of this technique is the relative simplicity of the method. However, this technique presents some limitations:

- This technique is best suited for soil with a continuous air phase in order to induce an equal pore-air pressure value throughout the specimen. The entire air phase in the pore space must be interconnected to the surface of the sample. In that sense, the degree of saturation of the soil cannot be at a level where the gas phase is discontinuous (Romero, 1999).
- Special care is required to install the porous ceramic discs into the device. These stones must be saturated with water before being in contact with the soil specimen to guarantee the best barrier to the air phase. Furthermore, the continuity between soil water and water in the ceramic disc is assumed to correctly impose matric suction. The saturation of ceramic discs requires special techniques to assure the total removal of the free air inside the pore of ceramic. If the saturated ceramic disc is placed under a dry soil sample, it may immediately draw water up through the ceramic disc (Romero, 1999; Geiser, 1999).
- Even if the high air-entry value ceramic disk (HAED) is designed to avoid the passage of free air below a specific bubbling pressure, some air diffuses through the HAED, even at air pressures below the rated capacity (Romero, 1999; Padilla et al., 2006) (see Section 5.2.3.2). This produces an error in the water exchange volume measurement (for drained test) or in the water pressure measurement (for undrained test). A diffused air volume indicator can be used in conjunction with the measuring system to flush and measure the volume of diffused air (Fredlund and Rahardjo, 1993; Lagny, 1996).
- If free water is connected to the sample through the two faces of the soil specimen, during a wetting stage, there are two wetting front advancing and air can be trapped inside the sample (Romero, 1999). In that configuration, the total saturation of the sample may be impossible on the wetting path.

Osmotic technique

The osmotic technique is based on the process of osmosis. If a difference of chemical concentration is maintained between two fluid solutions in contact, a difference of pressure is induced between the two fluids in order to equilibrate the chemical potential, the pressure increasing in the fluid at higher concentration. When applied to geotechnical testing, this process can control the matrix suction within the soil. Practically, the difference of concentration between pure water inside the sample and a solution of polyethylene glycol (PEG) outside the sample is maintained by a semi-permeable membrane. This membrane stops the large PEG molecules while water molecules can pass through it. The PEG solution is placed in a reservoir big enough to ensure a constant concentration despite water exchange occurring through the membrane between the sample and the solution (Cui and Delage, 1996). This reservoir is at atmospheric pressure. The relationship between osmotic pressure and PEG concentration is well known for two molecular weights (PEG 6000 and 20000) (Williams and Shaykewich, 1969). This relationship has been extended by Delage et al. (1998) for two other molecular weights (PEG 4000 and 1500) and for higher suctions. A large range of suctions can be imposed (up to 12 MPa).

The adaptation of this technique for geotechnical testing was made by Kassiff and Ben Shalom (1971) in an oedometric cell. Further, Kormonik et al. (1980), Delage et al. (1987) and Dineen and Burland (1995) used this technique, respectively, with an oedometric cell, a hollow cylinder triaxial apparatus and a standard triaxial apparatus.

The main advantages of the osmotic technique are detailed in the following (partially reported by Delage et al. (1987)):

- The suction condition can be imposed on the two faces of the sample. It reduces to half the distance of drainage inside the sample, which makes the suction equilibrium faster. Furthermore, the water permeability of the semi-permeable membrane is on the same order of magnitude as the porous ceramic (for the axis translation technique), but the membrane is thinner than the porous stone. Thus, water crosses over the semi-permeable membrane faster than the ceramic disc, which also contributes to a faster suction equilibrium.
- The soil remains close to its natural condition, since no pore air pressure needs to be applied within the sample. The pore water pressure is negative as in nature.
- The continuity of the gas phase is not required. As a consequence, there is no limitation to the range of the degree of saturation of the soil specimen.
- A large range of suctions (from 0 kPa to 12 MPa) can be imposed. The upper suction limit is determined by the concentration of the PEG solution, above which precipitation occurs. Delage et al. (1998) enlarged the range of suction, previously limited to 1500 kPa (Williams and Shaykewich, 1969), by using lower molecular weight PEG (1500 and 4000) and thus increases the concentration above which precipitations occurs.
- These relatively high suctions can be obtained without particular safety devices, which are needed when high air or high water pressure is imposed (as in the case of the axis translation technique).

The main drawbacks are mainly related to the semi-permeable membranes:

- The fragility of the semi-permeable membrane, which is sensitive to bacterial attacks and has a low mechanical resistance to shearing, requires specific care in the experimental procedure in order to avoid the membrane spoiling.
- During the wetting path, the effectiveness of the semi-permeable membrane may be imperfect. Indeed, during this stage, PEG molecules can "accidentally" traverse the membrane (Delage et al., 2001). This leads to inaccurate results. Furthermore, the retention capacity for PEG molecules of most of the semi-permeable membranes is defined as greater than 90% (not 100 %). Actually, if pore water is contaminated by PEG molecules, the osmotic pressure is lower than the theoretical configuration based on pure pore water. Delage and Cui (2008) developed a device to suppress this undesirable effect by using a purifying system that eliminates the smaller PEG molecules in the solution.
- The actual molecular weight of polyethylene glycol is generally a bit lower that the prescribed molecular weight (for instance PEG 20000 is generally rated as greater than

17.000 on average, Dineen and Burland (1995)). This also contributes to a decrease in the efficiency of the semi-permeable membrane.

- Taibi et al. (2005) noticed that the membrane is very sensitive to high temperature. They observed modifications of the visual aspects of the dialysis membrane and significant dispersion of the experimental results in tests carried out at high temperatures (60 and 80°C). This alteration of the membrane due to temperature is sorely avoidable and no calibration procedure really exists.

Relative humidity technique

The relative humidity technique (also called vapour transfer technique) is based on the control of the relative humidity of the atmosphere surrounding the sample by means of an aqueous solution of a given chemical compound (a product at various concentrations or different saturated saline solutions). According to the relative humidity of the air, water exchange occurring by vapour transfer induces a given suction at equilibrium inside the sample.

The relationship between suction at equilibrium inside the soil sample and the relative humidity of the surrounding air is given by Kelvin's law:

$$p_a - p_w = \frac{\rho_w RT}{M_w} \ln h \tag{5.1}$$

where p_a and p_w are the air and water pressures, respectively, R is the constant of perfect gases ($R = 8.3143\ J/(mol.K)$), T is the temperature in Kelvin, M_w is the molar mass of water ($M_w = 0.018\,kg/mol$), ρ_w is the bulk density of water ($\rho_w = 1000\ kg/m^3$), and h is the relative humidity. To influence the relative humidity of air surrounding the sample, saturated saline solutions are generally used. Delage et al. (1998) reported the value of relative humidity obtained with different salts. The first application to geotechnical testing was performed by Esteban and Saez (1988).

The main advantage of this technique is that there is no upper limit on the applied suction, since very high suctions can be applied using dry atmospheres. Thus, this method is very suitable for imposing suction on fine materials that need very high suction to undergo significant desaturation. However, the use of this method is limited by some major drawbacks:

- As reported by Delage et al. (1998), the relationship between the kind of saturated saline solution and the relative humidity is not precisely known. Indeed, it has been noted that the relation linking the kind of saline solutions and the generated relative humidity differs according to the various handbooks. A 1% relative uncertainty in the relative humidity h gives a 1.38 MPa absolute uncertainty for the suction. This is only acceptable for very high suction, while this method is inappropriate for imposing low suction.
- The value of relative humidity imposed by the saturated saline solution depends on temperature (Delage et al., 1998). Furthermore, Kelvin's law also involves temperature. So, during a non-isothermal test, special care must be given to control with accuracy the temperature which affects the relation between the relative humidity of the air and the suction at equilibrium (Romero et al., 2001).
- Finally, vapour exchange processes controlling suction inside the sample are very slow, which leads to very long testing periods.

5.2.2.2 *Control of temperature*

As far as temperature imposition to the soil sample is concerned, Cekerevac (2003) provides a bibliographical overview of the different ways to apply heat to the sample. He outlined three main categories: i) heating by a circulating fluid, ii) heating by internal heaters and iii) heating by lateral heaters. One of the main problems encountered with thermo-mechanical experimental devices is related to the calibration required to correct errors in the measurement due to the temperature effects on the testing apparatus. Also, a good assessment of the delay and the difference in temperature between the temperature control in the heating system and the temperature evolution in the middle of the sample is required. In particular, great attention must be paid to apply a sufficiently low thermal rating during heating or cooling in order to avoid undesired pore water pressure generation inside the sample. This undesired pore water pressure may produce an overconsolidated behaviour of the sample by decreasing the mean effective stress.

5.2.2.3 *Volume measurements*

Contrary to the saturated conditions for which specimen volume change is directly related to the volume of exchanged water, when the air phase coexists with the water phase in the pore space, both air and water exchanges contribute to the volume variation of the soil specimen. In an oedometric cell, the volume variation of the sample is directly determined by the measurement of height variations (via a dial gauge). On the contrary, in the case of triaxial or isotropic cells, the volume change measurement is usually subject to calibrations and indirect procedures. Laloui et al. (2006) (see also Geiser et al. (2000)) summarized the more utilized methods for measuring volume changes in unsaturated soil specimens during triaxial compression tests. They classified them in three different categories: i) cell liquid measurements, ii) direct air and water volume measurements and iii) direct measurements of the sample. Since the device used in the experimental program was an oedometric cell (Section 5.2.3), the volume variation of the soil sample was directly measured by height variation through a dial gauge. Thus, a complete description of the existing techniques to measure the sample volume variation is out of the present scope. The reader may refer to Delage (2002), Laloui et al. (2006) or Hoyos et al. (2008) for a thorough treatment of the subject.

5.2.3 The developed THM oedometric cell

A new THM oedometric cell has been developed to carry out standard oedometric compression tests by controlling the temperature and suction of the sample and to determine water retention characteristics under different mechanical and thermal states. The initial concept of the cell was developed by Blaisonneau and Laloui (2002). This cell uses a cylindrical sample with a diameter of 80 mm and a height of 23 mm. Figure 5.1 displays the general scheme of this THM oedometric cell. The temperature T, the applied vertical pressure σ_v, the pore air pressure p_a and the pore water pressure p_w can be controlled using four independent devices. The output variables, water volume exchanges and vertical displacement are simultaneously measured. Based on the specificities of each suction imposition technique, summarized in Section 5.2.2.1, the axis translation technique has been chosen as the most suitable method to control the soil sample suction in our specific case. Figure 5.2 shows a picture of the cell structure with the different tubing connections.

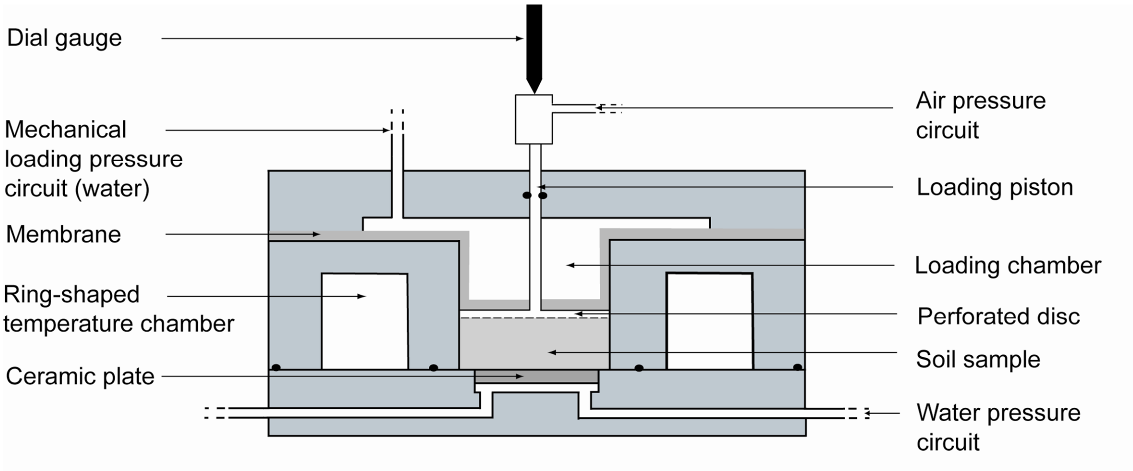

Figure 5.1 : General scheme of the THM oedometric cell.

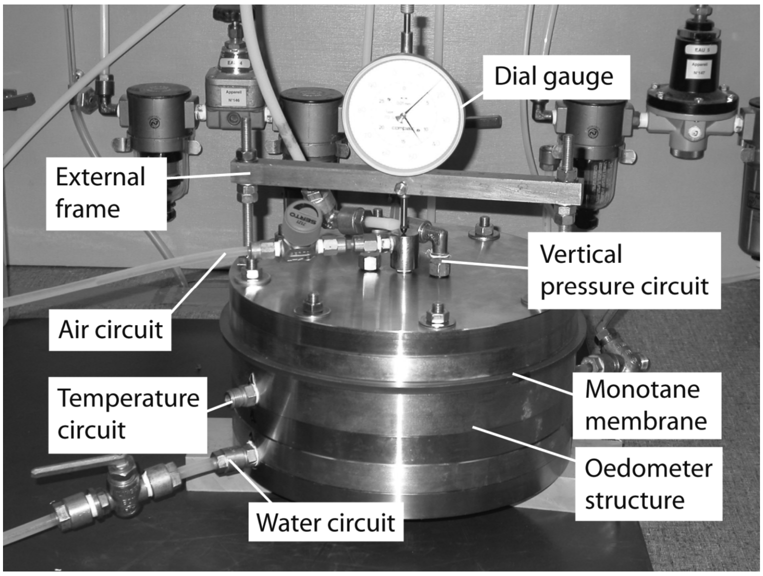

Figure 5.2 : Picture of the oedometric cell.

5.2.3.1 *Description of the oedometer*

The heating device consists of a ring-shaped chamber that surrounds the soil sample and is filled with circulating water heated to the required temperature by a cryostat, the DC10-K20 HAAKE. In order to reduce the ambient room temperature influence, the whole oedometer is located in an insulated box.

The vertical pressure is applied by a water controller in a loading chamber atop the sample. This pressure is transmitted to the sample via a water- and air-proof membrane made of a stretchable material (monothane 65A). This method for applying the vertical pressure ensures that the pressure is applied uniformly to the top of the soil sample. The pore air pressure is applied uniformly by an air controller via a loading piston that ends in a perforated disc that is in contact with the top surface of the sample, while the pore water pressure is controlled through a 500 kPa air-entry value ceramic disk (HAED) beneath the sample. These three controllers enable imposition of and/or measurement of pressures and/or volume changes.

The HAED was fixed to the periphery of the metallic oedometer with an epoxy resin, which ensures not only impermeability, but also permits differential dilatation between the ceramic disc and the oedometer with increasing temperature (no fine cracks appear upon heating).

Finally, the vertical displacement is measured with a dial gauge in contact with the loading piston that is fixed on an external frame. A computer continually stores the applied pressures, the measured volume exchanges and the vertical displacements, as measured by the dial gauge, while the temperature imposed by the cryostat is manually noted. All of these auxiliary devices are schematically represented in Figure 5.3.

In order to keep a constant temperature in the air and water controller chambers, thereby avoiding volume measurement variations due to temperature, a cooling chamber with a water bath at 20°C is added to the air and water circuit before the controller cells. To avoid pore water evaporation at high temperatures, a constant back-pressure of 80 kPa is maintained by the water controller and a water box is connected to the air pressure line to humidify the dried air before it reaches the sample (Figure 5.3).

5.2.3.2 *Calibration of the oedometer*

When performing THM experimental tests, the applied conditions (vertical stress, temperature, pore air and pore water pressures) and the measured data (exchanged fluid volume and vertical displacement) must be corrected in order to assess the real response of the soil sample, deducting the undesired disturbance of the measurements. In so doing, careful calibrations of the equipment must be made, including assessments of: i) the effect of friction between the membrane and the cell walls, ii) the cells' deformability under thermal and mechanical loadings, iii) the delay between the thermal variation in the heating system and the real temperature change within the sample, iv) the influence of thermal water dilatation in tubing on the water volume exchange measurements and v) the volume of water diffusing through the ceramic disk. The results of those calibrations are detailed in the following sections.

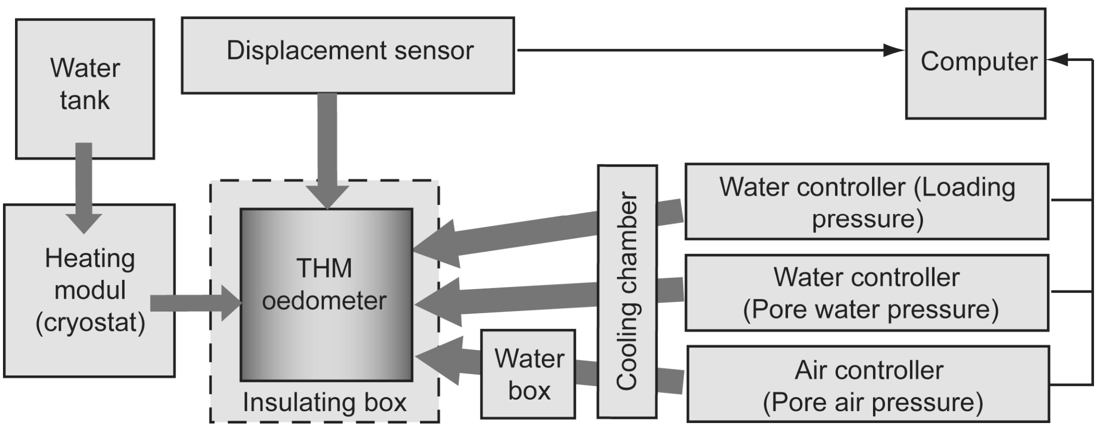

Figure 5.3: Schematic of oedometric cell environment and the auxiliary devices.

Effect of membrane friction

The vertical pressure transferred by the membrane to the sample differs from the pressure applied by the pressure controller in the loading chamber because of the friction occurring between this membrane and the oedometer wall. This difference has been quantified with respect to the applied vertical pressure during a mechanical loading and unloading by measuring the pressure of water placed in the sample chamber instead of soil. This calibration has been carried out at two different temperatures (20°C and 80°C). Figure 5.4 depicts the relationship between applied vertical pressure and the pressure measured inside the sample chamber. No difference has been observed between the loading and the unloading phases. The best-fit curves between the applied and measured vertical pressure are linear expressions with the following coefficient:

$$\begin{cases} P_{meas} = 0.934\ P_{appl} & \text{at } 20°\text{C} \\ P_{meas} = 0.952\ P_{appl} & \text{at } 80°\text{C} \end{cases} \tag{5.2}$$

where P_{appl} is the applied vertical pressure in the loading chamber and P_{meas} is the pressure measured in the sample chamber.

Deformability of the cell structure under mechanical loading

During mechanical loading, the cell structure is subject to deformation, which modifies the measurement of the vertical displacement. This effect must be subtracted from the total displacement recorded by the dial gauge in order to get the real deformation of the soil sample. This effect was quantified using an undeformable steel disc in the sample chamber. A loading-unloading cycle was performed on this steel disc at two temperatures (20°C and 80°C). Considering the disc undeformable, all the measured vertical displacements can be attributed to the deformation of the cell structure itself. Figure 5.5 shows the evolution of measured vertical displacement with respect to vertical load during this calibration process. The best fits are obtained with the following equations:

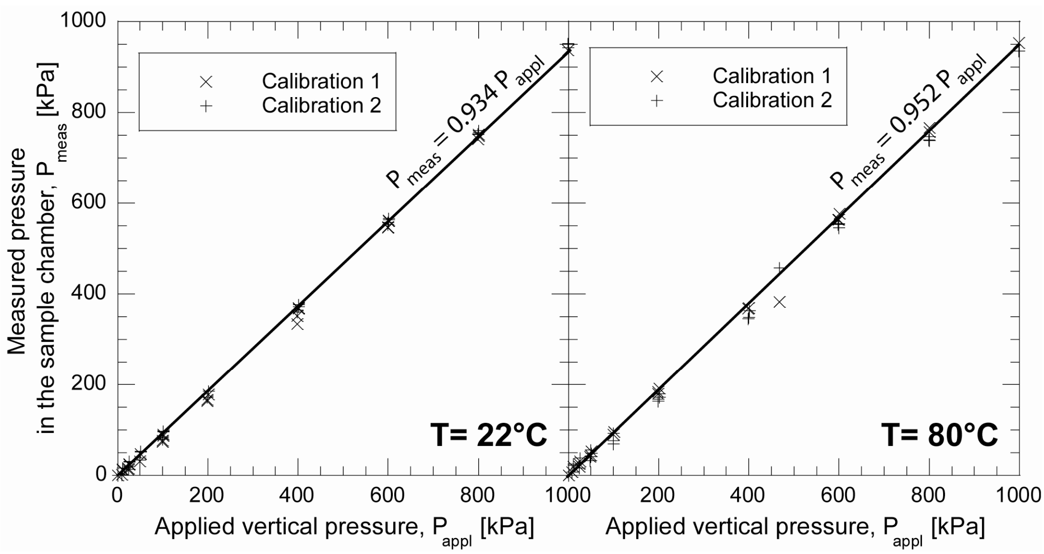

Figure 5.4: Calibration of the friction effect between the membrane and the oedometer wall.

$$\begin{cases} \Delta h_{cell} = 0.13 - 0.111 \ \log P_{appl} & \text{T=22°C, loading} \\ \Delta h_{cell} = 0.041 - 0.083 \ \log P_{appl} & \text{T=22°C, unloading} \\ \Delta h_{cell} = 0.203 - 0.166 \ \log P_{appl} & \text{T=80°C, loading} \\ \Delta h_{cell} = 0.111 - 0.14 \ \log P_{appl} & \text{T=80°C, unloading} \end{cases} \quad (5.3)$$

where Δh_{cell} is the measured vertical displacement due to the deformation of the cell. The dimensions of Δh_{cell} and P_{appl} are [mm] and [kPa], respectively.

Deformability of the cell structure under thermal loading

The influence of the undesired thermal effects on the measured soil sample deformation has also been investigated. Two thermal effects must be considered. On the one hand, (i) the thermal deformation of the cell structure affects the measurement of the vertical displacement. On the other hand, (ii) the thermal deformation of the oedometer ring may induce a certain loss of oedometric conditions by producing a small radial strain of the soil sample.

(i) The thermal deformation of the cell structure has been evaluated by measuring the vertical displacement of the piston during a thermal cycle from 20°C to 80°C in steps of 20°C with an inox sample in the sample chamber. The thermal dilatation coefficient of this inox sample being known, the measurement of the vertical displacement during the temperature cycle makes it possible to deduce the effect of the thermal deformation of the cell structure. This effect must be deducted from the total measurement of the vertical displacement in order to get the real deformation of the soil sample. Figure 5.6 shows the measured vertical displacement, distinguishing the effects of the inox sample dilatation and of the real thermal deformation of the cell structure.

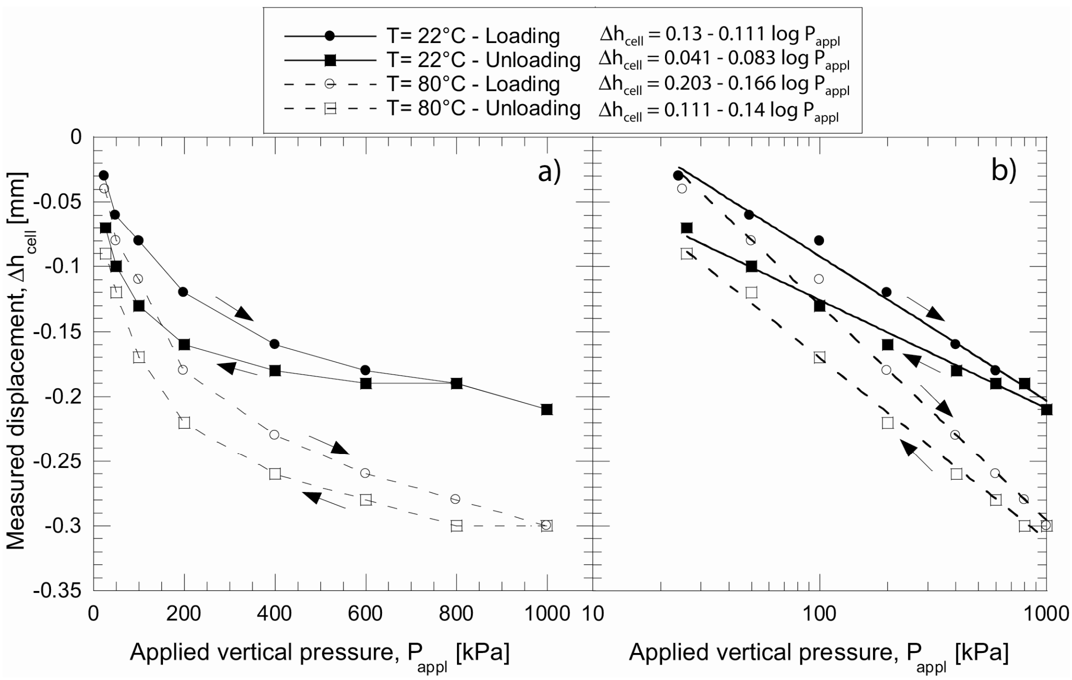

Figure 5.5: Calibration of the vertical displacement due to the deformability of the cell structure. (a) Measured displacement during loading-unloading on an undeformable steel disc; (b) best fitting in a logarithmic scale.

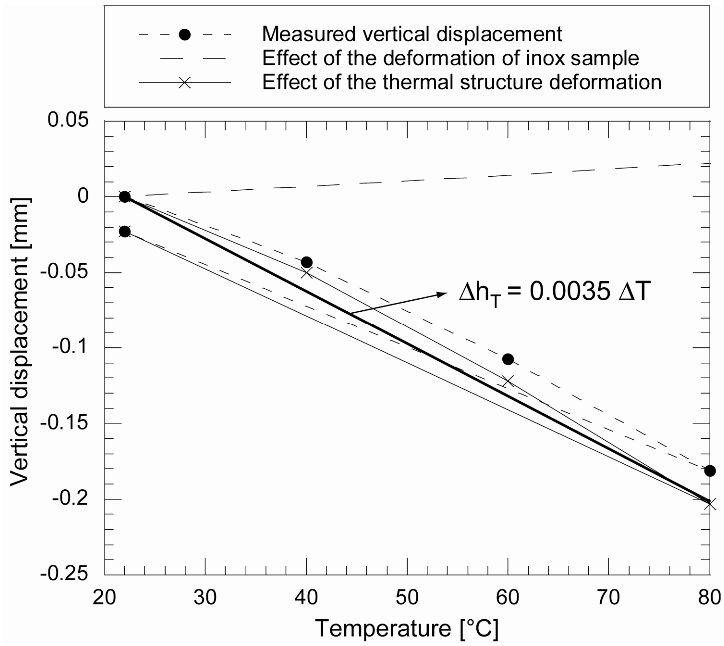

Figure 5.6: Effect of the thermal deformation of the cell structure on the measured vertical displacement.

The thermal deformation of the cell structure, Δh_T, in [mm], can be approximated according to the following linear equation:

$$\Delta h_T = 0.0035\ \Delta T \tag{5.4}$$

(ii) The thermal deformation of the oedometer ring has been experimentally quantified. To do this, several strain gauges were fixed on the oedometer structure in the circumferential, axial and radial directions while two thermal cycles were performed from 22°C to 80°C. Figure 5.7 shows the thermal strain evolution with respect to the applied temperature. The obtained results correspond to the theoretical thermal dilatation of the steel (1.65 10^{-5} $^{o}C^{-1}$). Romero (1999) proposes an equation to determine the thermal effect of oedometer ring deformation on the void ratio:

$$\frac{\Delta e}{1+e_0} = \frac{(2\bar{\beta}'_a - \bar{\beta}'_s)\Delta T}{1+\bar{\beta}'_s \Delta T} \tag{5.5}$$

where $\bar{\beta}'_s$ is the linear thermal expansion coefficient of the tested soil and $\bar{\beta}'_a$ is the linear thermal expansion coefficient of the ring. Based on the assumption of a linear thermal dilatation coefficient of soil, $\bar{\beta}'_s = 1\ 10^{-5}$, the effect of oedometer ring dilatation on the void ratio change is evaluated to be $\Delta e / (1+e_0) = 0.0013$ for a temperature variation of 60°C. This shows that the thermal expansion or contraction of the oedometric ring is partially compensated by the immediate response of the thermal strain of the soil particles. As a consequence, the thermal deformation of the cell does not significantly affect the oedometric conditions.

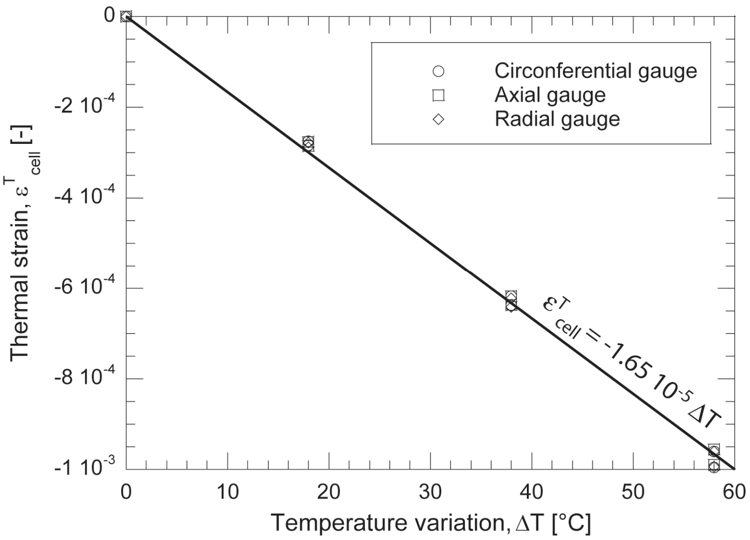

Figure 5.7: Thermal strain of the cell structure measured with strain gauges along two thermal cycles.

Delay in the heating process

The delay between the thermal variation in the heating system and the real temperature change in the middle of the sample has been quantified by performing a thermal cycle from 20°C to 80°C in steps of 20°C. A thermo-couple has been introduced into the middle of a soil sample made of the sandy silt used in the experimental program (Section 5.3.2). The results demonstrate a delay of about 80 minutes in reaching equilibrium between the heating system and the sample temperatures (Figure 5.8). At equilibrium, there is no significant difference between the measured temperatures in the heating system and the sample, which proves the efficiency of the isolating system. Thanks to the circulating water, thermal equilibrium is always maintained between the heating system and the ring-shaped chamber. Thus, the delay in the sample temperature evolution is due to the thermal diffusion process in the steel cell structure and in the soil sample.

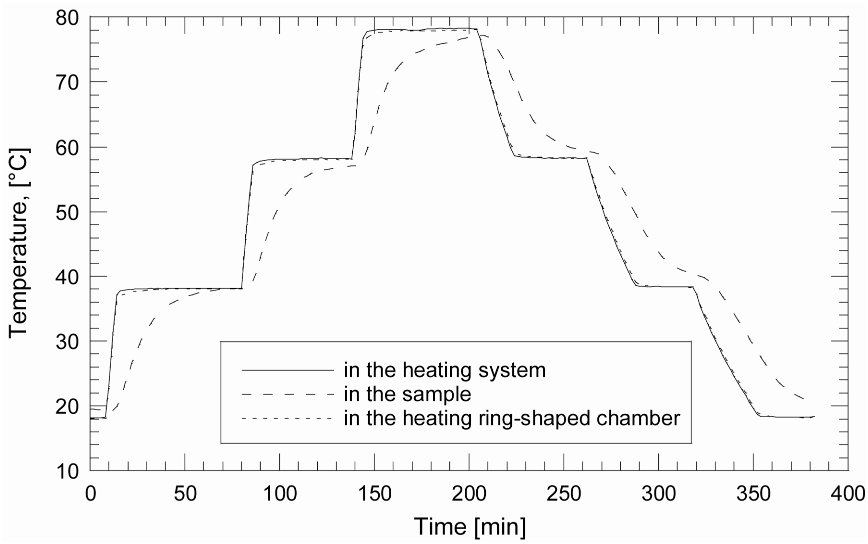

Figure 5.8: Evolution of temperature in the middle of the soil sample in comparison with the temperature in the heating system.

Effect of water thermal dilatation in tubing

Temperature variation of the oedometer induces a thermal volume change in all of the constituents. In particular, the drainage system is strongly affected by temperature variation. The volume of the ceramic disk, the drainage line and the water filling them is modified by a temperature change, which makes the measurement of the real water expelled or soaked up by the sample spurious, if no calibrations are performed. In order to calculate the real exchanged volume of water, it is necessary to quantify this undesired volume change of the drainage system during non-isothermal paths. To this end, an inox sample was placed in the sample chamber, a water back-pressure of 80 kPa was applied and a thermal cycle was performed. Figure 5.9 shows the water volume soaked up by the water controller connected to the water drainage line during this thermal cycle. In order to determine the water retention capacity of the soil sample throughout the tests, this water volume must be subtracted from the total volume variation measured by the water controller.

This volume change of the drainage system during a thermal cycle from 22°C to 80°C $\Delta V_{w,1}^{T}$ can be evaluated according to the following parabolic equations:

$$\begin{cases} \Delta V_{w,1}^{T} = -74.63 - 0.0126\ T + 0.1368\ T^{2} & \text{Heating phase} \\ \Delta V_{w,1}^{T} = -213.43 + 3.4975\ T + 0.1132\ T^{2} & \text{Cooling phase} \end{cases} \tag{5.6}$$

This non-linear expression is partially due to the temperature-dependence of the thermal expansion coefficient of water (Equation (5.8)). In addition to this volume change in the drainage system, the water in the pore space of the soil sample is also subject to volume variation due to temperature. This volume variation also contributes to the total volume measurement of the water controller. This effect must be deducted in order to get the real volume of water expelled or soaked up by the soil sample. It can be determined according to the following equation:

$$\Delta V_{w,2}^{T} = \beta_w'\ V_{voids}\ S_r \left(T - T_0\right) \tag{5.7}$$

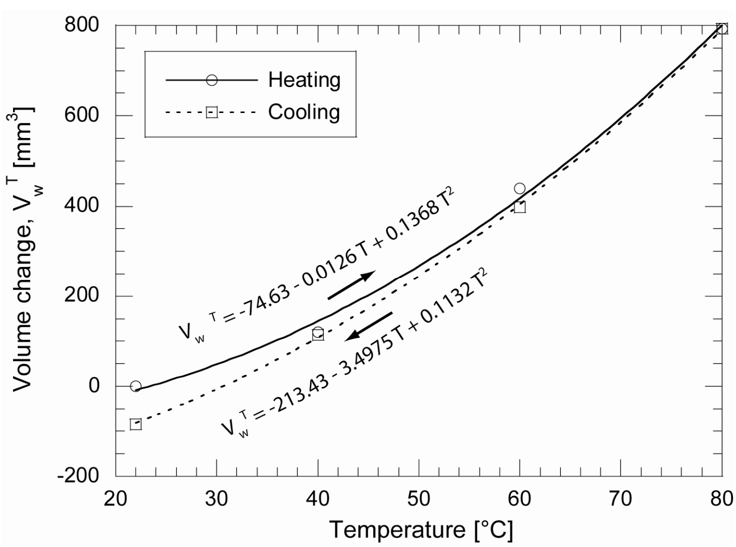

Figure 5.9: Volume change of drainage system during a thermal cycle (22°C-80°C-22°C).

where V_{voids} is the volume of void in the soil sample, S_r is the degree of saturation of the sample and β'_w is the volumetric thermal dilatation coefficient of water. The degree of saturation of the sample being unknown (it depends on $\Delta V^T_{w,2}$), this equation needs to be solved using an iterative process.

The volumetric thermal dilatation coefficient of water, β'_w, has been determined using an expression based on temperature and pore water pressure (Baldi et al., 1988).

$$\beta'_w = \alpha_0 + (\alpha_1 + \beta_1 T)\ln m\, p_w + (\alpha_2 + \beta_2 T)(\ln m\, p_w)^2 \tag{5.8}$$

where $\alpha_0 = 4.5\ 10^{-4}\ °C^{-1}$, $\alpha_1 = 9.15\ 10^{-5}\ °C^{-1}$, $\alpha_2 = 6.38\ 10^{-6}\ °C^{-1}$, $\beta_1 = -1.2\ 10^{-6}\ °C^{-2}$, $\beta_2 = -5.76\ 10^{-8}\ °C^{-2}$, and $m = 15\ MPa^{-1}$.

Air diffusion through ceramic disks

Even if a high air-entry value ceramic disk (HAED) is designed to prevent the passage of free air below a specific bubbling pressure, some air diffuses through the HAED, even at air pressures below the rated capacity (Romero, 1999; Padilla et al., 2006). Diffused air has a tendency to accumulate underneath the HAED, resulting in an error in the specimen water volume measurement. In addition to this air diffusion process through the HAED, soil water evaporation through the top coarse porous stone connected to the air pressure line is another major effect that must be considered in order to get the real water volume exchanged by the soil sample.

The volume of diffused air accumulated beneath the HAED is recorded as water expelled from the sample while evaporated water volume is recorded as water taken up by the sample. Depending on the suction values applied, one or the other could prevail, or else they could cancel each other out (Airo Farulla and Ferrari, 2005).

Air diffusion through the HAED is the consequence of three successive processes. First, in the soil sample air is submitted to a pressure imposed by the air controller. Under this pressure, a given amount of air is dissolved into the soil pore water according to Henry's law. Second, this dissolved air is diffused through the pore water in the ceramic disk according to Fick's law. Finally, below the HAED, the pressure of fluid decreases, which leads to a certain amount of air being desorbed from the water and forming bubbles in the drainage line, again according to Henry's law. Water evaporation is regulated by the vapour pressure gradient between pore voids and air overlying the sample. The water box connected to the air pressure line, aimed at humidifying the dried air before exposing it to the sample, enables one to limit the evaporation process, but not to completely avoid it. Romero (1999) discussed in detail the physical aspects of the phenomenon and suggested a procedure to detect and correct its effects on the sample water volume change measurements.

Air diffusion through the HAED combined with the evaporation of water through the top coarse porous stone are processes that prevent equilibrium in the water volume exchange recorded by the water controller. As a consequence, when soil reaches equilibrium between the applied suction, the degree of saturation, the applied stress and the void ratio of the soil, a constant rate of water volume exchange is recorded by the water controller. This rate corresponds to the difference between water evaporation through the top porous stone and air diffusion through the

HAED. The calibration of this air exchange, depending on applied suction, has been obtained from this measured rate of water volume exchange at equilibrium. Figure 5.10 reports this rate of water volume exchange at equilibrium for the four tests performed under unsaturated conditions. The air diffusion through the HAED being higher than the water evaporation, the water controller records that water is continuously expelled from the sample. The temperature of the test does not seem to affect the balance between the volume of diffused and evaporated water. The volume of air diffused through the ceramic disc certainly increases with temperature. Nevertheless, this effect is probably compensated for by an increase of water evaporation. Based on Figure 5.10, the following expression has been used for the calibration:

$$\Delta V_{w \to a} = 1.3\ 10^{-3} \left(p_a - p_w \right) \quad [\mathrm{mm^3/min}] \tag{5.9}$$

where p_a and p_w are the pore air and pore water pressures. The applied suction is the difference between these two pressures.

An example of water volume exchange recorded by the water controller in parallel with the applied vertical stress and the measured vertical displacement is reported in Figure 5.11. Those data are the uncorrected measurements. Under saturated conditions (the first part of the test), the contraction of the sample due to the mechanical loading expels a high volume of water from the specimen. Also, during the application of the suction at 300 kPa, the soil specimen is desaturated and water flows out from the soil sample. Under such suction, the soil is very dry ($S_r \approx 0.2$, see Figure 5.14), so the subsequent mechanical loading does not produce a water flow through the water drainage line. During that phase, all the recorded water volume change is due to the balance between water evaporation and air diffusion through the HAED. Figure 5.11b focuses on the water volume exchange during that mechanical loading. Whatever the mechanical loading, the rate of water volume exchange recorded by the water controller remains approximately constant. This indicates that the contraction of the sample, recorded by the dial gauge, does not produce any change in the water flow. The slope of the curve, $\Delta V_w - t$ in Figure 5.11b, corresponds to the balance between the rates of water evaporation and air diffusion through the HAED at that suction.

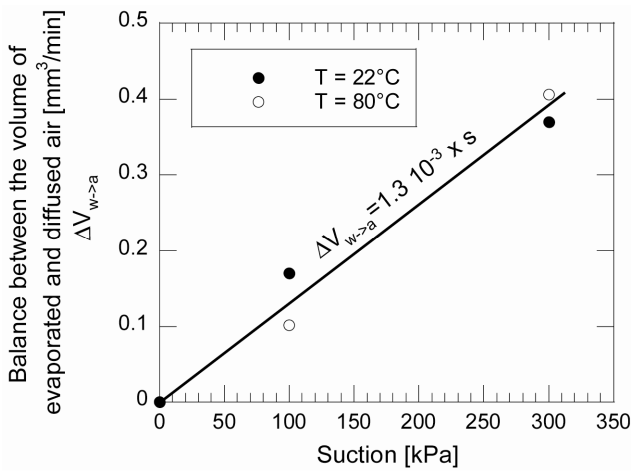

Figure 5.10: Balance between volumes of evaporated water through the top coarse porous disc and diffused air through the ceramic disc with respect to the applied suction.

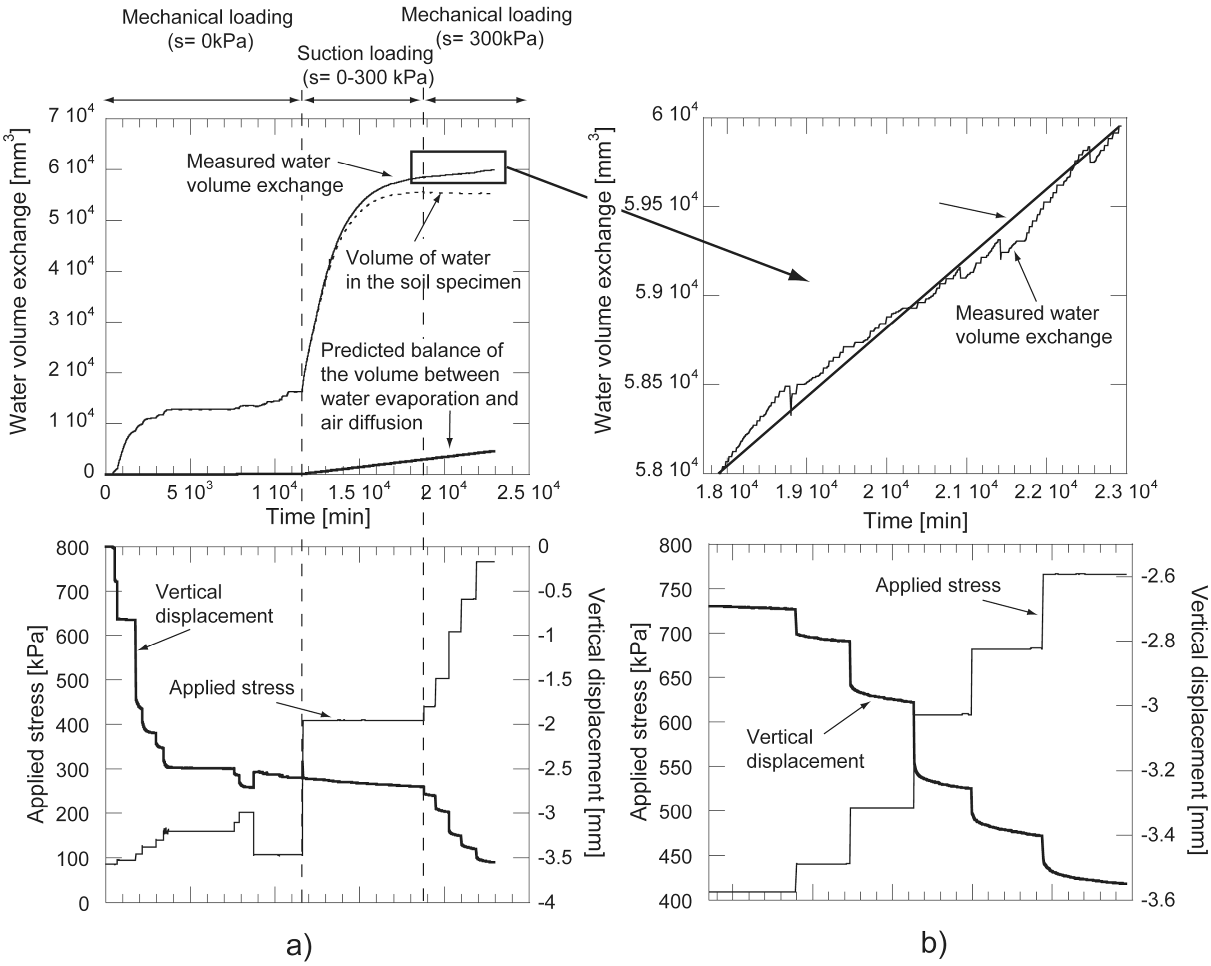

Figure 5.11 : Evolution of water volume exchange in parallel with vertical displacement and applied stress (uncorrected measurements). (a) The entire 0-T80S300 test; (b) Focus on the mechanical loading under unsaturated condition (s=300 kPa).

5.2.3.3 *Saturation of the ceramic disk*

The 500 kPa air-entry value ceramic disc must be fully saturated with water in order to be efficient. A previously established procedure was carried out to saturate the stone before each test. That procedure consists of six pressurized cycles applied with an additional water controller through the air circuit. The water flowing across the ceramic stone is recorded by the water controller connected to the water drainage line. Each cycle is 60 minutes of a 400 kPa vertical pressure under drained conditions, followed by 10 minutes of a 400 kPa vertical pressure under undrained conditions (Geiser, 1999). The water volume exchange is measured during the drained conditions. After two or three cycles, the permeability of the ceramic stone reaches its saturated permeability of 3 10^{-10} m/s (Ubals Picanyol, 2006).

A film of water is left over the ceramic disc when no test is being performed. In this way, the ceramic stone saturation is ensured, preventing the possibility of its desaturation due to air contact.

5.3 Experimental program

5.3.1 Introduction

Aiming to study the effect of the thermo-hydro-mechanical conditions on the compressibility indices and on the preconsolidation stress of soil, an experimental program has been designed using the developed oedometric cell. As discussed in Chapter 3 and Chapter 4, it is generally accepted that the preconsolidation pressure decreases with increasing temperature and increases with increasing suction. However, the combined effect of temperature and suction on the compressibility properties of soils has rarely been investigated in a systematic way. This experimental program aims to fill this gap in the experimental data pertaining to the thermo-hydro-mechanical behaviour of fine-grained soils.

After presenting the specific material characteristics, the thermo-hydro-mechanical paths and the main results are given. These experimental data are compared with the results obtained in a parallel set of experiments performed by a research group at Montpellier II University. Finally, those experimental evidences are interpreted, all together, in light of the THM constitutive framework. In particular, the effects of suction and temperature on the compressibility and the preconsolidation pressure of the soil are addressed.

5.3.2 Preparation and characteristics of the material

The soil examined is a sandy silt (USCS classification: CL-ML) from the region of Sion (Switzerland). This soil has already been the subject of many studies (Laloui et al., 1997; Geiser et al., 1998; Geiser et al., 2006). Its index properties are: $w_L = 25.4\%$, $w_P = 16.7\%$, $I_P = 8.7\%$. The grain-size distribution curve is presented in Figure 5.12. The clayey fraction represents 8%, the silty one about 72% and the sandy one about 20%.

Special care was taken in the sample preparation to ensure the reproducibility of the initial state. The sample preparation procedure consisted of mixing a known mass of dry soil with de-aired and demineralised water to an initial water content of $w = 1.5w_L$ (i.e. $w = 38\%$). This water-content value was assumed to be large enough to produce a slurry with no internal fabric. To remove the air bubbles trapped in the slurry, the soil was vibrated. The initial void ratio, e_0, at the slurry state varied between 0.8 and 1. This preparation procedure is similar to that described in a previous experimental study performed on this soil and was elaborated upon by Geiser (1999).

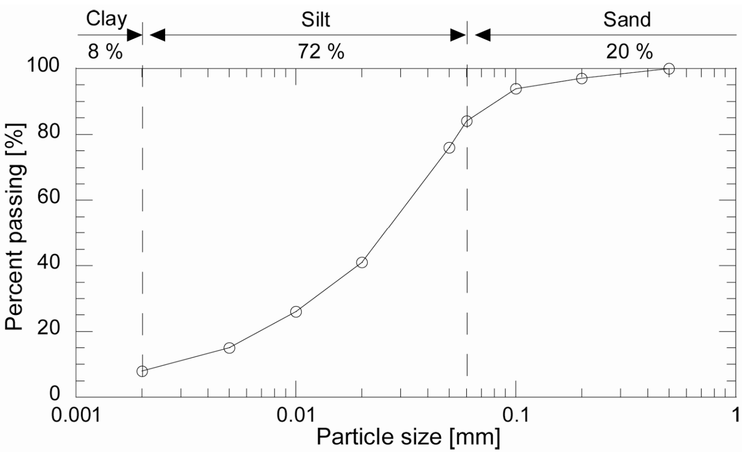

Figure 5.12: Grain size distribution of Sion silt.

5.3.3 Experimental layout

Figure 5.13 presents the different paths of the tests with numbers corresponding to the different steps detailed in the following. The tests start from a saturated state corresponding to the slurry obtained after the preparation process ($s = 0$ kPa, $w = 38\%$, $0.8 < e < 1$) [1]. From that state, a mechanical loading [2] (σ'_{vc0}) - unloading [3] (σ'_{v0}) cycle is applied to establish the vertical preconsolidation stress for the sample ($\sigma'_{vc0} \approx 100$ kPa). Then, the thermal loading is carried out to reach the desired temperature T_i through several steps long enough to avoid excess pore water pressure (e.g. 10°C every 3 hours) [4]. Afterwards, the sample is dried until the required suction value s_i [5] is reached. The test is ended with a conventional mechanical consolidation [6] which enables determination of the vertical preconsolidation stress and the compressibility indices for the couples (s_i, T_i). These oedometric tests were carried out for 3 suction values (0, 100 and 300 kPa) and 2 temperatures (22 and 80°C), with one duplication (0 kPa and 22°C), for a total of 7 tests.

All these tests are reported in Table 5.1. For each of these, the following are specified: the established preconsolidation stress (σ'_{vc0}), the temperature, the suction, the void ratio (e_0) and the mechanical stress (σ'_{v0}) corresponding to the state of the specimen just before the mechanical consolidation.

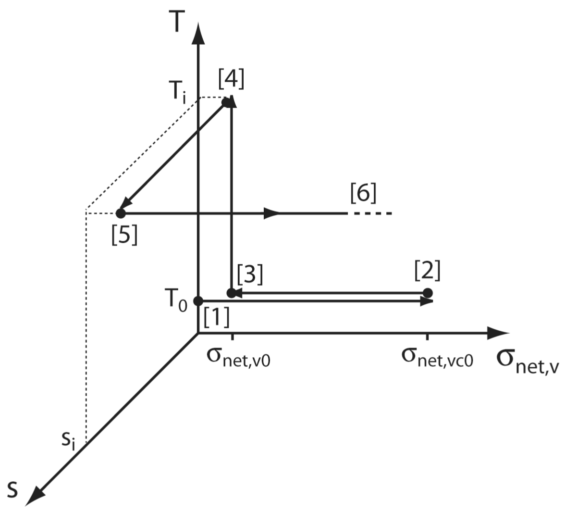

Figure 5.13: The different steps of the oedometric tests (T: temperature, s: suction, $\sigma_{net,v}$: vertical net stress).

Tests	σ'_{vc0} [kPa]	T [°C]	s [kPa]	e_0 [-]	σ'_{v0} [kPa]
O-T22S0-1	250	22	0	0.71	15
O-T22S0-2	134	22	0	0.85	1
O-T80S0	99	80	0	0.90	11
O-T22S100	100	22	100	0,66	71
O-T80S100	91	80	100	0.99	71
O-T22S300	100	22	300	0.74	121
O-T80S300	100	80	300	0.74	114

Table 5.1: THM tests and the parameters defining the state, just before the last mechanical consolidation.

5.3.4 Experimental results[1]

First, in order to express the experimental results in term of the generalized effective stresses (Section 4.2.2.2), the water retention information (e.g. the degree of saturation with respect to suction) of the Sion silt is needed. The water retention curve of the material has been determined from three different sources. First, independent of this experimental program, Peron et al. (2007) established, in desorption, the relationship between the degree of saturation and the suction of the Sion silt with a pressure plate apparatus (Figure 5.14). That measurement was made at ambient temperature and an initial void ratio of 0.75, which is quite close to the void ratio achieved in the present study's compression tests. This curve shows an air-entry suction of 50 kPa. Second, the degree of saturation has been extracted from the present oedometric tests by monitoring the water volume exchanges. Finally, similar tests performed under isotropic conditions at University Montpellier II (France) contributed additional points to the retention curve. In spite of careful calibrations, it has been observed that the water exchange volume measured in the oedometric and isotropic cells is not as accurate as that measured using the pressure plate apparatus test. Thus, with this method, an absolute error of +/- 5% in the degree of saturation value can be expected. Nevertheless, the degree of saturation versus suction relationships obtained from the oedometric and isotropic tests are also reported in Figure 5.14. In spite of these uncertainties, the results are quite close to the curve obtained by Peron et al. (2007).

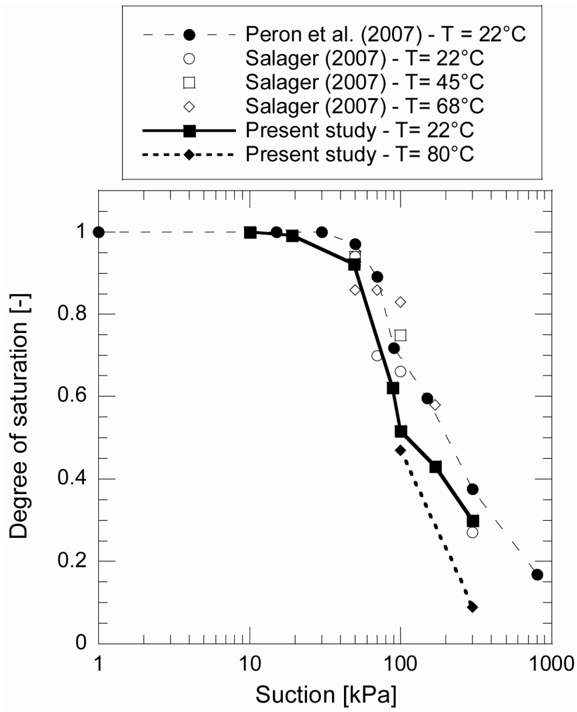

Figure 5.14: Retention curve determined for the desorption of Sion silt. Comparison between data obtained from the present study (oedometric cell), from Peron et al. (2007) (pressure plate apparatus) and from the experiment performed at University Montpellier II (isotropic cell).

[1] Salager S., François B., El Youssoufi M.S., Laloui L. and Saix C. (2008). Experimental investigations on temperature and suction effects on compressibility and pre-consolidation pressure of a sandy silt. *Soils and Foundations* 48(4): 453-466.

It is generally known that the retention curve depends slightly on temperature (Salager et al., 2006; Romero et al., 2001) and also on dry density (an important effect for high degrees of saturation but slight for low degrees of saturation) (Gallipoli et al., 2003a; Salager et al. 2007b). In this case, the present study seems to show a decrease of the retention capability with an increase in temperature. However, this trend is not confirmed by the tests performed in Salager (2007), where the points at 22°C, 45°C and 68°C are close to each other. It has been concluded that, for this soil and for the considered temperature range, there is no predominant thermal effect on the obtained retention curve. These effects may exist, but appear to be lower than the accuracy of the degree-of-saturation measurement. Moreover, the retention hysteresis usually observed under the drying-wetting cycle is not considered in the present case because only monotonic drying paths were performed. Because of all these considerations, the degree of saturation will be determined through its univocal relationship with suction using the curve established by Peron et al. (2007). Therefore, the three imposed suctions of the experimental program (50, 100 and 300 kPa) correspond to three particular degrees of saturation (0.96, 0.7 and 0.37, respectively).

The experimental results of the last compression paths at different temperature and suction levels are reported as both net and generalized effective stress references in Figure 5.15 and Figure 5.16, respectively. It is of particular interest to display compression curves as net stresses because they represent the data directly obtained from the experiments, although the results will not be interpreted using this reference. By considering the retention curve, the results obtained as the net stress reference (Figure 5.15) were transformed into the generalised effective stress reference using Equation (4.7), with $\chi = S_r$ (Figure 5.16). Consequently, the curves in the generalized effective stress reference are shifted forward by ($S_r \times s$) with respect to the results in the net stress reference. Because of the logarithmic scale of the abscissa, this shift is not simply a translation of the curve to the right, but it also changes the shape and tends to flatten it.

After comparisons of the curves in the generalized effective stress plane, they appear to exhibit normally consolidated lines that move forward with decreasing temperature and/or increasing suction. This will be analysed in the next section through quantification of the compressibility indices and the evolution of the vertical preconsolidation stress with respect to temperature and suction levels.

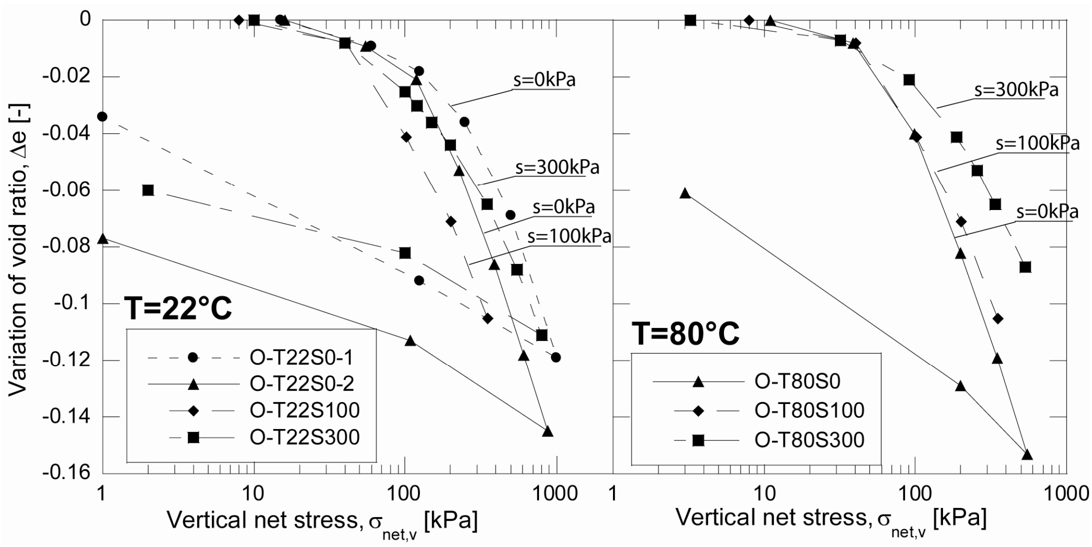

Figure 5.15: Oedometric compression paths at different temperature and suction levels, reported as net stress.

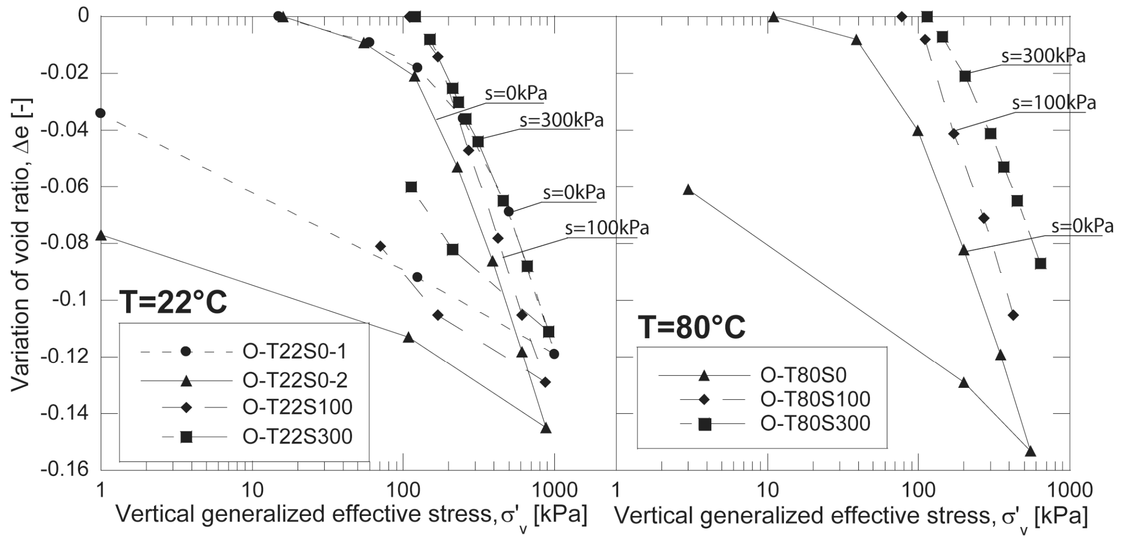

Figure 5.16: Oedometric compression paths at different temperature and suction levels, reported as generalized effective stress.

5.3.5 Analysis of the results

In this section, the effect of temperature and suction on the evolution of the compressibility indices and of the vertical preconsolidation stress (σ'_{vc}) are assessed. For all the tests, these parameters have been determined using the following method: i) the swelling index κ' is calculated from the elastic part of the loading path starting from the first point of mechanical loading. The unloading path is not available in all of the tests. However, when it is possible, κ' is also determined from the unloading elastic path. In this case, it is noted as κ'_{un}. In Figure 5.17, only the unloading modulus is reported. ii) Because all the tests are not performed using the same final mechanical state, the compression index λ' is measured in a given effective stress range, between 200 and 400 kPa. iii) Using these two results, the vertical preconsolidation stress, σ'_{vc}, and its corresponding void ratio, e_c, are determined by calculating the intersection of the swelling line (line of slope κ' and passing through the first points of mechanical loading) and the compression line (line of slope λ' and passing through the last points of mechanical loading).

In agreement with the hardening process, the yield limit changes with its void ratio. As a consequence, to compare the initial vertical preconsolidation stress applied to the soil, $\sigma_c^{e_{c0}}(T_0, s_0)$, corresponding to a void ratio e_{c0}, to the vertical preconsolidation stress determined after temperature and suction loadings, $\sigma_c^{e_c}(T_i, s_i)$, corresponding to a void ratio e_c, it is necessary to transpose these results to the equivalent void ratio. The correction, given by Atkinson and Bransby (1978), can be written as:

$$\sigma_c^{e_c}(T_0, s_0) = \sigma_c^{e_{c0}}(T_0, s_0)\exp\left(\frac{e_c - e_{c_0}}{\lambda'}\right) \tag{5.10}$$

Then, in order to estimate the temperature and suction effects on the vertical preconsolidation stress, the ratio $\sigma_c^{e_c}(T_i, s_i)/\sigma_c^{e_{c0}}(T_0, s_0)$ is used. To simplify the notation, this ratio, in terms of generalized effective stress, is noted as $\sigma'_{vc}/\sigma'_{vc0}$.

Table 5.2 reports the κ', κ'_{un}, λ' and σ'_{vc} parameters for all of the THM compression tests.

Figure 5.17 reports the compressibility indices (κ'_{un} and λ') of each compression test with respect to temperature (left graph) and suction (right graph). In general, this set of results does not exhibit a clear effect of temperature on the compressibility of the soils, at least for the range of temperatures considered in this experimental program. Concerning the suction effect, this variable seems to modify the compressibility indices even if, at this stage, a clear trend cannot be deduced from the few experimental results. This point will be further investigated in the next section where the results will be completed with additional experimental studies.

Figure 5.18 underlines, respectively, the effects of temperature (left graph) and suction (right graph) on the vertical preconsolidation stress. This yield limit clearly depends on the temperature and suction levels applied to the soil. The yield surface tends to shrink when the temperature increases, while it expands when the suction increases. In light of these experimental results, it is not easy to extract a quantitative expression to characterize the preconsolidation pressure evolution with respect to temperature and suction. This interpretation will be completed with the additional experimental results in the next section.

Tests	σ'_{vc} [kPa]	$\sigma'_{vc}/\sigma'_{vc0}$ [-]	κ' [-]	κ'_{un} [-]	λ' [-]
O-T22S0-1	251	1	0.012	0.012	0.048
O-T22S0-2	134	1	0.010	0.01	0.061
O-T80S0	76	0.76	0.018	0.017	0.066
O-T22S100	93	1.02	0.024	0.019	0.071
O-T80S100	99	0.99	0.008	0.019	0.071
O-T22S300	145	1.45	0.007	-	0.051
O-T80S300	120	1.2	0.005	0.01	0.054

Table 5.2: Preconsolidation pressure and compressibility indices obtained for the different THM tests.

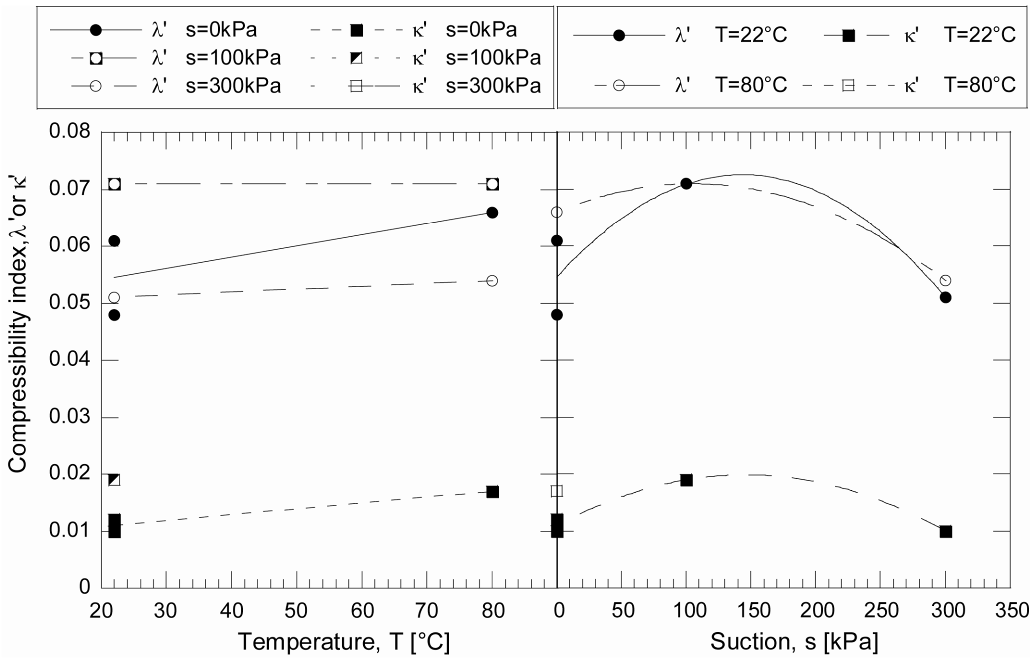

Figure 5.17: Evolution of the compressibility indices with temperature and with suction.

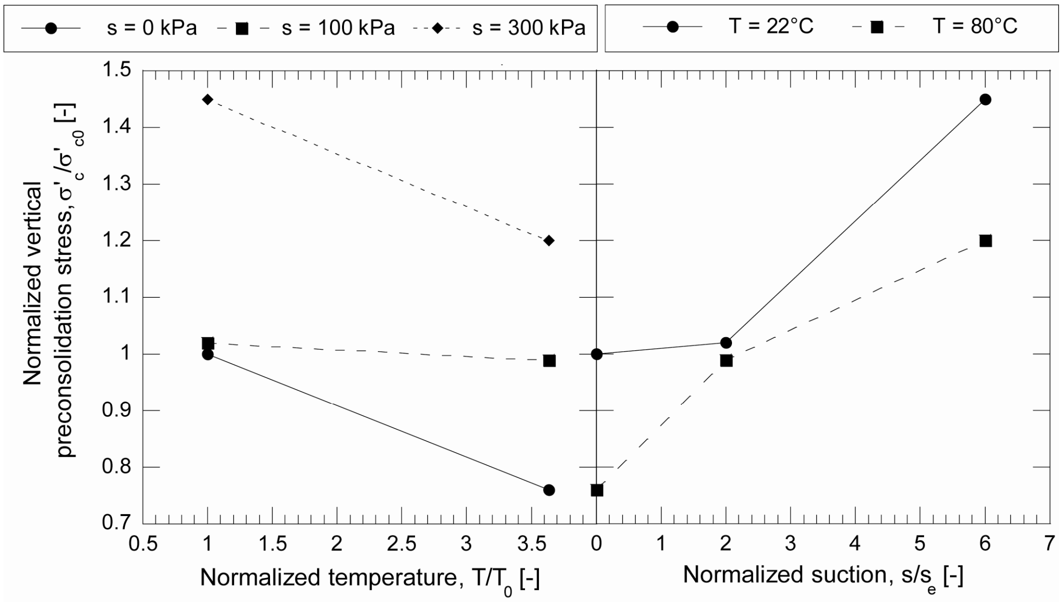

Figure 5.18: Evolution of the vertical preconsolidation stress with normalized temperature and suction. s_e is the air-entry suction

5.3.6 Comparison with other experimental results on Sion silt

As explained in Section 5.3.2, the mechanical behaviour of Sion silt has already been investigated in the past through several experimental programs under isothermal conditions (ambient temperature). Moreover, the experimental tests described in the previous sections were made in collaboration with a research group at the Montpellier II University (France), who performed similar tests under isotropic conditions at different suction and temperature levels (François et al., 2007a; Salager et al., 2008).

The effect of temperature and suction on the evolution of the compressibility indices and of the preconsolidation pressure (σ'_{vc} for the oedometric tests and p'_c for the isotropic ones), already presented in Figure 5.17 and Figure 5.18 for the present study, are combined with the most relevant results from Geiser (1999) and Salager (2007). This provides a wider experimental data base to deduce quantitative evolutions of the studied parameters with respect to temperature and suction.

5.3.6.1 *Evolution of the compressibility indices*

Figure 5.19 reports the compressibility indices of the considered tests with respect to temperature and suction. The filled points correspond to the oedometric tests, while the empty points report the results of isotropic compression tests. These results demonstrate an isotropic compression index that is half that of the oedometric one. This experimental evidence is not in accordance with the supposed similarity between isotropic and oedometric compressibilities for remoulded saturated clays. Indeed, the conventional soil mechanics hypothesis states that the compression index is independent of the stress ratio (i.e. the ratio between the deviatoric and the mean effective stress), provided that this ratio is kept constant throughout the compression test (Biarez and Hicher, 1994). Since the beginning of experimental tests on Sion silt (more than 10 years ago), this has been observed. Until now, however, no clear explanation has been found to justify this observation. A possible explanation could be linked to the evolution of compressibility with the stress level observed on Sion silt. In fact, the compression index continuously increases with increasing stress levels, which makes it difficult to define a rigorous value of λ'. To solve this problem, the compression index λ' was measured in a given effective stress range, between 200 and 400 kPa. The isotropic stress applied during isotropic tests is not equivalent to the vertical stress applied during oedometric tests. In that sense, even if a given stress range was fixed, the compression indices cannot be compared because of the different boundary conditions between isotropic and oedometric states.

In general, this set of results does not exhibit a clear effect of temperature on the compressibility of the soils, at least for the range of temperatures considered in this experimental program. This negligible thermal effect on the compressibility indices is in agreement with other experimental evidence, such as the results of Cekerevac and Laloui (2004) on saturated kaolin clay, or Tang et al. (2008) on compacted bentonite in an unsaturated state.

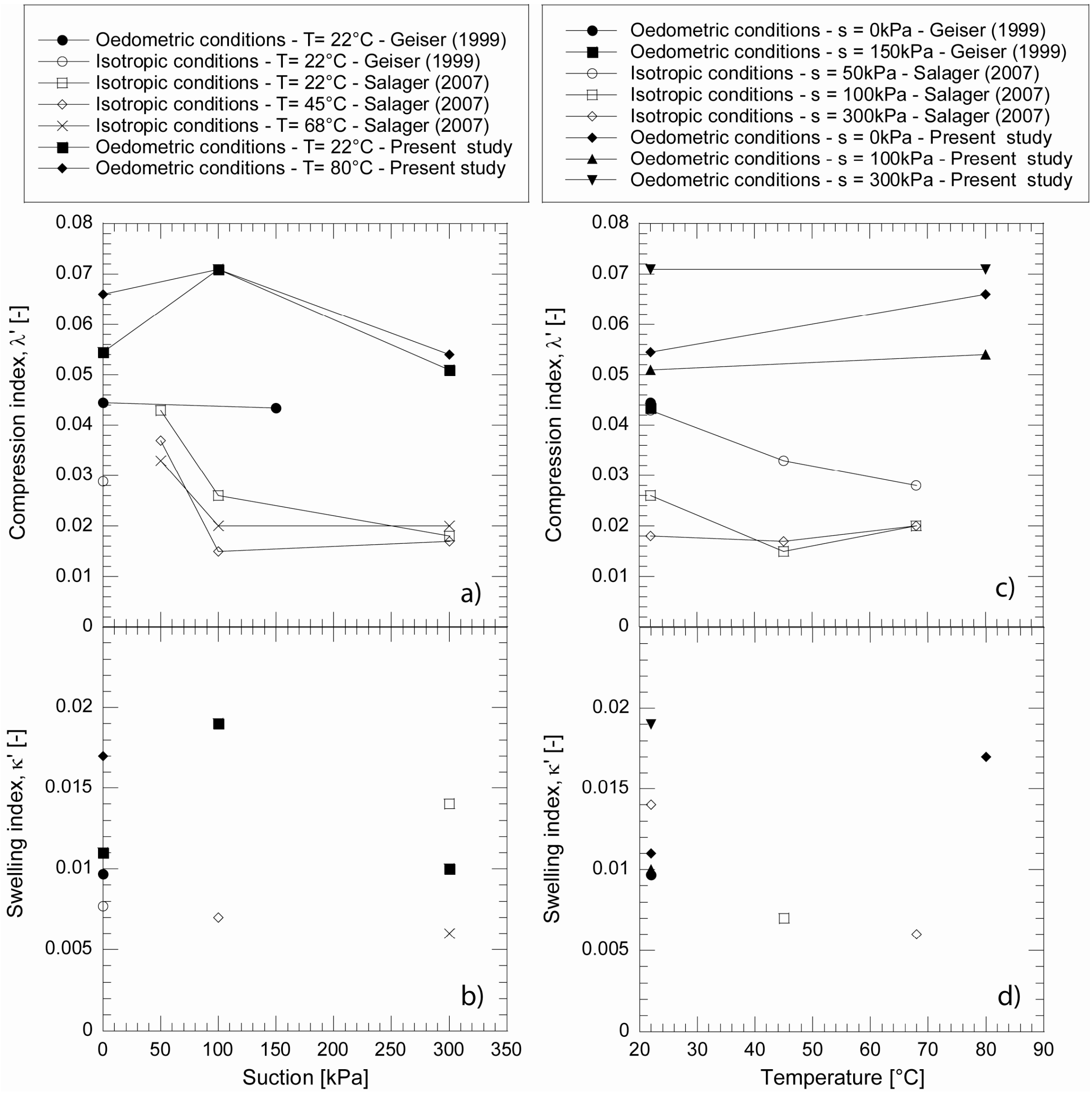

Figure 5.19: Evolution of the compressibility indices with temperature and with suction. Comparison of the results with other experimental results. a) Compression index versus suction, (b) Swelling index versus suction, (c) Compression index versus temperature, (d) Swelling index versus temperature.

As far as the suction effect is concerned, an increase of suction seems to induce a decrease in the compression index, at least for suction greater than the air-entry suction ($s_e \approx 50kPa$). A possible interpretation of this evolution should be that λ' increases with suction upon the air-entry suction, which initiate the desaturation process, and then for $s > s_e$, suction tends to reduce the soil compressibility. More experimental evidence from the same material is necessary to draw a conclusion about the trend of the swelling index with suction evolution.

5.3.6.2 *Evolution of the preconsolidation pressure*

The temperature and suction effects on the preconsolidation pressure, already presented in Figure 5.18 for the present study, is combined in Figure 5.20a and Figure 5.20b with other results. Those results confirm the decreasing trends of the preconsolidation pressure with temperature and its increase with suction. The spreading of the experimental evidence makes it difficult to deduce a precise quantitative law for the evolution of the preconsolidation pressure with temperature and suction. However, this evolution appears to be rapid for the low values of the two variables and becomes asymptotic for the higher ones. Consequently, a logarithmic function might be suitable to model these two phenomena.

As already discussed in Chapter 3, Laloui and Cekerevac (2003) proposed the following expression to represent the preconsolidation pressure decrease with heating in saturated conditions:

$$p'_c(T) = p'_{c0}\left(1 - \gamma_T \log\left(\frac{T}{T_0}\right)\right) \tag{5.11}$$

where p'_{c0} is the preconsolidation pressure at a reference temperature T_0, $p'_c(T)$ is the preconsolidation pressure at a given temperature T, and γ_T is a material parameter.

The form of Equation (5.11) is also suitable to predict the preconsolidation pressure increase with suction under isothermal conditions. In this expression, any suction lower than the air-entry value, s_e, is assumed to have no influence on the preconsolidation pressure (Nuth and Laloui, 2007):

$$p'_c(s) = \begin{cases} p'_{c0} & \text{if } s \le s_e \\ p'_{c0}\left(1 + \gamma_s \log\left(\dfrac{s}{s_e}\right)\right) & \text{if } s \ge s_e \end{cases} \tag{5.12}$$

where p'_{c0} is the preconsolidation pressure at saturation, $p'_{c0}(s)$ is the preconsolidation pressure at a given suction s, and γ_s is a material parameter. The proposed formulation has been validated on different material which has proven to provide a suitable fitting of experimental yield points (Nuth and Laloui, 2007). In the saturated domain (i.e for suction lower than the air-entry value), the capillary mechanisms are not activated. As a consequence, a positive suction can occur without affecting the preconsolidation pressure that remains equal to its saturated reference value.

Equations (5.11) and (5.12) can be combined to express the evolution of the preconsolidation pressure with temperature and suction (François and Laloui, 2007, 2008a):

$$p'_c(s,T)=\begin{cases} p'_{c0}\left(1-\gamma_T\log\left(\dfrac{T}{T_0}\right)\right) & \text{if } s\le s_e \\ p'_{c0}\left(1+\gamma_s\log\left(\dfrac{s}{s_e}\right)\right)\left(1-\gamma_T\log\left(\dfrac{T}{T_0}\right)\right) & \text{if } s\ge s_e \end{cases} \tag{5.13}$$

Figure 5.20c and Figure 5.20d displays this proposed analytical evolution for $\gamma_T = 0.46$ and $\gamma_s = 0.6$ and compares it with the experimental results. In spite of the discrepancy in the experimental results, this logarithmic law is in satisfactory agreement with the experiments.

5.3.6.3 *Discussion on the evolution of the preconsolidation pressure*

Experimental investigations of the separated effects of suction or temperature on the evolution of the size of the elastic domain have been performed by many authors. Those experimental programs demonstrated a clear decrease of the preconsolidation pressure with temperature and an increase of that pressure with suction. The present experimental study confirms that behavioural feature. However, a rigorous and systematic investigation of the combined effect of temperature and suction on the preconsolidation pressure has rarely been done in the past. The results obtained in the present study, in collaboration with a research group at Montpellier II University, bring noticeable advances in the characterisation of the compression behaviour of soil at different temperature and suction levels. Quantitative assessments have been proposed based on the logarithmic law describing the preconsolidation pressure decrease with temperature as proposed by Laloui and Cekerevac (2003).

The proposed evolution law requires only two additional parameters: γ_T, describing the decrease of the yield limit with temperature and γ_s, its increase with suction. It appears that γ_T depends on suction and γ_s on temperature, but the development of a more precise evolution law describing these relationships must be supported by further experimental evidence. In the present case, parameter variations are not important, so the mean values of γ_s and γ_T yield satisfactory results.

5.4 Conclusions

The combined effect of temperature and suction on the mechanical behaviour of soils has rarely been investigated in a systematic way. The experimental techniques that need to be developed in order to control and to measure the thermo-hydro-mechanical evolution of the soil sample require fine developments and calibrations. After a literature overview of the available techniques in mechanical soil testing under controlled temperature and suction conditions, the utilized oedometric cell with its required calibrations has been presented. The developed device has been used to perform a set of compression tests under different THM initial states on a sandy silt. The main objective of this experimental program was to study the influence of combined temperature and suction on the compressibility indices and on the preconsolidation stress. The results have been interpreted in light of the generalized effective stress. Moreover, the results of the present study have been compared with results obtained in a parallel set of experiments performed by a research group at Montpellier II University. The data tend to show that temperature has no prevailing effect on the compressibility indices. In contrast, an increase of suction induces a decrease in the compression index. The preconsolidation stress, however, is strongly influenced by both temperature and suction. A temperature increase tends to decrease the yield limit, while a suction increase enhances this limit, at least for suction higher than the air entry value. Finally, a quantitative logarithmic expression requiring two material parameters, one for the thermal evolution and another for the suction evolution, seems to describe these qualitative observations quite well.

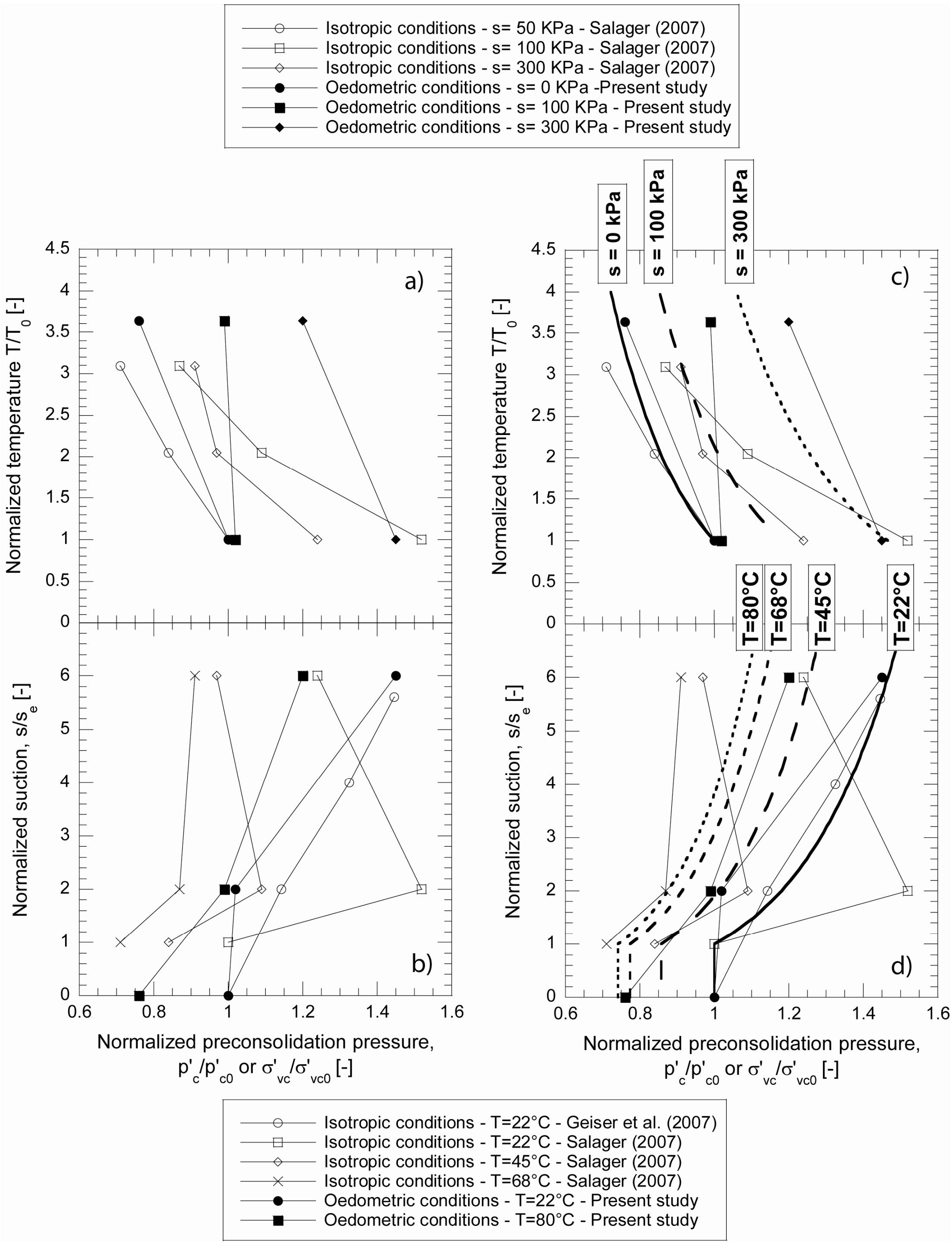

Figure 5.20: Evolution of the preconsolidation pressure with temperature and with suction. Comparison of the results with other experimental results. (a) Normalized preconsolidation pressure versus normalized temperature, (b) Normalized preconsolidation pressure versus normalized suction, (c) Logarithmic trends of the evolution of preconsolidation pressure with temperature, (d) Logarithmic trends of the evolution of preconsolidation pressure with suction.

Chapter 6

ACMEG-TS, a constitutive model for unsaturated soils under non-isothermal conditions

The problem of heat and mass transport in porous media is subject of great interest in many engineering disciplines. […]. In general, a major difficulty in the formulations is that they either completely ignore the matrix deformation or use the theory of elasticity in conjunction with the "state surface" approach to account for the strong non-linear deformation of the soil matrix. It is well established that vastly different volumetric responses can be obtained in an unsaturated soils, subject to identical increases of matric suction and net stress, but applied at different sequences. […]. An appropriate plasticity model must be invoked, in order to take into account the variation of yield surface with temperature and suction.[1]

---

[1] Khalili N. and Loret B. (2001). An elasto-plastic model for non-isothermal analysis of flow and deformation in unsaturated porous media: formulation. *International Journal of Solids and Structures*, 38: 8305-8330.

6.1 Introduction

As demonstrated in Chapter 4 through a literature analysis and in Chapter 5 through experimental investigations, variations in temperature and suction have a considerable influence on soils, not only in terms of mechanical response, but also on their water retention properties. It is challenging to understand and reproduce complex processes in which temperature and suction effects play a key role. In general, unsaturated and non-isothermal conditions are considered independent processes. However, coupling between temperature and water retention properties must be considered in order to cover the range of interactions affecting the mechanical response of soils.

In the last ten years, some useful insights were contributed to the field through the study of unsaturated constitutive relations under non-isothermal conditions (Gens, 1995b; Modaressi and Modaressi, 1995; Khalili and Loret, 2001; Wu et al., 2004; Bolzon and Schrefler, 2005). However, the first models in the field were limited by the lack of available experimental evidence focusing on thermal effects on the behaviour of unsaturated soils. Growing interest in the domain resulted in an increasing number of experimental results under both partially saturated and non-isothermal conditions, making it possible to improve existing constitutive approaches. In particular, the model developed in this chapter provides substantial advances concerning the temperature effect on water retention properties that directly affect the mechanical behaviour of materials.

From a constitutive point of view, a unified approach dealing with the thermo-plasticity of saturated and unsaturated soils in a highly-coupled framework is presented. The ACMEG-TS model uses two interconnected constitutive parts. The first dealing with the stress-strain relationship is an extension toward unsaturated conditions of the ACMEG-T model (Chapter 3), while the second focuses on the relationship between degree of saturation and suction considering the effects of stress and temperature states (François and Laloui, 2008a).

First, the existing constitutive approaches in this area are briefly described. Then, the mechanical and water retention parts of the constitutive model are introduced, including the stress framework used, while underscoring the interconnectivity of both parts. Following this, typical responses of the ACMEG-TS model on non-isothermal and unsaturated paths are given and, finally, some selected comparisons between model simulations and experimental results are presented for different combinations of temperature, suction and stress paths.

6.2 Previous constitutive contributions

6.2.1 The existing constitutive models

In parallel with the first laboratory tests dealing with unsaturated soils under non-isothermal conditions, as reviewed in Chapter 4, more advanced constitutive frameworks for soil responses under non-isothermal and unsaturated conditions were developed. Using the similarities between the structures of thermo-plastic model of Hueckel and Borsetto (1990) and the elastoplastic model for unsaturated soils of Alonso et al. (1990), Gens (1995b) joined both approaches in a more general model that involves suction and temperature effects. Despite the restricted experimental data available at that time, this initial work proposed a consistent constitutive framework using two independent stress variables, net stress and suction (see Section 4.2.2 for an explanation of the stress framework in unsaturated soils). At the same time, Modaressi and Modaressi (1995) extended an existing elastoplastic model with capillary hardening (Modaressi and AbouBerk, 1994) to include thermal effects with an already-developed thermoplastic model by Modaressi and Laloui (1997). The adopted stress framework was a pseudo effective stress that included the concept of capillary stress (Biarez et al., 1993; Kohgo et al., 1993).

In a unified treatment of the thermo-hydro-mechanical governing equations, Khalili and Loret (2001) presented a systematic elasto-plastic approach using the effective stress concept previously developed by Loret and Khalili (2000). In the continuation of the constitutive framework established by Gens (1995b), Wu et al. (2004) proposed advancing it by considering the coupling behaviour between suction and temperature, combined with the retention curve established by Fredlund and Xing (1994). The last major contribution to the field was made by Bolzon and Schrefler (2005). Based on recent experimental observations, the authors made some improvements to the original temperature-independent formulation previously developed, using a generalized effective stress approach (Bolzon et al., 1996).

6.2.2 Discussion on the existing constitutive models

A preliminary analysis of the main contributions in the field of constitutive modelling of partially saturated soils under non-isothermal conditions permits us to state the following:

- As with isothermal models, the choice of stress framework (two independent stresses or a single averaged stress) remains a matter of convenience.
- The earliest model (Gens, 1995b) was a combination of a separate thermo-plastic model for saturated soil with an elasto-plastic isothermal formulation for unsaturated soils. Due to the similarity of the constitutive structures, this association was possible with some substantial adaptation of the consistency equation.
- With increasing experimental evidence of the mechanical, water retention and thermal interactions in soils, water retention-temperature-stress-strain coupling effects were increasingly considered in models. However, due to the complexity of these processes, the inter-connected effects were never properly described in a consistent and unified approach.
- The retention properties of soils have often been expressed by fitting a curve, without considering the effects of density, temperature and water retention hysteresis.

With these observations in mind and with the goal of describing more accurately the global non-isothermal mechanical response of unsaturated soils, a comprehensive constitutive model, focusing on coupling aspects, is developed here. Figure 6.1 summarizes the interactions considered by the model and divides them into three categories. The interactions between the thermal, water retention and mechanical parts are fully coupled within a unified approach in the constitutive relations.

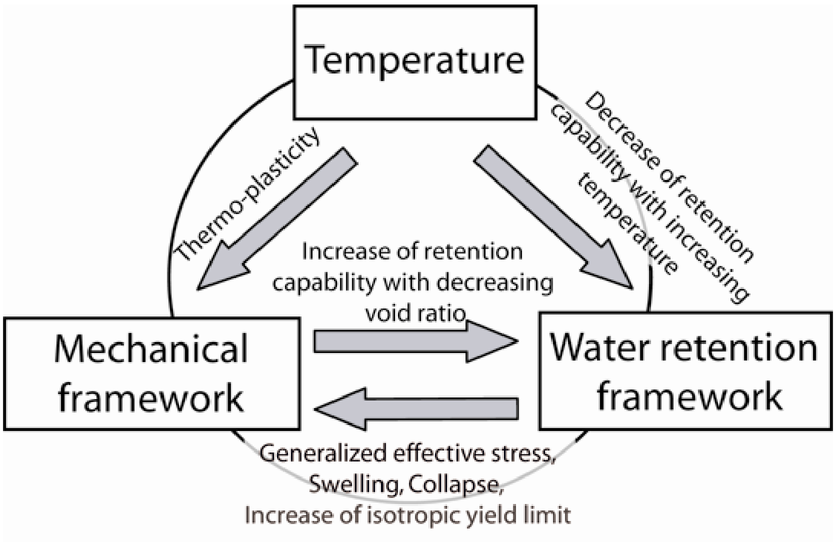

Figure 6.1 : Schematic overview of the interactions between the thermal, mechanical and water retention frameworks considered in the ACMEG-TS model.

6.3 The ACMEG-TS model[1]

6.3.1 Mechanical constitutive part

6.3.1.1 *Stress framework*

In light of the discussion on the choice of the stress framework for unsaturated soils addressed in Section 4.2.2, the ACMEG-TS model uses the generalized effective stress approach, which aims to use a single stress to describe the mechanical behaviour of unsaturated soils through combinations of mechanical stresses and fluid pressures (Nuth and Laloui, 2008). This averaged stress variable converts a multi–phase porous media into a mechanically equivalent, single-phase, single-stress state continuum according to the following expression:

$$\sigma'_{ij} = \left(\sigma_{ij} - p_a\delta_{ij}\right) + S_r\left(p_a - p_w\right)\delta_{ij} \tag{6.1}$$

where σ_{ij} is the total external stress tensor, p_a and p_w the air and water pore pressures, respectively, δ_{ij} Kroenecker's symbol and S_r the degree of saturation. This expression follows from Bishop (1959), in which the effective stress parameter is equal to the degree of saturation, as suggested by Bishop and Blight (1963) and by Schrefler (1984). Since the retention capacity of the soil depends on the thermo-hydro-mechanical conditions (suction level, suction paths followed, dry density and temperature), including the $S_r \times s$ product in the effective stress formulation itself creates a number of intrinsic thermo-hydro-mechanical connections. Furthermore, adopting a generalized effective stress creates noticeable advantages for the constitutive framework, such as simplifications in the expression of the yield surface, the uniqueness of the critical state line and a smooth and natural transition in stress variables from saturated to unsaturated conditions (Nuth and Laloui, 2008)

[1] François B. and Laloui L. (2008). ACMEG-TS: A constitutive model for unsaturated soils under non-isothermal conditions. *International Journal for Numerical and Analytical Methods in Geomechanics*, 32: 1955-1988.

In addition to this effective stress variable, a full description of the thermo-hydro-mechanical response of soils requires a consistent elasto-plastic framework. In particular, suction and temperature must be considered parameters that govern the evolution of the elastic limits. To this end, the constitutive relations of the ACMEG-TS model are presented in the next sections. The mechanical part of the model is an extension of the ACMEG-T model already addressed in Sections 2.3 and 3.5, so the following section details the specifics of the suction effect on the mechanical constitutive relations by completing them in the context of unsaturated conditions.

6.3.1.2 *Elastic component*

Similar to the thermo-mechanical elasticity under saturated conditions (Equation ((3.27)), the elastic part of the deformation is expressed as follows:

$$d\varepsilon_{ij}^{e} = E_{ijkl}^{-1} d\sigma'_{kl} - \beta_{\mathrm{T},ij} dT \tag{6.2}$$

The first term of Equation (6.2) is the contribution of the effective stress increment to the total elastic strain increment. According to Equation (6.1), this part may follow from total stress or fluid pressure variations. In that sense, $d\sigma'_{kl}$ collects the increments of external stress, suction, and degree of saturation within a unified stress variable. The expression for the elastic modulus as well as the thermal expansion coefficient can be found in Chapter 2 and Chapter 3, respectively (in particular, Equations (2.67), (2.68), (3.30) and (3.41)).

6.3.1.3 *Plastic component*

This section presents only the contribution of suction on the evolution of isotropic and deviatoric plastic mechanisms. The isothermal plastic mechanisms have been extensively presented in Section 2.3.3 while the temperature influence on the evolution of those yielding mechanisms has been addressed in Section 3.5.2.

Isotropic plastic mechanism

Similar to Equation (2.71), the yield limit, f_{iso}, of the isotropic plastic mechanism is expressed by :

$$f_{iso} = p' - p'_c \, r_{iso} \tag{6.3}$$

r_{iso} corresponds to the degree of plastification (mobilised hardening) of the isotropic yield limit (Equation (2.72)). The enhancement of the isotropic elastic domain with increasing suction is introduced through the evolution of the preconsolidation pressure p'_c (Figure 6.2). As experimentally observed in Section 5.3.6.2 (Equation (5.13)), the evolution of p'_c with combined temperature T and suction s can be expressed by a logarithmic function (François and Laloui, 2008a). In addition, the mechanical hardening produces an evolution of the preconsolidation pressure with the generated volumetric plastic strain ε_v^p (Equation (2.74)). Finally, the thermo-hydro-mechanical evolution of the preconsolidation pressure is expressed as:

$$p'_c = \begin{cases} p'_{c0} \exp\left\{\beta \varepsilon_v^p\right\}\left\{1-\gamma_T \log\left[T/T_0\right]\right\} & \text{if } s \le s_e \\ p'_{c0} \exp\left\{\beta \varepsilon_v^p\right\}\left\{1-\gamma_T \log\left[T/T_0\right]\right\}\left\{1+\gamma_s \log\left[s/s_e\right]\right\} & \text{if } s \ge s_e \end{cases} \tag{6.4}$$

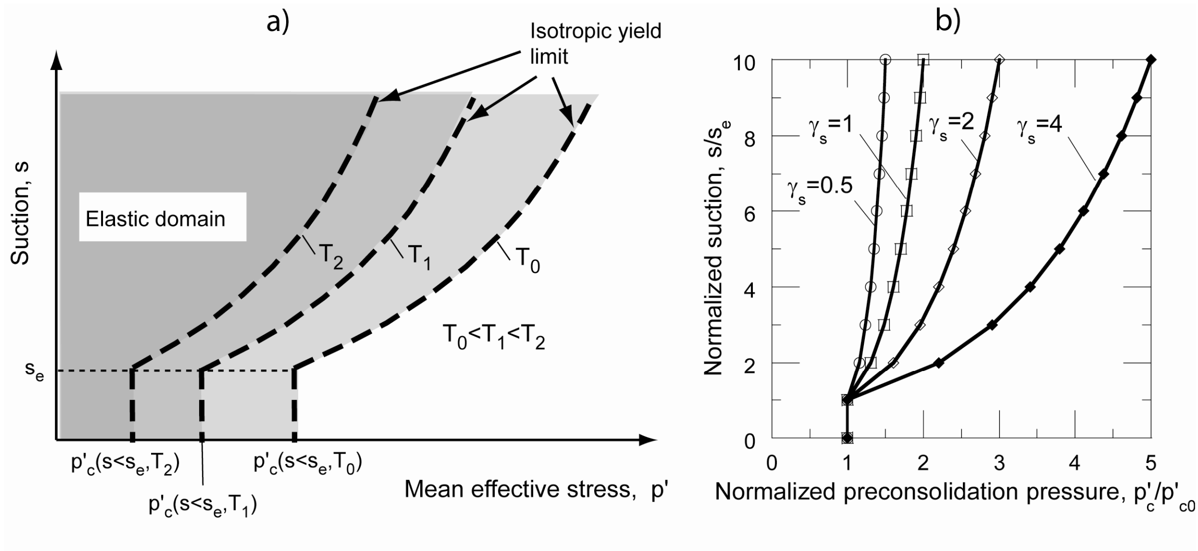

Figure 6.2 : Evolution of the isotropic yield limit with suction at difference temperatures (a) and its dependence on the γ_s parameter (b).

where β is the plastic compressibility modulus (the slope of the linear function in the $\left(\varepsilon_v^p - \ln p_c'\right)$ plane). γ_T and γ_s are the two material parameters needed to define the thermal and suction evolutions of the isotropic yield limit, respectively. T_0 is the reference temperature and s_e the air-entry suction.

The flow rule for the isotropic mechanism remains unchanged regarding the isothermal and saturated mechanism (Equation (2.75)).

Deviatoric plastic mechanism

Similar to Equation (2.76), the yield limit, f_{dev}, of the deviatoric plastic mechanism is expressed by (Hujeux, 1979):

$$f_{dev} = q - Mp'\left(1 - b\ \ln\frac{d\ p'}{p_c'}\right) r_{dev} = 0 \tag{6.5}$$

where b is a material parameter defining the shape of the deviatoric yield limit and d the ratio between the preconsolidation pressure, p_c', and the critical pressure, p_{cr}'. r_{dev}, in the same way as for the isotropic mechanism, is the degree of plastification of the deviatoric mechanism (Equation (2.78)). M is the slope of the critical state line in the ($q - p'$) plane (Equation (2.77)). The ACMEG-TS model assumes that the friction angle may depend on temperature (Equation (3.36)) but remains unaffected by suction change in the generalized effective stress reference, as noticed by Nuth and Laloui (2008).

The hardening and dilatancy rules of the deviatoric mechanism remain unchanged regarding to the isothermal mechanism under saturated conditions (Equations (2.79) to (2.84)).

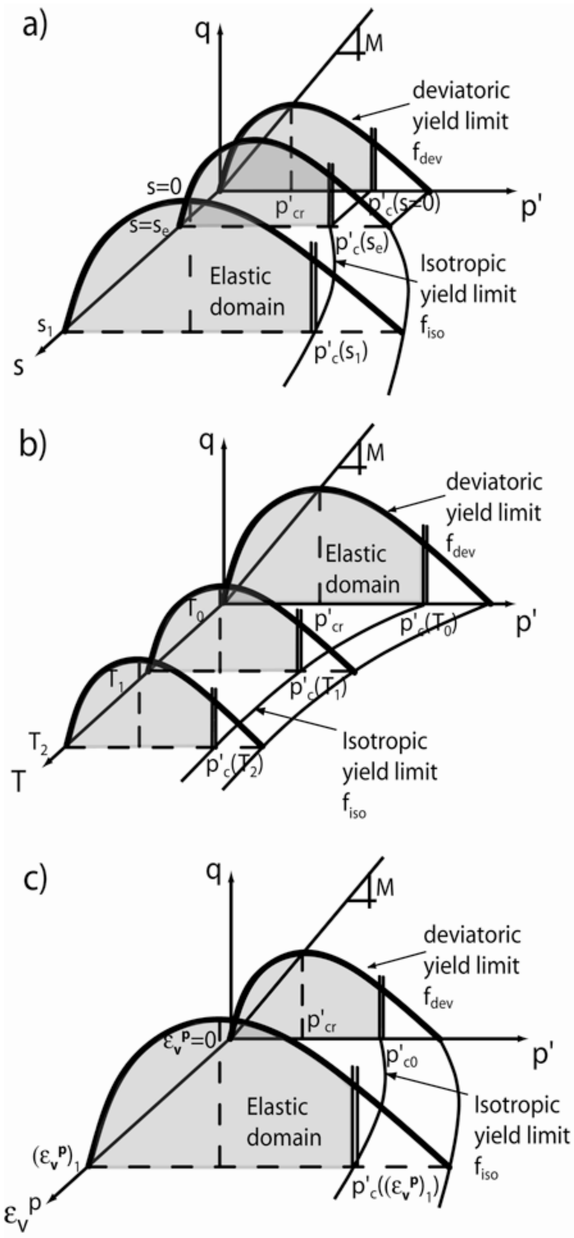

Figure 6.3 : Effect of (a) suction, (b) temperature and (c) volumetric plastic strain on the shape of coupled mechanical yield limits.

Coupling between the two plastic mechanisms

The shape of the elastic domain follows from the combinations of the deviatoric yield limit (Equation (3.35)) with the thermo-hydro-mechanical evolution of the preconsolidation pressure (Equation (6.4)). Figure 6.3 illustrates successively the effect of suction, temperature and generated volumetric plastic strain on the evolution of the elastic domain.

It must be noted that the temperature and suction dependence of the isotropic yield limit is a one-to-one relationship. Provided that the stress point remains in the elastic domain, a suction and/or a temperature cycle does not modify the final preconsolidation pressure with respect to the initial one, if the final state is identical to the initial one. On the contrary, the volumetric plastic strain produces irreversible modification of the isotropic yield limit. In other words, the volumetric plastic strain is a hardening variable, while temperature and suction are not.

The coupling between the two plastic mechanisms is similar to the ACMEG-T model under saturated conditions. However, inclusion of the derivative of the yield limits with respect to suction is required in the consistency conditions for multi-mechanism (Equation (3.38)) due to the evolution of both yield limits with suction level. The consistency condition of the two yielding mechanisms must be met simultaneously, requiring solution of two equations with two unknowns.

$$\begin{cases} \mathbf{dF} = \dfrac{\partial \mathbf{F}}{\partial \boldsymbol{\sigma}'} : d\boldsymbol{\sigma}' + \dfrac{\partial \mathbf{F}}{\partial s}.ds + \dfrac{\partial \mathbf{F}}{\partial \mathrm{T}}.d\mathrm{T} + \dfrac{\partial \mathbf{F}}{\partial \boldsymbol{\pi}}.\dfrac{\partial \boldsymbol{\pi}}{\partial \boldsymbol{\lambda}^{\mathbf{p}}}.\boldsymbol{\lambda}^{\mathbf{p}} = \mathbf{j} : d\boldsymbol{\sigma}' + \mathbf{i}.ds + \mathbf{t}.d\mathrm{T} - \mathbf{H}.\boldsymbol{\lambda}^{\mathbf{p}} \leq 0 \\ \boldsymbol{\lambda}^{\mathbf{p}} \geq 0 \ \ ; \ \ \mathbf{dF}.\boldsymbol{\lambda}^{\mathbf{p}} \geq 0 \end{cases} \tag{6.6}$$

$\boldsymbol{\sigma}'$ is the generalized effective stress vector and $\boldsymbol{\pi}$ the internal variable vector. $\mathbf{j}$ collects the stress-gradient and $\mathbf{t}$ the temperature-gradient of the loading function $\mathbf{F}$. $\mathbf{H}$ is the matrix of hardening moduli $H_{\alpha\beta} = -\partial f_{\alpha} / \partial \lambda_{\beta}^{p}$, $\boldsymbol{\lambda}^{\mathbf{p}}$ is the plastic multiplier vector and $\mathbf{dF} \leq 0$ expresses Prager's consistency condition extended to multiple dissipation processes. All those variables have been detailed in Section 2.3.3.2, for the isothermal model, and Section 3.5.2.2, for the temperature dependence. $\mathbf{i}$ collects the suction-gradient of the loading function. In the framework of generalized effective stress (Equation (6.1)), Borja (2004) proved that including suction in the argument of the yield functions is motivated by thermodynamic considerations. Within this adopted stress framework, $\boldsymbol{\sigma}'$ depends on s, which makes these two state variables dependent. In order to avoid the two effects of the suction increment (in $d\boldsymbol{\sigma}'$ and ds itself) in the consistency equation, numerical integration at the local (Gauss point) level is performed by considering suction fixed at its final value during the plastic corrector phase. In other words, as suggested by Borja (2004), there is no return map on the suction axis during numerical integration of the model, which makes ds equal to zero in Equation (6.6). There is no change in the consistency relations with respect to the saturated model, excepted that, at each time step, the value of the preconsolidation pressure is calculated considering the suction at the end of the time step through Equation (6.4).

6.3.2 Water retention constitutive part

The characteristics of water retention curve as experimentally observed in soils have been addressed in Section 4.2.4. The present section aims to reproduce the behaviour of the $S_r - s$ relationship from the constitutive point of view. In particular, the effects of density, temperature and hysteresis are properly considered.

6.3.2.1 *Drying and wetting mechanisms*

In terms of water retention response, desaturation is also a yielding phenomenon. Hysteresis in water retention behaviour is modelled as a plastic process, based on ideas similar to those of Wheeler et al. (2003). As long as the soil is drying, suction increases, and the degree of saturation, S_r, tends to decrease mainly when the air-entry suction s_e is reached. This concept may be compared with the irrecoverable volumetric strain produced during isotropic loading, mainly when the preconsolidation pressure is reached. So, as p_c' is the yield limit in the isotropic mechanical plane, s_e is the yield limit in the ($S_r - s$) plane. Under re-wetting, a hysteretic phenomenon occurs, also represented by a yielding process (Figure 6.4). A wetting-drying cycle activates two successive yield limits in the ($S_r - s$) plane (f_{dry} and f_{wet}, along the drying and wetting paths, respectively):

$$f_{dry} = s - s_d = 0 \tag{6.7}$$

$$f_{wet} = s_d s_{hys} - s = 0 \tag{6.8}$$

where s_d is the drying yield limit and s_{hys} a material parameter considering the size of the water retention hysteresis. If the initial state is saturated, the initial drying limit s_{d0} is equal to air-entry suction s_e and increases when suction overtakes s_e as follows:

$$s_d = s_{d0} \exp\left(-\beta_h \ \Delta S_r\right) \tag{6.9}$$

where β_h is the slope of the desaturation curve in the $\left(S_r - \ln s\right)$ plane (Figure 6.4).

Finally, because air-entry suction of the materials depends on temperature and dry density, s_{d0} is a function of temperature and volumetric strain (François and Laloui, 2007, 2008a,b):

$$s_d = s_{d0} \exp\left(-\beta_h \ \Delta S_r\right)\left\{1 - \theta_T \log\left[T/T_0\right] - \theta_e \log\left[1 - \varepsilon_v\right]\right\} \tag{6.10}$$

where θ_T and θ_e are material parameters describing the logarithmic evolution of air-entry suction with respect to temperature and volumetric strain, respectively (Figure 6.5). In this expression, s_{d0} corrrespond for the initial drying limit at ambient temperature T_0 and at zero volumetric strain. s_{d0} depends on the dry density of the material.

6.3.2.2 *Consistency conditions*

Because the retention response is governed by yielding mechanisms, the processes must be controlled by evolution laws that agree with both consistency equations and yield functions. The two following equations describe the flow rules of the drying mechanism activated when suction increases and of the wetting mechanism activated when suction decreases, respectively:

$$d\Delta S_r^{\ dry} = \lambda_{dry}^p \frac{\partial f_{dry}}{\partial s} = \lambda_{dry}^p \leq 0 \tag{6.11}$$

$$d\Delta S_r^{\ wet} = \lambda_{wet}^p \frac{\partial f_{wet}}{\partial s} = -\lambda_{wet}^p \geq 0 \tag{6.12}$$

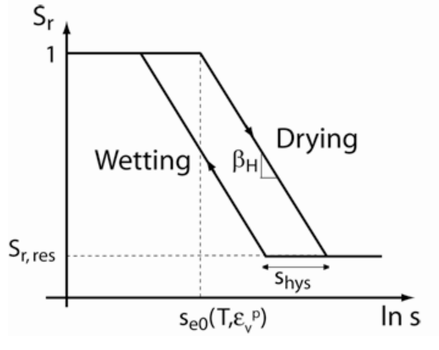

Figure 6.4 : Schematic representation of water retention curve modelling.

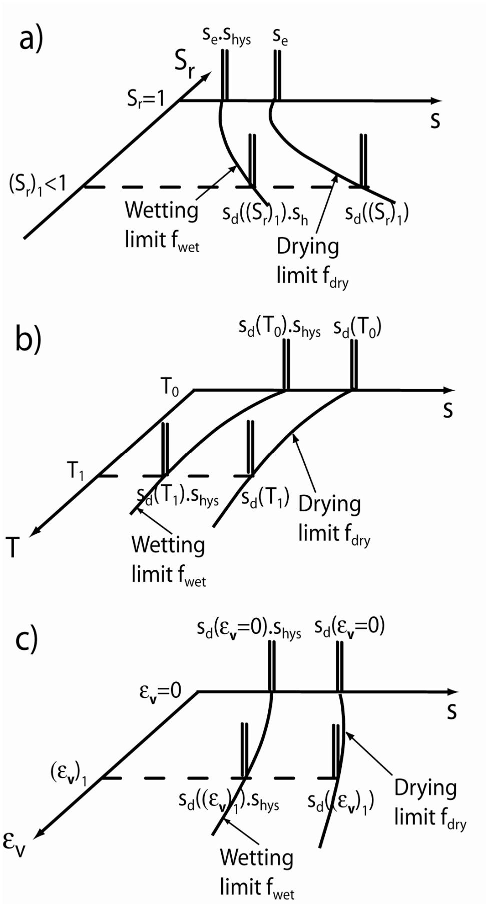

Figure 6.5 : Effect of (a) degree of saturation, (b) temperature and (c) volumetric strain on the shape of the drying and wetting limits.

As opposed to mechanical mechanisms, these two mechanisms of the water retention constitutive part cannot be active simultaneously, because they are activated in two opposite directions. As a consequence, the two plastic multipliers (λ_{dry}^p and λ_{wet}^p) are independent. Even if two consistency equations are needed to define the two water retention mechanisms, each equation must be satisfied independently, one for drying processes and the other for wetting processes. Moreover, these multipliers must be negative because an increase in suction tends to reduce ΔS_r. Within this framework, the current degree of saturation is obtained by summing the initial degree of saturation S_{r0} with its variations induced by drying and wetting mechanisms:

$$S_r = S_{r0} + \Delta S_r^{\ dry} + \Delta S_r^{\ wet} \tag{6.13}$$

The consistency conditions impose (François and Laloui, 2008c):

$$\begin{cases} \mathbf{dF_{hyd}} = \dfrac{\partial \mathbf{F_{hyd}}}{\partial s} ds + \dfrac{\partial \mathbf{F_{hyd}}}{\partial T} dT + \dfrac{\partial \mathbf{F_{hyd}}}{\partial \varepsilon_v} d\varepsilon_v + \dfrac{\partial \mathbf{F}}{\partial \boldsymbol{\pi}_{\mathbf{hyd}}} . \dfrac{\partial \boldsymbol{\pi}_{\mathbf{hyd}}}{\partial \boldsymbol{\lambda}_{\mathbf{hyd}}^{\mathbf{p}}} . \boldsymbol{\lambda}_{\mathbf{hyd}}^{\mathbf{p}} \leq 0 \ ; \ \boldsymbol{\lambda}_{\mathbf{hyd}}^{\mathbf{p}} \leq 0 \\ \mathbf{dF_{hyd}} . \boldsymbol{\lambda}_{\mathbf{hyd}}^{\mathbf{p}} \geq 0 \end{cases} \tag{6.14}$$

$\mathbf{F_{hyd}}$ is the yield function vector of the water retention constitutive part and $\boldsymbol{\pi}_{\mathbf{hyd}}$ the internal variables vector. s, T, ε_v^p are the three state variables of the retention part of the model. These hydraulic mechanisms count only one internal variable: the variation of degree of saturation ΔS_r. $\boldsymbol{\lambda}^{\mathbf{p}}_{\mathbf{hyd}}$ is the plastic multiplier vector of the water retention constitutive part.

In the numerical integration of Equation (6.14), temperature and volumetric strain are considered in their configuration at the end of the time step. Their values are therefore constant, making the second and third terms of Equation (6.14) useless. This latter can be simplified as following:

$$\mathbf{dF_{hyd}} = \frac{\partial \mathbf{F_{hyd}}}{\partial s} ds + \frac{\partial \mathbf{F}}{\partial \boldsymbol{\pi}_{\mathbf{hyd}}} \cdot \frac{\partial \boldsymbol{\pi}_{\mathbf{hyd}}}{\partial \boldsymbol{\lambda}^{\mathbf{p}}_{\mathbf{hyd}}} . \boldsymbol{\lambda}^{\mathbf{p}}_{\mathbf{hyd}} \leq 0 \ ; \qquad \boldsymbol{\lambda}^{\mathbf{p}}_{\mathbf{hyd}} \leq 0 \ ; \qquad \mathbf{dF_{hyd}} . \boldsymbol{\lambda}^{\mathbf{p}}_{\mathbf{hyd}} \geq 0 \tag{6.15}$$

$$\mathbf{dF_{hyd}} = \begin{pmatrix} df_{dry} \\ df_{wet} \end{pmatrix} \tag{6.16}$$

$$\boldsymbol{\lambda}^{\mathbf{p}} = \begin{pmatrix} \lambda^{p}_{dry} \\ \lambda^{p}_{wet} \end{pmatrix} \tag{6.17}$$

$$\frac{\partial \mathbf{F_{hyd}}}{\partial s} = \begin{pmatrix} \dfrac{\partial f_{dry}}{\partial s} \\ \dfrac{\partial f_{wet}}{\partial s} \end{pmatrix} = \begin{pmatrix} 1 \\ -1 \end{pmatrix} \tag{6.18}$$

$$\begin{aligned} \frac{\partial \mathbf{F}}{\partial \boldsymbol{\pi}_{\mathbf{hyd}}} \cdot \frac{\partial \boldsymbol{\pi}_{\mathbf{hyd}}}{\partial \boldsymbol{\lambda}^{\mathbf{p}}_{\mathbf{hyd}}} &= \begin{pmatrix} \dfrac{\partial f_{dry}}{\partial \Delta S_r} \dfrac{\partial \Delta S_r}{\lambda_{dry}} \\ \dfrac{\partial f_{wet}}{\partial \Delta S_r} \dfrac{\partial \Delta S_r}{\lambda_{wet}} \end{pmatrix} = \begin{pmatrix} s_d \beta_h \\ -s_d s_{hys} \beta_h \end{pmatrix} \\ &= \begin{pmatrix} s_{d0} \exp\left(-\beta_h \ \Delta S_r\right) \left\{1 - \theta_T \log\left[T/T_0\right] - \theta_e \log\left[1-\varepsilon_v\right]\right\} \beta_h \\ -s_{d0} \exp\left(-\beta_h \ \Delta S_r\right) \left\{1 - \theta_T \log\left[T/T_0\right] - \theta_e \log\left[1-\varepsilon_v\right]\right\} s_{hys} \beta_h \end{pmatrix} \end{aligned} \tag{6.19}$$

where T and ε_v^p correspond to the temperature and the volumetric strain at the end of the time step. For very high suctions, water retention conditions reach a residual state defined by the residual degree of saturation $S_{r,res}$. In this state, the degree of saturation can no longer vary, even if the suction increases. So, when S_r is equal to $S_{r,res}$, $d\Delta S_r^{dry}$ is null and Equation (6.15) can no longer be satisfied.

6.3.3 Some typical responses predicted by ACMEG-TS

In addition to elasto-plastic behaviour under saturated conditions, this framework for ACMEG-TS enables us to reproduce some non-linear and irreversible behaviours induced by suction and/or temperature changes. The following section explains the main mechanisms governing these processes. In particular, the swelling-collapse response depending on soil type, plasticity and stress level (measured in terms of OCR) is illustrated. The effects of temperature and dry density on the retention properties of soils are also addressed from a constitutive point of view. For the sake of clarity, mechanical $(\boldsymbol{\sigma}' - \boldsymbol{\varepsilon})$ and water retention $(S_r - s)$ plans are uncoupled, although both processes are actually fully interconnected. Those typical responses complete the set of schematic predictions addressed in Section 3.5.3 related to saturated conditions.

6.3.3.1 *Swelling-collapse on wetting*

The volumetric response of soils on wetting paths depends on soil type, plasticity and the overconsolidation ratio. This last is defined as the ratio of the preconsolidation pressure at a given suction (Equation (6.4)) on the mean generalized effective stress at the same suction (Equation (6.1)). Wetting (a suction decrease) induces a simultaneous drop in effective mean stress and yield limit. Nevertheless, the yield limit generally decreases faster than the effective mean stress. Under normally consolidated conditions, the stress state tends to surpass the yield limit upon wetting, which leads to hardening in order to satisfy the consistency condition (Figure 6.6a). This generates a wetting compaction, called wetting collapse. This compaction takes place as long as the suction is higher than the air-entry value (path A-B). On the contrary, when soil enters into the saturated domain (i.e. $s < s_e$), the wetting process occurs elastically, which correspond to a swelling. This behavioural feature is noticeable in experiments. For highly overconsolidated states, however, despite the possible plasticity inside the normally consolidated yield limit, the effective mean stress decreases faster than the yield limit, making the process elastic (swelling) (Figure 6.6b).

6.3.3.2 *Retention curve at different dry densities*

Due to the increase of air-entry suction s_e when the volumetric strain increases (Equation (6.10)), mechanical consolidation performed before the drying process changes the retention property of the material. Figure 6.7a shows three drying paths in the $(p' - s)$ plane performed at three different initial effective mean stresses. During the preliminary mechanical load under saturated conditions (paths A-B and A-C), volumetric strains are produced (Figure 6.7b), increasing the density of the material and therefore increasing the air-entry suction (Equation (6.10) - Figure 6.7c). Finally, when the soil is dried, the drying limit (the air-entry suction) is modified, and the three desaturation lines are parallel (Figure 6.7d). This schematic explanation illustrates the strong interconnection between the water retention and mechanical components of the model (H-M coupling).

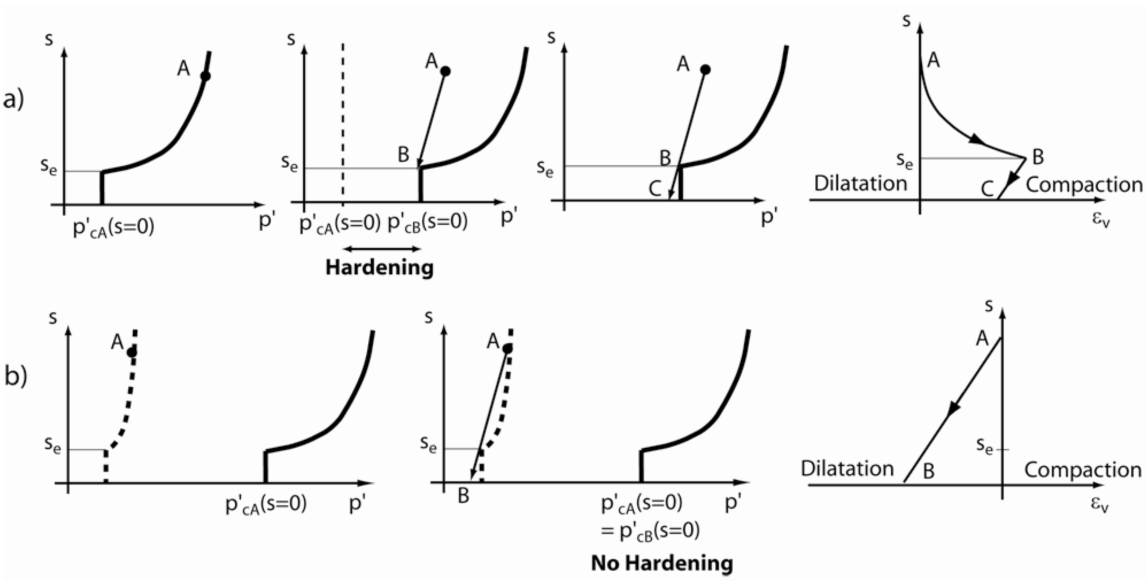

Figure 6.6 : Typical mechanical response on a wetting path: (a) wetting collapse of normally consolidated material, (b) swelling upon wetting of highly overconsolidated materials.

6.3.3.3 *Retention curve along a combined temperature and suction loading*

According to Equation (6.10), and in agreement with experimental evidence, a temperature increase provokes a drop in the drying limit (Figure 6.8). During drying, the water retention point is on the drying limit, and a thermal decrease of this limit induces a decrease in the degree of saturation, following the consistency condition (Equation (6.14)) and the corresponding flow rule (Equation (6.11)). Therefore, for the same suction, the retention capacity is lower at high temperatures than at room temperature. Heating induces desaturation under constant suction (Figure 6.8 - path B-C); this is representative of T-H coupling.

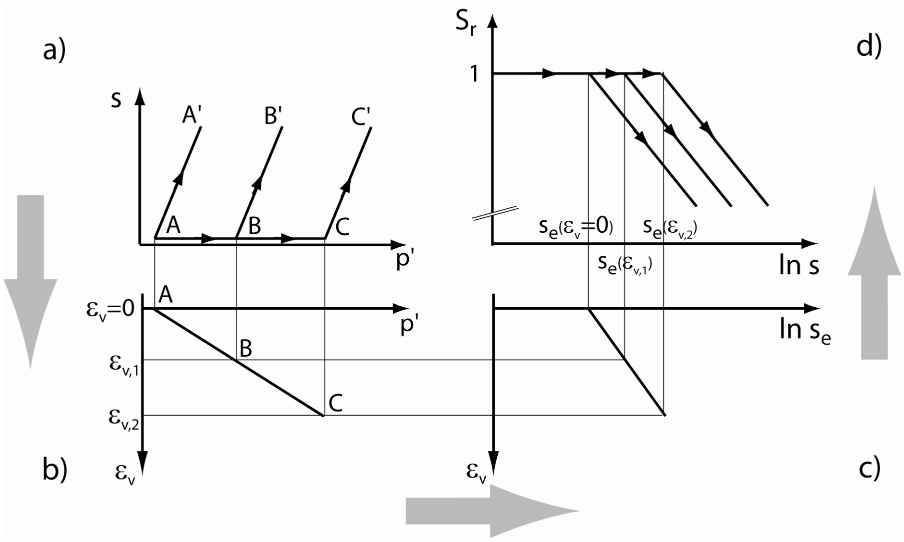

Figure 6.7 : Effect of the dry density of the material on its retention properties through volumetric strain.

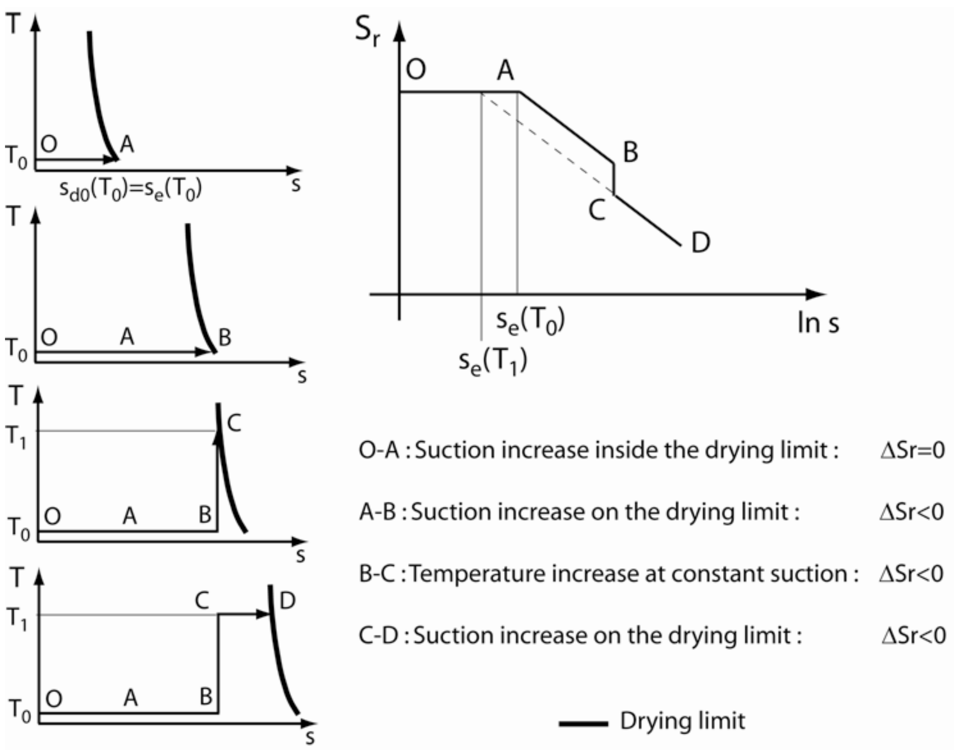

Figure 6.8 : Typical retention response along combined temperature and suction loading.

6.3.4 Validation of the ACMEG-TS constitutive model

The ACMEG-TS model has been validated with the results of different non-isothermal experiments under unsaturated conditions. In this section, numerical simulations are compared with the results of three distinct experimental programs: (i) the set of oedometric compression tests on Sion silt presented in Chapter 5, (ii) the tests on FEBEX bentonite (Lloret et al., 2004) and (iii) on MX80 bentonite (Tang, 2005; Tang et al., 2008) which were tested along coupled suction, temperature and mechanical paths.

First, some specific paths are used to calibrate the parameters of the different materials. For the simulations of Sion silt behaviour, the parameters of compressibility were calibrated from the test at ambient temperature under saturated conditions (O-T22S0-2), while the effect of temperature and suction on the evolution of the preconsolidation pressure was considered from the interpretation of experimental results in Chapter 5 ($\gamma_T = 0.46$ and $\gamma_s = 0.6$, Figure 5.20). For the two compacted bentonites, three isotropic compression tests at two temperatures and two suctions, one heating test on a highly overconsolidated soil and three drying-wetting tests at two temperatures and two dry densities are required to determine the isotropic parameters.

Because no deviatoric tests are available, deviatoric parameters are not considered in these simulations, with the exception of the elastic shear modulus of Sion silt and FEBEX bentonite, which affects their volumetric response under oedometric compression. The results and numerical simulations are displayed in the net stress reference $\left(\sigma_{ij,net} = \sigma_{ij} - p_a\right)$, although the model uses generalized effective stress. The net stress is the direct data monitored in the experiments, and remains the most convenient reference for presenting experimental results.

6.3.4.1 *Parameter determination*

In addition to the determination of the material parameters related to the thermo-mechanical behaviour of soils under saturated conditions (K_{ref} , G_{ref} , n^e , α , β , ϕ_0' , a , b , c , d , β_s' and γ_T), addressed in Section 3.5.5.1, the unsaturated conditions require consideration of additional parameters characterizing the soil behaviour. The only additional parameter for the mechanical part of the model (γ_s) is related to the effect of suction on the preconsolidation stress.

The slope of the logarithmic increase of the preconsolidation pressure with suction, γ_s is evaluated by comparing the values of the effective mean pressure corresponding to the inflection point of the compression curves (the preconsolidation pressure) obtained at two suctions:

$$\gamma_s = \frac{\dfrac{p_c'(s_1)}{p_c'(s_0)} - 1}{\log\left(\dfrac{s_1}{s_e}\right)} \tag{6.20}$$

where $p_c'(s_1)$ and $p_c'(s_0)$ are the preconsolidation pressures at suctions $s_1\left(> s_e\right)$ and $s_0\left(\le s_e\right)$ for two compressions tests performed at the same temperature. As discussed in the literature analysis (Section 4.2.3.2), the use of the generalized effective stress reference implies, for most materials, the uniqueness of the critical state line in a deviator stress versus mean effective stress plane for different levels of suction. Thus, the friction angle is assumed to be independent of the suction level.

Many of the parameters related to the water retention response can be determined using only one drying-wetting test. The air-entry suction s_{e0} is the suction corresponding to the intersection of the horizontal line $S_r = 1$ with the tangent of the linear part of the desaturation curve. β_h is the slope of the linear function ($\ln s - S_r$) when the air-entry suction is overcome. $S_{r,res}$ is the residual saturation characterizing the final plateau of the retention curve. s_{hys} is the ratio between suctions on wetting paths and drying paths, respectively, corresponding to the same degree of saturation on the linear part of the curve (Equation (6.8)); its value is between 0 and 1 (Figure 6.4).

In addition to the air-entry suction, s_{e0}, at reference temperature T_0 in the initial state $(\varepsilon_v = 0)$, one drying test at a high temperature is needed to obtain θ_T, which corresponds to the slope of the normalised plot of s_e / s_{e0} versus $\log(T/T_0)$. Moreover, one drying test at ambient temperature is needed after performing a mechanical loading cycle $(\varepsilon_v \neq 0)$ to obtain θ_e, which corresponds to the slope of the normalised plot s_e / s_{e0} versus $\log(1-\varepsilon_v)$.

Table 6.1 summarizes the material parameters determined for the three simulated materials. Notice again that deviatoric parameters are not considered in this set of simulations, as no deviatoric tests were available. However, in the case of deviatoric loading paths, no additional calibration test are needed with respect to the saturation state, because the critical state line is assumed unaffected by suction in the generalized effective stress reference. A brief academic example of triaxial test at different temperatures and suctions is presented in the next section to illustrate the performance of the model upon deviatoric loadings.

	Sion silt	**FEBEX bentonite**	**MX80 bentonite**
Elastic parameters			
K_{ref}, G_{ref}, n, β'_{s0} [MPa], [MPa], [-], [-]	30, 19, 0.5, 4.2 10^{-5}	16, 3.5, 1, 6.67 10^{-4}	1, -, 1.8, 2.10^{-4}
Isotropic plastic mechanical parameters			
β, γ_s, γ_T, c, r_{iso}^{ela} [-], [-], [-], [-], [-]	50, 0.6, 0.46, 0.001, 0.15	14.3, 16.1, 2.1, 0.02, 0.45	11, 18.4, 0.23, 0.015, 0.01
Deviatoric plastic mechanical parameters (fictive parameters)			
a, b, d, ϕ', r_{dev}^{ela}, g [-], [-], [-], [°], [-]	0.0035, 1, 2, 30, 0.01, 0		
Water retention parameters			
s_{e0}, β_h, θ_T, θ_e, s_{hys} [MPa], [-], [-], [-], [-]	0.05, 2.52, -, -, -	4, 8.64, 0.7, 10.8, 0.6	2, 7.06, -, 1.15, 0.5

Table 6.1: Model parameters for simulation of the response of Sion silt, Febex bentonite and MX80 bentonite.

6.3.4.2 *Validation on triaxial paths*

The simulations of the triaxial compression tests are performed using the parameters of Sion silt with additional fictive deviatoric plastic parameters (Table 6.1). The preconsolidation pressure p'_{c0} and the confining pressure $\sigma_{3,net}$ are assumed to be equal to 600 kPa and 400 kPa, respectively. This corresponds to an initial apparent overconsolidation ratio of 1.5. However, this value is calculated in net stress reference, assuming constant preconsolidation pressure. The real overconsolidation ratio depends on the suction and temperature levels, which affect the effective confining pressure ($\sigma'_3 = \sigma'_3(s)$) and the preconsolidation pressure ($p'_{c0} = p'_{c0}(s,T)$). In that sense, the higher the suction, the more overconsolidated the sample. On the other hand, the higher the temperature the less overconsolidated the sample. To make things clearer, the friction angle has been assumed to be temperature independent (i.e. $g = 0$).

Figure 6.9 reports the results of simulations for four different soil suctions and two temperatures. Even if the critical state line is not affected by suction, the apparent soil strength seems enhanced as suction increases (see Section 4.2.3.2). This is due to the increase of the initial effective confining stress with increasing suction. The shift of the effective confined stress with suction is controlled by the $S_r \times s$ product. It is worthwhile to note that, for the particular couples ($s = 150kPa$; $S_r = 0.56$) and ($s = 300kPa$; $S_r = 0.28$), the shifts in the effective confining pressures are equal. Consequently, the curves $s = 150kPa$ and $s = 300kPa$ reach the same critical state plateau.

By comparison of Figure 6.9a and Figure 6.9b, the effect of temperature on the shearing behaviour is mainly noticeable in the volumetric plane ($\varepsilon_1 - \varepsilon_v$). A temperature increase enhances the generated volumetric strain. Due to the temperature-induced decrease of the preconsolidation pressure, the hot specimen is closer to the normally consolidated state. The plasticity appears, therefore, faster in the hot sample than in the cold sample. Through the hardening process, this increase in the plasticity produces an increase in the contractile plastic volumetric strain.

This academic example shows that the effects of temperature and suction on the evolutions of the generalized effective stress and preconsolidation pressure affect the shearing behaviour of soils, even if the critical state line remains unchanged (at least in the generalized effective stress reference).

6.3.4.3 *Validation on Sion silt*

The experimental program performed on Sion silt consists in a set of oedometric compression tests at various temperature and suction levels aiming to study the effect of T and s on the compressibility indices and on the preconsolidation pressure (Chapter 5). The oedometric compressions have been performed at two temperatures (22 and 80°C) and three suctions (0, 100 and 300 kPa). The compressibility indices have been calibrated from the test at ambient temperature under saturated conditions and are assumed to be unaffected by temperature and suction applied during the test. Because of the lack of experimental evidence of the effect of dry density and temperature on the retention capacity of Sion silt, the water retention curve has been assumed fixed, whatever the temperature and dry density state. The calibrated curve is shown in Figure 6.10 and compared with the available experimental data.

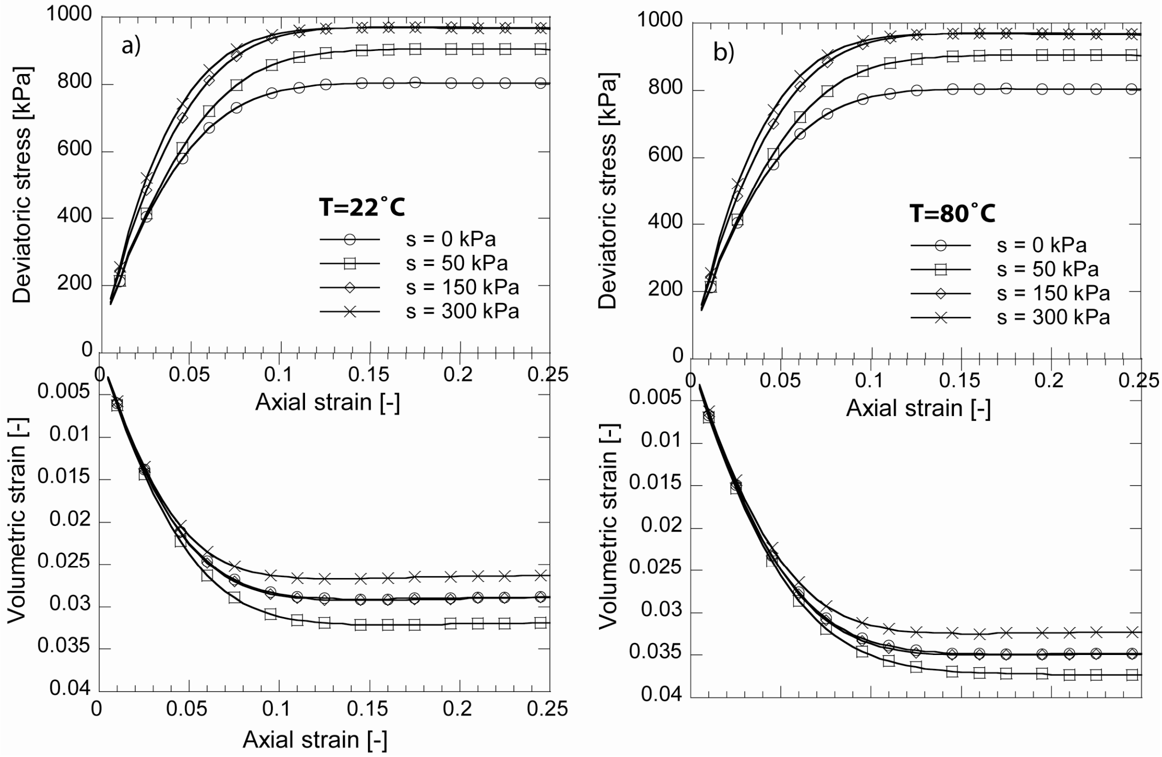

Figure 6.9 : Numerical simulation of triaxial compressions of Sion silt at four different suctions: a) ambient temperature (22°C); b) elevated temperature (80°C) (the deviatoric plastic parameters are fictive).

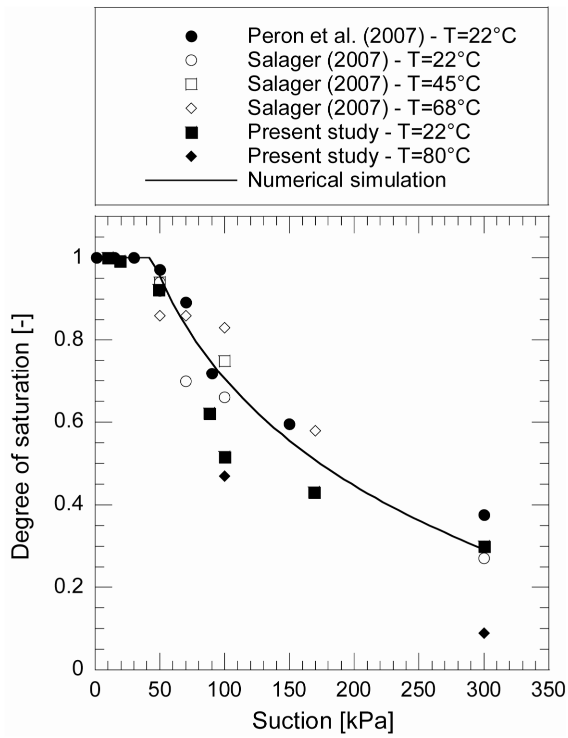

Figure 6.10 : Comparison between numerical simulation and experimental results of the water retention curve of Sion silt. The effects of temperature and dry density on the water retention curve have not been considered in the numerical curve.

The simulations of the oedometric compression tests start from the slurry state (i.e. quasi virgin state) in order to consider the entire THM history of the material before the final compression test under controlled temperature and suction conditions. The results of simulations compared with the experimental points are shown in Figure 6.11. The initial preconsolidation pressure of the slurry has been adjusted for each simulation to fit with experimental results. Indeed, during the setting up of the slurry in the oedometric cell, some little disturbances of the sample may lead to a slight overconsolidation of the specimen, which is different for each test.

In order to focus on the compression curves obtained under controlled temperature and suction conditions, the curves related to the final compression stages are presented in Figure 6.12. Those curves show the ability of ACMEG-TS to consider the shift of the normally consolidated line with temperature and suction change. Even if those effects are quite slight in such silty materials, the results appear to exhibit normally consolidated lines that move forward with decreasing temperature and/or increasing suction. The slope of the normally consolidated line is relatively well reproduced by the model, which is unaffected by temperature and suction. However, as mentioned in the interpretation of the compression curves (Section 5.3.6.1, Figure 5.19), the experimentally-observed compressibility of the material seems to decrease at a suction of 300 kPa, even in the generalized effective stress reference. This fact is not considered by the model, which means that the predicted vertical strains are slightly overestimated at a suction of 300 kPa.

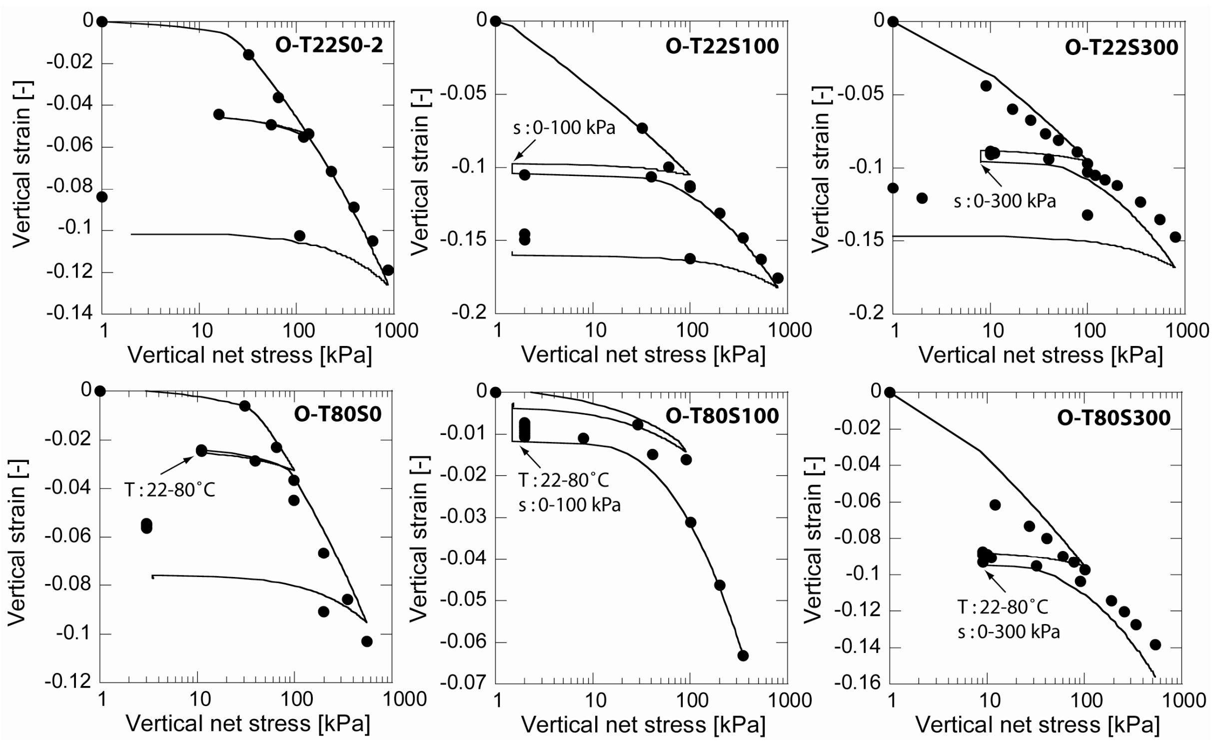

Figure 6.11 : Comparison between numerical simulations and experimental results of the set of oedometric compression tests on Sion silt, starting from the slurry state.

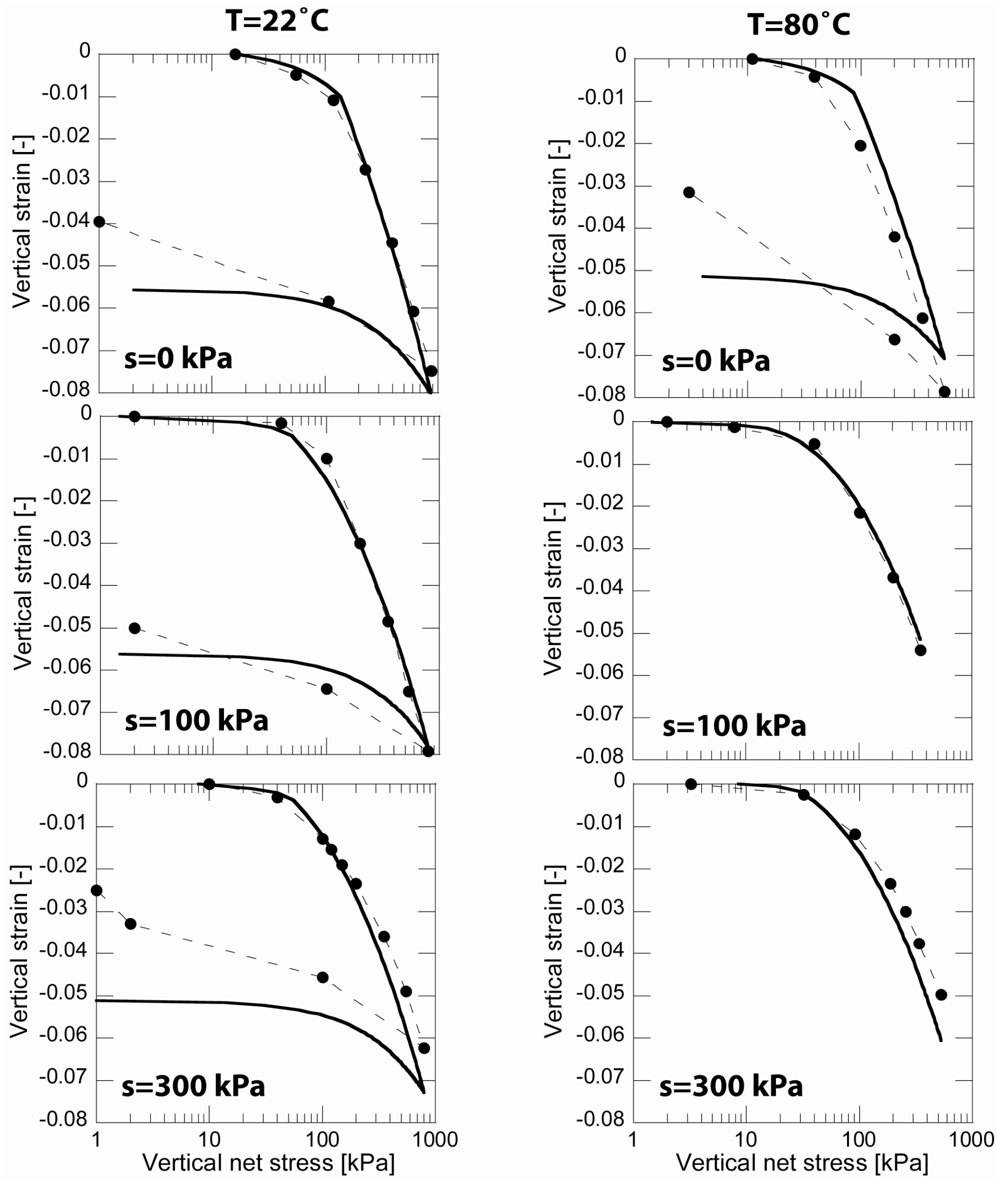

Figure 6.12 : Comparison between numerical simulations and experimental results of the set of oedometric compression tests on Sion silt. Focus on the final compression stages under controlled temperature and suction conditions.

6.3.4.4 *Validation on Febex bentonite*

The tests performed on Febex bentonite have an initial applied stress of 0.1 MPa and a compaction suction of about 127 MPa. In this set of experiments, 13 tests were simulated (ten from Lloret et al. (2004) and three from Romero et al. (2005)) (Figure 6.13). Of these tests, six were used to calibrate parameters (compression under saturated conditions (1) and under a suction of 14 MPa (3), compression at a suction of 127 MPa and 50 °C (6), drying at ambient temperature at two different densities (7) and (10) and at 60 °C (9)). The simulation results of these six tests are of back-predictions while the other eight are blind simulations. The material parameters used in this numerical modelling are given in Table 6.1.

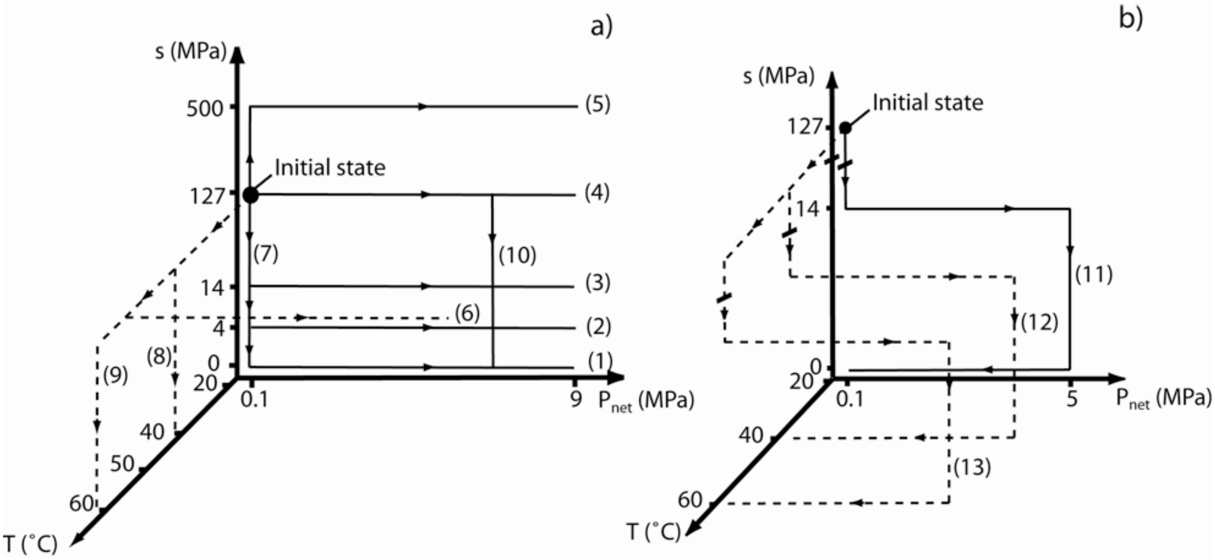

Figure 6.13 : Combined temperature, suction and mechanical experimental paths on Febex bentonite from (a) Lloret et al. (2004) and (b) Romero et al. (2005). Each test is numbered between brackets. References are made to the numbers between brackets in Figure 6.14 through Figure 6.16.

Figure 6.14a compares the numerical simulations with experimental results for oedometric compression tests at ambient temperature and 5 different suctions. The initial strain observed at 0.1 MPa net stress is due to the suction path from 127 MPa to the suction applied during compression. The subsequent compression paths clearly show the enhancement of the elastic domain with increased suction. The results of tests (1) and (3) were used to calibrate the material parameters, while simulations of the three others tests are blind predictions. Note that pure water is not able to handle very high tensions. Consequently, the case with suction at about 500 MPa challenges the validity of the concept of generalized effective stress framework, which may explain the model overestimation of the initial strain to reach this suction.

Figure 6.14b reproduces the numerical simulation of oedometric compression tests at two temperatures for natural hydroscopic suction (127 MPa). The initial strain observed for path (6) is due to the temperature increase and is governed by the thermal expansion coefficient. Figure 6.15 underscores the effect of temperature and dry density on the retention properties of the material. Figure 6.15a reproduces the retention curve observed for wetting at three different temperatures and compares results with numerical simulations. In the $(S_r - \ln s)$ plane, the shift of the wetting curve to the left with increased temperature is well reproduced by the model. Figure 6.15b illustrates water retention hysteresis in addition to the effect of density. At a given suction, the wetting path occurs at lower degree of saturation than the drying paths, which is representative of the hysteretic response of soil in the ($S_r - \ln s$) plane. For the simulation of test (10), a preliminary volumetric strain of 3%, corresponding to an increase in the dry density from 1.65 to 1.7 kg/m^3, induces a shift to the right of the subsequent wetting line; thus, the denser the soil, the higher the degree of saturation for the same suction.

The experimental paths of the results presented in Figure 6.16 can be divided into five steps: temperature application, wetting from a suction of 127 MPa to 14 MPa, application of a mechanical load from 0.1 MPa to 5 MPa net vertical stress, wetting to a suction of 0.1 MPa and finally mechanical unloading. As shown along path (6) (Figure 6.14b), at low external stress the temperature increase induces an elastic mechanical response of the bentonite (dilatation). Swelling is produced along the wetting paths, and the progressive change of the compression slope under oedometric compression mirrors the elasto-plastic behaviour. During subsequent wetting, the ACMEG-TS response exhibits a combination of elastic swelling and plastic collapse. The mechanisms governing this response are similar to those explained in Section 6.3.3.1. The experimental results do not exhibit such distinct collapse and swelling phases, but the global experimental strain throughout the wetting process fits well with the simulations. Finally, mechanical unloading takes place elastically. These complex combined temperature, suction and mechanical stress loadings prove the validity of the ACMEG-TS model.

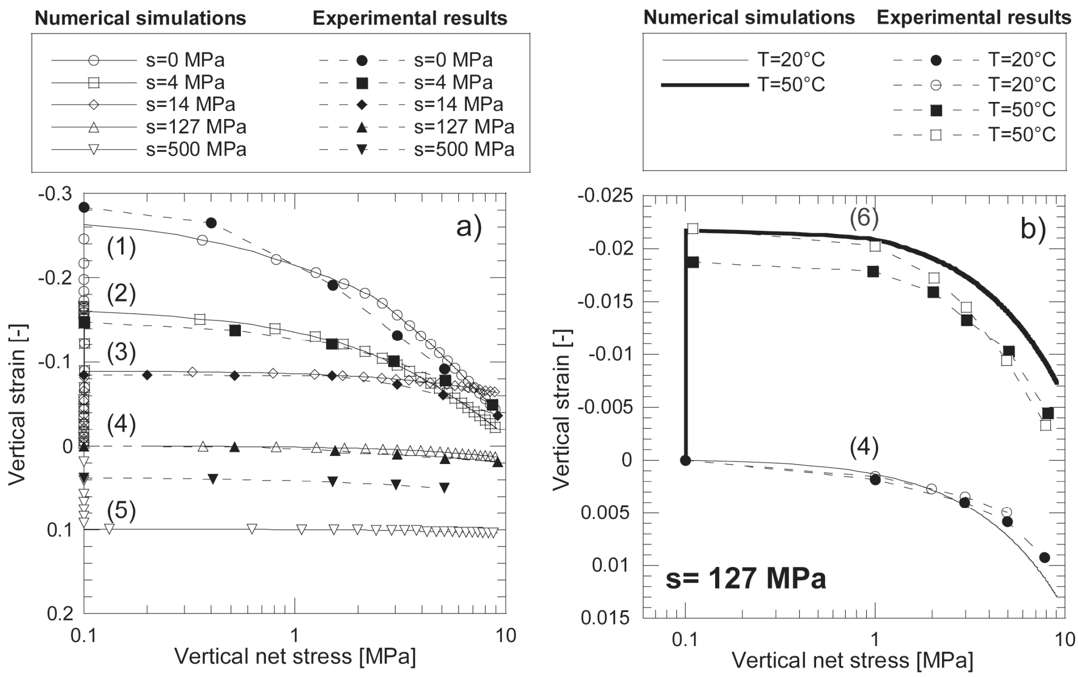

Figure 6.14 : Comparison between numerical simulations and experimental results on FEBEX bentonite – Oedometric compressions: (a) at ambient temperature and different suctions; (b) at 127 MPa of suction and two different temperatures.

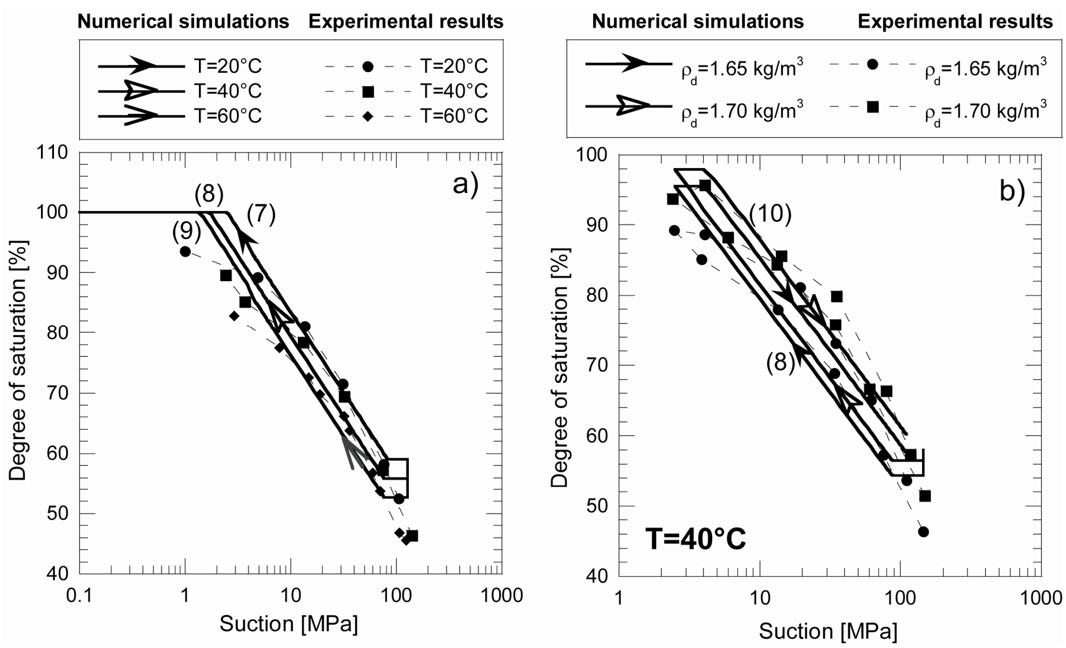

Figure 6.15 : Comparison between numerical simulations and experimental results on FEBEX bentonite – Retention curves: (a) at three different temperatures; (b) at two different dry densities.

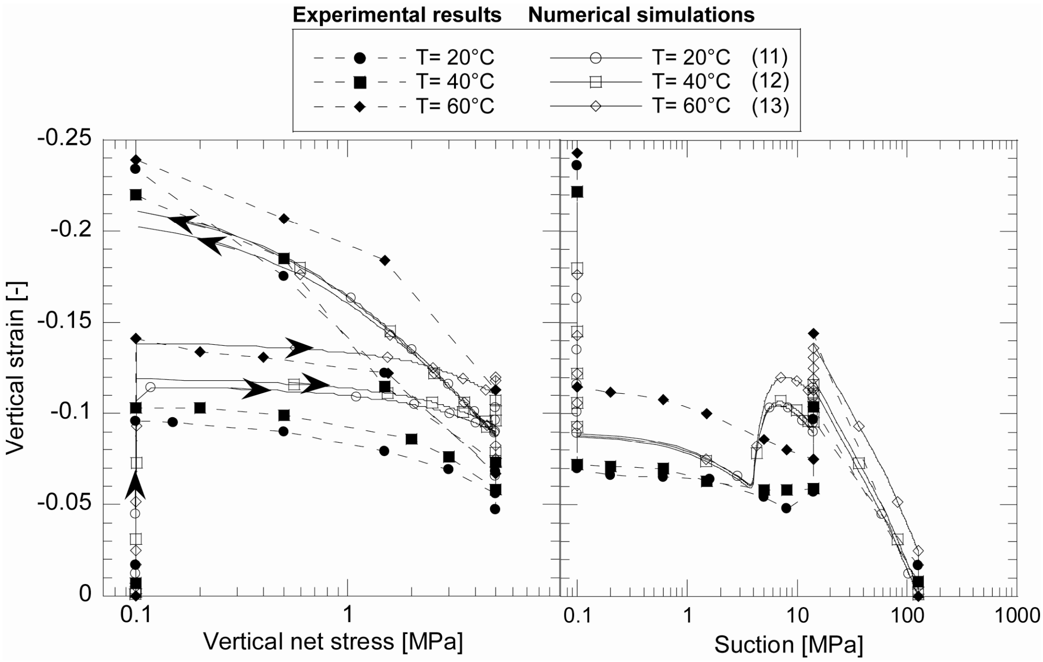

Figure 6.16 : Comparison between numerical simulations and experimental results on FEBEX bentonite – combined temperature, suction and mechanical paths.

6.3.4.5 *Validation on MX80 bentonite*

Table 6.2 reports the paths of tests on MX80 bentonite simulated with ACMEG-TS. Before the thermo-mechanical paths mentioned, the tests begin with applying suction from the initial compaction suction of 80 MPa, corresponding to a degree of saturation of 0.38. The tests (a), (b), (e) and (h) were chosen to calibrate the material parameters. The results of these tests were then back-predicted. The others tests were blindly simulated and compared with experimental results.

In this experimental program, the effect of the dry density on water retention information ($(S_r - s)$ relationship) is not available. The parameters of the water retention response (Table 6.1), at a given dry density were deduced from the water content versus suction and the void ratio versus suction relationships given by Tang (2005). Moreover, the effect of the dry density on the retention properties was assumed to be in agreement with the experimental observations of Cuisinier and Laloui (2004). These authors noted that no water is expelled during mechanical compression of compacted material under unsaturated conditions. Due to the double structure of the material, only the macropores collapse during a compression test. At high suctions, these pores are drained (without water). Therefore, the reduction in size of these pores does not induce water outflow. This consideration allowed us to fix the parameter θ_e, which determines the effect of the dry density on the retention curve. All the material parameters of MX80 bentonite are given in Table 6.1.

Figure 6.17 shows the water retention response of MX80 along a wetting path from the initial compaction suction (80 MPa) to 0.1 MPa. These simulation results are compared with the available experimental data.

Test number	Suction [MPa]	Successive TM paths		
(a)	39	T= 23.7-70-23.7 °C	p_{net}= 0.1-50-0.1 MPa	
(b)	39	p_{net}= 0.1-50-0.2 MPa		
(c)	39	T= 25-60 °C	p_{net}= 0.1-50-0.2 MPa	
(d)	39	T= 22.5-38.4 °C	p_{net}= 0.1-50-0.2 MPa	
(e)	110	p_{net}= 0.1-50-0.2 MPa		
(f)	110	T= 24.8-58 °C	p_{net}= 0.1-50-0.2 MPa	
(g)	39	p_{net}= 0.1-5 MPa	T= 24.9-80.5-60 °C	
(h)	9	p_{net}= 0.1-50-5-50 MPa		
(i)	9	T= 25-80-25-80 °C	p_{net}= 0.1-5 MPa	
(j)	110	p_{net}= 0.1-5 MPa	T= 22.5-80-22.5 °C	p_{net}= 5-40 MPa
(k)	110	p_{net}= 0.1-20 MPa	T= 24.9-80-24.9 °C	p_{net}= 20-30 MPa

Table 6.2 : Combined temperature, suction and mechanical experimental paths on MX80 bentonite (Tang, 2005). Each test is listed with letters between brackets. References are made to the letters between brackets in Figure 6.18 through Figure 6.20.

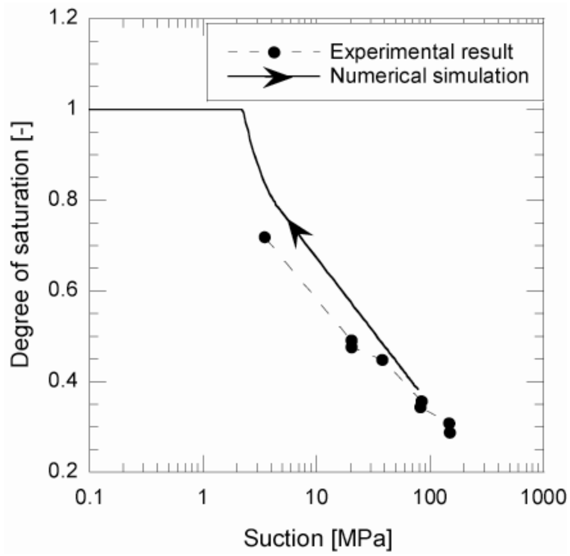

Figure 6.17 : Comparison between numerical simulation and experimental results (Tang, 2005) on MX80 bentonite – Retention curve on a wetting path. The experimental points were deduced from the water content and void ratio evolution during wetting.

Figure 6.18 compares numerical simulations with experimental results of isotropic compressions at ambient temperature for 3 different suctions. These three tests were used to calibrate model parameters. One can observe a significant increase of rigidity of MX80 bentonite with increased suction. This effect is quite well reproduced by ACMEG-TS due to the two suction contributions. First, through non-linear elasticity, an increase of suction means an increase in the generalized effective mean stress and then an increase in the bulk modulus. Second, the higher the suction, the larger the isotropic elastic domain, because of the effect of suction on the preconsolidation pressure (Equation (6.4)).

For lower suction (s= 9 MPa), the numerical simulations do not agree with experimental results for net stresses over 10 MPa. This is probably due to the double structure of MX80 bentonite induced by the fabrication process (compaction). At low suction, this compacted soil has two ranges of pore size, micro-pores and macro-pores. For low net stress, strain is induced by the collapse of macro-pores, so the soil rigidity is governed by the macrostructure. In a second phase, for higher net stress, all the macro-pores are collapsed, and strain is induced by rearrangement of particles inside aggregates (microstructure), which is characterized by a second rigidity. The

ACMEG-TS model does not consider this phenomenon, which is specific to double-structured soils. In the present case, the material parameters were calibrated with respect to the behaviour of the macrostructure.

Figure 6.19 underlines the effect of temperature on the isotropic compression response at suctions of 9 MPa, 39 MPa and 110 MPa, respectively. The temperature effect is clearly much lower than that of suction, presented in Figure 6.18. Indeed, the only perceptible effect is a slight shift of the normally consolidated line to the left when temperature increases. The volumetric responses of MX80 submitted to temperature changes are presented in Figure 6.20, for suctions of 9 MPa, 39 MPa and 110 MPa, under different constant net mean stresses. As already explained in Section 3.5.3.2, two main behaviours can be observed according to the overconsolidation ratio (OCR) of the soil. Thermal compaction is produced for OCR close to 1, while dilatation occurs for higher OCR. In this context, a suction increase decreases the thermal collapse tendency through the drastic increase of preconsolidation pressure with suction, inducing an increase of OCR. In spite of discrepancies with experimental results, ACMEG-TS is able to depict these complex mechanisms satisfactorily.

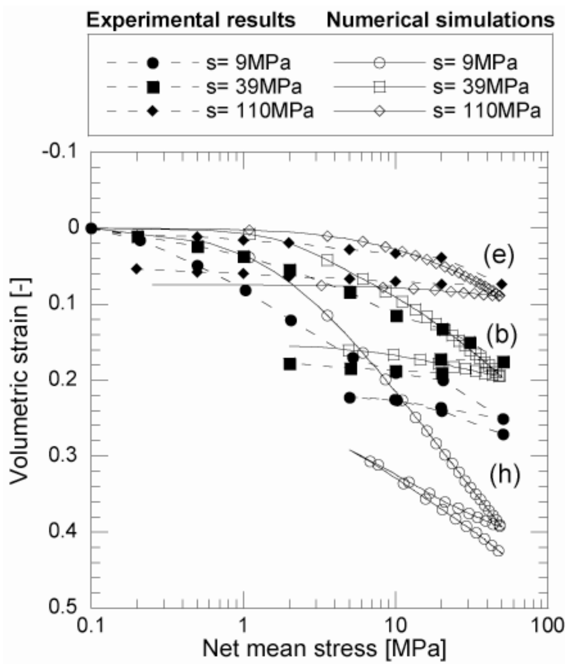

Figure 6.18 : Comparison between numerical simulations and experimental results (Tang, 2005) on MX80 bentonite – Isotropic compression tests at ambient temperature and 3 different suctions.

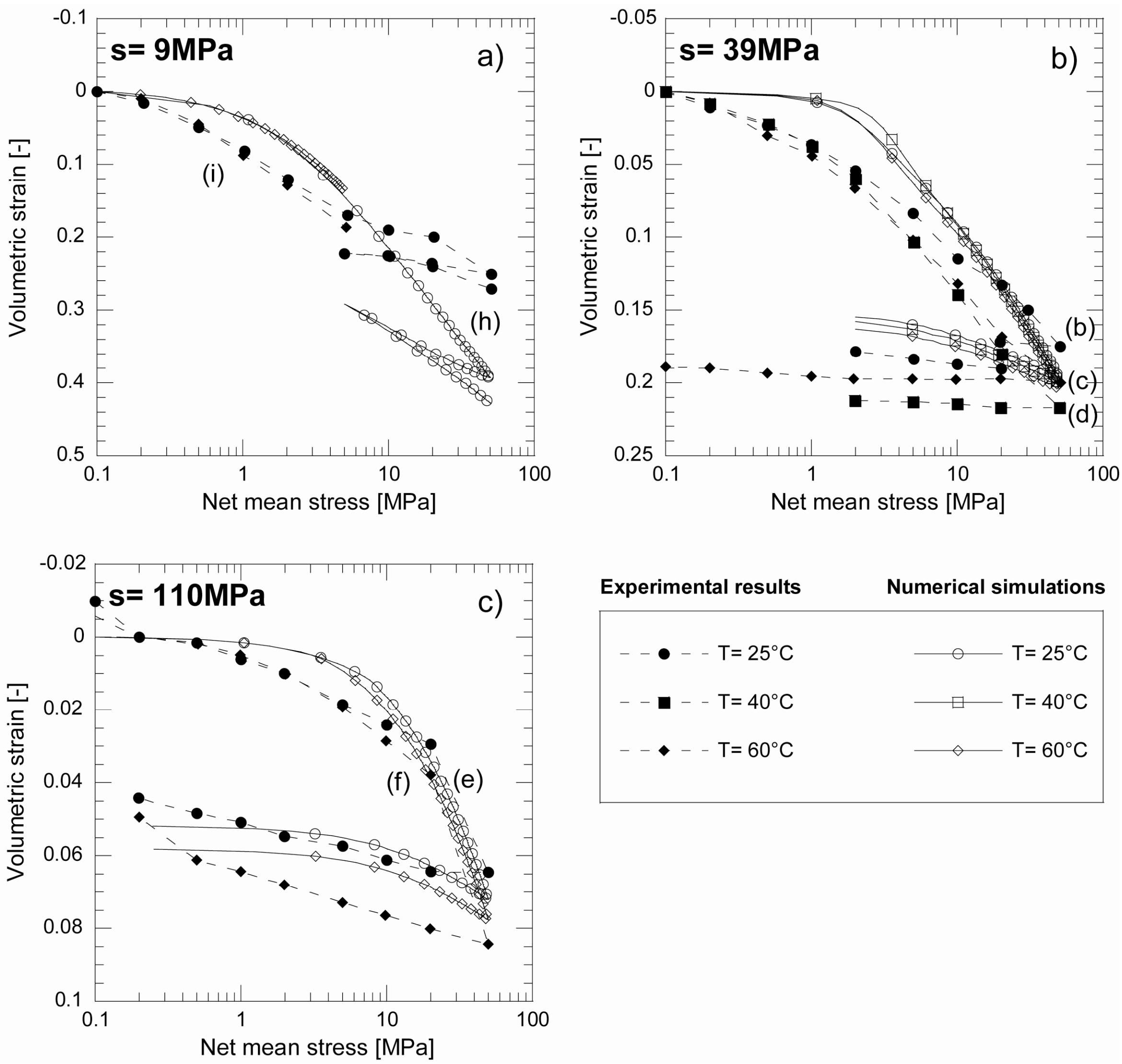

Figure 6.19 : Comparison between numerical simulations and experimental results (Tang, 2005) on MX80 bentonite – Isotropic compression tests at different temperatures and at suctions of (a) 9 MPa; (b) 39 MPa; (c) 110 MPa.

6.4 Conclusions

On the basis of the non-isothermal model for saturated soils developed in Chapter 3, a highly-coupled constitutive model dealing with non-isothermal and unsaturated conditions, named ACMEG-TS, has been developed. This model is based on two interrelated mechanical and water retention constitutive schemes. The single stress approach used (generalized effective stress) comprises a number of intrinsic thermo-hydro-mechanical connections that couple the schemes. Moreover, the water retention condition influences the isotropic mechanical behaviour by its effect on the preconsolidation pressure. Inversely, the mechanical state can modify the water retention curve (via the evolution of the air-entry suction). These two-way couplings depend on temperature.

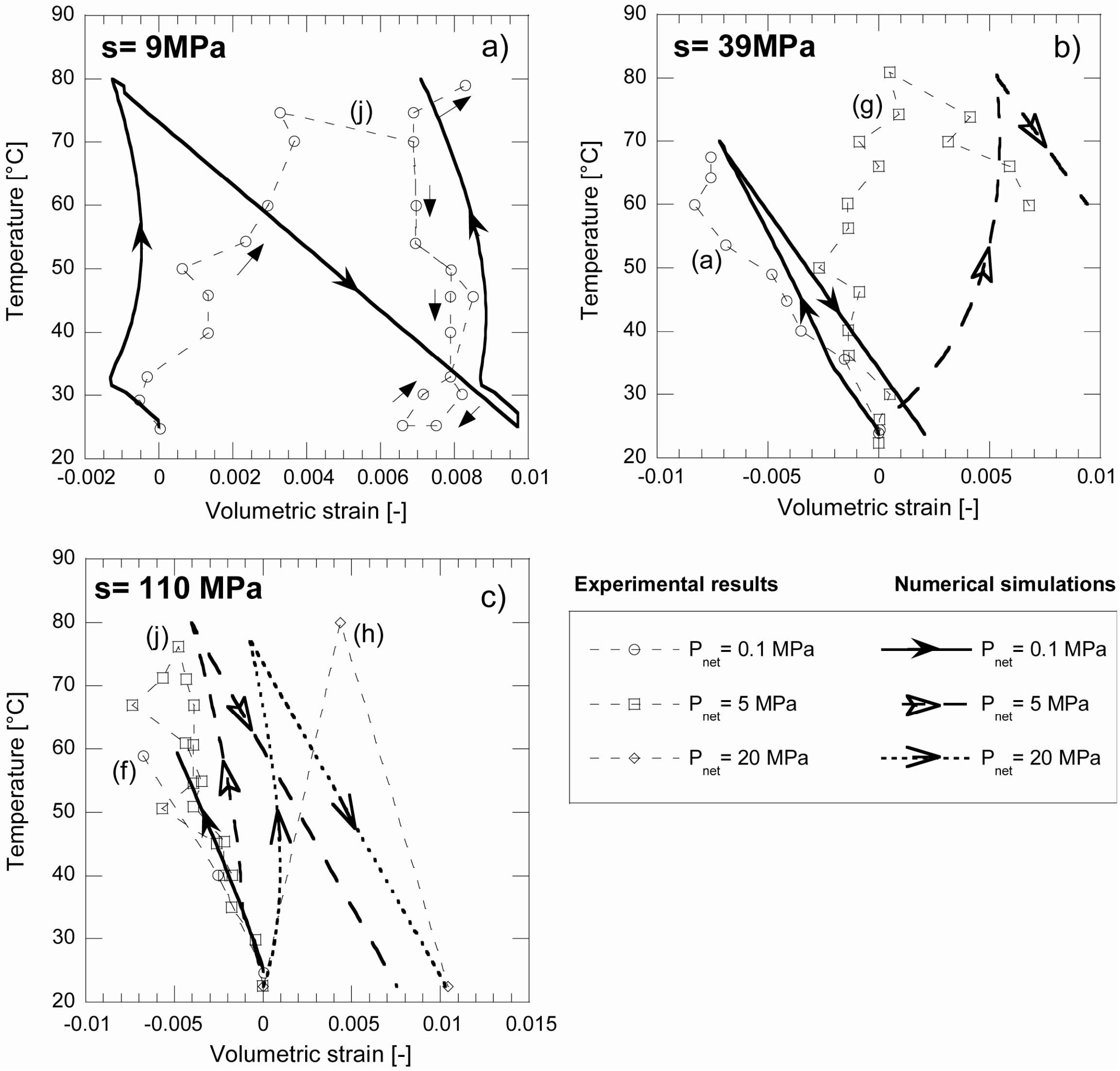

Figure 6.20 : Comparison between numerical simulations and experimental results (Tang, 2005) on MX80 bentonite – Thermal cycle at different net stresses and at suctions of (a) 9 MPa; (b) 39 MPa; (c) 110 MPa.

The constitutive relations for both schemes have been described. The mechanical part of the model is an extension to unsaturated conditions of the previously addressed ACMEG-T model, which uses two hardening mechanisms connected through volumetric plastic strain to consider the soil plasticity. As far as the water retention scheme is concerned, elasto-plasticity is used to describe the hysteretic behaviour and its dependency on the temperature and the dry density of the materials.

The proposed model has been validated by predictions of experimental results on three fine-grained materials: the Sion silt tested in Chapter 5 and two compacted clays (Febex and MX80 bentonites). These numerical simulations show that ACMEG-TS can reproduce the mechanical response of soils subject to coupled temperature, suction and external stress variations. Considering the phenomena induced by the variations of the three variables (temperature, suction and mechanical stress) as interconnected phenomena, ACMEG-TS constitutes an effective constitutive tool for modelling geomechanical problems governed by highly-coupled thermo-hydro-mechanical processes.

Section III

Application to nuclear waste disposal

Chapter 7

THM governing equations

The engineering problems in the field of Environmental Geomechanics generally involve a variety transport phenomena occurring in porous multiphase materials. Because the phases interact with each other, coupled phenomena are a very characteristic feature of these problems. […]. In addition, in Environmental Geomechanics, it is not uncommon to find nonisothermal situations and therefore, attention should be given to the mechanisms involving heat transport. The incorporation of a thermal component gives rise to numerous additional interactions between phenomena. Inevitably, a high degree of complexity ensues.[1]

[1] Gens A. and Olivella S. (2001). Clay barrier in radioactive waste disposal. *Revue Française de Génie Civil*, 5(6): 845-856.

7.1 Introduction

The finite element method is an efficient tool used to study the THM behaviour of geomaterials surrounding deep geological repositories for radioactive waste. As extensively discussed in the previous chapters, the combined effect of temperature and suction variations substantially affect the stress-strain behaviour of geomaterials. The multi-physics processes that must be considered include drying and wetting in non-isothermal conditions and heating-cooling in unsaturated conditions. In addition, thermo-hydraulic couplings such as temperature-induced water evaporation or condensation are of paramount importance. Therefore, these investigations require a numerical tool that considers the medium as a deformable three-phase medium in which heat and mass transfers occur, with possible exchanges between gas and water phases (Lewis and Schrefler, 1987; Olivella et al., 1994; Collin et al., 2002).

In this framework, the ACMEG-TS constitutive model, developed in the previous chapters, has been implemented in the finite element code LAGAMINE, developed at University of Liege (Charlier, 1987; Charlier et al., 2001; Collin et al., 2002; Collin, 2003). In this chapter, the governing balance equations are first introduced. Then, the constitutive relationships that assist in relating the balance laws with the nodal unknowns are presented. The finite element integration is briefly addressed. Implementation of the ACMEG-TS law in LAGAMINE is validated by comparison of numerical predictions from LAGAMINE and the solver LAWYER. Finally, the tool is validated by the means of a simple non-isothermal fully saturated consolidation, for which the numerical solution of the linear thermo-mechanical problem is known.

7.2 Governing equations

7.2.1 Introduction

Under unsaturated and non-isothermal conditions, the balance equations are obtained by considering that the soil is composed of solid matrix and voids filled with liquid and gas phases. The liquid phase is assumed to contain two species: liquid water and dissolved air. Similarly, the gas phase is composed of dry air and water vapour. Temperature changes in the medium may modify the liquid-vapour equilibrium. The distinction and the repartition between phases (liquid and gas) and species (air and water) are depicted in Figure 7.1.

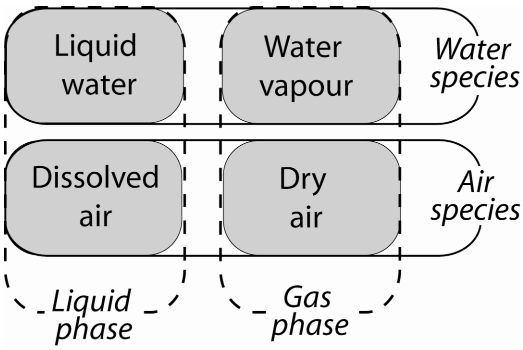

Figure 7.1 : Definition of the phases and chemical species that interact in the pore space (from Collin, 2003)

To uniquely describe the state of the material, four primary state variables are needed: gas pressure p_g, water pressure p_w, temperature T, and displacement vector $\mathbf{u}$. The intrinsic solid phase component is assumed to be incompressible (incompressible grains) while the water phase is slightly compressible. The solid, liquid, and water phases are assumed in thermal equilibrium, and a unique temperature is defined at each node. This assumption is justified by the relatively slow kinematics of the governing processes which allow a continuous thermal equilibrium between phases.

The compositional approach (Panday and Corapcioglu, 1989) is used to write the balance equations, which means that the mass balances are described for the components (also called species) present in the mixture rather than for the phases. Therefore, the conservation of mass of each chemical species (water and air) is assumed. Using this approach, the phase exchange term will cancel in the balance equations. In the following equations, the subscripts l, g, w, da, a, and v are related to the liquid phase, the gas phase, the liquid water, the dissolved air in water, the dry air, and the water vapour, respectively. The governing equations presented below are taken from Collin et al. (2002), Collin (2003) and Collin et al. (2006) where further details can be found.

7.2.2 Equilibrium and balance equations

The equilibrium and balance equations, as well as the water and heat flows, are expressed in the moving current configuration through a Lagrangian actualised formulation (Charlier, 1987). According to these assumptions, the mass balance equation of the solid skeleton is necessarily met. For a given mixture volume V, the mass balance equation reads (Collin et al., 2006):

$$\frac{\partial \rho_s (1-n) V}{\partial t} = 0 \tag{7.1}$$

where ρ_s is the density of solid grains, n the soil porosity, and t the time.

The mass conservation equations for the water and gas species are, respectively:

$$\underbrace{\frac{\partial}{\partial t}(\rho_w n S_r) + div(\rho_w \mathbf{f_l}) - Q_w}_{\text{Liquid water}} + \underbrace{\frac{\partial}{\partial t}(\rho_v n(1-S_r)) + div(\mathbf{i_v} + \rho_v \mathbf{f_g}) - Q_v}_{\text{Water vapour}} = 0 \tag{7.2}$$

$$\underbrace{\frac{\partial}{\partial t}(\rho_a n(1-S_r)) + div(\rho_a \mathbf{f_g} + \mathbf{i_a}) - Q_a}_{\text{Dry air in gas phase}} + \underbrace{\frac{\partial}{\partial t}(\rho_a H_s n S_r) + div(\rho_a H_s \mathbf{f_l}) - Q_{da}}_{\text{Dissolved air in water}} - = 0 \tag{7.3}$$

where ρ_w, ρ_v, and ρ_a are the bulk density of liquid water, water vapour, and dry air. $\mathbf{f_l}$ and $\mathbf{f_g}$ are the macroscopic velocity of the liquid and gas phases, respectively. $\mathbf{i_v}$ and $\mathbf{i_a}$ are the nonadvective flux of water vapour and dry air. S_r is the degree of saturation. The Henry's coefficient H_s, defining the proportion of dissolved air in the liquid phase, is taken equal to 0.017. Q_w, Q_v, Q_a, and Q_{da} are volume sources of liquid water, water vapour, dry air, and dissolved air in water, respectively.

The energy balance equation of the mixture has the following form:

$$\underbrace{\frac{\partial S_T}{\partial t}+L\frac{\partial}{\partial t}\left(\rho_v n\left(1-S_r\right)\right)}_{\text{Heat storage}}+\underbrace{div\left(\mathbf{f_T}\right)+L\frac{\partial}{\partial t}\left(\mathbf{i_v}+\rho_v\mathbf{f_g}\right)}_{\text{Heat transfer}}-Q_T=0 \tag{7.4}$$

where $\mathbf{f_T}$ is the heat flow and Q_T is a volume heat source. L is the latent heat of water vaporisation. The enthalpy of the system S_T is given by the sum of each component's enthalpy:

$$S_T=\rho C_p(T-T_0) \tag{7.5}$$

where ρ and C_p are the density and the specific heat of the mixture (solid matrix with voids filled by gas and liquid), respectively. Those parameters are deduced from the properties of each phase:

$$\rho C_p=nS_r\rho_w c_{p,w}+\left(1-n\right)\rho_s c_{p,s}+n\left(1-S_r\right)\rho_a c_{p,a}+n\left(1-S_r\right)\rho_v c_{p,v} \tag{7.6}$$

where ρ_s is the soil grain bulk density and $c_{p,w}$, $c_{p,s}$, $c_{p,a}$, and $c_{p,v}$ are the specific heat of liquid water, solid, dry air, and water vapour respectively.

The soil equilibrium equation is given by:

$$div\left(\boldsymbol{\sigma}\right)+\mathbf{b}=0 \tag{7.7}$$

where $\boldsymbol{\sigma}$ is the total (Cauchy) stress tensor, with compressive stress taken as positive, and $\mathbf{b}$ is the body force vector which is equal to $\rho\mathbf{g}$ if the only body force is gravity.

7.2.3 Constitutive relations

The conservation equations which govern the THM equilibrium of the system (Equations (7.1) to (7.7)) need to be expressed in terms of the primary state variables ($\mathbf{u}$, p_w, p_g, and T), after introduction of the constitutive relationships detailed below.

The liquid water bulk density depends on the pore water pressure p_w and temperature T through the water bulk modulus χ_w and the volumetric water thermal expansion coefficient β'_w:

$$\rho_w=\rho_{w0}\left(1+\frac{p_w-p_{w0}}{\chi_w}-\beta'_w\left(T-T_0\right)\right) \tag{7.8}$$

where ρ_{w0}, p_{w0}, and T_0 are the initial values of water bulk density, pore water pressure, and temperature, respectively. The bulk density of the water vapour is determined through the following equation:

$$\rho_v=\exp\left(\frac{\left(p_w-p_g\right)M_v}{R\,T\rho_w}\right)\frac{p_{v,0}M_v}{R\,T} \tag{7.9}$$

where p_w and p_g are the liquid water and gas pressures, respectively, M_v is the vapour molar mass (=0.018 kg/mol), T is temperature expressed in Kelvin, and $p_{v,0}$ is the saturated vapour pressure given by an experimental expression depending on temperature (Collin, 2003; Gerard et al., 2008):

$$p_{v,0} = a\exp\left(-b/T\right) \tag{7.10}$$

with $a = 112659MPa$ and $b = 5192.74K$ for temperature range between 273 K and 373 K.

The bulk density of dry air can be deduced considering that the gas phase is an ideal gas to which the Dalton law can be applied:

$$p_g = p_a + p_v \tag{7.11}$$

Consequently, the bulk density of dry air is:

$$\rho_a = \frac{p_a M_a}{R\,T} = \frac{\left(p_g - p_v\right)M_a}{R\,T} = \frac{p_g M_a}{R\,T} - \frac{\rho_v M_a}{M_v} \tag{7.12}$$

where M_a is the dry air molar mass (= 28.8 10^{-3} kg/mol).

The liquid phase motion is governed by the Darcy's law:

$$\mathbf{f_l} = -\frac{\mathbf{k_w}}{\mu_w}\left(\mathbf{grad}\left(p_w\right) + g\rho_w\mathbf{grad}\left(y\right)\right) \tag{7.13}$$

where $\mathbf{k_w}$ is the tensor of intrinsic water permeability, g the gravity acceleration, y the vertical, upward directed coordinate, and μ_w the dynamic viscosity of the water. This last parameter is assumed linearly dependent on the temperature:

$$\mu_w = \mu_{w0}\left(1 - \alpha_{w,T}\left(T - T_0\right)\right) \tag{7.14}$$

where μ_{w0} is the dynamic viscosity of water at initial temperature T_0 and $\alpha_{w,T}$ is a material parameter. In Equations (7.13) and (7.14), it is assumed that the ρ_w, k_w, and μ_{w0} are unaffected by the amount of dissolved air in the liquid phase.

The gas phase velocity is governed by the generalised Darcy's law for a multiphase medium:

$$\mathbf{f_g} = -\frac{\mathbf{k_g}}{\mu_g}\left(\mathbf{grad}\left(p_g\right) + g\rho_g\mathbf{grad}\left(y\right)\right) \tag{7.15}$$

where $\mathbf{k_g}$ is the tensor of intrinsic gas permeability, and μ_g is the dynamic viscosity of the gas. This last parameter is assumed to be linearly dependent on the temperature:

$$\mu_g = \mu_{g0}\left(1 - \alpha_{g,T}\left(T - T_0\right)\right) \tag{7.16}$$

where μ_{g0} is the dynamic viscosity of the gas at initial temperature T_0 and $\alpha_{g,T}$ is a material parameter.

The velocity of water vapour diffusion is related to the air bulk density gradient:

$$\mathbf{i_v} = n(1-S_r)\tau D\rho_g \mathbf{grad}\left(\frac{\rho_a}{\rho_g}\right) \tag{7.17}$$

where D is the air diffusion coefficient. The LAGAMINE finite element code uses the following expression based on the work of Philip and De Vries (1957):

$$D = 5.893\ 10^{-6}\frac{T^{2.3}}{p_g} \tag{7.18}$$

where D, T, and p_g are expressed in m^2/s, Kelvin, and Pascal, respectively. τ is the tortuosity of the material.

The heat transport is governed by conduction and convection:

$$\mathbf{f_T} = -\Gamma\mathbf{grad}(T) + c_{p,w}\rho_w\mathbf{f_w} + c_{p,a}(\mathbf{i_a} + \rho_a\mathbf{f_g}) + c_{p,v}(\mathbf{i_v} + \rho_v\mathbf{f_g}) \tag{7.19}$$

where Γ is the thermal conductivity of the mixture as deduced from the thermal conductivity of each phase:

$$\Gamma = \lambda_s(1-n) + \lambda_w nS_r + \lambda_g n(1-S_r) \tag{7.20}$$

where λ_s, λ_w, and λ_a are the thermal conductivity of solid, liquid water, and gas phase, respectively. Notice that, since the current configuration is defined following the skeleton movement, the thermal convection effect is implicitly taken into account.

The behaviour of the solid matrix is assumed to be governed by the generalized effective stress tensor $\boldsymbol{\sigma}'$:

$$\boldsymbol{\sigma}' = \boldsymbol{\sigma} - p_g\mathbf{I} + S_r(p_g - p_w)\mathbf{I} \tag{7.21}$$

where $\mathbf{I}$ is the identity matrix.

In this Lagrangian approach, the Cauchy strain tensor is used:

$$\boldsymbol{\varepsilon} = \frac{1}{2}(\mathbf{L} - \mathbf{L^T}) \tag{7.22}$$

where $\mathbf{L} = \frac{\partial\mathbf{u}}{\partial\mathbf{X}}$ is the displacement ($\mathbf{u}$) gradient defined in the global axis ($\mathbf{X}$) in the moving current configuration (Charlier et al., 2001). This strain tensor is related to the generalized effective stress tensor through the mechanical constitutive model:

$$d\boldsymbol{\sigma}' = \mathbf{C} : d\boldsymbol{\varepsilon} \tag{7.23}$$

where $\mathbf{C}$ is the mechanical constitutive tensor. This last equation is written in incremental form due to the non-linear behaviour of the solid matrix.

7.3 Finite element formulation

As the aim of this dissertation is not the development of advance finite element tools, this section briefly reports the finite element formulation used in the numerical simulation performed with the LAGAMINE finite element code. This part is mainly based on the papers of Charlier et al. (2001) and Collin et al. (2002) in which more detailed explanations are given.

For the model closure, the initial and boundary conditions are needed (Lewis and Schrefler, 1987). The initial conditions specify the full fields of state variables at time $t = 0$ in the entire domain Ω and on its boundary as:

$$p_w = p_{w0}, \quad p_g = p_{g0}, \quad T = T_0, \quad \mathbf{u} = \mathbf{u}_0 \quad \text{on } \Omega \tag{7.24}$$

The boundary conditions can be of Dirichlet's type on $\partial\Gamma_\pi$ for $t \geq 0$:

$$p_w = \hat{p}_w \text{ on } \partial\Gamma_w, \quad p_g = \hat{p}_g \text{ on } \partial\Gamma_g, \quad T = \hat{T} \text{ on } \partial\Gamma_T, \quad \mathbf{u} = \hat{\mathbf{u}} \text{ on } \partial\Gamma_u \tag{7.25}$$

or of Neumann's type on $\partial\Gamma_\pi^f$ for $t \geq 0$:

$$f_w = \left[-\frac{\mathbf{k_w}}{\mu_w}\left(\mathbf{grad}\left(p_w\right) + g\rho_w \mathbf{grad}\left(y\right)\right)\right].\mathbf{n} \quad \text{on } \partial\Gamma_w^f \tag{7.26}$$

$$f_g = \left[-\frac{\mathbf{k_g}}{\mu_g}\left(\mathbf{grad}\left(p_g\right) + g\rho_g \mathbf{grad}\left(y\right)\right)\right].\mathbf{n} \quad \text{on } \partial\Gamma_g^f \tag{7.27}$$

$$f_T = -\Gamma \mathbf{grad}\left(T\right).\mathbf{n} \quad \text{on } \partial\Gamma_T^f \tag{7.28}$$

$$\boldsymbol{\sigma}.\mathbf{n} = \mathbf{t} \quad \text{on } \partial\Gamma_u^f \tag{7.29}$$

where $\mathbf{n}$ is the unit normal vector. f_w, f_g, and f_T are the imposed water, gas, and heat fluxes, respectively. $\mathbf{t}$ is the imposed traction vector related to the total Cauchy stress tensor $\boldsymbol{\sigma}$. In addition, more complex conditions may be imposed at the boundary of the domain, such as unilateral contact with friction or interface behaviour conditions. Also, a thermal boundary condition considering radiation may be introduced.

A bi-dimensional large strain finite element is used (Charlier, 1987). As mentioned previously, that element possesses five degrees of freedom at each node: two displacements of the soil skeleton, a liquid water pressure, a gas (dry air + vapour) pressure, and a temperature. The elements used possess eight nodes and are isoparametric, that is to say that the coordinates, velocities, pore pressures (water and gas), and temperature are discretised by the same shape functions (Figure 7.2).

Numerical convergence to an accurate thermo-hydro-mechanical state is obtained through the stiffness matrix. At each calculation step, the THM state must respect the balance equations, (7.1) to (7.4), and the solid mechanics equilibrium (Equation (7.7)). These equations, also called field equations, are transformed into nodal values $\mathbf{F}$ (fluxes and forces) through interpolation functions. The internal and external nodal values are to be equal. If not, a new solution (that is, a new approximation of nodal fluid pressures, temperature, and displacements) has to be determined. Therefore, the nodal values at step *i*+1, $\mathbf{F}^{\mathbf{i+1}}$, are obtained from the value at step *i*, $\mathbf{F}^{\mathbf{i}}$, and a first-order prediction using the stiffness matrix $\mathbf{K}$:

$$\mathbf{F}^{\mathbf{i+1}} = \mathbf{F}^{\mathbf{i}} + \frac{\partial \mathbf{F}}{\partial \mathbf{x}} \Delta \mathbf{x} = \mathbf{F}^{\mathbf{i}} + \mathbf{K} \Delta \mathbf{x} \tag{7.30}$$

$\mathbf{x}$ is the vector of nodal values. The linearization of the problem induces an error in the prediction at step *i*+1 which is reduced until equilibrium is reached through an iterative procedure. A detailed integration procedure can be found in Gerard et al. (2008). The stiffness matrix associates the five degrees of freedom per node and can be schematised as follows (Collin et al., 2002):

$$\mathbf{K} = \begin{pmatrix} \underset{[2\times2]}{\mathbf{K_{MM}}} & \underset{[2\times1]}{\mathbf{K_{WM}}} & \underset{[2\times1]}{\mathbf{K_{GM}}} & \underset{[2\times1]}{\mathbf{K_{TM}}} \\ \underset{[1\times2]}{\mathbf{K_{MW}}} & \underset{[1\times1]}{\mathbf{K_{WW}}} & \underset{[1\times1]}{\mathbf{K_{GW}}} & \underset{[1\times1]}{\mathbf{K_{TW}}} \\ \underset{[1\times2]}{\mathbf{K_{MG}}} & \underset{[1\times1]}{\mathbf{K_{WG}}} & \underset{[1\times1]}{\mathbf{K_{GG}}} & \underset{[1\times1]}{\mathbf{K_{TG}}} \\ \underset{[1\times2]}{\mathbf{K_{MT}}} & \underset{[1\times1]}{\mathbf{K_{WT}}} & \underset{[1\times1]}{\mathbf{K_{GT}}} & \underset{[1\times1]}{\mathbf{K_{TT}}} \end{pmatrix} = \begin{pmatrix} \frac{\partial \mathbf{F_M}}{\partial \mathbf{x_M}} & \frac{\partial \mathbf{F_M}}{\partial p_w} & \frac{\partial \mathbf{F_M}}{\partial p_g} & \frac{\partial \mathbf{F_M}}{\partial T} \\ \frac{\partial \mathbf{F_W}}{\partial \mathbf{x_M}} & \frac{\partial \mathbf{F_W}}{\partial p_w} & \frac{\partial \mathbf{F_W}}{\partial p_g} & \frac{\partial \mathbf{F_W}}{\partial T} \\ \frac{\partial \mathbf{F_G}}{\partial \mathbf{x_M}} & \frac{\partial \mathbf{F_G}}{\partial p_w} & \frac{\partial \mathbf{F_G}}{\partial p_g} & \frac{\partial \mathbf{F_G}}{\partial T} \\ \frac{\partial \mathbf{F_T}}{\partial \mathbf{x_M}} & \frac{\partial \mathbf{F_T}}{\partial p_w} & \frac{\partial \mathbf{F_T}}{\partial p_g} & \frac{\partial \mathbf{F_T}}{\partial T} \end{pmatrix} \tag{7.31}$$

where $\mathbf{F_M}$ represents the nodal mechanical force, $\mathbf{F_W}$ the nodal water flux, $\mathbf{F_G}$ the nodal gas flux, $\mathbf{F_T}$ the nodal thermal flux, and $\mathbf{x_M}$ the nodal displacements. The four mechanical, water flow, gas flow, and thermal sub-matrixes ($\mathbf{K_{MM}}$, $\mathbf{K_{WW}}$, $\mathbf{K_{GG}}$ and $\mathbf{K_{TT}}$) are classical. All the other sub-matrixes are coupling matrixes.

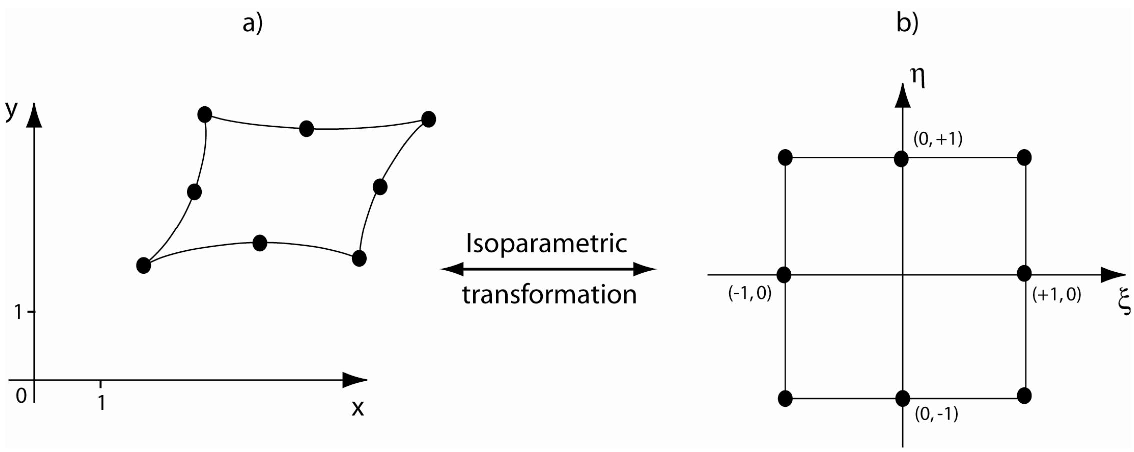

Figure 7.2 : Eight-noded bi-dimensional isoparametric element: (a) the finite element and (b) its corresponding parent element (from Collin, 2003).

7.4 Validation of implementation of the ACMEG-TS model

In order to validate the implementation of the ACMEG-TS constitutive model in the LAGAMINE finite element code, some validation simulations have been performed on one finite element of the LAGAMINE code and compared with the results obtained with the driver of the constitutive law, LAWYER, used in the previous chapters. The set of simulations that will be presented in Chapter 8 are used to compare the numerical results given by LAWYER and LAGAMINE. Those tests refer to selected laboratory tests on Boom clay: an isotropic consolidation test (Figure 7.3), two drained triaxial tests at two different confining pressures (Figure 7.4), and a thermomechanical test (Figure 7.5). In addition, Appendix D reports other comparisons of the numerical results obtained with both numerical tools on fictive thermo-hydro-mechanical paths. This series of numerical simulations validates the implementation on mechanical, thermal, and suction paths not only in terms of mechanical response but also concerning the water retention behaviour.

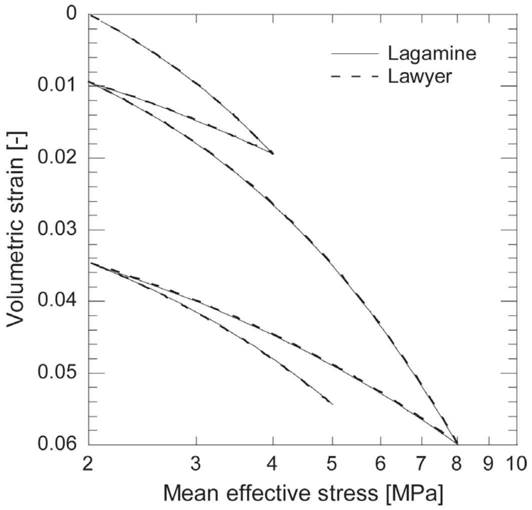

Figure 7.3 : Validation of the ACMEG-TS implementation in LAGAMINE. Comparison of numerical results of an isotropic compression test on Boom clay obtained with LAGAMINE and with the driver of the constitutive law LAWYER (TBoom 1, for comparison with experiment, see Figure 8.4).

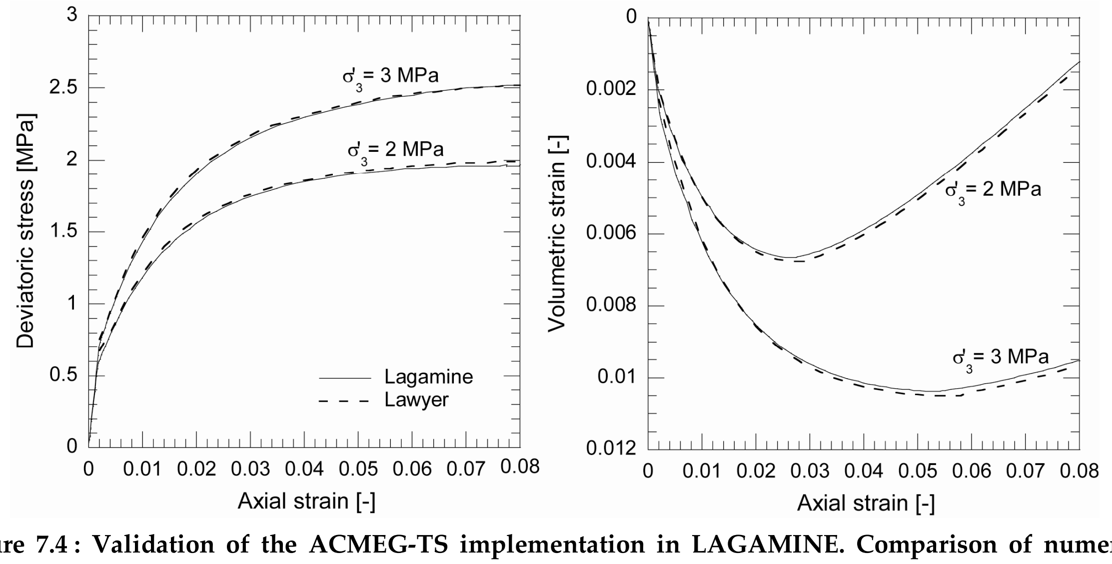

Figure 7.4 : Validation of the ACMEG-TS implementation in LAGAMINE. Comparison of numerical results of two triaxial tests on Boom clay obtained with LAGAMINE and with the driver of the constitutive law LAWYER (TBoom 2 and 3, for comparison with experiment, see Figure 8.5).

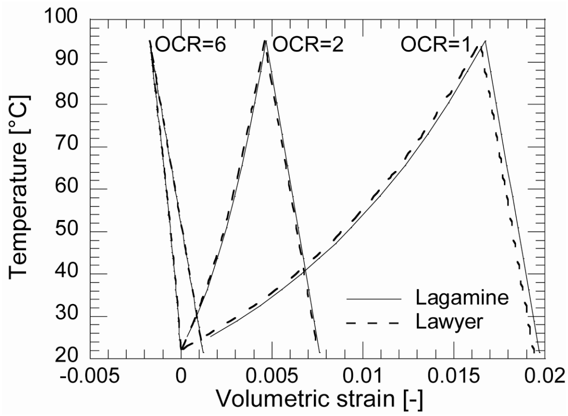

Figure 7.5 : Validation of the ACMEG-TS implementation in LAGAMINE. Comparison of numerical results of the Boom clay response upon three heating-cooling cycles obtained with LAGAMINE and with the driver of the constitutive law LAWYER (TBoom 9, for the comparison with experiment, see Figure 8.6).

7.5 Non-isothermal consolidation[1]

7.5.1 Introduction

The boundary value problem presented in this section aims to validate the finite element formulation and implementation of the ACMEG-T(S) constitutive law in the LAGAMINE finite element code. This first simple case deals with simulation of a non-isothermal fully saturated consolidation problem, for which the numerical solution of the linear thermo-mechanical problem is known (Aboustit et al., 1985). This example is a generalization of Terzaghi's unidimensional isothermal consolidation problem, in which thermal loading has been added to the conventional mechanical loading.

In addition, ACMEG-T, i.e. the version of the constitutive model that considers soil as water-saturated, has also been implemented in the COMES-GEO finite element code, developed by the research group of Prof. Schrefler et al. at University of Padova (see Sanavia et al., 2006, among others). Therefore, the problem has been modelled with the LAGAMINE finite element code and compared with the solutions obtained with the COMES-GEO code (Sanavia et al., 2008) and Aboustit's simulation.

A column of 7 m height is subjected to an external surface compressive load of 1.0 kPa and to a surface temperature jump of 50°C above the initial ambient temperature of 20°C. The material is initially water-saturated. The upper surface is drained ($p_w = 0\ Pa$), and the lateral and the bottom surfaces are insulated. Horizontal displacements are constrained along the vertical boundaries, and vertical displacements are constrained at the bottom surface. The column is discretized by 90 eight-node isoparametric elements for the LAGAMINE code while the COMES-GEO code uses the same mesh as the reference Aboustit's case, counting nine elements (Figure 7.6). The COMES-GEO and LAGAMINE codes use 3x3 and 2x2 Gauss integration points per element, respectively. The material parameters used in the computation are listed in Table 7.1. Plane strain conditions are assumed.

[1] Sanavia L., François B., Bortolotto R., Luison L. and Laloui L. (2008). Finite element modelling of thermo-elasto-plastic water saturated porous materials. *Journal of Theoretical and Applied Mechanics*, 38(1-2): 7-34.

7.5.2 Results

In Aboustit et al. (1985), the only available results are the vertical displacements of the top surface at eight different times. The time histories for the water pressure (Figure 7.7a), the temperature (Figure 7.7b), and the vertical displacement (Figure 7.7c) of several nodes of the mesh, depicted in Figure 7.6, show good agreement between the two obtained solutions, with the exception of some slight differences which are probably due to the different spatial and temporal discretisation of the problem. Moreover, the correspondence with the displacements obtained by Aboustit et al. (1985) tends to validate the finite element formulation used in the two codes.

Elastic parameters									**Diffusive law**			
K_{ref}	G_{ref}	p'_{ref}	n^e	β_s	ρ_s	ρ_w	n	k	λ_s	$c_{p,s}$	λ_w	$c_{p,w}$
[MPa]	[MPa]	[MPa]	[-]	[K^{-1}]	[kg/m^3]	[kg/m^3]	[-]	[m^2]	[W/(m K)]	[J/(kg K)]	[W/(m K)]	[J/(kg K)]
10	2.14	1	0	9 10^{-7}	2000	1000	0.2	4.6 10^{-17}	0.84	16760	0.84	4181

Table 7.1: Material parameters used in computation of the non-isothermal thermo-elastic consolidation example.

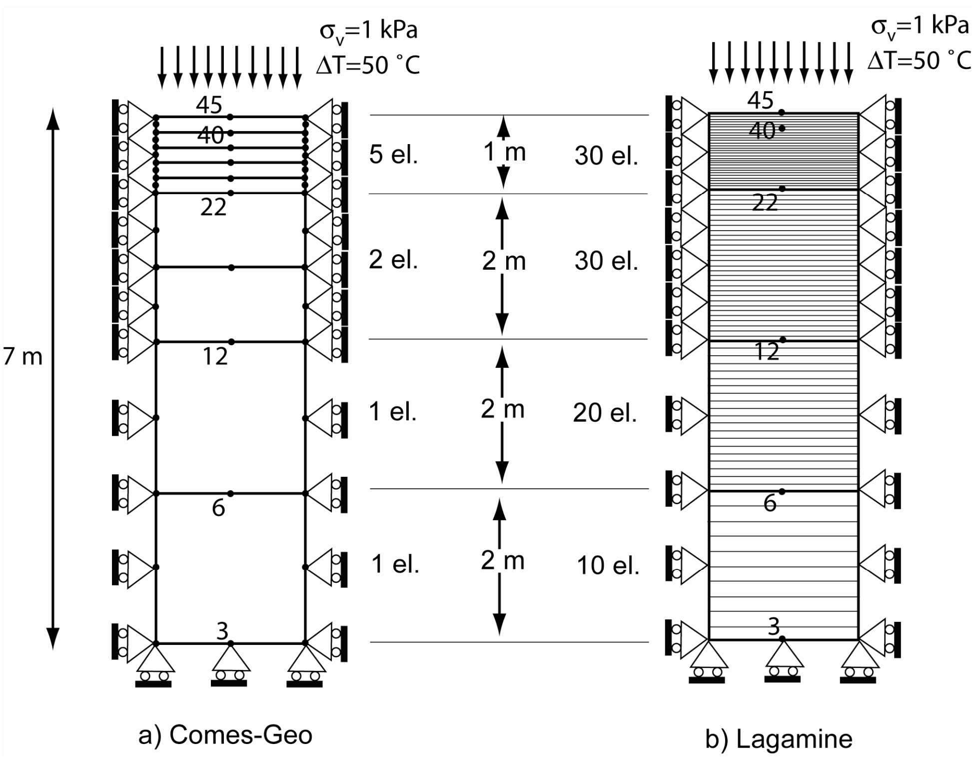

Figure 7.6 : Spatial discretisation and boundary conditions for the non-isothermal consolidation example.

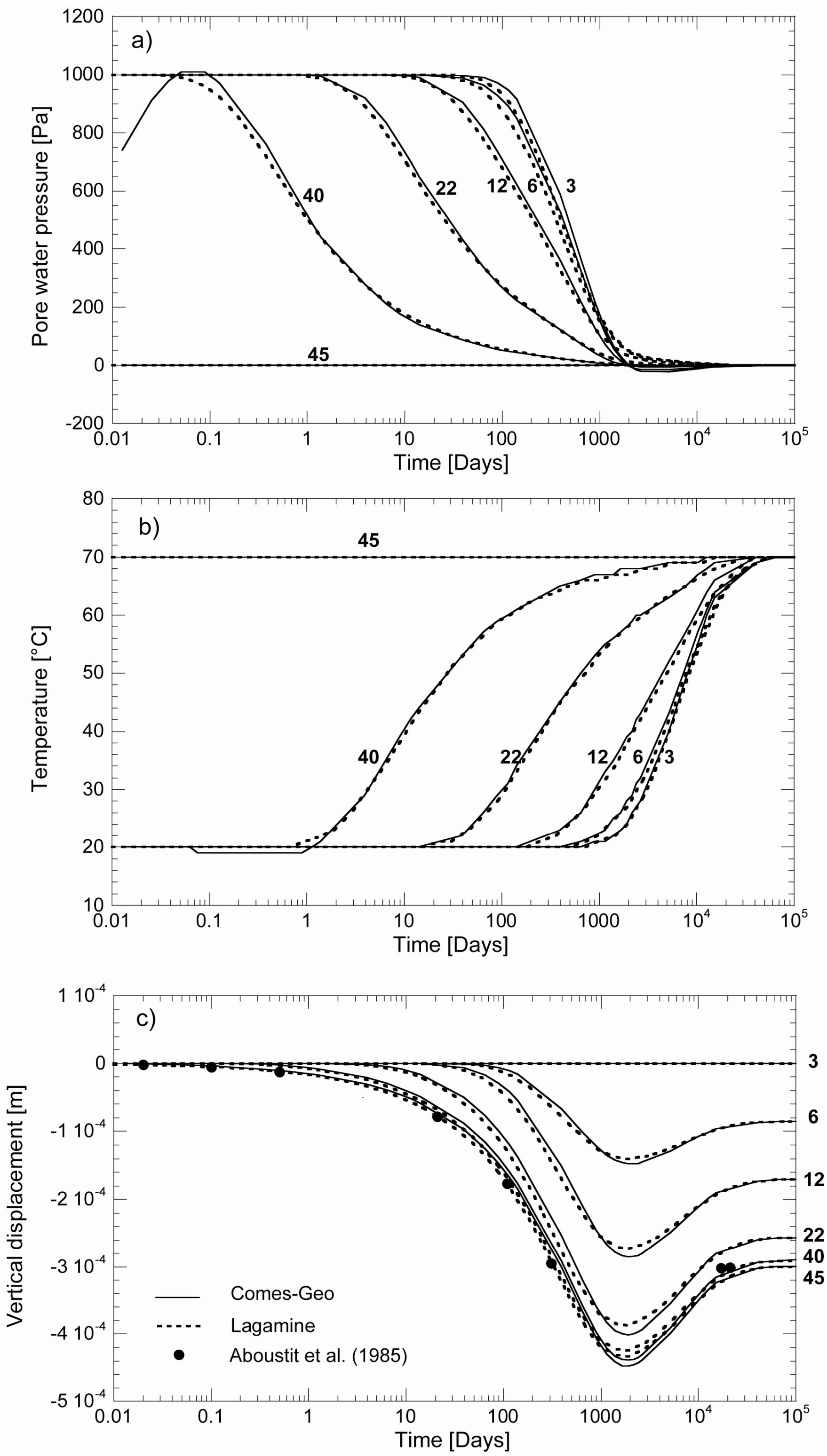

Figure 7.7 : Simulation of non-isothermal fully saturated consolidation problem in linear thermo-elasticity with two finite element codes (COMES-GEO and LAGAMINE): a) pore water pressure; b) temperature; c) vertical displacement. Comparison with the displacement obtained by Aboustit et al. (1985).

Upon application of the sudden vertical load, the pore water pressure increases immediately in the entire domain up to 1.0 kPa. Then, the pore water pressure dissipates progressively through the drained top surface. Temperature diffuses in the media from the top to the bottom, and the hydraulic and thermal diffusion processes have different characteristic times. The pore water pressure dissipates in 2000 days while the temperature field reaches equilibrium after 50000 days. This delay between hydraulic and thermal equilibrium explains the peak observed in the vertical displacement. Before the peak, settlement is mainly governed by the consolidation processes (i.e. dissipation of pore water pressure) while thermal dilatation is negligible. On the contrary, when pore water pressure is dissipated in the entire domain, the settlement is maximal and thermal expansion produces a swelling of the soil column in the post-peak phase.

In addition, this elastic non-isothermal consolidation has been extended towards elasto-thermoplastic analysis by reducing the preconsolidation pressure in order to obtain a mechanical and thermal hardening when loaded to 1 kPa. The results and interpretations of the thermo-plastic computations can be found in Sanavia et al. (2008) with the COMES-GEO code and in Laurent (2007) with the LAGAMINE code. This thermo-elasto-plastic case and the governing equations used by the COMES-GEO finite element code are extensively presented in Appendix E.

7.6 Conclusions

The modelling of boundary value problems in soils, such as those related to nuclear waste disposal, requires advanced mathematical models. The finite element method provides an efficient framework to discretize the field equations and the constitutive laws that govern non-homogeneous transient problems in porous media, in particular, in soils. The medium must be considered as a multiphase deforming porous medium in which heat and mass transfer occur. Also, there are strong couplings between water flow, heat flow, and soil mechanics which must be included in the mathematical formulation of the finite element code.

For this purpose, the mechanical, hydraulic, and thermal field equations implemented in the LAGAMINE finite element code have been presented. In addition, the constitutive laws that relate the field variables with the primary state variables (displacements, pore water pressure, pore gas pressure, and temperature) have been presented. The finite element formulation has been briefly introduced, focusing in particular on the stiffness matrix that associates the five degrees of freedom per node.

In order to accurately consider the stress-strain relations in soil affected by temperature and suction variations, the ACMEG-TS model has been implemented in the LAGAMINE finite element code. Validation of the implemented model was made by selected comparisons between model simulations with LAGAMINE and with the solver LAWYER for different combinations of thermo-hydro-mechanical loading paths.

Finally, a case of non-isothermal elastic consolidation was solved. The results have been compared with another solution obtained with the finite element code, COMES-GEO, and also with a known numerical solution from the literature. This validation case remains very simple but clearly points out that with a sufficiently general THM model, the main couplings between temperature, pore pressure and displacement occurring in fine soils may be reproduced in a relevant manner.

This numerical tool will be used in the next chapter to study the behaviour of soil surrounding nuclear waste disposal that includes strong non-linear stress-strain behaviour and highly coupled THM processes.

Chapter 8

Numerical simulation of processes relating to nuclear waste disposal

Barrier behaviour is highly complex, involving coupled thermo-hydro-mechanical phenomena that take place during heating and hydration of the clay barrier. Numerical analysis can be an effective way to bridge the gap between the theoretical and empirical understanding of the individual processes occurring and the resulting overall performance of the barrier.[1]

[1] Gens A., Garcia-Molina A.J., Olivella S., Alonso E.E. and Huertas F. (1998). Analysis of a full scale in-situ test simulating repository conditions. *International Journal for Numerical and Analytical Methods in Geomechanics*, 22: 515–548.

8.1 Introduction

The role of geomechanics in the feasibility study of nuclear waste disposal in deep geological formations is of paramount importance. In most of the concepts, the argillaceous materials constitute either the main barrier or an important element aimed at confining the nuclear waste and isolating it from the biosphere. The mechanical behaviour of the argillaceous barrier must be understood and predicted by means of numerical modelling. The geomaterials surrounding the radioactive waste undergo complex thermal, hydraulic and mechanical loadings with strong interactions between them. Such processes may involve unsaturated and non-isothermal conditions.

A rigorous modelling of the thermo-hydro-mechanical (THM) processes experienced by the confining soils requires advanced numerical tools that consider heat and fluid diffusion in addition to a highly non-linear stress-strain constitutive model. In that sense, the tools that have been developed and presented in the previous chapters will be used in order to study the soil response around the nuclear waste. The LAGAMINE finite element code, the governing equations of which have been presented in Chapter 7, combined with the ACMEG-T(S) constitutive model (Chapter 2, Chapter 3, and Chapter 6) is used.

The first section provides an explanation of the principle of nuclear waste disposal in deep geological formations. In particular, the role of geomechanics in the study of highly coupled THM processes around the waste is underlined. The second section studies, by the means of finite element computations, the THM responses of geomaterials involved in the confinement of heat-emitting nuclear waste. Three different in-situ or laboratory tests are modelled: a non-isothermal hollow cylinder test, a large scale in-situ heating test and a near-to-real experiment in relation with the Spanish reference concept of underground nuclear waste disposal in granitic formation. The conditions of the first two experiments are saturated while the third one is unsaturated.

8.2 Goal and principle of underground nuclear waste disposal[1]

8.2.1 Introduction

In all nuclear power generating countries, spent nuclear fuel and long-lived radioactive waste management is an important environmental issue. Disposal in deep clay geological formations is a promising option to dispose of these wastes. A safety case for a geological repository for high-level and/or long-lived radioactive waste aims at conveying reasoned and complementary arguments to illustrate and insure confidence in the performances of the disposal system. This need requires that, both in repository design and in performance assessment, all analyses and predictions about the behaviour of isolation barriers be based on robust science (Gera et al., 1996; Gens and Olivella, 2001). This implies a good understanding of the fundamental behaviour of the argillaceous materials and their modelling based on the best available knowledge.

[1] Laloui L., François B., Nuth M., Peron H., Koliji A. (2008) A thermo-hydro-mechanical stress-strain framework for modelling the performance of clay barriers in deep geological repositories for radioactive waste. *1st European Conf. on Unsaturated Soils, Durham, United Kingdom*: 63-80.

8.2.2 The multibarrier concept

The geological disposal of radioactive waste must be provided by a system that should (OECD, 2003):

- Isolate the wastes from the biosphere for extremely long periods of time, and
- Ensure that residual radioactive substances reaching the biosphere will be at concentrations that are insignificant compared, for example, with the natural background levels of radioactivity.

To increase the performance of the engineered barrier system (EBS), the multibarrier concept in the near-field of the waste was developed. This multi-protection generally consists of a solid waste form (e.g. vitrified high-level radioactive waste (HLW) or spent fuel), an overpack (or container), materials placed between the overpack and the surrounding rock (backfill or buffer materials), and finally the host formation (Chapman and Mc Kinley, 1987). Therefore, in many proposals for deep geological repositories, the argillaceous materials constitute either the main barrier or an important element of the multi-barrier system. They can be either the host material or engineered parts of the repository (buffer materials such as compacted swelling clays, most probably bentonite). Figure 8.1 schematically illustrates a possible concept of the barrier system.

Clay barriers provide waste isolation mainly by restricting the contact between the groundwater and waste containers and by limiting the migration of most radionuclides released from the waste (after container failure). These two functions result from the low permeability and high retention capability of clays. Therefore, the buffer material must have several specific properties in order to ensure efficient containment with high safety for the long term. These characteristics are related to sufficient mechanical properties under isothermal, non-isothermal, saturated, and unsaturated conditions, to liquid, air and thermal conductivities, to the nuclide filtration abilities and to manufacturability of the buffer material. Such required properties are summarized in Table 8.1.

The use of bentonite as a buffer material is the most possible solution in several national concepts. Bentonite is a clay mainly composed of smectite, which gives swelling properties to the clays due to its high water absorption capacity. Several experimental results on the THM behaviour of bentonite materials that could be used in radioactive waste storage sites have been reported in the literature in the last decade. Four well-known and largely studied bentonites are briefly presented below.

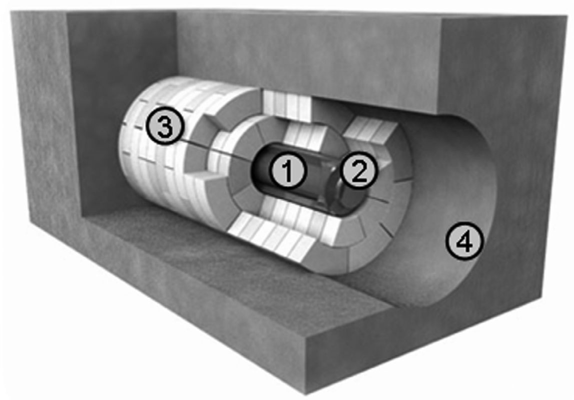

Figure 8.1 : The multi-barrier system: (1) nuclear waste; (2) steel canisters; (3) buffer material; (4) host material (from *www.grimsel.com/febex/febex_intro_1.htm*).

Function	Requirement	Property
Restriction of radionuclide migration	Restriction of groundwater movement	Low hydraulic conductivity (low permeability)
	Sorption of dissolved nuclides	High sorption coefficients
	Prevention of colloid migration	Colloid filtration function
	Buffering of changes in groundwater chemistry	Capability of chemical buffering
Technical feasibility of manufacturing/ installation	Possibility of filling gaps created during installation	Self-sealing ability
	Manufacturable and placement properties	Compaction properties
No significant impact on the engineered barriers for a specified period	Mechanical support of the overpack to ensure stability	Strength to support the overpack in a stable position
	To inhibit thermal alteration of vitrified waste and buffer	High thermal conductivity
	Stress buffering properties	Plasticity

Table 8.1: The function of the buffer material in parallel with its required properties (JNC, 1999)

The Febex bentonite extracted from the Cortijo de Archidona deposit (Almeria, Spain) is a material that has been selected in the ENRESA R&D plans as the most suitable material for backfilling and sealing the HLW repository and was tested over the last 10 years within the framework of the FEBEX project (ENRESA, 2000; Lloret et al., 2004; Villar, 2002, Villar et al., 2006). This clay is made of approximately 90% montmorillonite, giving it high swelling capacities upon wetting. Its liquid and plastic limits are 100% and 50%, respectively.

The FoCa Clay is a sedimentary clay from the Paris Basin. This clay is supplied by the SFBD French Company. Manufacturing consists in disaggregation and gentle grinding, drying at about 60°C and sieving. The maximum grain size is 4 mm. The clay is largely made of an interstratified clay (50% calcium beidellite and 50% kaolinite) (Imbert et al., 2005; Olchitzky, 2002).

Bentonite Kunigel V1 is a bentonite produced in Japan by Kunimine Industries. More than 90% of its grains are smaller than 74 μm. The properties and behavioural features of this bentonite have already largely been investigated under the supervision of the Japan Nuclear Cycle Development Institute (JNC, 1999; Komine and Ogata, 1994). The two main constituents are montmorillonite (48%) and quartz (34%). Its liquid and plastic limits are 416% and 21%, respectively.

MX-80, considered by many as the reference buffer material, is produced in the United States by the “American Colloid” society. The grain sizes are distributed between 10 μm and 1 mm (Tang, 2005). It is made of 75% montmorillonite and 15% quartz. Its liquid limit is approximately 450% while its plastic limit is around 50%.

After manufacturing of the bentonite powder, all of these materials are partially wetted to reach the desired water content, and eventually mixed with additive soil (sand or graphite) in different proportions to adjust the desired properties. They are subsequently compacted with a well-defined energy. This compaction induces particular properties in the bentonite (e.g. a double structure, expansive tendency under wetting).

8.2.3 Thermo-hydro-mechanical processes

In the first year following the construction of the underground disposal, the near-field, which can be defined as the zone altered by the presence of the radioactive waste (including the buffer materials and a portion of the host material adjacent to the waste location), is subjected to complex mechanical, hydraulic, and thermal solicitations with a great inter-dependence (THM couplings).

With the "intact state" of the host massif as the initial state with a generally anisotropic stress state, the first step is excavation. This process induces a stress redistribution due to opening, causing tension, compression and shear and leading to an Excavation Disturbed Zone (EdZ) in the host material around the excavation (Davies and Bernier, 2003).

After excavation and before HLW emplacement, the galleries are ventilated. During this stage, the excavated area plays a drainage role and a consolidation process occurs in the surrounding host material. In addition, a negative pore water pressure (suction) is acting on the field material; a strong suction gradient can develop between the gallery surface and the surrounding host material. In this situation, drainage and drying in the vicinity of the ventilated excavation are likely to be associated with radial cracking in the galleries.

After placing the canister and filling the gap between it and the host material with buffer material (i.e. blocks of compacted clay, initially unsaturated), the main action that affects the EBS is heating from the canister and hydration from the surrounding host material. This stage can be subdivided into several expected phases (summarized in Table 8.2):

- In the very early closure stage, the thermal flux from the vitrified waste into the buffer material occurs in unsaturated conditions at a constant water content (i.e. constant suction). The impact of the thermal load generated by the waste is particularly important as it will significantly affect the temperature and the stress far (more than 50 m) from the repository in the host material (TIMODAZ, 2007);
- During early closure, the resaturation process induced by the water flux from the surrounding rock/clay mass occurs in a media in which temperature progressively increases. The buffer material is subjected to wetting (suction decrease) and thermal swelling (and/or eventual collapse);
- The THM processes progress and the buffer material tends reaches a saturated state while the temperature is still increasing. In parallel, in the vicinity of the heat-emitting waste, the high temperature induces a desaturation process of the buffer material, which tends to shrink.
- Finally, in the very late closure stage, when the maximum of thermal power has been emitted by the vitrified waste, temperature around the repository is slowly falling and the buffer material is re-saturated (wetting process). The thermal and hydraulic gradients are largely lower than previously and progressively vanish. When the temperature has totally decreased, irreversible thermal strains predominate.

In terms of theoretical and constitutive studies of the processes encountered, the succession of different phases above clearly shows the necessity of using high-performance modelling tools to best approach the complex phenomena and interactions. The duration of each phase depends on the properties of the buffer and host materials as well as of the heat emitted by the vitrified waste.

Stage	Processes	Modelling
Excavation	Stress redistribution EDZ formation	Elasto-plastic (EP) model for saturated and isothermal conditions
Ventilation of the excavation	Consolidation process in the host material; Swelling and eventual desaturation of the host material	Hydro-mechanical coupling in unsaturated conditions
Early closure stage	Coupled thermal and hydraulic diffusion in a deformable media; Thermal and hydraulic swelling and/or collapse of the buffer material	Thermo-hydraulic (TH) diffusive law coupled with a THM-EP mechanical model for unsaturated conditions
Late closure stage	Desaturation of the buffer material due to thermal effects; Shrinkage	TH diffusive law coupled with a THM-EP mechanical model for unsaturated soil
Very late closure stage	Temperature decrease and wetting of the buffer material; Lower thermal and hydraulic gradient; Irreversible thermal strains	TH diffusive law coupled with a THM-EP mechanical model for unsaturated conditions considering wetting paths

Table 8.2: THM processes occurring in the life of underground nuclear waste disposal (Laloui et al., 2008).

8.2.4 Large scale in-situ simulation tests

In the coming years, safe and definitive solutions will likely be completed for managing the large quantities of high-level radioactive wastes. However, since this matter is urgent, yet concerns long time periods, the safety assessment of this option must be based mainly on predictions. Powerful simulation tools, such as THM finite element codes, are of paramount importance to realize this goal. To ensure their efficiency, the models that are expected to be used for safety assessment of radioactive waste repositories should be validated under characteristic loadings. To achieve this challenging task, simulations reproducing analogue studies or carefully selected experiments have to be performed. To this end, several large scale field heating tests were carried out in several underground laboratories. These experiments simulate the heat generation of a high-level radioactive canister, with or without the presence of backfill material between the heat source and the host formation, and measure the evolution of temperature, pore water pressure, displacement and in-situ stresses around the thermal source.

For instance, the FEBEX in-situ test was installed at the Grimsel Test Site Underground Laboratory, Switzerland, and is a near-to-real scale simulation of the Spanish reference concept of deep geological storage in crystalline host rock with blocks of compacted bentonite as a buffer material (Alonso et al., 2005). At the Kamaishi mine in Japan, a THM test was conducted where the heater was placed in the center of a pit and buffer material was compacted around the heater (Chijimatsu, 2001). A drift scale test was held in the Exploratory Studied Facilities at the Yucca Mountain, Nevada, USA. It involved heating a 5 m diameter, 47.5 m long drift for four years and measuring the thermal, hydrological, mechanical and chemical responses before, during and after the heating (Datta et al., 2004). The HE-D test in Mont-Terri Underground Laboratory, Switzerland, consists of a temperature increase in a main borehole in Opalinus clay with some instrumented surrounding boreholes controlling the evolution of the rock state (Hoxha et al., 2006). Finally, since the beginning of 80’s several large-scale heat-emission tests were designed in the HADES-URF laboratory in Mol, Belgium (Bernier and Neerdael, 1996). Among those tests, ATLAS, for Admissible Thermal Loading for Argillaceous Storage, was designed as part of the Interclay II programme (1990–1994) (Jeffries, 1995).

8.2.5 Conclusions

Assessing the performance of deep geological repositories for heat-generating radioactive waste requires reliable predictions of the THM behaviour of the clay barriers (the buffer material as well as the host rock/clay). This represents an important element of the waste isolation system. In order to provide reasonable assurance that clay barriers will ensure nuclear waste isolation, an understanding of their behaviour under a variety of environmental conditions is essential. The stress-strain material behaviours that need to be understood and modelled include drying and wetting in non-isothermal conditions and heating-cooling in non-saturated conditions.

In the next section, several laboratory or in-situ experiments, related to the THM behaviour of argillaceous materials involved in nuclear waste isolation, are simulated by the means of finite element methods. By predicting the behaviour of soils around heat-emitting radioactive waste with an advanced constitutive model implemented in a general THM finite element code, these simulations contribute to the understanding of the highly coupled THM processes occurring in the clay host formation surrounding a thermal source. When possible, the results are compared with experimental measurements and are interpreted in the light of the elasto-thermoplasticity of saturated and unsaturated soils.

8.3 Modelling of boundary value problems

8.3.1 Introduction

As concluded in the previous section, the assessment of the performance of deep geological repositories requires reliable predictions of the THM behaviour of the clay barriers. In that context, this section aims to study, by means of finite element computations, the THM responses of geomaterials involved in the confinement of heat-emitting nuclear waste. Two of the three studied experiments involve Boom clay as studied material. Consequently, the first section presents the thermo-mechanical characteristics of that clayey material. The parameters of the ACMEG-T model are calibrated on a series of laboratory experiments. Next, the calibrated parameters are used in the simulations of two boundary value problems dealing with saturated and non-isothermal conditions. Finally, the FEBEX experiment, which is a near-to-real in-situ test, is numerically simulated. This involves the use of an unsaturated and non-isothermal formalism.

For the simulation of the ATLAS and FEBEX in-situ tests, the obtained spatial and temporal distributions of the THM variables are given on a DVD support at the end of the manuscript. On this support, all the discussed concepts of this chapter are illustrated by the means of the evolution of isovalues around the heat source. That DVD provides didactic explanations on the kinematics of the processes that could occur around prospective nuclear wastes disposed in deep geological formations.

In addition, Appendix F presents an analysis of the isothermal mechanical behaviour of the Opalinus clay, which is a potential host formation in the Swiss concept of underground nuclear waste disposal. A large quantity of available laboratory tests has been compiled, and those experiment results have been simulated with the ACMEG model.

8.3.2 The Boom clay formation

8.3.2.1 *A possible host formation*

Boom clay is studied as a host geological formation for a radioactive waste deep geological repository in Belgium. In that framework, the underground research facility HADES-URF, aimed at studying the feasibility of a nuclear waste disposal in Boom clay, was built in Mol at a depth of 223 m (Figure 8.2).

Boom clay is a marine Rupelian deposit of overconsolidated clay. This deposit is of considerable stratigraphic and geotechnical significance in northeast Belgium (Mertens et al., 2004; Bouazza et al., 1996). As illustrated in Figure 8.3, its thickness is variable, but can be estimated to be 102 m in the Mol area. Within this area, the formation dips slightly (1-2°) toward the North-North-East and is surrounded by water-bearing sand layers (Bernier et al., 2007).

The main geotechnical properties of this plastic clay are collected from various sources in Table 8.3. The Boom clay is highly porous and has a higher mechanical strength than the average clayey material. Many of its properties are favorable to the choice of this formation as a geological barrier for radioactive waste disposal. In particular, its (i) very low permeability to fluid, (ii) good retention capacity of radionucleides, (iii) good stability for millions of years and (iv) self-sealing properties are of significant interest (TIMODAZ, 2007; Barnichon and Volckaert, 2003). At the depth of the HADES-URF gallery, Boom clay is slightly overconsolidated and the stress state is slightly anisotropic. The ratio between the minor and major principal stresses is difficult to establish. Thereby, the reported coefficient of earth pressure at rest has varied among authors. Table 8.4 summarizes the characteristics of the initial state of Boom clay at the depth of the HADES-URF laboratory, according to the analysis of different sources.

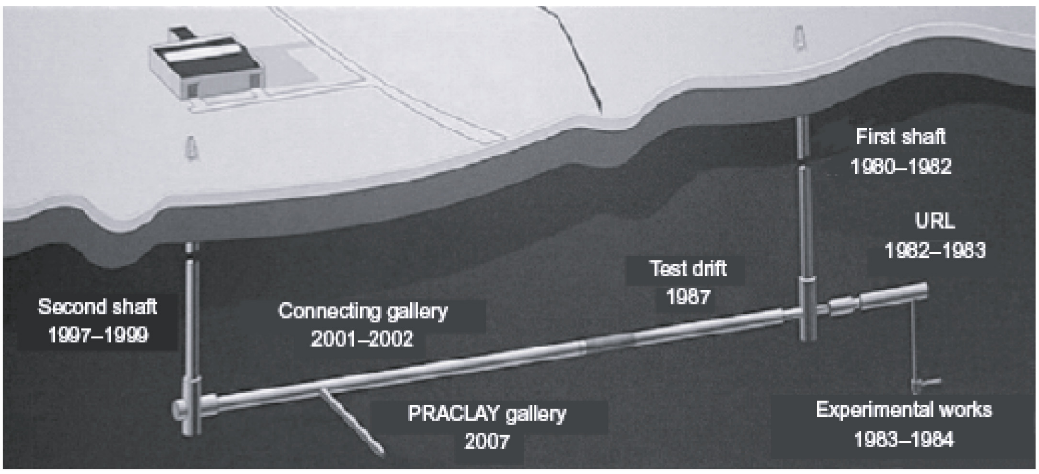

Figure 8.2 : Schematic view of the underground research facilities HADES-URF in Mol, Belgium (Bernier et al., 2007).

Parameter	Units	Symbol	Bernier et al. (2007)	Bastiaens et al. (2006)	Mertens et al. (2004)	Belanteur et al. (1997)	Dehandschutter et al., (2005)	Delage et al. (2000)	Gens et al. (2007)	Laloui (1993)	Baldi et al. (1987, 1991)	SCK-CEN (1997)
Bulk density (saturated)	g/cm^3	ρ_{sat}			1.9-2.1							1.9-2.1
Dry skeleton density	g/cm^3	ρ_d					1.9		1.61-1.78		1.9	
Porosity	%	n	39	39	36-40		35	40	>30		37.5	33-40
Solid density	g/cm^3	ρ_s				2.67						
Natural water content	%	w		30-40	19-24		25-30	24-30	>9.5			22-27
Natural degree of saturation	%	S_r										95-100
Liquid limit	%	w_L				59-76	70				66.6	70-83
Plastic limit	%	w_P				22-26	25					25-28
Unconfined compression strength	MPa	UCS	2	2	2.2-2.8				2			
Young's modulus	MPa	E	300	200-400	200-400				200-400	330		
Poisson ratio	-	υ	0.125	0.4-0.45	0.4		0.4			0.134		
Internal friction angle	°	ϕ_0'	18		11		18			19.5		
Cohesion	MPa	c'	0.3	0.5-1	0.396							0.6-1.2
Dilatancy angle	°	ψ	0-10							23		
Horizontal water permeability	10^{-19} m^2	$k_{w,h}$	2-4	~ 1			1	2.5-3.5.	2-5			4
Vertical water permeability	10^{-19} m^2	$k_{w,v}$	2-4	~ 1			1	2.5-3.5	2-5			2
Specific heat	J/(°C kg)	C_p										1400
Thermal conductivity	W/ (°C m)	Γ										1.69
Solid thermal dilatation coefficient	°C^{-1}	β_s'								$1.3.10^{-5}$	10^{-5}	

Table 8.3 : Literature review of Boom clay properties.

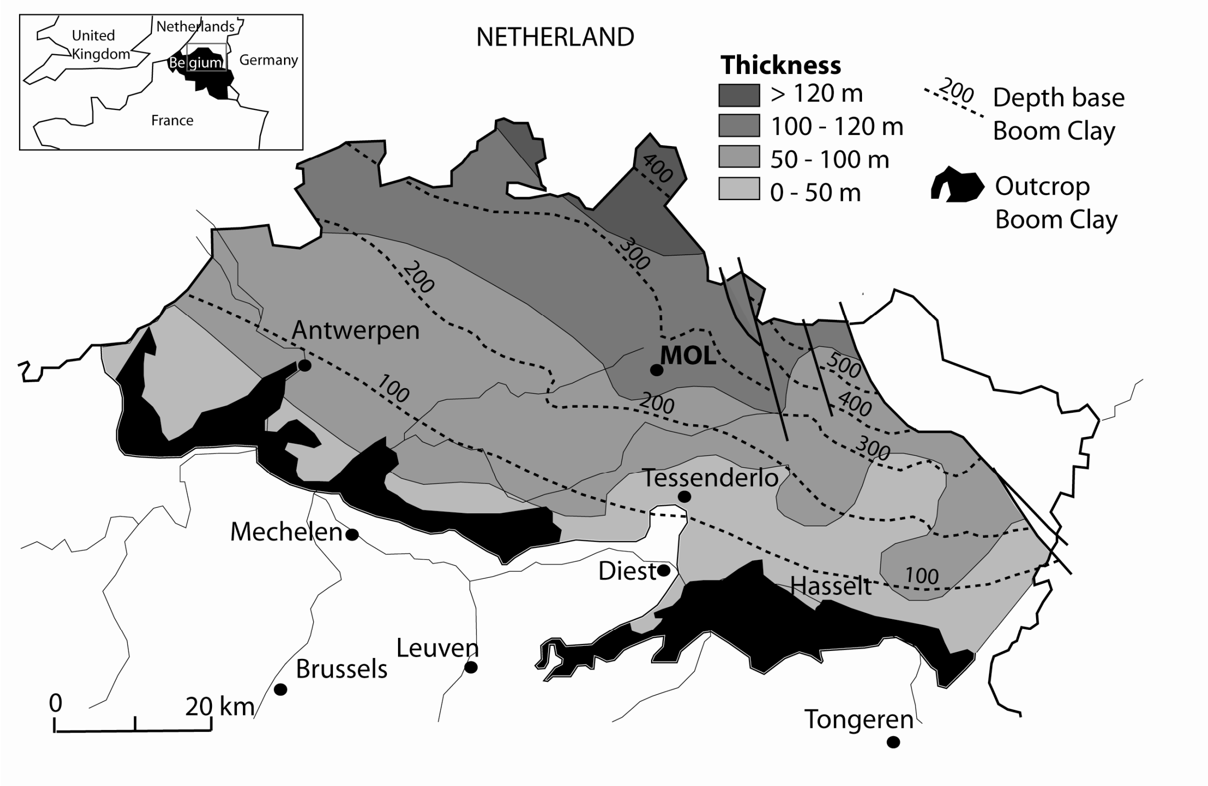

Figure 8.3 : Thickness and depth base of the Boom clay formation in Belgium (from Mertens et al., 2004).

Parameters	Units	Symbol	Bernier et al. (2007)	Bastiaens et al. (2006)	Bernier et al. (2002)	Horseman et al. (1987)	Mertens et al. (2004)	ONDRAF (2001)	Horseman et al. (1993)	Delage et al. (2007)	SCK-CEN (1997)	De Bruyn and Labat (2002)
Coeff. of earth press. at rest	-	K_0	1	~ 0.9	0.3-0.9	0.5-0.8	1	0.9	0.8	0.8-1		
Overconsolidation ratio	-	OCR	2.4	2.4		2.4						
Total vertical stress	MPa	σ_v	4.5	4.5			4.6				4.6	
Effective vertical stress	MPa	σ_v'	2.25	2.3		2.5	2.4			2.45		
Pore water pressure	MPa	p_w	2.25	2.2			2.2					
Preconsolidation pressure	MPa	p_{c0}'	5.4			6						
Temperature	°C	T										16.6

Table 8.4 : Literature synthesis of the THM in-situ state of Boom clay at a depth of 223 m.

8.3.2.2 *Mechanical parameters*

In terms of thermo-mechanical behaviour, Boom clay, as with all clayey soils, is subject to several disturbances when the temperature increases. Sections 8.3.3 and 8.3.4 address, by the means of the finite element method, the constitutive study of the Boom clay response in boundary value problems. The use of the ACMEG-T constitutive model to predict the behaviour of Boom clay in such problems requires the calibration of material parameters in agreement with its THM behaviour. To this end, the parameters of the ACMEG-T model have been determined from selected laboratory tests from Baldi et al. (1991): (i) an isotropic consolidation test (TBoom1), (ii) two drained triaxial tests at two different confining pressures (TBoom2 and TBoom3) and (iii) a thermo-mechanical test (TBoom9).

The TBoom1 experimental test consists of drained isotropic compression cycles (2; 4; 2; 8; 2; 5 MPa of mean effective stress) on Boom clay samples taken at the depth of HADES-URF, 223 m below the surface. The isothermal isotropic parameters of the model (K_{ref}, n^e, β, c, r^e_{iso}, p'_{c0}) were determined from this test and are reported in Table 8.5. A comparison between model simulation and TBoom1 experimental results is shown in Figure 8.4.

TBoom2 and TBoom3 are strain-controlled drained triaxial compression tests performed at a confining pressure of 2 MPa and 3 MPa, respectively. Strain reversals at 0.6% and 2.8% of axial strain for TBoom2, and at 0.56% and 2.13% of axial strain for TBoom3, were carried out in the experimental procedure but were not numerically simulated. The isothermal deviatoric parameters (G_{ref}, M, b, d, α, a, r^e_{dev}) were calibrated from these two results and are reported in Table 8.5. Figure 8.5 displays a comparison between experimental results and numerical simulations. Good agreement between both curves is obtained in the deviatoric plane, while the volumetric plane shows some discrepancies.

Elastic parameters		
K_{ref}, G_{ref}, n^e, β'_s	[MPa], [MPa], [-], [°C^{-1}]	130, 130, 0.4, 1.3 10^{-5}
Isotropic plastic parameters		
β, γ_T, c, r^e_{iso}	[-], [-], [-], [-]	18, 0.55, 0.012, 0.001
Deviatoric plastic mechanical parameters		
b, d, ϕ'_0, g, α, a, r^e_{dev}	[-], [-], [°], [-], [-], [-], [-]	0.6, 1.3, 16, 0.0085, 1, 0.007, 0.3

Table 8.5 : Set of the Boom clay thermo-mechanical parameters used for the ACMEG-T model in the simulation of the TIMODAZ benchmark (Section 8.3.3) and the ATLAS experiment (Section 8.3.4).

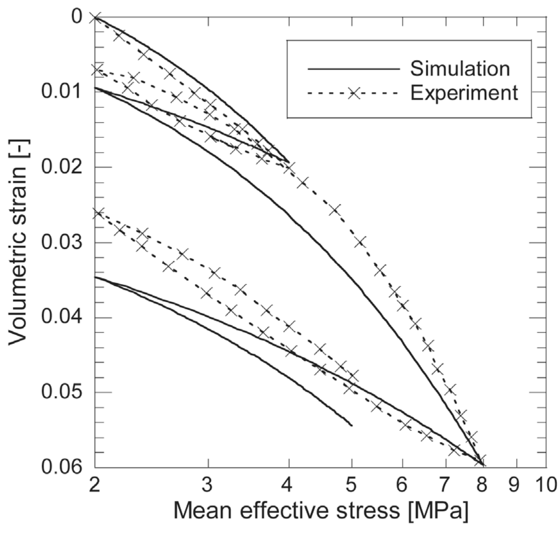

Figure 8.4 : Isotropic compression test (TBoom1 from Baldi et al., 1991): Comparison between numerical simulation and experimental results.

Finally, TBoom9 was used to determine thermo-mechanical parameters. Most of the isotropic parameters governing the mechanical response of the ACMEG-T model on thermal solicitations were already fixed from simulation of the TBoom1 test. Thereby, only two parameters needed to be adjusted: β_s' and γ_T, which control the thermo-elastic and the thermo-plastic part of the volumetric response of Boom clay, respectively. Among the three experimental curves at three different overconsolidation ratios (OCR), the choice was made to focus on the response of Boom clay at an intermediate OCR, which corresponds to an initial effective stress level at a depth of 223 m (Figure 8.6).

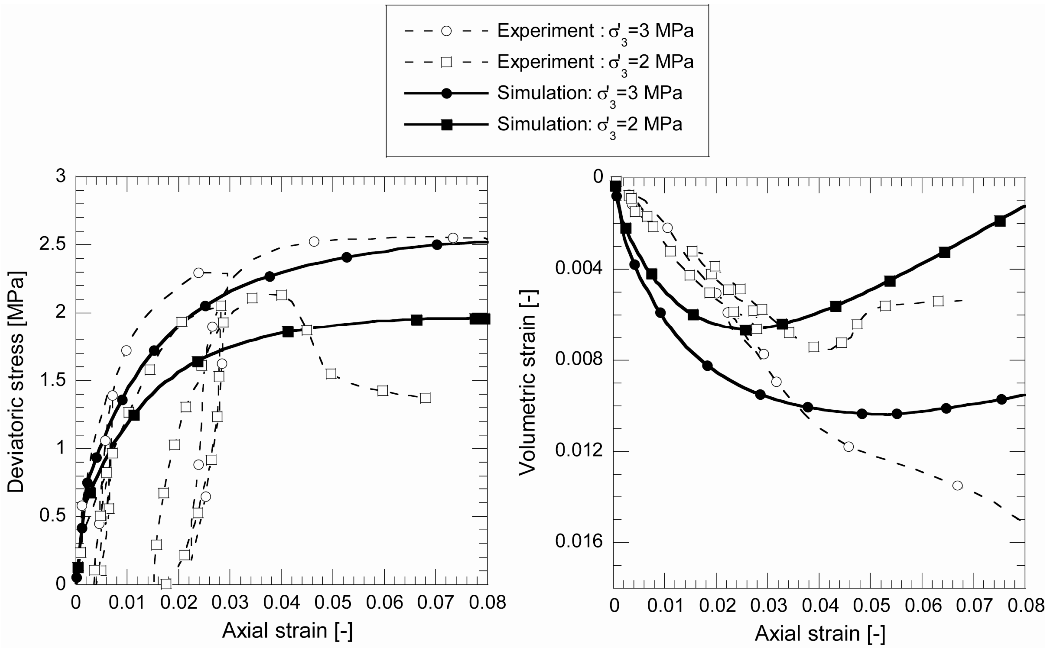

Figure 8.5 : Drained triaxial compression tests (TBoom2 and TBoom3 from Baldi et al., 1991): Comparison between numerical simulations and experimental results. σ_3' is the effective confining pressure.

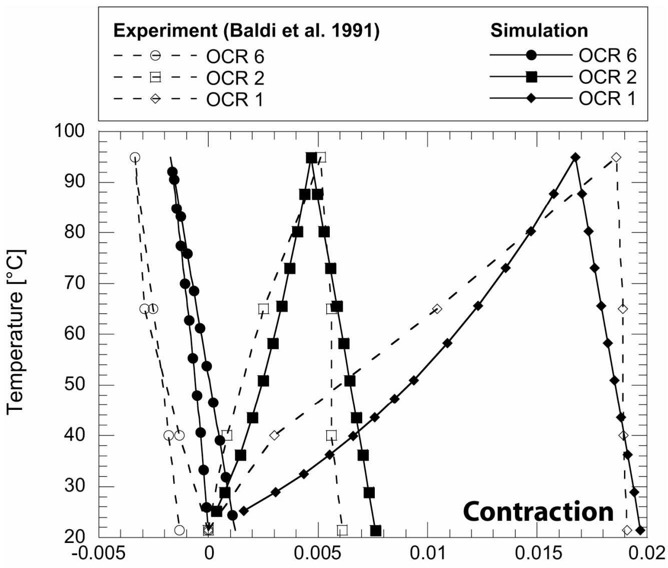

Figure 8.6 : Temperature cycle on sample at three different overconsolidation ratios (TBoom9 from Baldi et al. (1991)): Comparison between numerical simulations and experimental results.

8.3.2.3 *Material parameters of the diffusive model*

The parameters governing the thermal and hydraulic diffusion in Boom clay are directly established from a literature synthesis as gathered in Table 8.3. Their mean values over their variability domain have been selected. Table 8.6 reports the final diffusive parameters used in the numerical simulations. Generally, the thermal properties of Boom clay are given in terms of the average value of the water-solid mixture. The properties of the solid matrix were deduced from Equations (7.6) and (7.20), knowing the value of the specific heat and thermal conductivity of water. These parameters have been used in the numerical simulations of the ATLAS experiment (Section 8.3.4) while the diffusive parameters were given in the statement of the TIMODAZ benchmark.

Parameters	ρ_{w0}	ρ_s	n	k_w	χ_w	β'_w	μ_{w0}	$\alpha_{w,T}$	$c_{p,w}$	$c_{p,s}$	λ_w	λ_s
Units	[kg/m³]	[kg/m³]	[-]	[m²]	[Pa]	[°C⁻¹]	[Pa.s]	[°C⁻¹]	[J.kg⁻¹.°C⁻¹]	[J.kg⁻¹.°C⁻¹]	[W.m⁻¹.°C⁻¹]	[W.m⁻¹.°C⁻¹]
	1000	2670	0.39	$2\ 10^{-19}$	$2.2\ 10^{9}$	$3.5\ 10^{-4}$	0.001	0.011	4186	732	0.57	2.42

Table 8.6 : Set of the Boom clay parameters used in the diffusive law in the simulation of the ATLAS experiment.

8.3.3 TIMODAZ benchmark

8.3.3.1 *Introduction*

The TIMODAZ project is a four-year specific targeted project (2006-2010), co-funded by the European Commission, that investigates the thermal impact on the damaged zone around a radioactive waste disposal in clay host rocks. The priorities of the TIMODAZ project have been set on the study of the combined effect of the Excavation Damaged Zone (EDZ) and the thermal impact on the host rocks around a radioactive waste disposal. In particular, this project aims at studying the evolution of the damaged zone with time upon temperature evolution. An important objective of the project will be to perform predictive simulations of the large scale heater experiment PRACLAY that will be performed in the HADES underground research facility at Mol in Belgium (*http://www.timodaz.eu*).

In this context, it has been decided to propose a benchmark exercise to the modelling teams aimed at predicting the THM response of an experiment designed by a group of the project (LMR-EPFL). This experiment aims to carry out laboratory studies of the irreversible processes that develop in the EDZ around galleries in clayey formations and the impact of a thermal phase on their evolution. It consists in hollow cylinder samples of the Boom clay and Opalinus clay which are submitted to mechanical and thermal loadings fairly similar to the evolution that will be encountered around disposal galleries for heat-emitting radioactive waste. In the inner hole of the hollow cylinder, two phases of radial stress decrease along with a dissipation of pore water pressure are followed by a temperature cycle.

The benchmark exercise is performed before carrying out the experiment. In so doing, this first stage of simulation aims to compare the predictive results obtained with different constitutive models and different numerical tools. The results of those calculations will be compared with the experiment in a second step. However, due to schedule reasons, in this thesis, it has not been possible to face the model prediction with experiments. Moreover, only the simulation of the Boom clay behaviour has been performed.

8.3.3.2 *Modelling*

Description of initial and boundary conditions

The problem is treated as a one-dimensional process (radial-axisymmetrical) that is an idealization of the hollow cylinder sample. The geometry of the sample is illustrated in Figure 8.7. The internal and external radii are 7 mm and 42 mm, respectively. The clay sample is considered as homogeneous and isotropic. It is assumed to be fully saturated. The initial conditions considered are listed in Table 8.7. They are close to the one encountered in the Boom clay at the depth of the repository. Gravity is not considered in this modelling.

Variable	Units	Symbol	Value
Radial (x) total stress	[MPa]	σ_{r0}	4.5
Axial (y) total stress	[MPa]	σ_{y0}	4.5
Pore water pressure	[MPa]	p_w	2.2
Radial (x) effective stress	[MPa]	σ'_{r0}	2.3
Axial (y) effective stress	[MPa]	σ'_{y0}	2.3
Temperature	[°C]	T_0	16

Table 8.7 : THM initial state for the hollow cylinder simulation.

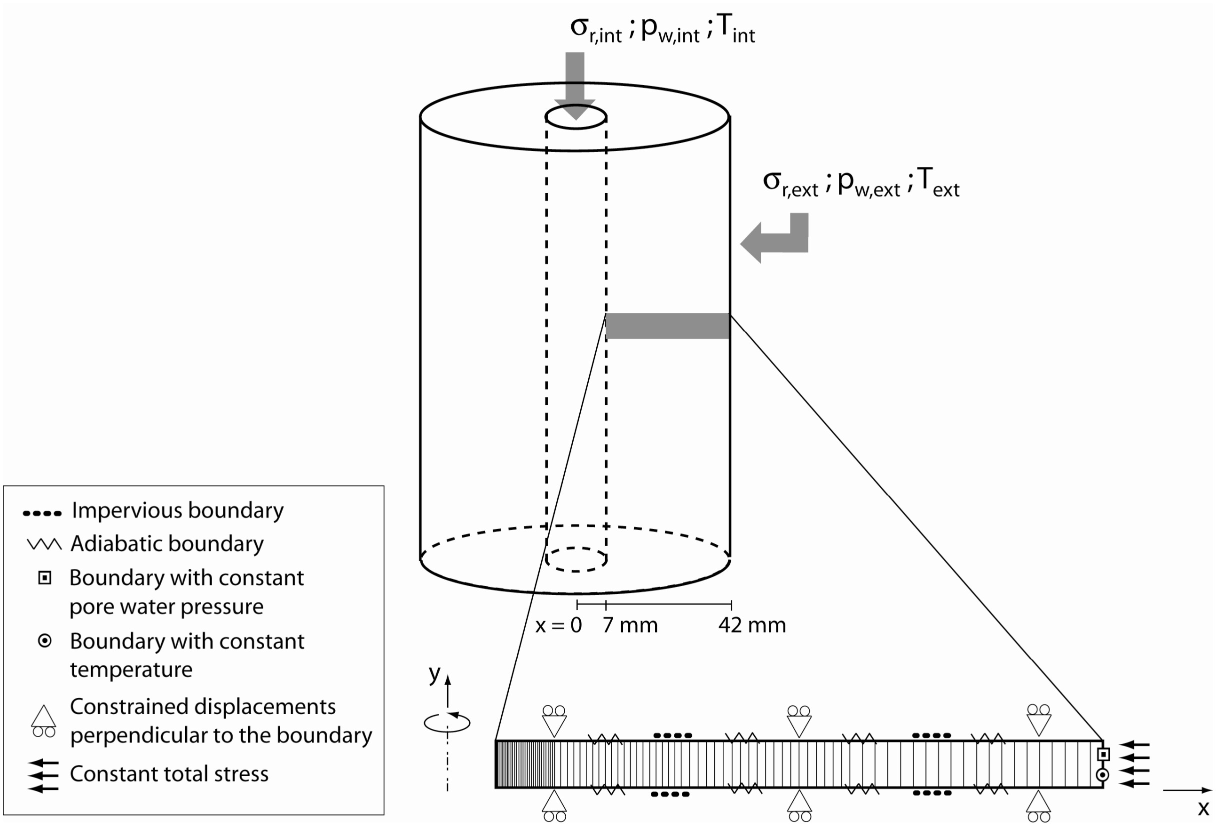

Figure 8.7 : Schematic of the hollow cylinder and its representation by a one-dimensional radial mesh under axisymmetrical condition.

The axial displacements (Y direction) are fixed along the two horizontal boundaries which are considered to be adiabatic and impervious. Constant total radial stress σ_r, pore water pressure p_w and temperature T, corresponding to the initial values, are maintained on the external boundary (Figure 8.7). On the contrary, on the internal boundary, the evolution of σ_r, p_w and T can be divided in three main phases (Figure 8.8). The first phase is a mechanical unloading along with a dissipation of the pore water pressure. It is similar to the hydro-mechanical evolution of the Boom clay state during the excavation of a gallery. The radial stress is kept at a non-zero value (i.e. 1 MPa) which could be assimilated to the action of the liner on the gallery wall. In the second phase, the unloading process goes further, down to 0.2 MPa of effective radial stress. This phase does not correspond to the experimental procedure but can help in the understanding, in a constitutive point of view, of the induced mechanical damage in the Boom clay. The last phase consists of the thermal phase with a temperature cycle in the inner hole which reproduces the real heat emission of radioactive waste.

Constitutive models and parameters

The aim of this benchmark is twofold: (i) To validate the numerical tools used by the different modelling teams through comparing simulation results on a relatively simple constitutive case without considering an advanced rheology of the material. (ii) To extend the study to the consideration of additional coupling effects with more advanced constitutive models.

With this double objective in mind, the numerical simulations were performed in two steps. In the first step, each modelling team used the same simple mechanical constitutive model (i.e. a perfectly plastic Drucker-Prager model, Drucker and Prager (1952)) imposed in the exercise statement. In the second step, liberty was given to use the model that each team considers as the most relevant regarding the Boom clay behaviour. For our modelling, the two steps of simulation were performed with the LAGAMINE code, using the Drucker-Prager model and the ACMEG-T model successively. The Drucker-Prager model is available in the constitutive model library of LAGAMINE.

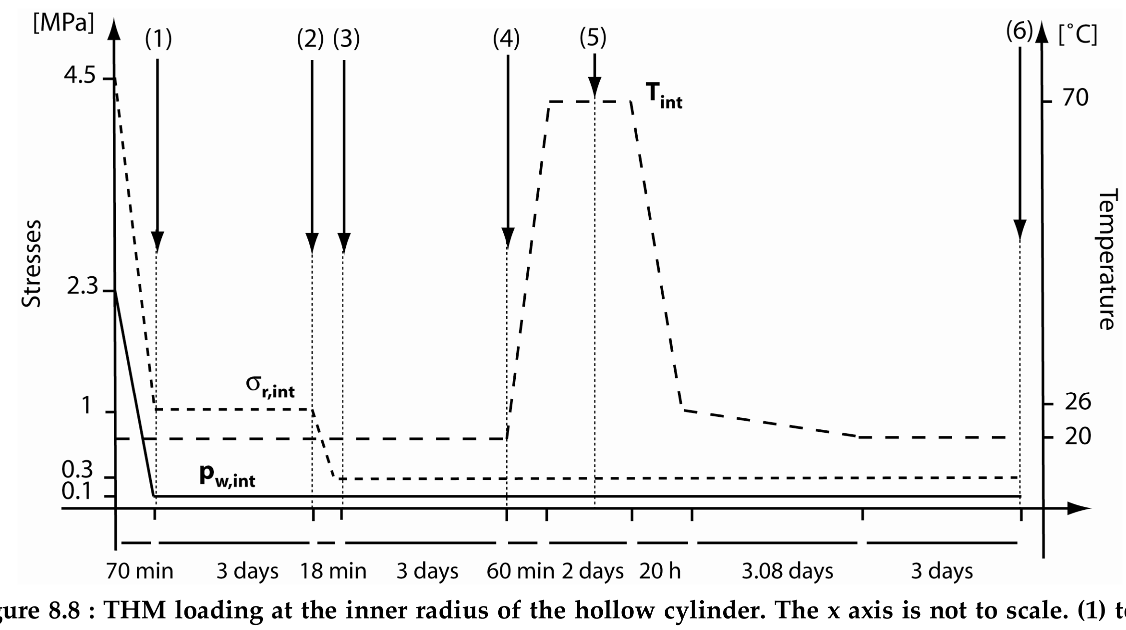

Figure 8.8 : THM loading at the inner radius of the hollow cylinder. The x axis is not to scale. (1) to (6) represent the times when results are reported in Figure 8.9.

The parameters governing the hydraulic and thermal diffusive processes, as well as the parameters of the Drucker-Prager constitutive model, were given in the benchmark statement. On the contrary, the ACMEG-T model parameters have been taken from the calibration presented in Section 8.3.2. The material parameters used in the computation are listed in Table 8.8.

Simulation results

At the time of thesis writing, three groups of modellers (Ulg, UJF, EPFL) had performed calculations with the perfectly plastic Drucker-Prager model. No significant differences have been observed between their results. With each group using the LAGAMINE finite element code, any disparity is impossible due to the model implementation or to the time and space integration. Then, in a second step, the ACMEG-T model was used.

The distribution in space for different times of the key variables is depicted in Figure 8.9. The times when the results are presented are reported in Figure 8.8. Those times have been chosen to be the most representative of the different loading steps. They correspond to the end of the first mechanical unloading (1), the end of the first equalization phase (2), the end of the second unloading phase (3), the end of the second equalization phase (4), the middle of the thermal phase (5) and the final state (6). Also, the variations in time of various variables at different locations are depicted in Figure 8.10. The three chosen locations are the inner radius (x = 7 mm), the middle of the hollow cylinder (x = 24.5 mm) and the outer radius (x = 42 mm).

Geomechanical parameters (Drucker-Prager model)			
Young elastic modulus	E	[MPa]	300
Poisson ratio	υ	[-]	0.125
Cohesion	c'	[kPa]	300
Friction angle	ϕ'	[°]	18
Dilatation angle	ψ	[°]	0
Hydraulic parameters			
Initial porosity	n	[-]	0.39
Intrinsic water permeability	k_w	[m^2]	4 10^{-19}
Water bulk density	ρ_w	[kg/m^3]	1000
Water dynamic viscosity	μ_w	[Pa.s]	10^{-3}
Liquid compressibility coefficient	$1/\chi_w$	[MPa]	5 10^{-4}
Thermal parameters			
Thermal conductivity	Γ	[W/(m.°C)]	1.35
Heat capacity	C_p	[J/(kg.°C)	2300
Solid specific mass	ρ_s	[kg/m^3]	2700
Solid thermal expansion coefficient	β'_s	[°C^{-1}]	10^{-5}
Liquid thermal expansion coefficient	β'_w	[°C^{-1}]	3 10^{-4}
Liquid dynamic viscosity thermal coefficient	$\alpha_{w,T}$	[°C^{-1}]	0.01

Table 8.8 : THM parameters used in the simulation of the hollow cylinder test with the Drucker-Prager constitutive model. The parameters of the ACMEG-T model have been taken from Table 8.5.

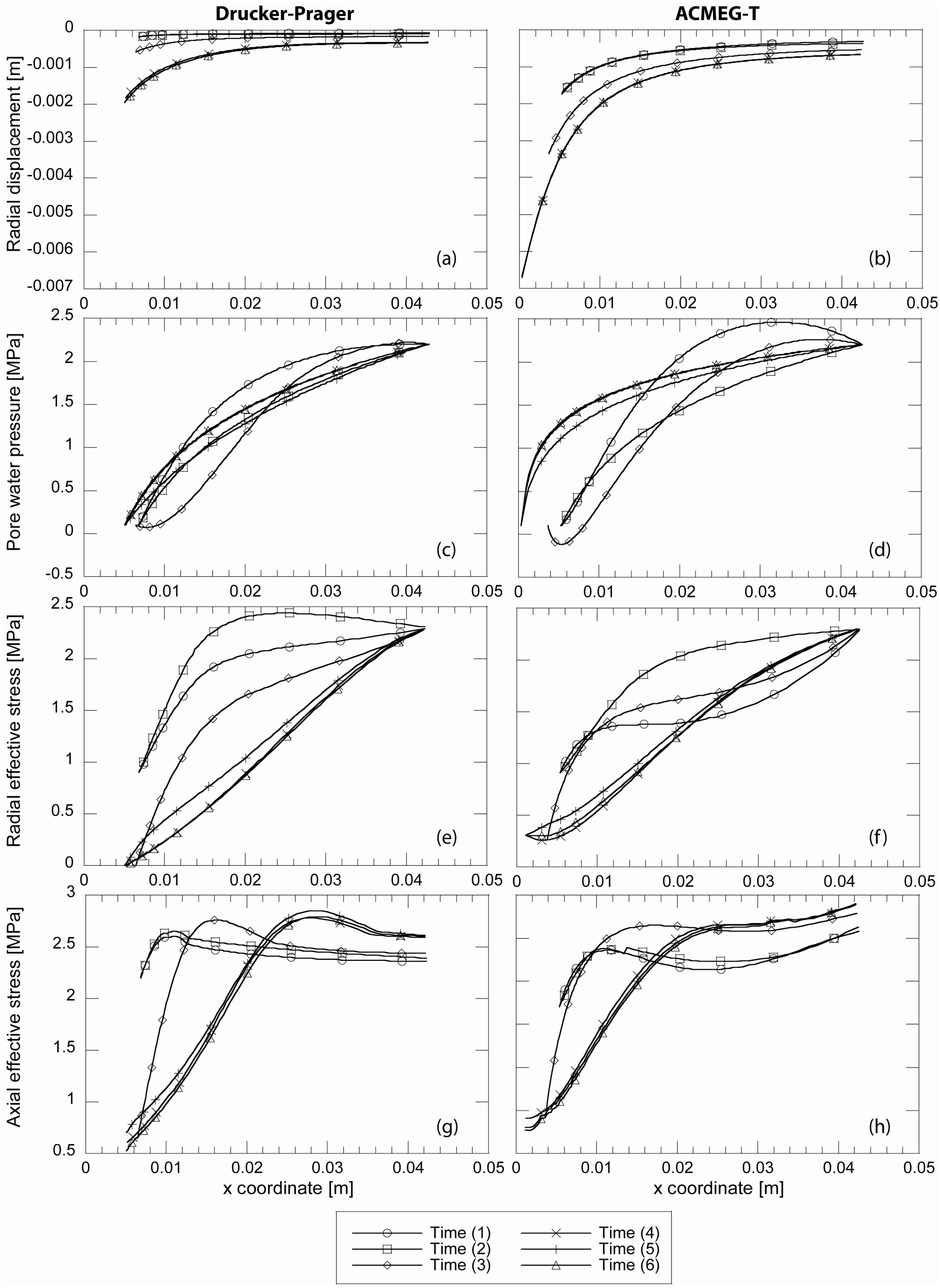

Drucker-Prager
ACMEG-T
Radial displacement [m]
Pore water pressure [MPa]
Radial effective stress [MPa]
Axial effective stress [MPa]
x coordinate [m]
(a)
(b)
(c)
(d)
(e)
(f)
(g)
(h)
Time (1)
Time (2)
Time (3)
Time (4)
Time (5)
Time (6)

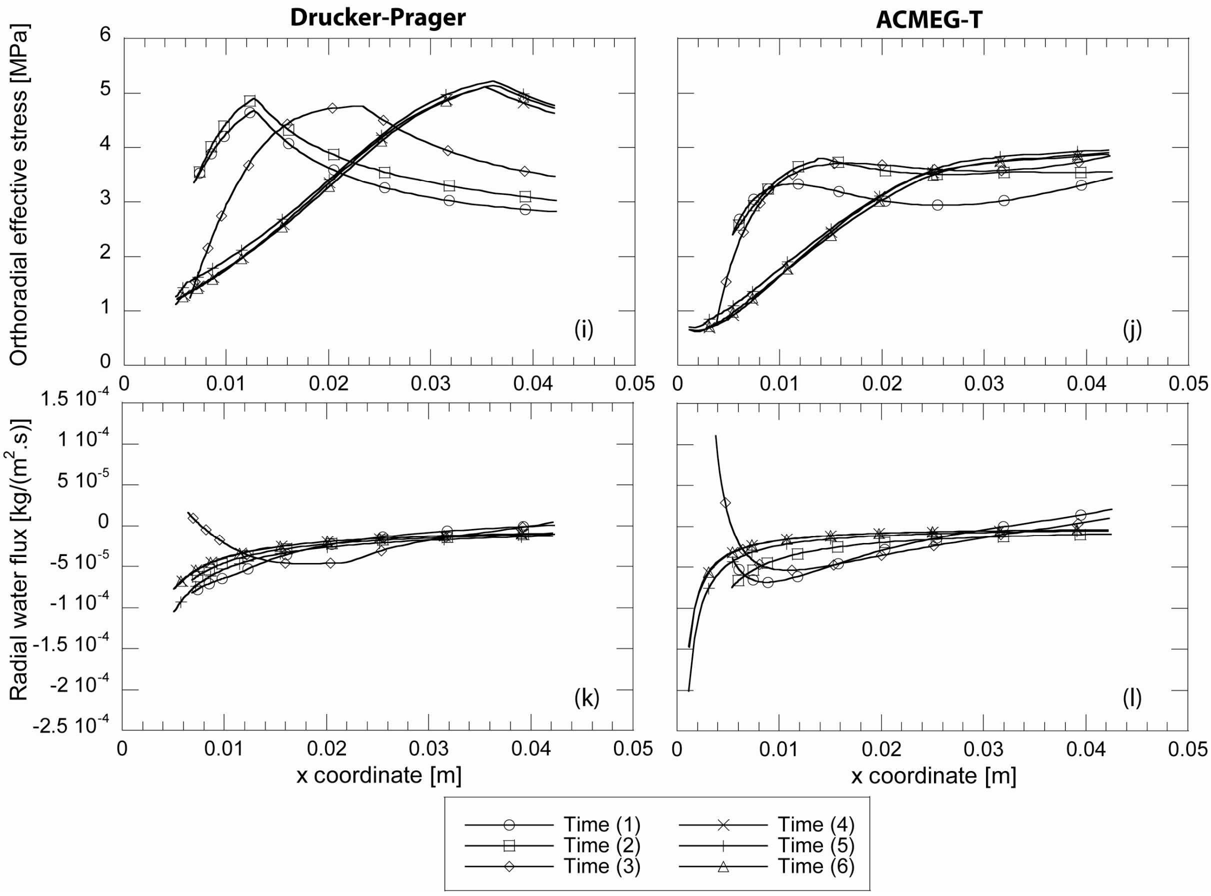

Figure 8.9 : For different times, distribution in space of computed (a, b) radial displacement, (c, d) pore water pressure, (e, f) radial effective stress, (g, h) axial effective stress, (i, j) orthoradial effective stress and (k, l) radial water flux. Comparisons between predictions using the Drucker-Prager model (left) and ACMEG-T model (right). The selected times (1) to (6) are reported in Figure 8.8.

The Drucker-Prager model predicts a 2 mm radial displacement of the inner face of the hollow cylinder which is mainly produced during the second mechanical unloading. The first unloading up to 1 MPa of radial effective stress and the thermal phase produce only negligible displacement (Figure 8.9a). On the contrary, ACMEG-T foresees a quasi-closure of the inner hole (6.8 mm of convergence on the 7 mm of initial radius) which is split up into 1.6 mm of convergence during the first unloading and the rest during the second unloading. Thermal loading does not induce additional convergence (Figure 8.9b).

In the evolution of pore water pressure, several hydro-mechanical coupling effects can be observed. Due to the higher strains and displacements generated by the ACMEG-T model with respect to those produced by the Drucker-Prager model, the hydro-mechanical couplings are more visible in the results of ACMEG-T. The effects of the first mechanical unloading and the drainage of the hole are twofold. In the internal part of the cylinder, the pore water pressure dissipates following the drop of the pore water pressure imposed at the inner boundary. On the contrary, in the external part of the cylinder, the pore water pressure increases due to a hardening process which tends to diminish the pore space. During the first equalization phase, the pore water pressure reaches equilibrium. During the second unloading, similar trends are observed. In addition, a softening effect is observed in the vicinity of the hole, inducing a drop in pore water pressure (Figure 8.9d). This hydro-mechanical effect produces a temporary inversion of the water flux from the inner hole to the soil (Figure 8.9l). The change of geometry predicted by ACMEG-T (e.g. a quasi-closure of the inner hole) considerably reduces the section for radial water seepage. Consequently, the water flux conservation requires that the water flux expressed per surface unit increases drastically in the vicinity of the quasi-closed hole (Figure 8.9k,l).

The evolution of the orthoradial effective stress predicted by the Drucker-Prager model clearly points out the propagation of the plastic zone through the hollow cylinder (Figure 8.9i). Indeed, the limit between the elastic and plastic zones is characterized by the peak of the orthoradial stress. The results of the simulation with the ACMEG-T model do not exhibit such a sharp transition between the elastic and plastic regions (Figure 8.9j). Indeed, due to the progressive mobilization of the plastic mechanisms, it is no longer possible to distinguish a clear elastic zone because the entire domain is plastic.

Figure 8.10a,b show that the temperature in the middle of the hollow cylinder evolves in parallel with the imposed temperature in the internal boundary. There is no transient process in the temperature diffusion. Consequently, the temperature propagation is governed by the thermal boundary conditions and not by thermal diffusion in the Boom clay. The difference in the temperature field predicted by the simulations with Drucker-Prager and ACMEG-T is due to the variation of geometry induced by the choice of the mechanical law. The distance between inner and outer faces is highly modified by the dilatant response predicted by ACMEG-T which produces a change of the thermal gradient in the cylinder. In terms of water flux evolution with time, Figure 8.10c,d show very limited transient periods followed by a long-time episode of steady-state. The decrease of radial water flux produced by the second unloading is due to the partial closure of the inner hole which increases the distance between internal and external pore water boundary conditions. In so doing, the hydraulic gradient decreases. During the temperature phase, the thermally-induced increase of the water permeability produces an increase of the radial water flux. The difference in radial water fluxes predicted by both simulations is due to the change of geometry.

Figure 8.11 depicts the followed stress paths in the $\left(p'-q\right)$ plane at three locations in the hollow cylinder: at the inner face (x = 7 mm), in the middle of the cylinder (x = 24.5 mm) and at the outer face (x = 42 mm). The prediction of the Drucker-Prager model clearly exhibits the elastic path until reaching the critical state line (Figure 8.11a). This plastic limit is reached at different steps in the loading procedure according to the location in the hollow cylinder. The first unloading produces plasticity in the near-field of the hole. This plastic zone progresses during the second unloading and reaches the middle of the cylinder during the second equalization phase. However, the external zone remains elastic during all the processes. On the contrary, the transition between elasticity and plasticity is not observable in the ACMEG-T prediction because progressive plasticity appears gradually in any location of the cylinder (Figure 8.11b). Due to the rapid decrease of the radial effective stress at the inner boundary, the unloading phases take place under quasi-undrained conditions in the middle of the cylinder. Then, the equalization phase enables the dissipation of excess pore water pressure, inducing an increase in the mean effective stress at constant deviatoric stress (a horizontal path in the $\left(p'-q\right)$ plane). Finally, the predictions with ACMEG-T reach the critical state faster than the simulation with the Drucker-Prager model. Indeed, the Drucker-Prager critical state is shifted upward due to the relatively high cohesion imposed in the benchmark statement.

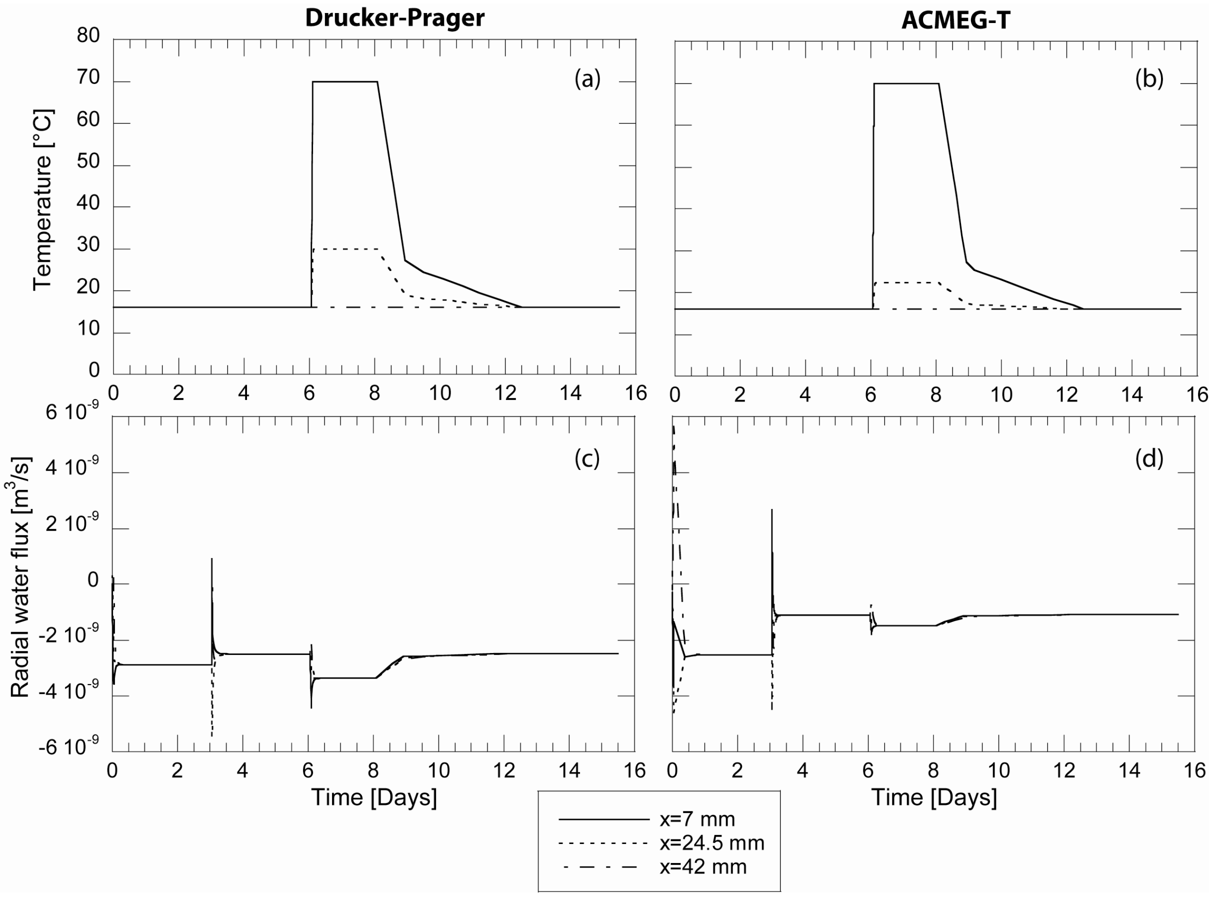

Figure 8.10 : At different locations, variations in time of (a, b) temperature and (c, d) radial water flux. Comparisons between predictions using the Drucker-Prager model (left) and ACMEG-T model (right).

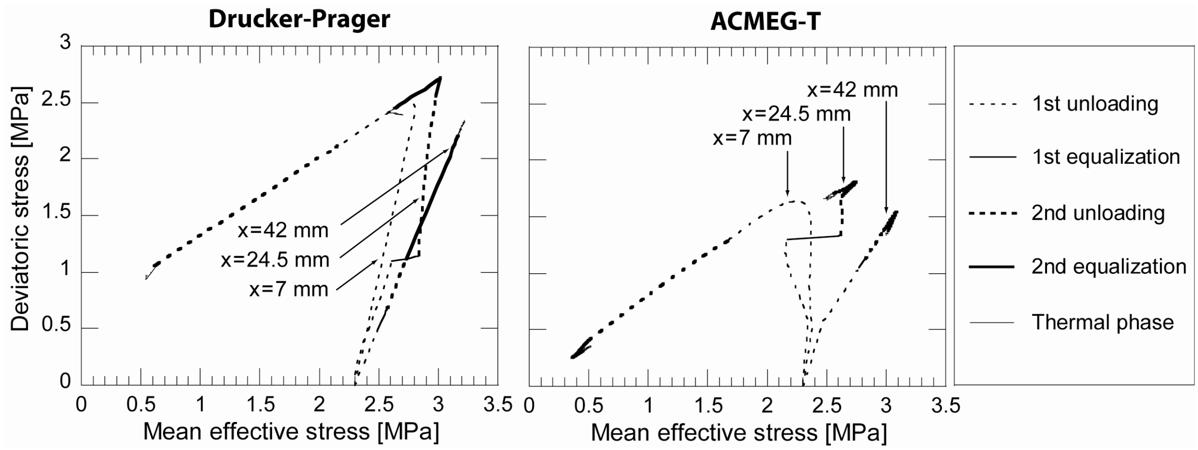

Figure 8.11 : Stress paths in the (p'-q) plane at three different radial coordinates (7 mm, 24.5 mm and 42 mm). Comparisons between predictions using the Drucker-Prager model (left) and ACMEG-T model (right).

Figure 8.12 presents the evolution of some plastic variables of the ACMEG-T model with respect to the radial coordinate. The two phases of mechanical unloading produces a drastic decrease in the mean effective stress in the vicinity of the hole along with an increase of the deviatoric stress. Consequently, the deviatoric plastic mechanism is mobilized in the softening part of the deviatoric yield limit, generating negative volumetric plastic strain. This plastic dilatancy strain reaches more than 12% at the inner hole face (Figure 8.12a).

On the contrary, the external part of the cylinder is subjected to plastic hardening characterized by positive volumetric plastic strain. However, this hardening effect is much lower (less than 1% of volumetric plastic strain) than the softening occurring in the inner part. This hardening part is mainly generated by the increase of the orthoradial stress around the softened zone, induced by stress redistribution. During the thermal phase, a small thermo-plastic hardening produces 2% of the volumetric plastic contraction strain in the first millimetres around the hole. The preconsolidation pressure evolution is directly related to the generated volumetric plastic strain and temperature (Equation (3.34)). In that sense, the hardening process in the external part produces a slight increase of the preconsolidation pressure p'_c (from 6 to 6.5 MPa), while the internal part is subjected to a huge decrease until it reaches less than 1 MPa (Figure 8.12b). Also, the thermal phase (time (5)) decreases p'_c in the whole cylinder domain. The porosity of Boom clay is strongly affected by the softening in the internal part which increases from 0.39 to 0.47 (Figure 8.12c). However, the thermal phase does not produce a significant additional alteration of the Boom Clay. Actually, the porosity distribution is almost similar before (time(4)), during (time (5)) and after (time (6)) the thermal phase. The degree of mobilization of the deviatoric plastic mechanism varies from 1 at the inner radius to 0.7 at the external radius at the end of the second equalization phase (Figure 8.12d).

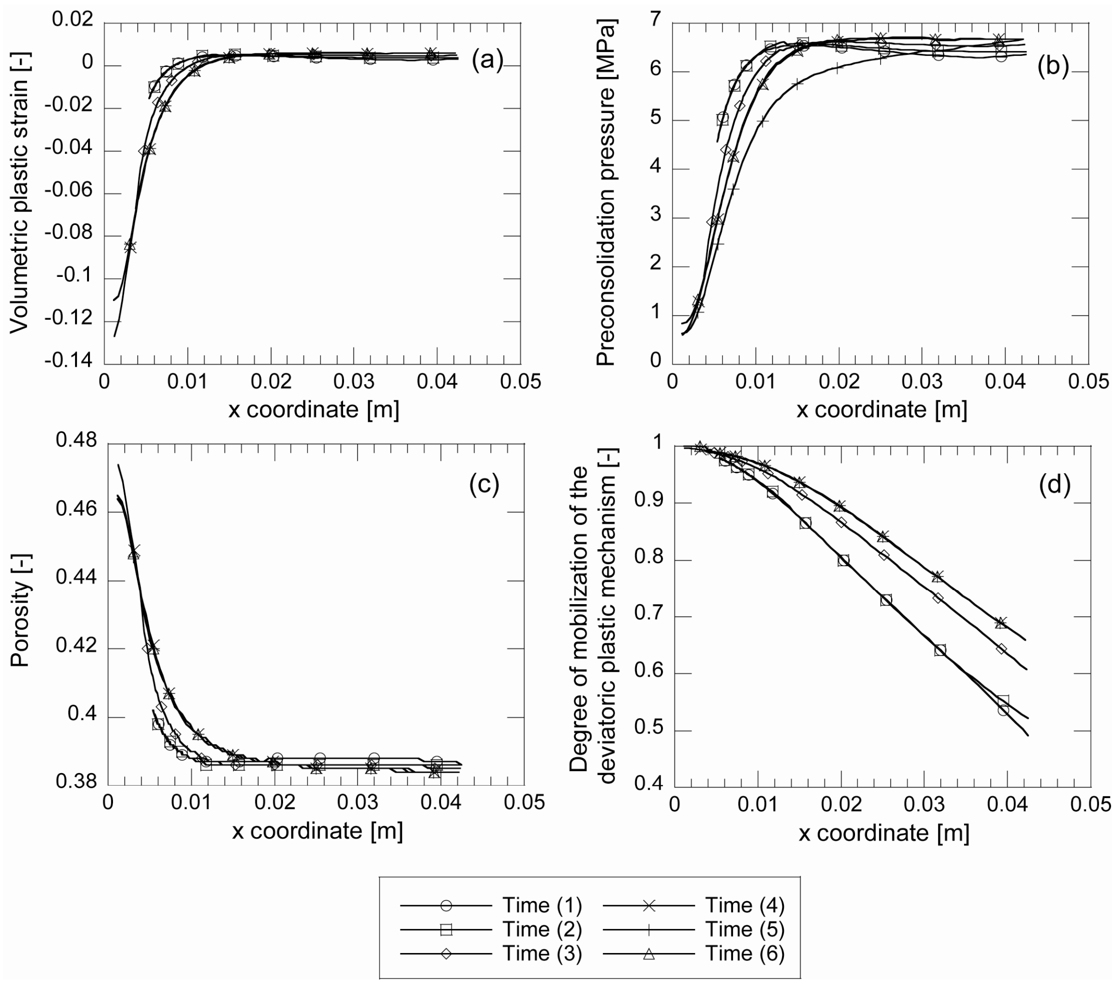

Figure 8.12 : For different times, distribution in space of computed volumetric plastic strain (a), preconsolidation pressure (b), porosity (c) and degree of mobilization of the plastic mechanism (d), predicted by the ACMEG-T model. The selected times (1) to (6) are reported in Figure 8.8.

8.3.3.3 *Conclusions*

The design of the hollow cylinder test aims at reproducing, in a laboratory, the THM evolution of Boom clay during the successive excavation, ventilation and heating phases. Numerical simulation of that experiment provides worthwhile information on the THM behaviour of Boom clay when submitted to such loadings. This simulation was organized in the framework of a benchmark exercise taking place in the context of the TIMODAZ project. The simulations have been performed with two distinct constitutive models: the Drucker-Prager model and the ACMEG-T model. The parameters of the ACMEG-T model were determined from calibration on laboratory tests while the Drucker-Prager model parameters were given in the benchmark statement. The Drucker-Prager model, which is an elastic perfectly-plastic model, predicts a sharp transition between the elastic and plastic states. On the contrary, the results obtained with the ACMEG-T model exhibit a progressive mobilization of the plastic mechanisms, and it is no longer possible to distinguish a clear elastic zone because the entire domain is plastic.

The numerical modelling reveals the drastic increase of the deviatoric stress in the inner part of the cylinder induced by the inner radial stress decrease. Dilatancy plastic strain is produced at the inner hole face, while the external part of the cylinder is subjected to slight plastic hardening characterized by positive volumetric plastic strain. The predicted convergence of the inner hole clearly depends on the model used. The Drucker-Prager model forecasts 2 mm of radial displacement while the ACMEG-T model predicts a quasi-closure of the inner hole (6.8 mm of convergence on the 7 mm of initial radius). Further analysis of the evolution of plastic parameters has been performed for simulations using the ACMEG-T model.

8.3.4 ATLAS in-situ test[1]

8.3.4.1 *Introduction*

The ATLAS experiment, conducted in the underground research facility HADES-URF in Mol (see Section 8.3.2.1), consists of a horizontal main borehole (19 m long) with heaters and two parallel boreholes (15.65 m long) with instrumentation, which have been drilled at 1.184 m and 1.515 m of the main borehole in the same horizontal plane (Figure 8.13) (De Bruyn and Labat, 2002). The central borehole is equipped with four electrical heaters, which are located in the last 8 meters of this borehole. The two instrumentation boreholes are equipped with one biaxial vibrating wire stress meter, four hydraulic flatjacks (FJ) and one piezometer. Two of the flatjacks measure the total horizontal radial stress, σ_x, while the others assess the total vertical stress, σ_z. The first heating phase started on 7th July 1993 at a power of 900W, provided by two of the four heaters. This phase lasted nearly 3 years. In June 1996, a second heating phase started at full power (1800W). Finally, almost one year later, the power was lowered to 0W. This cooling phase started in May 1997.

Aiming at validating the ACMEG-T constitutive model on a boundary value problem reproducing processes analogue to the ones encountered around a real nuclear waste disposal, this section reports the results of simulations of the ATLAS experiment. The obtained results are compared with in-situ measurements of the total stress, temperature and pore water pressure evolutions. Finally, those results are interpreted in the light of elasto-thermoplasticity (François et al., 2008).

[1] François B., Laloui L. and Laurent C. (2008) Thermo-hydro-mechanical interpretation of the response of Boom clay undergoing in-situ thermal loading. *Computers and Geotechnics.* (Accepted).

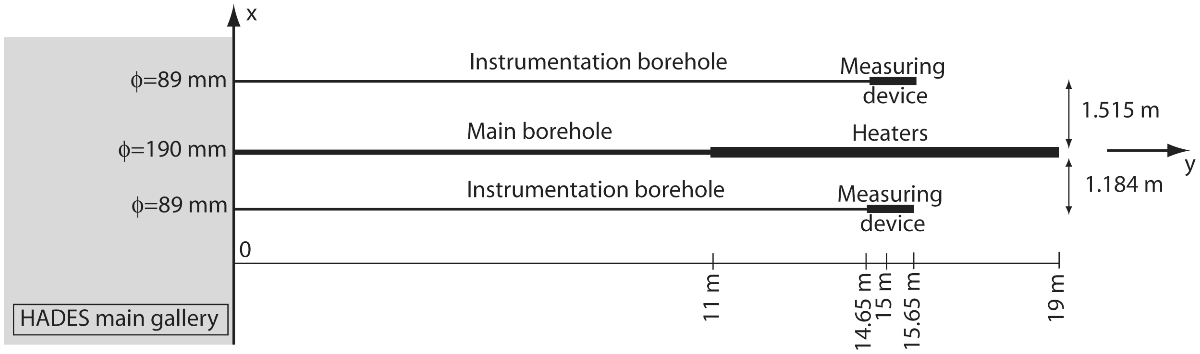

Figure 8.13 : Layout of the ATLAS experiment. View in the horizontal plane.

8.3.4.2 *Features of analysis*

The finite element computations were carried out with the LAGAMINE code. Because the properties and the stress state of the Boom clay formation has been considered homogeneous and isotropic for the considered area, an axisymmetric analysis was performed. The computation domain is assumed to be symmetric in revolution around the axis of the main borehole (Y axis in the present computation). Eight-noded 2D large strain finite elements were used. Water saturated conditions are assumed all along the THM processes. This assumption is consistent with observed results. The used mechanical and diffusive material parameters are reported in Table 8.5 and Table 8.6, respectively.

The modelled domain is included between the internal boundary, corresponding to the external radius of the main borehole, and an external fictive boundary, which was placed at a sufficient distance to limit as much as possible its influence on the computation. Preliminary calculation of heat propagation has shown that a temperature drop of 85°C at the inner boundary, as in the ATLAS experiment, induces an observable temperature change of the surrounding Boom clay in a 30 m radius zone, after 8 years, corresponding to the duration of experiments (Figure 8.14). In addition to this thermal effect, the diffusion of total stress and pore water pressure induced by this temperature modification must be considered around this 30 m radius zone. According to these considerations, an external radius of 100 m was chosen. It aims at limiting the effect of the external boundary conditions on the computational results and at keeping an acceptable time of calculation.

Two different geometries of the modelled domain were considered. Firstly, a slice of the Boom clay medium has been considered, perpendicularly to ATLAS main borehole, in the middle of the heaters, 15 m away from HADES-URF main gallery. This "one-dimensional axisymmetric" case was meshed assuming radial propagation of thermal and hydraulic fluxes. This first configuration neglects the possible dissipation of pore water pressure and temperature in the axial direction (i.e. in the direction of the main borehole). So, secondly, in order to avoid such a restriction, the slice of the Boom clay medium has been widened in the axial direction. This "two-dimensional axisymmetric" case was studied with a rectangular modelled domain of 100 m on 119 m lined by the external radius of both ATLAS central borehole and HADES-URF main gallery. Note that the distance of the external boundary to the heaters is the same (100 m) in both axial and radial directions. The finite element meshes of both cases are depicted in Figure 8.15.

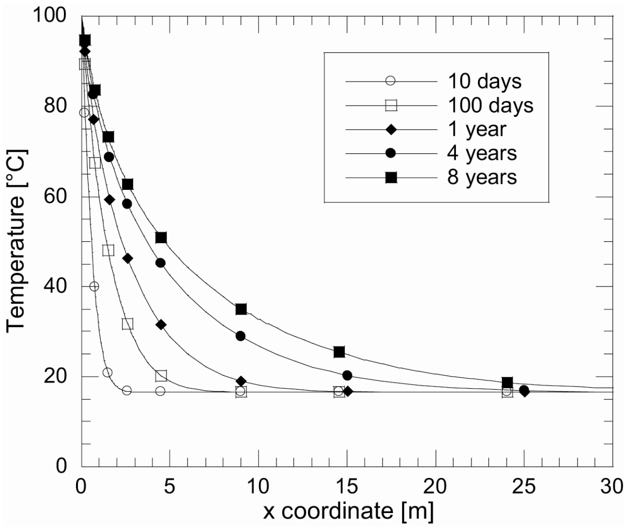

Figure 8.14 : Computed temperature distribution in the Boom clay medium at different times after a fictive 85°C temperature drop in the main borehole assuming a radial thermal propagation.

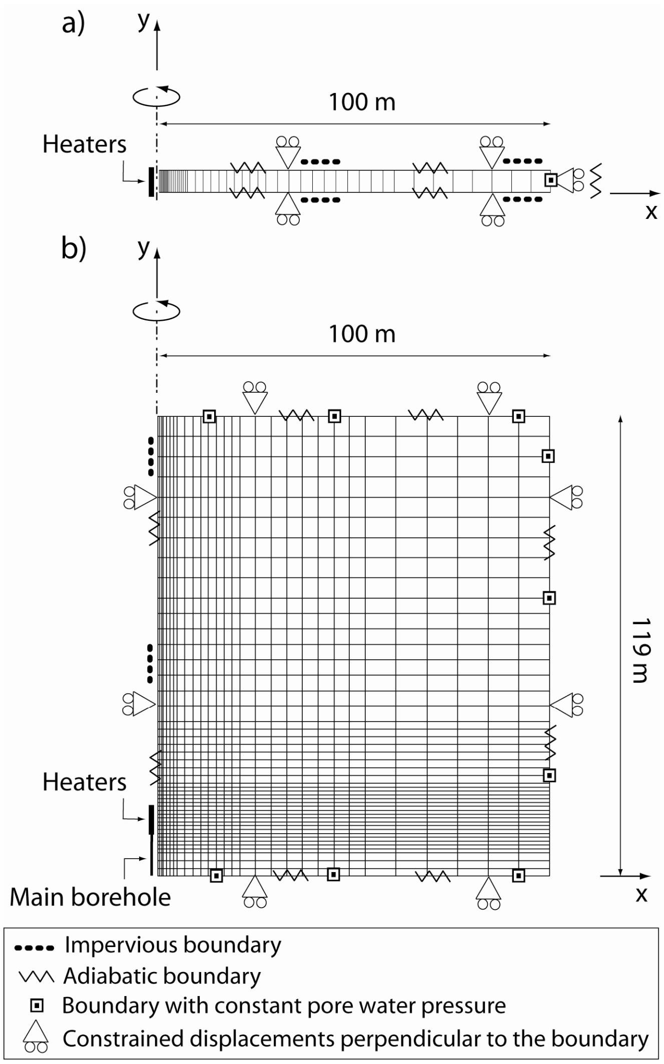

Figure 8.15 : Axisymmetric finite element meshes. (a) "One-dimensional axisymmetric" case; (b) "Two-dimensional axisymmetric" case. The y axis is the axis of symmetry of revolution.

8.3.4.3 *Initial conditions*

In the ATLAS experiment, the one-year period elapsed between the drilling of ATLAS boreholes, and the beginning of the heating phase was assumed to be long enough to render negligible the possible local disturbance of pore water pressure induced by the borehole drillings. Also, it was assumed that the ATLAS heater (placed at 15 m from the HADES-URF gallery) were out of the area in which the THM state is affected by the gallery. As a consequence, the THM initial conditions of Boom clay surrounding ATLAS experiment were assumed similar to the undisturbed in-situ state. So, the initial conditions of all computations were established in agreement with literature analysis, as gathered in Table 8.4 (Section 8.3.2.1) and are reported in Table 8.9. The initial time corresponds to the start of the first heating phase.

8.3.4.4 *"One-dimensional axisymmetric" simulations*

In this first set of simulations, the diffusive processes are restricted in the radial direction, which makes the modelled phenomena less accurate but drastically diminishes the time of calculation. This approach is very convenient in performing parametric studies and can be seen as pre-calculation to validate and optimize computation.

The two boundary conditions of the modelled domain are impermeable and adiabatic, and their displacements are constrained in the Y direction. At the external boundary, the pore water pressure and temperature are kept constant at their in-situ value (i.e. 2.025 MPa and 16.5 °C, respectively) while displacements are constrained in both directions. At the inner boundary, the surface is impermeable and displacements are constrained in both directions (due to the symmetry condition of the problem) (Figure 8.15a). In the ATLAS experiment, temperature was imposed with a constant heat power source in the heaters while in the simulations, temperature variation evolution was fixed at the inner boundary to reproduce the measurements recorded at the instrumentation boreholes thanks to calibrations and back-calculations. The evolution of imposed temperature at the inner boundary is depicted in Figure 8.16.

Figure 8.17 compares the temperature variations computed and measured at the level of the two instrumentation boreholes (i.e. at a distance of 1.184 m and 1.515 m from the axis of symmetry). A very good agreement has been obtained. Nevertheless, it is useful to mention that, because the aim of the analysis was interpretation, not prediction, thermal parameters and thermal solicitations at the main borehole were calibrated to meet agreement between simulation and experimental results. In term of pore water pressure, the evolution obtained by computation at the level of both instrumentation boreholes is compared with experiment in Figure 8.18. The intrinsic water permeability was adjusted at 2.10^{-19} m/s (Table 8.6) to fit with experimental observations.

Variable	Value
Vertical total stress, σ_z	4.5 MPa
Horizontal total stress, $\sigma_x = \sigma_y$	4.5 MPa
Pore water pressure, p_w	2.025 MPa
Preconsolidation pressure, p'_c	6 MPa
Overconsolidation ratio, OCR	2.4
Temperature, T	16.5°C

Table 8.9: Initial state of Boom clay considered in computations.

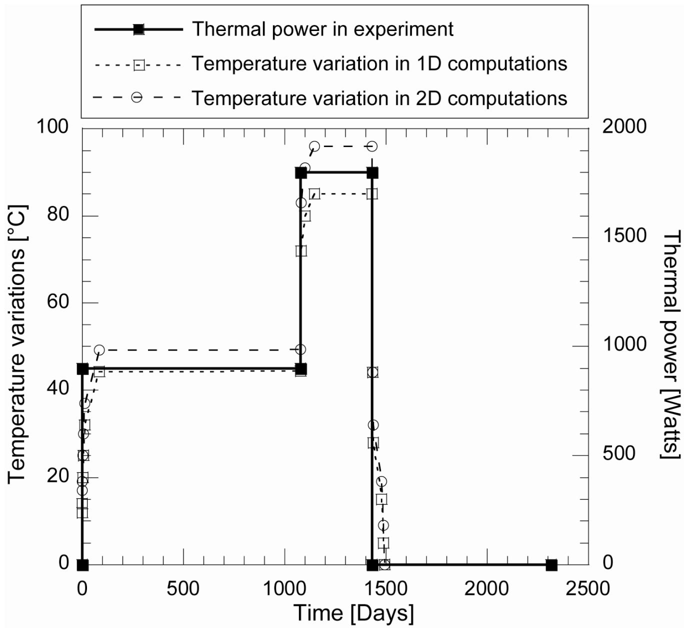

Figure 8.16 : Evolution with time of the imposed temperature at the heater level.

In addition, Figure 8.18 depicts also the computed pore water pressure assuming an elastic behaviour of the material. The comparison between the elastic and elastoplastic cases underlines that the thermo-plasticity brings a modification of about 20% of the excess pore water pressure obtained at a distance between 1 m to 1.5 m of the heat source. In the very near-field, this thermo-plastic contribution should be certainly higher, because thermo-plastic processes dominate in the vicinity of the heat source. Moreover, even if the results are quite good, the dissipation of pore water pressure computed at the end of both heating phases (i.e. when temperature seems to be stabilized) and the steep fall obtained in the early cooling phase are much lower than the experimental observations. This is mainly due to the restriction caused by the assumption limiting the diffusive processes only in the radial direction. To overtake this restrictive hypothesis, the following computations and the subsequent interpretations of the obtained results are performed in "two-dimensional axisymmetric" conditions.

8.3.4.5 *"Two-dimensional axisymmetric" simulations*

For reason of symmetry, the inner boundary condition is considered to be impermeable everywhere and adiabatic everywhere except along the heaters, where temperature variations are imposed according to Figure 8.16. Constant pore water pressure and temperature, equal to their initial values, are imposed in the three other boundaries. Displacements are prevented perpendicularly to each boundary (Figure 8.15b). The lower boundary perpendicular to the main borehole corresponds to the HADES-URF gallery. The axisymmetric conditions in the computations make the HADES-URF gallery act as a vertical plane perpendicular to the main borehole while, in reality, it stands only as a horizontal line. However, this boundary is 15 m from the heating source and therefore plays a minor role in the global THM response of the near-field formation.

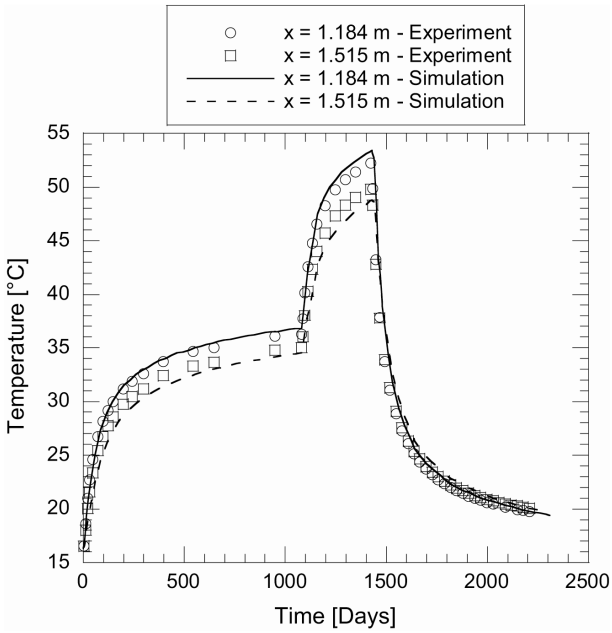

Figure 8.17 : Temperature variation versus time at the instrumentation boreholes: comparison between the numerical results and the experimental measurements, obtained using the one-dimensional axisymmetric approach. x is the distance between the instrumentation borehole and the axis of symmetry.

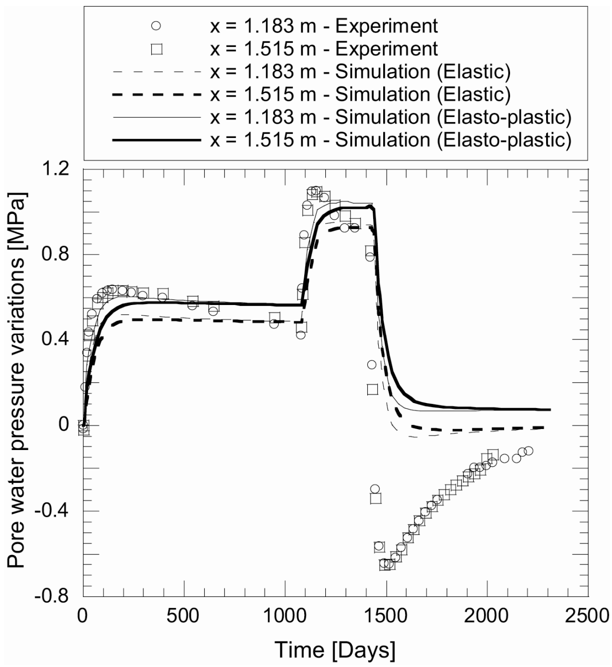

Figure 8.18 : Pore water pressure variation versus time at the instrumentation boreholes: comparison between the numerical results and the experimental measurements, obtained using the one-dimensional axisymmetric approach. The numerical results are given considering both thermo-elastic and thermo-elasto-plastic behaviour of Boom clay. x is the distance between instrumentation borehole and the axis of symmetry.

Figure 8.19 shows the temperature variation evolution at the level of both instrumentation boreholes and is very similar to Figure 8.17. This good agreement between experiment and simulation results from a calibration of the evolution of imposed temperature at the heater level (Figure 8.16), while the thermal diffusive parameters were unchanged with respect to the "one-dimensional axisymmetric" case. The computed pore water pressure evolution in the two instrumentation boreholes are represented in Figure 8.20 in both elastic and elasto-plastic conditions. Dissipations of pore water pressure at the end of both heating phases are well reproduced without any adjustments. Moreover, the reproduction of the steep fall observed in the early cooling phase, not reproduced by the "one-dimensional axisymmetric" simulations, is now close to the measurements. These improvements confirm the necessity to perform calculation accounting for flow diffusion in all three directions.

Variations in total stresses in both radial and orthoradial directions are represented in Figure 8.21 and Figure 8.22, respectively. Significant differences can be observed in the order of magnitude of numerical results and measurements. This lack of agreement between total stresses, numerically predicted and experimentally measured, was already noted in the framework of the Interclay benchmark results, as reported by Jeffries (1995). Until now, no consistent justification exists to explain such a difference. However, Bernier and Neerdael (1996) mentioned that the thermal dilatation of the measurement device may introduce significant disturbance in the recorded total stress. In that sense, the measured total stress may be overestimated because of temperature effects on the device itself.

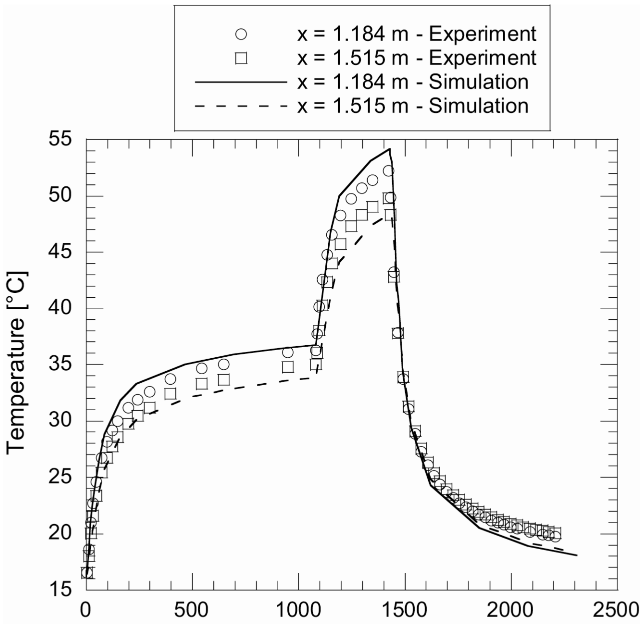

Figure 8.19 : Temperature variation versus time at the instrumentation boreholes: comparison between the measurements (Experiment) and the numerical results (Simulation), obtained using the two-dimensional axisymmetric approach. x is the distance between instrumentation borehole and the axis of symmetry.

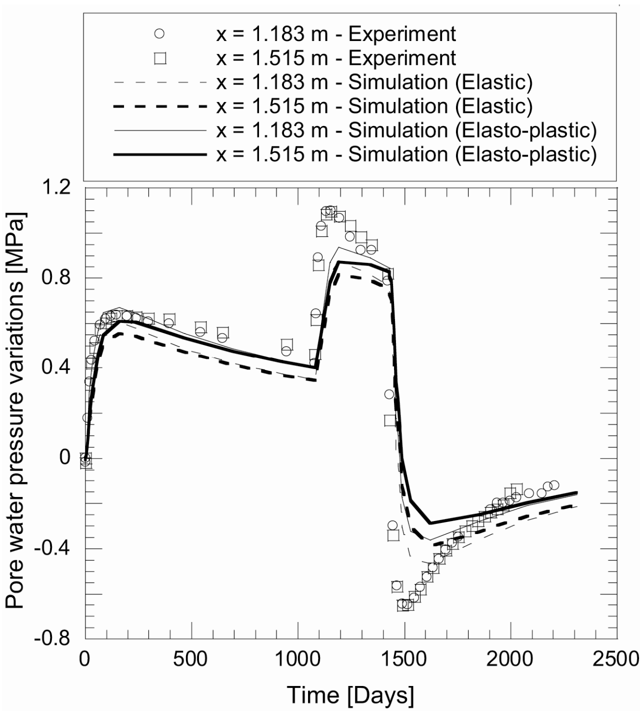

Figure 8.20 : Pore water pressure variation versus time at the instrumentation boreholes: comparison between the measurements (Experiment) and the numerical results (Simulation), obtained using the two-dimensional axisymmetric approach, in both thermo-elasticity and thermo-elastoplasticity. x is the distance between the instrumentation borehole and the axis of symmetry.

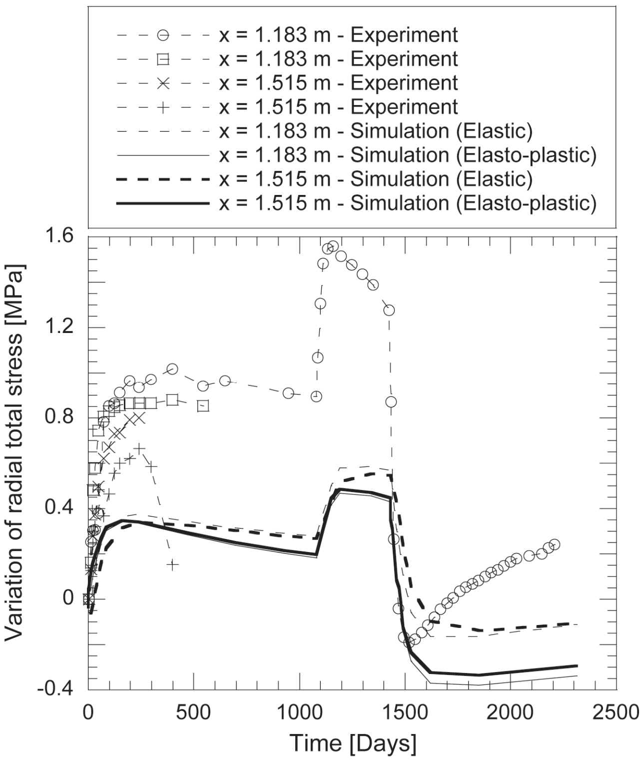

Figure 8.21 : Radial total stress variation at the instrumentation boreholes: comparison between the measurements (Experiment) and the numerical results (Simulation), obtained using the two-dimensional axisymmetric approach, in both thermo-elasticity and thermo-elastoplasticity. x is the distance between instrumentation borehole and the axis of symmetry.

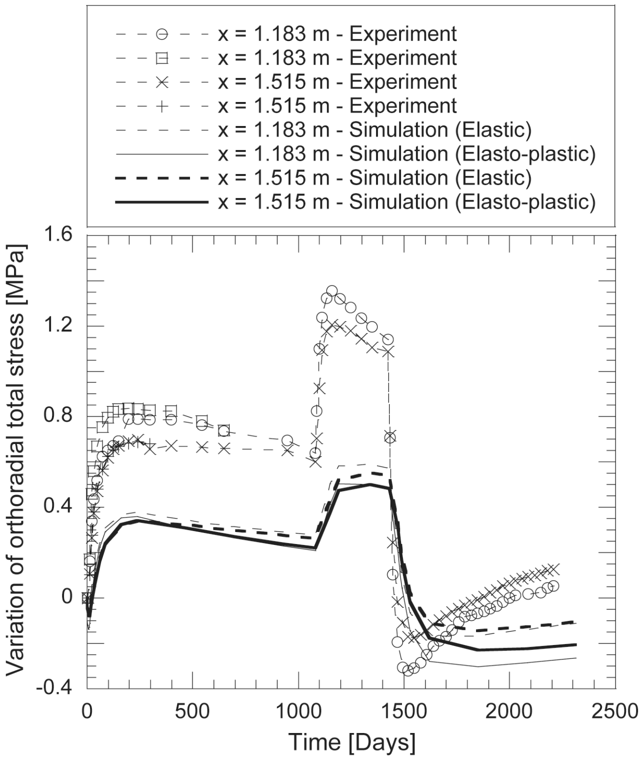

Figure 8.22 : Circumferential total stress variation at the instrumentation boreholes: comparison between the measurements (Experiment) and the numerical results (Simulation), obtained using the two-dimensional axisymmetric approach, in both elasticity and elasto-plasticity. x is the distance between the instrumentation borehole and the axis of symmetry.

8.3.4.6 *Interpretation in the near field*

As the aim of this work is the interpretation of the observed behaviour, the parameters of the study were partially determined thanks to independent laboratory experiments or literature reviews and partially calibrated to fit with some experimental observations in the two instrumentation boreholes. This part of the work has produced results in agreement with the experiment. This first step being validated, the aim is, now, to bring additional information about the different THM couplings occurring in Boom clay surrounding the heat source. To this end, the time evolution and the space distribution of some key variables of the diffusive and mechanical models in the near-field of the main borehole are presented and interpreted in the light of elasto-thermoplasticity.

Figure 8.23a shows that, after one year, temperatures obtained at the end of the first phase (which lasts 3 years) are already almost reached. Also, during the second phase, the temperature increases significantly in the near-field, but the size of the influenced area is similar in both phases. In other words, the thermal power of solicitation does not affect the size of the domain in which temperature variation occurs, at least for the range of temperature and time considered in the present study. The cooling of the medium is fast, and after 4.5 years (i.e. 6 months after the beginning of the cooling phase), the temperature is relatively close to the initial value everywhere in the medium.

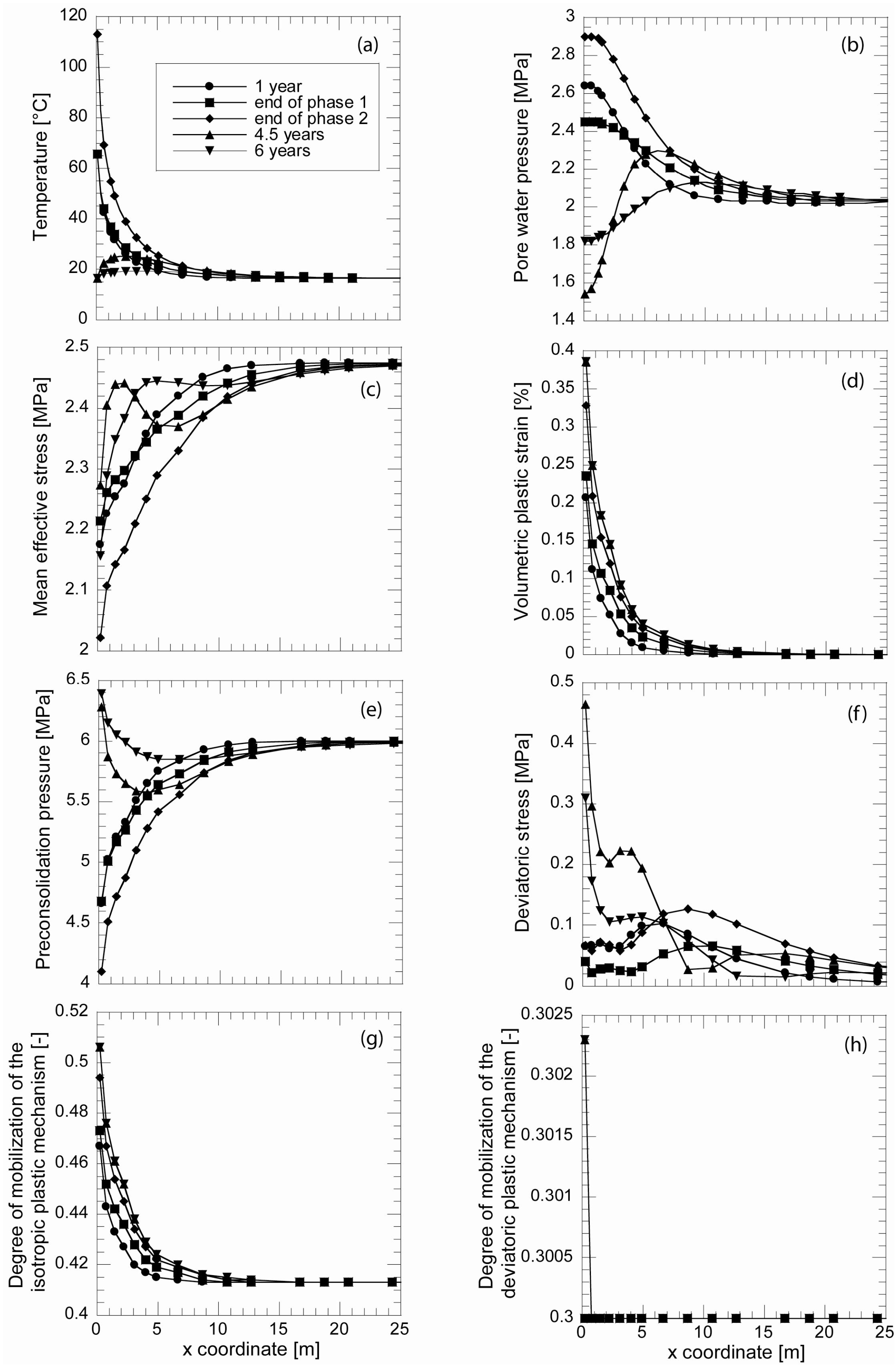

Figure 8.23 : For different times, distribution in space of computed (a) temperature, (b) pore water pressure, (c) mean effective stress, (d) volumetric plastic strain, (e) preconsolidation pressure, (f) deviatoric stress and degrees of mobilization of (g) isotropic and (h) deviatoric plastic mechanisms.

In addition to observations already discussed in the interpretation of Figure 8.20, Figure 8.23b clearly shows that excess pore water pressure is generated beyond the zone affected by temperature variation. Indeed, pore water pressure varies up to a distance of 20 m from the main boreholes while temperature change occurs only inside a radius of approximately 8 m. It proves that, due to hydraulic diffusive processes, the effect of temperature on the generated pore water pressure must be considered in a zone much larger than the area in which temperature is modified. Figure 8.23c highlights the decrease of mean effective stress mainly caused by an increase of pore water pressure. However, this process is not fully reversible. Indeed, at the end of ATLAS experiment (i.e. after 6 years), excess pore water pressure is almost dissipated (Figure 8.23b) while mean effective stress remains lower than its initial value. This effect is due to the thermo-plasticity, which produces irreversible volumetric strain (Figure 8.23d) and, as a consequence, induces a redistribution of effective stresses in the medium. The generated volumetric plastic strain induces a material hardening and leads to an increase of the preconsolidation pressure (Figure 8.23e). In other words, at the end of the THM processes, when temperature and pore water pressure have recovered their initial value, Boom clay characteristics have been modified, in the sense that the size of elastic domain has been enhanced. This behaviour over the whole temperature cycle is representative of thermal hardening.

The evolution of the deviatoric stress depicted in Figure 8.23f also results from the stress redistribution induced by the THM transient processes and by the irreversible volume change of Boom clay. Nevertheless, the magnitude of the deviatoric stress remains very low. Figure 8.5 clearly shows that 0.5 MPa of deviatoric stress has an insignificant effect in terms of generated deviatoric and volumetric strains. This observation underlines the predominance of isotropic processes compared to the deviatoric ones. This is corroborated with the evolution of the degree of mobilization of each plastic mechanism. The isotropic mechanism is activated all along the THM process (reaching 50 % of plastic mobilization, Figure 8.23g) while the deviatoric mechanism remains inactivated (its degree of mobilization keeps its initial value, Figure 8.23h).

Figure 8.24 shows the evolution of the radial displacement with time at different locations around the heat source. Even though volumetric response of Boom clay subject to heating under drained conditions, at such an OCR, is compaction (Figure 8.6), the obtained radial displacements during temperature increase, showing a dilatation of the near-field. This behaviour is caused by the temperature-induced pore water pressure. However, at the end of the ATLAS experiment, when pore water pressure is almost dissipated, an irrecoverable compaction strain is obtained in the near field and inward radial displacements occur.

Stress paths in the $(p' - q)$ plane are illustrated in Figure 8.25a, b and c, respectively, at distances of 0.21 m, 0.75 m and 1.45 m from the main borehole. In the early first phase, the mean effective stress p' decreases, as already explained in the interpretation of Figure 8.23c. Then, in the late first phase, p' increases. This increase seems mainly caused by the dissipation of the excess pore water pressure in the medium at the end of the heating phases. The evolution of the stress state during the second heating phase looks similar to the stress path caused by the first phase. The induced gradient of mean effective stress may cause the observed increase of the deviatoric stress. A rapid increase in both p' and q is observed in the early third phase (cooling phase) and is thought to be induced by the rapid decrease in pore water pressure at the beginning of this cooling phase. Also, one can observe that the smaller the coordinate x, the bigger the variations of both deviatoric stress q and mean effective stress p'. Indeed, the processes that occur in the medium are more intense close to the heaters.

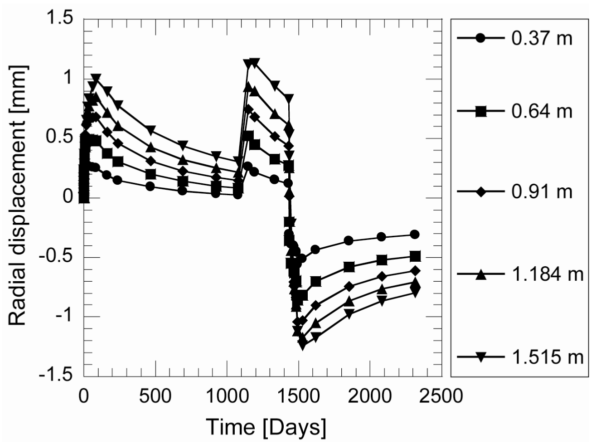

Figure 8.24 : At different locations, variations in time of displacements in the radial direction. Positive displacement corresponds to an outward displacement.

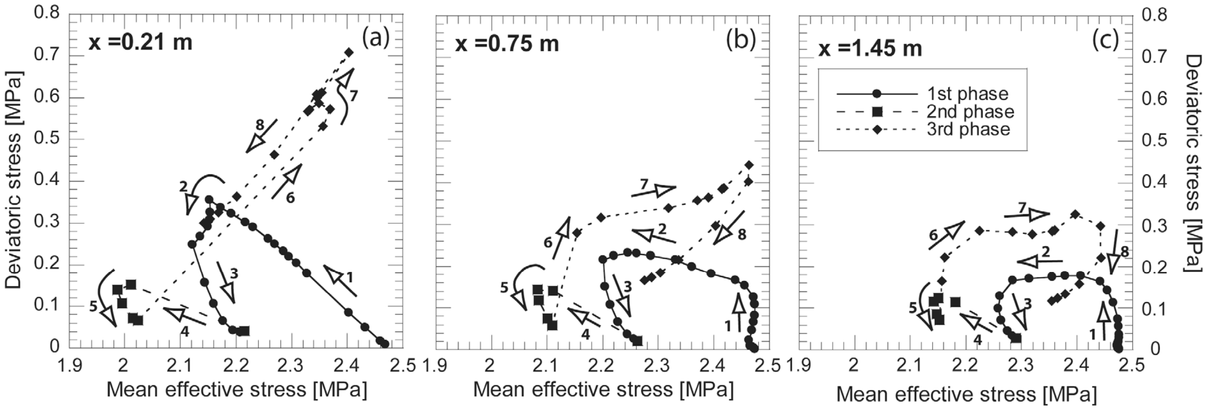

Figure 8.25 : Stress paths in the $(p'-q)$ plane, at (a) 0.21 m, (b) 0.75 m and (c) 1.45 m from the centre of the main borehole.

8.3.4.7 *Conclusions*

Following the need to understand and quantify the effect of temperature on the response of a candidate host formation (i.e. Boom clay) for radioactive waste disposal, a finite element modelling of an in-situ thermal experiment has been carried out.

The numerical simulation of the large-scale ATLAS experiment was achieved and the results were compared with in-situ measurements. This comparison clearly reveals the need to perform calculations accounting for flow diffusion in all three directions through a 2D axisymmetric analysis. An accurate reproduction of both pore water pressure dissipation and its steep fall in the early cooling phase is only possible with such a 2D axisymmetric approach. In addition, the use of a thermo-plastic constitutive model, supported by experimental evidence, offers noticeable advancement in the modelling of such phenomena. In particular the use of a consitent isotropic thermo-plastic mechanism improves of about 20% the prediction of the pore water pressure evolution around the heater. In that sense, the further interpretations of the obtained results show irreversible strains occurring in the near-field, which induce a redistribution of the effective stress in the medium.

The ACMEG-T model implemented in an advance finite element code permits substantial advancement in the understanding of the highly coupled processes occurring in a saturated clayey formation undergoing temperature variations.

8.3.5 FEBEX in-situ test

8.3.5.1 *Introduction*

The FEBEX (Full-scale Engineered Barriers EXperiment in crystalline host rock) in-situ test is a near-to-real experiment carried out in the underground laboratory at Grimsel (Switzerland). The FEBEX test has been designed in relation to the Spanish reference concept of underground nuclear waste disposal in a granitic formation. The gallery, excavated in the granitic rock of Aare Massif in central Switzerland, has a diameter of 2.28 m and a length of 71.4 m. Two heaters (0.95 m diameter and 4.54 m long, the same dimensions as the canisters of the reference disposal concept) were placed in the axis of the gallery at a 1 m distance from each other. The free space between the heaters and the granite was filled with compacted bentonite blocks on the last 17 m of the gallery. The 17 m long test zone was sealed by a concrete plug (Figure 8.26) (Lloret et al., 2004).

The purpose of this in-situ experiment was not only to demonstrate the technical feasibility of such a concept, but also to provide direct measurements in terms of temperature, fluid pressure, humidity, total stresses and deformation of the confining structure. Such information is worthwhile for the verification and the validation of mathematical models used to predict the coupled processes occurring in the near-field of nuclear waste disposal. Several numerical predictions or validations have already been reported in the literature (Gens et al., 1998, 2002; Alonso et al., 2005; Gens et al., 2004; Sugita et al., 2004; Rutqvist and Tsang, 2004; Nguyen et al., 2005).

In this section, predictions of the THM behaviour of compacted bentonite and host rock have been performed by the means of finite element simulations with the LAGAMINE code. It aims to validate the implementation of the ACMEG-TS model on complex highly coupled boundary value problems involving non-isothermal and unsaturated phenomena. Moreover, this near-to-real experiment enables the understanding of the main THM processes occurring in geomaterials around an underground nuclear waste disposal. As a preliminary modelling, a laboratory experiment reproducing the infiltration processes through the compacted bentonite has been modelled in order to validate the material parameters used. Then the in-situ FEBEX experiment was simulated.

This section successively presents the characteristics of the involved materials, the modelling of the infiltration test, the features of the performed numerical analysis of the in-situ test, the comparison of obtained results with in-situ measurements and further interpretations in terms of mechanical irreversibilities, coupling between mechanical, thermal and water retention responses and diffusion processes.

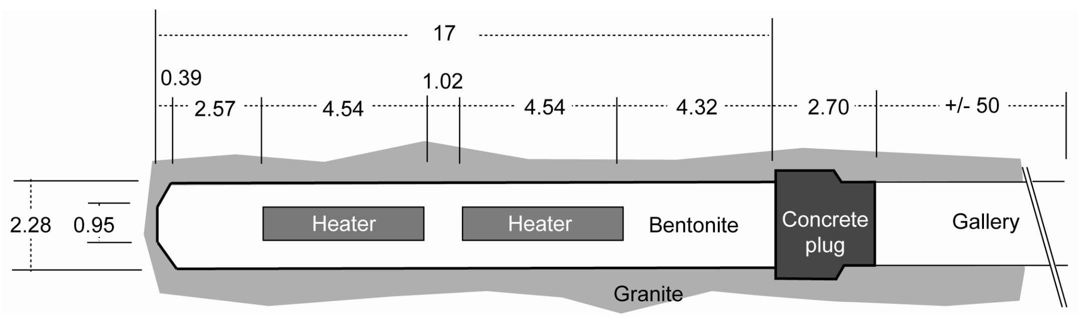

Figure 8.26 : Lay-out of the FEBEX in-situ test (dimension in meter).

8.3.5.2 *Material characteristics*

FEBEX bentonite

The clay barrier was constructed with highly compacted FEBEX bentonite blocks with a dry density of 1.77 g/cm³ (i.e. an initial void ratio of 0.52). This density is determined by considering the anticipated volume of construction gaps and a final dry density of the clay of 1.65 g/cm³ (i.e. a void ratio of 0.63). The initial water content of the blocks ranges from 12.5% to 15.5% (i.e. an initial degree of saturation from 55% to 67%). This compacted state corresponds to an initial suction of 80 MPa (Lloret et al., 2004).

The THM properties of the FEBEX bentonite have been extensively investigated over the last decade. Its mechanical behaviour under non-isothermal and unsaturated conditions has been characterized by the means of several experimental programs (Villar, 1999; ENRESA, 2000; Villar, 2002; Lloret et al., 2003, Villar and Lloret, 2004; Lloret et al., 2004; Romero et al., 2005, Villar et al., 2005a). In Chapter 6, a series of numerical simulations of oedometric tests on thermal, hydraulic and mechanical paths have been performed. It displays the parameters defining the isotropic mechanical behaviour as well as the water retention behaviour (Table 6.1). As far as the deviatoric mechanical behaviour of the FEBEX bentonite is concerned, there is a lack of relevant information on its characterization. Nevertheless, various triaxial tests were performed on samples of different dry densities and different unsaturated states (ENRESA, 1998, reported by ENRESA, 2000). On that basis, a friction angle of 30° has been selected in the computation. Due to the lack of additional information, the other deviatoric mechanical parameters have been assigned with usual values for such a kind of clay. The set of mechanical and water retention parameters are reported in Table 8.10.

The parameters governing the thermal and hydraulic diffusion in FEBEX bentonite are directly established from a literature synthesis. Villar (2002) reported the saturated hydraulic conductivity as a function of the dry density. The Kozeni-Karman relation enables one to relate the saturated permeability $k_{w,sat}$ with soil porosity n:

$$k_{w,sat} = k_{w0,sat} \frac{n^{EXPN}}{(1-n)^{EXPM}} \frac{(1-n_0)^{EXPM}}{n_0^{\ EXPN}} \tag{8.1}$$

Elastic parameters		
K_{ref} , G_{ref} , n^e , β_s'	[MPa], [MPa], [-], [°C^{-1}]	16, 3.5, 1, 6.67 10^{-4}
Isotropic plastic parameters		
β , γ_s , γ_T , c , r_{iso}^e , p_c'	[-], [-], [-], [-], [-], [MPa]	14.3, 16.1, 2.1, 0.02, 0.45, 4
Deviatoric plastic mechanical parameters		
b , d , ϕ_0' , g , α , a , r_{dev}^e	[-], [-], [°], [-], [-], [-], [-]	1, 1.5, 30, 0, 1, 0.001, 0.2
Water retention parameters		
s_{e0} , β_h , θ_T , θ_e , s_{hys}	[MPa], [-], [-], [-], [-]	4, 8.64, 0.7, 10.8, 0.6

Table 8.10 : Set of mechanical parameters of FEBEX bentonite used for the ACMEG-TS model in the simulation of the FEBEX in-situ test.

where $k_{w0,sat}$ is the saturated water permeability corresponding to the reference porosity n_0 and $EXPN$ and $EXPM$ are material parameters of the Kozeni-Karman relation. Figure 8.27 shows the good agreement of this relation for $k_{w0,sat} = 4\ 10^{-14} m/s$ corresponding to $n_0 = 0.37$ (i.e. $\rho_d = 1.7\ g/cm^3$) and $EXPN = EXPM = 6.5$.

In addition, the water permeability depends on the degree of saturation of the bentonite. Through a back-analysis of thermo-hydraulic bentonite properties from laboratory tests, Pintado et al. (2002) determined that the following relationship has the best agreement with $CKW1 = 2.9$:

$$k_w = k_{w,sat} k_{w,r} = k_{w,sat} S_r^{CKW1} \tag{8.2}$$

with S_r being the degree of saturation and $k_{w,r}$ the relative permeability. In addition, the water permeability is affected by its temperature through the thermal reduction of the viscosity of water (Equation (7.14)).

The thermal diffusion is governed by the mean approximation in function of the proportion of each phase in the bentonite:

$$\lambda = \lambda_s (1-n) + \lambda_w n S_r + \lambda_g n (1-S_r) \tag{8.3}$$

where λ_s, λ_w and λ_g are the thermal conductivities of the solid, the liquid water and the gas, respectively. This equation yields good agreement with experimental data for $(\lambda_s\ ;\ \lambda_w\ ;\ \lambda_a) = (0.7\ ;\ 2.1\ ;\ 0)\left[W/(m°C)\right]$ (Figure 8.28). The heat capacity of the solid matrix is $c_s = 1091\ J/(kg°C)$ (Gens et al., 1998).

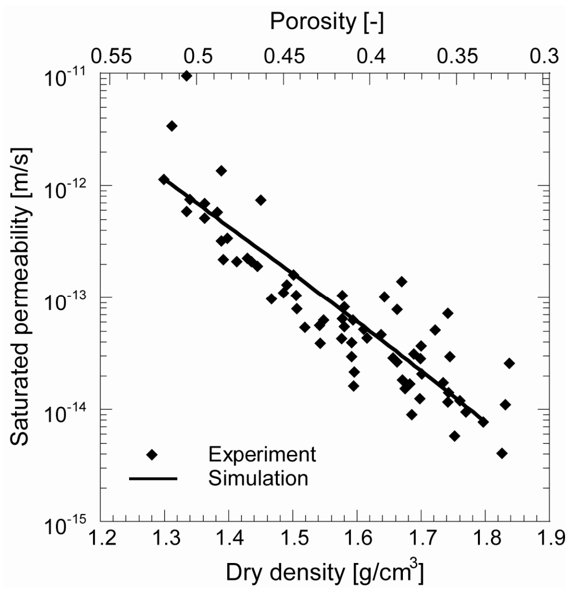

Figure 8.27 : Effect of dry density on the saturated permeability of FEBEX bentonite considered with the Kozeni-Karman relation.

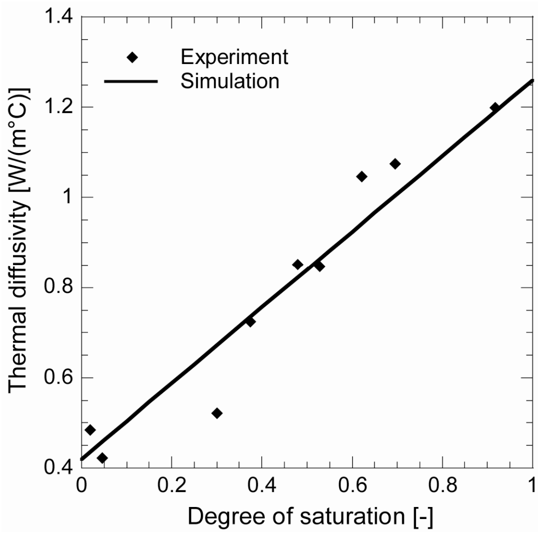

Figure 8.28 : Effect of the degree of saturation on the thermal diffusivity of FEBEX bentonite. Comparison between laboratory measurements (Gens et al., 1998) and simulation.

The gas phase is modelled as an ideal gas mixture composed of dry air and water vapour. Phase changes of water (evaporation-condensation, adsorption-desorption) and latent heat transfer are considered. Table 8.11 reports the material parameters of FEBEX bentonite in relation to the thermal and hydraulic diffusion processes. The parameters of the water retention curve have already been defined in Table 8.10.

Granite

The Grimsel test site has been excavated in a predominately granite and granodiorite rock mass that has been affected by various episodes of fracturing (ENRESA, 2000). In particular, in the test drift region, shear zones are of considerable area and govern the hydrogeological conditions of the massif. Hydraulic and mechanical properties of the Aare massif granite have been compiled in several internal reports and have been partially reported by Alonso et al. (2005) and Gens et al. (1998) (see also Sobolik et al., 2004 and Rutqvist and Tsang, 2004).

The mechanical behaviour of the granite is modelled by the Drucker-Prager model. The granite is assumed to be fully saturated even under negative pore water pressure. The water retention behaviour of granite is difficult to determine because the water flow mainly occurs in fractures. In that sense, even if negative pore water pressure is generated (mainly produced by the initial suction in bentonite that soaks water from granite), water is drained from the fractures but the granite matrix should remain saturated. Gens et al. (2002) studied by the means of a parametric approach the interaction between the engineered barrier and the host rock. It revealed a high degree of complexity with some paradoxical results due to the coupled nature of the thermal, hydraulic and mechanical phenomena that occur. Consequently, assuming granite as fully saturated may provide a useful solution. The mechanical, thermal and hydraulic parameters of the granite are reported in Table 8.11.

Other materials

The parameters of the steel of the heaters, as well as the concrete of the plug, have been ascribed in the range of usual parameters for those kinds of materials. Their mechanical behaviour has been assumed to be linear elastic. The steel is considered as impervious and the concrete plug as fully saturated. Table 8.11 reports the considered parameters for these two materials.

Thermal parameters			**Bentonite**	**Granite**	**Concrete**	**Canister**
Solid thermal conductivity	λ_s	[W/(m.°C)]	0.7	-	-	-
Water thermal conductivity	λ_w	[W/(m.°C)]	2.1	-	-	-
Air thermal conductivity	λ_a	[W/(m.°C)]	0	-	-	-
Global thermal conductivity	Γ	[W/(m.°C)]	-	3.34	1.7	-
Solid heat capacity	$c_{p,s}$	[J/(kg.°C)]	1091	-	-	-
Water heat capacity	$c_{p,w}$	[J/(kg.°C)]	4200	-	-	-
Gas heat capacity	$c_{p,a}$	[J/(kg.°C)]	1000	-	-	-
Global heat capacity	C_p	[J/(kg.°C)]	-	1000	750	-
Liquid thermal expansion coefficient	β'_w	[°C^{-1}]	4 10^{-4}	4 10^{-4}	4 10^{-4}	-
Solid thermal expansion coefficient	β'_s	[°C^{-1}]	6.77 10^{-4}	2.5 10^{-5}	1 10^{-5}	2.5 10^{-5}
Liquid dynamic viscosity thermal coefficient	$\alpha_{w,T}$	[°C^{-1}]	0.01	0.01	0.01	-
Hydraulic parameters						
Intrinsic water permeability	$k_{w0,sat}$	[m^2]	4 10^{-21}	4.5 10^{-19}	1 10^{-19}	
Fluid dynamic viscosity	μ_w	[Pa.s]	0.001	0.001	0.001	-
Kozeni-Karman coefficient 1	$EXPM$	[-]	6.5	0	0	-
Kozeni-Karman coefficient 2	$EXPN$	[-]	6.5	0	0	-
Relative permeability coefficient	$CKW1$	[-]	2.9	-	-	-
Volumetric parameters						
Initial porosity	n	[-]	0.4	0.01		0
Solid specific mass	ρ_s	[kg/m^3]	2700	2660	2500	7800
Water specific mass	ρ_w	[kg/m^3]	1000	1000	1000	-
Air specific mass	ρ_a	[kg/m^3]	1.18	-	-	-
Liquid compressibility	$1/\chi_w$	[Pa^{-1}]	3.33 10^{-10}	3.33 10^{-10}	3.33 10^{-10}	-
Mechanical parameters						
Young elastic modulus	E	[MPa]	See	5000	3000	20000
Poisson ratio	υ	[-]	Table 8.10	0.35	0.2	0.3
Cohesion	c'	[MPa]		5	-	-
Friction angle	ϕ'	[°]		33	-	-
Dilatation angle	ψ	[°]		0	-	-

Table 8.11 : Material parameters of the different materials involved in the simulation of the FEBEX in-situ test.

8.3.5.3 *The infiltration test*

Introduction

Non-isothermal infiltration tests through the bentonite, inside cylinders 60 cm in length and 7 cm in diameter, aim at simulating the water that saturates the barrier in a repository excavated in granitic rock. A temperature of 100°C is imposed at the bottom of the cylinder while granitic water is injected at ambient temperature (20–30°C) under a pressure of 1.2 MPa over the upper lid of the cell. In this way, a mean thermal gradient of 1.1–1.3°C/cm between the top and bottom of the sample is imposed (Lloret et al., 2004; Villar et al., 2005b). The available measurements during the tests are temperatures at 50, 40, 30, 20 and 10 cm from the heaters and the volume of water intake. The duration of the tests has been 6, 12 and 24 months. After dismantling, the water content, as well as the dry density, at different locations was measured. This data enables the validation of the bentonite material parameters used through the simulation of a relatively simple case.

Features of analysis

The problem is treated under axisymmetric conditions around the longitudinal axis of the cylinder. The modelled domain, 3.5 cm in width and 60 cm long, is meshed with 115 eight-noded isoparametric elements. Gas pressure has been fixed to atmospheric pressure at each node. Gravity is not considered. The mesh is refined in the vicinity of the water injection zone (in the top of the domain) (Figure 8.29). The temperature is imposed at 100°C in the bottom of the cylinder which is assumed impervious. At the top of the cylinder, the pore water pressure is fixed to 1.2 MPa and the temperature is maintained as a constant. The bentonite is considered as homogeneous and isotropic. The thermo-hydraulic initial conditions have been imposed as follows: $T_0 = 23°C$; $s_0 = 127 MPa$; $S_{r0} = 0.54$.

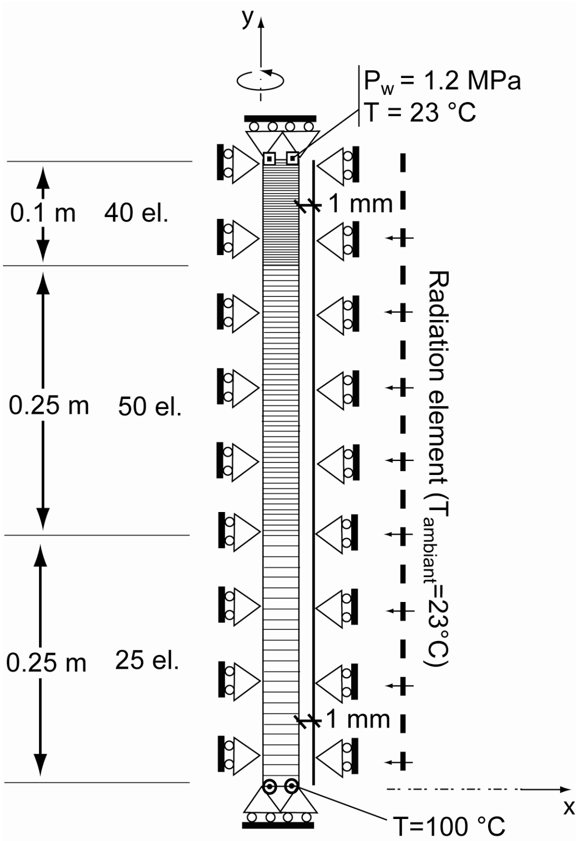

Figure 8.29 : Finite element mesh used in the simulation of the infiltration test in FEBEX bentonite. The y-axis is the axis of symmetry of revolution.

Several disturbing effects related to the experimental procedures needed to be considered or simplified in the numerical simulations in order to make the computations as close as possible to the experimental conditions. The construction gaps as well as the deformability of the cell have been considered in the computations by imposing a progressive horizontal displacement of the lateral cylinder wall up to 1 mm after 24 months (Figure 8.30). This is in agreement with the measured overall decrease of the dry density from an initial value of 1.65 g/cm^3 to 1.57 g/cm^3, for the 6 and 12-month tests, and to 1.55 g/cm^3, for the 24-month tests (Lloret et al., 2004).

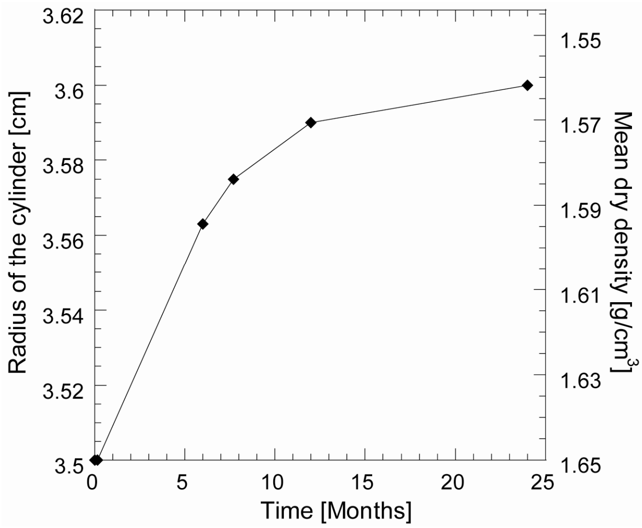

Figure 8.30 : Radial displacement of the cylinder wall imposed during simulation and its effect on the evolution of the mean dry density.

The laboratory temperature has a non-negligible effect on the temperature distribution measured inside the cylinder. Instead of a linear temperature evolution from 100°C at the bottom to 20-30°C at the top, there is a sharp decrease of temperature in the vicinity of the heater. As the cylinder is not insulated, the thermal boundary conditions of the lateral cylinder wall tend to cool the bentonite. To consider this, radiation elements were introduced as thermal boundary conditions along the sample. A temperature of 23°C was fixed as the laboratory temperature and the emissivity ε of the cylinder (Teflon) was ascribed to 0.4. The thermal flux q_{rad} through radiation from the cylinder to the laboratory is computed according to the Kirchhoff equation:

$$q_{rad} = \sigma\varepsilon\left(T_{cyl}^4 - T_{lab}^4\right) \tag{8.4}$$

where T_{cyl} and T_{lab} are the temperatures of the cylinder and of the laboratory ($T_{lab} = 23°C$). σ is the Stephan-Boltzmann constant ($\sigma = 5.67\ 10^{-8}\ W/(m^2K^4)$).

Finally, the daily and seasonal temperature variation of the injected water, from 20°C to 30°C, has not been considered. An averaged temperature of 23°C was fixed at the top surface.

Results

Figure 8.31 compares the results of simulations with the experimental measurements in terms of temperature, water content and dry density distributions in the axis of the cylinder as well as the evolution of the volume of water injected. First of all, the radiation elements, combined with accurate thermal diffusion and heat capacity of each phase of the bentonite, permit the reproduction of the sharp temperature decrease in the vicinity of the heater. At a location of 10 cm within the heater, simulations predict a temperature drop of 46.5°C (in comparison with 49°C, experimentally measured). Therefore, the thermal gradient is mainly concentrated in the bottom of the cylinder. The elevated temperature at the base of the cylinder produces an evaporation of water which diminishes the water content. In addition, that drying process induces shrinkage of the bentonite which is marked by an increase of the dry density at the bottom. On the contrary, at the top, the bentonite is wetted due to the water intake. That hydration process induces a swelling of the bentonite, except at the very top where numerical simulation predict a collapse phenomenon. That effect was not observed in the evolution of dry density experimentally measured. The cooler region is also resaturated through the vapour that arises from the drying of the bottom part, migrates and condensates in the top part.

In terms of water flux, the numerical simulation captures the main registered evolution of cumulative water intake. The good agreement validates the selected coefficient of permeability and its dependence with temperature, porosity and degree of saturation.

Conclusions

The numerical simulation of this relatively simple infiltration test provides clear evidence of the ability of the used numerical tools to reproduce, in both qualitative and quantitative viewpoints, the THM processes that occur in an engineered clay barrier. The study of those phenomena occurring mainly along the longitudinal axis in this infiltration test will be extended in three dimensions (2D axisymmetric) in the simulation of the in-situ FEBEX experiment. Through those simulations, the advancement in the understanding of the involved processes brought by the ACMEG-TS model will be further discussed. In so doing, the focus will be made on the effect of temperature and water retention conditions on the mechanical response of the buffer material.

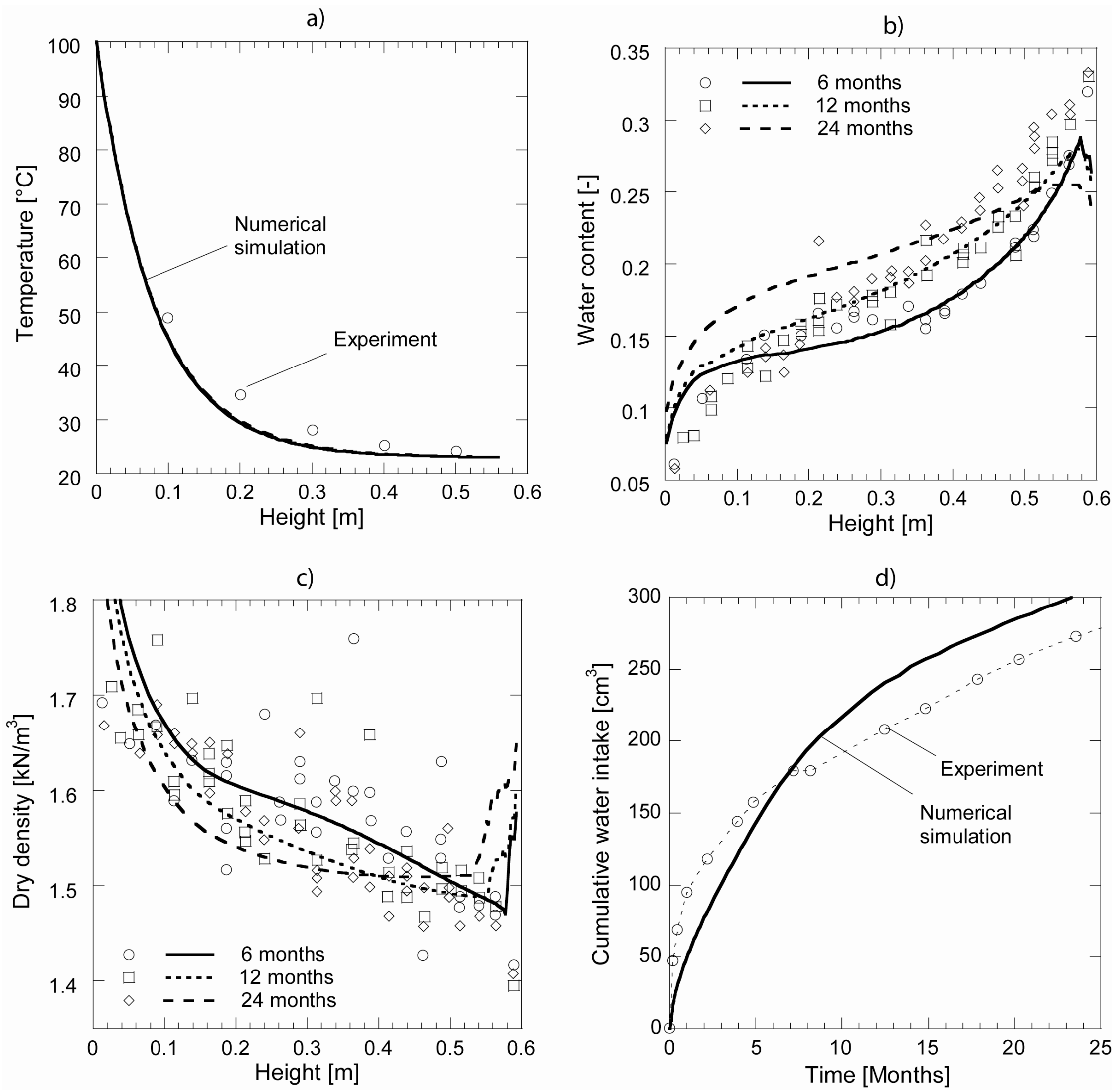

Figure 8.31 : Results of the simulation of the infiltration test in the 60 cm long cylinder compared with experiment: a) Temperature distribution; b) Water content distribution; c) Dry density distribution; d) Evolution of cumulative volume of water intake.

8.3.5.4 *Features of analysis of the FEBEX in-situ experiment*

The problem is treated under axisymmetric conditions around the y-axis, which is the axis of the test drift. Consequently, gravity is not considered. The domain is discretized with 2,693 eight-noded isoparametric elements and 8,312 nodes (Figure 8.32). The host rock is modelled in a domain of 61 x 130 m in the radial and longitudinal directions, respectively. It aims at considering a domain that is large enough to avoid undesired effects of the imposed boundary conditions in the far-field. The distance of the external boundary to the engineered barrier is the same (60 m) in both the axial and radial directions. In addition, the large modelled domain enables the modelling of the pore water pressure dissipation during the excavation stage. That preliminary purely hydraulic simulation provides a coherent initial state of the pore water pressure distribution in the granitic massif. Figure 8.33 compares the pore water pressure distribution at equilibrium after the excavation phase numerically simulated and measured in-situ in a borehole drilled before excavation (boreholes K1 and K2).

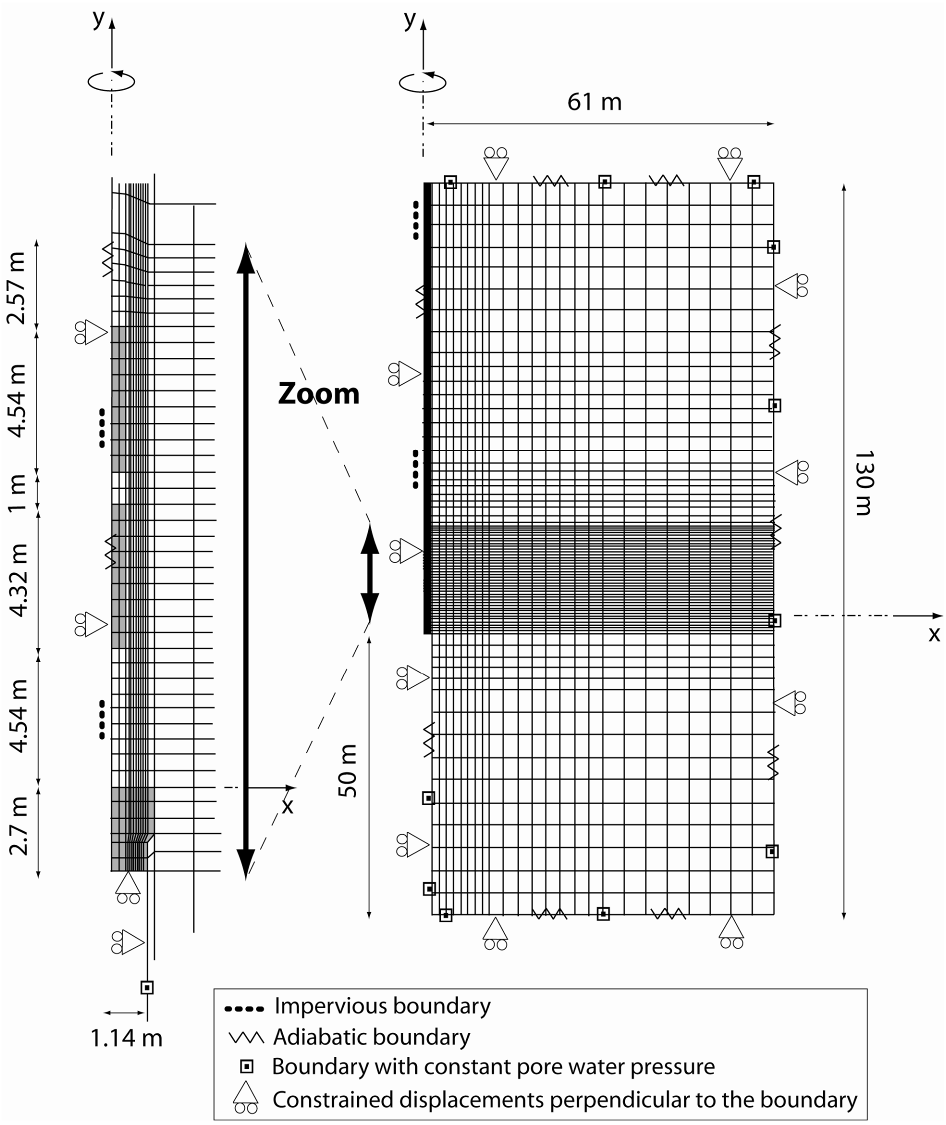

Figure 8.32 : Finite element mesh used in the simulation of the in-situ FEBEX experiment. The y axis is the axis of symmetry of revolution (y=0 corresponds to the bentonite/plug contact).

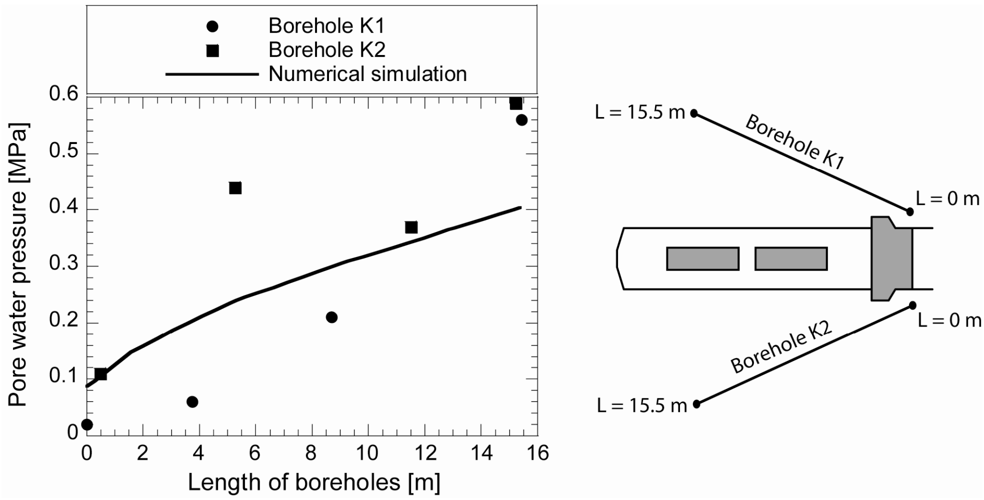

Figure 8.33 : Initial pore water pressure distribution in the two lateral K1 and K2 boreholes obtained after the simulation of the excavation phase. Comparison with the experimental measurements.

Due to symmetry, the inner boundary condition is considered to be impermeable and adiabatic. Constant pore water pressure and temperature, equal to their initial values, are imposed at each boundary of the domain. In particular, the access gallery wall, as well as the contact between concrete plug and access gallery, is assumed to be at atmospheric pressure and at 12°C. Displacements are prevented perpendicularly to each boundary, as well as for the gallery wall and the concrete plug (Figure 8.32). The initial pore water pressure in the host granite is determined through the preliminary hydraulic calculation of the excavation phase (Figure 8.33), while a suction of 80 MPa is considered in bentonite. The initial water pressure in the concrete plug is assumed to be atmospheric pressure. The initial temperature is equal to 12°C in the entire modelled domain.

As far as the mechanical state is concerned, the stress variable is the saturated Terzaghi's effective stress in the granite and the concrete plug, the generalized effective stress in the bentonite and the total stress in the canisters. An initial isotropic total stress of 28 MPa is imposed in the granite. The anisotropic stress state has not been considered in the simulation because of the axisymmetric formalism. In the bentonite, the external total stress is initially equal to zero, which corresponds to a generalized effective stress of 47.5 MPa (the initial product $S_r \times s$). The bentonite is assumed to be normally consolidated ($p'_{c0} = 4MPa$; $\gamma_s = 7$; $s = 80MPa$). The canister and the concrete plug are under zero stress. In the first time step, the unequilibrated stress between the bentonite (zero external stress) and granite (28 MPa of external stress) produces a convergence of the gallery towards the engineered barrier. It induces a stress increase in the bentonite.

In the finite element computation, several simplifications have been made with respect to the real case. In particular, the construction gap, evaluated to 5.53% of the emplacement volume (Alonso et al., 2005), has not been considered. This implies that the swelling pressure predicted by the numerical simulations will be overestimated. In addition, as already mentioned, gravity has not been considered. Also, the thermal loading in the canister has been controlled through temperature variation. On the contrary, in the experiment, the temperature ramp was imposed with a constant power of 1200 W per heater during an initial period of 20 days followed by a power of 2000 W per heater over the next 33 days until reaching the desired temperature of 100°C at the surface of the steel liner. In the simulation, the temperature evolution during the first 53 days has been imposed in agreement with the measurement obtained by temperature sensors in contact with heater (Figure 8.34). Throughout the computations the temperature was imposed at each node of the canister. Finally, the air pressure has been fixed to atmospheric pressure in the entire unsaturated domain. The simulation has been performed on the first 700 days of operation (i.e. 2 years). The initial time of computation corresponds to the start of the heating (February 27th 1997).

8.3.5.5 *Results of simulation compared with measurements*

Figure 8.35 reports the evolution of temperature with time in two sections of the engineered barrier and in two boreholes in the rock mass. In section D1 (Figure 8.35a), the temperature field reaches a quasi-steady-state after 100 days with a thermal gradient of about 60°C across 66 cm (from 95°C at x=0.48 m to 35°C at x=1.14 m). On the contrary, far from the heater (section B4, Figure 8.35b, and boreholes K1 and K2, Figure 8.35c), the temperature continuously increases, even after two years of heating. The results of the simulation show a relatively good agreement with in-situ measurements.

In terms of fluid pressures in the bentonite, sensors measured the evolution of the relative humidity of the bentonite in different sections. The numerical simulation displays the results as pore water pressure. Kelvin's law (Equation (5.1)) relates the suction with the temperature-dependent relative humidity. This transformation was done in order to compare numerical results with the in-situ measurement in terms of relative humidity. Figure 8.36 displays such a comparison in two different sections of the engineered barrier. The main difference between the numerical simulation and experiment takes places in the initial state and the subsequent 200 days. The simulation starts from a homogeneous relative humidity field equal to 60% (s = 80 MPa and T = 12°C), while the sensor measurements show an initial gradient of relative humidity in the considered section. However, after 200 days, the simulation and in-situ measurements exhibit very similar evolutions. Close to the heater, the bentonite is dried due to thermally-induced water evaporation. Vapour arising from that drying diffuses outwards and condensates in the cooler region, causing wetting of the bentonite in the outer part. In addition, hydration of the outer part also occurs due to the water inflows from granite. The numerical simulation is able to predict these phenomena.

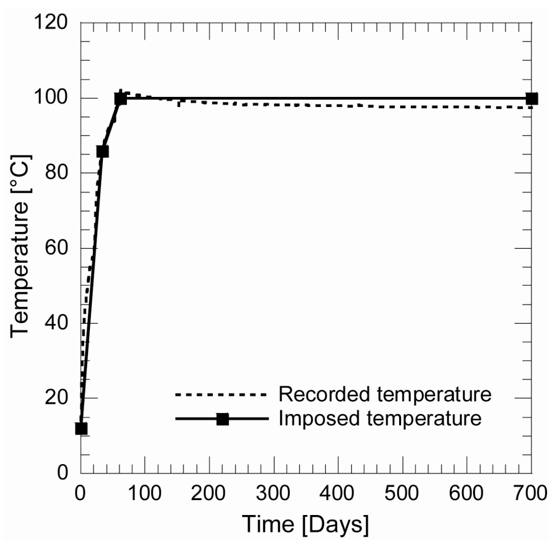

Figure 8.34 : Temperature evolution imposed in simulation compared with the recorded temperature at the heater surface.

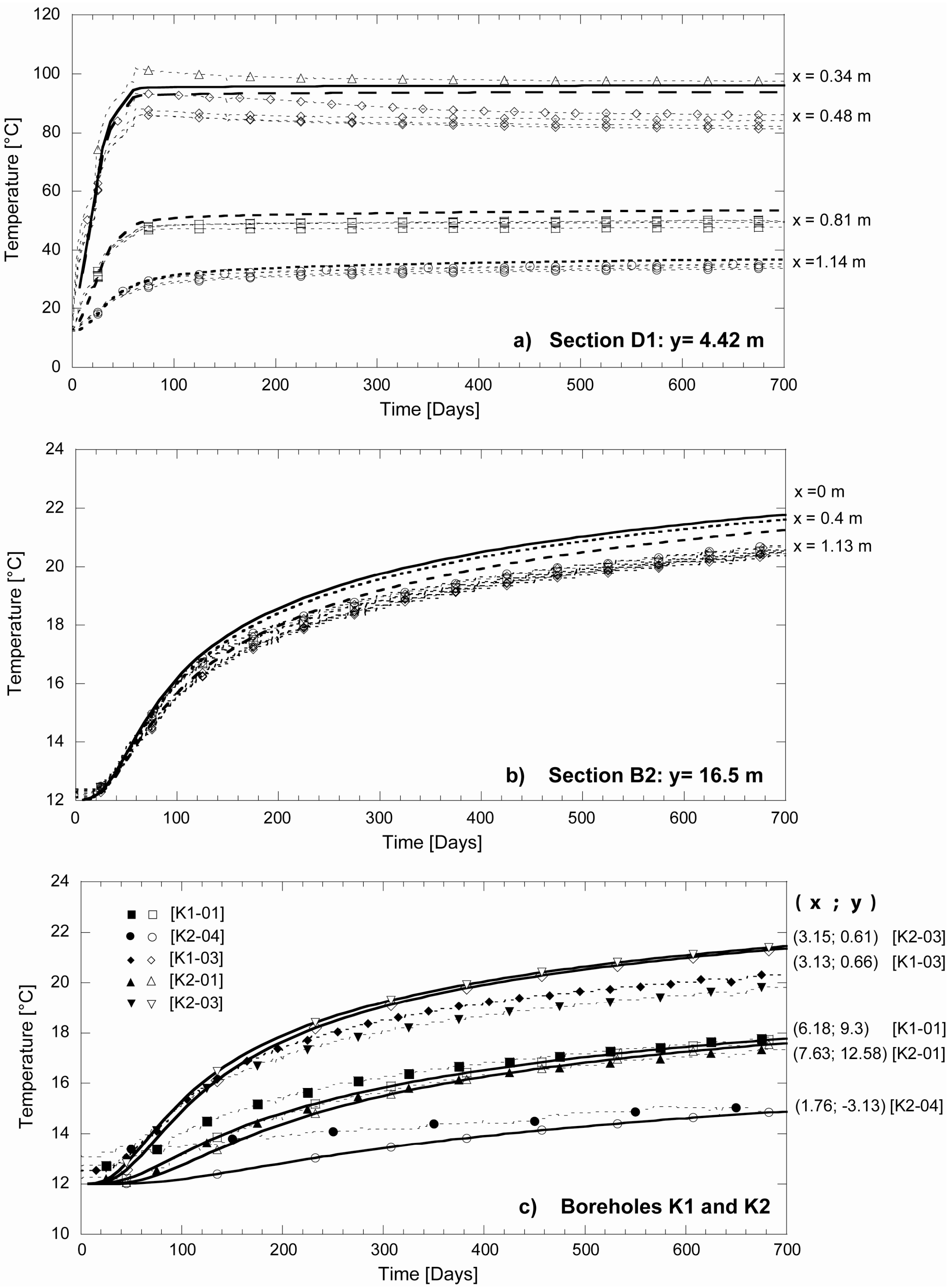

Figure 8.35 : Variation of temperature with time in two sections of the engineered barrier and in two boreholes in the host rock. Comparison between numerical predictions (bold lines) and experimental measurements (thin dashed lines).

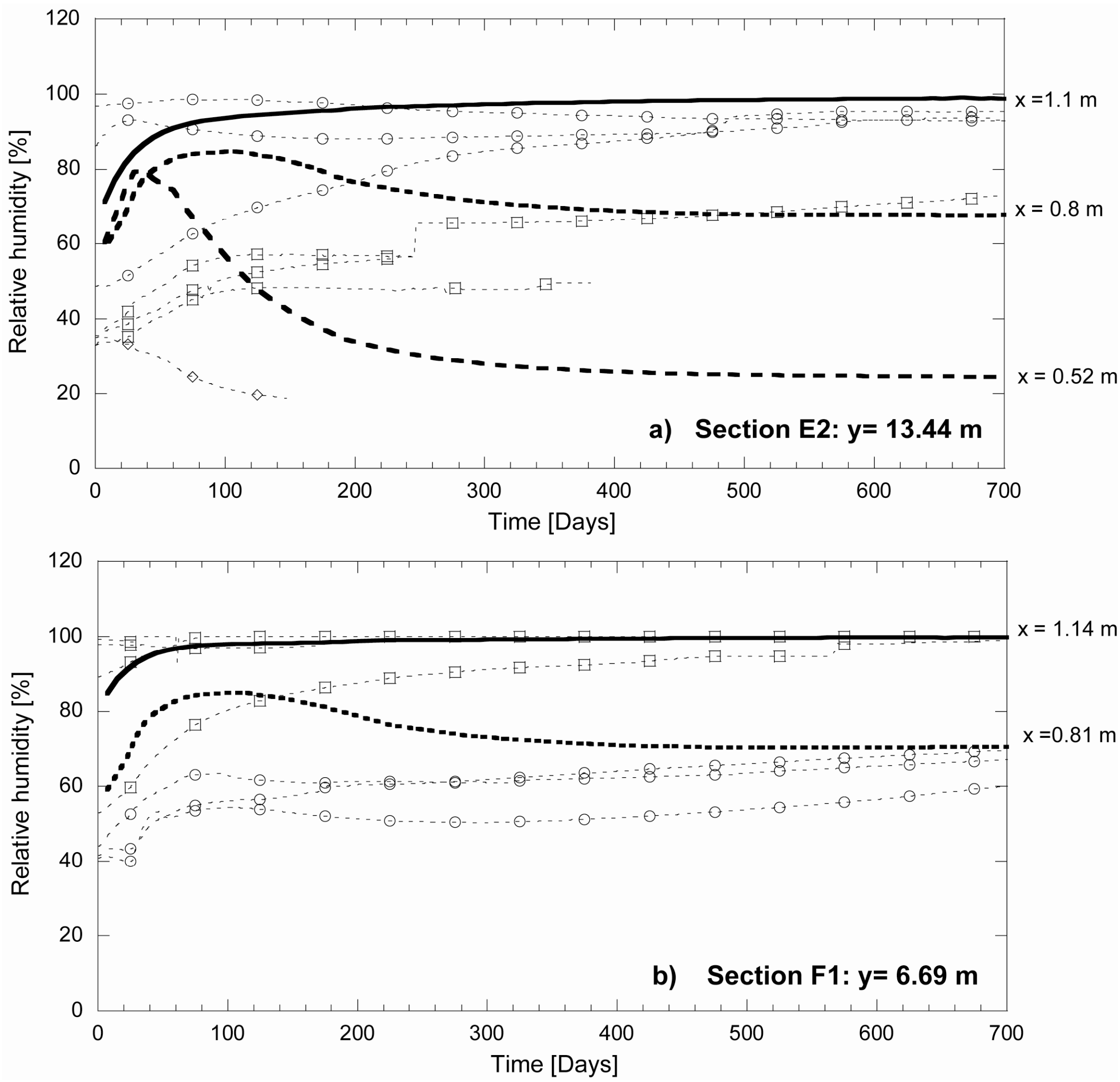

Figure 8.36 : Variation of relative humidity with time in two sections of the engineered barrier. Comparison between numerical predictions (bold lines) and experimental measurements (thin dashed lines).

Figure 8.37 displays the evolution of radial total stress measured at the granite-bentonite and bentonite-heater interfaces in two different sections. The stress sensor measurements show a progressive increase of the radial stress starting from zero up to about 2 MPa. On the contrary, the numerical simulation predicts a sharp increase of radial stress during the first days of operation and then a progressive decrease towards the values recorded by the stress sensors. That difference follows from the assumptions made in the definition of the initial state for the numerical simulations. On the one hand, the construction gaps, allowing a given free swelling of the bentonite before the generation of a swelling pressure, have not been considered in simulation. On the other hand, the excavation phase was simulated through a purely hydraulic calculation. In that sense, the convergence of the gallery wall takes place in the first days of the THM computations. That convergence produces a drastic increase of the external stress acting on the engineered barrier. However, in the real case, the bentonite is installed in the gallery after the gallery wall convergence.

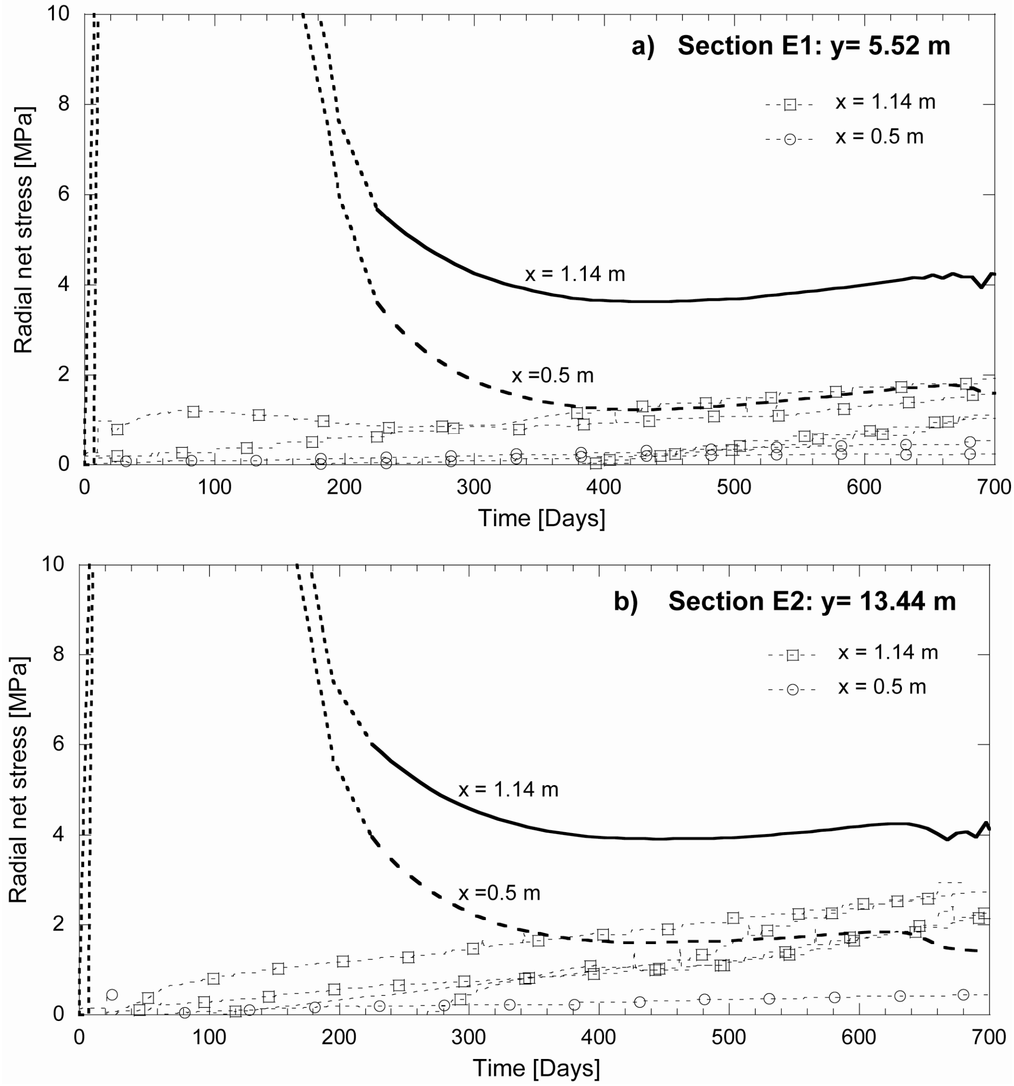

Figure 8.37 : Variation with time of radial net stress at the granite-bentonite (x=1.14 m) and bentonite-heater (x=0.5 m) interfaces. Comparison between numerical predictions (bold lines) and experimental measurements (thin lines).

Numerical simulations as well as sensor measurements show a stress gradient between the inner and the outer boundaries, the stress being higher at the outer boundaries. That phenomenon is due to the swelling of the buffer material due to the bentonite resaturation close to the granite in opposition to the shrinkage of the bentonite close to the heater. That point will be further discussed in the interpretation of results.

Figure 8.38 depicts the evolution of the pore water pressure in granite as recorded by sensors placed in two boreholes compared with the numerical simulation. The modelling predicts a negative pore water pressure in the granite during the first 100 or 200 days of operation, depending on the distance from the test drift. The suction in the granite is due to the bentonite that soaks up water from the host formation. In contradiction, the pore water pressure sensor does not record such negative water pressure in the granite. This difference may also be due to the initial state of the computation that considers the bentonite directly in contact with granite without considering the construction gap. In that sense, the bentonite directly soaks up water from granite in the computation while in reality construction gaps may act as a buffer zone.

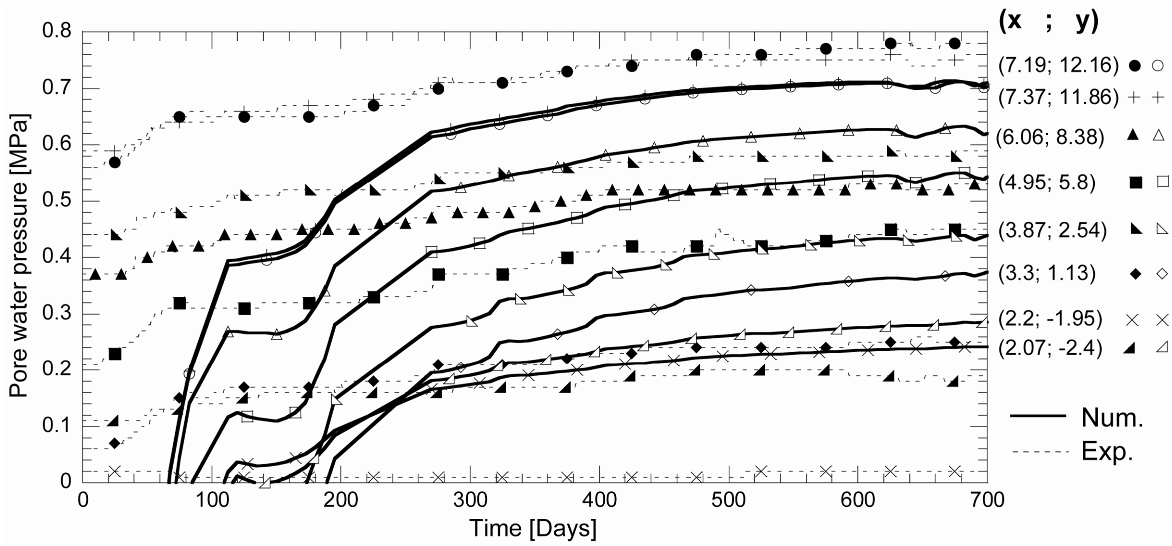

Figure 8.38 : Evolution of the pore water pression with time in granite. Comparison between results of simulation and sensor measurements.

8.3.5.6 *Interpretation of the results of simulation*

This section focuses on the THM processes that occur in the engineered clay barrier. The simultaneous heating (arising from the canister) and hydration (arising from the host formation) of the bentonite gives rise to interconnected phenomena that govern the complex response of the engineered barrier. The analysis of the numerical results, obtained by the means of the finite element simulation, permits a better understanding of these occurring THM processes. In Figure 8.39 to Figure 8.42, the evolution of the main THM variables is presented along the mid-plane section perpendicular to a heater.

The thermal loading of the canister produces a rapid increase of temperature in the inner part of the engineered barrier. At the outer part, the bentonite undergoes smaller temperature variations. At the point of contact with the host formation, the temperature is about 40°C (Figure 8.39a). In that sense, the engineered barrier acts as a thermal buffer aimed at reducing the temperature in the host formation. That positive effect of the bentonite avoids producing any significant thermally-induced damage in the host formation. Figure 8.39a also shows that a quasi-steady-state thermal regime is rapidly reached in the bentonite. After less than 6 months, the temperature does not continue to significantly evolve along the considered section.

At the inner boundary, the temperature increase produces, via water evaporation, a drying of the clay. Consequently, the degree of saturation decreases and the suction increases. Figure 8.39b shows that the suction rises up to more than 200 MPa after 24 months. It corresponds to a drop in the degree of saturation down to 0.6 (Figure 8.39c). The decrease of the saturation degree is relatively low due to two main effects. (i) The $S_r - s$ relation is a logarithmic relation in the desaturation phase. Accordingly, a high increase of suction produces only a limited decrease of the degree of saturation. (ii) Through the effect of the volumetric strain on the water retention capacity, the bentonite drying produces shrinkage and a subsequent increase of the degree of saturation for the same suction. This also limits the decrease of the degree of saturation with suction. This point will be further demonstrated in Figure 8.43.

At the outer boundary, the suction decreases and the degree of saturation increases. This is induced by two processes. (i) The higher water pressure of the granite than that in the buffer material implies a flow of water from granite to bentonite. This hydration process is the main contributor in resaturating the bentonite. (ii) Also, the vapour arising from the drying of the inner region diffuses through the engineered barrier and condensates in the cooler region.

An interesting transient effect occurs in the very short term. As the thermal diffusion is faster than the hydraulic diffusion in bentonite, the temperature produces an increase of the pore water pressure that has no time to dissipate in the short term. Consequently, after 1 month, the suction is lower than the initial suction everywhere in the domain (and the degree of saturation is higher) (Figure 8.39b and c). This transient effect dissipates by the means of hydraulic diffusion when the temperature reaches a quasi-steady-state regime.

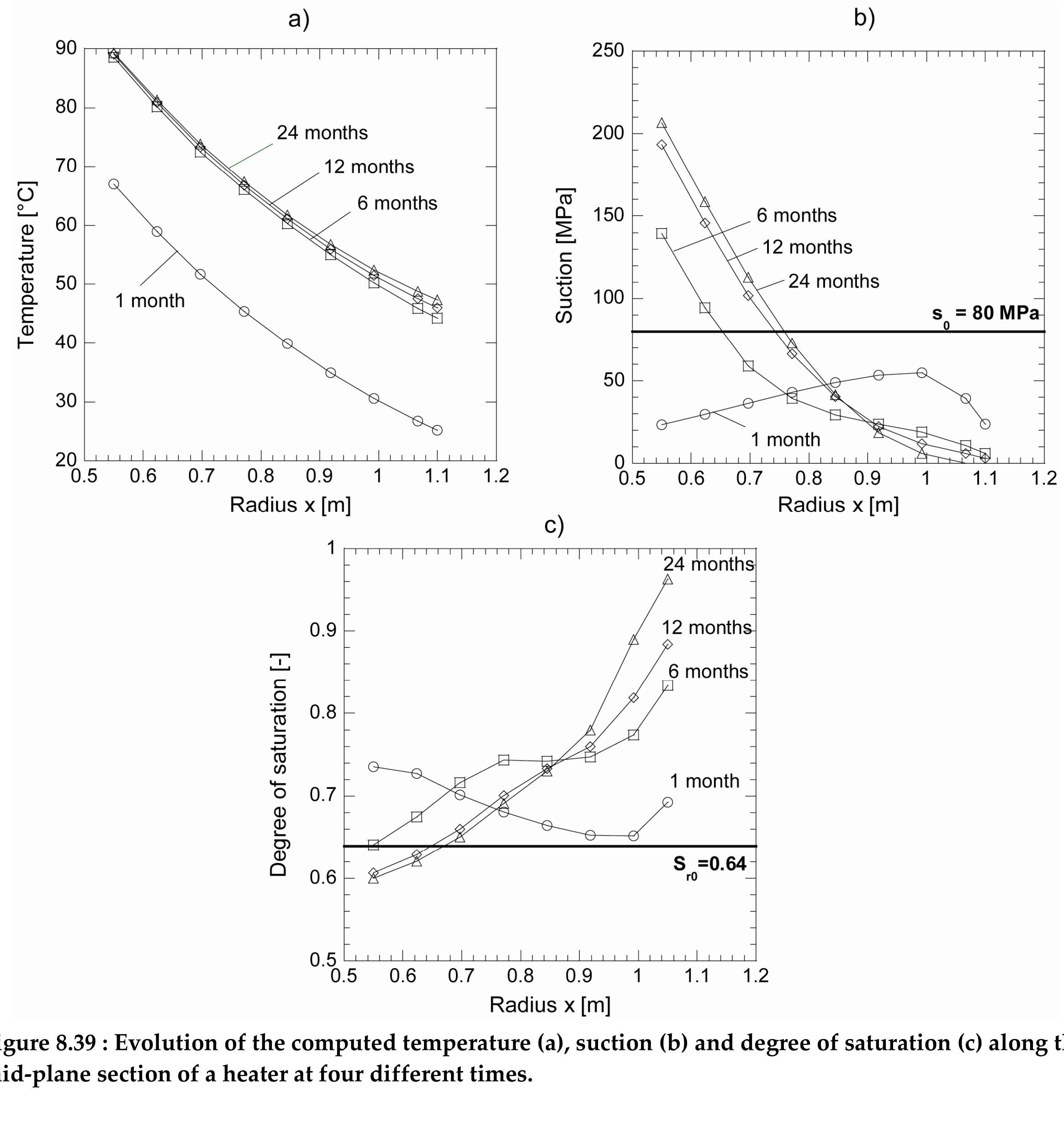

Figure 8.39 : Evolution of the computed temperature (a), suction (b) and degree of saturation (c) along the mid-plane section of a heater at four different times.

The distribution of the radial effective stress (Figure 8.40a) is the sum of the radial net stress (Figure 8.40b) and the product $S_r \times s$ (Figure 8.39b and c). As a consequence, the drying process in the inner part induces an increase of the radial effective stress while the hydration of the outer part decreases the radial effective stress. In terms of the radial net stress (Figure 8.40b), the sudden increase of the stress obtained after 1 month is due to the hypothesis of the initial state, as discussed in the previous section (Figure 8.37). Then, after 12 months, the radial net stress distribution reaches a quasi-equilibrium with values lower than 5 MPa. The mean generalized effective stress evolution is similar to the radial effective stress evolution (Figure 8.40c), higher in the inner part than in the outer part, because of the suction gradient. The deviatoric stress in the bentonite is mainly generated by two effects (Figure 8.40d). On the one hand, the differential displacement of the canister with respect to bentonite induces shearing in the inner part. On the other hand, the heterogeneous stress distribution induces a deviatoric component of the stress tensor. In particular, the gradient obtained in the radial stress distribution may cause the observed increase of the deviatoric stress.

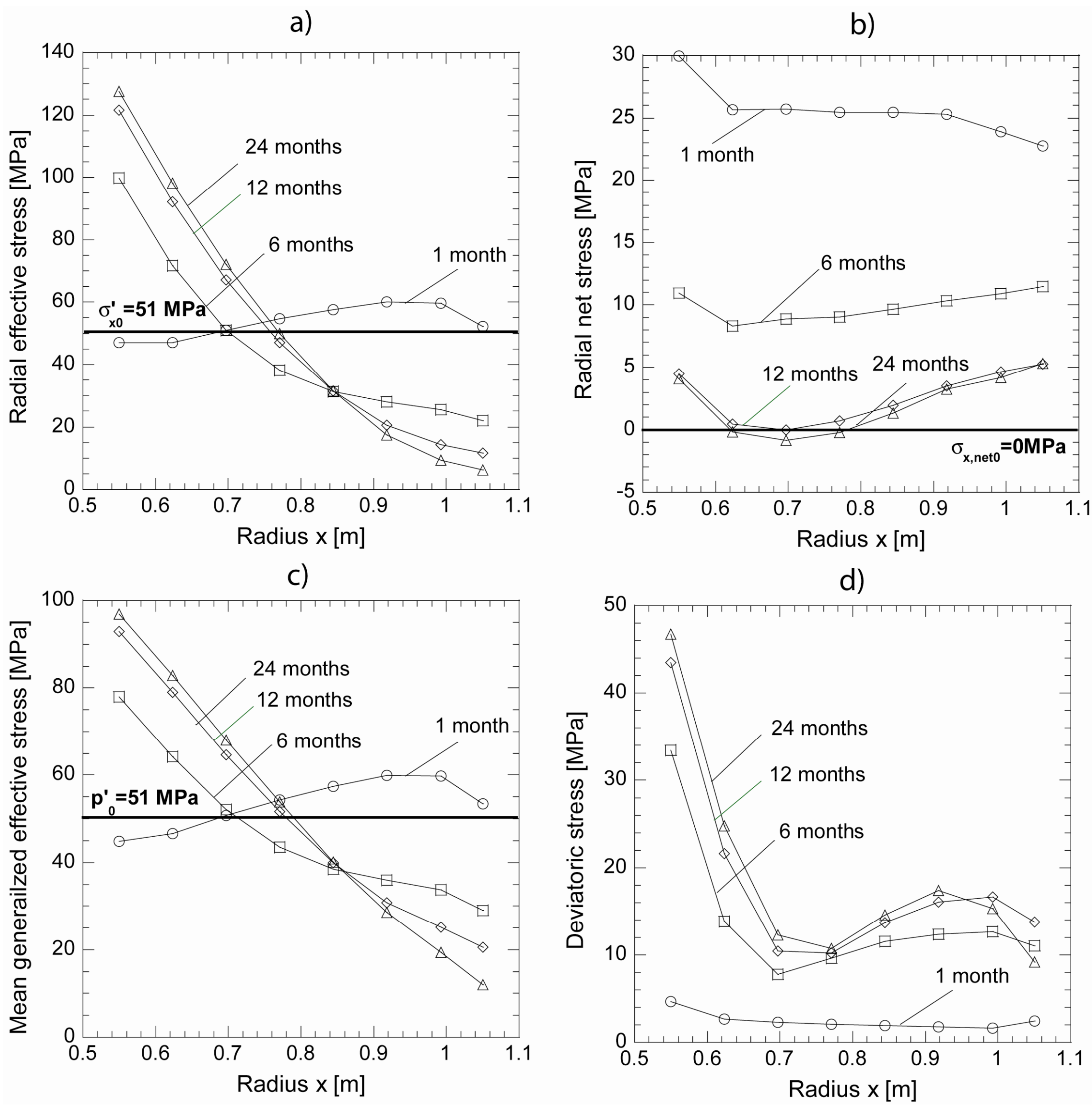

Figure 8.40 : Evolution of the computed radial effective stress (a), radial net stress (b), mean effective stress (c) and deviatoric stress (d) along the mid-plane section of a heater at four different times.

In Figure 8.41a, the distribution of volumetric strain shows a contraction of the bentonite in the inner part while the outer part dilates. This is consistent with the hydraulic processes that occur in the engineered barrier. The temperature-induced drying produces shrinkage while the hydration of the outer part produces swelling. In addition, the bentonite is also prone to plastic processes such as thermal and hydraulic collapse. Comparison between the total volumetric strain (Figure 8.41a) and the plastic volumetric strain (Figure 8.42b) reveals that almost the entire contractile strain in the inner part is plastic. These irreversible strains are produced by the drastic increase of the mean generalized effective stress in combination with the thermo-plasticity. On the contrary, in the outer part, the low contractile plastic strain (+/- 3%) is compensated by high elastic swelling strain (+/- 6%). In that sense, the obtained volumetric strain (3% of dilatation) in the outer part is the consequence of a combination of swelling and collapse phenomena. In terms of radial displacement, the contraction of the inner part, in addition to the dilatation of the outer part, produces an inward displacement of the engineered barrier. The numerical simulation predicts 18 mm of displacement in the centre of the barrier (Figure 8.41b). At the extremity of the considered section, the thermal expansion of the heater produces a radial displacement of about 1 mm. This is consistent with the thermo-elastic strain of the canister ($\Delta x = \beta_s' \times L \times \Delta T = 2.5\ 10^{-5} \times 0.475 \times 88 = 1\ mm$). At the other end of the considered section, the gallery wall convergence is about 1 mm.

Figure 8.42 exhibits the evolution of the plastic parameters in the considered section. The distribution of the preconsolidation pressure follows from the suction, the temperature and the generated volumetric plastic strain, according to Equation (6.4). Accordingly, the sudden decrease of suction during the first month of operation (Figure 8.39b) produces a drop of the preconsolidation pressure. Then, the preconsolidation pressure is controlled by the consistency condition, imposing that under full activation of the isotropic plastic mechanism $r_{iso} = 1$ (Figure 8.42c), the stress point lies on the isotropic yield limit. Thus, the preconsolidation pressure is equal to the mean generalized effective stress (Figure 8.42a and Figure 8.40b). The isotropic plastic mechanism reaches 100% of plastic mobilization (Figure 8.42c), while the mobilization of the deviatoric plastic mechanism is between 20% and 80% (Figure 8.42d). Therefore, the plastic processes are mainly isotropic even if a non-negligible deviatoric component takes place.

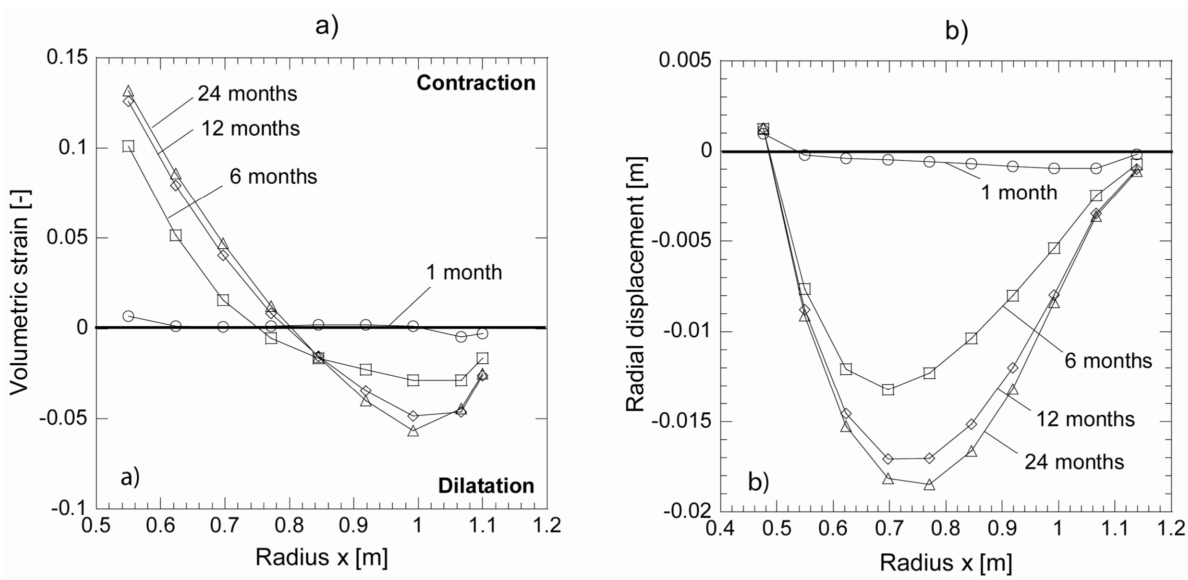

Figure 8.41 : Evolution of the computed volumetric strain (a) and radial displacement (b) along the mid-plane section of a heater at four different times.

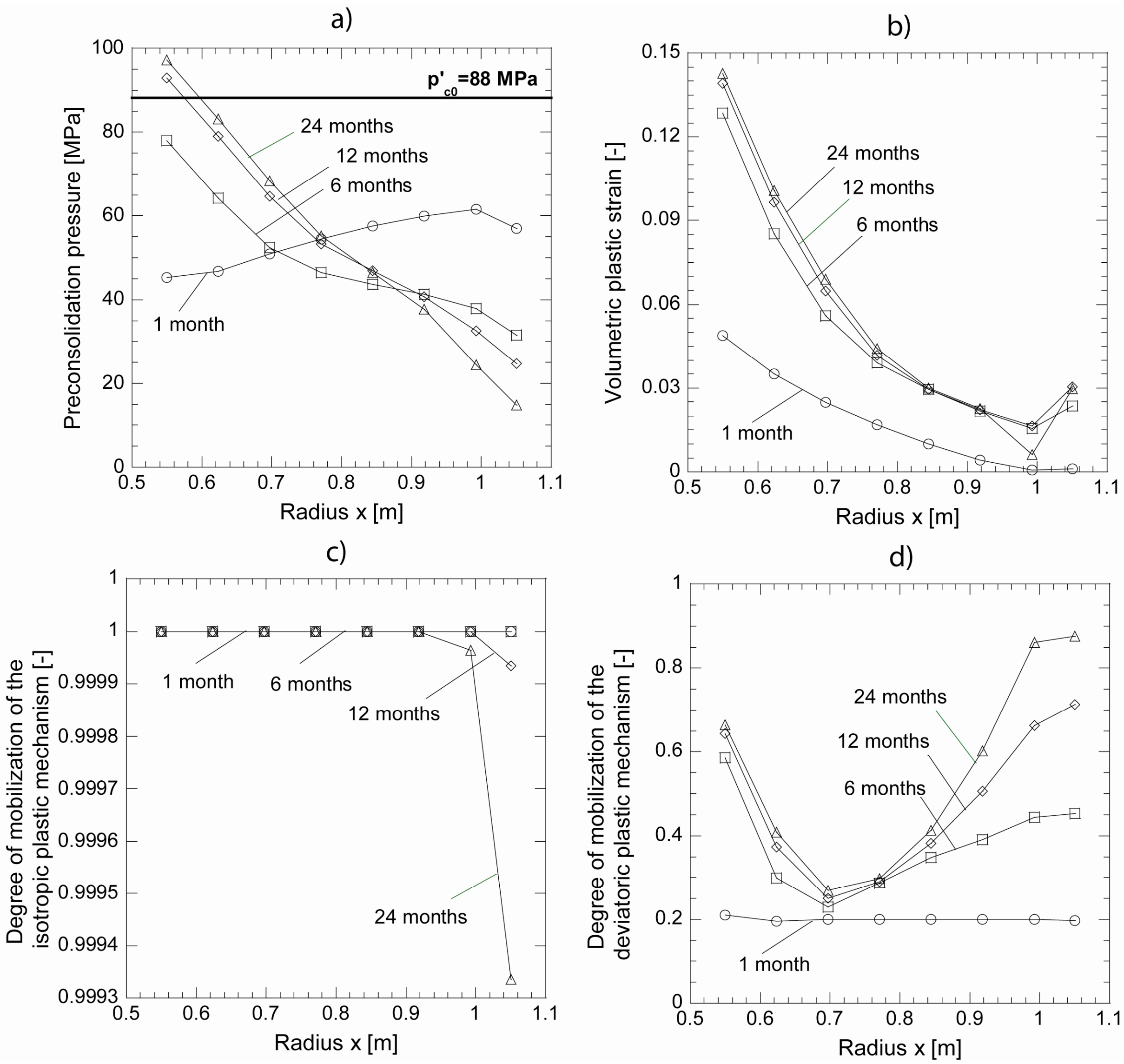

Figure 8.42 : Evolution of the preconsolidation pressure (a), the volumetric plastic strain and the degree of mobilization of the isotropic (c) and deviatoric (d) plastic mechanisms along the mid-plane section of a heater at four different times.

Until now, the analysis of the results of simulations has mainly revealed that the mechanical response of the material is, for a great part, due to the fluid pressure and temperature variations that occur in the bentonite. However, the reverse coupling, from the mechanics to the water retention behaviour, may also affect the THM response of the engineered barrier. In particular, the volumetric strain evolution influences the relation between degree of saturation and suction (Figure 8.43). Close to the heater (point 1), the bentonite undergoes shrinkage. It implies that its retention capacity increases. The point in the $S_r - s$ plane crosses over the uncoupled hydraulic hysteresis towards higher suctions. On the contrary, close to the granite (point 3), the bentonite undergoes swelling. Consequently, its water retention capacity decreases and the point in the ($S_r - s$) plane crosses over the hysteresis towards a lower suction value. Finally, far from the heater (point 2), the volumetric strain of the bentonite is very low and the water retention curve is not affected by the mechanical state.

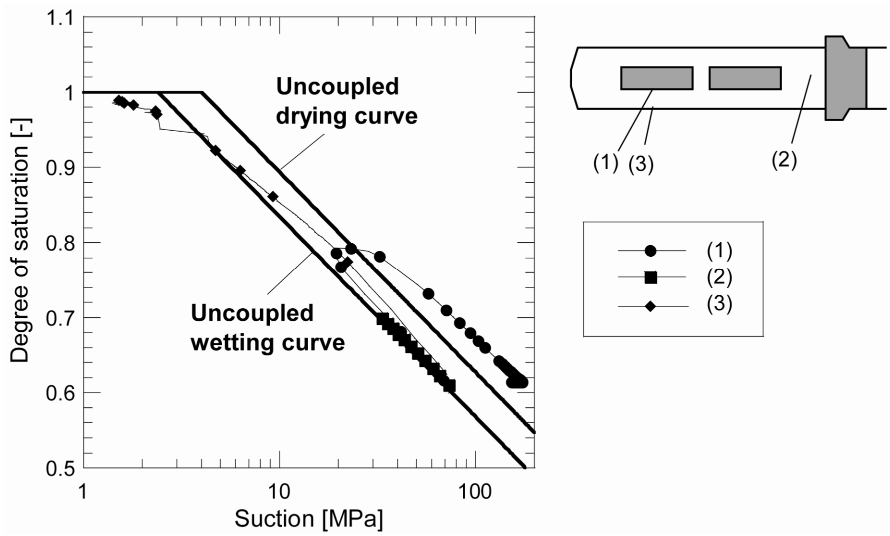

Figure 8.43 : Relation between suction and degree of saturation at three different locations of the engineered barrier.

8.3.5.7 *Conclusions*

The FEBEX in-situ test is a near-to-real experiment of nuclear waste disposal in granitic formation. The THM behaviour of the buffer material (made of FEBEX bentonite) and the surrounding host rock (granite) is monitored by the means of more than 600 sensors. The sensor measurements during the operation phase provide worthwhile information to validate numerical models aimed at predicting the behaviour of geomaterials involved in the confinement of nuclear waste. Many complex and interconnected THM phenomena occur in the engineered clay barrier.

The THM behaviour of the FEBEX bentonite is well-documented in the literature. The results of accurate laboratory experiments were used to calibrate the model parameters. The parameters of the ACMEG-TS model have been retrieved from the numerical simulations, performed in Chapter 6, of a series of oedometric tests. On the contrary, the parameters of the thermal and hydraulic diffusion models were extracted from the literature. In addition, a preliminary simulation of an infiltration test in bentonite undergoing thermal and hydraulic gradients was performed to validate the material parameters used.

The features of the finite element analysis have been presented. Then, the obtained numerical results have been compared with the available sensors measurements, in terms of temperature, fluid pressure, relative humidity and total stress evolutions in both the engineered barrier and granite. In spite of some restrictive assumptions in the initial state, the results of the simulation show good agreement with experiment. In a second step, the obtained results were interpreted in the light of elasto-thermo-plasticity of unsaturated soils. In particular, the effect of the suction and temperature variations on the computed volumetric strain was studied. Moreover, the coupling effects between water retention and mechanical behaviour were analysed as a two-way coupling.

Therefore, the use of a performing finite element code coupled with an advanced thermo-plastic constitutive model, using an unsaturated formalism, significantly advances our knowledge of the highly coupled processes occurring in a clayey formation, initially unsaturated, in the near-field of a heat-emitting radioactive waste.

8.4 Conclusions

In the coming years, safe and definitive solutions will likely be completed for managing the large quantities of high-level radioactive wastes that stem mainly from nuclear electricity production. Deep geological repositories constitute one of the most promising options to isolate such wastes from the human environment. In light of the great danger of a potential failure of these confining structures, analysis and predictions about the long-term behaviour of such disposal installations and their surrounding barriers should be based on robust science. In this context, the highly coupled THM phenomena that occur in the engineered and geological barriers must be captured adequately by means of numerical analysis.

Therefore, the primary aim of the simulations is to provide means for assessing and understanding the thermal, hydraulic and mechanical responses of the clayey materials and surrounding rock involved in the multi-barrier system. Consequently, the interpretation of the encountered results requires advanced constitutive and numerical tools in order to incorporate most of the soil behavioural features.

In this chapter, three boundary value problems relating to nuclear waste disposal have been analysed by the means of finite element simulations. The two first cases, the TIMODAZ benchmark and the ATLAS in-situ experiment, deal with non-isothermal saturated conditions, while the last case, the FEBEX in-situ experiment, involves unsaturated materials under non-isothermal conditions. In the analysis of the simulation results, the effect of the temperature and pore fluid pressure evolution on the induced mechanical response has been quantified. In particular, the elasto-plastic framework of the ACMEG-TS model enables an accurate interpretation of the irreversible processes that occur.

Clayey materials are prone to plastic strains; i.e. collapse under wetting, irreversible thermal strains or non-recoverable strains under mechanical loading. The order of magnitude of these plastic effects can be largely greater than the elastic strains, and they may have considerable impacts on the behaviour of soil surrounding heat-emitting radioactive waste. As far as unsaturated conditions are concerned, temperature increases may induce, via water evaporation, the drying of the engineered barrier. The vapour arising from this phenomenon diffuses through the barrier and condensates in the cooler region. Also, it has been observed that the engineered barrier undergoes thermal, hydraulic and stress gradients that may generate a deviatoric component of the stress tensor and imply shearing of the buffer material.

Chapter 9

Concluding remarks

In past decades, the effects of unconventional environmental loads on the mechanical behaviour of soils have been increasingly investigated for many geomechanical applications. Among these environmental loads, variations in temperature and humidity have a considerable influence on soils, not only in terms of mechanical response, but also on water retention properties. Engineering applications for which such effects are considered include high-level nuclear waste disposal. […]. Usually, unsaturated and non-isothermal conditions are considered independent processes. However, coupling between temperature and water retention properties must be considered to cover the range of interactions affecting the mechanical response of soils.[1]

[1] François B. and Laloui L. (2008) ACMEG-TS: A constitutive model for unsaturated soils under non-isothermal conditions. *International Journal for Numerical and Analytical Methods in Geomechanics*. DOI:10.1002/NAG712.

9.1 Conclusions

The present study has looked for a better understanding of the thermo-plasticity effects that soils may undergo when submitted to combined temperature, suction, and mechanical loadings. Soil is a multi-phase particulate material that may undergo irreversible changes in volume as the relative positions of the soil particles changes. In addition to external stress, temperature and suction variations may contribute to the irreversible volumetric straining of the soil. Such irreversible processes have been studied and modelled in order to investigate the response of the soil surrounding prospective nuclear waste disposal sites in deep geological formations.

The stress-strain-temperature-suction relationship in fine-grained soils has been studied via a three-part constitutive, experimental and numerical point of view, from which the following conclusions may be drawn.

9.1.1 Constitutive study

Modelling the complex non-linear and irreversible behaviour of soils, when submitted to combined temperature, suction and mechanical loadings, is a challenging task that requires advanced constitutive developments. In most of the cases, simple elastic and plastic models fail to reproduce, in a relevant manner, the thermo-hydro-mechanical response of the soil. A systematic approach that looks at the soil response as a combination of interconnected processes helps to explain the complex stress-strain relations in soils. Through a progressive analysis of the soil behaviour, Chapters 2, 3 and 6 present three successive evolutions of the developed mechanical constitutive model for fine-grained soils. Any constitutive model dealing with complex environmental actions on soils must start from a robust and straightforward bare-bones model. In that sense, the ACMEG model for isothermal and saturated conditions provides a robust stress-strain framework from which the ACMEG-T (for non-isothermal conditions) and ACMEG-TS (for non-isothermal and unsaturated conditions) models have been developed.

The framework of the model is based on the well-known Original Cam-Clay model. Thus, the ACMEG family models retain the concepts of classical elasto-plasticity and critical-state soil mechanics. In addition, the concept of multi-mechanism plasticity and bounding surface theory provides a major advance in the prediction accuracy. The Original Cam-Clay model has been shown to be a special case of the ACMEG model.

As far as non-isothermal conditions are concerned, thermo-plasticity is introduced as an addition to the classical thermo-elasticity. The main parameter that governs such thermo-plastic phenomena is the decrease of the preconsolidation pressure as the temperature increases. In addition, the friction angle at critical state may also vary with temperature. A clear explanation of the different model responses enables a good understanding of the constitutive mechanisms that are considered by the model.

The consideration of the soil as a three-phase medium introduces additional coupling effects and the need for a second stress variable to describe the mechanical behaviour of the soil. The ACMEG-TS model uses the generalized effective stress ($\boldsymbol{\sigma}'$) approach, which is a particular case of the Bishop's effective stress, coupled with the water retention curve via the $S_r \times s$ product. Accordingly, $\boldsymbol{\sigma}'$ and s are the two state variables that govern the mechanical behaviour of soils. Suction acts as a strengthening effect through a one-to-one relationship between suction and the preconsolidation pressure. In contrast, the friction angle at the critical state is assumed to be independent of the suction, which is justified by experimental evidence. In addition, a rigorous description of the water retention behaviour of soils is proposed through an elasto-plastic concept that includes the hydraulic hysteresis as well as the effect of temperature and dry density on the water retention capability of the soil. The two-way coupling between the retention and mechanics, including temperature effects, provides substantial advancements in the field of constitutive modelling of the thermal effect in partially saturated materials.

At each step of the development, the obtained constitutive model has been extensively validated by means of comparisons between experimental results, mainly from literature, and numerical predictions. Those comparisons have proven the ability of the model to reproduce the main features of the behaviour of soil when submitted to combined temperature, suction, and mechanical loading.

In addition, the characteristic experimental paths needed to calibrate the material parameters of the model have been presented. Most of the parameters have a physical significance, which makes it easy to comprehend the role of each. Moreover, it has been shown that, with a limited number of laboratory tests, the thermo-hydro-mechanical model parameters can be determined.

9.1.2 Experimental study

Due to the lack of experimental data that demonstrate the combined effect of temperature and suction on the mechanical behaviour of soils, we decided to undertake an experimental program that investigates the evolution, including the temperature and suction levels, of the preconsolidation pressure and the compressibility indices of a silty material (the Sion silt). A series of compression tests was performed in a temperature- and suction-controlled oedometer cell.

In that kind of test, many parameters must be controlled, and substantial precautions must be taken, to ensure accurate results. Devising a reliable experimental apparatus capable of working at elevated temperatures is a challenging task. The suction is imposed by means of the axis translation technique, while the temperature is controlled through a circulating water circuit in the structure of the oedometer. The calibration of the used experimental apparatus has been presented. In particular, the calibrations required us to correct errors in the measurement because temperature effects on the testing apparatus are of paramount importance.

In addition to the finespun calibrations of the apparatus, the one-month period needed to obtain a single experimental curve illustrates the arduous task of performing such unsaturated and non-isothermal tests on fine-grained soils. Nevertheless, such tests are essential to provide valuable information to validate the hypotheses taken in constitutive modelling. In that sense, this part of the work is complementary to the constitutive part.

In parallel with this work, a series of isotropic compression tests was performed on the same material in a companion experimental project at the University of Montpellier II (France). The combination of the two sets of experimental results provides a sufficient number of experimental curves to establish a quantitative assessment of the observed results. In particular, the preconsolidation stress appeared to be strongly influenced by both the temperature and suction. A temperature increase tends to decrease the yield limit, while a suction increase enhances this limit, at least for suction values higher than the air entry value. A quantitative logarithmic expression requiring two material parameters, one for the thermal evolution and another for the suction evolution, seems to describe these qualitative observations quite well. As far as compressibility is concerned, the data tend to show that temperature has no prevailing effect on the compressibility indices. In contrast, an increase of suction induces a decrease in the compression index.

9.1.3 Numerical study

In addition to the development of the constitutive models and the characterisation of the soil behaviour through laboratory experiments, the performance assessment of the future nuclear waste disposal in deep geological formations needs to introduce the concept developed at the laboratory scale into a numerical tool that solves boundary value problems. The field equations that govern the THM processes around nuclear waste have been presented. The medium is considered to be a deformable, three-phase medium in which heat and mass transfer occurs, with possible exchanges between the gas and water phases.

The resolution of those governing equations, which are highly coupled and non-linear, must be performed by means of an advanced numerical tool. The finite element method provides an efficient framework for solving such problems. The LAGAMINE finite element code developed at the University of Liege, in which the ACMEG-TS model has been introduced, has been used to perform the calculation presented in Chapter 8. Three THM problems were analysed in relation to the issue of nuclear waste disposal. The two first cases, the TIMODAZ benchmark and the ATLAS in-situ experiment, deal with non-isothermal saturated conditions, while the last case, the FEBEX in-situ experiment, involves unsaturated materials under non-isothermal conditions.

The three numerical simulations involve quite different stress paths: (i) an excavation phase followed by an unconfined heating-cooling cycle in the TIMODAZ benchmark, (ii) a confined heating-cooling cycle in the ATLAS in-situ test and (iii) a heating cycle under confined but unsaturated conditions, with resaturation from the host material in the FEBEX in-situ test. Each configuration includes their respective non-linearities and coupling effects.

(i) The excavation of the hollow cylinder is mainly a softening plastic process due to the dilatant response of the material. The subsequent heating does not produce a significant additional alteration of the material. (ii) On the contrary, the ATLAS experiment exhibits a thermal hardening process during the heating phase that involves a redistribution of the stress field around the heater. That feature is characteristic of the thermo-mechanical coupling occurring in the material. (iii) Finally, the simulation of the FEBEX in-situ test shows a high degree of coupling between the thermal, hydraulic, and mechanical processes that occur in the initially unsaturated bentonite. The main driving forces that control the behaviour of the buffer material are the hydration from the host material and the temperature-induced drying in the vicinity of the heater. Between these two opposed processes, a vapour transfer occurs from the hot region and condensate in the cooler one. The obtained results were interpreted in light of the elasto-thermo-plasticity of unsaturated soils. In particular, the effect of the suction and temperature variations on the computed volumetric strain was studied.

In the past, very few constitutive models including the thermo-plasticity and irreversible processes encountered in unsaturated soil mechanics have been developed. However, to the best of our knowledge, the limited number of such existing models had never been synthesized into a consistent numerical tool to study boundary value problems. In this way, the numerical simulations presented in this work constitute a real advancement in the understanding and the quantification of the different THM processes that occur around nuclear waste disposal sites. In the future, a rigorous safety assessment must be based on such calculations, i.e. those calculations that include the highly coupled and non-linear THM behaviour of the geomaterials involved in the confinement of radioactive waste.

9.2 Perspectives

The theoretical developments obtained in this work were applied in the context of the TIMODAZ project, which investigates the thermal impact on the damaged zone around a radioactive waste disposal site in clay host rocks. Within that framework, the current state of knowledge clearly reveals a series of gaps between the state of research and the need for understanding the THM processes that occur around a nuclear waste disposal site. Those gaps concern experimental as well as numerical and constitutive aspects.

From *an experimental point of view*, the materials that need to be characterized can be divided into two types: the geological barrier (natural host material) and the engineered barrier (hand-made material). Designing an experimental apparatus that controls the temperature, pore water pressure (positive or negative), and mechanical states in the entire soil specimen is an arduous task. With regard to the host material, the difficulties arise from its very low permeability, which makes it difficult to perform fully drained tests under temperature or stress loading. In addition, the high rigidity and the strong anisotropy of some materials make things more complicated. For the engineered barrier, the effect of temperature on the swelling and/or collapsing properties of bentonites needs further investigation. In this sense, a full experimental characterization of the THM behaviour of the soil involved in nuclear waste disposal will require, in the future, further developments of the existing experimental techniques.

From *a constitutive point of view*, the concepts that have been addressed in this thesis, which assume soil to be a isotropic material without induced or natural internal structure, should be adapted to consider the specificity of each studied soil. There are several constitutive aspects already developed for isothermal and saturated conditions that should be extend towards unsaturated and non-isothermal conditions. The models that consider the induced or natural mechanical anisotropy, the visco-plastic behaviour, the behaviour of bonded natural soils, or of double-structured soils should be extended to non-isothermal and unsaturated conditions.

Finally, from *a numerical point of view*, independent of the thermal aspects involved, there is a strong need to accurately predict, via finite element computation, the damaged zone produced during the excavation phase of the galleries of the nuclear waste disposal area. In addition, once this zone is well reproduced numerically, the effect of suction and temperature on that region should be predicted by means of numerical simulations. Moreover, the mechanical, thermal, and hydraulic anisotropy of the host material should require one to perform tri-dimensional computations in order to consider the aforementioned anisotropy in the calculations.

References

Aboustit B.L., Advani S.H. and Lee J.K. (1985). Variational principles and finite element simulations for thermo-elastic consolidation. *International Journal for Numerical and Analytical Methods in Geomechanics*, 9: 49-69.

Abuel-Naga H.M. (2005). Thermo-mechanical behavior of soft Bangkok Clay: experimental results and constitutive modeling. *PhD Thesis*, Asian Institute of Technology, Bangkok, Thailand.

Abuel-Naga H.M., Bergado D.T. and Bouazza A. (2007). Thermally induced volume change and excess pore water pressure of soft Bangkok clay. *Engineering Geology*, 89(1-2): 144-154.

Abuel-Naga H.M., Bergado D.T., Ramana G.V., Grino L., Rujivipat P. and Thet Y. (2006). Experimental evaluation of engineering behavior of soft Bangkok clay under elevated temperature. *Journal of Geotechnical and Geoenvironmental Engineering*, 132(7): 902-910.

Agar J.G., Morgenstern N.R. and Scott J.D. (1986). Thermal expansion and pore pressure generation in oil sands. *Canadian Geotechnical Journal*, 23: 327-333.

Airo Farulla C. and Ferrari A. (2005). Controlled suction oedometric tests: analysis of some experimental aspects. *International Symposium: Advanced Experimental Unsaturated Soil Mechanics*, Trento, Italy: 43-48.

Aitchison G.D. (1960). Relationships of moisture stress and effective stress functions in unsaturated soils. *Pore Pressure and Suction in Soils*, London, Butterworths: 47-52.

Alonso E.E., Gens A. and Josa A. (1990). A constitutive model for partially saturated soil. *Géotechnique*, 40(3): 405–430.

Alonso E.E., Vaunat J. and Gens A. (1999). Modelling the mechanical behaviour of expansive clays. *Engineering Geology*, 54: 173–183.

Alonso E.E., Alcoverro J., Coste F., Malinsky L., Merrien-Soukatchoff V., Kadiri I., Nowak T., Shao H., Nguyen T., Selvadurai A., Armand G., Sobolik S., Itamura M., Stone C., Webb S., Rejeb A., Tijina M., Maouche Z., Kobayashi A., Kurikami H., Ito A., Sugita Y., Chijimatsu M., Borgesson L., Hernelind J., Rutqvist J., Tsang C. and Jussila P. (2005). The FEBEX benchmark test: case definition and comparison of modelling approaches. *International Journal of Rock Mechanics and Mining Sciences*, 45(5-6): 611-638.

Atkinson J.H. and Bransby P.L. (1978). *The Mechanics of Soils - An Introduction to Critical State Soil Mechanics*, McGraw-Hill, London.

Aubry D. and Modaressi A. (1992). Strain-localization in multipotential elastoplasticity. *International Journal for Numerical Method in Engineering*, 34: 349-363.

Aubry D., Hujeux J.C., Lassoudiere F. and Meimon Y. (1982). A double memory model with multiple mechanisms for cyclic soil behaviour. *International Symposium on Numerical Models in Geomechanics*, Zurich.

Baldi G., Borsetto M. and Hueckel T. (1987). Calibration of mathematical models for simulation of thermal, seepage and mechanical behaviour of Boom clay: Final report, EUR 10924 EN. Luxembourg, Commission of the European Communities.

Baldi G., Hueckel T. and Pellegrini R. (1988). Thermal volume change of the mineral-water system in low-porosity clay soils. *Canadian Geotechnical Journal*, 25: 807-825.

Baldi G., Hueckel T., Peano A. and Pellegrini R. (1991). Developments in modelling of thermo-hydro-mechanical behaviour of Boom clay and clay-based buffer materials (Vol 1 and 2). *EUR 13365/1 and 13365/2*, Luxembourg.

Barnichon J.D. and Volckaert G. (2003). Observations and predictions of hydromechanical coupling effects in the Boom clay, Mol Underground Research Laboratory, Belgium. *Hydrogeology Journal*, 11: 193-202.

Bastiaens W., Bernier F. and Li X.L. (2006). An overview of long-term HM measurements around HADES URF. *EUROCK 2006 Multiphysics Coupling and Long Term Behaviour in Rock Mechanics*: 15-26.

Bear J. and Bachmat Y. (1986). *Introducing to Modelling of Transport Phenomena in Porous Media.* Kluwer Academie Publishers.

Belanteur N., Tacherifet S. and Pakzad M. (1997). Etude des comportements mécanique, thermo-mécanique et hydro-mécanique des argiles gonflantes et non gonflantes fortement compactées. *Revue Française de Géotechnique*, 78: 31-50.

Bernier F. and Neerdael B. (1996). Overview of in-situ thermomechanical experiments in clay: Concept, results and interpretation. *Engineering Geology*, 41: 51-64.

Bernier F., Li X.L., Bastiaens W. (2007). Twenty-five years' geotechnical observation and testing in the Tertiary Boom clay formation. *Géotechnique*, 57(2): 229-237.

Bernier F., Li X.L., Verstricht J., Barnichon J.D., Labiouse V., Bastiaens W., Palut J.M., Ben Slimane J.K., Ghoreychi M., Gaombalet J., Huertas F., Galera J.M., Merrien K., Elorza F.J., Davies C. (2002). CLIPEX: Clay Instrumentation Programme for the Extension of an Underground Research Laboratory. Commission of the European Communities, EUR20619, Luxembourg.

Biarez J. and Hicher P. (1994). *Elementary Mechanics of Soil Behaviour. Saturated Remoulded Soils*. Balkema.

Biarez J., Fleureau J.M. and Taibi S. (1993). Constitutive model for unsaturated granular media. *Proceeding of the 2nd International Conference on Micromechanics of Granular Media*, Birmingham.

Biot M.A. (1956). General solutions of the equations of elasticity and consolidation for a porous material. *Journal of Applied Mechanics*: 91-96.

Bishop A. and Donald I. (1961). The experimental study of partly saturated soil in the triaxial apparatus. *5th Int. Conf. on Soil Mechanics and Foundation Engineering*, Paris: 13-21.

Bishop A.W. (1959). The principle of effective stress. *Tecnisk Ukeblad*, 39, 859-863.

Bishop A.W. (1966). The strength of soils as engineering materials. 6th Rankine Lecture. *Géotechnique*, 16: 89-130.

Bishop A.W. and Blight G.E. (1963). Some aspects of effective stress in saturated and unsaturated soils. *Géotechnique*, 13: 177-197.

Bishop A.W., Alpan I., Blight G.E. and Donald I.B. (1960). Factors controlling the strength of partly saturated cohesive soils. *Conference Shear Strength Cohesive Soils, ASCE*: 503-532.

Blaisonneau A. and Laloui L. (2002). Phénomènes de transport dans les milieux poreux déformables multiphasiques. *Report COST Action P4 to the Swiss Federal Office for Education and Science*.

Blight G.E. (1966). Strength characteristics of dessicated clays. *Journal of Soil Mechanics and Foundations Division, ASCE*, 93 (SM2): 125-148.

Blight G.E. (1967). Effective stress evaluation for unsaturated soils. *Journal of Soil Mechanics and Foundations Division, ASCE*, 92 (SM6): 19-37.

Bock H. (2001). RA Experiment – Rock mechanics analyses and synthesis: Data report on rock mechanics. Mont Terri Project, Technical Report 2000-02.

Bolzon G. and Schrefler B.A. (2005). Thermal effects in partially saturated soils: a constitutive model. *International Journal for Numerical and Analytical Methods in Geomechanics*, 29(9): 861-877.

Bolzon G., Schrefler B.A. and Zienkiewicz O.C. (1996). Elastoplastic soil constitutive law generalized to partially saturated state. *Géotechnique*, 46: 279-289.

Borja R.I. (2004). Cam-Clay plasticity. Part V: A mathematical framework for three-phase deformation and strain localization analyses of partially saturated porous media. *Computer Methods in Applied Mechanics and Engineering*, 193: 5301-5338.

Bossart P., Meier P.M., Moeri A., Trick T. and Mayor J.C. (2002). Geological and hydraulic characterisation of the excavation disturbed zone in the Opalinus clay of the Mont Terri Rock Laboratory. *Engineering Geology*, 66: 19-38.

Bouazza A., Van Impe W.F. and Haegeman W. (1996). Some mechanical properties of reconstituted Boom clay. *Geotechnical and Geological Engineering*, 14: 341-352.

Boudali M., Leroueil S. and Srinivasa Murthy B.R. (1994). Viscous behaviour of natural clays. *13th International Conference on Soil Mechanics and Foundation Engineering*, New Delhi: 411-416.

Brandl H. (2006). Energy foundations and other thermo-active ground structures. *Géotechnique*, 56(2): 81-122.

Brooks R.H. and Corey A.T. (1964). Hydraulic properties of porous media. *Colorado State University, Hydrology Paper 3*.

Burger A., Recordon E., Bovet D., Cotton L. and Saugy B. (1985). *Thermique des Nappes Souterraines*. Lausanne, Presses Polytechniques Romandes.

Burghignoli A., Desideri A. and Miliziano S. (2000). A laboratory study on the thermomechanical behaviour of clayey soils. *Canadian Geotechnical Journal*, 37: 764-780.

Calladine C.R. (1963). Correspondence. *Géotechnique*, 13: 250-255.

Campanella R.G. (1965). Effect of temperature and stress on time-deformation behaviour of saturated clays. *PhD Thesis*, University of California, Berkeley.

Campanella R.G. and Mitchell J.K. (1968). Influence of temperature variations on soil behavior. *Journal of the Soil Mechanics and Foundation Division*, *ASCE*, 94: 709-734.

Casagrande A. (1936). The determination of the preconsolidation load and its practical significance. *Proceeding of the 1st International Conference of Soil Mechanics*, 3: 60-64.

Cekerevac C. (2003). Thermal effect on the mechanical behaviour of saturated clays: an experimental and constitutive study. *PhD Thesis*. EPFL, Lausanne.

Cekerevac C. and Laloui L. (2004). Experimental study of thermal effects on the mechanical behaviour of a clay. *International Journal for Numerical and Analytical Methods in Geomechanics*, 28(3): 209-228.

Chapman D.C. (1913). A contribution to the theory of electro-capillarity. *Philosophical Magazine*, 25: 475-481.

Chapman N.A. and McKinley I.G. (1987). *The Geological Disposal of Nuclear Waste*. John Wiley and Sons.

Charlier R. (1987). Approche unifiée de quelques problèmes non linéaires de mécanique des milieux continus par la méthode des éléments finis. *PhD Thesis*, Université de Liège.

Charlier R., Radu J.P. and Collin F. (2001). Numerical modelling of coupled transient phenomena. *Revue Française de Génie Civil*, 5(6): 719-741.

Chiffoleau S. and Robinet J.C. (1999). HE Experiment: Determination of the hydromechanical characteristics of the Opalinus clay. Mont Terri Project, Technical Report 98-36.

Chijimatsu M., Fujita T., Sugita Y., Amemiya K. and Kobayashi A. (2001). Field experiment, results and THM behavior in the Kamaishi mine experiment. *International Journal of Rock Mechanics and Mining Sciences*, 38: 67-78.

Clayton W.S. (1996). Relative permeability–saturation–capillary head relationships for air sparging in soils. *PhD Thesis*, Colorado School of Mines, Golden, Colorado.

Clotworthy A. (2000). Response of Wairakei geothermal reservoir to 40 years of production. *World Geothermal Congress*, Kyushu – Tohoku, Japan: 2057-2062.

Collin F. (2003). Couplages thermo-hydro-mécaniques dans les sols et les roches tendres partiellement saturés. *PhD Thesis*, Université de Liège.

Collin F., Chambon R. and Charlier R. (2006). A finite element method for poro mechanical modelling of geotechnical problems using local second gradient models. *International Journal of Numerical Methods in Engineering*, 65: 1749-1772.

Collin F., Li X., Radu J.P. and Charlier R. (2002). Thermo-hydro-mechanical coupling in clay barriers. *Engineering Geology*, 64: 179-193.

Costenza D., Viggiani G. and Tamagnini C. (2006). Directional response of a reconstituted fine-grained soil - Part I: Experimental investigation. *International Journal of Numerical and Analytical Methods in Geomechanics*, 30: 1283–1301.

Cui Y.J. and Delage P. (1996). Yielding and plastic behaviour of an unsaturated compacted silt. *Géotechnique*, 46(2): 291-311.

Cui Y.J., Delage P. and Sultan, N. (1995) An elasto-plastic model for compacted soils. *Unsaturated Soils*, Paris, Balkema: 703-709.

Cui Y.J. and Ye W.M. (2005). Modeling of thermo-mechanical volume change behavior of saturated clays. *Chinese Journal of Rock Mechanics and Engineering*, 24(21): 3903-3910.

Cui Y.J., Sultan N. and Delage P. (2000). A thermomechanical model for saturated clays. *Canadian Geotechnical Journal*, 37: 607-620.

Cuisinier O. and Laloui L. (2004). Fabric evolution during hydro-mechanical loading of compacted silt. *International Journal for Numerical and Analytical Methods in Geomechanics*, 28(6): 483-499.

Da Costa A.M., Cardoso C.D.O., Amaral C.D.S. and Andueza A. (2002). Soil-structure interaction of heated pipeline buried in soft clay. *International Pipeline Conference*: 457-466.

Dafalias Y. and Herrmann L. (1980). A bounding surface soil plasticity model. *International Symposium on Soils under Cyclic and Transient Loading*, Swansea: 335-345.

Dafalias Y. and Popov E.P. (1975). A model of non-linearly hardening materials for complex loadings. *Acta Mechanica*, 21: 173-192.

Dafalias Y. and Popov E.P. (1977). Cyclic loading for materials with vanishing elastic domain. *Nuclear Engineering Design*, 41: 293-302.

Datta R., Barr D. and Boyle W. (2004). Measuring thermal, hydrological, mechanical, and chemical responses in the Yucca Mountain drift scale test. *Coupled Thermo-Hydro-Mechanical-Chemical Processes in Geo-System*, Elsevier: 155-160.

Davies C. and Bernier F. (2003). Impact of the excavation disturbed or damaged zone (EDZ) on the performance of radioactive waste geological repositories. *Proceedings of a European Commission CLUSTER - Conference and Workshop*, Luxembourg.

De Boer R. and Ehlers W. (1990). The development of the principle of effective stress. *Acta Mechanica*, 83: 77-92.

De Bruyn D. and Labat S. (2002). The second phase of ATLAS: the continuation of a running THM test in the HADES underground research facility at Mol. *Engineering Geology*, 64: 309-316.

Dehandschutter B., Vandycke S., Sintubin M., Vandenberghe N. and Wouters L. (2005). Brittle fractures and ductile shear bands in argillaceous sediments: inferences from Oligocene Boom clay (Belgium). *Journal of Structural Geology*, 27(6): 1095-1112.

Dejarguin B., Karasev V. and Khromov E. (1986). Thermal expansion of water in fine pores. *Colloid and Interface Sciences*, 109(2): 586-587.

Del Olmo C., Fioravante V., Gera F., Hueckel T., Mayor J.C. and Pellegrini R. (1996). Thermomechanical properties of deep argillaceous formations. *Engineering Geology*, 41: 87-102.

Delage P. (2002). Experimental unsaturated soil mechanics. *3rd International Conference on Unsaturated Soils*, Recife, Brazil.

Delage P. and Cui Y.J. (2008). A novel filtration system for polyethylene glycol used in the osmotic method of controlling suction. *Canadian Geotechnical Journal*, 45: 421-424.

Delage P., Cui Y.J and De Laure E. (2001). Récents développement de la technique osmotique de contrôle de succion. *15th Int. Conf. on Soil Mechanics and Geotechnical Engineering*, Istanbul: 575-578.

Delage P., Howat M. and Cui Y. (1998). The relationship between suction and swelling properties in a heavily compacted unsaturated clay. *Engineering Geology*, 50(1-2) : 31-48.

Delage P., Le T.T., Tang A.M., Cui Y.J. and Li X.L. (2007). Suction effects in deep Boom clay block samples. *Géotechnique*, 57(2): 239-244.

Delage P., Sultan N. and Cui Y.J. (2000). On the thermal consolidation of Boom clay. *Canadian Geotechnical Journal*, 37: 343–354.

Delage P., Suraj De Silva G. and De Laure E. (1987). Un nouvel appareil triaxial pour les sols non-saturés. *9th European Conference on Soil Mechanics*, Dublin: 25-28.

Demarks K.R. and Charles R.D. (1982). Soil volume changes induced by temperature cycling. *Canadian Geotechnical Journal*, 19: 188-194.

Deng G. and Shen, Z.J. 2006. Numerical simulation of crack formation process in clays during drying and wetting. *Geomechanics and Geoengineering*, 1(1): 27-41.

Desai C.S. and Siriwardane H.J. (1984). *Constitutive Laws for Engineering Materials with Emphasis on Geological Materials.* Prentice-Hall Inc., New Jersey.

Despax D. (1976). Influence de la température sur les propriétés mécaniques des argiles saturées, *PhD Thesis*, Université de Grenoble, Grenoble.

Dierckx A. (1997). Boom clay in situ pore water chemistry. SCK•CEN report, BLG-734, Mol, Belgium.

Dineen K. and Burland J.B. (1995). A new approach to osmotically controlled oedometer testing. *Proc. of 1st Int. Conf. on unsaturated soils*, Paris: 459-465.

Dixon D., Gray M., Lingnau B., Graham J. and Campbell S. (1993) Thermal expansion testing to determinate the influence of pore water structure on water flow through dense clays. *46th Canadian Geotechnical Conference*, Saskatoon: 177-184.

Drucker D.C. (1958). The definition of a stable inelastic material. *Journal of Applied Mechanics*, 26: 101-106.

Drucker D.C. and Prager W. (1952). Solid mechanics and plastic analysis for limit design. *Quarterly of Applied Mathematics*, 10(2): 157-165.

Drucker D.C., Gibson R.E. and Henkel D.J. (1957). Soil mechanics and working hardening theories of plasticity. *Transaction of ASCE*, 122: 338-346.

Dusseault M.B., Wang Y. and Simmons J.V. (1988). Induced stresses near a fireflood front. *AOSTRA Journal of Research*, 4: 153-170.

ENRESA. (2000). Febex Project: Full-scale engineered barriers experiment for a deep geological repository for high level radioactive waste in crystalline host rock. Publicación técnica 1/2000.

Eriksson L.G. (1989). Temperature effects on consolidation properties of sulphide clays. *12th International Conference on Soil Mechanics and Foundation Engineering*. Rio de Janeiro, Vol.3: 2087-2090.

Escario V. (1969). Swelling of soils in contact with water at a negative pressure. *2nd Int. Conf. Expansive Clays*, Texas: 207-217.

Escario V. (1980). Suction controlled penetration and shear tests. *4th Int. Conf. Expansive Soils*, Denver: 781-797.

Escario V. and Saez J. (1986). The shear strength of partly saturated soils. *Géotechnique*, 36(3): 453-456.

Esteban V. and Saez J. (1988) A device to measure the swelling characteristics of rock samples with control of the suction up to very high values. *ISRM Symposium on Rock Mechanics and Power Plants*, Madrid.

Fei Y. (1995). Thermal expansion. *Mineral Physics and Cristallography. A Handbook of Physical Constants*: 22-44.

Finn F.N. (1951). The effects of temperature on the consolidation characteristics of remoulded clay. *American Society for Testing and Materials.* Report 126.

Fleureau J.M., Kheirbeksaoud S., Soemitro R. and Taibi S. (1993). Behavior of clayey soils on drying wetting paths. *Canadian Geotechnical Journal*, 30(2): 287-296.

François B. and Laloui L. (2007). A stress-strain framework for modelling the behaviour of unsaturated soils under non-isothermal conditions. *Springer Proceedings in Physics 113, Theoretical and Numerical Unsaturated Soil Mechanics*: 119-125.

François B. and Laloui L. (2008a). ACMEG-TS: A constitutive model for unsaturated soils under non-isothermal conditions. *International Journal for Numerical and Analytical Methods in Geomechanics,* 32: 1955-1988.

François B. and Laloui L. (2008b). Unsaturated soils under non-isothermal conditions: Framework of a new constitutive model. *GeoCongress08*, New Orleans, USA.

François B. and Laloui L. (2008c). ACMEG-TS: A unified elasto-plastic constitutive model to simulate coupled processes in non-isothermal unsaturated soils. *1st European Conf. on Unsaturated Soils, Durham, United Kingdom*: 539-545.

François B., Laloui L. and Laurent C. (2008). Thermo-hydro-mechanical interpretation of the response of Boom clay undergoing in-situ thermal loading. *Computers and Geotechnics*. (accepted).

François B., Nuth M., Laloui L. (2007b) Mechanical constitutive framework for thermal effects on unsaturated soils. *10th Int. Symp. on Numerical Models in Geomechanics, NUMOG X*, Rhodes, Greece : 9-13.

François B., Salager S., El Youssoufi M.S., Ubals Picanyol D., Laloui L. and Saix C. (2007a). Compression tests on a sandy silt at different suction and temperature levels. *ASCE Geotechnical special publication 157*, GeoDenver 2007.

Fredlund D.G. and Morgenstern N.R. (1976). Constitutive relations for volume change in unsaturated soils. *Canadian Geotechnical Journal*, 13: 261-276.

Fredlund D.G. and Morgenstern N.R. (1977). Stress state variables for unsaturated soils. *Journal of the Geotechnical Engineering Division, ASCE*, 103(GT5): 447-466.

Fredlund D.G. and Rahardjo H. (1993). *Soil Mechanics for Unsaturated Soils*. Wiley, New-York.

Fredlund D.G. and Xing A. (1994). Equation for the soil-water characteristics curve. *Canadian Geotechnical Journal*, 31: 521-532.

Gabrielsson A., Bergdahl U. and Moritz L. (2000). Thermal energy storage in soils at temperatures reaching 90°C. *ASME, Journal of Solar Energy Engineering*, 122(3): 3-8.

Gajo A. and Muir Wood D. (2001). A new approach to anisotropic, bounding surface plasticity: general formulation and simulations of natural and reconstituted clay behaviour. *International Journal of Numerical and Analytical Methods in Geomechanics,* 25: 207-241.

Gallipoli D., Gens A., Sharma R. and Vaunat J. (2003b). An elasto-plastic model for unsaturated soil incorporating the effects of suction and degree of saturation on mechanical behaviour. *Géotechnique*, 54(4): 293–295.

Gallipoli D., Wheeler S.J. and Karstunen M. (2003a). Modelling the variation of degree of saturation in a deformable unsaturated soil. *Géotechnique*, 53(1): 105-112.

Gautschi L. (2001). Hydrogeology of a fractured shale (Opalinus clay): Implications for deep geological disposal of radioactive wastes. *Hydrogeology Journal*, 9 (1): 97-107.

Gebrande H. (1982). Elasticity of rocks and minerals. *Numerical data and Functional Relationship in Science and Technology. Group V: Geophysics and Space Research* (1B), Springer, Berlin: 1-99.

Geiser F. (1999). Comportement mécanique d'un limon non saturé: Etude expérimentale et modélisation constitutive. *PhD Thesis*, EPFL, Lausanne, Switzerland.

Geiser F., Laloui L. and Vulliet L. (1998). Yielding of a remoulded sandy silt in saturated and unsaturated states. *2nd International Conference on Unsaturated Soils*, Beijing, China: 54-59.

Geiser F., Laloui L. and Vulliet L. (2000). On the volume measurement in unsaturated triaxial test. *Unsaturated Soil for Asia*, Singapor: 669-674.

Geiser F., Laloui L. and Vulliet L. (2006). Elasto-plasticity of unsaturated soils: laboratory test results on a remoulded silt. *Soils and Foundations*, 46(5): 545-556.

Geiser F., Laloui L. and Vulliet L. (2000). Modelling the behaviour of unsaturated silt. *Experimental Evidence and Theoretical Approaches in Unsaturated Soils*, Trento: 155-175.

Gens A. (1995a). Constitutive modelling: Application to compacted soils. *Unsaturated Soils*, Paris, Balkema: 1179-1200.

Gens A. (1995b). Constitutive laws. *Modern Issues in Non-saturated Soils*, Springer: 129-158.

Gens A. and Alonso E.E. (1992). A framework for the behaviour of unsaturated expansive clays. *Canadian Geotechnical Journal*, 29: 1013–1032.

Gens A. and Olivella S. (2001). Clay barrier in radioactive waste disposal. *Revue Française de Génie Civil*, 5(6): 845-856.

Gens A. and Potts D.M. (1988). Critical state model in computational geomechanics. *Engineering Computations*, 5: 178-197.

Gens A., Garcia-Molina A.J., Olivella S., Alonso E.E. and Huertas F. (1998). Analysis of a full scale in-situ test simulating repository conditions. *International Journal for Numerical and Analytical Methods in Geomechanics*, 22: 515–548.

Gens A., Guimaraes L.N., Garcia-Molina A. and Alonso E.E. (2002). Factors controlling rock-clay buffer interaction in a radioactive waste repository. *Engineering Geology*, 64: 297-308.

Gens A., Guimaraes L.N., Olivella S. and Sanchez M. (2004). Analysis of the THMC behaviour of compacted swelling clay for radioactive waste isolation. *Coupled Thermo-Hydro-Mechanical-Chemical Processes in Geosystems*: 317-322.

Gens A., Sanchez M. and Sheng D. (2006). On the constitutive modelling of unsaturated soils. *Acta Geotechnica*, 1: 137-147.

Gens A., Vaunat J., Garitte B. and Wileveau Y. (2007). In situ behaviour of a stiff layered clay subject to thermal loading: observations and interpretation. *Géotechnique*, 57(2): 207-228.

Gera F., Hueckel T. and Peano A. (1996). Critical issues in modelling the long-term hydro-thermo-mechanical performance of natural clay barriers. *Engineering Geology*, 41: 17-33.

Gerard P., Charlier R., Chambon R. and Collin F. (2008). Influence of evaporation and seepage on the convergence of a ventilation cavity. *Water Resources Research*, 44. DOI: 10.1029/2007WR006500.

Gerolymos N., Vardoulakis I. and Gazetas G. (2007). A thermo-poro-visco-plastic shear band model for seismic triggering and evolution of catastrophic landslides. *Soils and Foundations*, 47(1): 11-25.

Gouy G. (1919). Sur la constitution de la charge électrique à la surface d'un électrolyte. *Annale de Physique (Paris) Série 4*, 9: 457-468.

Graham J., Tanaka N., Crilly T. and Alfaro M. (2001). Modified Cam-Clay modelling of temperature effects in clays. *Canadian Geotechnical Journal*, 38: 608-621.

Grant S.A. and Salehzadeh, A. (1996). Calculation of temperature effects on wetting coefficients of porous solids and their capillary pressure functions. *Water Resources Research*, 32(2): 261-270.

Green A.E. (1956). Hypo-elastic and plasticity: II. *Journal of Rational Mechanics and Analysis*, 5: 725-734.

Hajal T. (1984). Modélisation élasto-plastique des sols par une loi multimécanismes: application au calcul pressiométrique. *PhD Thesis*, Ecole Centrale, Paris.

Hansen N.R. and Schreyer H.L. (1994). A thermodynamically consistent framework for theories of elasto-plasticity coupled with damage. *International Journal of Solids and Structures*, 31: 359-382.

Henkel D.J. and Sowa V.A. (1963). A discussion on symposium on laboratory shear testing of soils. *Symposium on Laboratory Testing of Soils, ASTM Special Technical Publication*, Ottawa, Canada: 104-107

Highway Research Board (1969). Effects of temperature and heat on engineering behavior of soils. *Special Report* 103, Washington, D.C.

Hill R. (1948). A variational principle of maximum plastic work in classical plasticity. *The Quarterly Journal of Mechanics and Applied Mathematics*, 1: 18-28.

Hill R. (1950). *The Mathematical Theory of Plasticity.* Clarendon Press, Oxford.

Ho D. and Fredlund D. (1982). Strain rates for unsaturated soil shear strenght testing. *7th South-East Asian Geotechical Conference*, Hong Kong: 787-803.

Holloway S. (1997). An overview of the underground disposal of carbon dioxide. *Energy Conversion Manage,* 38(S1): S193-S198.

Horseman S.T., Harrington J.F., Birchall D.J., Noy D.J. and Cuss R.J. (2006). Hydrogeologic analyses and synthesis (HA Experiment): Consolidation and rebound properties of Opalinus clay: A long-term, fully drained test. Mont Terri Project, Technical Report 2003-03 revised.

Horseman S.T., Winter M.G. and Entwistle D.C. (1987). Geotechnical characterisation of Boom clay in relation to the disposal of radioactive waste. Final report. EUR10987. Luxembourg, Commission of the European Communities.

Horseman S.T., Winter M.G. and Entwistle D.C. (1993). Triaxial experiments on Boom clay. *The Engineering Geology of Weak Rock*, Balkema, Rotterdam: 36-43.

Houston S.L., Houston W.N. and Williams, N.D. (1985). Thermo-mechanical behavior of seafloor sediments. *Journal of Soil Mechanics and Foundation Division*, ASCE, 111: 1249-1263.

Hoxha D., Jiang Z., Homand F., Giraud A., Su K. and Wileveau Y. (2006). Impact of THM constitutive behavior on the rock-mass response: case of HE-D experiment in Mont-Terri Underground Rock Laboratory. *EUROCK 2006 Multiphysics Coupling and Long Term Behaviour in Rock Mechanics*: 199-204.

Hoyos L., Laloui L. and Vassallo R. (2008). Mechanical testing in unsaturated soils. *Geotechnical and Geological Engineering.* DOI: 10.1007/s10706-008-9200-9.

Hueckel T. (1992a). Water-mineral interaction in hygromechanics of clays exposed to environmental loads: a mixture-theory approach. *Canadian Geotechnical Journal*, 29: 1071-1086.

Hueckel T. (1992b). On effective stress concept and deformation in clays subjected to environemntal loads: discussion. *Canadian Geotechnical Journal*, 29: 1120-1125.

Hueckel T. and Baldi G. (1990). Thermoplasticity of saturated clays: Experimental constitutive study. *Journal of Geotechnical Engineering*, 116(2): 1778-1796.

Hueckel T. and Borsetto M. (1990). Thermoplasticity of saturated soils and shales: Constitutive equations. *Journal of Geotechnical Engineering, ASCE*, 116(12): 1765-1777.

Hueckel T. and Pellegrini R. (1989). Modeling of thermal failure of saturated clays. *International Symposium on Numerical Models in Geomechanics – NUMOG*: 81-90.

Hueckel T. and Pellegrini R. (1991). Thermoplastic modeling of undrained failure of saturated clay due to heating. *Soils and Foundations*, 31(3): 1-16.

Hueckel T. and Pellegrini R. (1992). Effective stress and water pressure in saturated clays during heating-cooling cycles. *Canadian Geotechnical Journal*, 29: 1095-1102.

Hueckel T., Pellegrini R. and Del Olmo C. (1998). A constitutive study of thermo-elasto-plasticity of deep carbonatic clays. *International Journal of Numerical and Analytical Methods in Geomechanics*, 22: 549-574.

Hueckel T., Tutumluer E. and Pellegrini R. (1992). A note on non-linear elasticity of isotropic overconsolidated clays. *International Journal of Numerical and Analytical Methods in Geomechanics*, 16: 603–618.

Hujeux J.C. (1979). Calcul numérique de problèmes de consolidation élastoplastique. *PhD Thesis*, Ecole Centrale, Paris.

Hujeux J.C. (1985). Une loi de comportement pour le chargement cyclique des sols. *Génie Parasismique*, Les éditions de l'E.N.P.C., Paris: 287-303.

Hvorslev M.J. (1937). Uber die festigkeit-seigenschaffeten gestorter bindiger boden. *Ingeniorvidenskabelige skrifter* A, 45.

Imbert C., Olchitzky E., Lassabatère T., Dangla P. and Courtois A. (2005). Evaluation of a thermal criterion for an engineered barrier system. *Engineering Geology*, 81: 269-283.

Israelachvili J.N. and Adams G.E. (1978). Measurement of forces between two mica surfaces in aqueous electrolyte solutions in the range 0–100 nm. *Journal of Chemical Society, Faraday Transactions 1*, 74: 975 -1001.

Jamin F. (2003). Contribution à l'étude du transport de matière et de la rhéologie dans les sols non saturés à différentes températures. *PhD Thesis*. Université Montpellier II.

Jardine R.J., Gens A., Hight D.W. and Coop M.R. (2004). Developments in understanding soil behaviour. *Advances in Geotechnical Engineering. The Skempton Conference*, Thomas Telford: 103-206.

Jeffries R.M. (1995). Interclay II project. A coordinated benchmark exercise on the rheology of clays. Report on Stages 2 and 3. EUR16204EN. Luxembourg, Commission of the European Communities.

Jennings J.E. (1960). A revised effective stress law for use in the prediction of the behaviour of unsaturated soils. *Pore Pressure and Suction in Soils*, London, Butterworths: 26-30.

Jennings J.E.B. and Burland J.B. (1962). Limitations to the use of effective stresses in partly saturated soils. *Géotechnique*, 12: 125-144.

Jin M.S., Lee K.W. and Kovacs W.D. (1994). Seasonal variation of resilient modulus of subgrade soils. *ASCE, Journal of Transportation Engineering*, 120(4): 603-616.

JNC (1999). Project to establish the scientific and technical basis for HLW disposal in Japan. Technical report. Support report 2.

Jommi C. (2000). Remarks on the constitutive modelling of unsaturated soils. *Experimental Evidence and Theoretical Approaches in Unsaturated Soils*, Trento: 139–153.

Kaliakin V.N. and Dafalias Y.F. (1990). Theoretical aspects of the elastoplastic-viscoplastic bounding surface model for cohesive soils. *Soils and Foundations*, 30: 11-24.

Kassiff G. and Ben Shalom A. (1971). Experimental relationship between swell pressure and suction. *Géotechnique*, 21(3): 245-255.

Khalili N. and Khabbaz M.H. (1998). A unique relationship for x for the determination of the shear strength of unsaturated soils. *Géotechnique, 48*(5): 681-687.

Khalili N. and Loret B. (2001). An elasto-plastic model for non-isothermal analysis of flow and deformation in unsaturated porous media: formulation. *International Journal of Solids and Structures*, 38: 8305-8330.

Khalili N., Geiser F. and Blight G.E. (2004). Effective stress in unsaturated soils: Review with new evidence. *International Journal of Geomechanics*, 4(2): 115–126.

Khalili N., Habte M.A. and Valliappan S. (2005). A bounding surface plasticity model for cyclic loading of granular soils. *International Journal of Numerical Methods in Engineering*, 63: 1939–1960.

Kingery W.D, Bowen H.K. and Uhlmann D.R. (1976). *Introduction to Ceramics*, 2nd Edition. Wiley, New York.

Kohgo Y., Nakano M. and Miyazaki T. (1993). Theoretical aspects of constitutive modelling for unsaturated soils. *Soils and Foundations*, 33(4): 49-63.

Koiter W. (1960). General theorem for elastic-plastic solids. *Progress in Solids Mechanics*, North-Holland, Amsterdam: 165-221.

Koliji A. (2008). Mechanical behaviour of unsaturated aggregated soils. *PhD thesis*, No. 4011, Ecole Polytechnique Fédérale de Lausanne.

Komine H. and Ogata N. (1994). Experimental study on swelling characteristics of compacted bentonite. *Canadian Geotechnical Journal*, 31(2), 478-490.

Kormonik A., Livneh M. and Smucha S. (1980). Shear strength and swelling of clays under suction. *4th International Conference Expansive Soils*, Denver: 206-226.

Krepyshev N.V. (1958). Air cooling of the hearth bottom of no.2 blast furnace. *Metallurgist*, 2(11): 569-574.

Krieg R.D. (1975). A practical two-surface plasticity theory. *Journal of Applied Mechanics*, 42: 641-646.

Kuntiwattanakul P. (1991). Effect of high temperature on mechanical behaviour of clays. *PhD Thesis*, University of Tokyo, Tokyo.

Kuntiwattanakul P., Towhata I., Ohishi K. and Seko I. (1995). Temperature effects on undrained shear characteristics of clay. *Soils and Foundations*, 35(1): 147-162.

Lagny C. (1996). Comportement mécanique des sols fins sous fortes contraintes et fortes pressions négatives. *PhD Thesis*, Ecole Centrale, Paris.

Laloui L. (1993). Modélisation du comportement thermo-hydro-mécanique des milieux poreux anélastique. *PhD Thesis*, Ecole Centrale de Paris.

Laloui L. (2001). Thermo-mechanical behaviour of soils. *Environmental Geomechanics.* EPFL Press, Lausanne: 809-843.

Laloui L. and Cekerevac C. (2003). Thermo-plasticity of clays: An isotropic yield mechanism, *Computers and Geotechnics*, 30(8): 649-660.

Laloui L. and Cekerevac C. (2008). Non-isothermal plasticity model for cyclic behaviour of soils. *International Journal for Numerical and Analytical Methods in Geomechanics*, 32(5): 437-460.

Laloui L. and Nuth M. (2005). An introduction to the constitutive modelling of unsaturated soils. *Revue Européenne de Génie Civil*, 9(5-6): 651-669.

Laloui L., Cekerevac C. and François B. (2005) Constitutive modelling of the thermo-plastic behaviour of soils. *Revue Européenne de Génie Civil,* 9(5-6): 635-650.

Laloui L. and François B. (2008) ACMEG-T: A comprehensive soil thermo-plasticity model. *Journal of Engineering Mechanics.* (submitted).

Laloui L., Geiser F. and Vulliet L. (2001). Constitutive modelling of unsaturated soils. *Revue Française de Génie Civil*; 5(6): 797-807.

Laloui L., Geiser F., Vulliet L., Li X.L., Bolle A. and Charlier R. (1997). Characterization of the mechanical behaviour of an unsaturated sandy silt, *14th International Conference on Soil Mechanics and Foundation Engineering*, Hamburg: 703-706.

Laloui L., Nuth M. and Vulliet L. (2006). Experimental and numerical investigations of the behaviour of a heat exchanged pile. *International Journal for Numerical and Analytical Methods in Geomechanics*, 30: 763-781.

Laloui L., Peron H., Geiser F., Rifa'i A. and Vulliet L. (2006). Advances in volume measurement in unsaturated triaxial tests, *Soils and Foundations,* 46(3): 341-349.

Laloui L., François B., Nuth M., Peron H. and Koliji A. (2008). A thermo-hydro-mechanical stress-strain framework for modelling the performance of clay barriers in deep geological repositories for radioactive waste. *1st European Conf. on Unsaturated Soils*, Durham, United Kingdom: 63-80.

Lambe T.W. and Whitman R.V. (1969). *Soil Mechanics.* Wiley.

Lassoudiere F. (1984). Modélisation du comportement des sols sous sollicitations cycliques. *PhD Thesis*, Ecole Centrale de Paris.

Laurent C. (2007). Thermo-hydro-mechanical coupled modelisation in the context of nuclear waste storage. *Master Thesis*, EPFL, Lausanne.

Leclercq J. and Verbrugge J.C. (1985). Propriétés géomécaniques des sols non-saturés. *Compte-Rendus du Colloque sur le Travail du Sol*, Gembloux.

Leroueil S. and Hight D. (2003). Behaviour and properties of natural soils and soft rocks. *Characterisation and Engineering Properties of Natural Soils*: 29-254.

Leroueil S. and Marques M.E.S. (1996). Importance of strain rate and temperature effects in geotechnical engineering (State-of-the-art). *ASCE Geotechnical Special Publication*, 61: 1-59.

Lewis R.W. and Schrefler B.A. (1987). *The Finite Element Method in the Deformation and Consolidation of Porous Media*. John Wiley & Sons.

Likos W.J. and Lu N. (2004). Hysteresis of capillary stress in unsaturated granular soil. *Journal of Engineering Mechanics, ASCE*, 130(6): 646-655.

Lingnau B.E., Graham J., Yarechewski D., Tanaka N., andGray M.N. (1996). Effects of temperature on strength and compressibility of sand-bentonite buffer. *Engineering Geology*, 41 (1–4), 103–115.

Lloret A., Romero E. and Villar M. (2004). FEBEX II Project: Final report on thermo-hydro-mechanical laboratory tests. *Publicación técnica 10/2004*, ENRESA.

Lloret A., Villar M., Sanchez M., Gens A., Pintado X. and Alonso E.E. (2003). Mechanical behaviour of heavily compacted bentonite under high suction changes. *Géotechnique*, 53: 27-40.

Loret B. and Khalili N. (2000). A three phase model for unsaturated soils. *International Journal of Numerical and Analytical Methods in Geomechanics*, 31: 893-927.

Loret B. and Khalili N. (2002). An effective stress elastic-plastic model for unsaturated porous media. *Mechanics of Materials*, 34(2): 97-116.

Low P.F. (1979). Nature and properties of water in montmorillonite-water system. *Soil Science Society of America Journal*, 43: 651-658.

Lu N. and Likos W.J. (2004). *Unsaturated Soil Mechanics.* Wiley, New Jersey.

Maâtouk A., Leroueil S. and La Rochelle P. (1995). Yielding and critical state of collapsible unsaturated silty soil. *Géotechnique,* 45(3): 465-477.

Mandel W. (1965). Généralisation de la théorie de Koiter. *International Journal of Solids and Structures*, 1: 273-295.

Marques M.E.S., Leroueil S. and Almeida M.S.S. (2004). Viscous behaviour of the St-Roch-de-l'Achigan clay, Quebec. *Canadian Geotechnical Journal*, 41(1): 25-38.

Marschall P., Horseman S. and Gimmi T. (2005). Characterisation of gas transport properties of the Opalinus clay, a potential host rock formation for radioactive waste disposal. *Oil and Gas Science and Technology. Revue de l'Institut Français du Pétrole*, 60 (1): 121-139.

Masin D., Tamagnini C., Viggiani G. and Costenza D. (2006). Directional response of a reconstituted fine-grained soil - Part II: Performance of different constitutive models. *International Journal of Numerical and Analytical Methods in Geomechanics*, 30: 1303–1336.

Matyas E.L. and Radhakrishna H.S. (1968). Volume change characteristics of partially saturated soils. *Géotechnique*, 18(4): 432-448.

McKinstry H.A. (1965). Thermal expansion of clay minerals. *American Mineralogist,* 50: 212–222.

Mercury L., Azaroual M., Zeyen H. and Tardy Y. (2003). Thermodynamic properties of solutions in metastable systems under negative or positive pressures. *Geochimica et Cosmochimica Acta*, 67(10): 1769-1785.

Mertens J., Bastiaens W. and Dehandschutter B. (2004). Characterisation of induced discontinuities in the Boom clay around the underground excavations (URF, Mol, Belgium). *Applied Clay Science*, 26: 413-428.

Michalski E. and Rahma A. (1989). Modélisation du comportement des sols en élasticité: definition des parameters des modèles Hujeux-Cyclade et recherche des valeurs des parameters pour différents sols. Vol. 1 and 2. Rapport BRGM. 89 SGN 117 GEG.

Mitarai N. and Nori F. (2006). Wet granular materials. *Advances in Physics*, 55(1-2): 1-45.

Mitchell J. (1976). *Fundamentals of Soil Behavior*. Wiley.

Mitchell J.K., Boggs S.A., Rodenbaugh T.J., Chu F.Y., Ford G.L., Radhakrishna H.S. and Steinmanis J. (1979). EPRI Soils Research Program. *7th IEEE/PES Transmission and Distribution Conference and Exposition*: 108-116.

Modaressi A. and AbouBerk N. (1994). A unified approach to model the behaviour of saturated and unsaturated soils. *Proceeding of the 8th IACMAG*, Morgentown, USA.

Modaressi A. and Modaressi H. (1995). Thermoplastic constitutive model for unsaturated soils: a prospective approach. *Numerical Models in Geomechanics - NUMOG V*: 45-50.

Modaressi A., Modaressi H., Piccuezzu E. and Aubry D. (1989). Driver de la loi de comportement de Hujeux.

Modaressi H. and Laloui L. (1997). A thermo-viscoplastic constitutive model for clays. *International Journal for Numerical and Analytical Methods in Geomechanics*, 21(5): 313–315.

Mongiovi L. and Tarantino A. (1998). An apparatus to investigate on the two effective stresses in unsaturated soils. *2th International Conference on Unsaturated soils*: 422-425.

Moore C. and Mitchell J. (1974). Electromagnetic forces and strength. *Géotechnique*, 24(4): 627-640.

Moritz L. (1995). Geotechnical properties of clay at elevated temperatures. Report: *47*, Swedish Geotechnical Institute, Linköping.

Mroz Z. (1967). On the description of anisotropic workhardening. *Journal of the Mechanics and Physics of Solids*, 15: 163-175.

Mroz Z., Norris V. and Zienkiewicz O. (1978). An anisotropic hardening model for soils and its application to cyclic loading. *International Journal for Numerical and Analytical Methods in Geomechanics*, 2: 203-221.

Mroz Z., Norris V. and Zienkiewicz O. (1979). Application of an anisotropic hardening model in the analysis of elasto-plastic deformation of soils. *Géotechnique*, 29(1): 1-34.

Mroz Z., Norris V. and Zienkiewicz, O. (1981). An anisotropic, critical state model for soils subjected to cyclic loading. *Géotechnique*, 31: 451-465.

Muir Wood D. (1990). *Soil Behaviour and Critical State Soil Mechanics.* Cambridge University Press, Cambridge.

Neusinger R., Drach V., Ebert H.P. and Fricke J. (2005). Computer simulations that illustrate the heat balance of landfills. *International Journal of Thermophysics*, 26(2): 519-530.

Newitt D.M. and Conway-Jones J.M. (1958). A contribution to the theory and practice of granulation. *Transactions of the Institution of Chemical Engineers*, 36: 422–442.

Nguyen T.S., Selvadurai A.P.S. and Armand G. (2005). Modelling the FEBEX THM experiment using a state surface approach. *International Journal of Rock Mechanics and Mining Sciences*, 42: 639-651.

Ninham B.W. (1981). Surface forces – The last 30 Å. *Pure and Applied Chemistry*, 5: 2135-2147.

Nova R. and Wood D.M. (1979). A constitutive model for sand in triaxial compression. *International Journal for Numerical and Analytical Methods in Geomechanics*, 3: 255–278.

Nuth M. and Laloui L. (2007). New insight into the unified hydro-mechanical constitutive modeling of unsaturated soils. *3rd Asian Conference on Unsaturated Soils, Nanjing, China*: 109-125.

Nuth M. and Laloui L. (2008). Effective stress concept in unsaturated soils: clarification and validation of a unified framework. *International Journal of Numerical and Analytical Methods in Geomechanics*; 32(7): 771-801.

OECD (2003). Engineered barrier systems and the safety of deep geological repositories. State-of-the-art report. Nuclear Energy Agency. Organisation for Economic Co-operation and Development.

Olalla C., Martin M.E. and Sáez J. (1999). ED-B Experiment: Geotechnical laboratory tests on Opalinus clay rock samples. Mont Terri Project, Technical Report 98-57.

Olchitzky E. (2002). Couplage hydro-mécanique et perméabilité d'une argile gonflante non saturée sous sollicitations hydriques et thermiques. *PhD Thesis*. Ecole Nationale des Ponts et Chaussées, Paris.

Olivella S., Carrera J., Gens A. and Alonso E.E. (1994). Nonisothermal multiphase flow of brine and gas through saline media. *Transport in Porous Media*, 15: 271-293.

ONDRAF (2001). Technical overview of the SAFIR 2 report. Safety Assessment and Feasibility Interim Report 2. NIROND 2001-05 E.

Paaswell R.E. (1967). Temperature effects on clay soil consolidation. *Journal of the Soil Mechanics and Foundation Division*, *ASCE*, 93: 9-22.

Padilla J.M., Perera Y.Y., Houston W.N., Perez N. and Fredlund D.G. (2006). Quantification of air diffusion through high air-entry ceramic disks. *4th International Conference on Unsaturated Soils*, Arizona, USA: 1852-1863.

Panday S. and Corapcioglu M.Y. (1989). Reservoir transport equations by compositional approach. *Transport in Porous Media*, 4: 369–393.

Péron H. (2008). Desiccation cracking of soils. *PhD Thesis*, No. 4025, Ecole Polytechnique Fédérale de Lausanne.

Péron H., Hueckel T. and Laloui L. (2007). An improved volume measurement for determining soil water retention curves. *Geotechnical Testing Journal*, 30(1): 1-8.

Philip J.R. and De Vries D.A. (1957). Moisture movement in porous materials under temperature gradients. *Transactions, American Geophysical Union,* 38: 222-232.

Piccuezzu E. (1991) Lois de comportement en géomécanique. Modélisation, mise en œuvre, identification. *PhD Thesis*, Ecole Centrale, Paris.

Pietruszczak S. and Pande G.N. (1987). Multi-laminate framework of soil models – Plasticity formulation. *International Journal for Numerical and Analytical Methods in Geomechanics*, 11: 651–658.

Pintado X., Ledesma A. and Lloret A. (2002). Backanalysis of thermohydraulic bentonite properties from laboratory tests. *Engineering Geology*, 64: 91-115.

Plum L. and Esrig M.I. (1969). Some temperature effects on soil compressibility and pore water pressure. Special report, Report 103, Highway Research Board, Washington.

Prager W. (1949). Recent developments in mathematical theory of plasticity. *Journal of Applied Physics*, 20(3): 239-241.

Prager W. (1955). The theory of plasticity – a survey of recent achievements. *Proceedings of the James Clayton Lecture. The Institution of Mechanical Engineers*: 3-19.

Prager W. (1958). Non-isothermal plastic deformation. *Koninkklijk-Nederland Akademie Van Wetenschappen Te Amsterdam - Proceedings of the section of sciences- B*, 61, 176-182.

Prevost J.H. (1977). Mathematical modelling of monotonic and cyclic undrained clay behaviour. *International Journal of Numerical and Analytical Methods in Geomechanics*, 1: 195–216.

Prevost J.H. (1985). A simply plastic theory for frictional cohesionless soils. *Soil Dynamics Earthquake Engineering*, 4: 9–17.

Prevost J.H. and Popescu R. (1996). Constitutive relations for soils materials. *Electronic Journal of Geotechnics Engineering,* 9.

Pruess K. (2003). Numerical simulation of CO_2 leakage from a geologic disposal reservoir, including transitions from super- to sub-critical conditions, and boiling of liquid CO_2. U.S. Department of Energy; Information Bridge, Scientific and Technical Information.

Pusch R. (1987). Permanent crystal lattice contraction, primary mechanism in thermally induced alteration of Na-bentonite. *Scientific Basis for Nuclear Waste Management X.* MRS, Pittsburgh, 84: 792 802.

Pusch R. and Carlsson T. (1985). The physical state of pore water of Na-smectite used as barrier component. *Engineering Geology*, 21: 257–265.

Recordon E. (1993). Déformabilité des sols non saturés à diverses températures. *Revue Francaise de Géotechnique*, 65: 37-56.

Rizzi E., Maier G. and Willam K. (1996). On failure indicators in multi-dissipative materials. *International Journal of Solids and Structures*, 33(20-22): 3187-3214

Robinet J.C., Pakzad M. and Plas F. (1994). Un modèle rhéologique pour les argiles gonflantes. *Revue Française de Géotechnique*, 67: 57-67.

Robinet J.C., Pasquiou A., Jullien A., Belanteur N. and Plas F. (1997). Expériences de laboratoire sur le comportement thermo-hydro-mécanique de matériaux argileux remaniés gonflants et non-gonflants. *Revue Française de Géotechnique*, 81: 53-80.

Romero E. (1999). Characterisation and thermo-mechanical behaviour of unsaturated Boom clay: An experimental study. *PhD Thesis*, UPC, Barcelona.

Romero E., Gens A. and Lloret A. (2003). Suction effects on a compacted clay under non-isothermal conditions, *Géotechnique*, 53(1): 65-81.

Romero E., Gens A. and Lloret A. (2001). Temperature effects on the hydraulic behaviour of an unsaturated clay, *Geotechnical and Geological Engineering*, 19: 311-332.

Romero E., Gens A. and Lloret A. (2003). Suction effects on a compacted clay under non-isothermal conditions. *Géotechnique*, 53(1), 65-81

Romero E., Villar M. and Lloret A. (2005). Thermo-hydro-mechanical behaviour of two heavily overconsolidated clays. *Engineering Geology*, 81: 255-268.

Roscoe K.H, Schofield A.N. and Wroth C.P. (1958). On the yielding of soils. *Géotechnique*, 8: 22-52.

Roscoe K.H. and Burland J.B. (1968). On the generalised stress-strain behavior of wet clay. *Engineering Plasticity* (eds Heyman J & Leckie FA), Cambridge University Press, Cambridge: 535-609.

Russell A.R. and Khalili N. (2004). A bounding surface plasticity model for sands exhibiting particle crushing. *Canadian Geotechnical Journal*, 41: 1179–1192.

Russell A.R. and Khalili N. (2006). A unified bounding surface plasticity model for unsaturated soils. *International Journal of Numerical and Analytical Methods in Geomechanics*, 30:181–212.

Rutqvist J. and Tsang C.F. (2002). A study of caprock hydromechanical changes with CO_2-injection into a brine formation. *Environmental Geology*, 42: 296-305.

Rutqvist J. and Tsang C.F. (2004). A fully coupled three-dimensional THM analysis of the FEBEX in-situ test with the ROCMAS code: Prediction of THM behaviour in a bentonite barrier. *Coupled Thermo-Hydro-Mechanical-Chemical Processes in Geosystems*: 143-148.

Saix C. (1991). Consolidation thermique par chaleur d'un sol non saturé. *Canadian Geotechnical Journal*, 28: 42-50.

Saix C. and Jouanna P. (1990). Appareil triaxial pour l'étude du comportement thermique de sols non saturés. *Canadian Geotechnical Journal*, 27: 119-128.

Saix C., Devillers P. and El Youssoufi M.S. (2000). Eléments de couplage thermomécanique dans la consolidation de sols non saturés. *Canadian Geotechnical Journal*, 37: 308-317.

Salager S. (2007). Etude de la rétention d'eau et de la consolidation de sols dans un cadre thermo-hydro-mécanique. *PhD Thesis*, Université Montpellier 2, Montpellier, France.

Salager S., El Youssoufi M.S. and Saix C. (2007a). Influence of temperature on the water retention curve. *2nd International Conference on Mechanics of Unsaturated Soils*, Weimar, Germany: 251-258.

Salager S., El Youssoufi M.S. and Saix C. (2007b). Experimental study of the water retention curve as a function of void ratio. *ASCE Geotechnical special publication 157*, GeoDenver 2007.

Salager S., François B., El Youssoufi M.S., Laloui L. and Saix C. (2008). Experimental investigations on temperature and suction effects on compressibility and pre-consolidation pressure of a sandy silt. *Soils and Foundations*, 48(4): 453-466.

Salager S., Jamin F., El Youssoufi M.S. and Saix C. (2006). Influence de la température sur la courbe de rétention d'eau de milieux poreux. *Compte Rendu de Mécanique*, 334: 393-398.

Sanavia L., François B., Bortolotto R., Luison L. and Laloui L. (2008). Finite element modelling of thermo-elasto-plastic water saturated porous materials. *Journal of Theoretical and Applied Mechanics*, 38(1-2): 7-34.

Sanavia L., Pesavento F., Schrefler B.A. (2006). Finite element analysis of non-isothermal multiphase geomaterials with application to strain localization simulation. *Computational Mechanics*, 37(4): 331-348.

Sanchez M., Gens A., Guimaraes L. and Olivella S. (2005). A double structure generalized plasticity model for expansion materials. *International Journal of Numerical and Analytical Methods in Geomechanics*, 29: 751–787.

Santamarina J.C. (2001) Soil behavior at the microscale: Particle forces. *Proc. Symp. Soil Behavior and Soft Ground Construction*, MIT.

Schofield A. and Worth P. (1968). *Critical State Soil Mechanics*, McGraw-Hill, London.

Schrefler B.A. (1984). The finite element method in soil consolidation (with applications to surface subsidence). *PhD Thesis*. University College of Swansea, C/Ph/76/84.

SCK-CEN (1997). HADES TOUR GUIDE. Notebook. 5th edition.

Semenza E. and Ghirotti M. (2000). History of the 1963 Vaiont slide: The importance of geological factors. *Bulletin of Engineering Geology and the Environment*, 59(2): 87-97.

She H.Y. and Sleep B.E. (1998). The effect of temperature on capillary pressure-saturation relationships for air-water and perchloroethylene-water systems. *Water Resources Research*, 34(10): 2587-2597.

Sheng D., Sloan S.W., Gens A. (2004). A constitutive model for unsaturated soils: thermomechanical and computational aspects. *Computational Mechanics*, 33(6): 453-465.

Simpson B. (1973). Finite element applied to problems of plane strain deformation in soils. *PhD Thesis*. Cambridge University.

Sivakumar V. (1993). A critical state framework for unsaturated soils. *PhD Thesis*. University of Sheffield, Sheffield.

Skempton A.W. (1960b). Significance of Terzaghi's concept of effective stress. *From Theory to Practice in Soil Mechanics*. Wiley, New-York.

Skempton A.W. (1960a). Effective stress in soils, concrete and rocks. *Pore Pressure and Suction in Soils*. Butterworths, London: 4-16.

Skempton A.W. and Bishop A.W. (1950). The measurement of the shear strength of soils. *Géotechnique*, 2: 90-108.

Skempton A.W. and Golder H.Q. (1948). The angle of shearing resistance in cohesive soils at constant water content. *2nd International Conference of Soil Mechanics*, 1: 185-192.

Smith N. and Salt G. (1988). Predicting landslide mobility; An application to the East Abbotsford slide, New Zealand. *5th Australian.-New Zealand Conference in Geomechanics,* Sydney: 567-573.

Sobolik S., Webb S., Kobayashi A. and Chijimatsu M. (2004). Hydromechanical response of jointed host granitic rock during excavation of the Febex tunnel. *Coupled Thermo-Hydro-Mechanical-Chemical Processes in Geosystems*: 125-130.

Sorey M.L. (2000). Geothermal development and changes in surfacial features: examples from the western United States. *Proceedings World Geothermal Congress*, Kyushu – Tohoku, Japan: 705-711.

Sridharan A. and Venkatappa Rao G. (1973). Mechanisms controlling volume change of saturated clays and the role of the effective stress concept. *Géotechnique*, 23(3): 359-382.

Sugita Y., Chijimatsu M., Ito A., Kurikami H., Kobayashi A. and Ohnishi Y. (2004). THM simulation of the full-scale in-situ engineered barrier system experiment in Grimsel test site in Switzerland. *Coupled Thermo-Hydro-Mechanical-Chemical Processes in Geosystems*: 119-124.

Sultan N. (1997). Etude du comportement thermo-mécanique de l'argile de Boom: Expériences et modélisation. *PhD Thesis*, Ecole Nationale des Ponts et Chaussée, Paris.

Sultan N., Delage P. and Cui Y.J. (2002). Temperature effects on the volume change behaviour of Boom clay. *Engineering Geology*, 64: 135–145.

Taibi S., Ghembaza M. and Fleureau J. (2005). On the suction control techniques in studying the THM behavior of unsaturated soils. *International Symposium: Advanced Experimental Unsaturated Soils Mechanics*, Trento, Italy: 69-75.

Tamagnini R. (2004). An extended cam-clay model for unsaturated soils with hydraulic hysteresis. *Géotechnique*, 54(3): 223-228.

Tanaka N., Graham J. and Crilly T. (1997). Stress-strain behavior of reconstituted illitic clay at different temperatures. *Engineering Geology*, 47 : 339-350

Tang A.M. (2005). Effet de la température sur le comportement des barrières de confinement. *PhD Thesis*, Ecole Nationale des Ponts et Chaussées, Paris.

Tang A.M., Cui Y.J and Barnel N. (2008). Thermo-mechanical behaviour of a compacted swelling clay. *Géotechnique*, 58(1). 45-54.

Taylor D.W. (1948). *Fundamentals of Soil Mechanics*, Wiley, New-York.

Terzaghi K. (1936). The shearing resistance of saturated soils and the angle between the planes of shear. *1st International Conference on Soil Mechanics and Foundations Engineering*, Cambridge 1: 54-56.

Terzaghi K. (1943). *Theoretical Soil Mechanics*, London. Chapman and Hall.

Thury M. and Bossart P. (1999). The Mont Terri rock laboratory, a new international research project in a Mesozoic shale formation, in Switzerland. *Engineering Geology*, 52: 347-359.

Tidfors M. and Sällfors S. (1989). Temperature effect on preconsolidation pressure. *Geotechnical Testing Journal*, 12(1): 93-97.

TIMODAZ (2007). Thermal impact on the damaged zone around a radioactive waste disposal in clay host rocks. Deliverable 2. State of the art on THMC. Euratom European Project.

Touret O., Pons C., Tessier D. and Tardy Y. (1990). Study on distribution of water in saturated Mg2+ clays with high water content. *Clay minerals*, 25(2): 217-223.

Towhata I., Kuntiwattanakul P., Seko I. and Ohishi K. (1993). Volume change of clays induced by heating as observed in consolidation tests. *Soils and Foundations*, 33(4): 179-183.

Ubals Picanyol D. (2006). Oedometric compression tests on unsaturated soils: Thermal and structural effects, *Master Thesis*, EPFL - UPC, Lausanne.

Van Genuchten M.T. (1980). A closed-form equation for predicting the hydraulic conductivity of unsaturated soils. *Soil Science Society of America Journal*, 44: 892–898.

Van Olphen H. (1977). *An Introduction to Clay Colloid Chemistry.* 2^{nd} Edition. Wiley.

Vanapalli S.K. and Fredlund D.G. (2000). Comparison of empirical procedures to predict the shear strength of unsaturated soils using the soil-water characteristic curve. *Advances in Unsaturated Geotechnics, GSP 99, ASCE*, Reston: 195-209.

Vardoulakis I. (2002). Dynamic thermo-poro-mechanical analysis of catastrophic landslides. *Géotechnique*, 52(3): 157-171.

Verwey E. and Overbeek J. (1948). *Theory of Stability of Lyophobic Colloids – The Interaction of Soil Particles Having an Electric Double Layer*, Elsevier Publishing Company, Inc.

Viani B.E., Low P.F. and Roth C.B. (1983). Direct measurement of the relation between interlayer force and interlayer distance in the swelling of montmorillonite. *Journal of Colloid and Interface Science*, 96(1): 229-244.

Vicol T. (1990). Comportement hydraulique et mécanique d'un sol fin non-saturé: application à la modélisation. *PhD Thesis*, ENPC, Paris.

Villar M. (1999). Investigation of the behaviour of bentonite by means of suction-controlled oedometer tests. *Engineering Geology*, 54: 67-73.

Villar M. (2002). Thermo-hydro-mechanical characterisation of a bentonite from Cabo de Gata: A study applied to the use of bentonite as sealing material in high level radioactive waste repositories. Publicación técnica 04/2002, ENRESA.

Villar M. and Lloret A. (2004). Influence of temperature on the hydro-mechanical behaviour of a compacted bentonite. *Applied Clay Sciences*, 26: 337-350.

Villar M., Garcia-Sineriz J.L., Barcena I. and Lloret A. (2005a). State of the bentonite barrier after five years operation of an in-situ test simulating a high level radioactive waste repository. *Engineering Geology*, 80: 175-198.

Villar M., Martin P.L. and Barcala J.M. (2005b). Modification of physical, mechanical and hydraulic properties of bentonite by thermo-hydraulic gradients. *Engineering Geology*, 81: 284-297.

Villar M.V., Perez del Villar L., Martin P., Pelayo M., Fernandez A., Garralon A., Cuevas J., Leguey S., Caballero E., Huertas F., Jimenez de Cisneros C., Linares J., Reyes E., Delgado A., Fernandez-Soler J. and Astudillo J. (2006). The study of spanish clays for their use as sealing materials in nuclear waste repositories: 20 years of progress. *Journal of Iberian Geology*, 32(1): 15-36.

Von Mises R. (1928). Mechanik der plastischen formaenderung von kristallen. *Zeitschrift für Angevandte Mathematik und Mechanikm*, 8: 161-185.

Vulliet L., Laloui L. and Schrefler B. (2002). *Environmental Geomechanics*, EPFL Press, Lausanne.

Wang Z., Wang, H. and Cates M.E. (2001). Effective elastic properties of solid clays. *Geophysics*, 66(2): 428-440.

Wheeler S.J. and Sivakumar V. (1995). An elasto-plastic critical state framework for unsaturated soil. *Géotechnique*, 45(1): 35–53.

Wheeler S.J. and Karube D. (1995). Constitutive modeling. *Unsaturated Soils*, Paris, Balkema: 1323-1356.

Wheeler S.J., Sharma R.S. and Buisson M.S.R. (2003). Coupling of hydraulic hysteresis and stress-strain behaviour in unsaturated soils. *Géotechnique*, 53(1): 41–54.

Wiebe B., Graham J., Tang X. and Dixon D. (1998). Influence of pressure, saturation and temperature on the behaviour of unsaturated sand-bentonite. *Canadian Geotechnical Journal*, 35: 194-205.

Williams G.P. and Gold L.W. (1977). Ground temperatures. *Canadian Building Digest 180*.

Williams J. and Shaykewich C. (1969). An evaluation of polyethylene glycol (P.E.G.) 6000 and P.E.G. 20.000 in the osmotic control of soil water matric potential. *Canadian Journal of Soil Science*, 49: 397-401.

Wroth C.P. (1971). Some aspects of the elastic behaviour of overconsolidated clays. *Stress-Strain Behavior of Soils*. Roscoe Memorial Symposium. Cambridge University: 241-252.

Wu W., Li X., Charlier R. and Collin F. (2004). A thermo-hydro-mechanical constitutive model and its numerical modelling for unsaturated soils. *Computer and Geotechnics*, 31: 155-167.

Yu H.S. (2006). *Plasticity and Geotechnics.* Springer Publishers.

Yu H.S., Khong C.D. and Wang J. (2006). Experimental evaluation and extension of a simple critical state model for sand. *Granular Matter*, 7: 213-225.

Zerhouni M.I. (1991). Rôle de la pression interstitielle négative dans le comportement des sols - application au calcul des routes. *PhD Thesis*. Ecole Centrale Paris.

Zienkiewicz O. and Mroz Z. (1984). Generalized plasticity formulation and application to geomechanics. *Mechanics of Engineering Materials*: 655-679.

Appendix A

Stress-strain conventions

A.1 Stress tensor

The stress component σ_{ij}, which is a force per unit area, can be defined as follows:

$$\sigma_{ij} = \lim_{A_i \to 0} \left(\frac{F_j}{A_i} \right) \tag{A.1}$$

where F_j is the force in the direction j, and A_i is the area normal to the direction i (Desai and Siriwardane, 1984).

In three dimensions, the stress state can be represented by a 3×3 tensor:

$$\sigma_{ij} = \begin{pmatrix} \sigma_{11} & \sigma_{12} & \sigma_{13} \\ \sigma_{21} & \sigma_{22} & \sigma_{23} \\ \sigma_{31} & \sigma_{32} & \sigma_{33} \end{pmatrix} \tag{A.2}$$

In this dissertation, the components of stresses are expressed in vector form as:

$$\{\boldsymbol{\sigma}\}^T = \begin{pmatrix} \sigma_{11} & \sigma_{22} & \sigma_{33} & \sigma_{12} & \sigma_{13} & \sigma_{23} \end{pmatrix} \tag{A.3}$$

The components σ_{11}, σ_{22}, and σ_{33} are assumed positive when they are compressive. The positive quantities of shear and normal stresses are shown in Figure A.1.

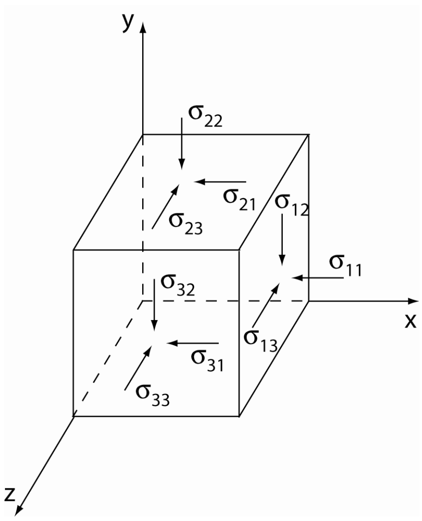

Figure A.1 : Components of a stress tensor in a general 3D configuration.

The stress tensor reported in Equation (A.2) is symmetric, that is:

$$\sigma_{ij} = \sigma_{ji} \tag{A.4}$$

The stress tensor possesses three independent invariants which can be defined in a number of ways. A usual way is:

$$\overline{I}_{1\sigma} = \sigma_{ii} = tr(\boldsymbol{\sigma}) \tag{A.5}$$

$$\overline{I}_{2\sigma} = \frac{1}{2}\sigma_{ij}\sigma_{ji} = \frac{1}{2}tr(\boldsymbol{\sigma})^2 \tag{A.6}$$

$$\overline{I}_{3\sigma} = \frac{1}{3}\sigma_{ij}\sigma_{kl}\sigma_{li} = \frac{1}{3}tr(\boldsymbol{\sigma})^3 \tag{A.7}$$

The mean stress p, commonly used in soil mechanics, is defined from the first invariants:

$$p = \frac{\overline{I}_{1\sigma}}{3} = \frac{\sigma_{11} + \sigma_{22} + \sigma_{33}}{3} \tag{A.8}$$

The stress tensor can be decomposed into two symmetric tensors, the deviatoric stress tensor and the hydrostatic (or spherical) stress tensor:

$$\sigma_{ij} = s_{ij} + \frac{1}{3}\sigma_{kk}\delta_{ij} = \begin{pmatrix} \sigma_{11} - p & \sigma_{12} & \sigma_{13} \\ \sigma_{21} & \sigma_{22} - p & \sigma_{23} \\ \sigma_{31} & \sigma_{32} & \sigma_{33} - p \end{pmatrix} + \begin{pmatrix} p & 0 & 0 \\ 0 & p & 0 \\ 0 & 0 & p \end{pmatrix} \tag{A.9}$$

The deviatoric stress, commonly used in soil mechanics, is defined from the second invariant of the deviatoric stress tensor:

$$\begin{aligned} q &= \sqrt{3}\sqrt{\overline{I}_{2s}} = \sqrt{\frac{3}{2}}\sqrt{s_{ij}s_{ji}} = \sqrt{\frac{3}{2}}\left[\left(\sigma_{ij} - p\delta_{ij}\right)\left(\sigma_{ji} - p\delta_{ji}\right)\right]^{\frac{1}{2}} \\ &= \frac{\sqrt{2}}{2}\left[(\sigma_{11} - \sigma_{22})^2 + (\sigma_{22} - \sigma_{33})^2 + (\sigma_{33} - \sigma_{11})^2 + 6\ (\sigma_{12}^2 + \sigma_{13}^2 + \sigma_{23}^2)\right]^{\frac{1}{2}} \end{aligned} \tag{A.10}$$

When the stress tensor is known at a point, it is always possible to find a new coordinate system (by rotating the original coordinate system) for which the stress tensor is diagonal. The directions of this new coordinate system are called the principal directions, and the planes having normal vectors pointing in the principal directions are called principal planes. On these planes, the shear stresses are zero:

$$\sigma_i = \begin{pmatrix} \sigma_1 & 0 & 0 \\ 0 & \sigma_2 & 0 \\ 0 & 0 & \sigma_3 \end{pmatrix} \tag{A.11}$$

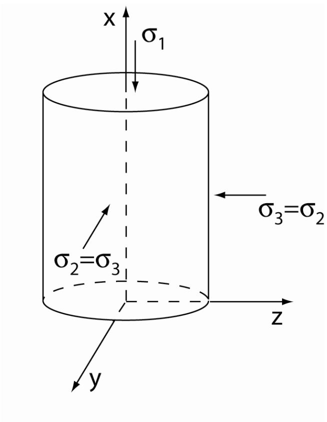

Figure A.2 : Component of stress tensor in the triaxial configuration.

Under triaxial conditions usually reproduced in laboratory experiments, the stress state is a particular case of the principal stress state for which $\sigma_2 = \sigma_3$ (Figure A.2). In that case, the mean stress and the deviatoric stress (Equations (A.8) and (A.10)) are reduced to:

$$p = \frac{\sigma_1 + 2\sigma_3}{3} \tag{A.12}$$

$$q = \sigma_1 - \sigma_3 \tag{A.13}$$

A.2 Strain tensor

A strain is a ratio between the magnitude of deformations and the extents of the undeformed configurations (Desai and Siriwardane, 1984). There are several ways to define a strain component. In this dissertation, all strains are defined as the Cauchy strains. The component of this strain in the *X* direction is:

$$\varepsilon_x = \frac{l_{x,0} - l_x}{l_{x,0}} = 1 - \frac{l_x}{l_{x,0}} \tag{A.14}$$

where l_x is the length of the deformed body in the *X* direction and $l_{x,0}$ is the length of the original (i.e. undeformed) body in the same direction. Equation (A.14) considers a reduction of length (contraction) as a positive strain, such as in this dissertation. In three dimensions, the strain state of a body can be represented by a 3×3 tensor:

$$\varepsilon_{ij} = \begin{pmatrix} \varepsilon_{11} & \gamma_{12} & \gamma_{13} \\ \gamma_{21} & \varepsilon_{22} & \gamma_{23} \\ \gamma_{31} & \gamma_{32} & \varepsilon_{33} \end{pmatrix} \tag{A.15}$$

In this dissertation, the components of stresses are expressed in vector form as:

$$\{\boldsymbol{\varepsilon}\}^T = \begin{pmatrix} \varepsilon_{11} & \varepsilon_{22} & \varepsilon_{33} & \gamma_{12} & \gamma_{13} & \gamma_{23} \end{pmatrix} \tag{A.16}$$

Note that the strain tensor is symmetric ($\gamma_{ij} = \gamma_{ji}$).

The invariants of the strain tensor are usually expressed as follows:

$$\overline{I}_{1\varepsilon} = \varepsilon_{ii} = tr(\boldsymbol{\varepsilon}) \tag{A.17}$$

$$\overline{I}_{2\varepsilon} = \frac{1}{2}\varepsilon_{ij}\varepsilon_{ji} = \frac{1}{2}tr(\boldsymbol{\varepsilon})^2 \tag{A.18}$$

$$\overline{I}_{3\varepsilon} = \frac{1}{3}\varepsilon_{ij}\varepsilon_{kl}\varepsilon_{li} = \frac{1}{3}tr(\boldsymbol{\varepsilon})^3 \tag{A.19}$$

The volumetric strain ε_v, commonly used in soil mechanics, is equal to the first invariants of the strain tensor:

$$\varepsilon_v = \overline{I}_{1\varepsilon} = \varepsilon_{11} + \varepsilon_{22} + \varepsilon_{33} \tag{A.20}$$

The strain tensor can be decomposed into two symmetric tensors, the deviatoric strain tensor and the volumetric (or spherical) strain tensor:

$$\varepsilon_{ij} = e_{ij} + \frac{1}{3}\varepsilon_{kk}\delta_{ij} = \begin{pmatrix} \varepsilon_{11} - (\varepsilon_v/3) & \gamma_{12} & \gamma_{13} \\ \gamma_{21} & \varepsilon_{22} - (\varepsilon_v/3) & \varepsilon_{23} \\ \gamma_{31} & \gamma_{32} & \varepsilon_{33} - (\varepsilon_v/3) \end{pmatrix} + \begin{pmatrix} \varepsilon_v/3 & 0 & 0 \\ 0 & \varepsilon_v/3 & 0 \\ 0 & 0 & \varepsilon_v/3 \end{pmatrix} \tag{A.21}$$

The deviatoric strain, commonly used in soil mechanics, is defined from the second invariant of the deviatoric strain tensor:

$$\begin{aligned} \varepsilon_d &= \frac{2\sqrt{3}}{3}\sqrt{\overline{I}_{2e}} = \frac{\sqrt{6}}{3}\sqrt{e_{ij}e_{ji}} \\ &= \frac{\sqrt{2}}{3}\left[(\varepsilon_{11} - \varepsilon_{22})^2 + (\varepsilon_{22} - \varepsilon_{33})^2 + (\varepsilon_{33} - \varepsilon_{11})^2 + \frac{3}{2}\ (\gamma_{12}^2 + \gamma_{13}^2 + \gamma_{23}^2) \right]^{\frac{1}{2}} \end{aligned} \tag{A.22}$$

In the principal coordinates, the shear strains acting on the principal planes are zero. Consequently, the strain tensor is diagonal:

$$\varepsilon_i = \begin{pmatrix} \varepsilon_1 & 0 & 0 \\ 0 & \varepsilon_2 & 0 \\ 0 & 0 & \varepsilon_3 \end{pmatrix} \tag{A.23}$$

Under triaxial conditions, the horizontal (radial) strains are equal ($\varepsilon_2 = \varepsilon_3$). In that case, the volumetric strain and the deviatoric strain (Equations (A.20) and (A.22)) are reduced to:

$$\varepsilon_v = \varepsilon_1 + 2\varepsilon_3 \tag{A.24}$$

$$\varepsilon_d = \frac{2}{3}(\varepsilon_1 - \varepsilon_3) \tag{A.25}$$

A.3 References

Desai C.S. and Siriwardane H.J. (1984). *Constitutive Laws for Engineering Materials with Emphasis on Geological Materials*. Prentice-Hall Inc., New Jersey.

Appendix B

Solver of the constitutive law

B.1 Introduction

In Chapters 2, 3 and 6, the numerical integration of the constitutive equations of the ACMEG, ACMEG-T and ACMEG-TS models has been done using the driver of constitutive equations LAWYER developed at Ecole Centrale Paris (Modaressi et al., 1989). The existing Hujeux model, already modified by Laloui (1993) at the BRGM (Bureau de Recherche Géologique et Minière, France) and Cekerevac (2003) at EPFL, has been completed in order to introduce the constitutive model developed in this thesis. It involves the programming of new parameters and variables in the existing code. In particular, the stress framework was modified to take into account the generalized effective stress and the double-way coupling between water retention and stress-strain behaviour.

A simplified algorithm of the integration of the constitutive equations is presented in Figure B.1. The loading can be stress- or strain-controlled, independently for the six components of the stress or strain tensor. Through the resolution of a linear system using an auxiliary elastic matrix, the stress increments are transformed in equivalent strain increments which are the input data for the resolution of the elasto-plastic stress-strain equations. An iteration procedure permits to reach the convergence of the solution. A return mapping algorithm is used that permit at each iteration to correct the elastic predictions considering the plastic component of the strain tensor.

This appendix presents the FORTRAN sub-routines that calculate the degree of saturation with respect to suction, temperature and volumetric strain (sub-routine HYDRIC) and the stress-strain relationship thanks to a return mapping type algorithm (sub-routine ACMEG that called the ACMEGDEV and ACMEGISO subroutines).

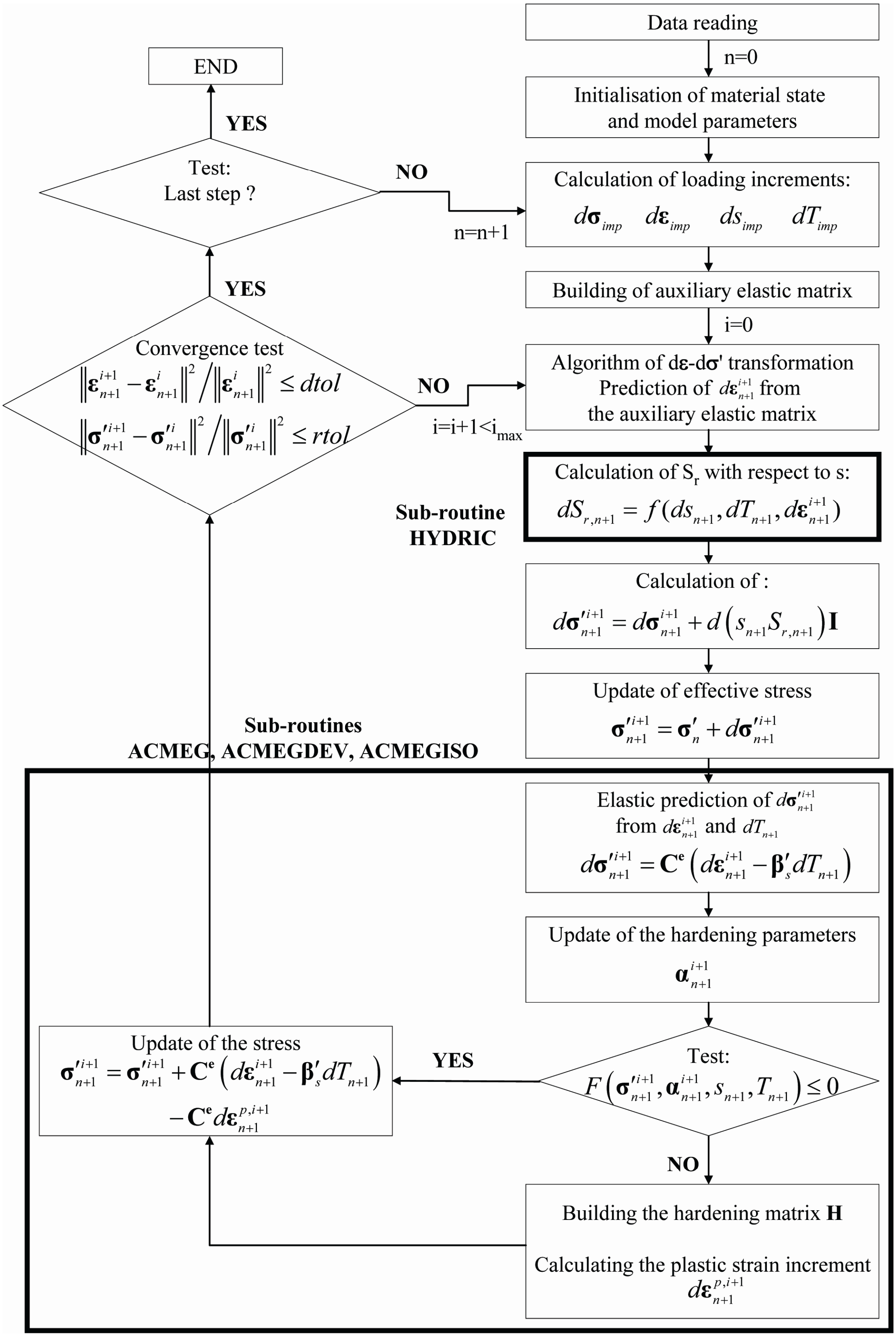

Figure B.1 : Flow chart of the algorithm of integration of the constitutive equations in LAWYER (modified from Koliji, 2008).

B.2 FORTRAN sub-routines

```
*
---------------------------------------------------------------------------------------------------------------------------
---------------------------------------------------------------------------------------------------------------------------
*
      SUBROUTINE HYDRIC (SUCTION, TEMP, T0, EPSV, BETAH, SHYS,
     . TETAT, TETAE, RETINI, AIREV, SRES, DSUC, SATUR, ISTRA)
*
      DATA ZERO/0.D0/, ONE/1.D0/
*
      IF (SUCTION.LT. 1.E-07) THEN
      SATUR=ONE
      GO TO 17
      ENDIF
      DELTASR=SATUR-ONE
****
****  For the first step of calculation (ISTRA(11)=1), the degree of saturation is initialized
****
              IF (ISTRA(11).EQ.1) THEN
              DELTASR=(((-ONE/BETAH)*LOG(SUCTION/AIREV))*(ONE-RETINI))
     .        +(((-ONE/BETAH)*LOG(SUCTION/AIREV/SHYS))*RETINI)
              IF (DELTASR.GT.ZERO) DELTASR=ZERO
              IF (DELTASR.LT.(SRES-1)) DELTASR=SRES-ONE
              ENDIF
          SEMODIF=AIREV*exp(-BETAH*DELTASR)
          DSE = (ONE-TETAT*LOG((TEMP)/T0)+TETAE*LOG(ONE-EPSV))
          SEMODIF = DSE * SEMODIF
****
****  Drying Phase
****  "Plastic" mechanism limited by SEMODIF
****
          SEUILH1 = SUCTION - SEMODIF
              IF (SEUILH1) 11, 11, 12
11            XLAMDAH1=0
              GOTO 13
12            XLAMDAH1=-SEUILH1/SEMODIF/BETAH
13        DELTASR=DELTASR+XLAMDAH1
*
              IF (DELTASR.LT.SRES-1) THEN ! Cut for Sr=Sr,residual
              DELTASR=SRES-ONE
              ENDIF
****
****  Wetting Phase
****  "plastic" mechanisms limited by SEMODIF*SHYS
****
          SEUILH2 = (SEMODIF * SHYS) - SUCTION
          IF (SEUILH2) 14, 14, 15
14            XLAMDAH2=0
              GOTO 16
15            XLAMDAH2=-SEUILH2/SEMODIF/SHYS/BETAH
              DSRDPW = ONE/(BETAH*(SUCTION-DSUC))
```

```
16              DELTASR=DELTASR-XLAMDAH2
*
                    IF (DELTASR.GT.0) THEN   ! Cut for Sr=1
                    DELTASR=0
                    ENDIF
*
                SATUR = ONE+DELTASR   ! update of the degree of saturation
17              CONTINUE
*
---------------------------------------------------------------------------------------------------------------------
---------------------------------------------------------------------------------------------------------------------
*
        SUBROUTINE ACMEG (XKI, XGI, PREF, XN, SINPHI, ALFA, BETA, A, B, C, D,
     .  PCI, RAYELA, DLTELA, TDILAS, XNTEM, DEV, GAMA, TEMP0, GAMAS, OMEGA,
     .  NSIG, SIG, EPSN, DEPS, RAY, IPEL, EVP, PRECONS, QK, DELTAT, TEMPE,
     .   ITHERMO, ISUC, VARIAS, SUCTION, PC, DEVP, PCINI, TETAT, TETAE, AIREV,
     .   NUMRET)
*
        IMPLICIT DOUBLE PRECISION (A-H,O-Z)
*
        DIMENSION PHI(NSIG+1,2),FIDSIG(2),PSI(NSIG,2),CPSI(NSIG+1,2),
     .  HRAY(2),XLRAY(2),HB(2),IMEC(2),HH(6),DEPSP(NSIG),
     .  XLAMDA(2),SIGD(NSIG),DEP(NSIG),DEPS(NSIG),SEUIL(2),ACTIF(2)
*
        DIMENSION SIG(NSIG),EPSN(NSIG),RAY(2),IPEL(2),DP(1),DSIG(NSIG)
*
        TEMPRA =0.0
        DEPSP(:) =0.0
        HH(:) =0.0
        PSI(:,:) =0.0
        DEPSV =DEPS(1)+DEPS(2)+DEPS(3)
****
****     In this version of the code, BETA (the plastic compressibility) may vary with suction
****
        BETAM=BETA+OMEGA*SUCTION
*
        IF (ITHERMO.EQ.1) THEN
****
****    (ITHERMO=1)Non linear thermo-elasticity: thermal expansion coefficient depends on temperature and
****    stress state
****
        IF (DELTAT.LT.0) THEN
        TDILAS1 =TDILAS/300 * ((PCI/P)**XNTEM) * (100 - TEMPE - DELTAT)
        ELSE
        TDILAS1 =TDILAS/300 * ((PCI/P)**XNTEM) * (100 - TEMPE)
        ENDIF
        ENDIF
*
        IF (ITHERMO.EQ.2) THEN
****
****     (ITHERMO=2) Linear thermo-elasticity: thermal expansion coefficient is constant
```

```
****
        TDILAS1 =TDILAS/3
        ENDIF
        DEPT = TDILAS1 * DELTAT
****
****     (ITHERMO=0) Isothermal problem: No thermal expansion
****
        IF (ITHERMO.EQ.0) DEPT=0
****
****    PC=PCINI*exp(BETA*EPSVP) written in the incremental form because BETA may vary with suction
****    during the loading
****
        PC = PCINI*(1+(BETAM*DEVP)+(((BETAM*DEVP)**2)/2)
    .  +(((BETAM*DEVP)**3)/6)+(((BETAM*DEVP)**4)/24)
    .  +(((BETAM*DEVP)**5)/120)+(((BETAM*DEVP)**6)/720))
*
        DEP(:) =0.0
        P = (SIG(1)+SIG(2)+SIG(3)) / 3.
        IF (P .LT. -1.E-07) GO TO 32
        P = -1. E-07
*
32      CONTINUE
        DO 111 I=1,3
111     SIGD(I) = SIG(I) - P
        DO 222 I=4,NSIG
222     SIGD(I) = SIG(I)
*
        SIGDII=0.
        DO 333 I=1,3
333     SIGDII=SIGDII+SIGD(I)*SIGD(I)
        DO 444 I=4,NSIG
444     SIGDII=SIGDII+2.*SIGD(I)*SIGD(I)
*
        SIGDII=SIGDII**.5
****
****    Non linear elasticity
****
        XG = (P/(PREF)) ** XN
        XK = XKI * XG
        XG = XGI * XG
        XG2 = XG * 2.
        BE = XG * .6666666667D0
        AE = XK + BE + BE
        BE = XK - BE
*
        DSIG(1) = AE * (DEPS(1)-DEPT) + BE * (DEPS(2)+DEPS(3)-2*DEPT)
        DSIG(2) = AE * (DEPS(2)-DEPT) + BE * (DEPS(3)+DEPS(1)-2*DEPT)
        DSIG(3) = AE * (DEPS(3)-DEPT) + BE * (DEPS(1)+DEPS(2)-2*DEPT)
        DSIG(4) = XG2* DEPS(4)
        IF (NSIG.LT.6) GOTO 80
        DSIG(5) = XG2* DEPS(5)
```

```
        DSIG(6) = XG2* DEPS(6)
*
80      DP(1) = (DSIG(1)+DSIG(2)+DSIG(3))/3
****
****    Evolution of the preconsolidation pressure with temperature and suction
****
        EPSV=EPSN(1)+EPSN(2)+EPSN(3)
        IF (NUMRET.EQ.17) THEN
        SE=AIREV*(1.D0-TETAT*LOG((TEMPE)/TEMP0)+TETAE*LOG(1.D0-EPSV))
        ELSE
        SE=AIREV
        ENDIF
*
        IF (ITHERMO.GT.0) THEN
        TEMPRA = TEMPE - TEMP0
        DN = D*(1-GAMA*LOG((TEMPRA+TEMP0)/TEMP0))
        if (DN.LT.0.01*D) DN=0.01*D
        ELSE
        DN = D
        ENDIF
*
        IF (ISUC.GT.0.AND.SUCTION.GT.SE) THEN
        DN = DN*(1+GAMAS*LOG((SUCTION)/SE))
        ENDIF
****
****    Call of the routines that check the activation of the isotropic and/or deviatoric mechanisms
****
        CALL ACMEGDEV (SINPHI, ALFA, BETA, A, B, C, D, PCI, RAYELA, DEV, TEMP0,
   .    NSIG, SIG, PHI(1,1), PSI(1,1), CPSI(1,1), SEUIL(1), FIDSIG(1),
   .    HRAY(1), XLRAY(1), IPEL(1), RAY(1), TEMPRA, SIGDII, DN, PC,
   .    AE, BE, XG2, DSIG, ACTIF(1), DELTAT, ITHERMO)
*
        CALL ACMEGISO(SINPHI, BETA, A, B, C, D, PCI, DLTELA, GAMAT, DEV, TEMP0, NSIG,
   .    SIG, PHI(1,2), PSI(1,2), CPSI(1,2), SEUIL(2), FIDSIG(2),
   .    HRAY(2), XLRAY(2), IPEL(2), RAY(2), TEMPRA, DP(1), SIGDII, DN, PC, P,
   .    AE, BE, DSIG, ACTIF(2), DELTAT, ITHERMO, GAMAS, SE, SUCTION, VARIAS)
****
****    Determination of the number of active plastic mechanisms (NMEC= 0, 1 or 2)
****    + Construction of the hardening matrix
****
103     NMEC = 0
*
        DO 120 K = 1, 2
        XLAMDA(K)=0.D0
        IF (IPEL(K) .LE. 0) GOTO 120
        NMEC = NMEC + 1
        HH(4+K) = ACTIF(K)
        HH((2*K)-1)=HRAY(K)+(PHI(5,K)*CPSI(5,K))
        IF (NSIG.EQ.6) HH((2*K)-1)=HH((2*K)-1)+(PHI(6,K)*CPSI(6,K))+(PHI(7,K)*CPSI(7,K))
        DO 110 I = 1, 4
        HH((2*K)-1)=HH((2*K)-1)+PHI(I,K)*CPSI(I,K)
```

```
        HH((2*K))=PHI(I,(2/K))*CPSI(I,K)
110     CONTINUE
120     CONTINUE
****
****    Calculation of the plastic multipliers
****
*
150     IF (NMEC-1) 200, 250, 300
*
200     DEVP=0.D0
        GOTO 350
****
****    One plastic mechanism is active
****
250     IF (IPEL(1) .EQ. 1) THEN
        XLAMDA(1)=HH(5)/HH(1)
        XLAMDA(2)=0
        ELSE
        XLAMDA(1)=0
        XLAMDA(2)=HH(6)/HH(3)
        ENDIF
        GOTO 315
****
****    The two plastic mechanisms are active
****
300     XLAMDA(1)=HH(6)-(HH(5)*HH(3)/HH(4))
        XLAMDA(1)=XLAMDA(1)/(HH(2)-(HH(1)*HH(3)/HH(4)))
        XLAMDA(2)=(HH(6)-(HH(2)*XLAMDA(1)))/HH(3)
****
****    Plastic strain rate and hardening
****
315     DO 320 K = 1, 2
        EVP = EVP + XLAMDA(K)*CPSI(4,K)
        DEVP= DEVP+ XLAMDA(K)*CPSI(4,K)
        RAY (K) = RAY (K) + XLAMDA(K)*XLRAY(K)
        RAY (K) = MIN (RAY(K),1.D0)
        DO 320 I = 1, NSIG
320     DEP(I) = DEP(I)+(XLAMDA(K)*PSI(I,K))
****
**** Calculation of the elasto-plastic stresses
****
350     SIG(1) = SIG(1) + DSIG(1) - AE*DEP(1) - BE*(DEP(2)+DEP(3))
        SIG(2) = SIG(2) + DSIG(2) - AE*DEP(2) - BE*(DEP(3)+DEP(1))
        SIG(3) = SIG(3) + DSIG(3) - AE*DEP(3) - BE*(DEP(1)+DEP(2))
        SIG(4) = SIG(4) + DSIG(4) - XG2*DEP(4)
        IF (NSIG.LT.6) GOTO 370
        SIG(5) = SIG(5) + DSIG(5) - XG2*DEP(5)
        SIG(6) = SIG(6) + DSIG(6) - XG2*DEP(6)
*
370     CONTINUE
        RETURN
```

```
        END
*
------------------------------------------------------------------------------------------------------------------------------------------------
------------------------------------------------------------------------------------------------------------------------------------------------
*
        SUBROUTINE ACMEGDEV (SINPHI, ALFA, BETA, A, B, C, D, PCI, RAYELA, DEVT,
     .  TEMP0, NSIG, SIG, PHI, PSI, CPSI, SEUILK, FIDSIG, HRAY, XLRAYA,
     .  IPL, RAY, TEMPRA, SIGDII, DN, PC, AE, BE, GMA2, DSIG, ACTIF,
     .  DELTAT, ITHERMO)
*
        IMPLICIT DOUBLE PRECISION (A-H,O-Z)
*
        DIMENSION PHI(*), PSI(*), CPSI(*), RAY(*), DQDSIG(3),DSIG(NSIG)
     .  DEV(3),CPSIPHI(1),SINPSIM(1),SIG(NSIG)
*
        ACTIF = 0.0
        CPSI(4)=0.0
        PK = (SIG(1) + SIG(2) + SIG(3))/3
        IF (PK.GT.0) PK=-1e-7
        QK = 1.224744 * SIGDII
****
****    Effect of temperature on the friction angle at critical state
****
        IF (ITHERMO.GT.0) THEN
        TEMEVA = TEMPRA * DEVT
        SINPHT = ((18+(3*TEMEVA))*SINPHI - (9*TEMEVA))
        SINPHT = SINPHT/(18-(3*TEMEVA)+(TEMEVA*SINPHI))
        ELSE
        SINPHT = SINPHI
        ENDIF
****
****     FMKRAY = deviatoric yield limit
****
        FACPK = SINPHT * (1. - B *  LOG(PPP*D/PC/DN))
        FMK = PK * FACPK
        RAYK = RAY(1)
        FMKRAY = FMK * RAYK
        FACHRY = 1.
****
****    Test on the deviatoric yield limit
****
12      SEUILK = QK - FMKRAY
****
****     Calculation of dF/dEPSVP (=PHI(4))
****
150     TEMP = SINPHT * B * RAYK
        PHIV2 = (-FACPK*RAYK + TEMP)/3
        PHI(4) = TEMP * PK * BETA
****
****    Calculation of dF/dtime = SUM of dF/dSIG(I)*dSIG(I)/dtime + dF/dTEMP *dTEMP/dtime
****
```

```
        IF ( QK-0.000001 ) 160,160,165
*
160     QK = 0.000001          ! to avoid the division by zero in the next equations
165     DQDSIG(1) = 3*((SIG(1)-PK)/QK)/2
        DQDSIG(2) = 3*((SIG(2)-PK)/QK)/2
        DQDSIG(3) = 3*((SIG(3)-PK)/QK)/2
*
        PHI(1) = DQDSIG(1) + PHIV2
        PHI(2) = DQDSIG(2) + PHIV2
        PHI(3) = DQDSIG(3) + PHIV2
        PHI(5) = 3 * SIG(4) / QK
        IF (NSIG.LT.6) GOTO 180
        PHI(6) = 3 * SIG(5) / QK
        PHI(7) = 3 * SIG(6) / QK
*
180     CONTINUE
****
****    FIDSIG = dF/dSIG * dSIG/dtime
****
        FIDSIG = PHI(1)*DSIG(1)+PHI(2)*DSIG(2)+PHI(3)*DSIG(3)+PHI(5)*DSIG(4)
        IF (NSIG.LT.6) GOTO 200
        FIDSIG = FIDSIG + PHI(6)*DSIG(5)+PHI(7)*DSIG(6)
*
200     CONTINUE
****
****FIDTEM = dF/dTEMP * dTEMP/dtime
****
        IF (ITHERMO.GT.0) THEN
        THI1 = - PK * (1. - B * LOG(PK/PC) )
        THI2 = THI1 * RAY(1)
        THJ1 = 3 * DEVT * (SINPHI - 3)
        THJ2 = (18-(3*TEMEVA)+(TEMEVA*SINPHI))
        THJ3 = ((DEVT*SINPHI) - (3*DEVT))
        THJ5 = ((18 * SINPHI)+(3*TEMEVA*SINPHI)-(9*TEMEVA))
        THJ6 = THJ2**2
        THK1 = THJ1/THJ2
        THK2 = THJ3*THJ5
        THK3 = THK2/THJ6
        THF  = THI2*(THK1-THK3)  ! = dF/dTEMP
        FIDTEM = THF * DELTAT
        ELSE
        FIDTEM = 0
        ENDIF
****
****    Test of the activation of the deviatoric mechanism
****
        ACTIF = SEUILK + (FIDSIG+FIDTEM)
*
        IF ( ACTIF ) 310, 310, 340
*
310     IF (IPL .LT. 0 .OR. FIDSIG .GE. 0) GO TO 320
```

```
****
****    Unload (change of the direction of loading: The stress point is on the yield limit
****    but there is no hardening)
****
        IF (IPL .EQ. 1) RAY(1) = MAX (RAY(1) , QK/FMK)
        IPL = -1
        FMKRAY = FMK * RAYELA
        RETURN
****
****    In the elastic domain (mechanism non active)
****
320     IPL = -1
        RETURN
****
****    The mechanism is active: calculation of hardening parameters
****
340     IPL = 1
****
****    PSI = dG/DSIG with G = plastic potential
****
        PSI(1) = (DQDSIG(1)+((SINPHT-(QK/PK))*ALFA/3))
        PSI(2) = (DQDSIG(2)+((SINPHT-(QK/PK))*ALFA/3))
        PSI(3) = (DQDSIG(3)+((SINPHT-(QK/PK))*ALFA/3))
        PSI(5) = PHI(5)
*
        CPSI(1) = AE*PSI(1) + BE*PSI(2) + BE*PSI(3)
        CPSI(2) = BE*PSI(1) + AE*PSI(2) + BE*PSI(3)
        CPSI(3) = BE*PSI(1) + BE*PSI(2) + AE*PSI(3)
        CPSI(5) = GMA2*PSI(5)
*
        IF (NSIG.LT.6) GOTO 400
        PSI(6) = PHI(6)
        PSI(7) = PHI(7)
        CPSI(6) = GMA2*PSI(6)
        CPSI(7) = GMA2*PSI(7)
*
400     CONTINUE
****
****    CPSI (4) = dEVP/dEDP
****
        CPSI(4) = (SINPHT-(QK/PK))*ALFA
****
****    HRAY= dF/dRAY  (/DEDP)
****
        HRAY = 1. - RAYK
        HRAY = HRAY*HRAY / A
        XLRAYA = HRAY * FACHRY
        HRAY = HRAY * FMK
        RETURN
        END
*
```

```
------------------------------------------------------------------------------------------------------------------------
------------------------------------------------------------------------------------------------------------------------
*
      SUBROUTINE ACMEGISO (SINPHI, BETA, A, B, C, D, PCI, DLTELA, GAMA, DEVT,
     .     TEMP0, NSIG, SIG, PHI, PSI, CPSI, SEUILC, FIDSIG, HRAY, XLDLTA,
     .     IPL, DELTAA, TEMPRA, DP, SIGDII, DN, PC, P, AE, BE, DSIG, ACTIF,
     .     DELTAT, ITHERMO, GAMAS, SE, SUCTION, VARIAS)
*
      IMPLICIT DOUBLE PRECISION (A-H,O-Z)
*
      DIMENSION PHI(*), PSI(*), CPSI(*), DELTAA(*), CPSIPHI(1), SIG(NSIG), DSIG(NSIG)
*
10    ACTIF=0.0
      CPSI(4)=0.0
****
****  Determination of isotropic yield limit (FACDLT=preconsolidation pressure*RAY)
****
      FACISO = -DN * PC
****
****  For unloading, reversibility of the isotropic plastic radius (RAY(2)= DELTAA(1))
****
      DERIVT=DELTAA(1)*PC*DN*GAMA/(TEMPRA+TEMP0)
     .     /(1-GAMA*LOG((TEMPRA+TEMP0)/TEMP0))*DELTAT
*
      IF (SUCTION.GT.SE) THEN
      DERIVS=-(DELTAA(1)*PC*DN*GAMAS/SUCTION)
     .     /(1+GAMAS*LOG((SUCTION/SE)))*VARIAS
      ELSE
      DERIVS=0
      ENDIF
*
      P1=P+DP
      IF ((DP + DERIVT + DERIVS).GT.0) DELTAA(1) = (P1/PC/DN)+DLTELA
*
      IF (DELTAA(1).LT.DLTELA) DELTAA(1) = DLTELA
      IF (DELTAA(1).GT.1) DELTAA(1) = 1
*
      DLTISO = DELTAA(1)
      FACDLT = FACISO*DLTISO
****
****  Test on the isotropic yield limit
****
12    SEUILC = -P - FACDLT
****
****  Calculation of dF/dtime = SUM of dF/dSIG(I)*dSIG(I)/dtime
****  + dF/dTEMP *dTEMP/dtime
****
40    PHI(1) = -1 / 3.   ! dF/dSIG(I) = dF/dP * dP/dSIG(I)
      PHI(2) = PHI(1)
      PHI(3) = PHI(1)
****
```

```
****      Calculation of dF/dEPSVP (=PHI(4))
****
          PHI(4) = -PC * BETA * (DN*DELTAA(1))
****
****      FIDSIG = dF/dSIG * dSIG/dtime
****
          FIDSIG = -(DSIG(1)+DSIG(2)+DSIG(3))/3.
****
****      FIDTEM = dF/dTEMP * dTEMP/dtime
****
          IF (ITHERMO.GT.0) THEN
          FIDTEM=((FACDLT/(1-GAMA*LOG((TEMPRA+TEMP0)
    .     /TEMP0)))*GAMA*(1/((TEMPRA+TEMP0)*2.303)))*DELTAT
          ELSE
          FIDTEM=0
          ENDIF
*
50        ACTIF = SEUILC+(FIDSIG+FIDTEM)
*
          IF ( ACTIF+0.00001*P ) 320,320,340
****
****      In the elastic domain (mechanism non active)
****
320       IPL = -1
          RETURN
****
****      The mechanism is active: calculation of hardening parameters
****
340       IPL = 1
****
****      PSI = dG/DSIG with G = plastic potentiel
****
          PSI(1) = -1 / 3.
          PSI(2) = PSI(1)
          PSI(3) = PSI(1)
          PSI(4) = 0
*
          CPSI(1) = (AE+2.*BE) * PSI(1)
          CPSI(2) = CPSI(1)
          CPSI(3) = CPSI(1)
          CPSI(4) = -1
*
          XLDLTA = 1 - DELTAA(1)
          XLDLTA = XLDLTA*XLDLTA
          XLDLTA = XLDLTA/ C
          HRAY = PC*DN*(-XLDLTA)
          RETURN
          END
*
------------------------------------------------------------------------------------------------------------------------
```

B.3 References

Cekerevac C. (2003). Thermal effect on the mechanical behaviour of saturated clays: an experimental and constitutive study. *PhD Thesis*, EPFL, Lausanne.

Koliji A. (2008). Mechanical behaviour of unsaturated aggregated soils. *PhD thesis*, No. 4011, Ecole Polytechnique Fédérale de Lausanne.

Laloui L. (1993). Modélisation du comportement thermo-hydro-mécanique des milieux poreux anélastique. *PhD Thesis*, Ecole Centrale de Paris.

Modaressi A., Modaressi H., Piccuezzu E. and Aubry D. (1989). Driver de la loi de comportement de Hujeux.

Appendix C

Numerical application of temperature effect on interaction stress between particles

C.1 Introduction

This appendix presents a numerical application of the theoretical developments exposed in Section 3.2 dealing with the thermal effect on the microstructural aspects of clayey soils. In that section, the equations quantifying the interaction forces between clay platelets are exposed based on the concept of double layer theory. In this appendix, this theoretical development is applied in the particular case of Boom clay. The first section assesses the physico-chemical variables of Boom clay needed to solve the equations governing the equilibrium between particles under isothermal conditions. In the second section, a temperature increase is considered. Finally, the macroscopic thermal expansion of Boom clay predicted from this approach at the micro-scale is compared with thermal expansion of Boom clay measured from a macroscopic experiment.

C.2 Isothermal aspects

From the equations presented by Van Olphen (1977) (Equations (3.2) to (3.7), in Chapter 3 and recalled below), it is possible to compute the interaction stress between platelets of clay depending on the properties of the electrolyte solution and on the clay density:

$$\sigma_R = 2n_0kT\left(\cosh u - 1\right) \tag{C.1}$$

$$\frac{dy}{d\xi} = -\left(2\cosh y - 2\cosh u\right)^{1/2} \tag{C.2}$$

$$\text{For } y = z \qquad \left(\frac{dy}{d\xi}\right)_0 = \frac{4\pi e_0 \upsilon \sigma_c}{DkT\kappa} \tag{C.3}$$

$$\int_z^u \left(2\cosh y - s\cosh u\right)^{-1/2} dy = -\kappa\frac{\delta}{2} \tag{C.4}$$

$$\kappa = \left(\frac{8\pi n_0 e_0{}^2 \upsilon^2}{DkT}\right)^{1/2} \tag{C.5}$$

$$\sigma_A = \left(\frac{A}{6\pi}\right)\left[\left(\frac{1}{\delta}\right)^3 - \frac{2}{(\delta+t)^3} + \frac{1}{(\delta+2t)^3}\right] \tag{C.6}$$

All the variables of Equations (3.2) to (3.7) have been defined in Chapter 3. In the following, those variables are assessed for the particular case of Boom clay.

Considering that all the pore water is adsorbed water, the thickness of adsorbed water (corresponding to half of the inter-particle distance δ) may be quantified through the porosity n and the specific surface SS of Boom clay. The in-situ porosity of Boom clay is 0.37, and its specific surface is around 180 m^2/g (Delage et al., 2000):

$$\frac{\delta}{2} = \frac{w}{SS\rho_w} = \frac{e}{SS\rho_s} = \frac{n}{(1-n)SS\rho_s} = \frac{0.37}{0.63\times180\times2.67\ 10^6} = 1.22\ 10^{-9}\,m = 1.22\ 10^{-7}\,cm \tag{C.7}$$

The charge density at the surface of the platelet is deduced from the cation exchange capacity CEC (= 300 meq/kg for Boom clay, Robinet et al. (1997)) and the specific surface (Mitchell, 1976):

$$\sigma_c = \frac{CEC}{SS} = \frac{300}{180\times10^3} = 1.66\ 10^{-3} meq/m^2 = 4.83\ 10^8 esu/m^2 = 4.83\ 10^4 esu/cm^2 \tag{C.8}$$

The electrolyte concentration n_0 may be deduced from the molarity M of the Boom clay water. Boom clay pore water is of the sodium bicarbonate type ($NaHCO_3$) with a concentration of about 1.5 10^{-2} mol/l (Dierckx, 1997):

$$n_0 = N_0 10^{-3} M = 6.02\ 10^{23}\times10^{-3}\times1.5\ 10^{-2} = 9.03\ 10^{18}\,ions/cm^3 \tag{C.9}$$

Equations (3.6) and (3.4) respectively give the values of κ and $(dy/d\xi)_0$ for $T = 293K$, $D = 80$, $e_0 = 4.81\,10^{-10}\,esu$, $k = 1.38\ 10^{-16}\,ergs/K$, and $\upsilon = 1$:

$$\kappa = \left(\frac{8\pi\times9.03\ 10^{18}\times\left(4.81\,10^{-10}\right)^2\times1^2}{80\times1.38\ 10^{-16}\times293}\right)^{1/2} = 4.03\ 10^6\,cm^{-1} \tag{C.10}$$

$$\left(\frac{dy}{d\xi}\right)_0 = \frac{4\pi\times4.81\,10^{-10}\times1\times4.83\ 10^4}{80\times1.38\ 10^{-16}\times293\times4.03\ 10^6} = 22.3 \tag{C.11}$$

From the tables of Van Olphen (1977), for $(dy/d\xi)_0 = 22.3$, $\kappa = 4.03\ 10^6\,cm^{-1}$ and $\delta/2 = 1.22\ 10^{-7}\,cm$, it can be deduced that $u = 3.358$. From Equation (3.2), the repulsive pressure is:

$$\begin{aligned}\sigma_R &= 2\times9.03\ 10^{18}\times1.38\ 10^{-16}\times293\times(\cosh 3.358 - 1)\\ &= 9.77\ 10^6\,dyne/cm^2 = 977\ kPa\end{aligned} \tag{C.12}$$

If a 4 nm mean thickness of the clay particle is assumed, the Van der Waals attraction between platelets is (Equation (3.7)):

$$\sigma_A = \left(\frac{2.2\ 10^{-13}}{6\pi}\right)\times\left[\left(\frac{1}{2.44\ 10^{-7}}\right)^3 - \frac{2}{\left(2.44\ 10^{-7}+4\ 10^{-7}\right)^3} + \frac{1}{\left(2.44\ 10^{-7}+2\times 4\ 10^{-7}\right)^3}\right] \tag{C.13}$$
$$= 725871\ dyne/cm^2 = 72\ kPa$$

It yields to the interaction stress between particles:

$$\sigma_{R-A} = \sigma_R - \sigma_A = 977 - 76 = 901\ kPa \tag{C.14}$$

This computation can easily be reproduced for different inter-particle distances and surface charge densities, which gives the theoretical curve in Figure C.1. The Boom clay value ($M = 1.5\ 10^{-2}\ mol/l$ and $n = 0.37$) corresponds to a particular point on these curves. Figure C.1 clearly reveals that the repulsive force increases when inter-particle distance decreases. Also, an increase of the charge density of the solute builds up the repulsive force.

The in-situ total stress of Boom clay is around 4.5 MPa (quasi-isotropic) and the pore water pressure is 2.025 MPa. So, it seems that the difference between total stress and pore water pressure is supported by both interaction stress σ_{R-A} and stress contact between particles σ^* in agreement with the parallel connection model (Equation (3.9)):

$$\sigma^* = \sigma - p_w - \sigma_{R-A} = 4.5 - 2.025 - 0.9 = 1.575\ MPa \tag{C.15}$$

However, a reminder is needed that this development remains purely theoretical. Even if the trend is often similar to the experimental observations, it is a delicate task to deduce the precise stress state from such micro-scale considerations.

C.3 Temperature effect

The thermal dependency of the interaction stress between particles is easily noticeable in Equations (3.2) to (3.6). In addition, the dielectric constant of water depends on temperature as follows (for temperatures between 273 K and 373 K):

$$D = -0.316\ T + 173 \qquad T \text{ in } Kelvin \tag{C.16}$$

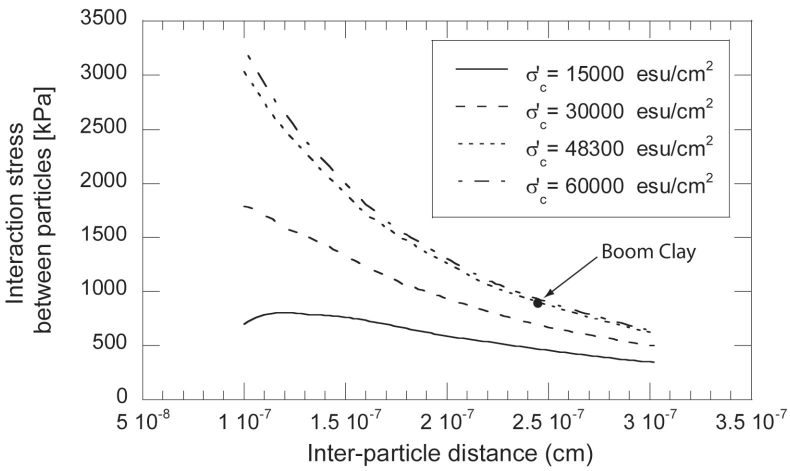

Figure C.1 : Evolution of the interaction stress between particles with respect to the inter-particle distance of Boom clay, for four different surface charges σ'c. The natural Boom clay is one particular point of this graph.

For the physical values of Boom clay, the effect of temperature on the relation between the inter-particle distance and the interaction stress, deduced from Equations (3.2) to (3.7), is sketched in Figure C.2. Conversely, for a given inter-particle distance, the evolution of the interaction stress between particles may be drawn with respect to temperature (Figure C.3). In particular, these theoretical considerations based on the diffuse double layer theory predict an increase of the repulsion stress with increasing temperature. The Hamaker constant A governing the Van der Waals attraction has been assumed to be independent of temperature.

When the temperature increases, all the constituents of soils (i.e. solid minerals, adsorbed and free waters) dilates. The thermal expansion of each constituent depends on its mineral type. The mineralogical composition of Boom clay is reported in Table C.1, along with the density, the bulk modulus and the thermal expansion coefficient of each component.

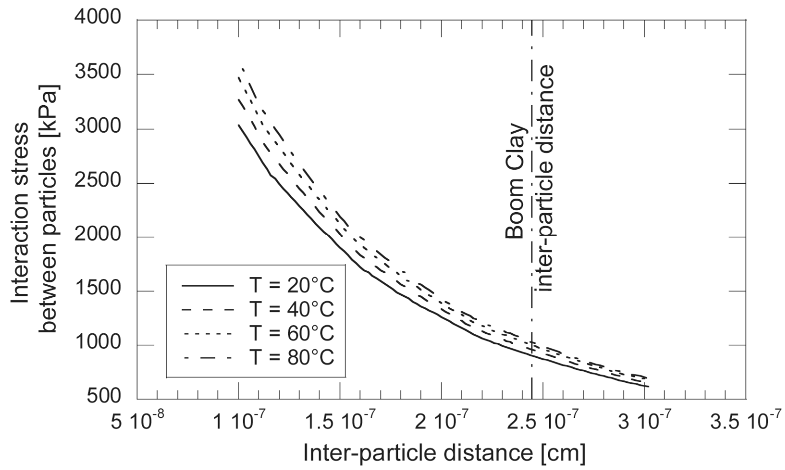

Figure C.2: Evolution of the interaction stress between particles with respect to the inter-particle distance of Boom clay, for four different temperatures T.

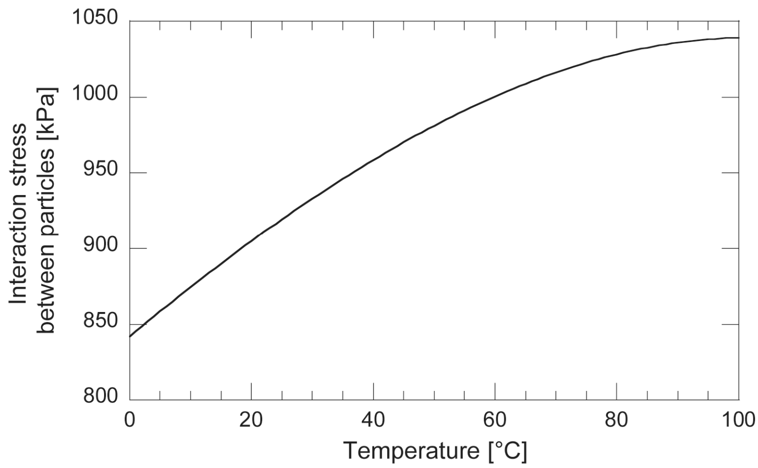

Figure C.3 : Evolution of the interaction stress between particles of Boom clay with respect to the temperature, for the inter-particle distance of natural Boom clay.

Mineral	Mass fraction [%] (Baldi et al., 1987)	Bulk density [kg/m³]	Bulk modulus [GPa]	Thermal expansion coefficient [10^{-6} °C^{-1}]
Kaolinite	30	2442	46	29
Quartz	28	2650	38	32
Illite	20	2706	60	17
Smectite	22	2394	9	36

Table C.1: Mineralogical composition of Boom clay with the density, the bulk modulus and the thermal expansion coefficient of each component, taken from Table 3.1 and Table 3.2.

In addition to the solid skeleton, the properties of adsorbed water must be considered. If it is assumed that all water of Boom clay is adsorbed water, the volume fraction of adsorbed water corresponds to the porosity ($n = 0.37$, Delage et al. (2000)). The bulk density of adsorbed water may vary from 1000 kg/m³ for water far from the surface of the particle to 1400 kg/m³ for the first layer of water molecules at the solid surface (Baldi et al., 1988). So, a mean adsorbed water density of 1200 kg/m³ has been selected. Without any precise information on the bulk modulus of such adsorbed water, a modulus similar to that of free water was considered ($K = 2\ GPa$). The mean volumetric thermal expansion coefficient of water in the vicinity of a clay platelet is around 4.5 10^{-4} °C^{-1}.

The mass fraction of adsorbed water in Boom clay may be assessed as follows:

$$\begin{aligned}\%ads\ wat &= \frac{n\ \rho_{ads\ wat}}{n\ \rho_{ads\ wat} + (1-n)\rho_s} \\ &= \frac{0.37\times1200}{0.37\times1200 + 0.63\times(2442\times0.3 + 2650\times0.28 + 2706\times0.20 + 2394\times0.22)} \\ &= 21.7\ \%\end{aligned} \quad \text{(C.17)}$$

where $\rho_{ads\ wat}$ and ρ_s are the bulk density of the adsorbed water and of the solid skeleton, respectively. So, the mass fraction of each mineral component with respect to the fully soil-adsorbed water mixture is: 23.4% (Kaolinite), 21.9% (Quartz), 15.6% (Illite), 17.2% (Smectite). From Equation (3.13) which quantifies the global thermal expansion coefficient of a composite material β'_s, the Boom clay thermal expansion coefficient may be assessed:

$$\begin{aligned}\beta'_s &= \frac{\dfrac{29\times0.234\times46}{2442} + \dfrac{32\times0.219\times38}{2650} + \dfrac{25\times0.156\times60}{2706} + \dfrac{39\times0.172\times9.3}{2650} + \dfrac{450\times0.217\times2}{1200}}{\dfrac{0.234\times46}{2442} + \dfrac{0.219\times38}{2650} + \dfrac{0.156\times60}{2706} + \dfrac{0.172\times9}{2650} + \dfrac{0.217\times2}{1200}} \times 10^{-6} \\ &= 4.18\ 10^{-5}\ °C^{-1}\end{aligned}$$

(C.18)

In addition to the effect of expansion of each constituent on the macroscopic thermal dilation of the medium, the stress distribution between solid particles and adsorbed water may be modified due to a temperature change. The difference between total stress and pore water pressure in Boom clay is supported by both the interaction stress σ_{R-A} and the contact stress between particles σ^*, in agreement with the parallel connection model (Equation (C.15)). So, the volumetric strain undergone by Boom clay under a temperature increase should be governed by (Equation (3.21)):

$$d\varepsilon_v = -\frac{K}{K+\xi_\delta}\left(\frac{\xi_T}{K}+\beta_s'\right)dT \tag{C.19}$$

From Equation (3.15), the ξ_δ and ξ_T variables may be evaluated as follows:

$$\xi_\delta = \frac{d\sigma_{R-A}}{d\delta}\delta \tag{C.20}$$

$$\xi_T = \frac{d\sigma_{R-A}}{dT} \tag{C.21}$$

These values can be obtained from derivative of the curves in Figure C.1 and Figure C.3, respectively. The values of ξ_δ and ξ_T are reported in Figure C.4, with respect to the inter-particle distance and temperature, respectively.

ξ_δ may be evaluated to -1.45 MPa for $\delta = 2.44\ nm$ (Figure C.4a), while ξ_T varies from 2.94 kPa/°C at 293 K to 0.33 kPa/°C at 353 K (Figure C.4b). The bulk modulus of Boom clay is around 400 MPa (Mertens et al., 2004). With those values in Equation (3.21), the evolution of the thermal expansion of Boom clay with temperature varying from 293 *K* (20 °C) to 368 *K* (95 °C) is drawn in Figure C.5. This theoretical curve compares well with the experimental result of Baldi et al. (1991) from heavily overconsolidated Boom clay. This good agreement between the prediction of the double layer theory and macroscopic experimental results clearly reveals that the effect of adsorbed water on the thermal expansion of a soil-water mixture is not only related to the thermal expansion of the adsorbed water, but also to the thermal degradation of this water layer.

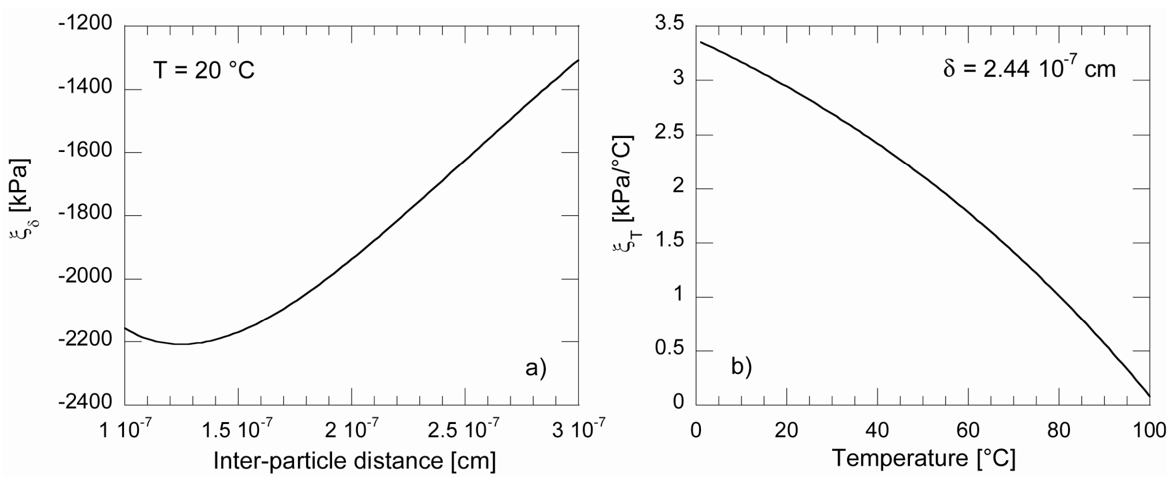

Figure C.4: Evolution of the ξ_δ (a) and ξ_T (b) variables with respect to the inter-particle distance and the temperature, respectively, in the case of Boom clay.

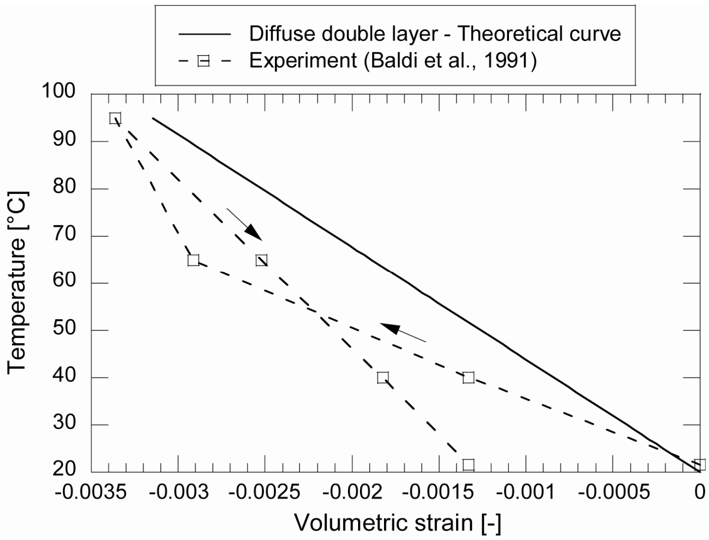

Figure C.5: Comparison between experiment and prediction through the diffuse double layer theory of the thermal expansion of highly overconsolidated Boom clay.

C.4 References

Baldi G., Borsetto M. and Hueckel T. (1987). Calibration of mathematical models for simulation of thermal, seepage and mechanical behaviour of Boom clay. EUR 10924 EN. Luxembourg, Commission of European Communities.

Baldi G., Hueckel T. and Pellegrini R. (1988). Thermal volume change of the mineral-water system in low-porosity clay soils. *Canadian Geotechnical Journal*, 25: 807-825.

Baldi G., Hueckel T., Peano A., Pellegrini R. (1991). Developments in modelling of thermo-hydro-mechanical behaviour of Boom clay and clay-based buffer materials (Vol 1 and 2). EUR 13365/1 and 13365/2. Luxembourg, Commission of the European Communities.

Delage P., Sultan N. and Cui Y.J. (2000). On the thermal consolidation of Boom clay. *Canadian Geotechnical Journal*, 37: 343–354.

Dierckx A. (1997). Boom clay in situ pore water chemistry. SCK•CEN report, BLG-734, Mol, Belgium.

Mertens J., Bastiaens W. and Dehandschutter B. (2004). Characterisation of induced discontinuities in the Boom clay around the underground excavations (URF, Mol, Belgium). *Applied Clay Science*, 26: 413-428.

Mitchell J. (1976). *Fundamentals of Soil Behavior*. Wiley.

Robinet J.C., Pasquiou A., Jullien A., Belanteur N. and Plas F. (1997). Expériences de laboratoire sur le comportement thermo-hydro-mécanique de matériaux argileux remaniés gonflants et non-gonflants. *Revue Française de Géotechnique*, 81: 53-80.

Van Olphen H. (1977). *An Introduction to Clay Colloid Chemistry.* 2nd Edition. Wiley.

Appendix D

Validation of the implementation of the ACMEG-TS model

In order to validate the implementation of the ACMEG-TS constitutive model in the LAGAMINE finite element code, some validation simulations have been performed on one finite element of the LAGAMINE code and compared with the results obtained with the driver of the constitutive law LAWYER. The used material parameters correspond to the Boom clay, as described in Section 8.3.2.2. However, the parameters related to the unsaturated behaviour are fictive (Table D.1). Figure D.1 presents a series of numerical simulations of triaxial compressions at two confining pressures, two temperatures and three suctions levels. Figure D.2 deals with a combined isotropic thermo-hydro-mechanical path as detailed in Table D.2.

Elastic parameters		
K_{ref} , G_{ref} , n^e , β_s'	[MPa], [MPa], [-], [°C^{-1}]	130, 130, 0.4, 4 10^{-5}
Isotropic plastic parameters		
β , γ_s , γ_T , c , r_{iso}^e , p_c'	[-], [-], [-], [-], [-], [MPa]	18, 16.1, 0.2, 0.012, 0.001, 6
Deviatoric plastic mechanical parameters		
b , d , ϕ_0' , g , α , a , r_{dev}^e	[-], [-], [°], [-], [-], [-], [-]	0.6, 1.3, 16, 4.5 10^{-4}, 1, 0.007, 0.3
Water retention parameters		
s_{e0} , β_h , θ_T , θ_e , s_{hys}	[MPa], [-], [-], [-], [-]	0.5, 4, 0.5, 2, 0.6

Table D.1: Parameters used in the simulations performed to compare the results obtained with LAWYER and LAGAMINE in Figure D.1 and Figure D.2.

	p_{net} [MPa]	s [MPa]	T [MPa]
O	0.1	0	20
A	0.1	5	20
B	10	5	20
C	10	5	80
D	10	1	80
E	0.1	1	80
F	0.1	1	20
G	0.1	0	20

Table D.2: Thermo-hydro-mechanical paths followed in the numerical simulation presented in Figure D.2.

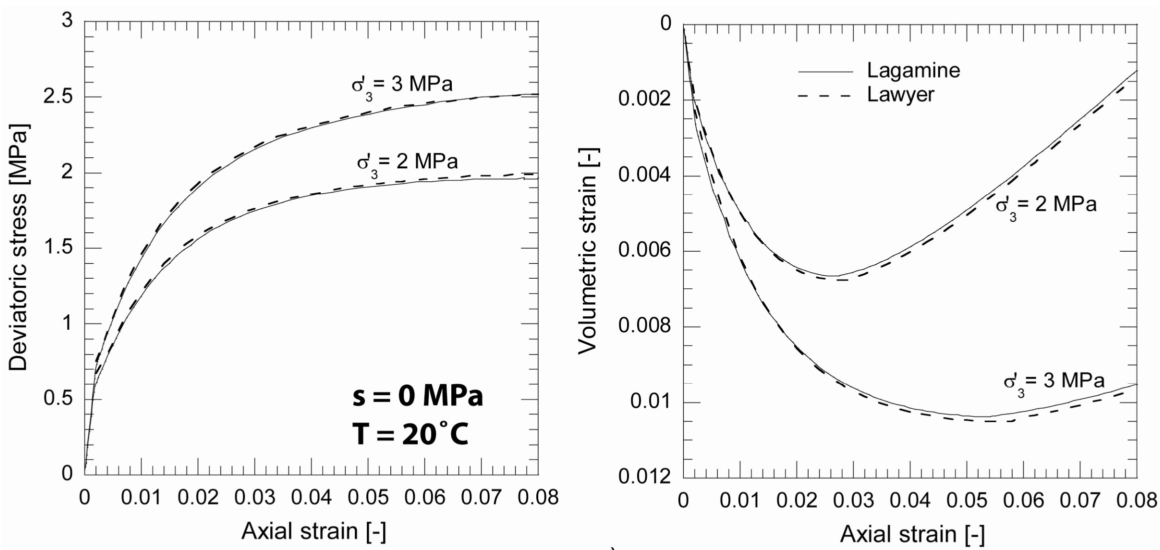

Deviatoric stress [MPa]
Axial strain [-]
σ'3 = 3 MPa
σ'3 = 2 MPa
s = 0 MPa
T = 20°C
Volumetric strain [-]
Lagamine
Lawyer

a)

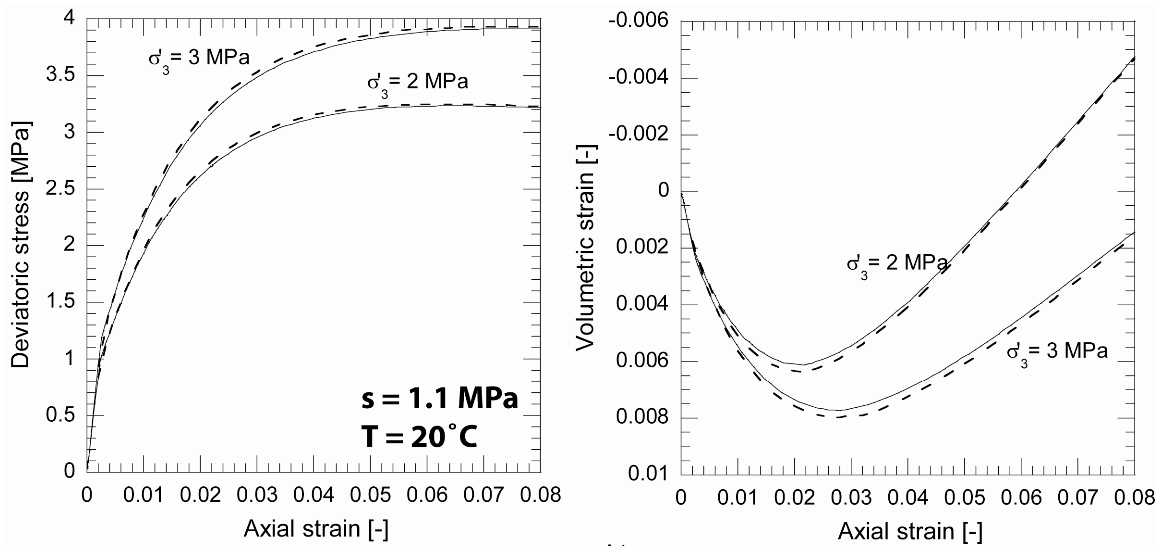

Deviatoric stress [MPa]
Axial strain [-]
σ'3 = 3 MPa
σ'3 = 2 MPa
s = 1.1 MPa
T = 20°C
Volumetric strain [-]

b)

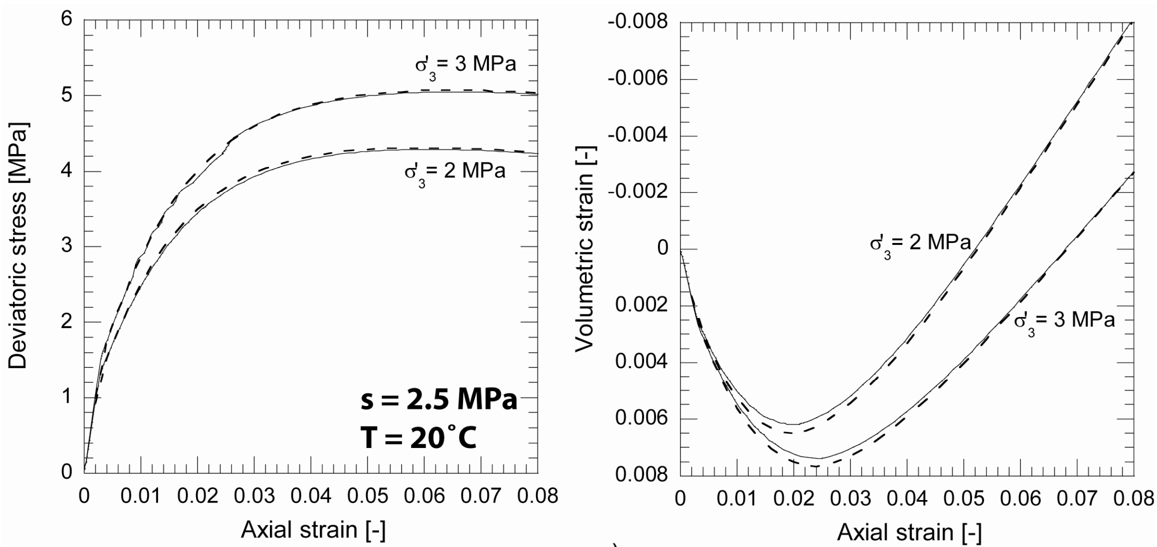

c)

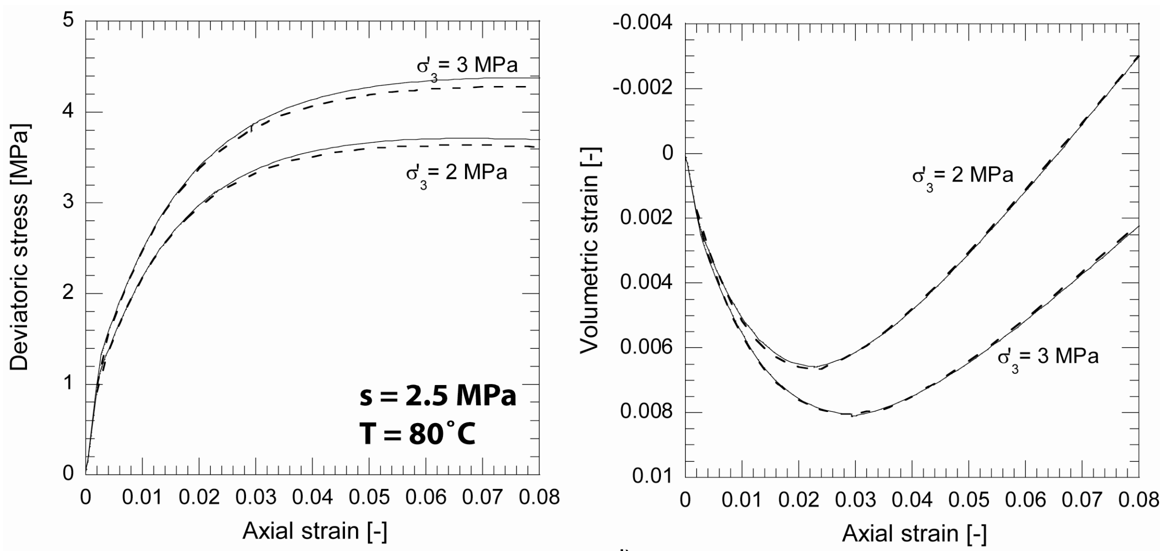

d)

Figure D.1 : Validation of the ACMEG-TS implementation in LAGAMINE. Comparison of numerical results of a series of triaxial tests at different suction and temperature values obtained with LAGAMINE and with the driver of the constitutive law LAWYER.

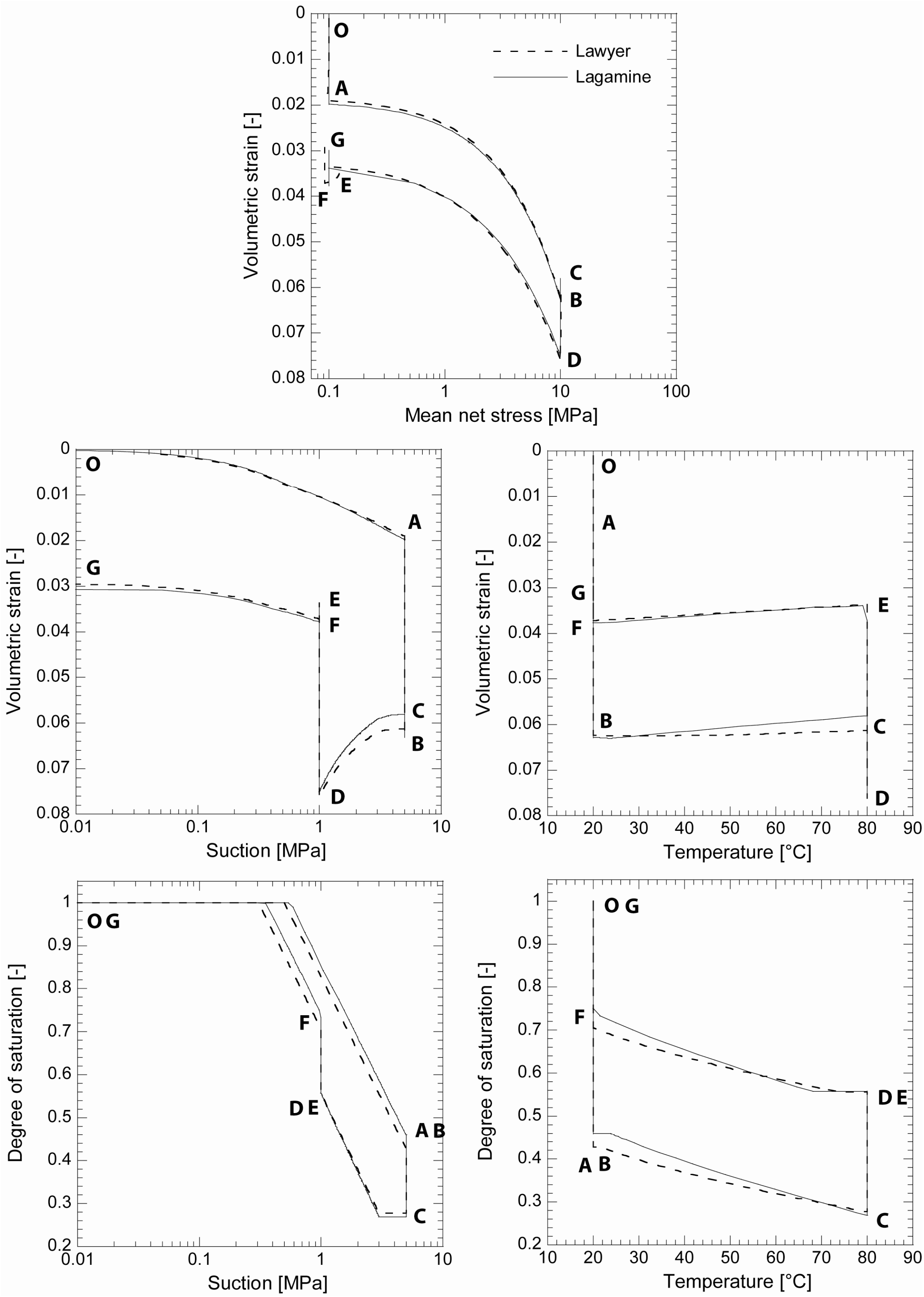

Figure D.2 : Validation of the ACMEG-TS implementation in LAGAMINE. Comparison of numerical results of a combined thermo-hydro-mechanical loading in different planes obtained with LAGAMINE and with the driver of the constitutive law LAWYER.

Appendix E

Modelling of thermo-elasto-plastic water saturated materials

This appendix reproduces the paper *"Finite element modelling of thermo-elasto-plastic water saturated materials"*, by Sanavia L., François B., Bortolotto R., Luison B. and Laloui L. in Journal of Theoretical and Applied Mechanics, 38(1-2): 7-24, 2008. This paper presents the validation of the implementation of the ACMEG-T model in the COMES-GEO finite element code.

Journal of Theoretical and Applied Mechanics, Sofia, 2008, vol. 38, Nos 1–2, pp. 7–24

FINITE ELEMENT MODELLING OF THERMO-ELASTO-PLASTIC WATER SATURATED POROUS MATERIALS*

Lorenzo Sanavia
Dipartimento di Costruzioni e Trasporti, Università degli Studi di Padova, Via Marzolo 9, 35-131 Padova, Italy,
e-mail: lorenzo.sanavia@unipd.it

Bertrand François
Soil Mechanics Laboratory, Ecole Polytechnique Fédérale Lausanne, EPFL, 1015 Lausanne, Switzerland,
e-mail: bertrand.francois@epfl.ch

Roberto Bortolotto, Loris Luison
Dipartimento di Costruzioni e Trasporti, Università degli Studi di Padova, Via Marzolo 9, 35-131 Padova, Italy,
e-mails: roberto.bortolotto@unipd.it, loris.luison@unipd.it

Lyesse Laloui
Soil Mechanics Laboratory, Ecole Polytechnique Fédérale Lausanne, EPFL, 1015 Lausanne, Switzerland,
e-mail: lyesse.laloui@epfl.ch

Dedicated to Professor Bernhard A. Schrefler on the occasion of his 65th birthday

[Received 10 July 2007. Accepted 25 February 2008]

Abstract.The purpose of this paper is to present a new finite element formulation for the hydro-thermo-mechanical analysis of elasto-plastic multiphase materials based on Porous Media Mechanics.

To this end, the ACMEG-T thermo-plastic constitutive model for saturated soils has been implemented in the finite element code COMES-GEO.

Validation of the implemented model is made by selected comparison

*The authors would like to thank the University of Padua (UNIPD 60A09-5407/06), the Foundation "Cassa di Risparmio di Padova e Rovigo" and the Swiss State Secretariat for Education and Research SER (*Grant* OFES C04.0021) for their financial support.

between model simulation and experimental results for different combinations of thermo-hydro-mechanical loading paths. A case of non-isothermal elasto-plastic consolidation is also shown.
KEY WORDS: thermo-elastoplasticity, water saturated porous materials, finite element method, isotropic compression test, triaxial test, consolidation.

1. Introduction

In recent years, increasing interest in thermo-hydro-mechanical analysis of geomaterials is observed, because of a wide spectrum of their engineering applications. Typical examples belong to Environmental Geomechanics, where some challenging problems are of interest, as for example the case of the nuclear waste isolation and of geothermal structures.

A step in the development of a suitable physical, mathematical and numerical model for the simulation of geo-environmental engineering problems is presented here. To this end, the general ACMEG-T thermo-elastoplastic constitutive model for saturated soils [1], [2] has been implemented in the finite element code COMES-GEO for the analysis of non-isothermal elasto-plastic porous materials [3].

In this paper we summarize the mathematical formulation for non-isothermal elasto-plastic water saturated porous materials in Section 2. The material is considered as made of a solid phase and open pores, which are filled with one fluid, and is modelled as a deforming porous continuum where heat conduction and convection and water advection are taken into account [4], [5]. The elasto-plastic behaviour of the solid skeleton is assumed homogeneous and isotropic; the effective stress state is limited by two temperature dependent yield surfaces, with non associated plastic flow, as presented in Section 3. The macroscopic balance equations are discretized in space and time within the finite element method for coupled problems, e.g. [4]. In particular, a Galerkin procedure is used for the discretisation in space, and the Generalised Trapezoidal Method for the time integration (see Section 5). Small strains and quasi-static loading conditions are assumed.

Validation of the implemented model by selected comparison between model simulation and experimental results for different combinations of thermo-hydro-mechanical loading paths is presented in Section 6. A case of non-isothermal elastic and elasto-plastic consolidation is described.

A review of non-isothermal thermo-hydro-mechanical models and of thermo-elasto-plastic constitutive formulations for soils is beyond the scope of this paper; the interested reader can find it in [3], [4] and [1], [2], respectively.

2. Macroscopic balance equations

A full mathematical model necessary to simulate Thermo-Hydro-Mechanical (THM) transient behaviour of fully and partially saturated porous media was developed in [4], [5] and [6] using averaging theories following [7] (see also [8]). The model for water saturated porous materials is briefly summarized in the present section for sake of completeness.

The porous medium is treated as two-phase system composed of the solid skeleton (s) with open voids filled with water (w).

At the macroscopic level the porous material is modelled by a substitute continuum of volume B with boundary ∂B that simultaneously fills the entire domain, instead of the real fluid and the solid which fill only a part of it. In this substitute continuum each constituent π has a reduced density which is obtained through the volume fraction $\eta^\pi(\boldsymbol{x},t) = dv^\pi(\boldsymbol{x},t)/dv(\boldsymbol{x},t)$, where $\boldsymbol{x}$ is the vector of the spatial coordinates and t is the current time ($\pi = s, w$). Heat conduction, heat convection and water flow due to pressure gradient inside the pores are taken into account. The solid is deformable and non-polar, and the fluid, solid and thermal fields are coupled. Local thermal equilibrium between solid matrix and liquid phase is assumed. The state of the medium is described by pore water pressure p^w, absolute temperature T and displacements of the solid matrix $\mathbf{u}$. Pore pressure is defined as compression positive for water, while stress is defined as tension positive for the solid phase.

Before presenting the balance equations used in the present case, it is useful to mention that the full mathematical model and its implementation in the COMES-GEO finite element code consider the soil as a non-isothermal three-phase media in which not only water but also a gas phase may fill the void space. In this complete formulation, which is not addressed here, the gas phase is modelled as an ideal gas mixture composed of dry air and water vapour. Phase changes of water (evaporation-condensation, adsorption-desorption) and latent heat transfer are considered [4], [5], [6], [8]. A recent development which considers the air dissolved in the liquid phase and its desorption at lower water pressure is presented in [9].

The balance equations of the implemented model are now summarized. These equations are obtained assuming the porous medium to be constituted of incompressible solid and water constituent; the process is considered as quasi-static and developed in the geometrically linear framework.

The linear momentum balance equation of the mixture in terms of effective Cauchy's stress $\boldsymbol{\sigma}'(\boldsymbol{x},t)$ assumes the form,

$$\mathrm{div}\left(\boldsymbol{\sigma}' - p^w\,\mathbf{1}\right) + \rho\,\mathbf{g} = \mathbf{0}, \tag{1}$$

where $\rho = [1-n]\,\rho^s + n\rho^w$ is the density of the mixture, $n(\boldsymbol{x},\mathrm{t})$ the porosity, $\mathbf{g}$ is the gravity acceleration vector and $\mathbf{1}$ the second order identity tensor.

The mass conservation equation for the water is,

$$\rho^w \operatorname{div} \boldsymbol{v}^s - \operatorname{div}\left(\rho^w \frac{\mathbf{k}}{\mu^w}\left[\operatorname{grad}(p^w) - \rho^w \mathbf{g}\right]\right) - \rho^w \beta_{sw} \frac{\partial T}{\partial t} = 0, \tag{2}$$

where $\boldsymbol{v}^s$ is the solid velocity, $\mathbf{k}(\boldsymbol{x},t)$ is the intrinsic permeability tensor and $\mu^w(\boldsymbol{x},t)$ the water viscosity. $\beta_{sw}(\boldsymbol{x},t) = [1-n]\beta_s + n\beta_w$ is the cubic thermal expansion coefficient of the medium, β_s and β_w being the solid and water cubic thermal expansion coefficient, respectively. In equation (2), the water flux has been described using the Darcy law.

The energy balance equation of the mixture has the following form,

$$(\rho C_p)_{\mathit{eff}} \frac{\partial T}{\partial t} - \left(\rho^w C_p^w \frac{\mathbf{k}}{\mu^w}\left[\operatorname{grad}(p^w) - \rho^w g\right]\right) \cdot \operatorname{grad} T - \operatorname{div}\left(\chi_{\mathrm{eff}} \operatorname{grad} T\right) = 0, \tag{3}$$

where $(\rho C_p)_{\mathit{eff}} = (1-n)\,\rho^s C_p^s + n\rho^w C_p^w$ is the effective thermal capacity of porous medium, C_p^s and C_p^w the specific heat of solid and water, respectively, and χ_{eff} the effective thermal conductivity of the porous medium. This balance equation takes into account the heat transfer through conduction and convection (see [4], [5]) and neglects the terms related to the mechanical work induced by density variations due to temperature changes of the phases and induced by volume fraction changes.

3. Constitutive equations

The thermo-elastoplastic behaviour of the solid skeleton is described by the general ACMEG-T thermo-plastic constitutive model for water saturated soils developed in [1], [2], [10] within the rate-independent elasto-plasticity theory for geometrically linear problems.

The most relevant experimental results for the constitutive description of the soil behaviour will be summarized in the following, before the description of the constitutive model (see e.g. [2] for a comprehensive description).

When studying thermo-mechanical behaviour of soil, some specific experimental observations must be considered in the constitutive development. In particular, irreversible processes induced by temperature changes may induce thermo-plastic processes in soils. These irreversible effects strongly depend on the stress level measured in terms of OverConsolidation Ratio (OCR). Under Normally Consolidated conditions (NC), soils contracts when it is heated and a significant part of this deformation is irreversible upon cooling. The behaviour over the whole cycle indicates the irreversibility of strain due to thermal loading, which is representative of thermal hardening. On the contrary, the highly overconsolidated states produce mainly reversible dilation when heated. Between these states, an intermediate one (low OCR) first produces dilation, then a tendency toward contraction on heating paths.

In addition, several results from the literature show a decrease in the preconsolidation pressure with increasing temperature. Finally, under undrained conditions, when soil is heated, the higher thermal expansion of water than that of the solid skeleton induces pore water pressure increase. Indeed, a temperature increase tends to enhance the pore space of the material proportionally to the thermal expansion coefficient of the solid skeleton. Nevertheless, this effect is more than counterbalanced by the thermal dilation of water. Moreover, when the soil tends to collapse during heating (due to thermo-plastic behaviour of NC soils), the undrained conditions make the decrease of pore space impossible, which provokes an additional increase in pore water pressure.

The ACMEG-T model considers a non-linear thermo-elasticity coupled with a multi-dissipative thermo-plasticity in order to reproduce all the thermo-mechanical features of behaviour exposed above.

The elastic part of the deformation is expressed as following:

$$d\boldsymbol{\varepsilon}^e = \mathbf{D}^{-1} d\boldsymbol{\sigma}' + \boldsymbol{\beta}_{\mathrm{T}} dT, \tag{4}$$

$\mathbf{D}$ is the mechanical elastic tensor defined by the non-linear bulk and shear modulus, K and G, respectively,

$$K = K_{ref} \left(\frac{p'}{p'_{ref}} \right)^{n^e}, \qquad G = G_{ref} \left(\frac{p'}{p'_{ref}} \right)^{n^e}, \tag{5}$$

p' is the effective mean stress, n^e the non-linear elasticity exponent, p'_{ref} the reference pressure, K_{ref} and G_{ref} the bulk and shear modulus at the reference pressure, respectively. $\boldsymbol{\beta}_{\mathrm{T}}$ is the thermal expansion tensor. Considering an isotropic thermal dilatation, one can express the thermal expansion tensor as $\boldsymbol{\beta}_{\mathrm{T}} = \frac{1}{3}\beta_s \mathbf{1}$ with β_s being the volumetric thermal expansion coefficient of the solid skeleton.

The material plasticity is induced by two coupled mechanisms: an isotropic and a deviatoric mechanism. The yield functions of the two mechanical thermo-plastic mechanisms, f_{iso} and f_{dev}, representing the isotropic and deviatoric yield limits, respectively, restricting the effective stress state $\boldsymbol{\sigma}'(\boldsymbol{x},t)$, take the following expressions (Fig. 1):

$$f_{iso} = p' - p'_c r_{iso}, \qquad f_{dev} = q - Mp'\left(1 - b\ln\frac{dp'}{p'_c}\right) r_{dev} = 0, \tag{6}$$

where q is the deviatoric stress. Each of the yield limits evolves through the generation of plastic strains. During loading, the volumetric plastic strain governs the evolution of p'_c and r_{iso}, while deviatoric plastic strains control the evolution of r_{dev}.

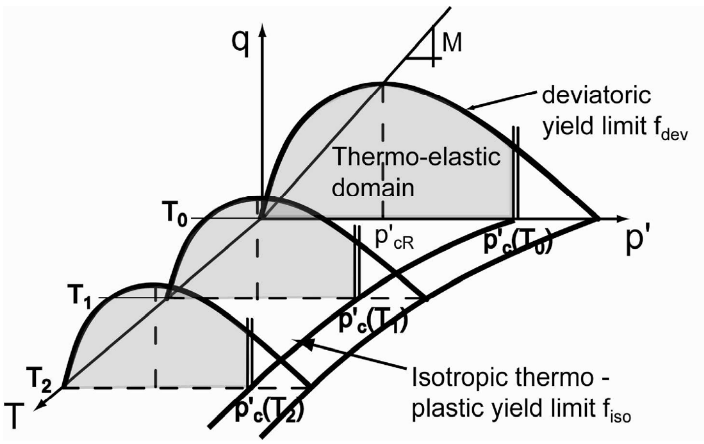

Fig. 1. Yield limits for the ACMEG-T thermo-mechanical elasto-plastic framework. q: shear stress, p': mean effective stress, T: temperature, p'_c: critical pressure

The preconsolidation pressure, p'_c, depends on the volumetric plastic strain ε_v^p and temperature [1]:

$$p'_c = p'_{c0T_0}\exp\left\{\beta\varepsilon_v^P\right\}\{1 - \gamma_T \log\,[T/T_0]\}\,, \tag{7}$$

where p'_{c0T_0} is the initial value of the preconsolidation pressure at the reference temperature, T_0, while β and γ_T are material parameters.

r_{iso} and r_{dev} correspond to the degree of plastification (mobilised hardening) of the isotropic and deviatoric yield limits, respectively. This enables a progressive evolution of the isotropic yield limit during loading and a partial comeback of this limit during unloading. The evolution of r_{iso} during loading is linked to the volumetric plastic strain induced by the isotropic mechanism $\varepsilon_v^{p,iso}$:

$$r_{iso} = r_{iso}^e + \frac{\varepsilon_v^{p,iso}}{c + \varepsilon_v^{p,iso}}, \tag{8}$$

where c and r_{iso}^e are material parameters. In the same way, the evolution of r_{dev} during loading is linked to the deviatoric plastic strain ε_d^p:

$$r_{dev} = r_{dev}^e + \frac{\varepsilon_d^p}{a + \varepsilon_d^p}, \tag{9}$$

where a and r_{dev}^e are material parameters. For more completeness about the equations of this progressive mobilised hardening, the readers may refer to [11], or more recently, to [10].

The deviatoric yield limit described by equation (6) counts three additional material parameters. b and d govern the shape of the yield limit and M is the slope of critical state line, which may depend on temperature,

$$M = M_0 - g\,(T - T_0)\,, \qquad M_0 = \frac{6 \sin \phi_0'}{3 - \sin \phi_0'}, \tag{10}$$

where ϕ_0' is the friction angle at critical state at the reference temperature T_0 and g defines the linear evolution of M with temperature T.

The flow rule of the isotropic mechanism is associated, while the deviatoric one is not and assumes the following forms:

$$\mathrm{d}\boldsymbol{\varepsilon}^{p,iso} = \lambda_{iso}^p \frac{\partial g_{iso}}{\partial \boldsymbol{\sigma}'} = \frac{\lambda_{iso}^p}{3}\mathbf{1}, \tag{11}$$

$$\mathrm{d}\boldsymbol{\varepsilon}^{p,dev} = \lambda_{dev}^p \frac{\partial g_{dev}}{\partial \boldsymbol{\sigma}'} = \lambda_{dev}^p \frac{1}{Mp'}\left[\frac{\partial q}{\partial \boldsymbol{\sigma}'} + \alpha\left(M - \frac{q}{p'}\right)\frac{1}{3}\mathbf{1}\right]. \tag{12}$$

The plastic multipliers, λ_{iso}^p and λ_{dev}^p, are determined using Prager's consistency equation for multi-dissipative plasticity [12], [13], [14]. α is a material parameter.

4. Initial and boundary conditions

For the model closure the initial and boundary conditions are needed. The initial conditions specify the full fields of state variables at time $t = t_0$ in the whole domain and on its boundary as: $p^w = p_0^w$, $T = T_0$, $\mathbf{u} = \mathbf{u}_0$ on $B \cup \partial B$.

The Boundary Conditions (BCs) can be of Dirichlet's type on ∂B_π for $t \geq t_0$:

$$p^w = \hat{p}^w \text{ on } \partial B_w, \qquad T = \hat{T} \text{ on } \partial B_T, \qquad \mathbf{u} = \hat{\mathbf{u}} \text{ on } \partial B_u \tag{13}$$

or of Neumann' BCs type on ∂B^q_π for $t \geq t_0$:

$$
\begin{aligned}
&\rho^w \frac{\mathbf{k}}{\mu^w}\left[-\operatorname{grad}(p^w)+\rho^w \mathbf{g}\right]\cdot \mathbf{n} = q^w \quad \text{on } \partial B^q_w,\\
&\chi_{\mathit{eff}}\operatorname{grad}(T)\cdot\mathbf{n} = \alpha_c(T-T_\infty)+q^T \quad \text{on } \partial B^q_T,\\
&\boldsymbol{\sigma}\cdot\mathbf{n}=\mathbf{t} \quad \text{on } \partial B^q_t,
\end{aligned}
\tag{14}
$$

where $\mathbf{n}(\boldsymbol{x},t)$ is the unit normal vector, $q^w(\boldsymbol{x},t)$ and $q^T(\boldsymbol{x},t)$ are the imposed water and heat fluxes, respectively, and $\mathbf{t}(\boldsymbol{x},t)$ is the imposed traction vector related to the total Cauchy stress tensor $\boldsymbol{\sigma}(\boldsymbol{x},t)$. $\alpha_c(\boldsymbol{x},t)$ is the convective heat transfer coefficient and $T_\infty(\boldsymbol{x},t)$ is the temperature in the far field.

5. Finite element formulation

The finite element model is derived by applying the Galerkin procedure for the spatial integration and the Generalised Trapezoidal Method for the time integration of the weak form of the balance equations of Section 2 (e.g. [4]). In particular, after spatial discretisation within the isoparametric formulation, the following non-symmetric, non-linear and coupled system of equation is obtained,

$$
\begin{bmatrix} \mathbf{C}_{ww} & \mathbf{C}_{wt} & \mathbf{C}_{wu} \\ \mathbf{C}_{tw} & \mathbf{C}_{tt} & \mathbf{C}_{tu} \\ \mathbf{0} & \mathbf{0} & \mathbf{0} \end{bmatrix} \frac{\partial}{\partial t} \begin{bmatrix} \bar{\mathbf{p}}^w \\ \bar{\mathbf{T}} \\ \bar{\mathbf{u}} \end{bmatrix} + \begin{bmatrix} \mathbf{K}_{ww} & \mathbf{K}_{wt} & \mathbf{0} \\ \mathbf{K}_{tw} & \mathbf{K}_{tt} & \mathbf{0} \\ \mathbf{K}_{uw} & \mathbf{K}_{ut} & \mathbf{K}_{uu} \end{bmatrix} \begin{bmatrix} \bar{\mathbf{p}}^w \\ \bar{\mathbf{T}} \\ \bar{\mathbf{u}} \end{bmatrix} = \begin{bmatrix} \mathbf{f}_w \\ \mathbf{f}_t \\ \mathbf{f}_u \end{bmatrix}, \tag{15}
$$

where the solid displacements $\mathbf{u}(\boldsymbol{x},t)$, the pore water pressure $p^w(\boldsymbol{x},t)$ and the temperature $T(\boldsymbol{x},t)$ are expressed in the whole domain by global shape function matrices $\mathbf{N}_u(\boldsymbol{x})$, $\mathbf{N}_w(\boldsymbol{x})$, $\mathbf{N}_T(\boldsymbol{x})$ and the nodal value vectors $\bar{\mathbf{u}}(t)$, $\bar{\mathbf{p}}^w(t)$, $\bar{\mathbf{T}}(t)$.

In a more concise form the previous system is written as $\mathbf{G}(\mathbf{X}) = \mathbf{C}\dfrac{\partial \mathbf{X}}{\partial t} + \mathbf{K}\mathbf{X} - \mathbf{F} = \mathbf{0}$, where $\mathbf{X} = \left[\bar{\mathbf{p}}^w, \bar{\mathbf{T}}, \bar{\mathbf{u}}\right]^T$ is the solution vector.

Finite differences in time are used for the solution of the initial value problem over a finite time step $\Delta t = t_{n+1} - t_n$. Following the Generalised Trapezoidal Method, equations (15) are rewritten at time t_{n+1} using the relationships

$$
\left.\frac{\partial \mathbf{X}}{\partial t}\right|_{n+\theta} = \frac{\mathbf{X}_{n+1}-\mathbf{X}_n}{\Delta t}, \quad \mathbf{X}_{n+\theta} = [1-\theta]\mathbf{X}_n + \theta\mathbf{X}_{n+1}, \quad \text{with } \theta \in [0,1]. \tag{16}
$$

Linearized analysis of accuracy and stability suggest the use of $\theta \geq 0.5$. In the example section, implicit one-step time integration has been performed ($\theta = 1$).

After time integration the non-linear system of equations is linearized, thus obtaining the equations system that can be solved numerically (in compact form)

$$\left.\frac{\partial \mathbf{G}}{\partial \mathbf{X}}\right|_{\mathbf{X}_{n+1}^{i}} \Delta \mathbf{X}_{n+1}^{i+1} \cong -\mathbf{G}(\mathbf{X}_{n+1}^{i}) \tag{17}$$

with the symbol $(\bullet)_{n+1}^{i+1}$ to indicate the current iteration $(i+1)$ in the current time step $(n+1)$ and where $\partial \mathbf{G}/\partial \mathbf{X}$ is the Jacobian matrix. Details concerning the matrices and the residuum vector of the linearized equations system can be found in [3].

Owing to the strong coupling between the mechanical, thermal and the pore fluid fields, a monolithic solution of (17) is preferred using a Newton scheme. Finally, the solution vector $\mathbf{X}$ is then updated by the incremental relationship $\mathbf{X}_{n+1}^{i+1} = \mathbf{X}_{n+1}^{i} + \Delta \mathbf{X}_{n+1}^{i+1}$.

6. Numerical results

In this section, the validation of the implementation of ACMEG-T thermo-plastic constitutive model for saturated soils is presented and discussed by comparison between experimental and finite element results at element level and by solving a reference case of non-isothermal consolidation taken from the literature [15].

6.1. Validation at the element level

The first set of examples deals with the simulation of isothermal isotropic and triaxial compression tests. The case of isotropic compression is represented by a mechanical compression test on silty sand under saturated conditions [16]. This test is simulated with an axisymmetric finite element analysis under isotropic load: $\sigma'_r = \sigma'_z = \sigma'_\theta = p'$, $\tau_{rz} = \tau_{z\theta} = \tau_{\theta r} = 0$. The initial effective stress is characterized by a mean compressive pressure $p' = -10$ kPa and a deviatoric stress $q = 0$ kPa. This compression test consists of a $[-100;$ $-10;$ $-200;$ $-10;$ -550 kPa$]$ loading-unloading cycle. The material parameters used in the computation are listed in Table 1.

The analysis was performed discretizing the geometry successively with one and one hundred linear element(s) and with one 8-node element. The comparison between the experimental and the finite element results shows a good agreement, independently of the spatial discretisation (Fig. 2). This first very simple example of numerical simulation under isotropic compression path shows the capability of the ACMEG-T model to reproduce the progressive plasticity of materials. The transition between purely elastic behaviour and the total mobilisation of plasticity is smooth as experimentally observed.

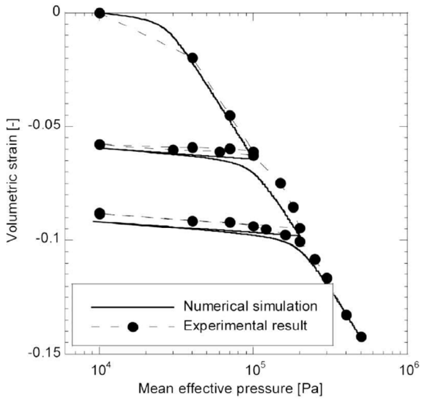

Fig. 2. Isothermal isotropic compression test: Comparison between the experimental and the finite element results

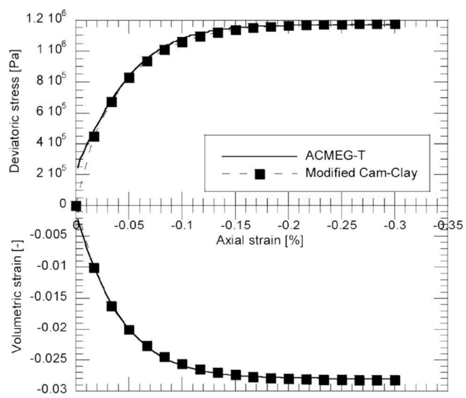

Fig. 3. Isothermal triaxial compression test: Comparison between Modified Cam-Clay simulation and the finite element results

The second example simulates triaxial compression test on normally consolidated sample submitted to an initial mean pressure p' of -800 kPa, without deviatoric component and by imposing a vertical displacement of the upper surface. This example uses a fictive material for which the material parameters have been arbitrary chosen to correspond to well-known Modified Cam-Clay model. Indeed, ACMEG-T model can be seen has an extension of the Modified Cam-Clay model. The material parameters used in the computation are listed in Table 1. Figure 3 shows that, by selecting adequate parameters, the ACMEG-T response gives identical results than the Modified Cam-Clay simulated with a commercial code.

These two first examples tend, first, to validate the implementation of the isothermal part of ACMEG-T model in the COMES-GEO code and, secondly, to prove the capability of the constitutive model to reproduce the response of soils submitted to classical mechanical paths.

As a second part of the validation process, the next simulations show the efficiency of the model implemented in COMES-GEO to reproduce soil behaviours under non-isothermal conditions. To this end, two sets of experiments are simulated numerically. The first one consists of heating-cooling cycles on soils having different degree of consolidation (OCR = 1; 2; 6), as performed by [17]. The material parameters are listed in Table 1. The initial mean pressure

Table 1. Material parameters used in the computation of the (1) Isothermal isotropic compression, (2) Isothermal triaxial compression, (3) Heating-cooling cycle, (4) Triaxial compression at two different temperatures

	Elastic parameters					Isotropic plastic parameters					Deviatoric plastic parameters						
	K_{ref}	G_{ref}	p'_{ref}	n^e	β_s	$p'_{c_0T_0}$	β	c	r^e_{iso}	γ_T	b	d	ϕ'_0	α	a	r^e_{dev}	g
	[MPa]	[MPa]	[MPa]	[–]	[K^{-1}]	[MPa]	[–]	[–]	[–]	[–]	[–]	[–]	[°]	[–]	[–]	[–]	[–]
(1)	460	690	−1	1	/	−0.028	−22	0.001	0.001	/	/	/	/	/	/	/	/
(2)	131	78	−1	1	/	−0.8	−44	0.001	1	/	1	2	−25	1	0.001	1	/
(3)	150	130	−1	1	3E–5	−6	−47	4E–4	0.01	0.18	/	/	/	/	/	/	/
(4)	70	30	−1	0.68	/	−0.6	−21	0.055	0.01	0.075	0.5	2.75	−22	2	0.0035	0.1	2.9E–5

Table 2. Material parameters used in the computation of the non-isothermal consolidation example – (1) Thermo-elastic case, (2) Thermo-elastoplastic case

	Elastic parameters					Isotropic plastic parameters					Diffusive law						
	K_{ref}	G_{ref}	p'_{ref}	n^e	β_s	$p'_{c_0T_0}$	β	c	r^e_{iso}	γ_T	ρ^s	ρ^w	n	k	λ_s	c_s	λ_w	c_w
	[MPa]	[MPa]	[MPa]	[–]	[K^{-1}]	[Pa]	[–]	[–]	[–]	[–]	[kg/ [m^3]	[kg/ m^3]	[–]	[m^2]	[W/ (m K)]	[J/ (kg K)]	[W/ (m K)]	[J/ (kg K)]
(1)	10	2.14	−1	0	9E–7	−1E10	/	/	1	0	2000	1000	0.2	4.6E–17	0.84	16760	0.6	4181
(2)	10	2.14	−1	0	9E–7	−800	−20	0.001	0.001	0.2	2000	1000	0.2	4.6E–17	0.84	16760	0.6	4181

is of -6.0 MPa, -3.0 MPa and −1.0 MPa for OCR = 1; 2; 6, respectively.

The comparison between the experimental and the finite element results shows a very good agreement, as it can be seen in Fig. 4. This specific response of soil depending on the stress state is very representative of thermo-plastic effects, as already mentioned in Section 3.

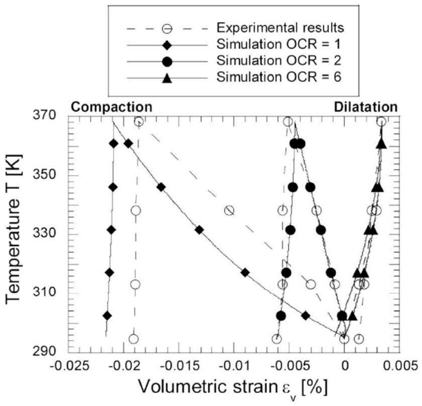

Fig. 4. Heating-cooling at different OCR: Comparison between the experimental [17] and the finite element results

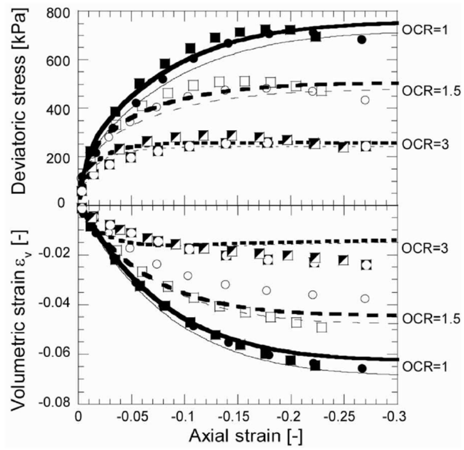

Fig. 5. Simulation of triaxial shear tests under different confining pressures ($p'_c = -600$ kPa). Circle (square) points: Experimental results at T = 22 °C (T = 90 °C) [18]. Thin (thick) lines: numerical simulations at T = 22 °C (T = 90 °C)

The second set of experiments consists of triaxial tests on kaolin clay at two different temperatures (22 °C and 90 °C) and under different OCR [18]. The cases of OCR = 1, 1.5 and 3 have been simulated at both temperatures. The comparison between the experimental and finite element results are depicted in Fig. 5 and reveal a good capability of the ACMEG-T model implemented in the COMES-GEO code to describe the thermal effects on the deviatoric response of soil, as observed experimentally. In particular, equation (6) coupled with equations (7) and (10) clearly shows that temperature induces a change in the deviatoric yield limit, through the modification of preconsolidation pressure and friction angle, and so modifies the stress-strain response of soil when temperature changes.

6.2. Boundary value problem

The following example aims to validate the finite element formulation solving an initial boundary value problem. It deals with the simulation of a non-isothermal fully saturated consolidation problem, for which the numerical solution of the linear thermo-mechanical problem is known [15].

A column of 7 m height and 2 m width is subjected to an external surface compressive load of 1.0 kPa and to a surface temperature jump of 50 K above the initial ambient temperature of 293.15 K. The material is initially water saturated. The upper surface is drained ($p^w = 0$ Pa); the lateral and the bottom surfaces are insulated. Horizontal displacements are constrained along the vertical boundaries and vertical displacements are constrained at the bottom surface. The column is discretized by nine eight-node isoparametric elements (Fig. 6). Furthermore, 3×3 Gauss integration points are used. The material parameters used in the computation are listed in Table 2. Gravity forces are taken into account. Plane strain conditions are assumed.

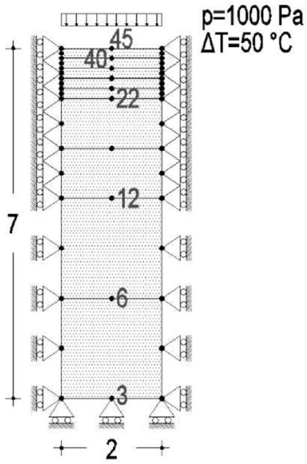

Fig. 6. Spatial discretisation and boundary conditions for the non-isothermal consolidation example

The case studied in [15], which assumed constant Young modulus ($E =$ 6.0 MPa) and Poisson ratio ($\nu = 0.4$) and constant cubic thermal expansion coefficient, is used as validation example. To this aim, the results of [15] as published in [4] and labelled "Aboustit *et al.*" in the Figs 7 and 8, are used to compare the solution obtained with the finite element formulation proposed in this paper and labelled "ACMEG-T". The time histories for the water pressure (Fig. 7(a)), the temperature (Fig. 7(b)) and the vertical displacement (Fig. 7(c)) of several nodes of the mesh show the coincidence of the two solutions. The linear behaviour of the thermo-mechanical problem adopting the

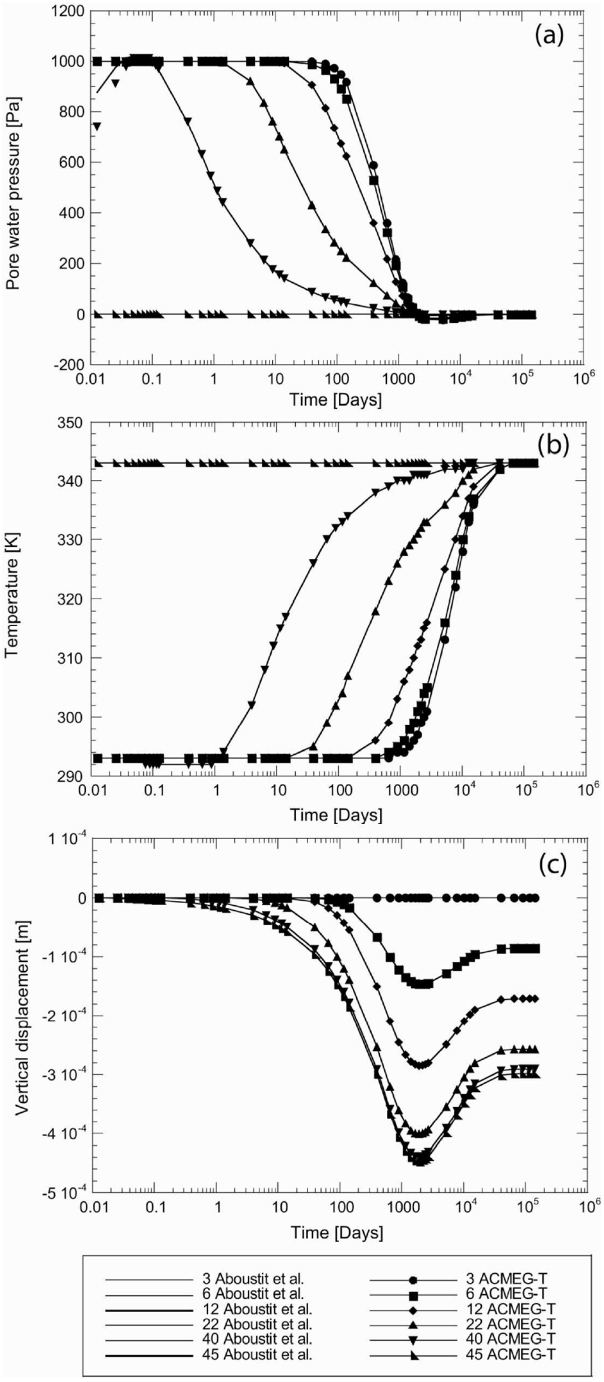

Fig. 7. Simulation of non-isothermal fully saturated consolidation problem using linear thermo-elasticity and comparison with results of [4]. Evolution of pore water pressure (a), temperature (b) and vertical displacement (c)

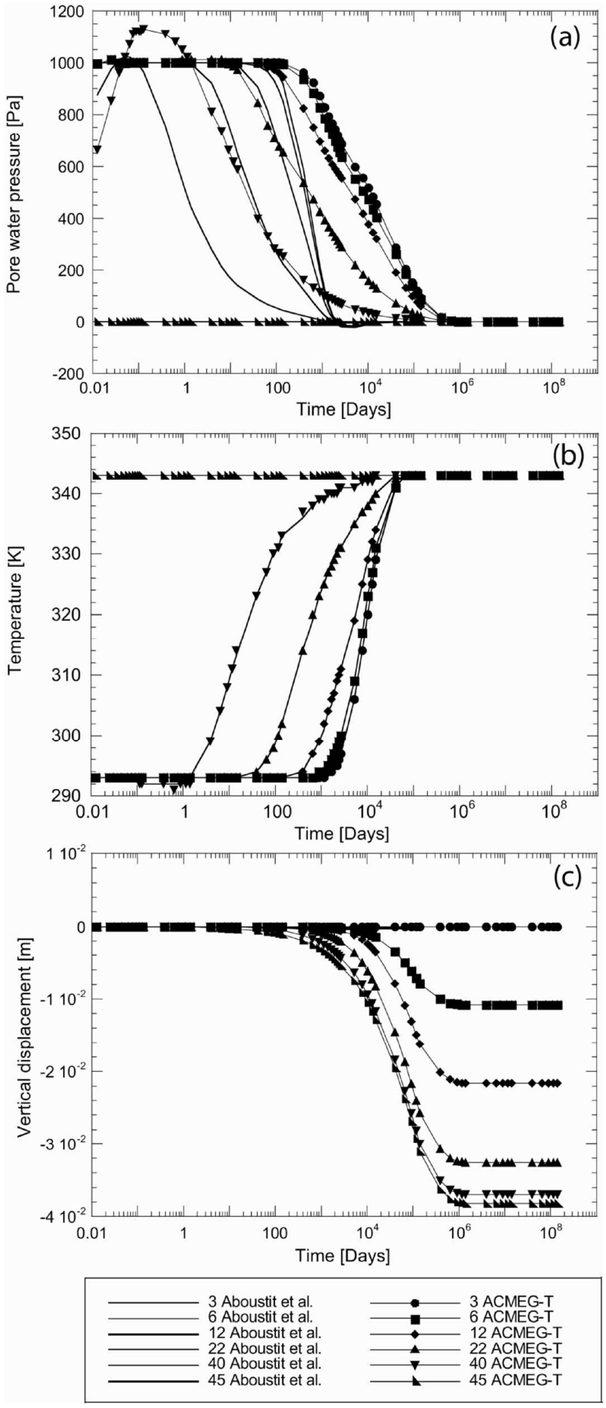

Fig. 8. Simulation of non-isothermal fully saturated consolidation problem using thermo-elastoplasticity and comparison with results of [4]. Evolution of pore water pressure (a), temperature (b) and vertical displacement (c)

ACMEG-T model is obtained by using the mechanical moduli independent of the stress state ($n^e = 0$).

As shown all along the present paper, soils are often subject to irreversible processes induced by thermal effect. In this context, the last simulation extends the problem of Fig. 6 towards thermo-elastoplastic analysis. The material parameters are listed in Table 2, where it can be observed that the linear elasticity is kept for comparison with the previous simulation; thermo-plasticity is introduced by reducing the preconsolidation pressure to get a mechanical and thermal hardening when loaded to 1 kPa and introducing the decrease of the isotropic yield surface with temperature.

The comparison between the elastic and the elasto-plastic solution shows that the inclusion of the plasticity effects delays the dissipation of pore water pressure in time (Fig. 8(a)), because of the reduced thermo-plastic stiffness of the solid skeleton with respect to the elastic one. Moreover, the predicted water pressures at the same time station are therefore higher than those from the elastic analysis.

Temperature evolution is almost not modified with respect to the previous simulation, as it can be observed in Fig. 8(b). Indeed, because parameters of thermal conduction and convection are almost independent of porosity changes, at least for this range of volumetric strain, equation (3) remains almost unaffected by mechanical change. On the contrary, the time history for the vertical displacements appears to be strongly affected by thermo-plastic behaviour of the solid skeleton. In particular, an increase of two order of magnitude for the vertical displacements is observed (Fig. 8(c)), that makes negligible the thermal component that can be observed in Fig. 7(c).

7. Conclusions

A coupled finite element formulation for thermo-elastoplastic water saturated geomaterials based on Porous Media Mechanics was presented. To this end, the ACMEG-T thermo-plastic constitutive model for saturated soils has been implemented in the finite element code COMES-GEO for the analysis of non-isothermal elastoplastic multiphase solid porous materials.

Validation of the implemented model was made by selected comparison between model simulation and experimental results for different combinations of thermo-hydro-mechanical loading paths. A case of non-isothermal elastic or elasto-plastic consolidation was solved.

The model has been obtained as a result of a research in progress on the thermo-hydro-mechanical modelling of multiphase geomaterials undergoing inelastic strains. The validation case addressed in this paper remains very simple but clearly points out that with a sufficiently general thermo-hydro-mechanical model, the main THM couplings occurring in fine soils may be reproduced in a relevant manner. In particular, thermo-elastoplastic effects coupled with transient water and heat flow can be numerically analysed. That constitutes a powerful tool to address many geoenvironmental problems.

REFERENCES

[1] Laloui, L., C. Cekerevac. Thermo-Plasticity of Clays: An Isotropic Yield Mechanism. *Computers and Geotechnics,* **30** (2003), 649–660.

[2] Laloui, L., C. Cekerevac, B. François. Constitutive Modelling of the Thermo-Plastic Behaviour of Soils. *Revue Européenne de Génie Civil*, **9** (2005), No. 5–6, 635–650.

[3] Sanavia, L., F. Pesavento, B. A. Schrefler. Finite Element Analysis of Non-isothermal Multiphase Geomaterials with Application to Strain Localization Simulation. *Computational Mechanics,* **37** (2006), No. 4, 331–348.

[4] Lewis, R. W., B. A. Schrefler. The Finite Element Method in the Static and Dynamic Deformation and Consolidation of Porous Media, J. Wiley, Chichester, 1998.

[5] Gawin, D., B. A. Schrefler. Thermo-Hydro-Mechanical Analysis of Partially Saturated Porous Materials. *Engineering Computations*, **13** (1996), No. 7, 113–143.

[6] Schrefler, B. A. Mechanics and Thermodynamics of Saturated-Unsaturated Porous Materials and Quantitative Solutions. *Applied Mechanics Review*, **55** (2002), No. 4, 351–388.

[7] Hassanizadeh, M., W. G. Gray. General Conservation Equations for Multi-Phase System: 1. Averaging Technique. *Adv. Water Res.*, **2** (1979), 131–144.

[8] Schrefler, B. A., L. Sanavia. Coupling Equations for Water Saturated and Partially Saturated Geomaterials. *Revue Française de Génie Civil*, **6** (2002), 975–990.

[9] Gawin, D., L. Sanavia. Modelling of Cavitation and Rapid Water Desaturation of Porous Media Considering Effects of Dissolved Air. *Transport in Porous Media* (Accepted).

[10] Laloui, L., B. François. ACMEG-T: A Comprehensive Soil Thermo-Plasticity Model. (Submitted).

[11] Hujeux, J. C. Une loi de comportement pour le chargement cyclique des sols, In: Génie Parasismique. Les éditions de l'E.N.P.C, Paris, 1985, 287–302.

[12] Prager, W. Non-Isothermal Plastic Deformation. *Koninkklijk-Nederland Akademie Van Wetenschappen Te Amsterdam – Proceedings of the Section of Sciences – B*, **61** (1958), 176–182.

[13] Rizzi, E., G. Maier, K. Willam. On Failure Indicators in Multi-Dissipative Materials. *International Journal of Solids and Structures*, **33** (1996), No. 20–22, 3187–3214.

[14] Simo, J. C., T. J. R. Hughes. Computational Inelasticity, Springer, New York, 1998.

[15] Aboustit, B. L., S. H. Advani, J. K Lee. Variational Principles and Finite Element Simulations for Thermo-Elastic Consolidation. *Int. J. Num. Anal. Meth. Geomech.*, **9** (1985), 49–69.

[16] Jamin, F. Contribution à l'étude du transport de matière et de la rhéologie dans les sols non saturés à différentes temperatures, PhD Thesis, Université Montpellier 2, 2003.

[17] Baldi, G., T. Hueckel, A. Peano, R. Pellegrini. Developments in Modelling of Thermo-Hydro-Geomechanical Behaviour of Boom Clay and Clay-Based Buffer Materials, Report: 13365/2 EN, Commission of the European Communities, 1991.

[18] Cekerevac,C., L. Laloui. Experimental Study of the Thermal Effects on the Mechanical Behaviour of a Clay. *International Journal of Numerical and Analytical Methods in Geomechanics*, **28** (2004), 209–228.

Appendix F

Benchmark exercise on constitutive modelling of the mechanical behaviour of Opalinus clay

F.1 Introduction

The Mont Terri Project is an international research project for the hydrogeological, geochemical and geotechnical characterisation of a clay formation (Opalinus clay). The results of the experiments carried out in the context of this research project provide input for assessing the feasibility and safety of this type of host rock as a repository for radioactive waste (Thury and Bossart, 1999; Bossart et al., 2002; Marschall et al., 2005). In this framework, during more than ten years, many experimental tests have been performed on core materials extracted in a series of boreholes drilled in different directions.

A large quantity of available laboratory tests aiming to characterize the mechanical response of Opalinus clay has been analysed. The data were extracted from project-specific documents supplied by NAGRA. Those tests mainly consist in uniaxial compression tests, triaxial tests, direct shear tests and a few oedometric compression tests. The review of the laboratory experiments reveals the difficulty to obtain fully-controlled hydro-mechanical conditions, not only in the boundary conditions but mainly inside the specimen. The very low compressibility, the low porosity, the high mechanical and hydraulic anisotropy and the very low permeability make difficult the carrying out of accurate experimental tests. Among the available experimental data, 18 uniaxial tests, 33 triaxial tests, 6 direct shear tests and 2 oedometric compression tests were selected. Those tests have been chosen for their systematic, detailed and repeated experimental procedure. They provide valuable evidence to gain a comprehensive understanding on the mechanical behaviour of Opalinus clay.

Based on the results of some selected laboratory tests, a benchmark exercise was performed. It aims to investigate the capability of the ACMEG constitutive model to reproduce the most relevant features of the mechanical behaviour of the Opalinus clay. Given the results of conventional tests conducted on triaxial and oedometric paths, the behaviour of the Opalinus clay under different stress paths are predicted by the means of blind simulations.

F.2 Opalinus clay

Opalinus clay consists of indurated dark grey micaceous claystones (shales). The clay-mineral content ranges from 40 to 80 % in weight (9–29% illite, 3–10% chlorite, 6–20% kaolinite, and 4–

12% illite/smectite mixed layers in the ratio 70/30). 10 % of the clay minerals are capable of swelling. Others minerals are quartz (14%), calcite (13%), siderite (3%), ankerite (0–3%), feldspars (1%), pyrite (1.1%), and organic carbon (<1%) (Gautschi, 2001).

The in-situ hydraulic conductivity of the Opalinus clay is evaluated to about 2×10^{-13} m/s for undeformed rock (Thury and Bossart, 1999). Table F.1 summarizes the mean physical properties of this material according to Bock (2001).

F.3 Compilation of the mechanical tests

Due to the anisotropy of Opalinus clay, the mechanical response of the clay is highly affected by the direction of loading with respect to the bedding plane. As a consequence, three different directions of loading have been considered in the compilation of the triaxial and uniaxial tests: bedding planes parallel (P-Sample), perpendicular (S-Sample) and with an inclination of 45°C (Z-Sample) with respect to the loading direction (Figure F.1).

All the tests compiled in this section were performed on samples extracted from boreholes cored from the Mont-Terri underground laboratory at a depth of approximately 300 m. This corresponds to a preconsolidation pressure around 20 MPa. In all these tests, the water content is not controlled and is assumed to be constant (i.e. equal to the natural water content).

Figure F.2 to Figure F.4 gather the uniaxial and triaxial tests according to the three loading directions (P-Sample, S-Sample and Z-Sample, respectively). Same scales and ornaments of axis were used for each graph (axial strain [0-4%] and deviatoric stress [0-60 MPa] in order to help the comparison between each result.

Property	Symbol	Value	Units
Bulk density in natural conditions	ρ	2450	kg/m^3
Bulk dry density	ρ_d	2340	kg/m^3
Grain density	ρ_s	2710	kg/m^3
Water loss porosity	n	12.1	%
Specific surface	SS	112-147	m^2/g
Water content in natural conditions	w	6.1	%
Atterberg limits	w_L	38	%
	w_P	23	%

Table F.1: Physical properties of Opalinus clay

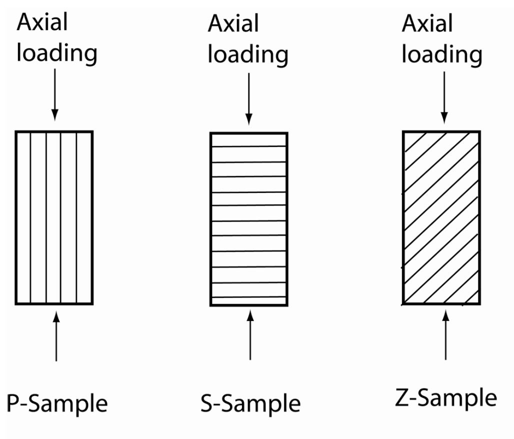

Figure F.1: Orientation of bedding with respect to the loading direction in P-, S- and Z- samples

Similar procedure was used for each test:

(i) The desired hydrostatic confining pressure (0, 5, 10 or 15 MPa) is first applied to the sample.
(ii) A fluid pressure of about 0.3 MPa is then applied to the sample from both sides (above and below).
(iii) Consolidation of the sample is made over a period of 24 hours.
(iv) The axial load is then increased with a strain rate of 10^{-6} s^{-1}.

Due to the extremely low permeability of the material, the axial strain rate of 10^{-6} s^{-1} does not guarantee a fully dissipation of excess pore water pressure generated by the mechanical loading. As a consequence, a constitutive analysis of the mechanical response of Opalinus clay using the effective stress approach is delicate. For this reason, all the results presented in this section are reported in the total stress reference.

Qualitatively, Figure F.2 to Figure F.4 show a relatively high spreading in results. The material exhibits a very high rigidity in its elastic part followed by a very short hardening process before the brittle failure. However when the confining pressure increases the axial strain at failure increases, reaching a maximum of 3.5% for a confining pressure of 15 MPa. Therefore, the brittleness seems to decrease when the confining level increase. In the volumetric plane, the experimental results exhibit unconsistent response. Thereby, the dilatancy behaviour of Opalinus clay is difficult to characterize.

Figure F.5 shows the results of two oedometric compressions tests. They consist in long term consolidation tests in which axial stresses are controlled in sharp steps during which the specimen is allowed to adjust to the new stress state in order to obtain a fully drained response. The two tests show a very similar behaviour even though the initial state of the material is different. The test conducted by Chiffoleau and Robinet (1999) reaches very high vertical stress and supply several experimental points on the unloading path, making this test more valuable for a constitutive interpretation.

Figure F.6 displays the results of direct shear tests under four different normal stress levels. Tests were carried out in direct shear boxes of 30 cm*30 cm with a shearing area for the specimen of around 900 cm^2. This shearing surface consists of open joints. The rate of deformation was set at 4.10^{-3} mm/s until reaching a maximum relative displacement of approximately 7.5 mm (Olalla et al. 1999).

In Figure F.6, the shear stress versus relative displacement results present a first linear behaviour almost directly followed by a plateau. The shear stress corresponding to this plateau increases with the increasing normal stress. Those responses do not exhibit high peak which make that the peak and residual strength are quite similar. This kind of results enables to characterize the mechanical behaviour of fractures in the Opalinus clay.

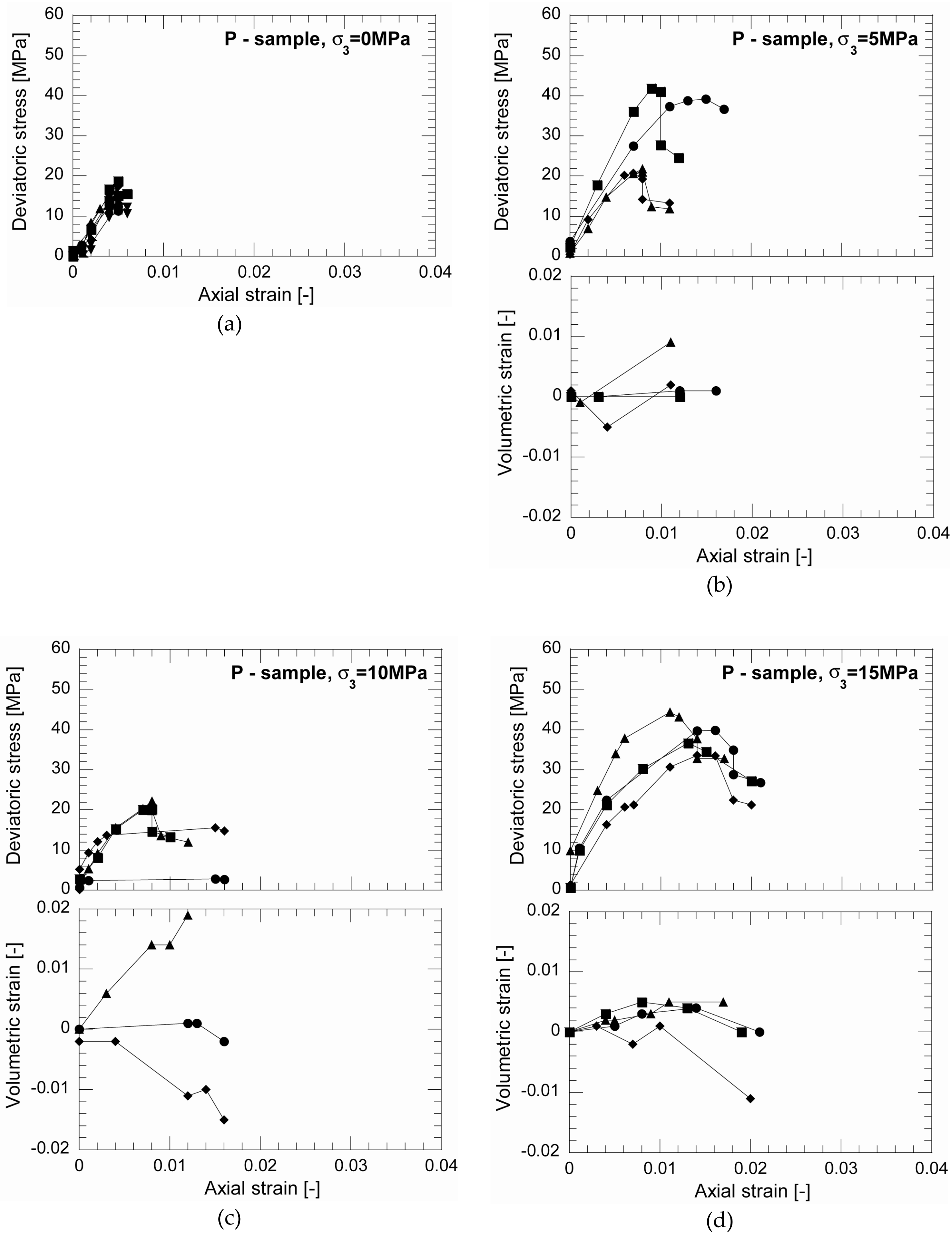

Figure F.2: Compilation of triaxial tests on Opalinus clay with the axial loading parallel to the bedding orientation (P-samples). The confining pressures are (a) 0 MPa; (b) 5 MPa; (c) 10 MPa; (d) 15 MPa.

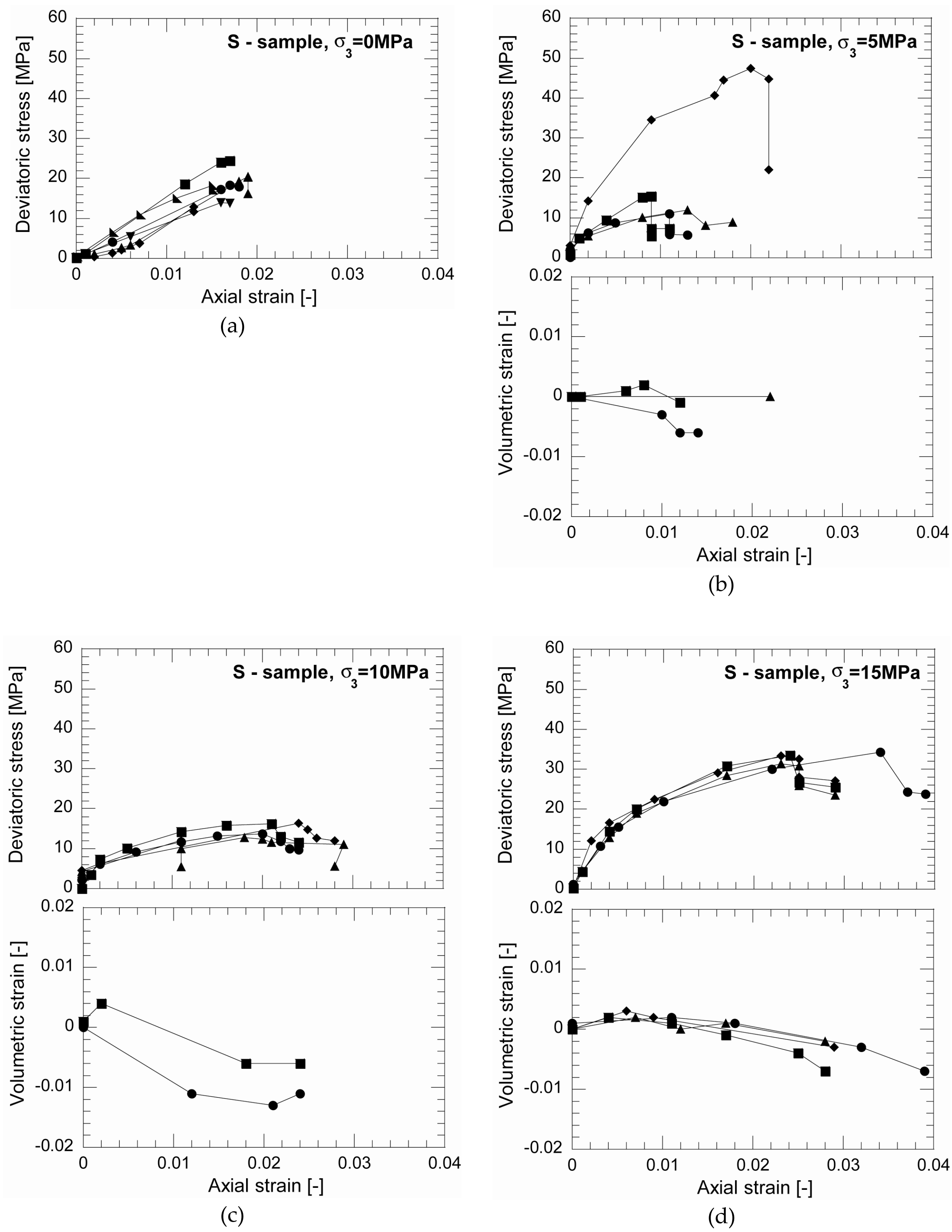

Figure F.3: Compilation of triaxial tests on Opalinus clay with the axial loading perpendicular to the bedding orientation (S-samples). The confining pressures are (a) 0 MPa; (b) 5 MPa; (c) 10 MPa; (d) 15 MPa.

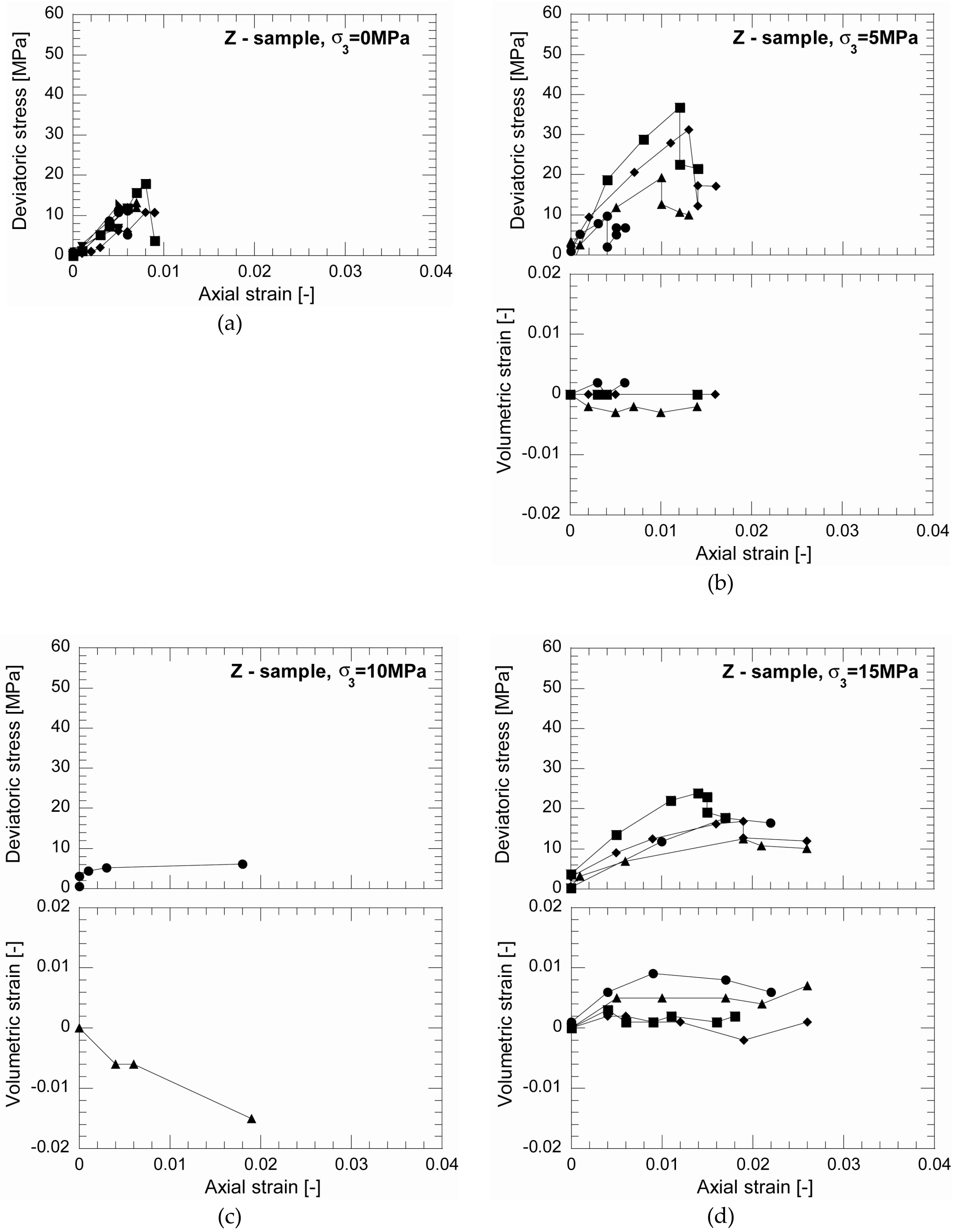

Figure F.4: Compilation of triaxial tests on Opalinus clay with the axial loading oriented at 45° with respect to the bedding orientation (Z-samples). The confining pressures are (a) 0 MPa; (b) 5 MPa; (c) 10 MPa; (d) 15 MPa.

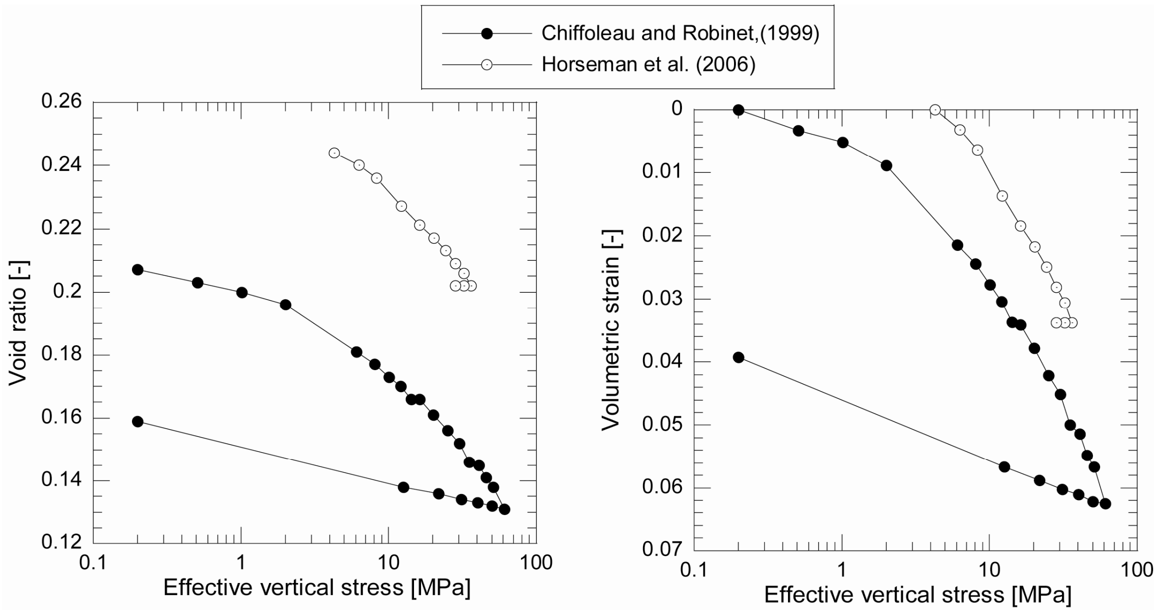

Figure F.5: Oedometric compression tests on Opalinus clay.

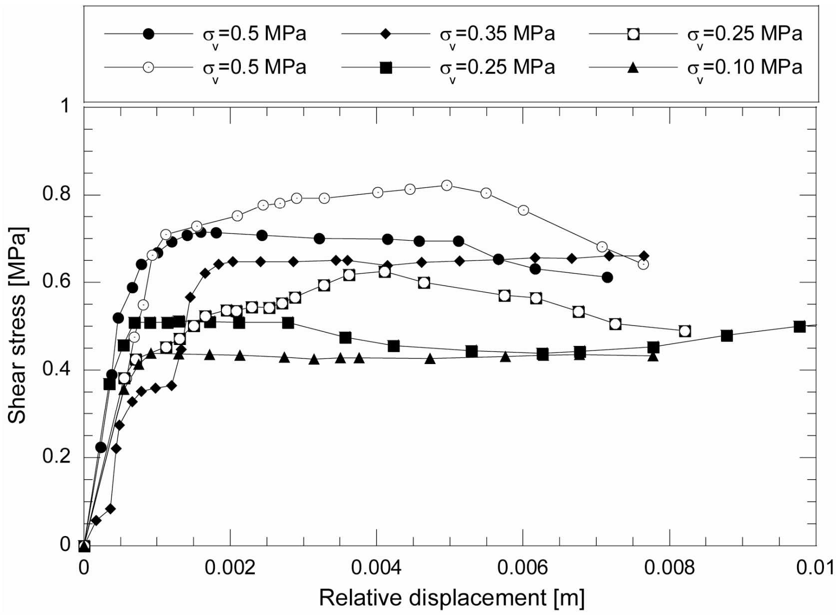

Figure F.6: Direct shear tests on open joints of Opalinus clay at different normal stress levels (σ_v).

F.4 Interpretation of results

The Young modulus of the Opalinus clay has been determined on the curves of the compiled triaxial tests. Because unloading paths at low axial strain are not available, the Young moduli corresponding to each test was calculated on the linear part of the loading curve for axial strain lower than 0.6%. This procedure does not guarantee to obtain the true elastic rigidity of the material because even at very low strain, some irreversible processes may occur (hardening, closure or occurrence of microcracks, …). So, those obtained Young moduli correspond to secant moduli. In Figure F.7, they are reported with respect to the applied confining pressure. It is observed that the Young modulus depends on the direction of loading and on the applied confining pressure. In spite of the spreading in obtained results, interpolations with power expressions were drawn for each direction of loading, leading to the following expressions:

$$E = 3017\ (\sigma_3)^{0.158}\quad [MPa]\qquad \text{(P-sample)}$$
$$E = 1162\ (\sigma_3)^{0.5}\quad [MPa]\qquad \text{(S-sample)}\qquad \text{(F.1)}$$
$$E = 2000\quad [MPa]\qquad \text{(Z-sample)}$$

where σ_3 is the confining pressure.

The ultimate strength of the Opalinus clay has been characterized from the compiled triaxial tests by drawing the deviatoric stress at the peak value with respect to the mean stress (Figure F.8). Due to the brittleness of Opalinus clay, failure generally occurs before reaching a residual state. So, it was not possible to deduce the critical state line of the material. However, the strength at peak state is valuable information in the case of Opalinus clay because it corresponds to the ultimate strength of the material. This strength at peak state strongly depends on the direction of loading. The highest friction angle at peak is observed for sample loaded parallel to the bedding orientations while the loading inclined at 45° with respect to the bedding orientation displays the lowest value of friction angle. On the contrary, the cohesion does not seem to be affected by the loading direction.

Table F.2 gathers the cohesion (c_{p-q}^{peak}) and the slope of the line characterizing the peak strength (M_{peak}) in the (p-q) plane and the classical cohesion (c^{peak}) and friction angle (ϕ^{peak}), in the sense of Mohr-Coulomb criterion. The relations between both c_{p-q}^{peak} and c^{peak} and both M_{peak} and ϕ^{peak} are expressed according to the following relations:

$$\phi^{peak} = Sin^{-1}\left(\frac{3M^{peak}}{6+M^{peak}}\right) \quad ; \quad c^{peak} = c_{p-q}^{peak}\,\frac{\mathrm{Tan}\ \phi^{peak}}{M^{peak}} \qquad \text{(F.2)}$$

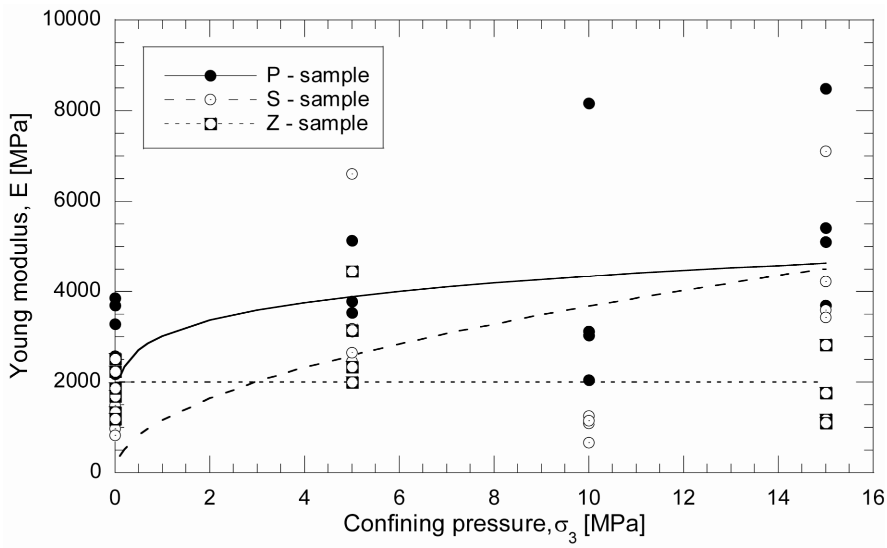

Figure F.7: Young modulus measured on the triaxial loading paths, for axial strain lower than 0.6%, expressed with respect to the applied confining pressure. Interpolations with power expressions are drawn for each direction of loading (P-sample, S-sample and Z-sample) according to Equation (F.1).

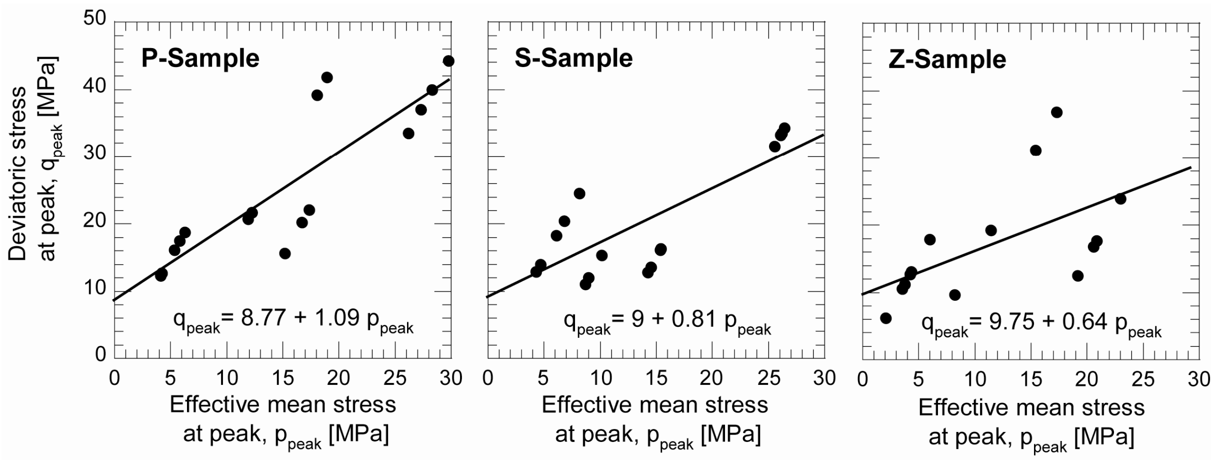

Figure F.8: Ultimate strength of the Opalinus clay (peak value) observed on the compiled triaxial tests. Results have been distinguished according to the direction of loading. Linear interpolations between obtained points have been drawn.

	c_{p-q}^{peak} [MPa]	M_{peak} [-]	c^{peak} [MPa]	ϕ^{peak} [-]
P-sample	8.77	1.09	4.17	27.4
S-sample	9	0.81	4.24	20.9
Z-sample	9.75	0.64	4.6	16.8

Table F.2: Characteristics of the line defining the peak strength of Opalinus clay, in the (p-q) plane (c_{p-q}^{peak} and M_{peak}) and in the Mohr-Coulomb plane (c^{peak} and ϕ^{peak}).

The oedometric curve obtained by Chiffoleau and Robinet (1999) in Figure F.5 enables to deduce the compressibility indices of Opalinus clay: the compression index λ=0.033 and the swelling index κ=0.0049. It implies β=43.2 (the plastic compressibility). Also the preconsolidation pressure p_c' can be evaluated to 13 MPa which is lower than the value often assigned to Opalinus clay around the Mont-Terri tunnel (15-20 MPa).

Finally, the direct shear tests reported in Figure F.6 permit to represent the line of peak and residual shear stress of the open joints with respect to their normal stress (Figure F.9). It can be observed that higher the normal stress, higher the difference between peak and residual strength. At low normal stress, the peak and residual strength are similar. In other words, it means that the cohesions at peak (c^{peak}) and at residual (c) states are similar while the friction angle at peak (ϕ^{peak}) is higher than the one at residual state (ϕ).

Table F.3 summarizes the cohesion and friction angle at both peak and residual states deduced from the compiled direct shear tests.

State	Cohesion [MPa]	Friction angle [°]
Peak	0.369	39
Residual	0.397	26.7

Table F.3: Cohesion and friction angle at the peak and residual states deduced from the direct shear tests on open joints of Opalinus clay.

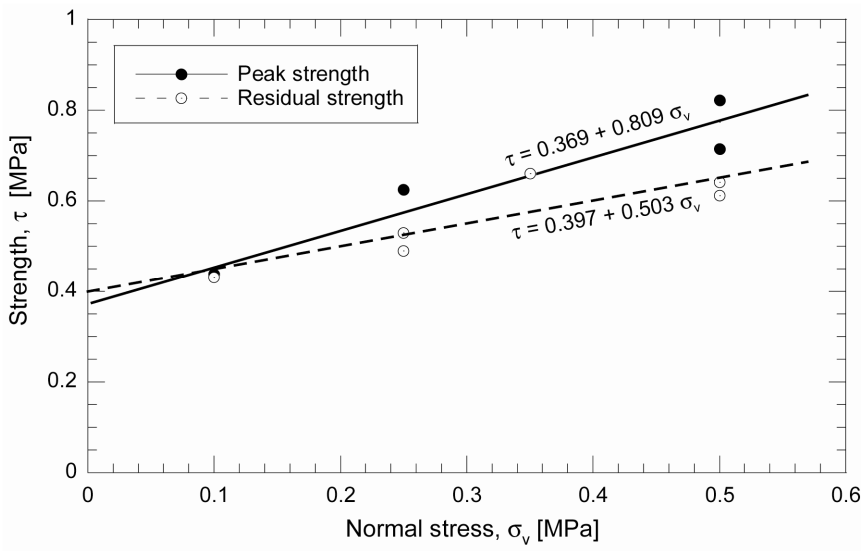

Figure F.9: Peak and residual shear strengths with respect to the normal stress deduced from the direct shear tests on open joints reported in Figure F.6.

F.5 Benchmark exercise

The oedometric compression tests and the uniaxial and triaxial tests have been simulated using the ACMEG model. The material parameters were determined based on the interpretation of the experimental results presented in the previous section. Due to the lack of accuracy in the volumetric plane, the Poison ratio is difficult to assess. It has been assumed equal to 0.15. The Young modulus was assumed affected by the loading direction and by the stress level, as observed in Equation (F.1).

Isotropic plastic parameters have been established from the oedometric compression tests. Those parameters are assumed independent of the loading direction. However, additional oedometric tests in different loading directions should be useful to confirm this point.

The deviatoric plastic parameters b, d, α and r_{dev}^{ela} where calibrated using the triaxial tests at 5 MPa of confining pressure in the 3 loading directions (P-sample, S-sample and Z-sample). The α parameter characterizes the post-peak behaviour. In such a brittle material, the specimen often fails after the peak which makes difficult to represent this post-peak behaviour with a constitutive model based on the assumptions of homogeneous specimen. So, α was fixed equal to 1, by default. Finally, the friction angles were determined using experimental interpretation in Table F.2. The ACMEG model does not consider cohesion. So, ϕ' is an equivalent friction angle assuming that the critical state line starts from origin in the ($p' - q$) plane. As observed in the experiment interpretation, the friction angle is affected by the loading direction. The set of material parameters used in the simulation with the ACMEG model is reported in Table F.4.

Figure F.10 reports the comparison of experimental results and numerical simulation of the oedometric compression test. The preconsolidation pressure of 13 MPa seems in good agreement with the experiments. However, the transition between elastic part (governed by the elastic modulus) and the elasto-plastic part (governed by the plastic compressibility) is more progressive in experiment than in the numerical simulation.

Elastic parameters			P-sample	S-sample	Z-sample
K_{ref}	[MPa]	Bulk modulus at a reference mean effective pressure p'_{ref} (=1MPa)	1515	590	1000
G_{ref}	[MPa]	Shear modulus at a reference mean effective pressure p'_{ref} (=1MPa)	1250	490	825
n	[-]	The exponent of non-linear elasticity	0.158	0.5	0
Isotropic plastic parameters					
p'_{c0}	[MPa]	Initial preconsolidation pressure	13	13	13
β	[-]	Plastic compressibility modulus	43	43	43
r_{iso}^{ela}	[-]	Radius of the isotropic elastic domain	0.01	0.01	0.01
c	[-]	Control of the progressive plasticity inside the external isotropic yield limit	0.05	0.05	0.05
Deviatoric plastic parameters					
b	[-]	Control the shape of the deviatoric yield limit	1	1	1
d	[-]	Ratio between the Cam-Clay critical pressure and the preconsolidation pressure	1.3	1.3	1.3
ϕ'	[°]	Friction angle at critical state	33	26	23
α	[-]	Flow rule parameter	1	1	1
r_{dev}^{ela}	[-]	Radius of the deviatoric elastic domain	1	1	1

Table F.4: Material parameters of the Opalinus clay for the ACMEG model.

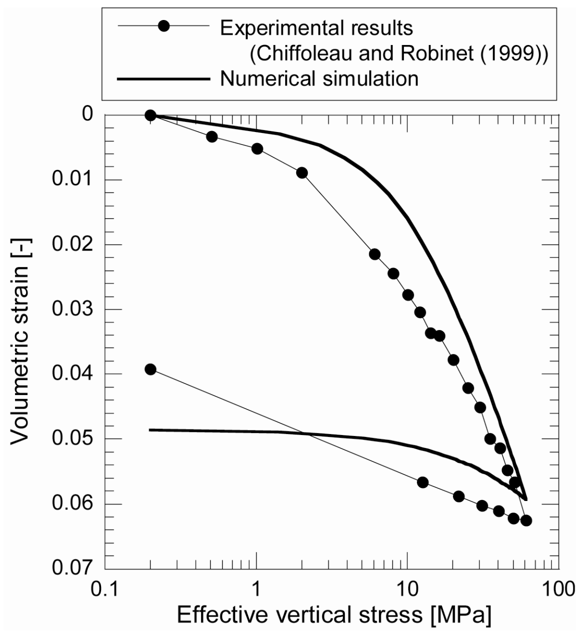

Figure F.10: Oedometric compression tests on Opalinus clay. Comparison between numerical simulation and experimental result.

Figure F.11 to Figure F.13 compare experimental results and numerical simulations of the uniaxial and triaxial compression tests in the three loading directions (P-sample, S-sample and Z-sample, respectively). Those results are expressed in the deviatoric (q versus ε_1) and volumetric (ε_v versus ε_1) planes. The anisotropic and non-linear elasticity seems to reproduce well the pre-peak response of Opalinus clay in the deviatoric plane. The peak strength, governed by the friction angle ϕ' and the parameters b and d, is quite well reproduced by the numerical simulations. However, in the volumetric plane, the results of simulation disagree with experimental observations. This may be due to the hypothesis of fully drained conditions assumed in the numerical simulations, while experimental conditions are partially undrained (due to the very low permeability of Opalinus clay).

F.6 Conclusions

The Opalinus clay is an indurated claystone exhibiting very low permeability, high rigidity, brittleness in its post-peak behaviour and mechanical anisotropy. All those characteristics makes difficult to carry out accurate experimental tests on this material. In particular, the hydro-mechanical conditions inside the specimen are delicate to control. Indeed, due to the very low permeability, fully drained conditions are often complicated to obtain within reasonable experimental deadlines.

A large quantity of available laboratory tests (uniaxial, triaxial and oedometric compressions tests, as well as direct shear tests) aiming to characterize the mechanical response of Opalinus clay has been analysed, interpreted in the light of elasto-plasticity and simulated using ACMEG model. In this context, the material parameters were deduced from the interpretation of the experimental results. Despite the ACMEG model has not been specifically developed for such stiff materials, the numerical simulations shows good agreement with experimental results. In particular, in uniaxial and triaxial tests, the pre-peak responses in the deviatoric plane as well as the peak strengths are well predicted by the model. On the contrary, the volumetric responses of the model disagree with experimental observations. It may be due to the hypothesis of fully drained conditions assumed in the numerical simulations while in experiment, conditions are partially undrained (due to the very low permeability of Opalinus clay).

As far as mechanical anisotropy is concerned, not only the elastic modulus but also the friction angles are affected by the loading directions. Therefore, the bedding orientation seems to govern the mechanical response of the material. The ACMEG model does not consider such anisotropy in the mechanical response. Nevertheless, this feature of behaviour has been considered by changing the K_{ref}, G_{ref}, n and ϕ' parameters according to the type of triaxial and uniaxial tests (P-, S- or Z-samples).

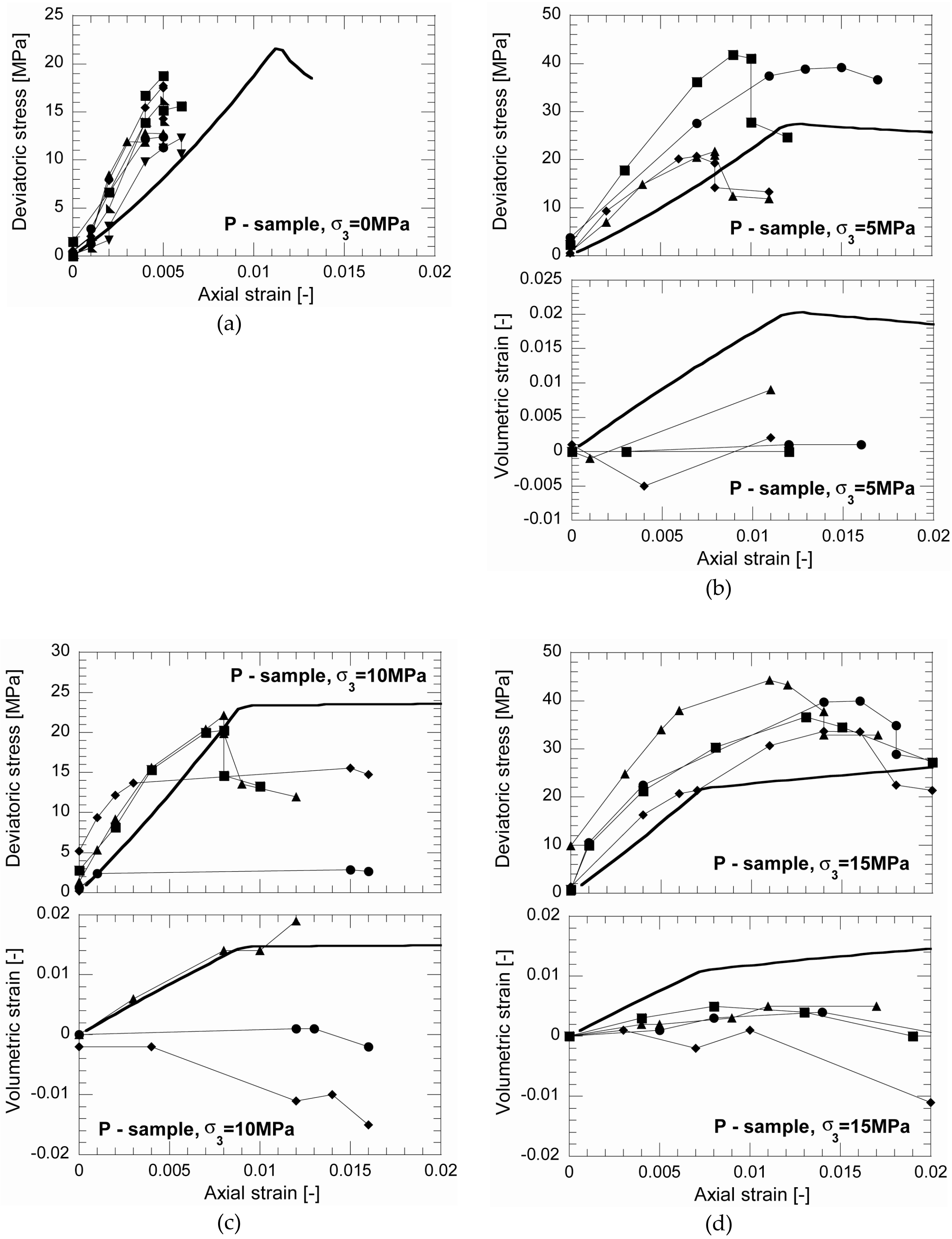

Figure F.11: Comparison between numerical simulations and experimental results of triaxial tests on Opalinus clay with the axial loading parallel to the bedding orientation (P-samples). The confining pressures are (a) 0 MPa; (b) 5 MPa; (c) 10 MPa; (d) 15 MPa.

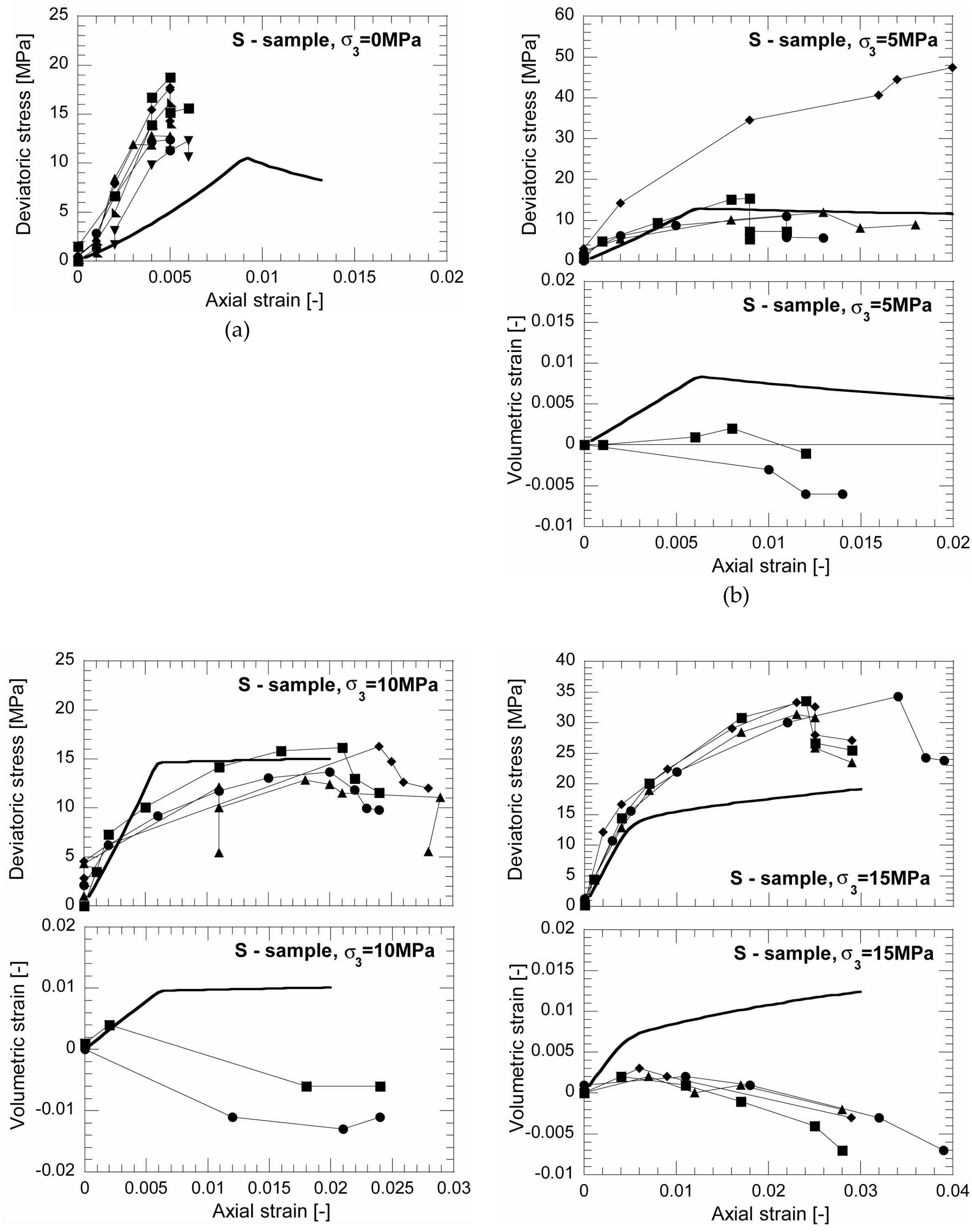

Figure F.12: Comparison between numerical simulations and experimental results of triaxial tests on Opalinus clay with the axial loading perpendicular to the bedding orientation (S-samples). The confining pressures are (a) 0 MPa; (b) 5 MPa; (c) 10 MPa; (d) 15 MPa.

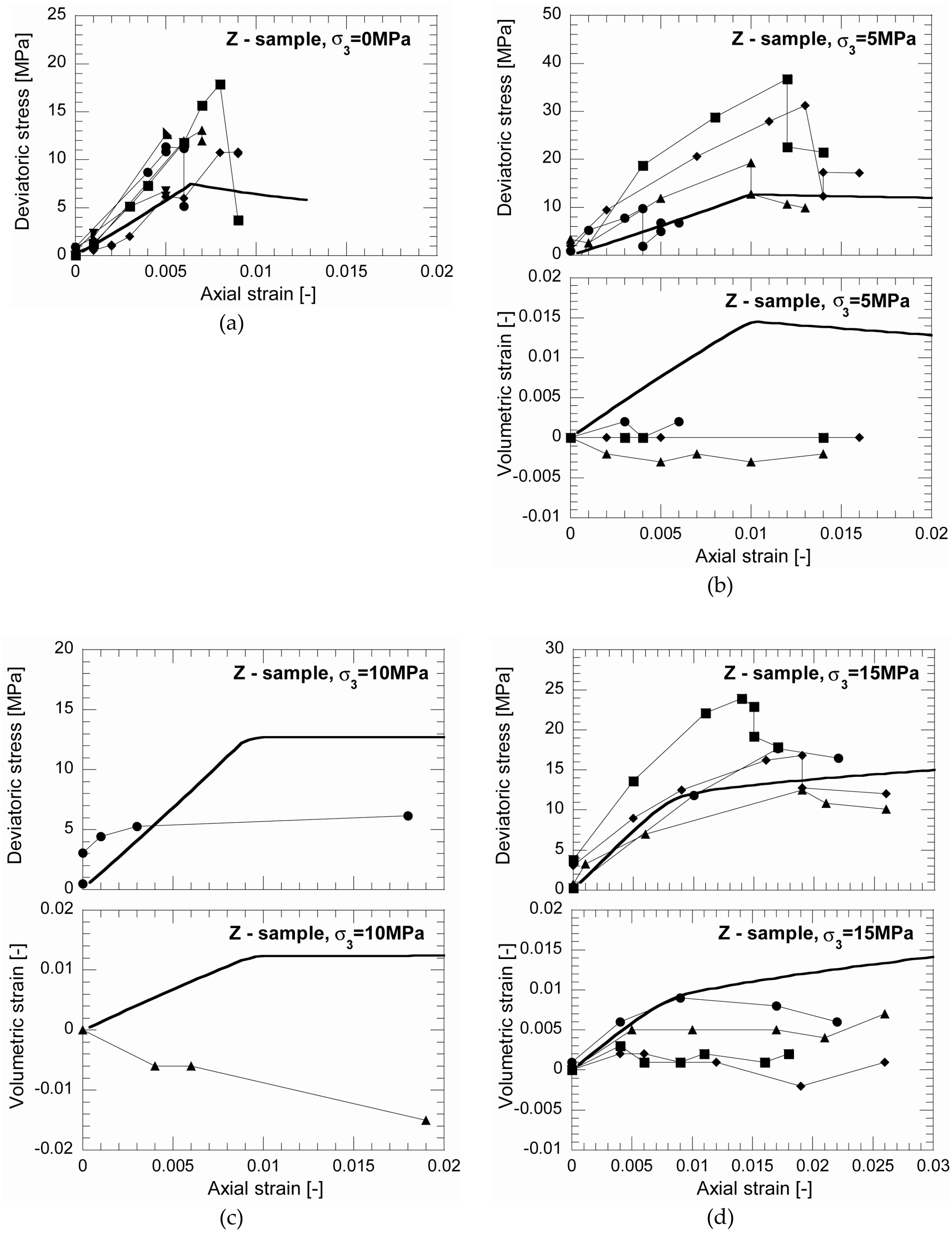

Figure F.13: Comparison between numerical simulations and experimental results of triaxial tests on Opalinus clay with the axial loading oriented at 45° with respect to the bedding orientation (Z-samples). The confining pressures are (a) 0 MPa; (b) 5 MPa; (c) 10 MPa; (d) 15 MPa.

F.7 References

Bossart P., Meier P.M., Moeri A., Trick T. and Mayor J.C. (2002). Geological and hydraulic characterisation of the excavation disturbed zone in the Opalinus clay of the Mont Terri Rock Laboratory. *Engineering Geology*, 66: 19-38.

Bock H. (2001). RA Experiment – Rock mechanics analyses and synthesis: Data report on rock mechanics. Mont Terri Project, Technical Report 2000-02.

Chiffoleau S. and Robinet J.C. (1999). HE Experiment: Determination of the hydromechanical characteristics of the Opalinus clay. Mont Terri Project, Technical Report 98-36.

Horseman S.T., Harrington J.F., Birchall D.J., Noy D.J. and Cuss R.J. (2006). Hydrogeologic analyses and synthesis (HA Experiment): Consolidation and rebound properties of Opalinus clay: A long-term, fully drained test. Mont Terri Project, Technical Report 2003-03 revised.

Gautschi L. (2001). Hydrogeology of a fractured shale (Opalinus clay): Implications for deep geological disposal of radioactive wastes. *Hydrogeology Journal*, 9 (1): 97-107.

Marschall P., Horseman S. and Gimmi T. (2005). Characterisation of gas transport properties of the Opalinus clay, a potential host rock formation for radioactive waste disposal. *Oil and Gas Science and Technology. Revue de l'Institut Français du Pétrole*, 60 (1): 121-139.

Olalla C., Martin M.E. and Sáez J. (1999). ED-B Experiment: Geotechnical laboratory tests on Opalinus clay rock samples. Mont Terri Project, Technical Report 98-57.

Thury M. and Bossart P. (1999). The Mont Terri rock laboratory, a new international research project in a Mesozoic shale formation, in Switzerland. *Engineering Geology*, 52: 347-359.

Curriculum Vitae

BERTRAND FRANÇOIS

Chemin du Furet, 8
1018 Lausanne, Switzerland
Phone (Mobile): +41 (0)76.307.50.21
e-mail : bertrand.francois@epfl.ch
webpage: http://people.epfl.ch/bertrand.francois

PERSONAL INFORMATION

Marital status :	Single
Country of citizenship :	Belgium
Date of birth :	3 november 1981
Place of birth :	Charleroi (Belgium)

EDUCATION

2005-now : **PhD thesis** : "Thermo-plasticity of fine-grained soils at varaious saturation states: Application to nuclear waste disposal"
Ecole Polytechnique Fédérale de Lausanne (EPFL) - Soil Mechanics Laboratory (LMS)
Under the supervision of Prof. L. Laloui

2004 : **Civil Engineer diploma**
Université de Liège (Ulg)

2004 : **Master thesis** : "Numerical modelling of the hydro-mechanical behaviour of Triesenberg's landslide (Liechtenstein)"
Ecole Polytechnique Fédérale de Lausanne (EPFL)

1999-2004 : **Bachelor and Master studies** : Civil Engineering
Université de Liège (Ulg)

PROFESSIONAL EXPERIENCE

2005-now : **Teaching assistant**
Ecole Polytechnique Fédérale de Lausanne (EPFL) - Soil Mechanics Laboratory (LMS)

"Soil Mechanics" - Civil Engineering - Teacher: Prof. L. Vulliet
"Geotechnics and Foundations" - Environmental Engineering - Teacher: Dr. M. Gencer
"Underground Seepage" - Civil Engineering - Teacher: Prof. L. Laloui

2004 : **Research and teaching assistant**
Ecole Polytechnique Fédérale de Lausanne (EPFL) - Soil Mechanics Laboratory (LMS)

SKILLS

Languages : **French**
Mother tong
English
Fair written and oral, fluent in academic writing
Dutch
Basic notions written and oral

Computers : **Classical software**
Word, Excel, PowerPoint, Illustrator, Photoshop,…
Finite element code dedicated to soil mechanics
Z_SOIL, Lagamine
Programming
FORTRAN

Additional skills :Laboratory experiments in Soil Mechanics

SCIENTIFIC PUBLICATIONS

Journals :

Laloui L., Cekerevac C., **François B.** (2005) Constitutive modelling of the thermo-plastic behaviour of soils. *Revue Européenne de Génie Civil* 9, 5-6, pp.635-650.

François B., Tacher L., Bonnard C., Laloui L., Triguero V. (2007) Numerical modelling of the hydrogeological and geomechanical behaviour of a large slope movement: The Triesenberg landslide (Liechtenstein). *Canadian Geotechnical Journal* 44(7) - pp. 840-857.

François B., Laloui L. (2008) ACMEG-TS: A constitutive model for unsaturated soils under non-isothermal conditions. *International Journal for Numerical and Analytical Methods in Geomechanics,* 32, pp 1955-1988.

Sanavia L., **François B.**, Bortolotto R., Luison L., Laloui L. (2008) Finite element modelling of thermo-elasto-plastic water saturated porous materials. *Journal of Theoretical and Applied Mechanics,* 38, 1-2, pp 7-34.

Salager S., **François B.**, El Youssoufi M.S., Laloui L., Saix C. (2008) Experimental investigations on temperature and suction effects on compressibility and pre-consolidation pressure of a sandy silt. *Soils and Foundations* 48(4), pp. 453-466.

Laloui L., **François B.** (2008) ACMEG-T: A soil thermo-plasticity model. *Journal of Engineering Mechanics.* (Accepted).

François B., Laloui L., Laurent C. (2008) Thermo-hydro-mechanical interpretation of the response of Boom clay undergoing in-situ thermal loading. *Computers and Geotechnics.* (Accepted).

Hueckel T., **François B.**, Laloui L. (2008). Explaining thermal failure in saturated clays. *Géotechnique.* (Accepted).

Chapter of books :

François B., Bonnard Ch., Laloui L., Triguero V. (2006) Numerical modeling of the hydro-mechanical behaviour of a large slope movement: the Triesenberg landslide. *In: Numerics in geotechnics and structures, Eds. T. Zimmermann & A. Truty, Elmepress Int.*, pp. 81-102.

Master thesis :

François B. (2004) Modélisation numérique du comportement hydro-mécanique de la zone instable du versant de Triesenberg (Liechtenstein). *Master Thesis, EPFL, Lausanne.*

Conference proceedings :

François B., Laloui L.* (2007) A stress-strain framework for modelling the behaviour of unsaturated soils under non-isothermal conditions. *Springer Proceedings in Physics 113, Theoretical and Numerical Unsaturated Soils Mechanics,* pp. 119-126

François B.*, Salager S., El Youssoufi M. S., Ubals Picanyol D., Laloui L., Saix C. (2007) Compression Tests on a Sandy Silt at Different Suction and Temperature Levels. *ASCE Geotechnical Special Publication 157.*

François B., Nuth M.*, Laloui L. (2007) Mechanical constitutive framework for thermal effects on unsaturated soils. *Proceeding of the 10th Int. Symp. on Numerical Models in Geomechanics, NUMOG X, Rhodes, Greece,* pp. 9-13.

François B., Laloui L. (2007) A fully coupled thermo-mechanical model for unsaturated soil. *2nd International Conference on Porous Media and its Applications in Science, Engineering and Industry, Hawaai.*

François B.*, Laloui L. (2008) Unsaturated soils under non-isothermal conditions: Framework of a new constitutive model. *GeoCongress08, New Orleans, USA.*

François B.* (2008) Un modèle de comportement thermo-plastique pour les sols-non-saturés: Application aux stockages de déchets nucléaires. *26eme Rencontres Universitaires de Génie Civil, Prix René Houpert, Nancy.*

Laloui L.*, **François B.**, Nuth M., Peron H., Koliji A. (2008) A thermo-hydro-mechanical stress-strain framework for modelling the performance of clay barriers in deep geological repositories for radioactive waste. *1st European Conf. on Unsaturated Soils, Durham, United Kingdom*, pp 63-80.

François B.*, Laloui L. (2008) ACMEG-TS: A unified elasto-plastic constitutive model to simulate coupled processes in non-isothermal unsaturated soils. *1st European Conf. on Unsaturated Soils, Durham, United Kingdom*, pp. 539-545.

François B., Bonnard Ch., Laloui L.* (2008) Investigation of the geomechanical aspects of a large landslide by means of a finite-element method: a case study. *12^{th} IACMAG Conference. Goa, India,* pp. 4577-4585.

Laloui L.*, **François B.** (2008) Numerical simulation of an in-situ underground experiment for nuclear waste storage. *12^{th} IACMAG Conference. Goa, India,* pp. 2345-2355.

Extended abstracts and posters:

Laloui L.* and **François B.** (2006) A THM stress-strain framework for modelling the performance of argillaceous materials in deep repositories for radioactive waste. *Mont Terri, 10 years anniversary workshop, St-Ursanne, Switzerland.*

Laloui L. and **François B.** (2007) New insights in the thermomechanical modelling of soils. *International Conference on Thermo-Mechanical Modeling of Solids, Paris.*

François B., Nuth M., Laloui L. (2007) A constitutive approach to address the thermal and hydric impacts in the concept of deep radioactive waste repositories. *3rd international meeting on Clays and Natural and Engineered Barriers for Radioactive Waste Confinement, Lille, France.*

Luison L., **François B.***, Bortolotto R., Sanavia L., Laloui L. (2007) Finite element modelling of thermo-elasto-plastic water saturated porous materials. *18th ALERT Workshop, Poster Session, Aussois, France.*

Laloui L., **François B.*** (2008) Thermo-hydro-mechanical simulation of Atlas in situ large-scale test in Boom clay. *19th ALERT Workshop, Session Multiphysics of Multiphase Materials. Aussois, France.*